UNIVERSITÉ DE SHERBROOKE

Faculté de génie

Département de génie chimique et de génie biotechnologique

SYNTHÈSE FISCHER-TROPSCH À BASSE TEMPÉRATURE POUR LA PRODUCTION DE CARBURANTS SYNTHÉTIQUES SUR DES CATALYSEURS NANOMÉTRIQUES DE FER ET DE COBALT SUPPORTÉS PAR LE CARBONE

Thèse de doctorat

Spécialité: génie chimique

James ALUHA-LULIZI

B.Ed(Sc.)(Hons.)(KU); B.Tech(Bus.Admin.)(UNISA); M.Sc(Chem.), M.Eng(Chem.)(WITS).

Jury: Prof. Nicolas ABATZOGLOU (Université de Sherbrooke, QC – Directeur)
Prof. Nadi BRAIDY (Université de Sherbrooke, QC – Codirecteur)
Prof. Ajay DALAI (University of Saskatchewan, SK – Codirecteur)
Prof. François GITZHOFER (Université de Sherbrooke, QC – Rapporteur)
Prof. Ryan GOSSELIN (Université de Sherbrooke, QC)
Prof. Mehrab MEHRVAR (Ryerson University, ON)

Sherbrooke, (QC), CANADA Février 2017

UNIVERSITÉ DE SHERBROOKE

Faculty of Engineering

Department of Chemical Engineering and Biotechnological Engineering

LOW-TEMPERATURE FISCHER-TROPSCH SYNTHESIS FOR PRODUCTION OF SYNTHETIC FUELS USING NANOMETRIC CARBON-SUPPORTED IRON AND COBALT CATALYSTS

A thesis submitted for the degree of Doctor of Philosophy

in Chemical Engineering

by

James ALUHA-LULIZI

B.Ed(Sc.)(Hons.)(KU); B.Tech(Bus.Admin.)(UNISA); M.Sc(Chem.), M.Eng(Chem.)(WITS).

Jury: Prof. Nicolas ABATZOGLOU (Université de Sherbrooke, QC – Director)

Prof. Nadi BRAIDY (Université de Sherbrooke, QC – Co-director)

Prof. Ajay DALAI (University of Saskatchewan, SK – Co-director)

Prof. François GITZHOFER (Université de Sherbrooke, QC – Reporting)

Prof. Ryan GOSSELIN (Université de Sherbrooke, QC)

Prof. Mehrab MEHRVAR (Ryerson University, ON)

Sherbrooke, (QC), CANADA February 2017

Dedication

To my Parents, who took me to school,

Baba,

Joshua Lulizi Adamba,

for making great sacrifices and teaching me the value of integrity and hard work; and

Mama,

Terry Edaro née Aore,

who has faithfully and fervently prayed to God for my success over the years.

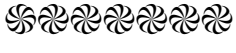

Résumé

Ce travail met en évidence le potentiel que la technologie des plasmas présente dans l'élaboration, en une seule étape, des catalyseurs de la synthèse Fischer-Tropsch (SFT), alors que les méthodes habituelles ou conventionnelles comme l'imprégnation et la précipitation sont des voies de production multi-étapes du matériau catalytique. Les nouveaux catalyseurs ont été mis en œuvre à partir d'espèces monométalliques ayant comme support le carbone (Fe/C, Co/C) pour développer des bimétalliques (Co-Fe), des ternaires (Mo-Co-Fe, Ni-Co-Fe) qui ont été ensuite formulés avec la présence de promoteurs (Au/Ni-Co-Fe). Du fait que la préparation par plasma thermique de ces catalyseurs nanométriques supportés par le carbone soit relativement récente, cela permet d'envisager des perspectives d'applications avec des retombées industrielles, car les hautes températures caractéristiques des plasmas permettent de générer des carbures de fer (Fe_3C, Fe_5C_2) très importants dans le processus catalytique de SFT. Des efforts de quantification de toutes les phases de carbures ont été effectués à l'aide de la diffraction des rayons X (DRX), tandis que l'analyse quantitative à l'aide du Rietveld (AQR) n'a été que partiellement concluante à cause de la taille nanométrique des matériaux étudiés qui est en dessous des limites de détection instrumental.

Avec des aires spécifiques de BET comprises entre 35 et 93 $m^2.g^{-1}$, les catalyseurs sont typiques de matériaux poreux et présentent ainsi un avantage pour la SFT car les transformations réactionnelles ne sont pas limitées par les phénomènes de transfert de masse. La microscopie électronique à transmission (MET) et la microscopie électronique à balayage (MEB) couplées avec la Spectroscopie à rayons X à dispersion d'énergie (EDX) et la cartographie des rayons X (cartographie X) ont montré une grande dispersion des particules métalliques dans la matrice de carbone, indiquant ainsi l'absence d'agglomération sur les échantillons frais et post réactionnels. Les caractérisations par la spectroscopie Raman et la Spectroscopie photoélectronique par rayon X (XPS) ont mis en évidence un support de catalyseur essentiellement graphitique. Les analyses par la spectroscopie d'absorption des rayons X (SAX), par la spectroscopie de structure près du front d'absorption des rayons X (XANES) ont confirmé que le catalyseur Co/C obtenu par plasma contenait des carbures (Co_3C) qui n'ont pu être révélés par XPS.

Le test catalytique initial a été effectué en réacteur à lit fixe à 503 K (230°C), sous une pression de 3 MPa avec une vitesse volumique spatiale (VVH) de 6 000 $cm^3.h^{-1}.g^{-1}$, pour une durée de 24 heures. Par la suite, les tests ont été performés dans un réacteur triphasique agité continu (3-φ-CSTSR) opérant de façon isotherme pendant 24 heures à des températures de 493–533 K (220–260°C), sous 2 MPa et à VVH = 3 600 $cm^3.h^{-1}.g^{-1}$. Tous les catalyseurs étudiés ont été actifs pour la SFT, produisant des fractions de gasoline (essence) et de diesel mais avec des sélectivités qui dépendaient de la proportion de métal présent dans le catalyseur et des conditions réactionnelles.

À 493 K, le catalyseur le plus actif a été Co/C, obtenu par plasma, avec 40% de conversion qui contraste avec les 32% du meilleur catalyseur commercial Fe/C. Ces performances ont été comparées avec celles d'autres catalyseurs synthétisés par plasma Fe/C (25% de conversion) et 80%Co-20%Fe/C (10%), tandis que 50%Co-50%Fe/C, 30%Co-70%Fe/C n'ont montré aucune activité. Le catalyseur Co/C a été aussi le plus sélectif pour la formation de gasoline; mais à 533 K il a généré des quantités excessives de CH_4 (46%) et CO_2 (19%); ce qui a conduit à l'idée de synthétiser des bimétalliques Co-Fe/C qui ont permis d'abaisser la sélectivité en CH_4 ou CO_2 en dessous de 10%, pour une conversion de CO dépassant 40%. De même, les catalyseurs contenant du Ni (Ni-Co-Fe/C) ont été plus actifs avec des conversions de CO dépassant 50% avec des sélectivités en gasoline (38%) plus élevées qu'en diesel (20%). Ce catalyseur bimétallique a aussi favorisé la formation importante de CH_4 (23%) et de CO_2 (14%) beaucoup plus que dans le cas du solide Co-Fe/C.

Globalement, le catalyseur bimétallique Co-Fe et sa variante acidifiée (exemple Mo-Co-Fe) ont été plus sélectifs en diesel (~ 55%). L'influence du prétraitement a été examinée et, selon la composition des catalyseurs, ceux qui ont été initialement réduits par CO avaient montré une amélioration de la sélectivité en diesel (50–67%); ces performances se sont avérées meilleures par rapport à celles des solides initialement réduits par H_2 (45–55%). En outre, les catalyseurs aux concentrations élevées en cobalt, ainsi que ceux prétraités sous hydrogène ont généré plus d'eau que ceux prétraités ou réduits par CO.

La présence d'atomes d'or comme promoteur dans le catalyseur Ni-Co-Fe/C (Au/Ni-Co-Fe/C) a non seulement ralenti l'activité de Ni-Co-Fe/C, mais aussi a diminué sa capacité à former l'eau, bien que n'ayant eu aucun impact significatif sur la sélectivité en composés hydrocarbonés.

Mots clés:

Technologie de synthèse de nanomatériaux par plasma inductif, synthèse de Fischer-Tropsch, catalyseurs supportés par le carbone

Abstract

This work reveals the potential plasma technology presents in producing highly active catalysts for Fischer-Tropsch synthesis (FTS), while simultaneously contracting catalyst production into a single step, which is a certain departure from the traditional multi-step methods such as impregnation or precipitation. Novel catalysts proposed were carbon-based, developed from single metal (Fe/C, Co/C) to bimetallic (Co-Fe), ternary (Mo-Co-Fe, Ni-Co-Fe) and then the promoted Au/Ni-Co-Fe formulations. Since the preparation of nanometric carbon-supported catalysts by plasma is a relatively new phenomenon, it offers the Fischer-Tropsch catalysis prospects of future commercial applications, because of the high temperatures that are achieved in plasma create Fe carbides (Fe_3C, Fe_5C_2), which are assumed to account for Fe-based FTS catalysis. An attempt to fully quantify the carbide phases in the samples by X-ray diffraction (XRD) and Rietveld Quantitative Analysis (RQA) was only partially successful due to the nanometric nature of the materials existing below the instrument's detection limits.

With BET specific surface areas of 35–93 $m^2.g^{-1}$, the catalysts were found to be non-porous, a characteristic that is advantageous because Fischer-Tropsch reaction would operate away from mass transfer limitations. Transmission Electron Microscopy (TEM) and Scanning Electron Microscopy (SEM) coupled with Energy Dispersive X-ray Spectroscopy (EDX) and X-ray mapping indicated high dispersion of the metal moieties in the carbon matrix, with no signs of nanoparticle agglomeration both in the fresh and used samples. Raman and X-ray Photoelectron Spectroscopy (XPS) characterized the support as highly graphitic, mixed with amorphous carbon arising from substantial defects in the graphite. Evidence from X-ray Absorption Spectroscopy (XAS) using X-ray Absorption Near Edge Structure (XANES) analysis confirmed that plasma synthesized Co/C catalyst contained some carbides (Co_3C), which went undetected by XPS.

Initial catalyst testing was performed in the fixed-bed reactor at 503 K (230°C), 3 MPa pressure, and gas hourly space velocity (GHSV) of 6 000 $cm^3.h^{-1}.g^{-1}$ of catalyst for 24 h. Elaborate tests were further executed in a 3-phase continuously stirred-tank slurry reactor (3-φ-CSTSR) isothermally operated between 493–533 K (220–260°C) at 2 MPa

pressure, and GHSV = 3 600 $cm^3.h^{-1}.g^{-1}$ of catalyst, for 24 h. It was observed that all catalysts were active for FTS, producing both gasoline and diesel fractions, but selectivity depended on the amount of metal in the catalyst or the reaction conditions.

The most active catalyst at 493 K was the plasma-synthesized Co/C that showed 40% CO conversion, which was benchmarked against the commercial Fe/C at 32%. This performance was compared to the plasma-synthesized Fe/C (25% CO conversion) and 80%Co-20%Fe/C (10% CO conversion), while both the 50%Co-50%Fe/C and 30%Co-70%Fe/C were inactive. The plasma-synthesized Co/C was also more selective towards the gasoline fraction, but at 533 K it generated excessive CH_4 (46%) and CO_2 (19%) prompting the development of the Co-Fe/C bimetallics, which exhibited less than 10% selectivity towards CH_4 or CO_2 at over 40% CO conversion. Similarly, Ni-containing catalysts (Ni-Co-Fe/C) were relatively more active than the bimetallics, exhibiting over 50% CO conversion with higher selectivity towards the gasoline fraction (38%) than towards diesel (20%). The Ni-Co-Fe/C catalysts also produced excessive CH_4 (23%) and CO_2 (14%), than the Co-Fe/C bimetallics.

Overall, the Co-Fe bimetallics and the acidified Co-Fe catalyst (i.e. Mo-Co-Fe/C) were more selective towards diesel formation (~55%). When the effect of pre-treatment medium was investigated, depending on catalyst composition, the CO-reduced catalysts showed enhanced selectivity for diesel fraction (50–67%) than catalysts reduced in H_2 (45–55%). In addition, it was observed that catalysts containing high concentration of Co as well as those reduced in H_2 generated more H_2O than those reduced in CO, and the presence of Au (that is, in Ni-Co-Fe/C) not only depressed the Ni-Co-Fe/C catalyst activity, but it also lowered its capacity to form H_2O, although it had no significant impact on the catalyst's hydrocarbon selectivity.

Keywords:

Induction Plasma Synthesis Technology of Nanomaterials, Fischer-Tropsch Synthesis, Carbon-Supported Catalysts

Acknowledgements

1. This project work was conducted under the auspices of the ***Canadian BioFuelNet NCE*** (National Centre of Excellence), and I thank them for their generosity in financial support and the opportunities they accorded me to expand my professional network through conferences and other fora.

2. I am greatly indebted to my supervisors **Prof. Nicolas Abatzoglou** and **Prof. Nadi Braidy** (***Université de Sherbrooke***), for their constant availability, expertise and proficiency in guiding me.

3. I wish to immensely appreciate **Prof. Ajay Dalai** (***University of Saskatchewan***) my supervisor, with whom I had an effective collaboration, and together with the help of my PhD compatriot, **Mr. Philip Boahene** who gave me a jumpstart when I successfully tested my catalysts in the 2-phase fixed-bed reactor.

4. My special appreciation goes to **Prof. Yongfeng Hu** (***Canadian Light Source, CLS)*** in Saskatoon for excellent reception and generously providing me with access to the Soft X-ray Microcharacterization Beamline (SXRMB) of the Synchrotron.

5. I confer special recognition to **Dr. Jasmin Blanchard**, **Ms. Carmina Reyes Plascencia, Mr. Henri Gauvin** and **Mr. Jacques Gagné** (***Université de Sherbrooke***),) for their friendship and technical expertise in the labs; **Ms. Aimee MacLennan** (***CLS Synchrotron***) for XANES analysis; all the personnel at the ***Centre de Caractérisation des Matériaux*** (***CCM, Université de Sherbrooke***) for expediting sample characterization: **Mrs. Irène Kelsey Lévesque** and **Mr. Carl St.-Louis** for BET surface area analysis, **Dr. Kim Doan Nguyen Thi** for Raman spectroscopy, **Mrs. Sonia Blais** for XPS and elemental analysis by carbon ignition, **Mr. Charles Bertrand** for Microscopy (SEM and TEM), and **Mr. Stéphane Gutierrez** for XRD analysis.

6. I am forever grateful to **Dr. Kossi Béré** and **Prof. François Gitzhofer** (***Université de Sherbrooke***) who, without reservation provided me with all the expertise and technical support I required to operate the Plasma equipment for catalyst synthesis.

7. Many blessings to my immediate family that has been my anchor in life: To my most gracious wife, **Mrs. Roselidah Anyango Aluha**, who has endured listening to my daily PhD progress reports, prepared warm nice meals and done everything to keep me sane for the last 3 years; to my sons, **Mr. Glenn Leitzy**, and **Master Daniel Balozi,** and my daughter **Miss Ruth Sindavi** for their indescribable cooperation, having created a peaceful environment at home for my studies, and seeing them every day has given me a sense of purpose in life.

Declaration

I, _____ declare that this thesis is my own, original and unaided work. It is being submitted for the degree of Doctor of Philosophy at the Université de Sherbrooke. It has not been submitted for any degree or examination in any other University.

_____

Signed

At Sherbrooke on 11-Nov-2016.

List of Symbols

α	Probability of the hydrocarbon-chain growth in FTS
$K\alpha$	Emission line when an electron transitions to the innermost "K" shell (principal quantum number 1)
φ	Phase (3-φ = 3 phase: gas, liquid, solid)
χ	as in χ-Fe_5C_2 = Hägg carbide
χ^2	Chi-square as a measure of a curve's goodness of fit
λ	Wavelength of the incident X-ray radiation in XRD analysis
$x\mu(E)$	Absorption coefficient in XAS analysis
π	Unsaturated carbon-carbon bonds
2θ	Angle on X-ray diffractogram

List of Acronyms

Symbols	**Description (Units)**
A_i	Relative area under peak for hydrocarbon with *i* carbon atoms (%)
Ar	Argon
ASAP	Accelerated Surface Area Porosimeter (Micromeritics Unit)
BCC	Body-centered cubic structure
B.E.	Binding Energy
BET	Brunauer-Emmett-Teller (expression used for surface area analysis)
BTL	Biomass-To-Liquid
C	Carbon
C_4–C_{12}	Gasoline fraction
C_{13}–C_{20}	Diesel fraction

C_{16}	*n*-Hexadecane
C_{21+}	High molecular hydrocarbons, such as waxes
CH_4	Methane
[—CH_2—]	Alkene monomer unit
C_nH_{2n+2}	Alkanes
CNF	Carbon Nano-Filaments
CNT	Carbon Nano-Tubes
Co or Co^o	Cobalt or metallic cobalt
CO	Carbon monoxide
CO_2	Carbon dioxide
Co/C	Cobalt catalyst supported on carbon
Co_2C, Co_3C	Cobalt carbides
CoO, Co_3O_4	Cobalt oxides: cobalt (II) oxide, cobalt (II).(III) oxide
CSTR	Slurry-Continuous Stirred Tank Reactor
CSTSR	Continuous Stirred-Tank Slurry Reactor
CTL	Coal-To-Liquid
df	Film thickness, of GC column (μm)
EDX	Energy Dispersive X-ray Spectroscopy
e.s.d	Estimated standard deviation
Fe or Fe^o	Iron or metallic iron
FCC	Face-centered cubic (crystal structure)
Fe/C	Iron catalyst supported on carbon
FeO, Fe_2O_3 Fe_3O_4	Iron oxides: Ferrous oxide, hematite and magnetite
Fe-NanoCat®	Commercial Fischer-Tropsch nano-hematite catalyst
FID	Flame-Ionization Detector
FTS	Fischer-Tropsch Synthesis

Fe_xC_y	Iron carbides: Fe_2C, Fe_3C, Fe_3C_7, Fe_5C_2 or Fe_7C_3	
GC	Gas Chromatography	
GHSV	Gas Hourly Space Velocity	$(ml.g_{cat}^{-1}.h^{-1})$
GOF	Goodness of fit: $(\chi^2) = (R_{wp}/R_{exp})^2$	
GTL	Gas-To-Liquid	
HCP	Hexagonal closed packing (crystal structure)	
He	Helium	
H_2	Hydrogen	
H_2O	Water	
ID	Inner Diameter, of GC column	(mm)
L	Length	(m)
LT-FTS	Low-Temperature Fischer-Tropsch Synthesis	
N_2	Nitrogen	
N2.5	Gas purity for CO; two nines = 99.5%	
N4.5	Gas purity for H_2 and Ar; four nines = 99.995%	
O_2	Oxygen	
P	Pressure	(kPa)
R_{exp}	Expected R or the "best possible R_{wp}" factor;	
RF	Radio-Frequency	(MHz)
$R_{profile}$	Minimized quantity during fitting procedures (by least-squares)	
RQA	Rietveld Quantitative Analysis	
R_{wp}	Weighted profile (R-factor): ratio of peak intensity to background	
P-XRD	Powder X-ray Diffraction	
S	Selectivity	(%)
SCCM	Standard cubic centimetres per minute	

SEM	Scanning Electron Microscopy
SLPM	Standard litres per minute
SPS	Suspension plasma-spray technology
T	Temperature (K)
TCD	Thermal Conductivity Detector
TG-DTA	Thermogravimetric – Differential Thermal Analysis
TEM	Transmission Electron Microscopy
TOS	Time-on-stream
TPR	Temperature Programed Reduction
WGS	Water-gas shift reaction
XANES	X-ray Absorption Near-Edge Structure
XAS	X-ray Absorption Spectroscopy
XPS	X-ray Photoelectron Spectroscopy
XRD	X-ray Diffraction
3φ-CSTSR	Three-Phase Continuously-Stirred Tank Slurry Reactor

TABLE OF CONTENTS

LIST OF FIGURES

LIST OF TABLES

1. INTRODUCTION

1.1. Background

Fischer-Tropsch catalysis was discovered by Franz Fischer and Hans Tropsch in the 1920's, and today the process has been commercially exploited to generate synthetic automobile fuels such as gasoline and diesel among other valuable hydrocarbon products (Khodakov *et al*., 2007). Since then, the Fischer-Tropsch synthesis (FTS) has been studied extensively (Dry, 2002), but not exhaustively; with four metals, namely cobalt, iron, nickel and ruthenium exhibiting great potential for industrial application (Dry, 1990).

In the entire scheme, the industrial FTS process converts a mixture of syngas (H_2 and CO) in a specified ratio to form polymeric chains of liquid hydrocarbons with a widespread distribution of products as represented by Equations (1.1) to (1.7) given in Table 1.1.

Table 1.1 Equations showing the complexity of FTS reaction

Target	Reaction	Designation
Alkanes	$(2n+1)\ H_2 + n\ CO \rightarrow C_nH_{2n+2} + n\ H_2O$	Eqn. (1.1)
Alkenes	$2n\ H_2 + n\ CO \rightarrow C_nH_{2n} + n\ H_2O$	Eqn. (1.2)
Water-gas shift	$H_2O + CO \rightarrow CO_2 + H_2$	Eqn. (1.3)
Methane	$3\ H_2 + CO \rightarrow CH_4 + H_2O$	Eqn. (1.4)
	$4\ H_2 + CO_2 \rightarrow CH_4 + 2\ H_2O$	Eqn. (1.5)
Alcohols	$2n\ H_2 + n\ CO \rightarrow C_nH_{(2n+1)}OH + (n-1)\ H_2O$	Eqn. (1.6)
	$(n+1)\ H_2 + (2n-1)\ CO \rightarrow C_nH_{(2n+1)}OH + (n-1)\ CO_2$	Eqn. (1.7)

Equation (1.1) indicates that hydrogen-rich feed-streams favour the production of alkanes, while hydrogen-poor feed-streams favour alkene production as given by Equation (1.2), and the water-gas shift (WGS) reaction given in Equation (1.3) can be a valuable source of CO or H_2 in the system depending on the prevailing reaction conditions (Khodakov, 2009).

Currently, FTS operates in two modes: the high-temperature process between 573–623 K (300–350°C) using Fe-based catalysts to produce gasoline and linear low molecular mass olefins, while the low-temperature process operates between 473–513 K (200–240°C), with either Fe or Co catalysts that produce high molecular mass linear waxes (Dry, 2002).

Since FTS is a versatile process, it has capacity to consume different feedstocks such as natural gas, coal or biomass, from which their respective names are attributed as gas-to-liquid (GTL), coal-to-liquid (CTL) and biomass-to-liquid (BTL) processes (de Klerk and Furimsky, 2011). The hydrocarbons thus produced are comparable to the conventional liquid fuels derived from crude oil when refined.

1.2. Problems associated with Fischer-Tropsch synthesis

1.2.1. Today's challenges in FTS

From the considerable amount of information currently in literature (Jacobs *et al*., 2013), the FTS chemical process may be considered a success story in the commercial production of synthetic fuels, although major challenges still exist. Areas that still have potential for further examination include issues related to reactor-choice, catalyst type and process chemistry, as summarised in Table 1.2.

Overarching concerns include the high costs in capital investment involved in commissioning the FTS plant and the need to improve heat and mass transfer efficiencies during operation. Critical to lowering the overall effectiveness of the FTS process, less complex, but effective catalyst synthesis approaches must be applied. This is in addition to addressing issues of catalyst longevity, regeneration and deactivation due to fouling, metal agglomeration, oxidation or poisoning and change of support properties such as loss of surface area due to pores collapsing. Moreover, during operation, depressing H_2O production as well as minimizing the selectivity towards CO_2 and CH_4 is vital.

Table 1.2 Summary of potential research areas in FTS catalysis

Property	Challenge	Ref.
Reactor-choice	**1**. Lowering the high capital costs for the FTS process	(Vosloo, 2001)
	2. Increasing thermal efficiency due to: (i) Energy losses from the plant, which escalates operational costs (ii) Inordinate temperature profiles in tube reactors	
Catalyst issues	**3**. Catalyst synthesis methods: create less complex, but effective approaches	(Zhang *et al*., 2009)
	4. Carburization: promotes Fe-based catalyst, but poisons Co catalyst	(Ding *et al*., 2009)
	5. Catalyst deactivation: due to (i) Coking	(Tsakoumis *et al*., 2010) (Pour *et al*., 2008)
	(ii) Sintering	(Dry, 2002)
	(iii) Metal re-oxidation in Fe-based catalysts (iv) Metal re-oxidation in Co-based catalysts	(Li *et al*., 2001) (van Berge *et al*., 2000), (van de Loosdrecht *et al*., 2007)
	(iv) Sulphur intolerance - sulphur poisoning as an irreversible process	(Chew and Bhatia, 2008) (Dry, 1990), (Vosloo, 2001)
	6. Catalyst regeneration	(Tavasoli *et al.*, 2008)
Process chemistry	**7**. Methane selectivity: minimizing CH_4 formation	(Schulz, 1999)
	8. Production of CO_2 (as an inert component in FTS)	(Riedel and Schaub, 2003)
	9. Presence of H_2O and its management: (i) WGS activity (ii) Effect of H_2O in FTS (iii) Removal of H_2O in FTS	(Li *et al*., 2002), (Hilmen *et al*., 1999) (Dry, 2002) (Dalai and Davis, 2008) (Rohde *et al*., 2008)

1.2.2. Research areas of interest

Current research interests centered on FTS catalysis can be divided into three general areas namely: catalyst synthesis, testing and characterization as summarized in Figure 1.1 for the convenience of our discussion in this work.

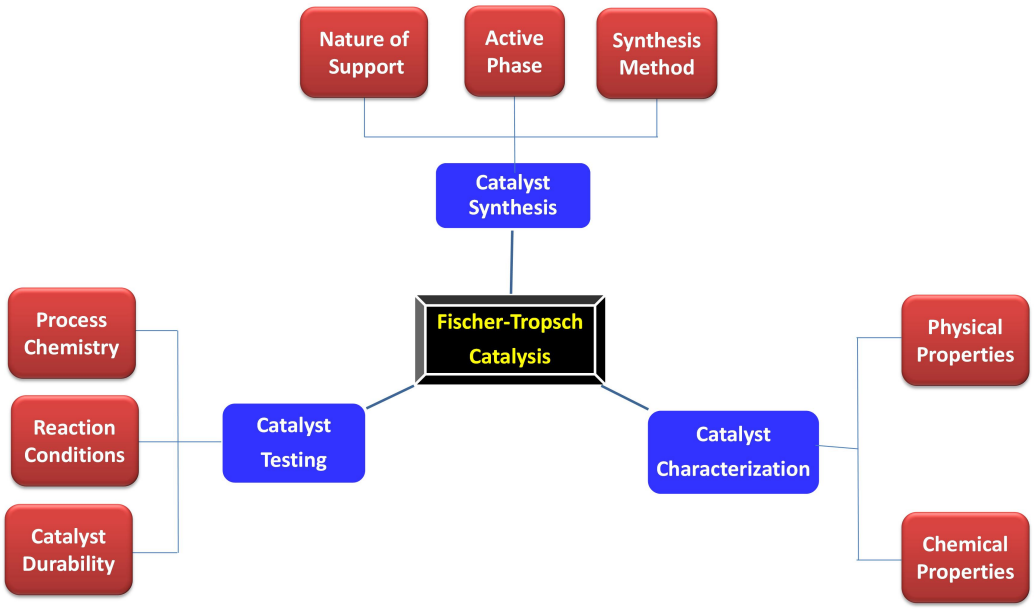

Figure 1.1 Summary chart of research design indicating key areas of FTS catalysis

Under catalyst synthesis, three aspects that impact FTS were considered, that is, the choice of catalyst synthesis method, the type of support used and the active metallic phase. Highlights in catalyst testing included how the test conditions influence the FTS product spectrum. In catalyst characterization, a number of analytical techniques were used to probe the physico-chemical properties of the catalytic materials in order to elucidate and relate the probable nature of the active species in FTS, and the operating conditions under which these species were generated.

Due to the numerous convoluted constraints (involving time, personnel, instrumentation, financial support, etc.), this project focussed only on a few aspects of advancing research on catalyst synthesis and FTS process chemistry. Figure 1.2 presents the complete dissection, with attention directed at the areas highlighted in green.

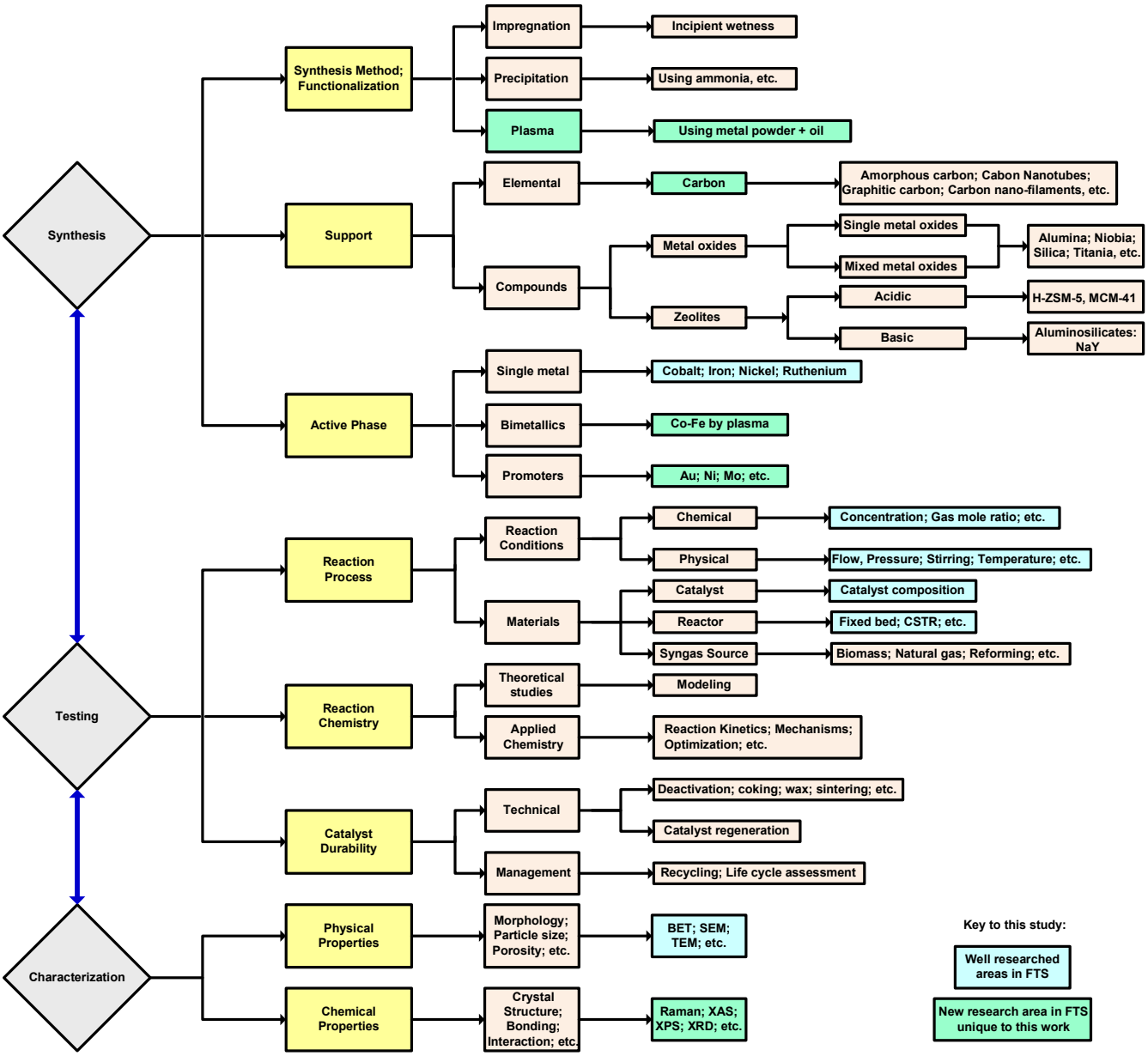

Figure 1.2 Global view of FTS catalysis

Under catalyst synthesis, plasma spray was the method of choice, generating the carbon support *in situ*. The catalysts' active phase was studied iteratively from single-metal formulations (Co/C or Fe/C) to Co-Fe bimetallics, which were then promoted using various other metals such as Au, Mo, and Ni. For commercial applications, attractive FTS catalysts must effectively suppress production of H_2O, CH_4 and CO_2 in addition to inhibiting metal re-oxidation. In catalyst testing, our reactor of choice was the 3-phase continuously-stirred tank slurry reactor (3-φ-CSTSR), although initial tests and validation of the results was conducted in the fixed-bed reactor.

One of the highlights on the reaction process chemistry was the influence of test conditions on the FTS product spectrum. Some reaction conditions were simulated to mimic a syngas composition with a biomass origin, construed to be richer in CO with a H_2:CO ratio < 2. A selection of analytical techniques was employed to characterize the catalysts for their physical and chemical properties with an intention of elucidating on how these properties could possibly influence the FTS reaction.

1.3. Objectives of this work

1.3.1. Previous research

For Co-based catalysts, it has been agreed almost unanimously that the FTS reaction occurs on the metallic species, and formation of the oxide is a source of catalyst deactivation (Jacobs *et al*., 2013). However, for the Fe-based catalysts, controversy still persists with some authors asserting that both magnetite and metallic Fe are active for FTS while the carbides are inactive. Yet another school of thought advances that WGS reaction occurs on magnetite sites, while FTS takes place on the carbide sites (Huyser *et al*., 2010; p.185). The authors state that the non-polar Fe-carbide surface could be responsible for the production of paraffins and olefins while the polar Fe-oxide surface could be responsible for light hydrocarbon production, olefins and oxygenates. For this reason, other authors claim that the non-stoichiometric Fe-oxide-carbide complex is the active phase (Herranz *et al*., 2006). Original findings published by this research group has demonstrated the benefit of plasma method in creating the Fe carbides, which are thought to be indispensable in FTS (Blanchard *et al*., 2010), although the reaction mechanism is not yet clear.

1.3.2. Current research

The principal objective of this work therefore, was to develop novel, yet highly active catalysts that might find commercial application in FTS. A choice catalyst should:

(a) Be nanometric and non-porous, exhibiting high external surface area, but with low porosity in order to eliminate diffusion and mass transfer limitations during FTS;
(b) Be supported by an inert material such as graphite (Bezemer *et al*., 2006), with a support that is yet to be commercialized giving it scope for industrial application;
(c) Contain active metallic Co nanoparticles or Fe carbides species (Li *et al*., 2001).

This study aimed to include a comparative assessment of different aspects of the FTS process, such as sample preparation methods, determining the properties and performance of the catalysts (Co-only, Fe-only, Co-Fe bimetallics and those promoted with Au, Ni and Mo) as measured by their catalytic activity and selectivity, especially with regard to the variant presence of metallic, carbidic and possibly oxidic species in the materials.

1.4. Originality of this work: gaps in Fischer-Tropsch research

Synthesis of carbon-supported catalysts for the FTS process using induction suspension plasma-spray (SPS) technology is a relatively new phenomenon (Blanchard *et al*., 2010). Plasma application shows potential for higher efficiency in contrast to conventional catalyst preparation methods, because it achieves shortened preparation time, attains uniform and highly distributed active species (Liu *et al*., 2002), and the materials exhibit superior performance (Rutkovskii *et al*., 2000).

The use of SPS application is unique to this research project, but so far only the Fe/C catalyst had successfully been synthesised. In this work, the focus was on three areas where little attention has been given:

(i) Synthesis of bimetallic (Co-Fe) catalysts using induction SPS technology,
(ii) The use of *in situ* produced carbon support in FTS catalysts, and
(iii) Catalyst characterization by Synchrotron light (XAS).

The successful production of the following FTS catalysts is therefore reported for the first time: the single metal Co/C formulation, the Co-Fe/C bimetallics, and the Ni-Co-Fe/C and Mo-Co-Fe/C ternary systems by plasma method, where one (Ni-Co-Fe/C) was promoted with Au, and this was in addition to the testing and characterization of such novel materials.

1.5. Hypotheses tested and the expected outcomes

Six hypotheses were tested in this study, ranging from synthesis method to catalyst composition and performance, thus:

(i) *Plasma method of catalyst synthesis*: Three methods of catalyst synthesis were used to test the efficiency of the catalysts in FTS, and it was postulated that materials synthesized by plasma technology were comparatively superior in performance (Rutkovskii *et al*., 2000) to other catalysts, with evenly distributed metal components in the support matrix (Liu *et al*., 2002), devoid of the metal nanoparticle agglomeration in the samples.

(ii) *Catalyst selectivity for diesel fraction production*: Since the alpha value (α) for Co lies in the range of 0.70–0.80 and Fe operates between 0.50–0.70 (Dry, 1982), plasma-synthesized catalysts targeting for a mean metal nanoparticle size of about 10 nm were expected to produce more of the diesel than the gasoline fraction because the smaller the particle, the higher the α-value (Khassin *et al*., 1998). Usually, high α-values at low temperature favour production of diesel and high molecular-mass hydrocarbons (e.g. waxes), with less of gasoline and low molecular-weight compounds.

(iii) *Choice of Co-Fe bimetallics*: In selecting the 3 bimetallic compositions, it was expected that the 50%Co-50%Fe and 30%Co-70%Fe formulations would comprise identical intermetallic phases, while the 80%Co-20%Fe sample would exhibit unique properties since its Co-Fe intermetallic phases are different, according to the Co-Fe binary-phase diagrams (Okamoto, 2008).

(iv) *Presence of nickel in Co-Fe bimetallics*: Since it has been reported that Ni could replace Re as a reduction and activity promoter in Co-based FTS catalyst (Rytter *et al*., 2010), in this study it was postulated that Ni addition to the Co-Fe/C bimetallic catalysts could boost production of the shorter hydrocarbon-chain molecules, because Ni promotes early molecular desorption by lowering its activation energy (Enger and Holmen, 2012).

(v) *Presence of gold*: It was proposed that incorporation of Au in the Ni-Co-Fe/C sample could keep Co in metallic form by decreasing its propensity for oxidation (Ahmad *et al*., 2013); while the synergistic effect of Au-Ni-Fe could enhance LT-WGS reaction that enriches the feed-gas with H_2, thereby improving FTS (Venugopal *et al*., 2003b).

(vi) *Presence of molybdenum*: It was advanced that catalyst synthesis of Mo-Co-Fe/C by plasma would create Mo-carbides, which are selective for olefin production (Vo and Adesina, 2011). Increased surface acidity by Mo-addition to Co-Fe/C bimetallic would augment the electron-withdrawing character in the catalyst and enhance production of the diesel fraction (Cooper *et al*., 2008).

2. LITERATURE REVIEW

2.1. FTS process chemistry

2.1.1. The FTS catalyst

Four metals (Co, Fe, Ni and Ru) display high activity for FTS, but only Co and Fe have commercially been exploited since they exhibit a considerable variation in the products depending on the reaction conditions. The Ru catalyst is the most active FTS catalyst, working at the lowest reaction temperature of only 423 K (150°C), and yielding products of high molecular weight, but it is expensive (Fechete *et al*., 2012). On the other hand, Ni forms nickel carbonyls at high pressure, and it produces mainly CH_4 at higher temperatures, a tendency that is less pronounced with Co or Ru (Schulz, 1999).

In tandem, much attention in literature has been given to cobalt (Eschemann *et al*., 2014), (Ma *et al*., 2011), and iron catalysts (Dry, 1990), (Lohitharn and Goodwin Jr., 2008). Additional studies of bimetallics to improve their catalytic performance have emerged and they include Fe-Cu (Pour *et al*., 2010b), Co-Mn (Morales *et al*., 2007), Fe-Mn (Tao *et al*., 2006), and Co-Fe (Lögdberg, 2007). For example, synthesis based on Fe^{2+} disproportionation in a highly basic medium leads to well crystallized metal-spinel composite material, $\left[Co^0_{\alpha}.Fe^0_{(1-\alpha)}\right]_{\gamma}.[Co_xFe_{3-x}O_4]$ having a direct effect on the catalyst reactivity, with 0.5 being the best ratio (Wang *et al*., 2003).

Furthermore, the promotional effect on Co and Fe catalysts has been reported using a myriad of elements that include among others, Au (Ahmad *et al*., 2013), Ba, Be, and Ca (Luo and Davis, 2003), Mg (Yang *et al*., 2006), and Pt (Chu *et al*., 2007). For example, increasing the basicity of a catalyst surface by addition of Ca, Mg or La influences the rate constant of the FTS reaction (Pour *et al*., 2010a), while K promotes selectivity for olefin production (Zhao *et al*., 2008), but restrains the formation of CH_4 and light hydrocarbons in Fe-Mn catalysts (Yang *et al*., 2004).

Since an effective Co catalyst must be in the metallic state, Au improves Co reducibility because it has been observed that the strong metal-support interaction in for example, Co/Al_2O_3 catalyst hinders Co reduction (Ahmad *et al*., 2013).

It is noted that the seamless transition in the application of single-metal catalysts to bimetallics and then to complex catalytic materials is an indication of the rapid technological advances that have been achieved in FTS research.

2.1.2. FTS catalyst performance

Three critical factors that determine the viability of commercializing a new FTS catalyst are the life, activity and product selectivity of the catalyst (Dry, 2002). Since Shell's fixed-bed reactor catalyst can last over 5 years, it implies that in today's commercial plant, the immediate issue may not be the catalyst's lifespan *per se* (Davis, 2007). Rather, selectivity remains the principle concern of any new catalyst employment in industry. It has been established that at low temperature, Co exhibits higher hydrogenation activity, while Fe is more versatile and may be manipulated to increasingly produce branched hydrocarbons, alkenes and oxygenates depending on reaction conditions and promoter effect. Selectivity towards the production of wax as a heavy FTS product has also been treated with sufficient interest (Pinna *et al*., 2003).

Ordinarily, promoters in Fe catalysts can vary its selectivity properties in a wide window, while selectivity-linked promoters in the Co catalyst have been limited to date, because they have an unfavourable effect on the catalytic activity (Davis, 2007). Since H_2O greatly impacts on the selectivity of CO to CH_4 in Co catalysts, promoter choice and process conditions are key to lowering CH_4 production (Yang *et al*., 2014). In some cases, raising the basicity of the catalyst surface can worsen the FTS reaction rate due to increased activation energy. For example, the activation energy of promoted Fe-catalysts using La, Mg and Ca was determined to be 70, 78 and 92 $kJ.mol^{-1}$, respectively (Pour *et al*., 2010a).

2.1.3. Characterization of the active catalyst phase

The nature and operation of the active species in the FTS catalysts has been of substantial interest to the researcher, and has been studied using many characterization techniques, including BET surface area, Microscopy (SEM/TEM coupled with EDX), XRD, TPR, XAS (XANES/EXAFS), and XPS, among others (Ernst *et al*., 1999). It has been observed that Co, Ni, and Ru remain in the metallic state under FTS conditions, but often the catalyst composition changes with time on stream (TOS).

To probe these changes, some *in situ* characterization techniques such as laser Raman spectroscopy, magnetic measurements and Mössbauer spectroscopy have provided significant real-time evidence of the active Fe species (Herranz *et al*., 2006). When subjected to FTS conditions, several phases were identified, including metallic Fe, oxides (Fe_2O_3, Fe_3O_4 and Fe_xO), and various different forms of carbides, Fe_xC (Bahgat, 2006).

Some studies on carbon-supported Fe catalysts for FTS have shown that partially reduced Fe oxide influences both catalyst activity and selectivity. Reduction of fresh Fe_3O_4 catalysts has led to the formation of a non-stoichiometric iron-oxide-carbide species, which is less stable, but more active and more selective towards olefin formation than the known χ-Fe_5C_2 carbide. This implies that total reduction of the catalyst to metallic state or pure Fe carbides is not beneficial to the FTS reaction (Bengoa *et al*., 2007).

The formation and composition of these Fe phases depend on the process conditions, catalyst deactivation and catalyst composition (Davis, 2009). Where the Fe carbide species were responsible for Fischer-Tropsch activity, oxidation of the Fe carbide to Fe oxide led to catalyst deactivation (Li *et al*., 2001). In order to improve on catalysts durability, some bimetallic Fe-Co/C alloys were prepared by mechanical alloying. Their nanostructure properties and the local ordering around Fe and Co atoms were examined using XRD and EXAFS (Yoo *et al*., 2006). Since catalyst-synthesis by plasma in this work was expected to generate various species of Co-Fe nano-alloys supported in a carbon matrix, such characterization techniques (SEM, EDX, TEM, XRD, XAS, XPS) at our disposal, which have been successfully used in other studies could be employed to determine the composition of the catalysts so-synthesized.

2.1.4. FTS reaction mechanism

Although there are many views on the possible mechanism of interactions between CO and H_2 leading to the formation of alkanes, alkenes or the production of oxygenates such as aldehydes and alcohols, today there appears to exist some convergence of opinion from old literature and recent findings in support of an oxygenate species as a more probable chain propagator (James *et al*., 2012).

Nevertheless, there is a rival mechanism to the "oxygenated monomer" one, with considerable evidence that validates its proposition. The "carbene-mechanism" has three possible routes: the alkyl, alkenyl and the alkylidene mechanisms. It has been advanced that the CO molecule dissociates upon adsorption on active FTS catalysts, a phenomenon that occurs even at low temperatures. The CO is first reduced to its elemental state and later converted to metal-CH_2 via metal-CH bonds (Thomas and Thomas, 1997; p.528).

This theory has been confirmed by the assertion that H_2 surface concentration is the key parameter in determining the reactivity of adsorbed CO, with various carbon pathways being suggested for either hydrocarbon-chain growth, or chain termination that leads to massive CH_4 formation. Indeed, it has recently been shown that the dominating CO activation pathway is via hydrogen-assisted CO dissociation (Yang *et al*., 2013).

2.2. FTS process engineering

2.2.1. Choice of FTS test reactor

Most FTS laboratory tests are either conducted in the continuous-flow fixed-bed reactor (Ali *et al*., 2011), or 3-φ-CSTSR (Hayakawa *et al*., 2006), but sometimes also in the Berty reactor, which intrinsically behaves like a CSTR (Botes and Böhringer, 2004). In industry reactors have high capital costs generally, and each type has its pros and cons. For example, the cost of a slurry reactor is 20–40% lower than the cost of a fixed-bed reactor with the same capacity (Khadzhiev and Krylova, 2011).

Lower catalyst loading in the slurry reactor decreases catalyst consumption per tonne of product. In addition, there is a greater possibility of on-line addition or removal of catalyst in the slurry reactor, allowing for longer reactor operations (Dry, 2002). Nevertheless, catalyst attrition is more rampant in the slurry reactor than in the fixed-bed reactor due to the vigorous stirring involved (Hou *et al*., 2008), and should any catalyst poison such as H_2S enter the reactor, all of the catalyst will be deactivated, whereas in a fixed-bed reactor all the H_2S would be adsorbed by the top layers of catalyst, leaving the balance of the catalyst bed unscathed (Dry, 2002).

FTS being highly exothermic, heat transfer considerations limit the maximum conversion per pass in fixed-bed processes, whereas the slurry bed is more isothermal and so can operate at higher average temperatures resulting in greater conversions (Fox, 1993). The main areas of energy loss in large plants include syngas generation and syngas conversion sections, condensation of H_2O produced during FTS and the inefficient recovery of energy from low-pressure steam (Vosloo, 2001).

The differential pressure across the slurry reactor is normally lower than in the fixed-bed reactor, which reduces gas compression costs. Other incidental costs are governed by plant capacity, quality of feedstock and nature of the FTS products, type of process technology applied, in addition to storage, handling facilities such as buildings, utilities and service facilities (Brennan, 1998).

2.2.2. FTS reaction conditions

Key factors that influence the FTS product spectrum include reaction temperature, pressure, choice of catalyst, and composition of feed-stream gases (Farias *et al*., 2008). Higher temperatures have been perceived to lower the average chain length of the product molecules and favour both the selective formation of CH_4 and the deposition of carbon, which leads to catalyst deactivation, especially with the Fe catalyst (Schulz, 1999).

Generally, higher pressure is desirable in terms of reactor sizing, but it also increases the CO conversion to FTS products since the reaction is accompanied by a reduction in volume (van Steen and Schulz, 1999), and for Fe catalysts, the rate of reaction increases with higher partial pressure of H_2 and lower partial pressure of H_2O (Pour *et al*., 2010a).

On the other hand, it has been observed that the Co catalyst gives higher conversions in comparison to the Fe catalyst with syngas mixtures originating from natural gas, which is richer in H_2 (ratio H_2:CO ≈ 2:1), besides giving higher selectivity towards the paraffins (Calderone *et al*., 2013).

Over a Co catalyst, approximately two H_2 molecules react with one molecule of CO to form one hydrocarbon unit [-CH_2-] and one H_2O molecule, see Equation (1.2). This (molar H_2:CO usage ratio) is normally taken as 2.1 and for the Co catalyst the required ratio is 2.15 or may be as low as 1.7 for the Fe catalyst in the low-temperature (LT-FTS). At higher temperatures, WGS given in Equation (1.3) rapidly goes into equilibrium to allow the CO_2 to convert to FTS products via the reverse-WGS reaction.

Theoretically, all of the H_2, CO and CO_2 can be converted to FT products if the syngas has a ratio of [H_2:(2CO+3CO_2)]≈1.05 (Dry, 2002). Since the Fe catalyst inherently performs the WGS reaction, it enriches the feedstock by generating additional H_2 gas back into the FTS reaction (Spath and Dayton, 2003). It has been observed that Au supported on Fe_2O_3 is an effective low-temperature (LT-WGS) reaction catalyst particularly when associated with FTS-active metals such as Ru (Venugopal *et al*., 2003a), or Ni although the Au-Co combination is relatively poorer at the LT-WGS reaction (Venugopal *et al*., 2003b).

2.3. Current developments in FTS catalysis

2.3.1. Application of biomass feedstock

In principle, syngas may be produced from any hydrocarbon feedstock (e.g. fossil fuel, natural gas, coal or biomass). However, the Co catalyst is usually preferred for syngas obtained from natural gas with the H_2:CO ratio ≥ 2 (Davis, 2007) because it is richer in H_2, but the Fe catalyst is preferred with syngas derived from coal (with H_2:CO = 0.5–1.0). Syngas feedstock of biomass origin (bio-syngas) has the H_2:CO ratio in the range between 0.6–1.1 (Hu *et al*., 2012). Today, due to the impact of greenhouse gases experienced from fossil fuels there is mounting interest in the application of bio-syngas in FTS because bio-syngas is a renewable source (Jahangiri *et al*., 2014).

Biomass is apparently one of the most abundant and cheapest renewable resources of hydrocarbons in nature, and for commercial production of gasoline or diesel, the lowest cost path would be the most favourable. Since Co catalysts are more sensitive to sulphur-poisoning than Fe catalysts, and given the relative higher cost of Co to Fe, more efficient removal of sulphur is expected for the FTS reaction than with the Fe catalysts, which are more sulphur tolerant (Chew and Bhatia, 2008). A bio-syngas feedstock will therefore involve minor costs in syngas clean-up, particularly from sulphur, whose presence only appears in minute quantities (Hu *et al*., 2012).

2.3.2. Carbon supported catalyst materials

The active catalyst phase, usually in metallic form may come unsupported (Gaube and Klein, 2008), or supported on pristine metal oxides like alumina (Visconti *et al*., 2009), silica (Escalona *et al*., 2009), titania (Zennaro *et al*., 2000), or zeolites (Kang *et al*., 2010). High activity and selectivity towards aromatic products in the FTS has been attributed to the strong acidity and the unique porosity found in the HZSM-5 zeolite (Jong and Cheng, 1995). The use of mixed metal-oxide supports such as SiO_2-TiO_2 (Jongsomjit *et al*., 2006), ZrO_2-Al_2O_3 or ZrO_2-SiO_2 (Jacobs *et al*., 2002) has also been reported.

On one hand, it has been observed that strong interaction between the metallic phase and the support may improve catalytic activity (Jacobs *et al*., 2002), but it may also be detrimental on the other hand due to the formation of irreducible metal-support compounds such as $CoAl_2O_4$ because CoO becomes chemically incorporated in the Al_2O_3 support (Jacobs *et al*., 2013). Moreover, pore size and acid properties can influence the metal-support interactions that may form well-defined phases such as cobalt silicate (Co_2SiO_4), aluminate ($CoAl_2O_4$), lanthanate ($LaCoO_3$) (Ernst *et al*., 1999), or titanate ($CoTiO_3$) (Voss *et al*., 2002).

Today, carbon supports are receiving substantial attention because of their inertness and capacity to be modified to produce diverse porous microstructures (Fu and Li, 2015). Since the active metal phase of the catalyst does not interact strongly with the carbon support, many authors have observed higher activity in carbon-supported catalysts than in those supported on metal oxides (Xiong *et al*., 2015).

Limited interaction of the metal with the support makes carbon attractive, and with growing significance because carbon exists in a variety of forms and morphologies, such as activated carbon (Ma *et al*., 2007), carbon nano-tubes (Chen *et al*., 2006), graphitic nano-fibres (Bezemer *et al*., 2006), carbon nano-filaments (Jankhah *et al*., 2008), carbon spheres with mean size 600 nm (Dlamini *et al*., 2015), carbon black, glassy carbon, ordered mesoporous carbon, and diamond (Xiong *et al*., 2015), graphene nano-sheets (Moussa *et al*., 2014), or reduced graphene oxide (Cheng *et al*., 2016). Graphene is a two-dimensional, one-atom thick layer of graphite, while graphite has multiple irregular layers of naturally formed graphene. Graphene oxidation results into an O-rich surface, whose reduction leads to reduced graphene oxide that can be used as a catalyst support.

Various preparation techniques have been employed to produce different types of carbon supports. For example, in industry carbon black is produced by the incomplete combustion of heavy petroleum products such as tar (Xiong *et al*., 2015). Carbon spheres can be synthesized by the hydrothermal treatment of sucrose solution (Dlamini *et al*., 2015), or by a chemical vapor deposition method (Xiong *et al*., 2011), while carbon nano-filaments have been produced by the dry-reforming of ethanol using CO_2 gas (Blanchard *et al*., 2008). Some authors have prepared carbon nanotubes using organogels (Chen *et al*., 2006), and others catalytically generated carbon nanofibers of the fishbone-type from syngas using a 5-wt% Ni/SiO_2 growth catalyst (Bezemer *et al*., 2006). Activated carbon may be produced by treating biomass (e.g. coconut shell) with phosphoric acid (H_3PO_4) at optimized conditions of activation temperature, time and reactant mass ratio (Gratuito *et al*., 2008). With enhanced mechanical support for metal particle anchorage, nano-carbon materials are now finding many applications in industry.

While activated carbon offers highly porous supports with enhanced BET specific surface area (often exceeding 10^3 $m^2.g^{-1}$), graphitic carbon in particular, provides good electrical and thermal conductivity properties through electron tunneling, and it exhibits high reactivity because of the unsaturated valences at the edges of its graphitic layers. Its surface area can be considerably enhanced by mechanical stretching or expansion along its crystallographic c-axis (Serp and Machado, 2015; p.6).

Different authors have effectively deposited the active metallic phase of the catalyst on the preformed carbon supports through various methods such as impregnation (Trépanier *et al*., 2009a), incipient-wetness impregnation (Ma *et al*., 2007), or deposition/precipitation using K_2CO_3 or urea (van Steen and Prinsloo, 2002). At other times the metallic phase and the carbon support could be simultaneously generated *in situ* by for example, the plasma-spray technology (Blanchard *et al*., 2010).

Since catalyst activity has been found to be directly related to both the stability of the metal nanoparticles in the active phase and the degree of reducibility of the metal species (Xiong *et al*., 2015), other factors perceived to enhance the performance of carbon-supported catalysts include higher metal loading and use of promoters (Trépanier *et al*., 2009a). Increasing the metal loading has been seen to improve both CO conversion and C_{5+} selectivity. However, where application of bimetallic formulations has been attempted, it was observed that the alloy with intermetallic ratio of Co:Fe = 1 was not a critical component in enhancing both the activity and selectivity of the carbon-supported catalyst, but rather a Co-rich combination being most significant, with a metal ratio close to Co_2Fe (Dlamini *et al*., 2015).

A Co-based catalyst promoted with Ru through impregnation method was perceived to enhance metal reducibility and dispersion, while simultaneously decreasing the average metal cluster sizes. It was observed that both Ru and K promote selectivity for higher molecular-weight hydrocarbons (Trépanier *et al*., 2009a). In addition, chemical activation of the carbon support in order to improve catalyst performance has been found to be very beneficial. For example, carbon nanotubes (CNTs) can be functionalized by acid treatment in order to increase the number of defect sites in the support's crystal structure. These defects are considered to be the anchoring positions for metal nanoparticles (Abbaslou *et al*., 2009), with the results indicating increased BET surface area, higher metal dispersion and lower mean particle size, in addition to better catalyst reducibility and FTS activity (Trépanier *et al*., 2009b).

2.3.3. Catalyst synthesis through plasma technology

Various techniques have been employed to prepare FTS catalysts, which include among others, impregnation (Voss *et al*., 2002), precipitation (Riedel and Schaub, 2003), co-precipitation (Cai *et al*., 2010), micro-emulsion method (Zamani, 2015), ion-exchange (Tang *et al*., 2003), carbon-vapour deposition (CVD) (Xiong *et al*., 2011), spray-drying technology (Zhao *et al*., 2008), and the rapid quenching of skeletal Fe of nano-crystalline dimensions to produce expanded lattice with low coordination number (Xu *et al*., 2014). Currently, interest in plasma technologies for application in FTS is on the rise (Blanchard *et al*., 2010), because of its proposed advantages that include superior catalyst performance (Rutkovskii *et al*., 2000), shortened preparation time, production of highly distributed active species, enhanced catalyst lifetime, and overall lower energy requirements, especially with cold plasma applications (Liu *et al*., 2002).

2.3.4. Nanotechnology: application of nano-catalytic materials

Since plasma technologies inherently produce nano-catalysts that may ultimately find use in FTS, such materials present numerous benefits and current trends in research indicate movement toward the widespread application of nanometric catalysts. For example, it has been noted that increasing the catalyst pellet size of a catalyst in FTS results in the reaction becoming more diffusion controlled than kinetically controlled and consequently, the amount of CH_4 produced increases (Davis, 2007).

Besides, it has also been shown that the rate of carbide formation depends on the average metal particle size. Additionally, Fe catalysts with smaller particles have been observed to be more resistant to oxidation by the CO_2 and H_2O produced during FTS (Raupp and Delgass, 1979). In Co-based FTS catalysts, selectivity has been seen to be considerably dependent on the metal particle size; and the smaller the particle, the higher the probability of producing longer-chain hydrocarbons (Khassin *et al*., 1998).

However, there is also low turnover frequency in smaller Co particles (< 7 nm) due to stronger CO adsorption (den Breejen *et al.*, 2009). Other authors concur that metal nanoparticles smaller than 6 nm lead to both poor activity and inferior selectivity towards the C_{5+} fractions (Bezemer *et al*., 2006). These studies bring to the fore the significant role nanometric materials will play in the future of FTS catalysis.

Moreover, catalyst reactivity has been linked to H_2 exposure because CO molecules dissociate more efficiently on the larger Co nanoparticles (15 nm) than on the smaller ones (4 nm), and higher exposure of Co nanoparticles to H_2 has been found to enhance CO dissociation rates (Tuxen *et al*., 2013). Therefore, higher H_2 concentrations favour chain termination and lead to production of shorter-chain hydrocarbons (Madon and Iglesia, 1993). It is then recommended that a choice FTS catalyst should have metal nanoparticles within a narrow range of about 6–8 nm (Bezemer *et al*., 2006). This assertion has been supported by kinetic studies indicating that the FCC structure of Co metal tends to favour the H-assisted CO dissociation mechanism (Liu *et al*., 2013).

3. EXPERIMENTAL DESIGN

3.1. Catalyst synthesis

3.1.1. Materials and reagents

Raw materials used in this research included: 99.8% Co metal (particle size: 1–10 μm), 99.95% Mo, 99.99% CoO and 99.5% $CoO.Co_2O_3$ from Aldrich (Milwaukee, WI, U.S.A); 99.9+% Fe metal (1–10 μm), 99.5% FeO, Fe_2O_3, 99.99% $FeO.Fe_2O_3$, $Fe(NO_3)_3.9H_2O$, and $Co(NO_3)_2.6H_2O$ from Alfa Aesar (Tewksbury, MA USA); pure Ni powder from CuLox Technologies Inc. (Naugatuck, CT, USA); Commercial Fe-NanoCat® from Mach I (King of Prussia, PA, USA), 99.9+% Chloroauric acid [$AuCl_3.4H_2O$] from Sigma-Aldrich (Oakville, ON, Canada); high purity gases from PRAXAIR (Sherbrooke, QC, Canada): H_2 (N5.0), CO (N2.5), Ar (N5.0); 68% nitric acid and 29% ammonia solution from ACE Chemicals Co (Camden Park, SA, Australia); mineral oil (Fisher Scientific, Ottawa, ON, Canada) with catalog name "O122-4, Mineral Oil, Heavy; USP/FCC (Paraffin Oil, Heavy)", and 99% n-hexadecane solvent (Fisher Scientific, Whitby, ON, Canada).

3.1.2. Summary of catalyst synthesis procedures

In order to correlate the effect of synthesis method to catalyst performance, all the single-metal catalysts (Co/C and Fe/C) supported on carbon were prepared as follows:

(a) Metal deposition on freshly synthesized carbon nanofilaments (CNFs) by

(i) Impregnation, or

(ii) Precipitation; and

(b) By *in situ* generation of carbon-supported metal nanoparticles through plasma.

3.1.3. Production of carbon nanofilaments (CNFs)

The CNFs were synthesized through dry-reforming of ethanol (C_2H_5OH) in a CO_2 stream at 838 K (565^oC) according to a patented process developed by this research group (Abatzoglou *et al*., 2010). The expression in Equation (3.1) summarizes the reaction.

$$C_2H_5OH\ (l)\ +\ CO_2\ (g)\ \rightarrow\ CO\ +\ 2\ H_2\ (g)\ +\ 2\ H_2O\ (l)\ +\ 2C\ (s)\quad \text{Eqn. (3.1)}$$

A stream of C_2H_5OH and CO_2 mixture was left to flow over a 17-g steel strip with dimensions of 413 mm x 25 mm x 0.5 mm, at a constant rate of 1 O atom for every C atom ($C_2H_5OH + CO_2 = 3C + 3O$), where some 0.3 $g.min^{-1}$ of liquid C_2H_5OH reacted with CO_2 at a flow rate of 160 SCCM at room temperature and barometric pressure (298 K, 101.325 kPa), and the reaction left to proceed for about 4–6 h (Blanchard *et al*., 2008).

The resulting CNFs were then functionalized by acid-activation (using 4 M HNO_3 acid) where 250 cm^3 of 68% concentrated acid (15.8 M) was dissolved in a liter of solution of distilled H_2O. About 50 g of the CNFs were refluxed with 4 M HNO_3 at 368 K for 3 h (Abatzoglou and Plascencia, 2014). Activation by acid treatment was to create metal anchorage sites on the CNFs.

3.1.4. Catalyst synthesis by impregnation

Catalyst samples were synthesized while aiming for a 40% metal-mass loading: 33.7 g of $Co(NO_3)_2.6H_2O$ and 10.2 g of acid-activated CNF support were mixed with just enough water to produce a thick homogenous paste, which was left to evaporate slowly to dryness in an oven set at 373 K (100^oC) for 15 h. An analogous Fe-based catalyst was made using 45.4 g of $Fe(NO_3)_3.9H_2O$ and 9.4 g of acid-activated CNF support. The resulting catalyst precursor was then calcined at 563 K (290^oC) in a current of Ar flowing at 400 SCCM for 10 h, after which the material was cooled to room temperature in the same gas stream.

3.1.5. Catalyst synthesis by precipitation

Comparable Co/C and Fe/C catalysts aiming at 40% metal-mass loading in the final catalysts were prepared from 0.11 M metal salts solutions using a mass of 31.6 g of $Co(NO_3)_2.6H_2O$ or 45.1 g of $Fe(NO_3)_3.9H_2O$ respectively. For metal precipitation, 25 cm^3 of 29% (or 15 M) NH_4OH solution was dissolved to make 250 cm^3 of solution (0.15 M) using distilled H_2O, from which 100 cm^3 was drawn and added instantaneously to 10.0 g of acid-activated CNF support. The ensuing thick homogenous paste was warmed gently for 30 min on a water bath set at 343 K (70^oC) to evaporate excess ammonia.

The sample was then vacuum-filtered and flashed several times with a liter of distilled H_2O. The residue was left to oven-dry at 373 K for 10 h, and later calcined at 563 K in a current of pure inert gas (Ar) flowing at 400 SCCM for 10 h, and then cooled to room temperature in the same gas stream.

3.1.6. Catalyst synthesis by plasma

Figure 3.1 shows a diagram of the radio frequency (RF) plasma-spray equipment, which also appears in the article provided in Appendix A (Aluha *et al*., 2016a).

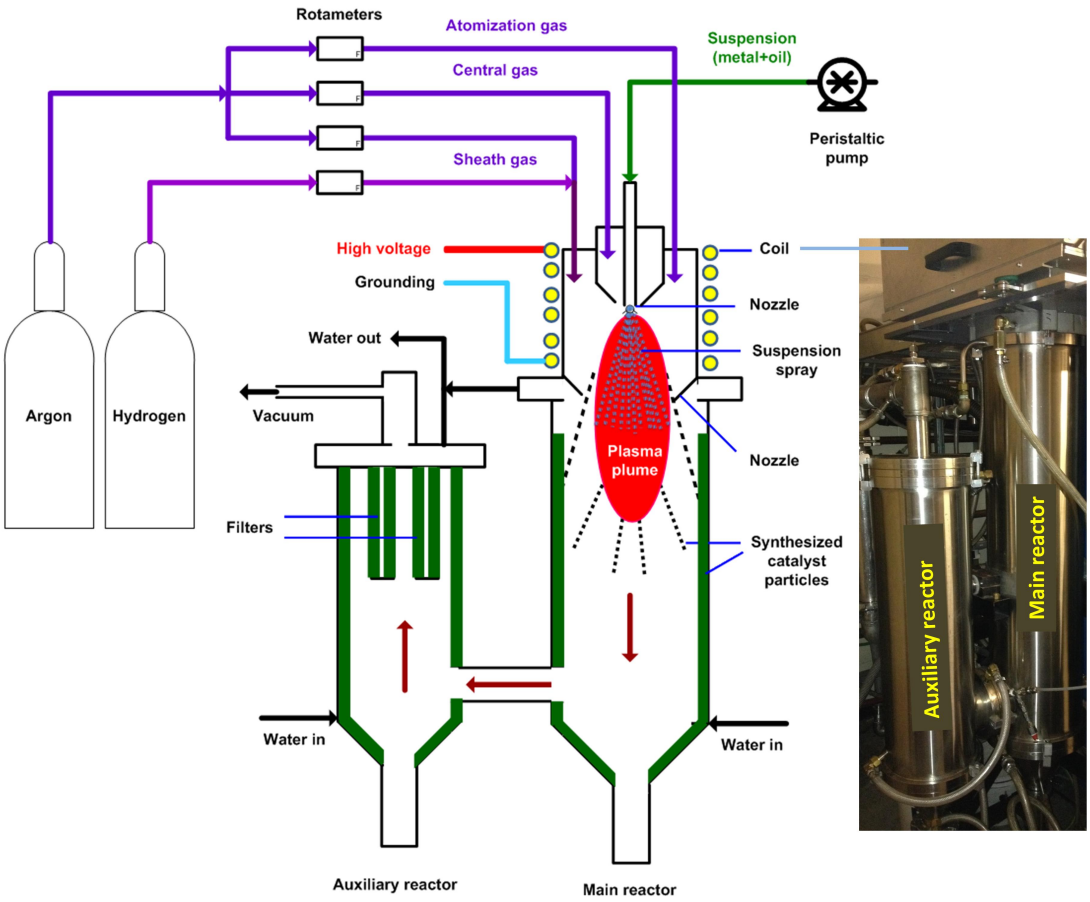

Figure 3.1 Graphic showing equipment for the plasma spray technique

The HF-60 kW SPS system operates on the PL-50 coil and the subsonic nozzle. In the sheath of the flame, the gas flow rates were set at 75 SLPM for Ar and 10 SLPM for H_2 while the other Ar gas flow rates were 23 SLPM (Central) and 10.4 SLPM (Powder). The voltage was set at about 6.6 kV, current at 4.4 A and 0.5 A (grounding) to provide a 29-kW power output.

In catalyst preparation, a mass of 60 g of the metal (Co-only, Fe-only or both in a predetermined ratio) were mixed with 300 cm^3 of mineral oil for at least two hours in order to form a homogeneous suspension, which was then injected directly into the plasma spray at a flow rate of 8.2 $cm^3.min^{-1}$. Table 3.1 provides the various targeted catalyst formulations that were produced.

Table 3.1 Mass of metal required to create the plasma-spray suspensions

Catalyst sample (expected wt% loading)	**Mass of metals (g)**			
	Co	**Fe**	**Ni**	**Mo**
100%Fe/C	-	60	-	-
30%Co-70%Fe/C	18	42	-	-
50%Co-50%Fe/C	30	30	-	-
70%Co-20%Fe-10%Mo/C	42	12	-	6
70%Co-20%Fe-10%Ni/C	42	12	6	-
70%Co-25%Fe-5%Ni/C	42	15	3	-
80%Co-20%Fe/C	48	12	-	-
100%Co/C	60	-		

The conditions for the SPS system were monitored constantly to ensure consistency, where voltage was set at 6.6 kV, current at 4.4 A, and 0.5 A (for grounding), fixed pressure set at 250 Torr (33 kPa), initial pressure below 30 Torr (4 kPa) and final pressure at 300 Torr (40 kPa). After catalyst synthesis, which gives about 70 g of the material per batch, the feather-light material was harvested and tested for the Fischer-Tropsch activity.

3.2. Catalyst testing

3.2.1. Reactor designs and set-up

In this study, initial tests were performed in a fixed-bed reactor, whose design is presented in Appendix B (Aluha et al., 2015) and further, in a 3-φ-CSTSR whose design is shown in Figure 3.2, also appearing in the article provided in Appendix C (Aluha *et al*., 2016b).

When compared, reactors applicable to Fe-based catalysts, but operating at lower temperatures have received less attention than their Co-based counterparts since Fe-based catalysts usually exhibit lower yields of diesel and wax (Ebert, 2013). In our case, the 3-φ-CSTSR was employed in order to obtain mainly the diesel fraction and waxes and was commissioned with capability to function in either batch mode or continuous flow.

In the 3-φ-CSTSR, the feed syngas ($CO + H_2$) was bubbled through inert oil (hexadecane), in which catalyst particles were suspended. High conversion of the feed gas to liquid products can be achieved by vigorous mixing, which provides an intimate gas-catalyst contact with a uniform temperature distribution in a relatively small reactor volume (Kreutz *et al*., 2008). Vigorous mixing with the stirrer set at 2 000 rpm provided effective heat transfer mechanisms besides depressing the accumulation of H_2O during reaction. In addition, a special sampling column was set up in such a way that the slurry (solid catalyst in hexadecane solvent) could be isolated from the reactor occasionally for α-value determination with TOS without interrupting the process.

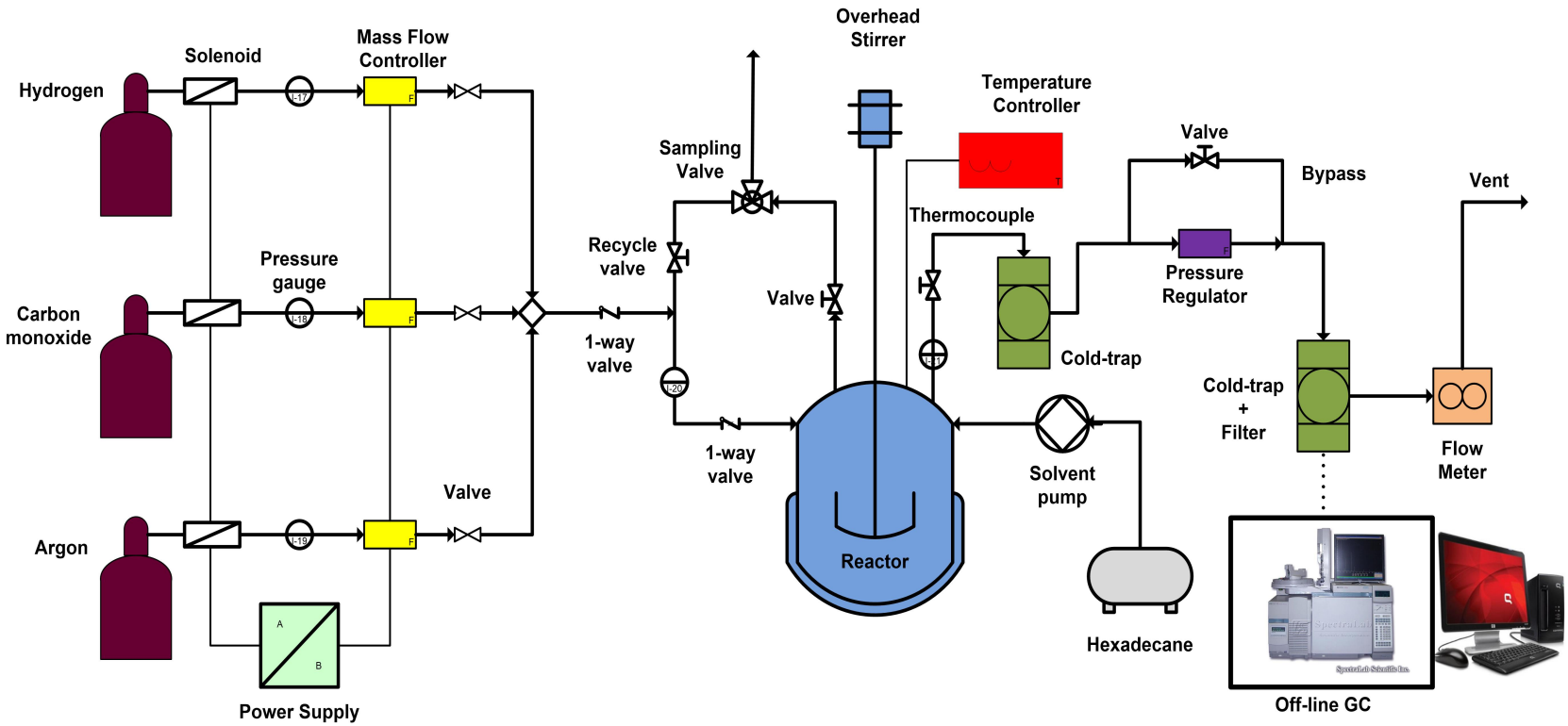

Figure 3.2 Schematic showing the entire reactor-system design of the 3-φ-CSTSR

3.2.2. FTS reaction conditions

Using a high-pressure, stainless-steel vessel supplied by Autoclave Engineers (Erie, PA, U.S.A) operated isothermally between 493–533 K (220–260°C) at 2 MPa pressure, about 5 g of the catalysts was loaded into the reactor and the gas feed adjusted to a space velocity (GHSV) of about 3 600 $cm^3.h^{-1}.g^{-1}$ of catalyst. Since these nanometric materials have been observed to be pyrophoric, great care was taken when handling and the catalyst was pre-treated *in situ* (before the FTS reaction ensued) at 673 K (400°C) for 24 h under reducing conditions of pure H_2 or CO flowing at 250 $cm^3.min^{-1}$.

Pre-treatment normally activates the catalyst by gasifying most of the carbon matrix surrounding the metal moieties to essentially form CH_4 and other light hydrocarbons, leaving behind nanometric Fe or Co catalysts predominantly in the metallic form. Product analysis was carried out offline in two Varian CP-3800 Gas Chromatographs; one dedicated for gas injections, while the other was dedicated for liquid samples only.

3.2.3. Determination of catalyst activity

About 10% Ar was included in the FTS gas feed stream for mass balance determination (Bahome *et al*., 2005), where the catalyst activity was calculated from gas-phase analysis using Equation (3.2) by the amount of CO converted, thus:

$$CO\ (\%) = \left[\frac{CO_{in} - CO_{out}}{CO_{in}}\right] \times \left[\frac{Ar_{in}}{Ar_{out}}\right] \times 100 \qquad \text{Eqn. (3.2)}$$

3.2.4. Determination of catalyst selectivity

In the liquid-phase, the selectivity of each product (S_i') was calculated from the area under its corresponding peak (A_i) on the GC chart, and then divided by the total sum area of all the peaks from C_5 and above as shown in Equations (3.3) and (3.4), thus:

$$S_i' = \left(\frac{A_i}{A_5 + A_6 + A_7 + \cdots A_n}\right) \qquad \text{Eqn. (3.3)}$$

The selectivity (S) of any product (C_i) in liquid-phase was determined by the equation:

$$S_{C_i} = \frac{S_i'}{100}\, x\, (100 - P) \qquad \text{Eqn. (3.4)}$$

where C_i = hydrocarbon product with i carbon atoms

i = number of carbon atoms, i = 5, 6, 7, ….n, and

S_i' = selectivity calculated from the area under each peak (A_i).

P = the total CO conversion to the gas-phase products (as %)

3.2.5. Determination of α-values from ASF distribution

Generally, the catalyst's alpha value (α), which denotes the probability for hydrocarbon-chain growth (Wang *et al*., 2003), is predicted from the Anderson-Schulz-Flory (ASF) distribution (van der Laan and Beenackers, 1999) by several mathematical expressions shown below.

$$\frac{M_n}{n} = (1-\alpha)^2 . \alpha^{(n-1)} \qquad \text{Eqn. (3.5)}$$

$$ln\, \alpha = n\, ln\, \alpha + ln\left[\frac{(1-\alpha)^2}{\alpha}\right] \qquad \text{Eqn. (3.6)}$$

$$\alpha = \frac{M_{n+1}}{M_n} = \frac{r_p}{(r_p + r_t)} \qquad \text{Eqn. (3.7)}$$

where: M_n = mole fraction of a hydrocarbon with chain length n

n = number of total carbon atoms

α = probability of chain growth (α < 1)

(1 - α) = probability of chain termination

r_p = the rate of chain propagation

r_t = the rate of chain termination

Thus, the α-values were obtained by the least-squares linear regression of Equation (3.5) in the logarithmic form expressed as Equation (3.6), where $\log(M_n/n)$ is plotted against *n*, the hydrocarbon-chain length (Bartholomew and Farrauto, 2006; p.403). A catalyst's α-value, whose meaning is interpreted to be the relationship between the rate of chain propagation and the rate of chain termination as shown in Equation (3.7) is usually given as a range, and depends on the nature of the material and the reaction conditions such as the FTS temperature (low or high).

3.3. Catalyst characterization

Various analytical techniques were utilized in characterizing both the fresh and spent catalysts. The following methods were attempted: Thermogravimetric analysis (TGA) for metal-mass loading in the catalysts using the TGA-DTA Setsys 2400 instrument (Setarum, Hillsborough, NJ, U.S.A), Brunauer-Emmett-Teller (BET) surface area analysis by means of an Accelerated Surface Area Porosimeter (ASAP) 2020 (Micromeritics, Norcross, GA, U.S.A), Raman Spectroscopy using a Micro-Raman LabRam-800 Spectrometer (Horiba Ltd., Kyoto, Japan), Scanning Electron Microscopy (SEM) coupled with Energy Dispersive X-ray (EDX) Spectroscopy and X-ray mapping performed on a Hitachi S-4700 instrument (Hitachi, Tokyo, Japan), while the Transmission Electron Microscopic (TEM) imaging for particle size analysis was conducted on a Hitachi H-7500 Microscope (Hitachi, Tokyo, Japan). Phase analysis by X-ray Diffraction (XRD) was performed on a Philips X'pert PRO X-ray Diffractometer (PANalytical, EA Almelo, The Netherlands), X-ray Photoelectron Spectroscopy (XPS) was done using a Kratos Axis Ultra DLD spectrometer (Shimadzu, Manchester, England), and X-ray Absorption Spectroscopy (XAS) particularly by the X-ray Absorption Near Edge Structure (XANES) analysis was conducted at the Synchrotron (Canadian Light Source (CLS), Saskatoon, SK, Canada).

3.3.1. BET surface area analysis

The BET physisorption analysis was carried out using liquid nitrogen at 77 K (–196°C), and pressure ~1 kPa (below 10 μmHg) in a Micromeritics ASAP 2020 instrument, shown in Figure 3.3. Prior to the analysis, the samples were degassed at 423 K (150°C) for about

50 hours and evacuated until a pressure of less than 1 kPa was obtained in the sample holder. Porosity information on specific surface area, average pore size and pore distribution was extracted from the plotted isotherms.

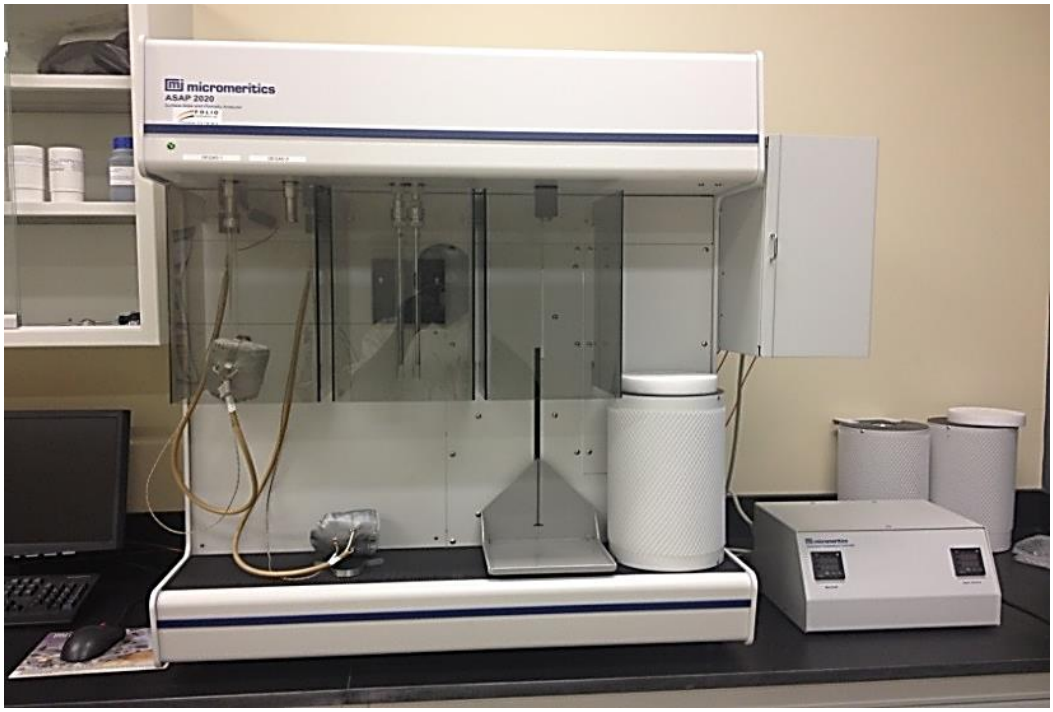

Figure 3.3 The Micromeritics ASAP 2020 instrument

3.3.2. Microscopy: SEM and TEM

Morphological properties of the catalysts were examined on a Hitachi S-4700 SEM instrument shown in Figure 3.4. The microscope captured both secondary and backscattered images, and with an X-Max Oxford EDX spectrometer for elemental analysis, X-ray mapping was used to visually indicate the degree of dispersion of the metals in the carbon matrix. On the other hand, metal-particle size distribution was analyzed on a Hitachi H-7500 TEM, fitted with W filament and operated at an accelerating electron beam of 120 kV. Images were captured in bright field mode on a bottom-mounted AMT 4k x 4k CCD Camera System Model X41 and the Nano-measurer 1.2 “Scion Imager” software aided particle size analysis.

Figure 3.4 The Hitachi S-4700 Scanning Electron Microscope

3.3.3. Thermogravimetric analysis

A number of difficulties were associated with samples analysis, one of them being the indigestible nature of graphite. This rendered the conventional elemental analysis by inductively-coupled plasma mass spectrometry (ICP-MS) method unreliable. Therefore, only the metal mass loading of the single-metal catalysts (Co/C and Fe/C) was determined using thermogravimetric analysis, and it was conducted on a Setaram Setsys 2400 calorimetric system, equipped with a 1 873 K TG-DTA sensor. Less than 25 mg of the sample in an alumina crucible was heated from ambient temperature (~293 K) to 1 273 K at a heating rate of 10 $K.min^{-1}$, first in an inert atmosphere using Ar and then in 20% O_2 balanced in Ar. From the results, it was interpreted that the mass loss recorded was related to the amount of carbon burned (to form CO_2), leaving behind the bare metal, from which the atomic mass and hence the metal loading in the catalyst was calculated.

3.3.4. Raman spectroscopy

Since graphite is Raman active, the degree of graphitization in the catalyst support was determined on a LabRam-800 spectrometer equipped with a microscope, a He-Ne 632.8

nm laser and a N_2-cooled charge-coupled device detector. To avoid sample overheating during measurements, laser beam power was kept below 2 mW through 50x objective lens, focusing the excitation light on a spot size of 3 μm in diameter. Weak Raman signals were accumulated for a period of 30 min to 1 h to obtain a good signal/noise ratio. The MicroRaman module was favored for this analysis because FT-Raman spectra reproducibility of the samples was poor.

3.3.5. X-ray diffraction (XRD) studies

Figure 3.5 is an image of the Philips X'pert PRO Diffractometer from PANalytical used for the powder-XRD analysis in this study. Having been fitted with Ni-filters for the Cu Kα radiation produced at 40 kV and 50 mA with wavelength alpha1 as (λ = 1.540598Å), the instrument was set in the Bragg-Brentano configuration with PIXcel-1D detector and operated on the factory-installed Analytical Data Collector software.

Figure 3.5 The Philips X'pert PRO Diffractometer used for XRD analysis

The XRD patterns were recorded in the range of 5° and 110° [2θ] angle at a scanning speed of about 3° [2θ].min^{-1}, step size of 0.040° [2θ] angle and time of 0.0395 sec per step; corresponding to a scan time of 24 min. The anti-scatter and divergent slits were

fixed at 1°. Data collection and analysis was conducted using the Materials Data Inc. software: the *MDI JADE 2010* (version 2.6.6 @ 2014 Feb 21). The collected data was compared with the *Powder Diffraction Files* in the Database (version 4.13.0.2), using the PDF-4+ software 2013 (version 4.13.0.6), published by the International Centre for Diffraction Data (ICDD). Phase quantification by Rietveld Quantitative Analysis (RQA) using Equation (3.8) was attempted in order to determine the various amounts of each species in the fresh and used catalysts (Rietveld, 1969).

$$W_p = \frac{S_p(ZMV)_p}{\sum_{i=1}^{n} S_i(ZMV)_i} \qquad \text{Eqn. (3.8)}$$

where W_p = relative weight fraction of phase p in a mixture of n phases,

S_p = Rietveld scale factor,

Z = number of formula units per cell,

M = mass of the formula unit (in atomic mass units), and

V = the unit cell volume (in $Å^3$).

In RQA, curve fitting was done using the High Score Plus software, with the modelling fully describing the shape, width and systematic errors in the positions of the Bragg peaks. The procedure ensured that all reflections in the XRD pattern were explicitly included for calculation, while reducing the effects of preferred orientation, considering factors such as the structural parameters of the crystal, peak profile parameters, micro-absorption and particle statistics, all being refined as part of the same analysis (Kniess *et al*., 2012).

3.3.6. X-ray Photoelectron Spectroscopy (XPS) analysis

In XPS analysis, the sample is irradiated with mono-energetic x-rays that emit photoelectrons from the surface of the sample. An electron energy analyzer determines the binding energy of the photoelectrons. From the binding energy and the intensity of a photoelectron peak, the identity of the element, its chemical state and quantity are determined.[1] XPS is generally a surface technique used to analyze the surface composition

[1] Web site source: https://www.phi.com/surface-analysis-techniques/xps.html, Accessed on 2014-08-05.

of materials, and in this work, the analysis was performed on a Kratos Axis Ultra DLD spectrometer, see Figure 3.6.

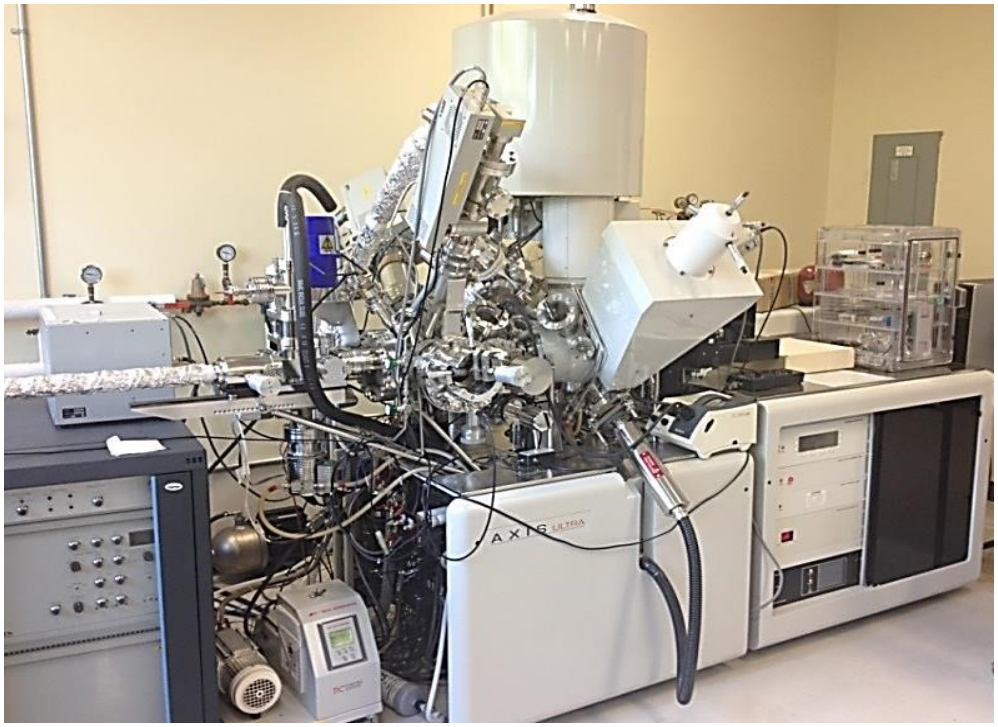

Figure 3.6 The Kratos Axis Ultra DLD spectrometer for XPS analysis

The Al*Kα* monochromatized line (1 486.6 eV) was used for excitation with 225-W of applied power. The analyzer was operated in a constant pass energy mode (*E*pass = 160 eV for survey scans; *E*pass = 20 eV for high resolution scans). The instrument's work function was calibrated to give a binding energy (BE) of 83.96 eV for the Au 4f7/2 line for metallic gold. The spectrometer dispersion was adjusted to give a BE of 93.62 eV for the Cu 2p3/2 line of metallic copper.

A charge neutraliser was used on all samples to compensate for the charging effect and when needed (mostly for non-conductive samples) the binding energies were referenced to the adventitious carbon, C 1s core level (284.8 eV).[2] No charge corrections were done on the charged samples, e.g. the CNFs. The powdered catalysts were pressed into a thin pellet

[2] Web site source: http://www.xpsfitting.com, Accessed on 2014-08-02.

in a powder sample holder, and an oval area of 300 x 700 micron was examined (Chu *et al*., 2007), while Casa XPS software (version 2.3.16) was used for data analysis.

3.3.7. X-ray Absorption Spectroscopy (XAS) by the Synchrotron

The X-ray absorption spectra at both the Co and Fe K-edges were measured using Synchrotron light, at the *Canadian Light Source* (CLS, in Saskatoon, Canada). Figure 3.7 shows the images of the XAS reaction cell (at the top) and the Soft X-ray Microcharacterization Beamline (SXRMB) hutch at the bottom.

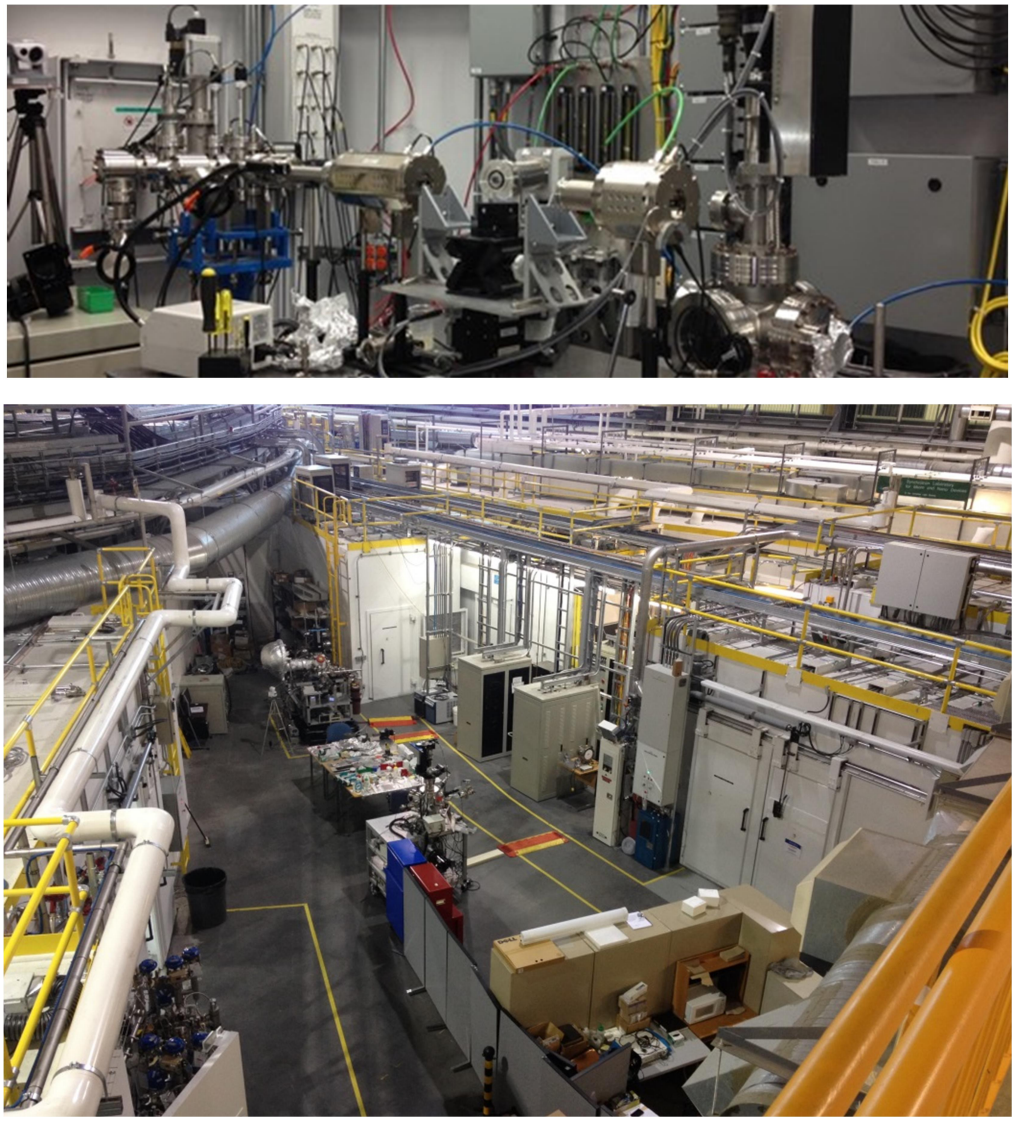

Figure 3.7 The CLS Synchrotron Facility in Saskatoon

Table 3.2 gives the K-edge energies for the elements in our single metal Co/C and Fe/C catalysts and XAS measurements, which were conducted both in the transmission mode and by fluorescence, with two ionization chambers used for X-ray detection.

Table 3.2 The K-edge and XAS limits for the various elements

Metal foil	K-edge (eV)	XAS spectrum (eV)
Fe	7 110	7 000 – 7 300
Co	7 709	7 600 – 8 400

The Si(111) double-crystal monochromator was calibrated by setting the first inflection point of the K-edge spectrum of the elements in question. Data collection ensued within the determined range for about 20–30 min per element. Using Athena software, the conventional procedure of background correction followed by data normalization were performed before further treatment of the XANES analysis (Ravel and Newville, 2005). Various reference compounds were used in the study, including Co foil, CoO, crystalline $Co(NO_3)_2$ and Co_3O_4 for the Co-based catalysts. Similarly, for Fe-based catalysts, Fe foil, FeO, Fe_2O_3, crystalline $Fe(NO_3)_3$ and Fe_3O_4 were used.

4. RESULTS

4.1. Reactor set-up for catalyst testing

Images of the commissioned catalyst testing rig are presented in Figure 4.1. From the left are cylinders containing feedstock gases whose flow rate was adjusted by the mass flow controllers, while the solenoids entailed a shut-off safety mechanism. The feedstock gases streamed to the right into the reactor whose internal pressure was regulated by the Brooks® controller and read-out unit by means of a back-pressure regulator. The peristaltic pump delivered hexadecane solvent into the reactor before the FTS reaction ensued, while at the terminal was a flow meter to determine the exit gas flow rate. Preliminary catalyst testing and results validation was performed in fixed-bed reactor.[3]

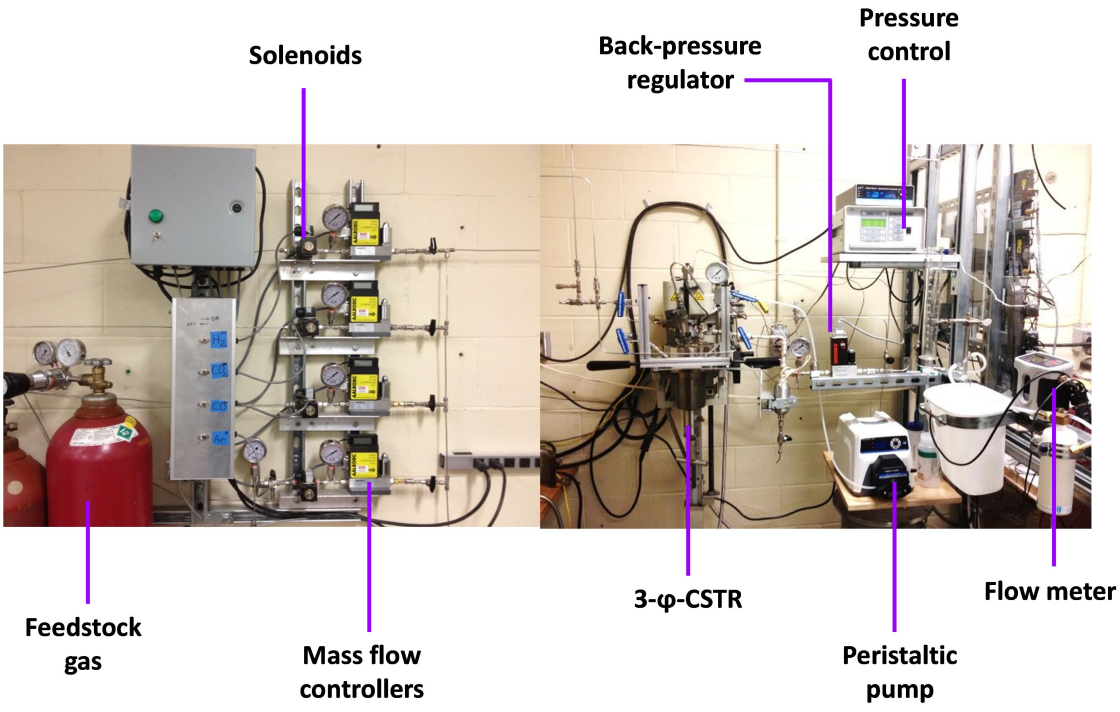

Figure 4.1 The final 3-φ-CSTSR set-up for the FTS with an offline GC system

[3] Fixed-bed reactor tests: Courtesy of Prof. Ajay Dalai (Department of Chemical Engineering, University of Saskatchewan), with whom we share a platform on the Canadian BiofuelNet (BFN).

4.2. Overview: evolution of catalyst selection criteria

Initial work sought to establish the most effective synthesis method for the carbon-supported nanometric catalysts (Aluha *et al*., 2015a), attached in Appendix B. This was followed by the synthesis of more complex binary and ternary metallic systems, and a full account of the synthesis method is attached in Appendix A (Aluha *et al*., 2016a). A comparative study was undertaken to evaluate plasma-synthesized samples alongside those prepared by other traditional methods such as impregnation or precipitation. Since the plasma-synthesized samples were found to be relatively more active, samples prepared by impregnation or precipitation methods were abandoned.

It was observed that at the higher space velocity (6 000 $cm^3.h^{-1}.g^{-1}$ of catalyst) where tests were performed in fixed-bed reactor, the Fe catalyst was more active (with ~30% CO conversion) than the Co catalyst (20%). However, at higher conversions achieved at the lower space velocities (of 3 600 $cm^3.h^{-1}.g^{-1}$ of catalyst), the Co catalyst became more active with over 40% CO conversion against 25% for Fe catalyst tested in the 3-φ-CSTSR. This observation concurs with literature data (Davis, 2007).

The principal target in testing these catalysts was selectivity towards the diesel fraction. Preliminary tests in the 3-φ-CSTSR were performed at 493 K using the plasma-synthesized single metal Co/C and Fe/C catalysts. Their respective CO conversions were 45 and 25%, with massive wax production observed with the Co/C sample. Details of the experimental procedures, results and discussions are available in the attachment of Appendix C (Aluha *et al*., 2016b).

In order to lower wax formation by the Co/C catalyst and enrich the diesel fraction, the temperature was raised to 533 K because it has been established that higher temperatures tend to produce shorter-chain hydrocarbons. It was observed that the higher temperature significantly improved catalyst activity to complete CO conversion. This was however accompanied by poor selectivity towards the FTS fuels (S_{fuels} = 27%), where S_{fuels} was the combined selectivity for gasoline and diesel fractions; and in this discussion, it comprises C_5–

C_{20}. The overall Co/C selectivity towards the diesel fraction (C_{13}–C_{20}) as our targeted product was a paltry 19%. Figure 4.2 provides this information as a summary spatial chart offering the rationale and complete process of examining the materials for their performance at 533 K, 2 MPa pressure; and GHSV = 3 600 $cm^3.h^{-1}.g^{-1}$ of catalyst in the 3-φ-CSTSR.

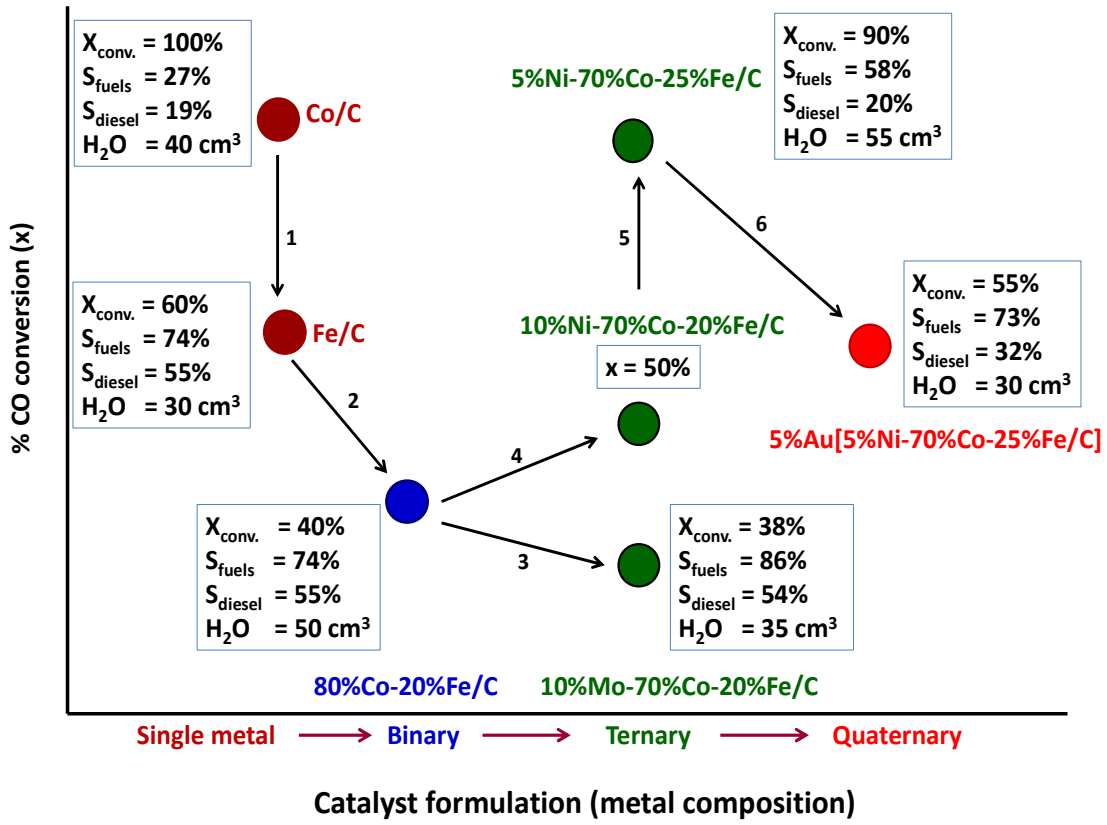

Figure 4.2 A mind map showing the process of catalyst development from the single-metal Co/C, Fe/C to bimetallic Co-Fe/C, ternary (Ni-Co-Fe/C and Mo-Co-Fe/C) and quaternary (Au-Ni-Co-Fe/C) systems tested at 533 K, 2 MPa

Comparatively, at 533 K, the Fe/C catalyst showed lower activity (60% CO conversion), but with better overall selectivity towards the fuels (S_{fuels} = 74%), moving from Co/C catalyst (step 1). Selectivity towards the diesel fraction was 55% compared to 19% in Co/C. The Fe/C catalyst also formed less CO_2 (10%) than in the Co/C catalyst (20%), and Fe/C generated significantly less CH_4 (5%) in comparison to the 46% produced by the Co/C (Aluha *et al.*, 2016b).

Further catalyst evaluation in order to improve on selectivity towards the diesel fraction was attempted using the Co-Fe/C bimetallics (step 2), and the 80%Co-20%Fe/C catalyst acted as the bimetallic representative. This is because it had metal nanoparticle size comparable to those of the single metal catalysts having a mean size in the range of 9–11 nm. Besides, it also had identical metal proportions with the other materials under examination, that is, Co (~70%) and Fe (~20%) (Aluha and Abatzoglou, 2016).

Therefore, the application of bimetallics only led to a marginal difference when compared to the Fe/C catalyst operated at 533 K, since S_{fuels} (selectivity for diesel + gasoline) remained unchanged (at 55%), prompting the exploration of the ternary systems (step 3 and 4). In addition, the Co-Fe/C bimetallic was relatively worse off in suppressing H_2O production because it generated more of it when compared to the Co/C and Fe/C catalysts.

On the other hand, the addition of 10%Ni to the Co-Fe/C bimetallic (step 4) increased CO conversion by 10% (from 40% to 50%), and yet the addition of only 5%Ni (step 5) improved the activity by an additional 50% to 90% CO conversion. This means that promotional effect of Ni only required small amounts to function effectively. Whereas the Co-Fe/C bimetallic catalyst gave S_{fuels} selectivity of 74%, with only 3% CO_2, 10% CH_4 and 50 cm^3 H_2O, the presence of 5%Ni produced excessive quantities of CO_2 (14%), CH_4 (23%), and 55 cm^3 of H_2O. This means that Ni leads to early molecular desorption.

Since the selectivity of 5%Ni-Co-Fe/C catalyst towards S_{fuels} was 58% with only 20% apportioned towards the diesel fraction, the Ni-Co-Fe ternary was further modified by the addition of Au (step 6) leading to improve the selectivity towards S_{fuels} to 73% from 58%, and towards the diesel fraction (from 20% to 32%), but at the expense of catalytic activity (dropping from 90% to 55% CO conversion). Further discussion on catalyst promotion with Au can be found in the article currently under publication review process (Aluha and Abatzoglou, 2017a). On the other hand, both the Co-Fe/C and Mo-Co-Fe/C catalysts had almost identical catalytic activity (~40% CO conversions), but the presence of Mo demonstrated overall improved selectivity towards S_{fuels} from 74% in the Co-Fe bimetallic to 86% (step 3), and it also minimized H_2O production of (35 cm^3). An article on the catalyst promotion by Ni and Mo has been accepted for publication (Aluha and Abatzoglou, 2017b).

4.3. Evaluation of single-metal Co/C and Fe/C catalysts

4.3.1. The effect of synthesis method on catalyst activity

It has been advanced that catalysts prepared by SPS technology display superior performance, and in this work, preliminary results of the plasma-synthesized Fe/C catalyst tested in the fixed-bed reactor showed about 30% CO conversion per pass while the Co/C catalyst yielded about 20% CO conversion (503 K, 3 MPa pressure, and GHSV = 6 000 $cm^3.h^{-1}.g^{-1}$ of catalyst). Analogous Co/C and Fe/C catalysts prepared by impregnation or by precipitation method exhibited CO conversions of about 7% under similar reaction conditions, confirming the assertion that plasma-synthesized catalysts had superior attributes (Aluha *et al.*, 2015a).

Catalyst selectivity tended more towards the diesel range, which was the target hydrocarbon fraction in this work, shown as follows: 71% (Fe/C by plasma), 56% (Co/CNF by impregnation), and 51% (Fe/CNF by precipitation), except for the plasma-synthesized Co/C catalyst that was richer in the gasoline range with 60% selectivity.

From these findings, a rational basis of choosing an effective FTS catalyst was developed and used to rapidly establish SPS technology as one of the most promising approaches for future application in the synthesis of high quality catalysts. Figure 4.3 articulates the proposition that the plasma-spray method shrinks catalyst production into a single step, having intrinsic potential for seamless scale-up. Initial pictorial appears online as a graphical abstract in a journal article attached in Appendix B (Aluha *et al.*, 2015a), where further details on this aspect are availed.

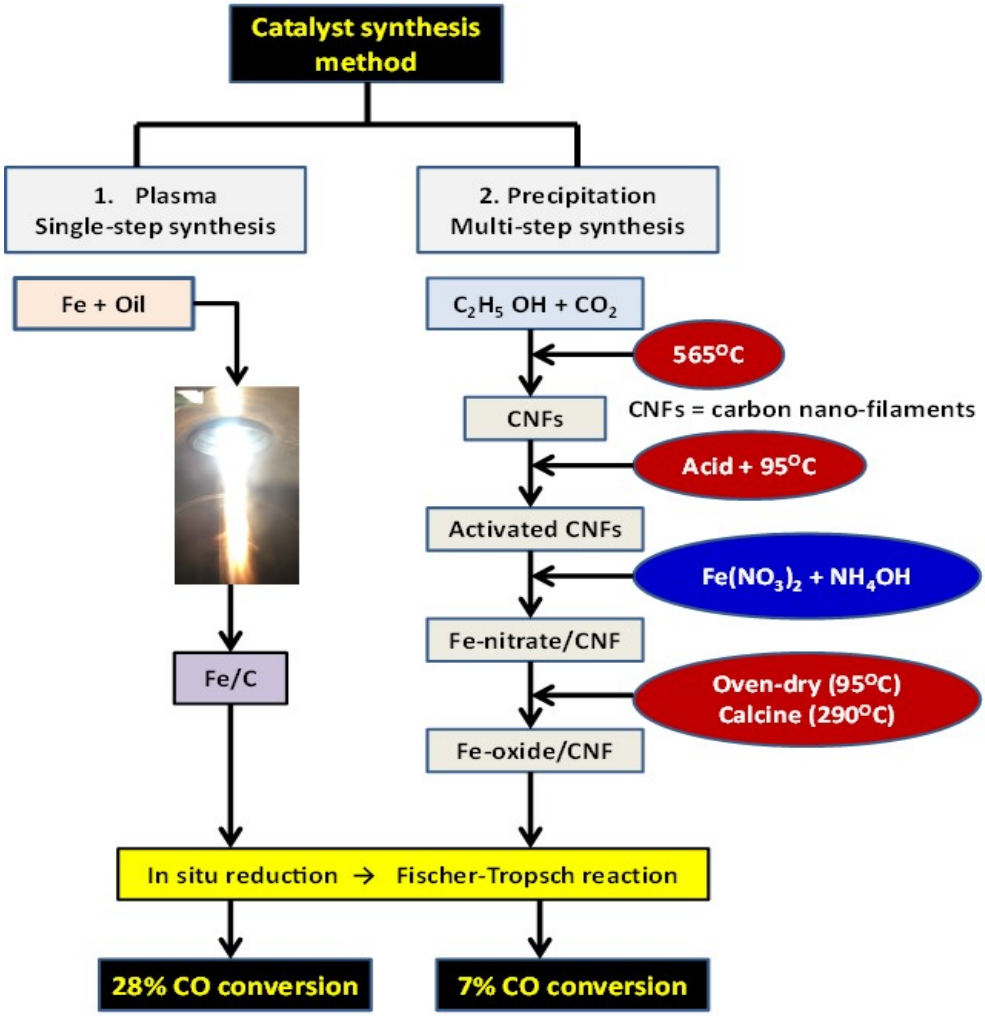

Figure 4.3 Comparing SPS with other multi-stage catalyst synthesis methods [4]

4.3.2. Error analysis and reproducibility

Activity tests were repeated about 5 times at the onset of the project for the Co/C catalyst only and the CO conversion consistently found to be ~40% (±5%) depending on the time on stream (when tested at 220°C, 2 MPa), with the activity sometimes steadily increasing over time. Analysis of the Fe/C catalyst was repeated twice and found to be very sensitive to the pre-treatment conditions with maximum of 25% (±5%) when pretreated at 400°C and minimum of ~10% (±5%) when pretreated at 320°C. Since these were considered to be random errors, all the other catalytic systems tested were expected to lie within the same error margins.

[4] Web source: http://pubs.acs.org/doi/abs/10.1021/acs.iecr.5b03003, Accessed on 2016-11-01.

4.3.3. Possible mechanism for catalyst synthesis in plasma

It was postulated that during catalyst synthesis in plasma, the metal particles vaporize, while the suspension oil is thermally cracked. As the carbonaceous gases in the plasma interact with the metal species (e.g. Fe) to produce Fe carbides (Fe_xC_y), the same gases react with the H_2 of the sheath gas to generate mainly CH_4, allowing for its convenient exit from the reactor. The remaining carbon then begins to accumulate on the metal nanoparticle moieties and on the cooler walls of the plasma reactor. XRD analysis has indicated the presence of Fe_3C phase in our samples, and from known phase diagrams, Fe_3C forms at temperatures above 1 373 K, below which Fe_3C decomposes into graphitic carbon and austenite (FCC structure), or into the α-Fe (BCC structure) below 973 K (Digges *et al.*, 1966). See full discussion in the article provided in Appendix A.

4.3.4. Catalyst characterization

Below is a synopsis of the characterization results of the single-metal Co/C and Fe/C catalysts. Details of this work can be found in Appendix B (Aluha *et al.*, 2015a). Elemental analysis by TGA-DTA indicated that the atomic mass loading of the metals onto the carbon support in the freshly plasma-synthesized Co/C and Fe/C catalysts was approximately 0.25g/g (or 25-wt%) of Fe/C or Co/C mass-by-mass (Aluha *et al.*, 2016b).

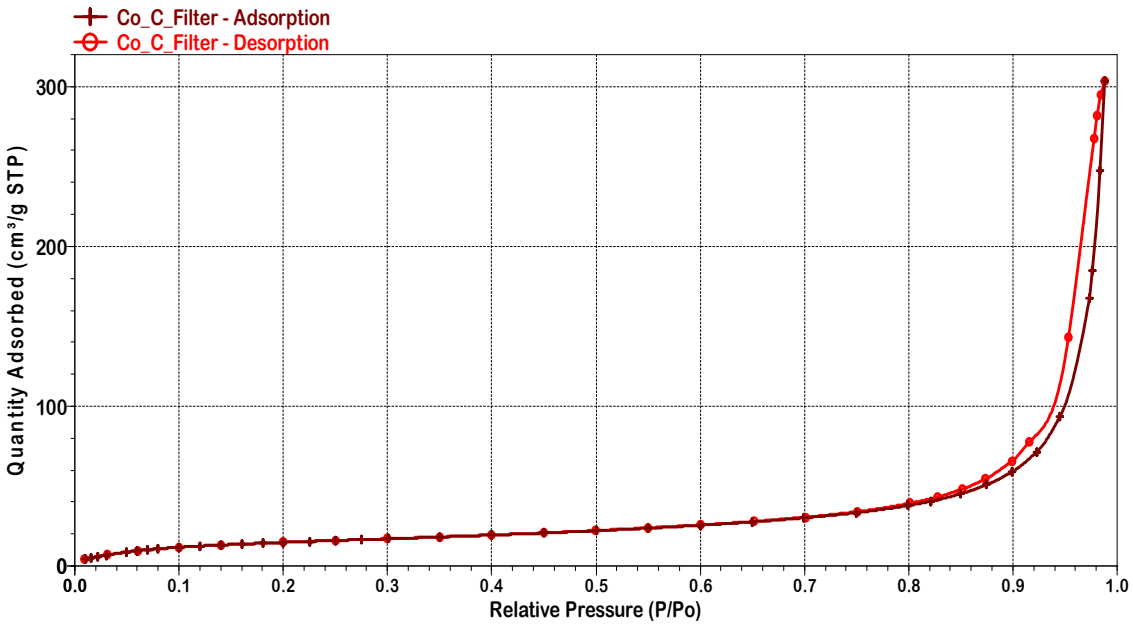

Figure 4.4 BET adsorption-desorption isotherm of plasma-synthesized Co/C catalyst

The BET specific surface areas of the plasma-derived Co/C and Fe/C catalysts were approximately 93 and 55 $m^2.g^{-1}$ respectively, while those of the catalysts supported on CNFs varied between 106 and 176 $m^2.g^{-1}$. In all cases, the catalysts' adsorption-desorption isotherms were near superimposable, represented by Figure 4.4. Both low surface area and limited hysteresis defined the catalysts to be non-porous.

SEM images showed poor metal dispersion and particle agglomeration in samples prepared by impregnation or precipitation. However, the plasma-synthesized catalysts indicated uniform distribution of the metal nanoparticles in the carbon support. Evidence through TEM imaging of the plasma-synthesized Fe/C catalyst provided in Figure 4.5 showed high dispersion and homogenous distribution of the metal nanoparticles in the carbon matrix, and this alludes to the consistency in the quality of the materials. Further, image analysis of the fresh catalysts before and after use in FTS reaction indicated no sintering of metal particles during reaction. The mean metal nanoparticle size remained at approximately 11 nm, and this confirmed the reliability of plasma technology as a method of choice in catalyst synthesis.

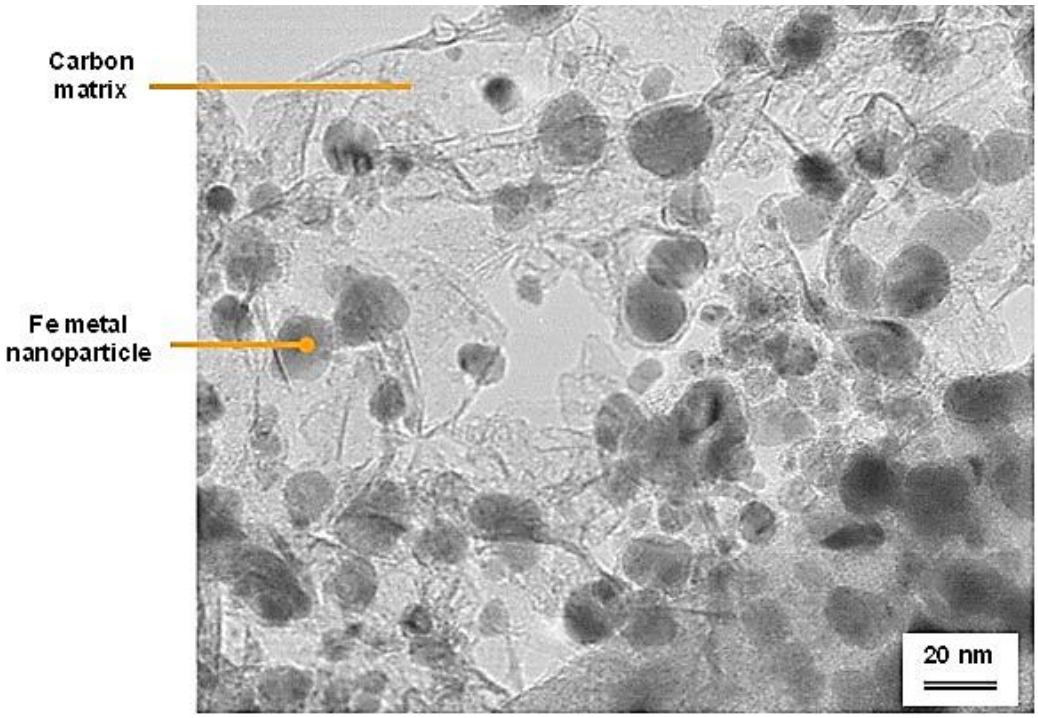

Figure 4.5 TEM image of the plasma-synthesized Fe/C catalyst

Analysis by Raman spectroscopy showed that during functionalization, the acid-treated nanofilaments (CNFs) had diminished G-bands due to loss of graphitization, leading to structural defects that increase amorphicity (D-band). On the other hand, the plasma-synthesized samples had dominant G-bands as a sign of ensuing graphitization in the support and therefore had more of the ordered graphitic structure (Osswald *et al*., 2012).

Normally, the ordered graphitic carbon is assigned the G-line at around 1580–1600 cm^{-1}, while the disordered carbon form (D-line) around 1350 cm^{-1} contains defective graphitic sites and may portray varying intensities, position, and width in different nano-crystalline and amorphous carbons, even in samples without widespread graphitic ordering (Ferrari and Robertson, 2000).

XRD analysis coupled with RQA modelling indicated the concurrent presence of metallic and carbidic species in the fresh plasma-synthesized catalysts. The Co/C catalyst comprised ~39% Co^0 and ~7% Co_3C, while the Fe/C catalyst showed ~26% Fe_3C alongside two different phases of metallic Fe^0 amounting to ~34% (cubic FCC = 20.9%; taenite = 13.1%). Appendix C provides details of this discussion (Aluha *et al*., 2016b).

XPS analysis confirmed results from XRD that samples prepared through impregnation or precipitation method had significant amount of metal oxides. The $\pi \rightarrow \pi^*$ electron transitions observed in XPS as the broad peak at about 290 eV, above the carbon peak (at 284 eV) indicated presence of graphitic carbon in the samples. Raman spectroscopy and XRD analysis also confirmed presence of graphite. However, the main aim of performing XPS analysis was to identify metal carbides, and despite the substantial and concomitant presence of both the metal and carbon in the materials, there was no significant sign of chemical bonding between them. The metal-carbide peak was expected to appear just below the carbon satellite peak, but it was absent (Aluha *et al*., 2015a).

Generally, analysis by XANES indicated that samples synthesized by plasma were more likely to trace the spectrum of the metal standards than those prepared by impregnation or precipitation. For example, the freshly-precipitated catalysts showed that they contained

oxidic species (possibly Co^{3+}) since their K-edge was seen at higher energies than those of the CoO (or Co^{2+}) standards. This observation confirmed findings by both XPS and XRD analysis, which indicated that the precipitated Co/CNF catalyst indeed composed Co_3O_4. Nevertheless, a peak shift was detected in the used plasma-synthesized Fe/C sample, drifting towards the oxidized state as shown in Figure 4.6, yet it was still catalytically active. Since it has been shown that intrinsic catalyst deactivation originates from metal oxidation, this observation could be pointing either towards catalyst deactivation, which is most unlikely, or indicating a synergy arising from the co-existence of both Fe carbides and oxides that might be crucial for FTS catalysis.

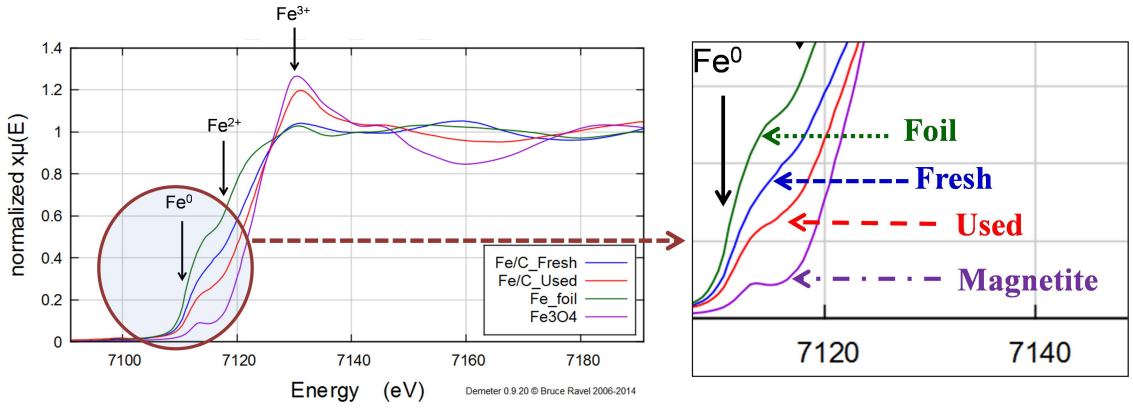

Figure 4.6 XANES spectra for fresh and used plasma-synthesized Fe/C samples compared with Fe^0 and Fe_3O_4 standards

The latter opinion concurs with the assertion that formation of the non-stoichiometric iron-oxide-carbide species, which is less stable, but more active than the known χ-Fe_5C_2 carbide might be at play in our plasma-synthesized Fe/C catalyst (Bengoa *et al.*, 2007). Further details to this discussion involving both the Co/C and Fe/C catalysts is found in Appendix B (Aluha *et al.*, 2015a).

4.4. Benchmarking Co/C and Fe/C catalysts

4.4.1. Summary: reaction conditions

Granting that the plasma-derived catalysts were the most active in FTS, a study was conducted benchmarking them against the commercial nano-hematite (Fe-NanoCat®) catalyst

currently available in the market. Since the two single-metal catalysts (Co/C and Fe/C) that were synthesized through plasma were being projected for commercial application, they were tested in realistic LT-FTS conditions in a 3-φ-CSTSR operating at 493 K, 2 MPa pressure, and GHSV = 3 600 $cm^3.h^{-1}.g^{-1}$ of catalyst. A rundown of the findings is given below, with full account of the discussion provided in Appendix C (Aluha *et al*., 2016b).

4.4.2. Catalyst activity

The plasma-synthesized Co/C catalyst was observed to be comparatively more active and more stable online than the plasma-synthesized Fe/C catalyst. Catalyst activity decreased in the order of Co/C >> Fe-NanoCat® > Fe/C with their respective CO conversions being 42%, 32% and 25% as shown in Figure 4.7.

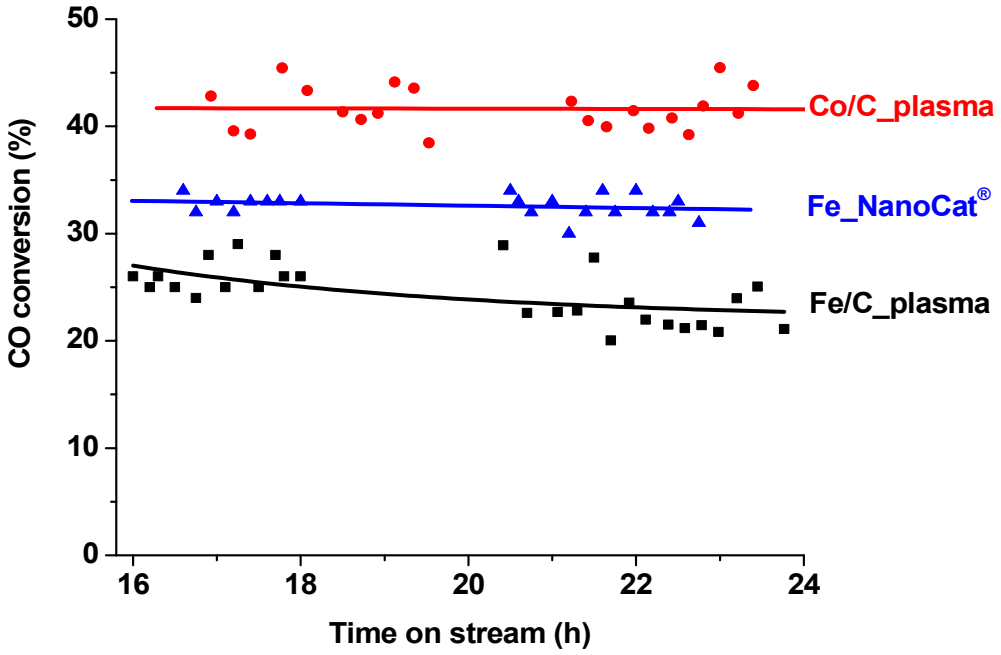

Figure 4.7 Catalyst activity of the plasma-synthesized Co/C and Fe/C tested for FTS at 493 K, 2 MPa, benchmarked against the commercial Fe-NanoCat®

4.4.3. Catalyst selectivity

For the targeted diesel fraction (C_{13}-C_{20}), catalyst selectivity decreased in the order of Fe/C >> Co/C > Fe-NanoCat® (with 51%, 31% and 22% respectively). Figure 4.8(a) shows the

product spectrum of the catalyst at 493 K, with ~95% selectivity towards hydrocarbon production (at >40% CO conversion). This differed sharply with the product spectrum obtained at 533 K as shown in Figure 4.8(b), which was obtained at almost total CO conversion, with combined selectivity of over 65% towards CH_4 and CO_2 alone. It was observed that the Fe/C catalyst at 55% CO conversion had a selectivity of 5% towards CH_4 and 15% towards CO_2 presumably due to WGS reaction. Compare it with the Co/C catalyst (at ~45% CO conversion), with selectivity of only 1% toward CO_2 at 493 K.

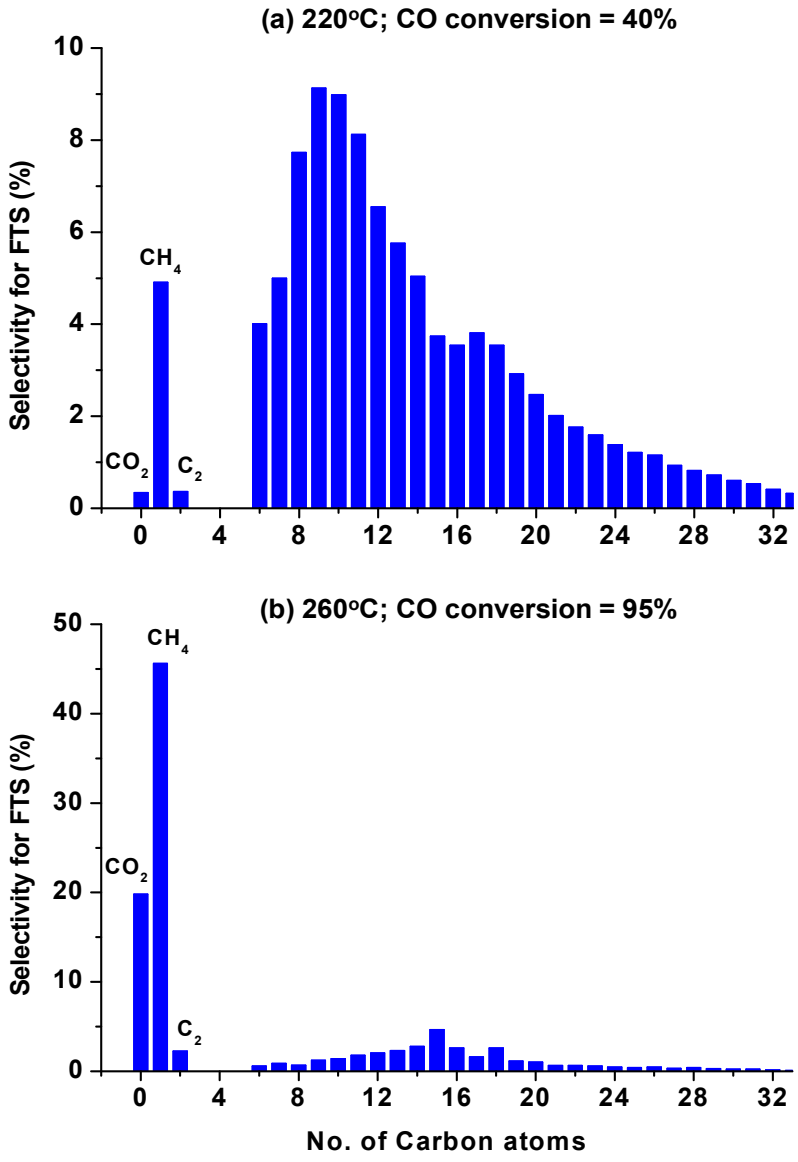

Figure 4.8 FTS product spectrum of Co/C catalyst at (a) 493 K, and (b) 533 K

4.4.4. ASF distribution

Figure 4.9 provides section extracts of a GC trace that demonstrates the progressive polymerization with TOS using the plasma synthesized Co/C catalyst in the liquid-phase. Two Co/C samples from the same batch were tested under similar reaction conditions (493 K, 2 MPa), indicated as run 1 shown in Figure 4.9 and run 2, whose data involving another sample test was graphically transmuted into Figure 4.10 that displays a shift in the FTS product distribution from the short-chain to longer chain hydrocarbons with TOS. Full details of this work can be found in the article presented in Appendix D (Aluha *et al*., 2017).

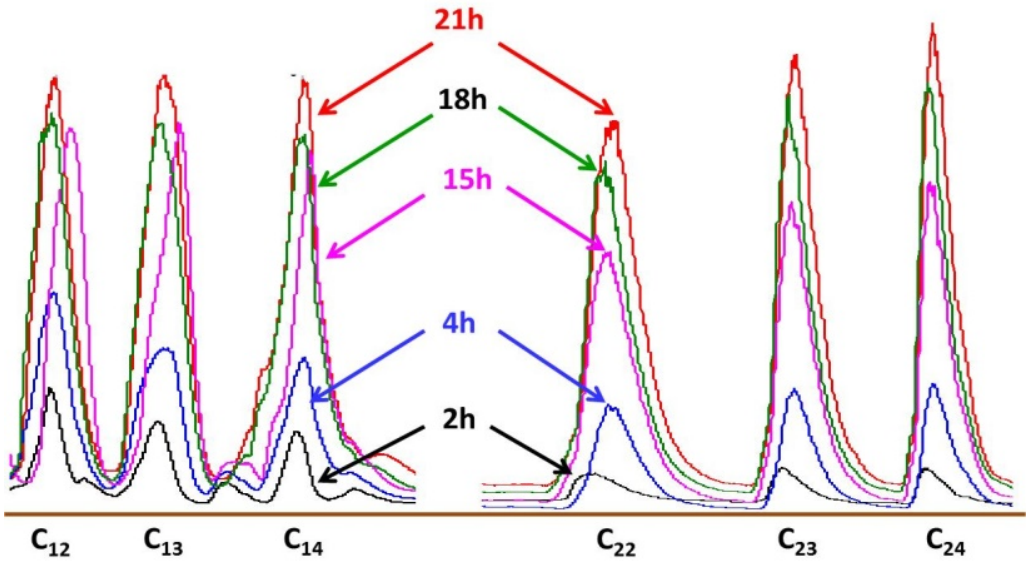

Figure 4.9 GC chart with overlaid spectra for the first Co/C sample (run 1) portraying gradual increase of FTS products with TOS

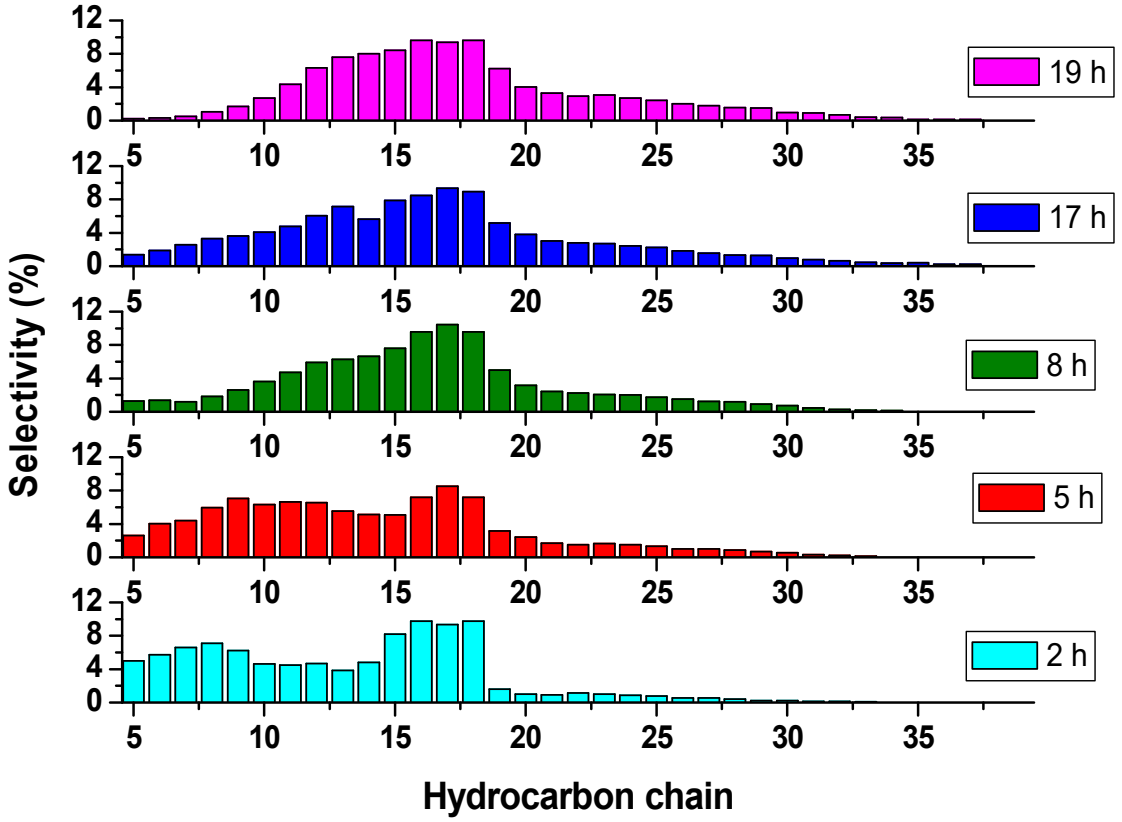

Figure 4.10 Liquid-phase analysis for the second Co/C sample (run 2) showing catalyst selectivity (at 493 K, 2 MPa pressure) at various TOS

Figure 4.11 provides the plots for $\log(M_n/n)$ vs. n in order to determine the α-value of the plasma-synthesized Fe/C and Co/C catalysts, which were found to match the commercial Fe-NanoCat® at high n values. Their α-values for $n \geq 10$ were identical, in the range of 0.83–0.86. Similarly, for hydrocarbon chains of carbon numbers between 8 and 16, the plasma-synthesized Co/C maintained its α-value of 0.83. However, the Fe-based catalysts gave a different impression, with the commercial Fe-NanoCat® exhibiting α-value of 0.71 as predicted in literature for the Fe-based catalysts, where $\alpha = 0.5–0.7$ (Dry, 1982), while the plasma-synthesized Fe/C, $\alpha = 1.00$.

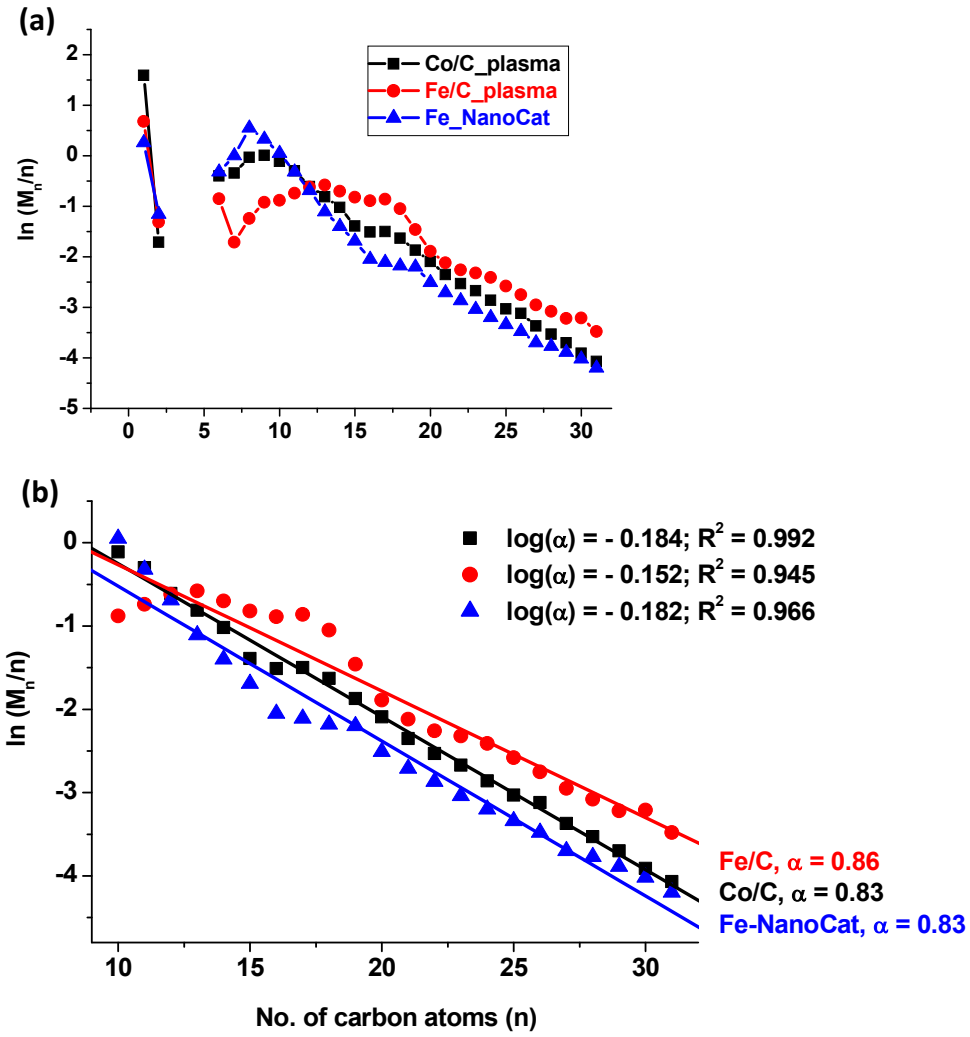

Figure 4.11 Plots of log (M_n/n) vs. n for (a) plasma-synthesized catalysts (Co/C and Fe/C) compared to commercial Fe/C, tested at 493 K, 2 MPa; and (b) with linear regression at high molecular weights

4.4.5. Effect of feed composition (H_2:CO ratio)

When various syngas compositions were applied, higher α-values were obtained from CO-rich feed streams, see Appendix D (Aluha *et al.*, 2017). Plots of log(M_n/n) against n generated for various H_2:CO ratios as shown in Figure 4.12 indicated that using CO-rich gases of H_2:CO ratio 1.0 or 1.5 results in high α-values (~0.93), although it came at the cost of low CO conversions of ~10% and ~20% CO conversion. This contrasted with the findings of using a H_2–rich feed stream (H_2:CO ratio = 2.0), which displayed lower α-value (~0.83), but at higher catalytic activity of ~40% CO conversion.

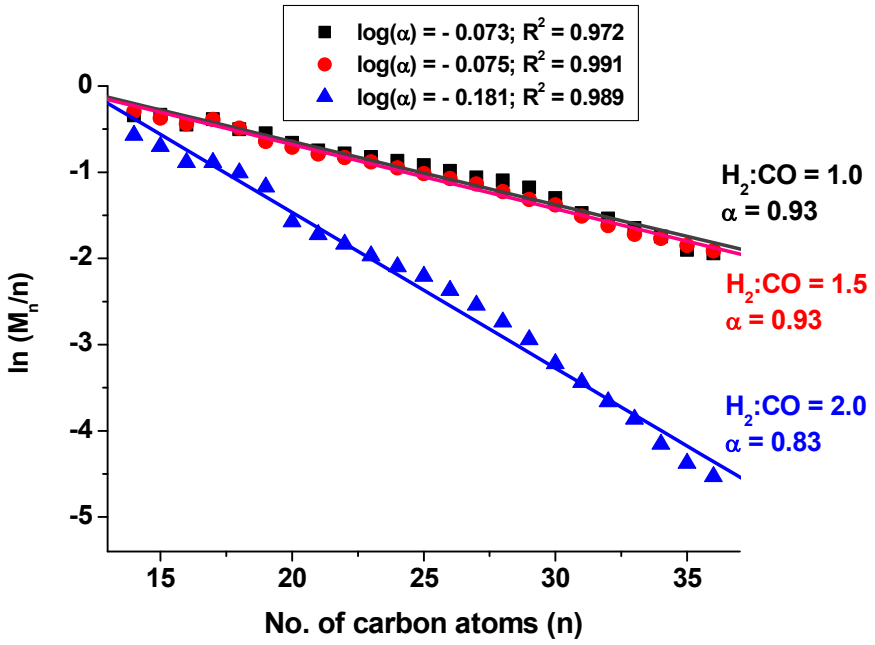

Figure 4.12 ASF distribution plots of the Co/C catalyst tested at 493 K, 2 MPa, displaying high α-values in CO-rich feed gases, but low α-values in H_2-rich feed gases after 24 h

4.5. The bimetallic effect: Co-Fe/C catalysts

Three bimetallic formulations, 30%Co-70%Fe, 50%Co-50%Fe and 80%Co-20%Fe were selected in order to test the hypothesis that the plasma-generated the 80%Co-20%Fe/C formulation was to exhibit unique properties while the other two 50%Co-50%Fe/C and 30%Co-70%Fe/C catalysts would contain identical intermetallic phases according to the Co-Fe binary phase diagrams (Okamoto, 2008). Results and a detailed discussion of the work on bimetallics is provided in Appendix E (Aluha and Abatzoglou, 2016), and Appendix F (Aluha *et al.*, 2015b), but here only highlights are provided.

4.5.1. Catalyst characterization

SEM imaging indicated uniform distribution of the metal moieties in all the samples. The gradual increase of the metal concentration in the materials is conspicuously evident in Figure 4.13; see the increasing red coloration for Co metal in the samples.

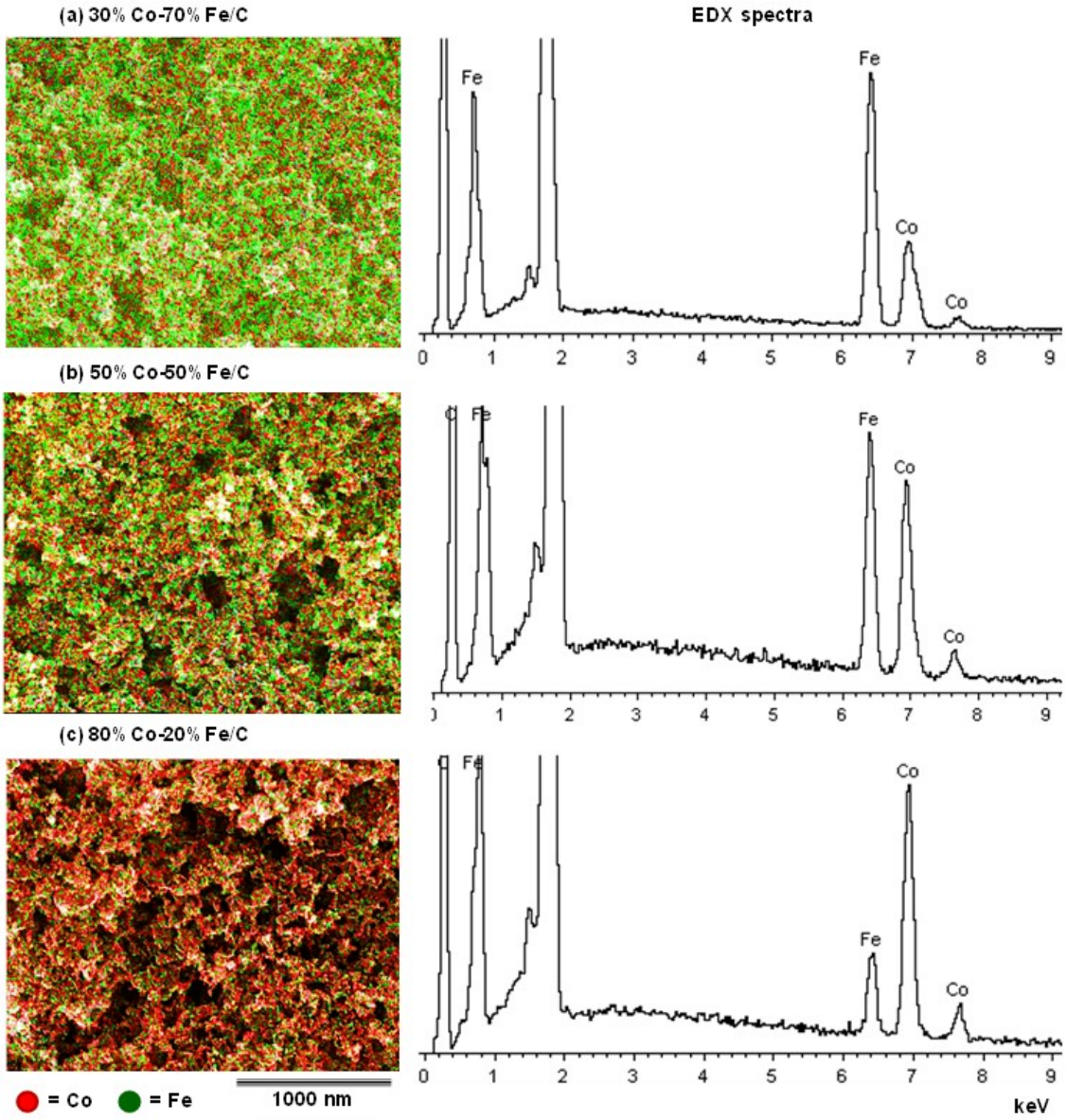

Figure 4.13 SEM imaging of Co-Fe/C bimetallics with EDX mapping

X-ray mapping by SEM analysis confirmed that the plasma-synthesized bimetallic catalysts were consistent in quality with the single metal Co/C and Fe/C catalysts as they equally showed high dispersion and uniform distribution of the metals in the carbon matrix. This observation was confirmed by EDX analyses, whose spectra are provided on the right with proportionate peak intensities appearing between 6 and 8 keV.

TEM imaging revealed some variation in the morphology of the three bimetallic catalysts. Figure 4.14 gives a sample micrograph of the plasma-synthesized 50%Co-50%Fe/C catalyst, while Figure 4.15 provides a summary of the particle size analysis in which 250 nanoparticles for each bimetallic sample were measured. The results indicated that both the 30%Co-70%Fe/C and 80%Co-70%Fe/C catalysts had similar nanoparticle distribution with a mean particle size of approximately 9 nm, with their respective standard deviation (**δ**) values being 3.2 and 3.4, while the 50%Co-50%Fe/C sample indicated a higher mean particle size of 14.4 nm, and it had a standard deviation of 5.0.

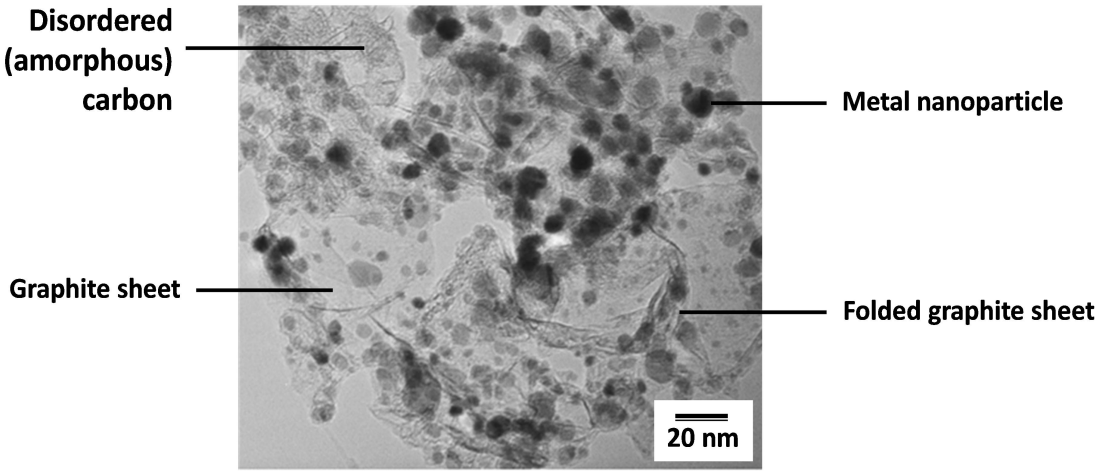

Figure 4.14 Sample TEM image for the 50%Co-50%Fe/C bimetallic catalyst

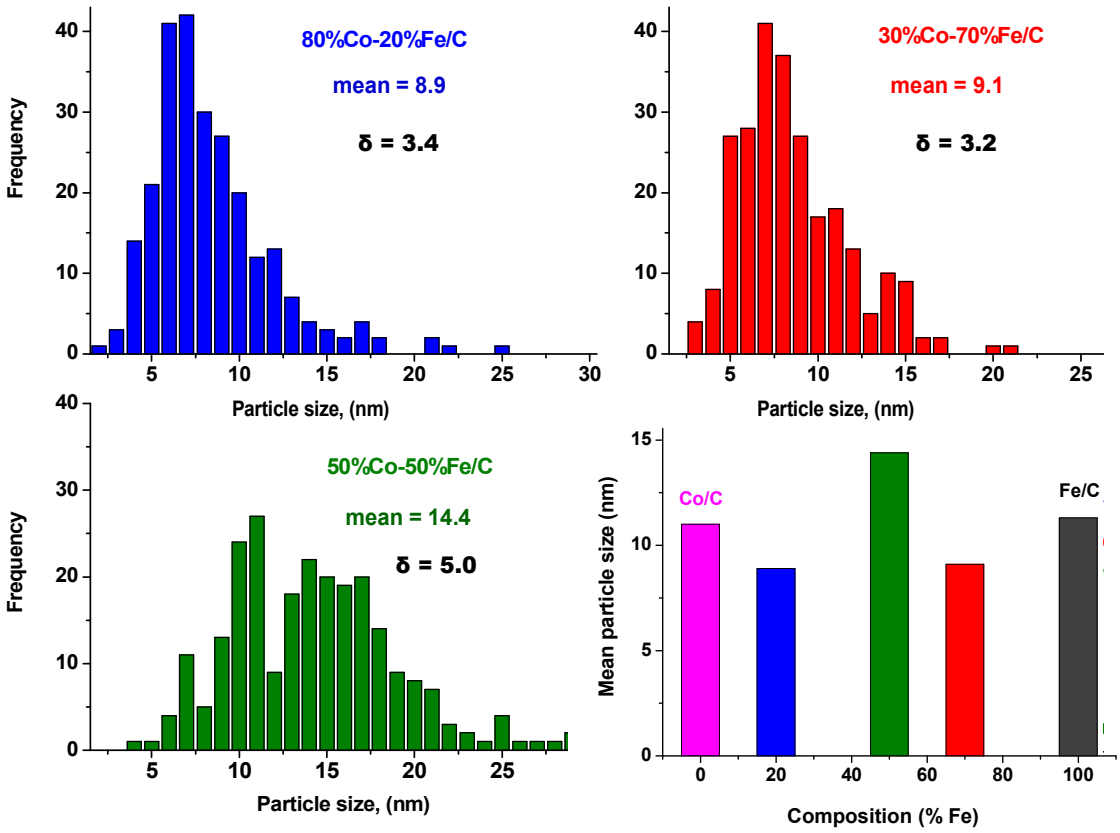

Figure 4.15 Particle size analysis by TEM imaging for the Co-Fe/C bimetallics

Analysis by XRD showed that all the Fe-containing catalysts had significant amounts of carbides (Fe_3C) as indicated by the major peak at 45° (2θ) angle, although the peak also overlapped with the cobalt's face centered cubic (FCC) and hexagonal close packing (HCP) peaks. Crystal planes of the CoFe (FCC) solid solution phase with reflections from their characteristic (111), (200) and (220) were observed at approximately [2θ] angles of 44°, 51° and 75°, respectively.

In addition, the (110), (200), (211) peaks of α-Co_7Fe_3 (BCC) phase were observed at about 45°, 66° and 84°, respectively (Lu *et al*., 2013). The Co_3Fe_7 seemed to share the same XRD peak positions with Co_7Fe_3 (Terakado *et al*., 2014). Figure 4.16 condenses phase analysis of the bimetallic samples by XRD, which shows overlaid XRD patterns of the bimetallics in comparison to the single Co/C and Fe/C catalysts as well as the corresponding pure metals that were injected into the plasma.

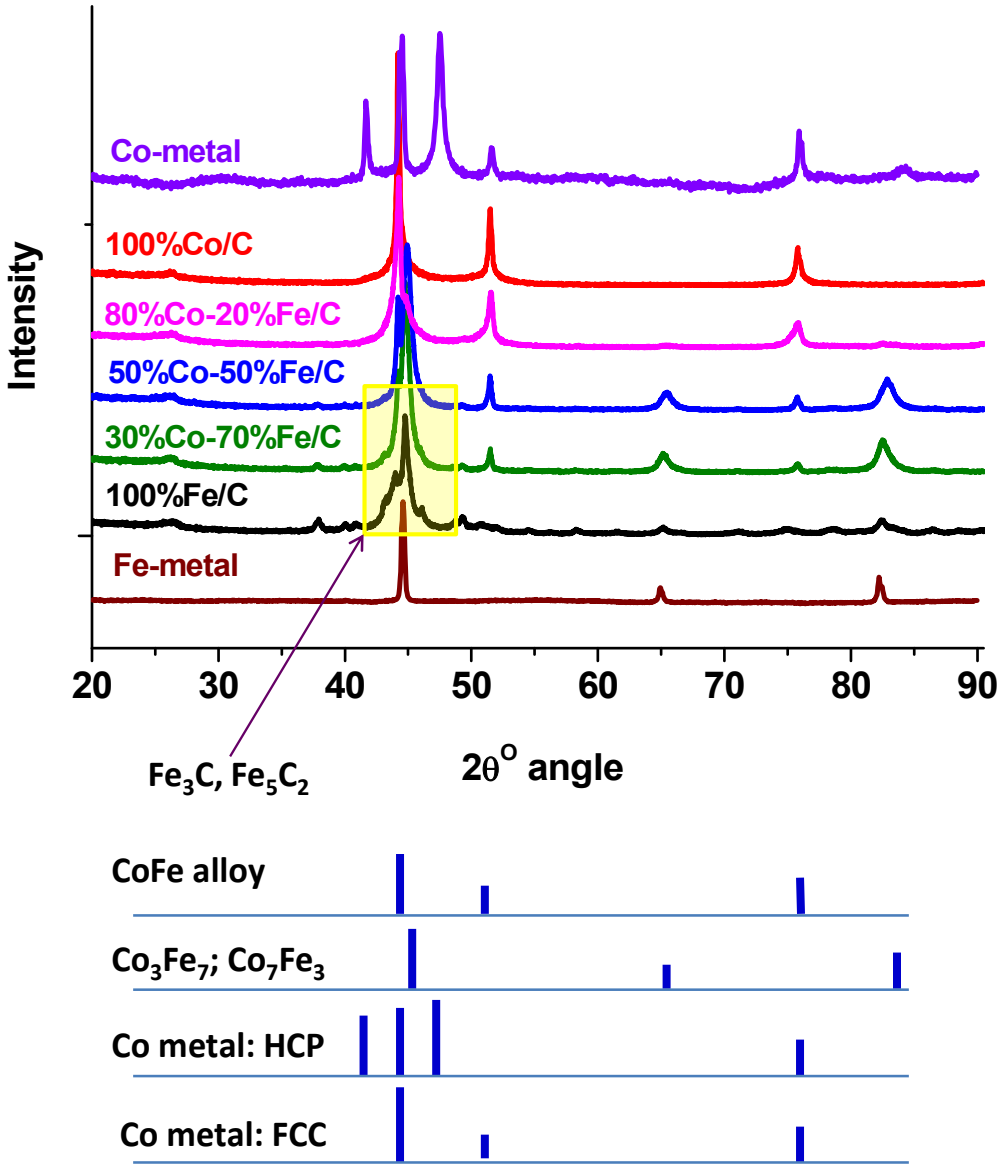

Figure 4.16 XRD patterns of the Co-Fe/C bimetallics compared to the single metal Co/C and Fe/C catalysts

Table 4.1 summarizes the RQA data of the species identified in bimetallic samples, which were benchmarked against the single-metal catalysts. The analysis indicated that each of those samples composed numerous phases, some of which could not be quantified fully. The residuals and pictorial results of the single metal Co/C, Fe/C catalysts and the Co-Fe/C bimetallics by RQA are attached in Appendix G.

Table 4.1 Summary Rietveld Quantitative Analysis (RQA) results by XRD

Properties	Catalyst composition				
Expected composition	**0% Fe**	**20%Fe**	**50%Fe**	**70%Fe**	**100%Fe**
Co_3C	6.7 (1)*	-	-	-	-
Fe_3C	-	5.3 (4)	6.6 (1)	8.9 (1)	26.0 (1)
Graphite-2H	54.1 (1)	27.0 (1)	29.0 (1)	32.0 (1)	40.0 (3)
Co (metal)	39.2 (2)	57.0 (1)	12.2 (1)	8.5 (2)	-
Fe (metal)	U^{∞}	3.5 (2)	27.0 (1)	25.0 (1)	34.0 (3)
FeCo intermetallic	-	11.0 (1)	25.0 (2)	25.0 (1)	-
R_{exp} (expected)	8.31	9.26	9.12	9.2	8.31
R_p (profile)	7.97	10.85	8.99	8.49	7.97
R_{wp} (weighted-profile)	10.50	14.39	12.48	11.69	10.50
GOF	1.60	$2.41^{\#}$	1.87	1.61	1.59

*6.7(1) = means phase composition = 6.7%; estimated standard deviation = 1;

U^{∞} = unquantifiable; beyond instrument's detection limits;

$GOF^{\#}$ = goodness of fit (χ^2) = $(R_{wp}/R_{exp})^2 \approx 1$; a value higher than 2 is unacceptable.

4.5.2. Catalyst performance in FTS

At 533 K, both the single metal and bimetallic catalysts showed good activity including total CO conversion for the Co/C catalyst, see Figure 4.17. However, poor selectivity disqualified the use of single metal Co/C catalyst at higher temperatures, while the Co-Fe/C bimetallics were almost inert at 493 K. Figure 4.18 summarizes the results comparing these materials at both 493 and 533 K.

When compared to the most active single-metal Co/C catalyst, it was observed that not only did the presence of Fe suppress the production of both CO_2 and CH_4 in the Fe-containing catalysts, but it also constrained H_2O formation. This revealed the beneficial impact Fe had in the catalysts, such that the more Fe there was, the less H_2O it generated. However, the lower temperature was most conducive for the selectivity of Co/C catalyst towards the gasoline (C_4–C_{12}) and diesel (C_{13}–C_{20}) fractions, since production of undesired products such as CO_2 and CH_4 was only prevalent at higher temperatures. Further discussion on bimetallics may be found in the published articles provided in Appendix E (Aluha and Abatzoglou, 2016), and in Appendix F (Aluha *et al.*, 2015b).

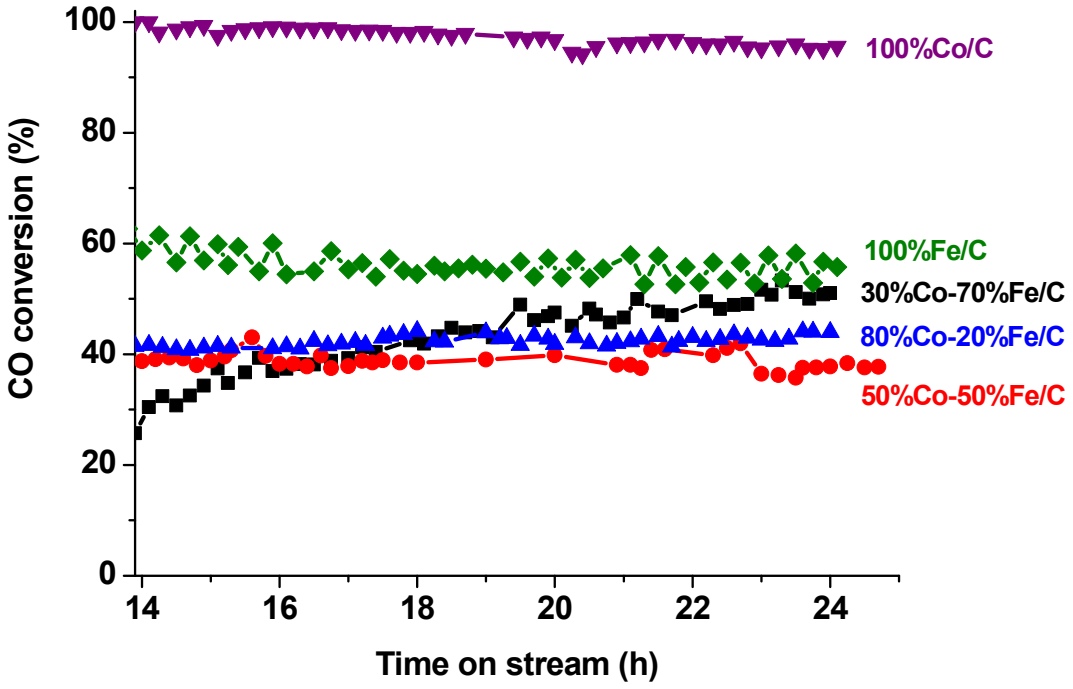

Figure 4.17 Activity plots for plasma-synthesised Co/C and Fe/C catalysts compared to the bimetallic Co-Fe/C catalysts tested at 533 K for 24 h

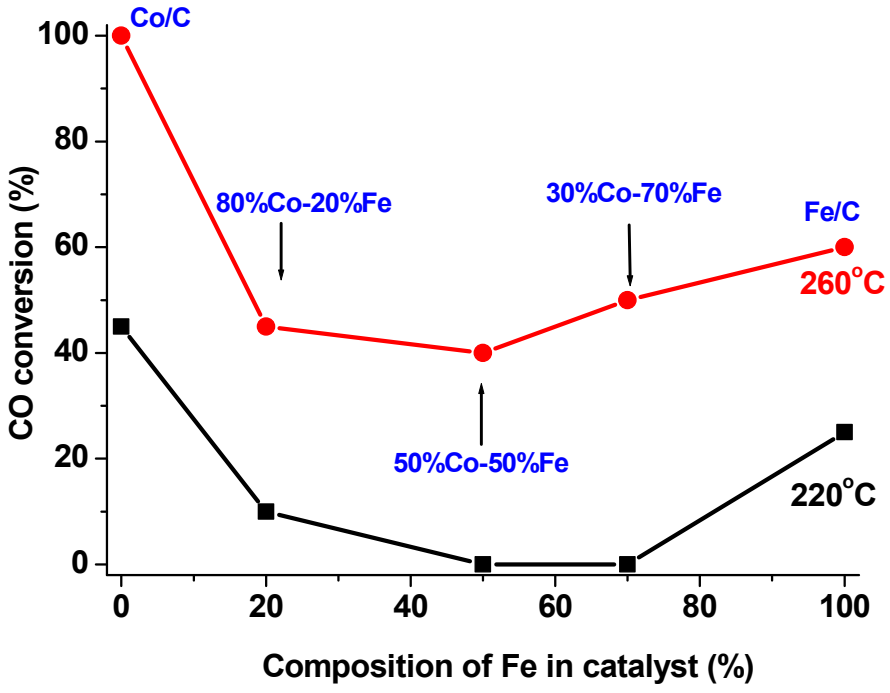

Figure 4.18 Activity plots for the plasma-synthesised catalysts with various metal compositions tested at 493 and 533 K (220° and 260°C)

4.6. Catalyst pre-treatment: H_2 versus CO

Catalyst activity of the Co-Fe/C bimetallics was compared with the *in situ* pre-treatment of the materials in two different reducing gases, H_2 or CO at 673 K for 24 h and details of the findings are discussed in Appendix E (Aluha and Abatzoglou, 2016), and a summarized version of the findings is provided in sections that follow.

4.6.1. Catalyst characterization

TEM images showed that the morphology of catalysts reduced in H_2 remained the same before and after FTS reaction (at 533 K for 24 h), while significant but identical changes were observed in the morphology of all the catalysts that were reduced in CO as indicated in the TEM image of Figure 4.19, with CNFs perceived to be growing away from the metal centres. Such growth in carbon nanotube (CNT) production is normally induced by metal oxide centres (Gore and Sane, 2011), which may be likened to the catalytic chemical vapour deposition of Ni-activated growth of CNFs. Similar structures have been described more effectively as the multi-wall carbon nanotubes (MWCNTs) (Tehrani *et al*., 2014).

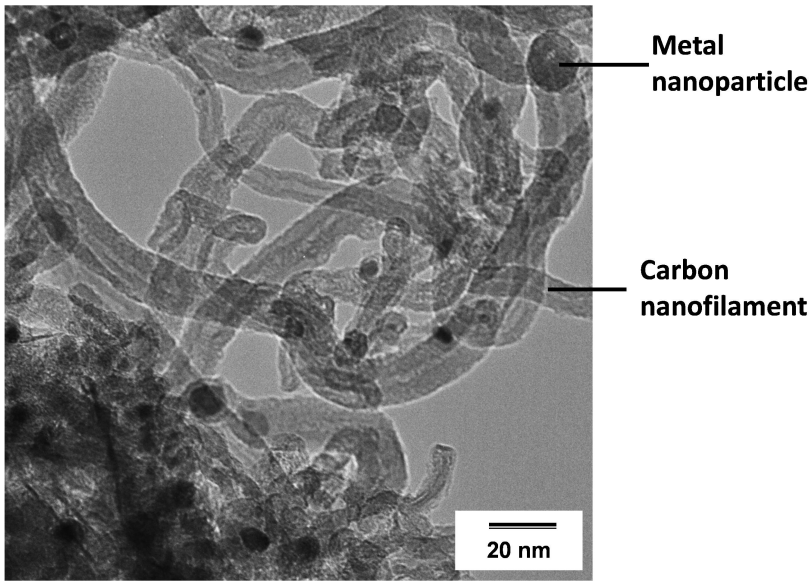

Figure 4.19 A TEM image of the CO pre-treated catalyst

XRD analysis alluded to the total absence of metal oxides and Co carbides in all the used samples, even after 24-h carburization with CO and a further 24 h in the presence of the CO-rich FTS feedstock (*ca*. 30% CO). This implies that plasma-synthesized catalysts may be resistant to deactivation notwithstanding the fact that thermodynamically, oxidation of the metal nanoparticles to form Co_3O_4 or Fe_3O_4 is highly favoured, and would lead to irreversible catalyst deactivation. The full discussion to this work is found in the article provided in Appendix E (Aluha and Abatzoglou, 2016).

4.6.2. Catalyst performance in FTS

All catalysts pre-treated in CO had identical activity of approximately 40% CO conversion at 533 K, and Figure 4.20 shows that their selectivity shifted towards the production of the diesel-range fractions.

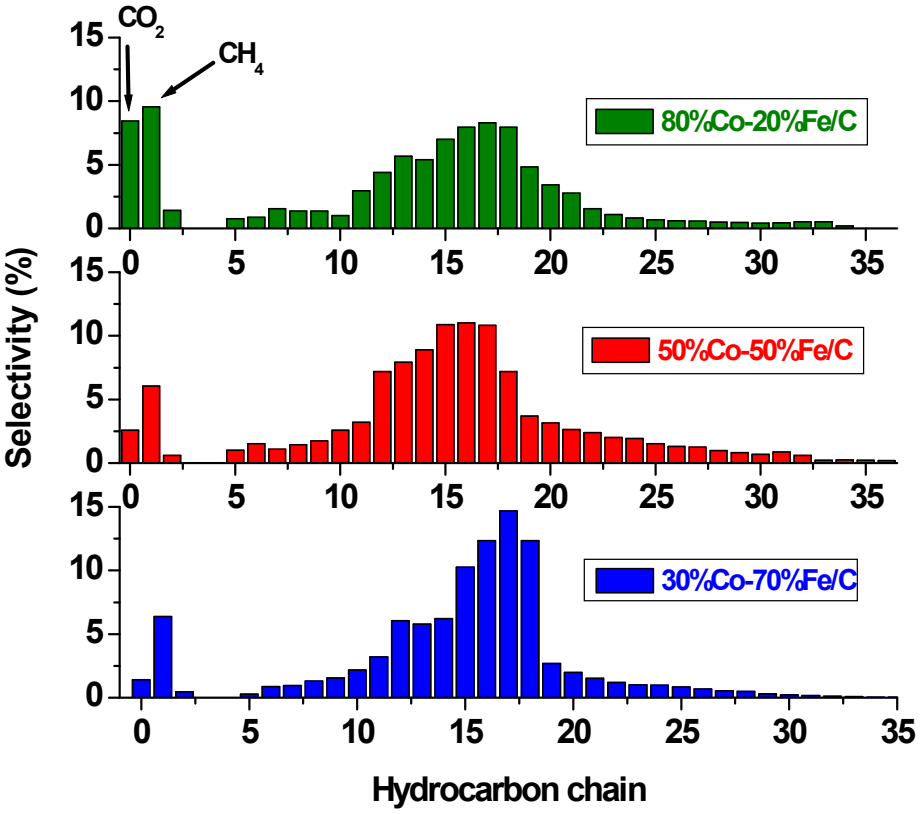

Figure 4.20 Product spectrum of Co-Fe/C bimetallic catalysts pre-treated in CO and tested at 533 K, 2 MPa

Increasing the Fe content in Co-rich catalysts diminished H_2O production by almost half in some case, when compared to H_2-reduced catalysts. However, H_2O production capacity was almost comparable in all CO-reduced catalysts. See details in Appendix E.

4.7. Promotional effect of Au, Ni and Mo in Co-Fe/C catalysts

A comparative study was carried out collating the catalytic performance and properties of the 80%Co-20%Fe/C catalyst with its corresponding promoted catalysts using either 10%Mo or 10%Ni and in this work, they are designated as Mo-Co-Fe/C and Ni-Co-Fe/C respectively. Details of this investigation have just been accepted for publication and the submitted manuscript before proofreading can be found in Appendix H (Aluha and Abatzoglou, 2017b). On the other hand, the Ni-Co-Fe/C was further modified by lowering the metal mass loading from 10%Ni to 5%Ni and then doping it with 5%Au. This formulation was designated as Au-Ni-Co-Fe/C, and a complete description of this work is currently under review. The original (unedited) manuscript is provided in Appendix I (Aluha and Abatzoglou, 2017a).

4.7.1. Catalyst characterization

Table 4.2 is a summary of the porosity measurements of all the materials under this investigation. Plotting the BET specific surface areas against increasing metal content, generally takes the shape of a crescent, with the single metal catalysts having lower surface areas than their bimetallic or ternary counterparts. Small pore volumes (*ca*. 0.4 $cm^3.g^{-1}$) alluded to the non-porous nature of all the plasma-synthesized materials.

In FTS, non-porous catalysts are recommended for eliminating diffusion limitations because porous materials inhibit mass transfer of high molecular-weight products, which clog the pores, eventually resulting in catalyst deactivation (Aluha *et al.*, 2016b). Figure 4.21 shows the identical nature of the plasma-synthesized catalysts (comparing bimetallic Co-Fe/C with ternary Mo-Co-Fe and Ni-Co-Fe) using the overlaid adsorption-desorption isotherms originating from N_2 physisorption tests.

Table 4.2 Porosity analysis of the catalyst materials by the BET method

Catalyst (expected composition)	BET Surface area ($m^2.g^{-1}$)		Average pore diameter (nm)*		Average pore volume ($cm^3.g^{-1}$)#	
	Auxiliary reactor	Main reactor	Auxiliary reactor	Main reactor	Auxiliary reactor	Main reactor
100%Co/C	55.5	54.4	27.4	28.3	0.38	0.39
80%Co-20%Fe/C	67.2	72.8	24.4	22.0	0.41	0.42
70%Co-20%Fe-10%Mo/C	85.0	77.0	25.5	22.5	0.54	0.43
70%Co-20%Fe-10%Ni/C	69.2	76.3	25.8	19.3	0.45	0.37
70%Co-25%Fe-5%Ni/C	92.6	88.7	20.6	19.1	0.48	0.42
50%Co-50%Fe/C	92.2	73.3	22.3	20.8	0.51	0.38
30%Co-70%Fe/C	91.1	73.1	22.6	18.9	0.51	0.34
100%Fe/C	72.2	35.4	21.6	32.6	0.40	0.28

* Single point adsorption total pore volume of pores less than 120 nm in diameter at P/Po = 0.98

Average pore diameter (4V/A by BET)

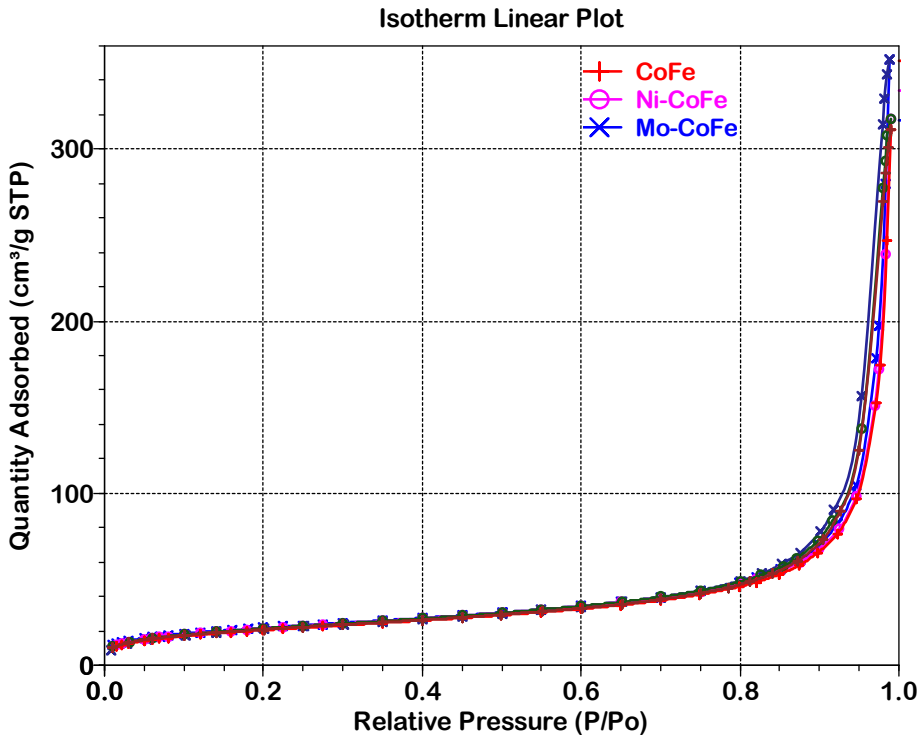

Figure 4.21 Overlaid isotherms of bimetallic and ternary catalysts collected from the main plasma reactor

Figure 4.22 indicates SEM imaging coupled with elemental X-ray mapping of the Ni-promoted catalysts. Notice the evidence of increasing blue coloration from 5-wt% Ni to 10-wt% Ni by mass-loading, proving the uniform metal dispersion in the carbon matrix. This was confirmed by TEM imaging because Figure 4.23 shows that no major variation existed between the metal dispersion in the two Ni-containing samples. Similarly, the used catalysts indicated very little transformation in the morphology of the metal nanoparticles even after over 50 h of thermal exposure as depicted by the TEM images in Figure 4.24. Normally, the mean metal nanoparticle size is in the range of 9–11 nm for the freshly synthesized samples. It was observed that by counting 250 nanoparticles per sample, the mean size for the used 10%Mo-70%Co-20%Fe/C catalyst was 9.7 nm, while for the used Au-promoted Ni-based catalyst, that is, 5%Au-[5%Ni-70%Co-20%Fe/C], the mean particle size was 11.0 nm.

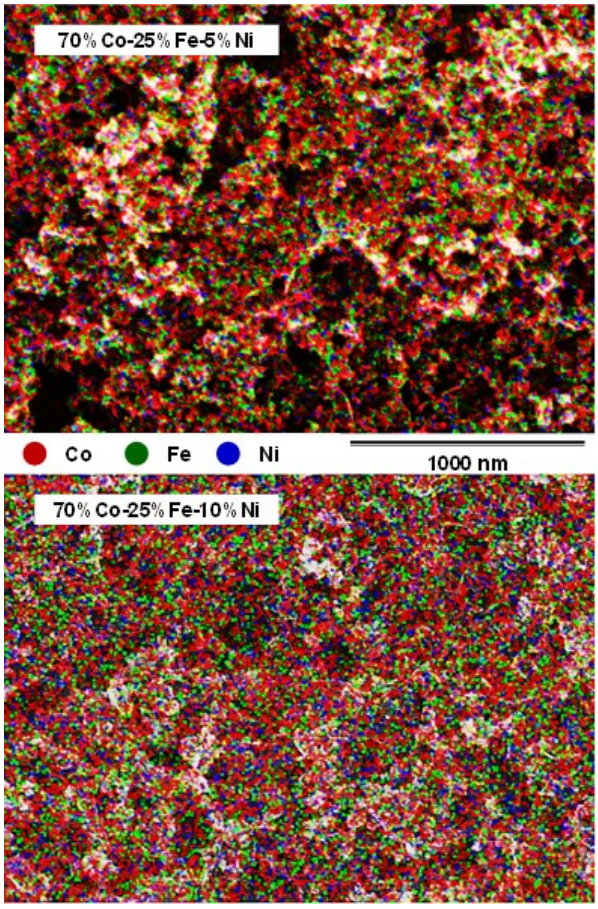

Figure 4.22 X-ray imaging of the fresh Co-Fe-Ni ternary catalysts by SEM indicating uniform metal dispersion

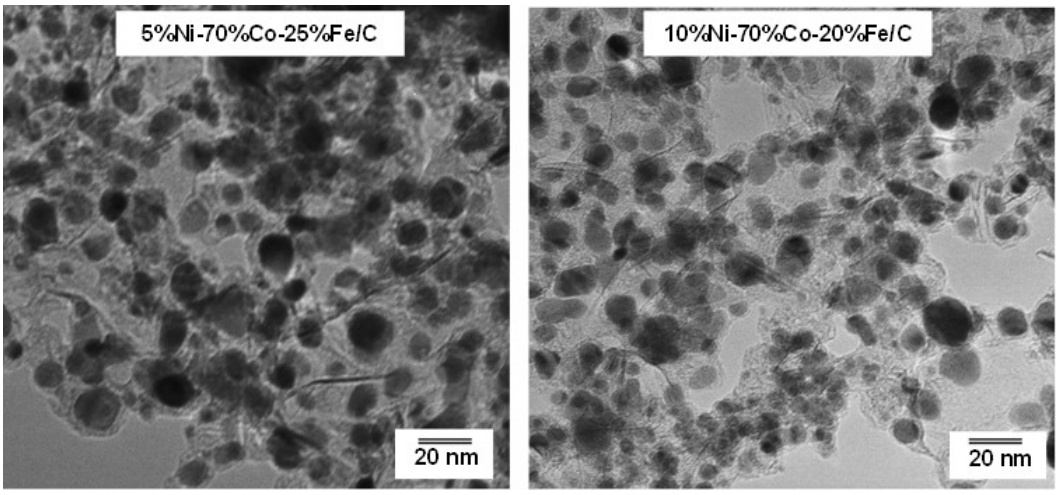

Figure 4.23 TEM images of fresh Ni-Co-Fe ternary catalysts

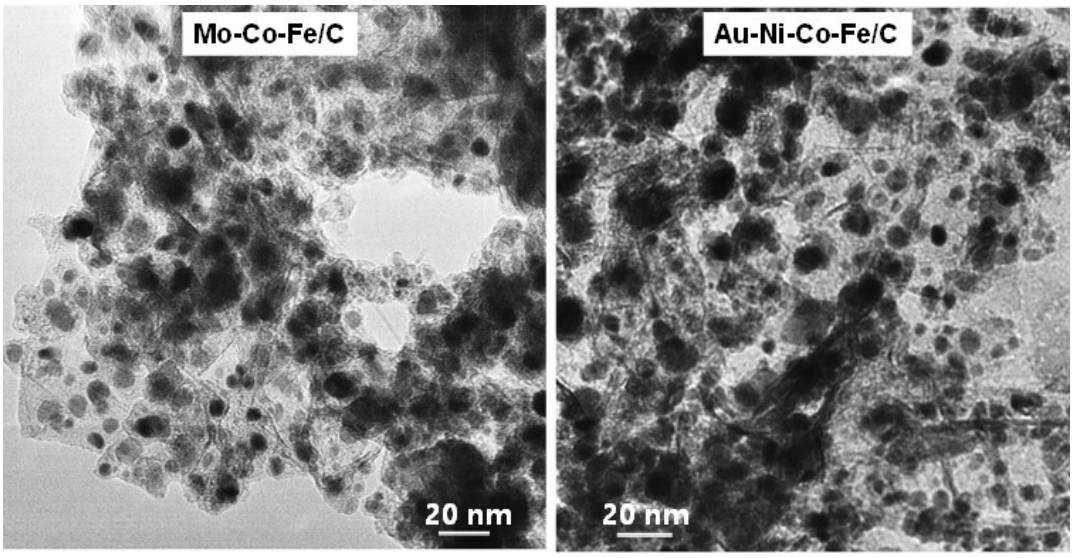

Figure 4.24 TEM images of used (a) Mo-Co-Fe/C, and (b) Au-promoted Ni-Co-Fe/C

4.7.2. Catalyst performance in FTS

Figure 4.25 portrays the activity of H_2–reduced ternary metal catalysts, benchmarked against the bimetallic 80%Co-20%Fe/C catalyst, while Figure 4.26 displays the corresponding selectivity of the given catalysts. It was observed that the Ni-Co-Fe/C formulation had the highest activity of ~90% CO conversion at 533 K, which dropped to ~60% upon addition of 5%Au on the 5%Ni-70%Co-20%Fe/C sample. The least active catalyst was the Mo-Co-Fe/C formulation with ~38% CO conversion.

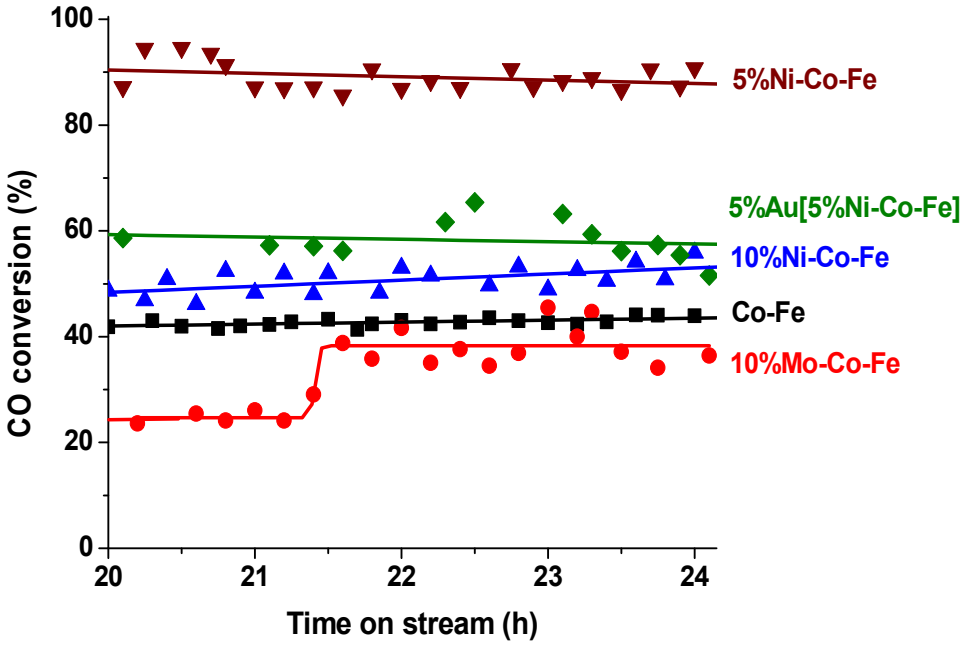

Figure 4.25 Activity plots (a) 80%Co-20%Fe/C; (b) 10%Mo-Co-Fe/C; (c) 10%Ni-Co-Fe/C; (d) 5%Ni-Co-Fe/C; and 5%Au-5%Ni-Co-Fe/C, tested at 533 K, 2 MPa

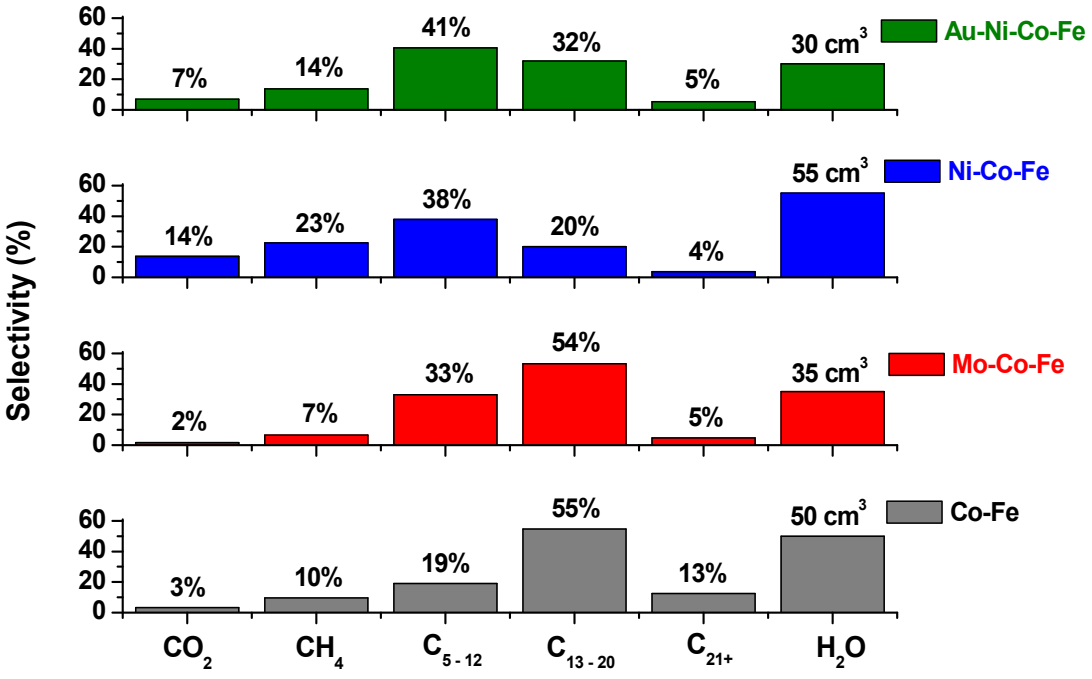

Figure 4.26 Plots comparing FTS fraction distribution for (a) 80%Co-20%Fe/C; (b) 10%Mo-Co-Fe/C; (c) 5%Ni-Co-Fe/C; and 5%Au-5%Ni-Co-Fe/C catalysts after 24 h of reaction at 533 K, 2 MPa

Although the Ni-promoted catalyst was very active, it was highly selective for CH_4 (23%). The addition of Au to the catalytic system significantly impacted the selectivity of the catalyst in the S_{fuel} range because it resulted in higher diesel production (from 20% to 32%). However, both catalysts produced gasoline-rich fractions (with 38% for Ni-Co-Fe, and 41% for Au-Ni-Co-Fe).

On the other hand, the addition of Mo to the Co-Fe bimetallic led to the production of a diesel-rich fraction, but at a lower CO conversion. Our findings are in agreement with other authors who observed that addition of Mo decreased the FTS activity of the Fe catalyst, but markedly enhanced the C_{12+} hydrocarbon selectivity (diesel fraction), while suppressing the C_2–C_8 hydrocarbon selectivity (Qin *et al*., 2009).

In 24 h, the Ni-Co-Fe/C sample produced the most H_2O (55 cm^3), at 90% CO conversion, while Au-Ni-Co-Fe/C formed only 30 cm^3 at 60% CO conversion, and 35 cm^3 for Mo-Co-Fe at 38% CO conversion. It was anticipated that promoting a catalyst with both of them could produce synergies where close proximity of Au-Ni to Fe_2O_3 in the sample would enhance LT-WGS reaction (Venugopal *et al*., 2003b).

In addition, Au was expected to prevent catalyst oxidation by enhancing the reducibility of the metals in the catalysts, because in commercial applications FTS catalysts that effectively suppress excessive H_2O production and remain in metallic state would be very attractive. Moreover, the acidic properties of Mo were understood to improve catalyst selectivity for the diesel fraction (Jong and Cheng, 1995).

Although a plasma-synthesized Co-Fe/C bimetallic catalyst promoted with Au, Mo or Ni has not been reported in literature, our preliminary analysis still found such materials promising for FTS. We therefore concluded that catalytic activity can still be improved by careful optimization of the pre-treatment procedure. Nonetheless, we observed that the presence of Ni enhanced lower molecular weight hydrocarbons with considerable CH_4 production, while surface acidity (from Mo) improved selectivity towards the gasoline fraction, and the presence of Au in the Ni-Co-Fe/C catalyst lowered H_2O generation.

4.7.3. ASF distribution

Figure 4.27 shows the determination of the catalysts' α-values, which were found to be above 0.81 at high C-numbers (C_{10+}), although the Co-Fe/C bimetallic had a higher value of 0.84. Addition of Ni to the Co-Fe/C catalyst, had no apparent impact, but addition of either Mo or Au lowered the α-value to 0.81. This means that higher production of the light hydrocarbons would be expected from the Mo- and Au-containing catalysts. The hump at around C_{16} is due to hexadecane solvent interference.

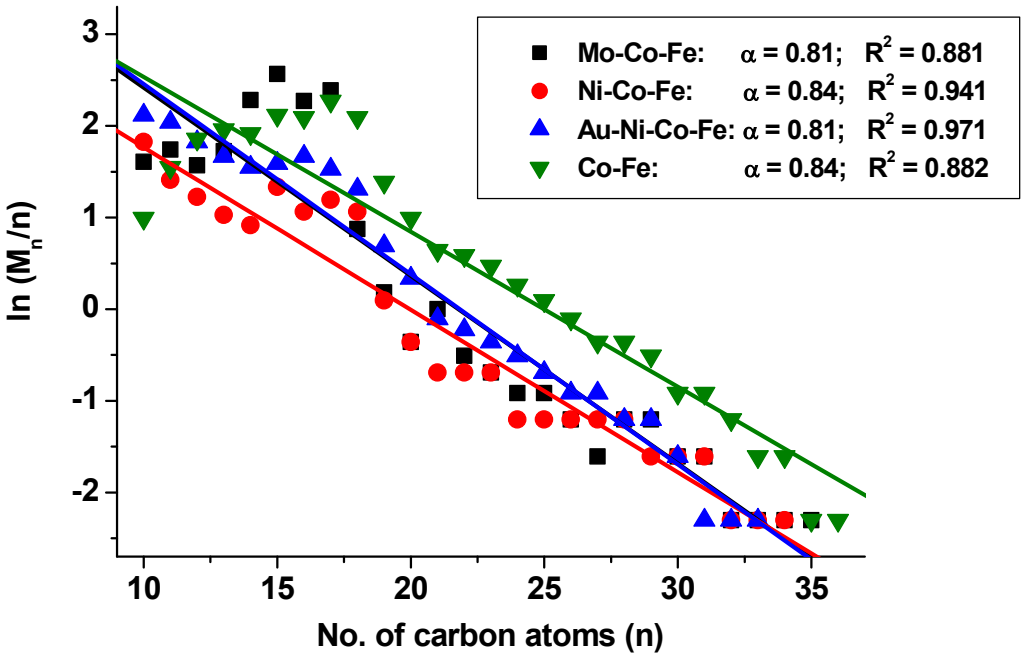

Figure 4.27 Graphical determination of α-values for Co-Fe/C catalyst promoted with Au, Mo and Ni tested at 533 K, 2 MPa

However, at lower C-numbers (C_{5-12}), all the promoted catalysts, that is, those containing Au, Mo or Ni far and above the Co-Fe/C bimetallic catalyst showed enhanced production of lower molecular weight hydrocarbons in the gasoline range with substantial amounts of CH_4 when compared to the Co-Fe/C bimetallic catalyst.

4.8. Mass balance determination

4.8.1. Determination of H_2 efficiency by water measurement

Since our analytical instruments do not discriminate between the various hydrocarbon groups, it was assumed that the principal product of this analysis was the alkene, (C_nH_{2n}) with the co-production H_2O, which is measurable. In applying this simple approach to estimate the catalytic behaviour of each catalyst with respect to H_2 consumption, without going into the complexities of FTS reaction such as the consequences of WGS reaction, the amount of H_2O formed was split in the same proportions as they appear in the selectivity data between CH_4 on one hand and overall FTS products (C_{5+}) on the other. Therefore, Figure 4.28 exemplifies a sample calculation performed using the bimetallic Co-Fe/C catalyst data (Aluha and Abatzoglou, 2017b).

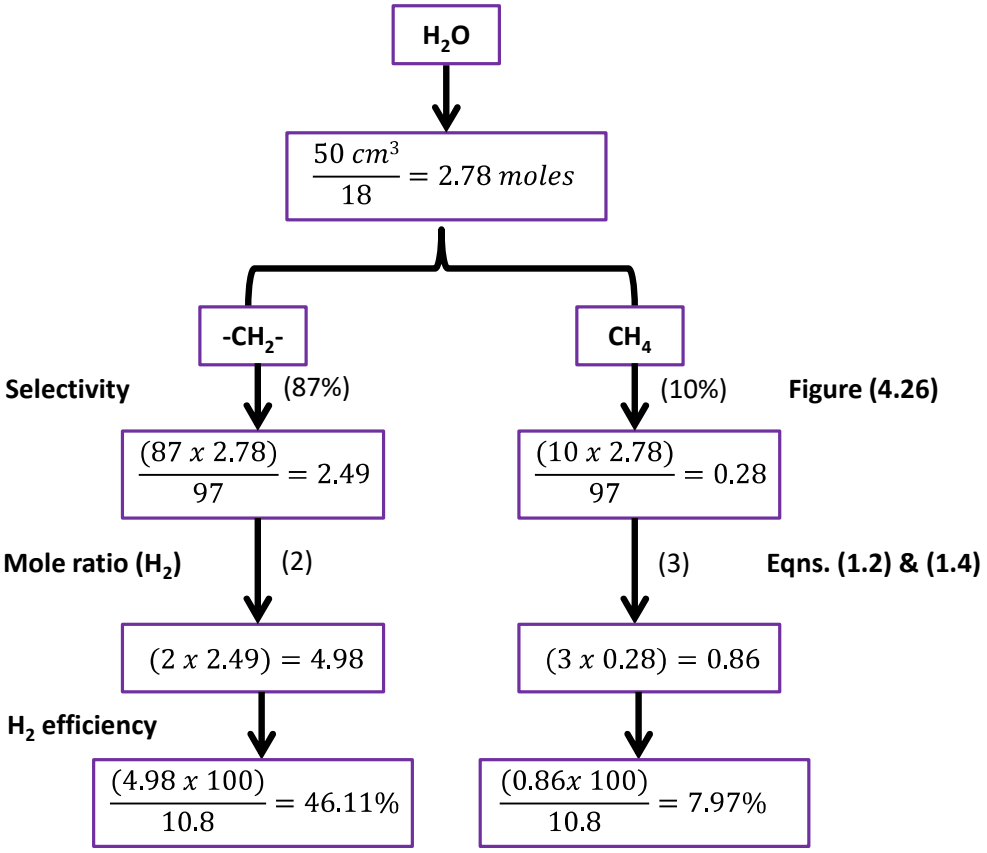

Figure 4.28: Sample calculation to determine the H_2 efficiency of the 80%Co-20%Fe/C catalyst after 24 h of reaction

Table 4.3 provides summary calculated results of all the nine plasma-synthesized catalysts. The total amount of H_2 gas that was delivered in the 24-h experiment was equivalent to 10.8 moles = (300 $cm^3.min^{-1}$) x (60% H_2) x (60 min.) x (24 h)/(24 000 cm^3 at RTP). From these findings, it was observed that at 260^oC, the ternary Mo-Co-Fe/C was the most H_2 efficient catalyst competing favourably with the Fe/C although the Mo-containing sample had a lower CO conversion. This implies that for every CH_4 molecule produced, there were ten -[CH_2]- monomers added to the hydrocarbon-growth chain in the Mo-Co-Fe/C formulation. The least H_2 efficient catalyst was the single-metal Co/C formulation, which produced two CH_4 molecules, for every one -[CH_2]- monomer. This performance was followed by the Ni-containing samples and amongst the bimetallic samples, the best performance was displayed by the 30%Co-70%Fe/C formulation.

4.8.2. Calculation of mass balance

Table 4.4 indicates the mass balance of the samples from the calculated and raw data of the H_2 and CO_2 gases exiting the FTS reactor. Fe-rich catalyst samples (comprising 100%Fe/C, 30%Co-70%Fe/C and 50%Co-50%Fe/C) had higher X_{CO} : X_{H2} ratios given as 3.0, 2.7 and 1.6 respectively. The same catalysts produced the minimum amount of H_2O possibly due to enhanced WGS reaction that generates surplus H_2 in the system. This makes it may seem like less of the H_2 feedstock is consumed. When the amount of H_2 exiting the reactor was added to that used in the FTS reaction, the mass balance was approximately 90+% in all cases. By subtracting the conversion of H_2 from that of CO one could estimate the effect of WGS reaction due to H_2 formation while concurrently generating equimolar amounts of CO_2. In this regard, some catalysts such as the 80%Co-20%Fe/C, 5%Ni-Co-Fe/C, 5%Au-Ni-Co-Fe/C and the Co/C indicated a close relationship while all the other formulations did not. Incidentally, the former had X_{CO} : X_{H2} ratios below 1.2.

Table 4.3 Determination of the H_2 efficiency per catalyst at 260^{0}C, 2 MPa

Catalyst	CO conversion, X_{CO} (%)	H_2O produced		Selectivity (%)		H_2 efficiency (%)		
		(cm^3)	moles	C_{5+}	CH_4	C_{5+}	CH_4	$[C_{5+}]:CH_4$
Co/C	100	40	2.22	32	46	17	36	0.5
Fe/C	60	30	1.67	83	5	29	3	9.7
30%Co-70%Fe/C	50	25	1.39	84	7	24	3	8.0
50%Co-50%Fe/C	40	30	1.67	81	10	28	5	5.6
80%Co-20%Fe/C	42	50	2.78	87	10	46	8	5.8
10%Mo-Co-Fe/C	38	35	1.94	91	6	33	3	10.0
10%Ni-Co-Fe/C	50	40	2.22	78	14	35	9	3.9
5%Ni-Co-Fe/C	89	55	3.06	62	23	41	23	1.8
5%Au-Ni-Co-Fe/C	60	30	1.67	78	14	26	7	3.7

Table 4.4 Mass balance determination from the H_2 efficiency per catalyst at 260°C, 2 MPa

Catalyst	Conversion, X (%)			Mass balance, H_2 (%)		Mass balance, CO_2 (%)	
	X_{CO}	X_{H2}	X_{CO} : X_{H2} ratio	F_{exit} (GC)*	Total (X_{H2} + F_{exit})	F_{exit} (GC)	(X_{CO} – X_{H2})
Co/C	100	86	1.16	12	98	20	14
Fe/C	60	20	3.00	67	87	11	40
30%Co-70%Fe/C	50	22	2.72	65	87	7	28
50%Co-50%Fe/C	40	25	1.60	62	87	10	15
80%Co-20%Fe/C	42	38	1.18	52	90	3	4
10%Mo-Co-Fe/C	38	27	1.41	62	89	2	11
10%Ni-Co-Fe/C	50	33	1.52	56	89	9	17
5%Ni-Co-Fe/C	89	78	1.14	20	98	12	11
5%Au-Ni-Co-Fe/C	60	51	1.18	49	100	7	9

* F_{exit} (GC)* = the measured residual gas concentration at the GC effluent

5. DISCUSSION

5.1. Evaluation of project objectives and hypotheses

5.1.1. Project objectives

Since the key objective of this work was to discover novel, yet highly active FTS catalysts that could find future commercial application, we accomplished this task by relying on the idea that was already established in synthesizing the single-metal Fe/C catalyst by SPS technology (Blanchard *et al*., 2010). Below are eight new catalysts that were successfully synthesized through plasma and are considered to be highly effective for FTS:

(i) 1 single-metal Co/C catalyst;

(ii) 3 Co-Fe/C bimetallics (containing 30%Co, 50%Co and 80%Co);

(iii) 3 ternary systems with Ni (5% or 10%), or Mo (10%) in 70%Co-20%Fe/C;

(iv) 1 Au-promoted quaternary system 5%Au on (5%Ni-70%Co-20%Fe/C).

5.1.2. Research hypotheses

The following were the outcomes of the six hypotheses that were tested in this study, thus:

(i) *Plasma technology is the most effective method of catalyst synthesis*: Three catalyst synthesis methods were used (precipitation, impregnation and plasma-spray), and the plasma approach produced the best performing materials, being 4 times more active. The plasma synthesized samples comprised evenly distributed metal components in the carbon support matrix, and no agglomeration of metal nanoparticles was witnessed in their samples. Therefore, our initial assumption was accurate.

(ii) *Plasma-synthesized catalysts are more selective towards diesel fraction*: Since the SPS method targeted catalysts with metal nanoparticles with a mean size of about 10 nm, catalyst selectivity aimed more towards production of diesel than the gasoline fraction. This was evident from the high α-values (0.7–0.9) exhibited by the catalysts. As expected, the hypothesis advanced was factual.

(iii) *Choice of Co-Fe bimetallics*: We selected 3 bimetallic compositions according to the known Co-Fe binary-phase diagram, hoping that, the plasma-generated 50%Co-50%Fe and 30%Co-70%Fe formulations would contain identical intermetallic phases while the 80%Co-20%Fe formulation would exhibit unique properties. Due to the nanometric nature of the samples, we were unable to conclusively resolve phase composition and quantification in the binary Co-Fe nano-alloys using XRD analysis or RQA. However, the 50%Co-50%Fe/C catalyst was the exceptional sample since it was more selective towards gasoline production and it had a mean particle size of 14.4 nm, while the other catalysts had a mean particle size in the range of 9–11 nm. Some of these results therefore deviated from our original hypothesis.

(iv) *Presence of nickel in Co-Fe bimetallics is beneficial in gasoline production*: We postulated that Ni addition to the Co-Fe/C bimetallic catalysts could boost production of the shorter hydrocarbon-chain molecules, because Ni promotes early molecular desorption by lowering its activation energy. Our prediction was correct and empirically verified.

(v) *Presence of Au coupled with Ni and Fe enhances both WGS and FTS reactions*: It was proposed that incorporation of Au in the Ni-Co-Fe/C sample could keep Co in the metallic form by decreasing its propensity for oxidation, while the synergistic effect of Au-Ni-Fe would enhance LT-WGS reaction that enriches the feed-gas composition with H_2 and improves FTS. These two assertions could not be proved experimentally from the results obtained. Nevertheless, the presence of Au in the sample seemed valuable in lowering H_2O production although it was not accompanied by a corresponding amount of CO_2 befitting WGS activity. Therefore, more advanced tests are required.

(vi) *Presence of Mo leads to diesel production*: It was posited that increased surface acidity by Mo addition to the Co-Fe/C bimetallic would augment the electron-withdrawing character in the catalyst to make it more selective toward the diesel fraction. Our prediction fell short of expectation because when compared to the Co-Fe/C formulation, the presence of Mo rather selectively increased the

gasoline fraction. On the other hand, the quantity of diesel produced by both the Co-Fe and Mo-Co-Fe catalysts remained relatively the same. Therefore, Mo is more selective towards the shorter-chain molecules.

5.2. The significance of these results

5.2.1. SPS as a targeted technology in catalyst synthesis

Sufficient evidence has indicated that the FT reaction mechanism by Fe-based catalysts depends on the presence of Fe carbides (Bengoa *et al*., 2007). The current approach applied in industry to generate these Fe carbides in the catalyst is to carburize Fe oxides with CO to enhance the FTS activity (Ding *et al*., 2009). However, the carburization process can act as a catalyst poison for the Co-based catalysts (Tsakoumis *et al*., 2010). Today, SPS technology stands as an alternative method to carburization in catalyst synthesis. It is perceived as an attractive method because it can easily generate these carbides at temperatures just above 727^{o}C (Okamoto, 1992).

In this work, it has been shown that all catalysts produced through SPS technology were both nanometric and non-porous, with a myriad of phases ranging from metallic to carbidic species. Since nanometric catalysts are imperative in overcoming mass transfer limitations in FTS, we aimed at producing both the active phase (containing the metallic moieties) and the carbon support in the nanometric range. The use of plasma is therefore an attempt to produce high quality catalysts by means of a less complex method, and it is hoped that plasma-synthesized catalysts will find a marketable application in the FTS process, particularly when supported on carbon. Although catalyst deactivation by carbon deposition is a major challenge when using non-carbon supported FTS catalysts, not all forms of carbon lead to deactivation (Moodley *et al*., 2010). In our case, since the catalysts were supported on nanometric carbon, no adverse effects have been observed in the catalyst performance so far.

5.2.2. Benefits of using non-porous catalysts

In polymerization reactions where a porous catalyst is bound to be blocked by larger molecules, it is imperative to operate away from diffusion limiting regimes. Having a non-porous catalyst with high surface area improves the rate of reaction, and this has been a major benefit derived from plasma-synthesized catalysts. For porous materials, reaction rate can be improved by increasing the gas-flow velocity in the reactor, or by decreasing the pellet size or diameter. Operating at sufficiently high velocities ensures that the reaction is not mass-transfer limited. It is noted that even for a given velocity, one can still operate within kinetically-limiting conditions. Therefore, small catalyst particles are recommended in order to operate out of the diffusion-controlled regimes.

Alternatively, on a non-porous particle, the rate of a reaction can be improved by enhancing the surface area of the catalyst, increasing the reactant concentration, or increasing the mass-transfer coefficient, since low resistance to diffusion enhances the reaction rate. Some studies have shown that in FTS, diffusivity is a function of molecular size or carbon number, catalyst properties and reaction conditions (James *et al*., 2012). Therefore, increasing residence time or decreasing diffusivity escalates hydrocarbon re-adsorption, resulting in higher chain-growth probability with increasing carbon number. High pressure, low temperature and low space velocity would increase reactant residence time, which favours hydrocarbon re-adsorption, and in turn promotes selectivity to heavier hydrocarbons. Consequently, highly porous catalysts restrict diffusion, when filled with liquid hydrocarbons produced during FTS.

Since our catalysts can be viewed as solid balls, the reaction takes place outside the catalyst and there are no mass-transfer limitations involved, particularly where turbulence is created in the system with high speed agitation (>2 000 rpm). The non-porous nature of our materials enables them to operate in the kinetically controlled regimes only, a valuable feature in FTS catalysis.

5.2.3. Effect of metal nanoparticle size on catalyst selectivity

Catalyst synthesis by SPS technique has been optimized to produce samples with mean metal particle size of about 9–11 nm. Plasma conditions can be varied to alter the final particle size of the catalyst through changes in gas or powder flow rate, as well as the resident time of the metal/oil suspension in the plasma. It was observed that catalysts with larger nanoparticles (e.g. Fe/C from Fe-NanoCat® with mean size of 21.1 nm; and the binary 50%Co-50%Fe/C formulation with mean size of 14.4 nm) were more selective towards gasoline production, while all the other catalysts with smaller metal nanoparticles with mean size of 9–11 nm were more selective towards the diesel fraction. This outcome was concurrent with other literature findings (den Breejen *et al*., 2009); making the plasma method an accurate and reliable approach in catalyst design, whose production has great potential for seamless scale-up.

5.2.4. ASF distribution and α-value determination

Overall, the effect of time on the probability of hydrocarbon-chain growth indicated that the true α-values of the catalyst could only be ascertained after 15 h on stream, when the catalyst was expected to be operating at steady state. The α-value for the plasma-synthesized catalysts were found to be in the range of 0.71–0.94, with the Fe-rich samples being inclined toward the lower end of the range. It has been observed that during FTS, a catalyst's α-value can be enhanced by applying higher pressure, lowering reaction temperature or decreasing the H_2:CO ratio (Bartholomew and Farrauto, 2006; p.403). This was real to our scenario as those catalysts operating at low H_2:CO ratios (of 1.0 or 1.5) gave α-values of 0.93 meaning that production of higher molecular-weight hydrocarbons would be favoured by either using blended Co-rich catalysts or by operating with CO-rich syngas feedstocks, typical of biomass origin.

5.2.5. Green chemistry: potential bio-syngas application

Since a number of studies have shown that CO adsorption on the catalyst precedes that of H_2, it is presumed that CO-rich gas feeds would be beneficial for FTS. Through the carbene reaction mechanism, FTS reaction begins with CO adsorption and its subsequent dissociation, followed by the dissociative adsorption of H_2 and finally the irreversible

hydrogenation of the adsorbed carbon species to form for example, an alkane (Bartholomew and Farrauto, 2006; p.405).

Although H_2 enhances dissociative CO adsorption, FTS feedstocks with elevated H_2 concentrations normally favour rapid chain termination, leading to the formation of shorter hydrocarbon chains (Madon and Iglesia, 1993). In this work, analysis performed at lower H_2:CO ratios < 2 produced high α-values (≈0.93) indicating the potential production of hydrocarbons with higher molecular-weight than when H_2:CO ratios ≈ 2 was applied. This finding points toward the potential application of these catalysts in CO-rich bio-syngas feedstocks that may become the standard FTS feedstock in future (Jahangiri *et al*., 2014).

Today, there is an increasing demand for efficient carbon utilization and the FTS bio-syngas conversion is a targeted alternative technology in reducing greenhouse emissions. Since sulphur selectively and irreversibly adsorbs on many metal catalysts to form sulphides, low sulphur content bio-syngas is appealing because of the lower pre-treatment costs it would attract in scrubbing sulphur-related impurities (Hu *et al*., 2012). Should dedicated plantations be developed as a major source of renewable biomass, targeted "clean wood" may produce bio-syngas with low levels of contaminants. In addition, since the bio-syngas is a CO-rich feedstock, should need arise for H_2-rich feedstocks, the H_2:CO ratio can be adjusted through WGS reaction by converting some of the CO to CO_2 and H_2 using steam. Removing the CO_2 would increase H_2 concentration and lower the amount of inert gases in the FTS process (Tijmensen *et al*., 2002).

5.2.6. Effect of catalyst reducing agent: H_2 vs. CO

In order to investigate the effect of reduction on catalyst performance, two gases were used: H_2 and CO. Reduction by CO generated carbon nanofilaments in all their catalyst supports, unlike with H_2 where reduction did not impact on the morphology of the catalysts at all. Nonetheless, in the past, it was advanced that carburizing Co may be detrimental to the catalyst (Ding *et al*., 2009), and that the use of CO pre-treatment should be avoided. In this work, catalyst synthesis by plasma has been shown to create a significant amount of carbides in the catalysts that seem to be beneficial to FTS reaction.

Further, catalyst reduction in CO was perceived to be more advantageous than reduction in H_2 in a number of ways, such that:

(i) CO-reduced catalysts did not suffer deactivation due to carburization;

(ii) CO-reduced catalysts were as active as those reduced in H_2 (with all the catalysts displaying 40–45% CO conversion) under identical test conditions;

(iii) CO-reduced catalysts cut H_2O production during FTS (in some cases by almost half) when compared to those reduced in H_2;

(iv) CO-reduced catalysts produced more diesel (C_{13}–C_{20}) than those reduced in H_2; diesel selectivity increased directly with the catalysts' Co content, in the order of 30%Co < 50%Co << 80%Co (respective selectivity = 51%, 60%, 67%).

Moreover, we think that in as much as the carbides may seem to be spectators in the FTS catalyst, they constitute a crucial phase that could be necessary during catalyst regeneration. In case of catalyst deactivation as a result of metal oxidation, the carbides present great potential for *in situ* catalyst regeneration, achieved through carburization, followed by reduction in H_2 (Kwak *et al.*, 2016), see Equation (5.1).

$$CoO \overset{CO}{\rightarrow} Co_2C \overset{H_2}{\rightarrow} Co \qquad Eqn.(5.1)$$

5.2.7. Promotional effect of Au, Mo and Ni in Co-Fe/C

In this work, all the elements that were selected to promote Co and Fe had a positive effect on both the catalyst activity and selectivity. The influence of surface acidity as enhanced by Mo addition in the Co-Fe/C catalysts was perceived to produce more gasoline (C_5–C_{12}). This is despite lowering the catalyst activity of Co-Fe/C catalyst marginally by 2–5%, but it was suspected that the catalyst was still in induction period. Other promoters, namely, Ni and the Au-Ni nexus were also seemingly more selective towards the gasoline fraction. With the presence of Au in Ni-Co-Fe/C catalyst, H_2O production dropped substantially.

However, enhancement of the WGS reaction by Au-Ni-Fe system could not be supported empirically because the process was not accompanied by a matching amount of CO_2 in the system. Since it has been observed that the acid sites of zeolites aid in cracking, isomerization and aromatization of FTS reactions, it was hoped that Mo addition in the samples could also achieve this, besides its ability to produce alcohols. Cracking longer-chain hydrocarbons and oligomerization of short-chain hydrocarbons would enrich gasoline and diesel range fractions (Hu *et al.*, 2012). The prolonged catalyst induction period witnessed in the Mo-promoted catalyst as shown in Figure 4.25, which was followed by a sudden increase in the catalytic activity after 20 h on stream might be due to the presence of MoO_3, which take much longer to be reduced as explained with the help of XPS data in the article presented in Appendix H, (Aluha and Abatzoglou, 2017b). The promotional effect of Au, Ni and Mo in the binary Co-Fe/C catalysts still needs further investigation.

6. CONCLUSION

In this work, comparative studies were conducted on a family of nine nanometric carbon-supported catalysts. The materials were developed iteratively from the less complex single metal (Fe/C, Co/C) catalysts to the composite bimetallic (Co-Fe), ternary (Mo-Co-Fe, Ni-Co-Fe) and the promoted Au/Ni-Co-Fe formulations. Initial tests conducted in a fixed bed reactor (at 503 K, 3 MPa pressure, with GHSV = 6 000 $cm^3.h^{-1}.g^{-1}$ of catalyst for 24 h) showed that plasma-synthesized catalysts were superior in performance to those catalysts prepared through the traditional multi-step precipitation or impregnation methods. Further tests conducted in the 3-φ-CSTSR at 2 MPa pressure, between 493–533 K using GHSV = 3 600 $cm^3.h^{-1}.g^{-1}$ of catalyst, for 24 h) indicated that all catalysts had capacity to produce both gasoline and diesel fractions, but selectivity depended on metal composition in the catalyst or the reaction conditions.

This work has demonstrated that the single-step induction SPS technology, which simplifies catalyst preparation, is an effective approach in the synthesis of highly active nanometric FTS catalysts and the following observations have been made in this study:

(i) All samples produced through the plasma technique had consistent physical properties as presented by microscopic (SEM/EDX, and TEM) analysis, besides showing unique porosity as given by BET surface area analysis, which alludes to the method's potential in making reproducible FTS catalysts and ultimate future scale-up.

(ii) The catalysts were monitored for early deactivation due to metal particle agglomeration. The plasma-synthesized samples did not show significant sintering, but those samples prepared by traditional methods of either impregnation or precipitation indicated metal particle agglomeration after 24 h of FTS reaction.

(iii) A large amount of wax, was generated by the Co/C catalyst (α = 0.83) at 220^{o}C. Although the FTS conditions have not been optimized, the catalyst had poor performance at higher temperatures (260^{o}C) since it produced vast quantities of CO_2 and CH_4 (with combined selectivity of ~65%). This

suggested that Co/C can only be useful at low-temperature operations, while the bimetallic and ternary formulations perform better at higher temperatures.

(iv) Catalyst pre-treatment at 400^{o}C by reduction in either H_2 or CO was an effective way of activating the catalysts. The morphology of H_2-reduced samples remained the same after FTS, while that of the CO-reduced samples produced carbon nanofilaments. Both pre-treatment methods did not lead to catalyst deactivation with TOS, particularly due to carburization from the CO.

(v) Since diesel fraction (C_{13}–C_{20}) was the target product in this work, it was observed that under identical test conditions, the CO-reduced catalysts produced more of diesel than those reduced in H_2 and catalyst reduction in CO considerably cut H_2O production during FTS (in some cases by almost half).

(vi) Promotion of the Co-Fe bimetallic using Mo almost doubled the catalyst's H_2-efficiency (C_{5+} : CH_4 ratio) from 5.8 to 10. At comparable CO conversion of ~40% (260^{o}C, 2 MPa), their C_{5+} selectivity values were 91% (α = 0.81) for Mo-Co-Fe and 87% (α = 0.84) for the Co-Fe/C catalyst. The most active catalyst, Co/C had a H_2-efficiency of 0.5 while that of the Fe/C catalyst stood at 9.7 under similar reaction conditions.

(vii) The addition of Au to the Ni-promoted formulation was found to be beneficial because it lowered the production of undesirable products such as CH_4 (from 23% to 14%), CO_2 (from 14% to 7%) and H_2O (from 55% to 30 cm^3) when compared to the Ni-Co-Fe/C. Besides, the Au-Ni-Co-Fe/C was more selective towards the diesel fraction (32%) when compared to Ni-Co-Fe/C (20%).

Since this research contemplated exploring a number of unique aspects to FTS that have not been attempted before, there is still wide latitude for future work, which may involve:

- Optimization of the reduction process (in CO, H_2 or the syngas);
- Catalyst durability and deactivation tests: Long runs (for over 1 000 h);
- Catalyst life cycle assessment: regeneration and retesting the used catalysts;
- Further catalyst characterization, which is still problematic. For example, attempting *in situ* analysis by the Synchrotron's XRD or EXAFS.

7. CONCLUSION (FRENCH)

Dans ce travail, des études comparatives ont été menées sur neuf catalyseurs nanométriques supportés par le carbone. Les matériaux ont été développés s de façon itérative à partir de catalyseurs monométalliques simples (Fe/C, Co/C) aux bimétalliques (Co-Fe), ternaires (Mo-Co-Fe, Ni-Co-Fe), et aux dopés Au/Ni-Co-Fe. Les tests catalytiques initiaux ont été effectués en réacteur à lit fixe (à 503 K, sous une pression de 3 MPa et une vitesse volumique spatiale (GHSV) de 6 000 $cm^3.h^{-1}.g^{-1}$, en 24 heures. Puis les tests ont été performés dans un réacteur triphasique agité continu (3-φ-CSTSR) opérant de façon isotherme pendant 24 heures à des températures de 493–533 K, sous 2 MPa et à GHSV = 3 600 $cm^3.h^{-1}.g^{-1}$, indiquant que tous les catalyseurs étudiés étaient capables de produire des fractions de gazoline (essence) et de diesel mais avec des sélectivités qui dépendaient de la quantité de métal présent dans le catalyseur ou des conditions réactionnelles.

Ce travail a démontré que la technologie de projection par plasma inductif, en une seule étape, est une meilleure approche dans la synthèse de catalyseurs nanométriques hautement actifs dans SFT et cette étude permet de faire les observations suivantes:

(i) Tous les échantillons produits par la technique des plasmas inductifs avaient des propriétés physiques mises en évidence par les analyses de microscopie (SEM/EDX et TEM) et montraient en outre, une porosité unique révélée par les mesures d'aire spécifique BET; ceci laisse présager de la capacité à reproduire les catalyseurs de SFT en production à plus grande échelle.

(ii) Les catalyseurs ont été suivi pour la désactivation précoce due l'agglomération des particules métalliques. Les échantillons synthétisés par plasma n'ont pas montré de frittage significatif alors que ceux obtenus par les méthodes traditionnelles par imprégnation ou par précipitation ont montré une agglomération des particules métalliques après 24 heures de réaction de SFT.

(iii) Une grande partie de cire provenait de l'activité du catalyseur Co/C (α = 0.83) à 493 K. Les conditions de réaction n'ayant pas été optimisées, le catalyseur a montré de faibles performances à plus haute température (533 K) avec une

production de CO_2 and CH_4 (avec des sélectivités totalisant ~65%). Cela pouvait suggérer que le catalyseur Co/C peut être opérationnel qu'à basse température, alors que les formulations bimétalliques et ternaires ont de meilleures performances à des températures plus élevées.

(iv) Le prétraitement des catalyseurs à 673 K par la réduction sous H_2 or CO a été bénéfique pour l'activation des catalyseurs. La morphologie des échantillons prétraités sous H_2 a été conservée après la SFT, tandis que ceux qui étaient réduits sous CO avaient conduit aux nanofilaments de carbone. Les deux méthodes de prétraitement n'ont pas donné des catalyseurs qui se désactivaient avec le temps d'activation, du fait de la carburisation par le CO en particulier.

(v) Comme les fractions de diesel (C_{13}–C_{20}) font l'objet d'intérêt dans ce travail, il avait été observé que sous des conditions de tests identiques, les catalyseurs prétraités avec CO produisaient plus de diesel que ceux prétraités avec H_2; autrement dit la réduction du catalyseur par le CO diminue considérablement la production d'eau (de moitié, dans certains cas), durant la réaction SFT.

(vi) Le dopage des catalyseurs bimétalliques Co-Fe par Mo a doublé l'efficacité de H_2 (rapport C_{5+} : CH_4) passante de 5.8 à 10. Pour une même conversion de CO à ~40% (533 K, 2 MPa), les sélectivités ont été de 91% (α = 0.81) pour Mo-Co-Fe et de 87% (α = 0.84) pour le catalyseur Co-Fe/C. Le catalyseur le plus actif, Co/C avaient une efficacité de H_2 de 0.5 tandis que celui de Fe/C était de 9.7 sous des conditions réactionnelles similaires.

(vii) L'ajout d'atomes d'or au catalyseur dopé au Ni (Ni-Co-Fe/C) a été bénéfique car la production de produits indésirables a été réduite, comme pour CH_4 (de 23% à 14%), pour CO_2 (de 14% à 7%) et pour H_2O (de 55% to 30%) comparativement au Ni-Co-Fe/C. En outre, le catalyseur Au-Ni-Co-Fe/C a été plus sélectif pour la production de diesel (32%) comparé à 20% pour Ni-Co-Fe/C.

Étant donné que cette recherche envisageait d'explorer un certain nombre d'aspects particuliers au SFT qui n'ont pas été tentés auparavant, il reste encore beaucoup de latitude pour les travaux futurs, qui peuvent comprendre:

- Optimisation du processus de réduction (CO, H_2 ou gaz de synthèse);
- Essais de durabilité et de désactivation: Longue durée (pour plus de 1 000 h);

• Évaluation du cycle de vie du catalyseur: régénération et réétalonnage des catalyseurs utilisés;

• Une autre caractérisation du catalyseur, qui reste problématique. Par exemple, la tentative d'analyse in situ par le synchrotron ou l'EXAFS.

8. BIBLIOGRAPHY

Abatzoglou, N., Gitzhofer, F., Blanchard, J., Vigier, K.D.O. & Gravelle, D. (2010). *Carbon sequestration and dry reforming process and catalysts to produce same*. USA patent application US 11/099 529; Patent No. 7794690 B2.

Abatzoglou, N. & Plascencia, C.R. (2014). *Ni-doped Carbon Nanofilaments (Ni-CNF): Preparation and use as reforming catalyst*. The 5th International Conference on Nanotechnology: Fundamentals and Applications. Conference Proceedings, Keynote Lecture V. Prague, Czech Republic. 1-8.

Abbaslou, R.M.M., Tavasoli, A. & Dalai, A K. (2009). Effect of pre-treatment on physico-chemical properties and stability of carbon nanotubes supported iron Fischer–Tropsch catalysts. *Applied Catalysis A: General,* 355, 33-41.

Ahmad, N., Hussain, S.T., Muhammad, B., Anderson, J.A., Ali, N. & Abbas, S.M. (2013). *Influence of gold promoter on Fischer Tropsch synthesis over Co/Al_2O_3 catalysts*. 10th International Bhurban Conference on Applied Sciences & Technology (IBCAST). Conference Proceedings, Volume: 978-1-4673-4426-5 (Electronic ISBN). IBCAST, Islamabad, Pakistan. 11-15.

Ali, S., Zabidi, N.A.M. & Subbarao, D. (2011). Correlation between Fischer-Tropsch catalytic activity and composition of catalysts. *Chemistry Central Journal,* 5:68, 1-8.

Aluha, J. & Abatzoglou, N. (2016). Synthetic fuels from 3-φ Fischer-Tropsch synthesis using syngas feed and novel nanometric catalysts synthesised by plasma. *Journal of Biomass and Bioenergy,* 95, 330-339.

Aluha, J. & Abatzoglou, N. (2017a). Gold-promoted plasma-synthesized Ni-Co-Fe/C catalyst for Fischer-Tropsch synthesis. *Gold Bulletin,* (Submitted).

Aluha, J. & Abatzoglou, N. (2017b). Promotional effect of Mo and Ni in plasma-synthesized Co-Fe/C bimetallic nano-catalysts for Fischer-Tropsch synthesis *Journal of Industrial and Engineering Chemistry,* (Accepted).

Aluha, J., Bere, K., Abatzoglou, N. & Gitzhofer, F. (2016a). Synthesis of nano-catalysts by induction suspension plasma technology (SPS) for Fischer-Tropsch reaction. *Journal of Plasma Chemistry and Plasma Processing,* 36, 1325-1348.

Aluha, J., Boahene, P., Dalai, A., Hu, Y., Bere, K., Braidy, N. & Abatzoglou, N. (2015a). Synthesis and characterisation of nanometric Co/C and Fe/C catalysts for Fischer-Tropsch synthesis: A comparative study using a fixed-bed reactor. *Journal of Industrial and Engineering Chemistry Research,* 54, 10661-10674.

Aluha, J., Braidy, N., Dalai, A. & Abatzoglou, N. (2015b). *Low-temperature Fischer-Tropsch synthesis with carbon-supported nanometric iron-cobalt catalysts*. 23rd European Biomass Conference and Exhibition (EUBCE). Conference Proceedings, Volume: 978-88-89407-516 (ISBN). EUBCE, Vienna, Austria, 988-994.

Aluha, J., Braidy, N., Dalai, A. & Abatzoglou, N. (2016b). Low-temperature Fischer-Tropsch synthesis using plasma-synthesised nanometric Co/C and Fe/C catalysts. *Canadian Journal of Chemical Engineering,* 94, 1504-1515.

Aluha, J., Hu, Y. & Abatzoglou, N. (2017). Effect of CO concentration on the α-value of plasma-synthesized Co/C catalyst in Fischer-Tropsch synthesis. *Catalysts,* 7(2), 69**,** 1-19.

Bahgat, M. (2006). Technology of Iron Carbide Synthesis. *Journal of Materials Science and Technology,* 22, 423-432.

Bahome, M.C., Jewell, L.L., Hildebrandt, D., Glasser, D. & Coville, N.J. (2005). Fischer–Tropsch synthesis over iron catalysts supported on carbon nanotubes. *Applied Catalysis A: General,* 287, 60-67.

Bartholomew, C.H. & Farrauto, R.J. (2006). *Fundamentals of industrial catalytic processes*, 2nd Edition. John Wiley & Sons Inc., Hoboken (New Jersey), USA, p.966.

Bengoa, J.F., Alvarez, A.M., Cagnoli, M.V., Gallegos, N.G. & Marchetti, S.G. (2007). Influence of intermediate iron reduced species in Fischer-Tropsch synthesis using Fe/C catalysts. *Applied Catalysis A: General,* 325, 68-75.

Bezemer, G.L., Bitter, J.H., Kuipers, H.P.C.E., Oosterbeek, H., Holewijn, J.E., Xu, X., Kapteijn, F., van Dillen, A.J. & de Jong, K.P. (2006). Cobalt particle size effects in the Fischer-Tropsch reaction studied with carbon nanofiber supported catalysts. *Journal of the American Chemical Society,* 128, 3956-3964.

Blanchard, J., Abatzoglou, N., Eslahpazir-Esfandabadi, R. & Gitzhofer, F. (2010). Fischer-Tropsch synthesis in a slurry reactor using a nano-iron carbide catalyst produced by a plasma spray technique. *Journal of Industrial and Engineering Chemistry Research,* 49, 6948-6955.

Blanchard, J., Oudghiri-Hassani, H., Abatzoglou, N., Jankhah, S. & Gitzhofer, F. (2008). Synthesis of nanocarbons via ethanol dry reforming over a carbon steel catalyst. *Chemical Engineering Journal,* 143, 186-194.

Botes, F.G. & Böhringer, W. (2004). The addition of HZSM-5 to the Fischer–Tropsch process for improved gasoline production. *Applied Catalysis A: General,* 267, 217-225.

Brennan, D. (1998). *Process Industry Economics: An international perspective.* Institution of Chemical Engineers, Rugby (Warwickshire), UK, p.294.

Cai, Z., Li, J., Liew, K. & Hu, J. (2010). Effect of La_2O_3-dopping on the Al_2O_3 supported cobalt catalyst for Fischer-Tropsch synthesis. *Journal of Molecular Catalysis A: Chemical,* 330, 10-17.

Calderone, V.R., Shiju, N.R., Curulla-Ferré, D., Chambrey, S., Khodakov, A., Rose, A., Thiessen, J., Jess, A. & Rothenberg, G. (2013). De Novo design of nanostructured iron–cobalt Fischer–Tropsch catalysts. *Angewandte Chemie International Edition,* 52, 4397-4401.

Chen, J., Xue, C., Ramasubramaniam, R. & Liu, H. (2006). A new method for the preparation of stable carbon nanotube organogels. *Carbon,* 44, 2142-2146.

Cheng, Y., Lin, J., Xu, K., Wang, H., Yao, X., Pei, Y., Yan, S., Qiao, M. & Zong, B. (2016). Fischer–Tropsch synthesis to lower olefins over potassium-promoted reduced graphene oxide supported iron catalysts. *ACS Catalysis,* 6, 389-399.

Chew, T.L. & Bhatia, S. (2008). Catalytic processes towards the production of biofuels in a palm oil and oil palm biomass-based biorefinery. *Bioresource Technology,* 99, 7911-7922.

Chu, W., Chernavskii, P.A., Gengembre, L., Pankina, G.A., Fongarland, P. & Khodakov, A.Y. (2007). Cobalt species in promoted cobalt alumina-supported Fischer–Tropsch catalysts. *Journal of Catalysis,* 252, 215-230.

Cooper, C.G., Nguyen, T.-H., Lee, Y.-J., Hardiman, K.M., Safinski, T., Lucien, F.P. & Adesina, A.A. (2008). Alumina-supported cobalt-molybdenum catalyst for slurry phase Fischer–Tropsch synthesis. *Catalysis Today,* 131, 255-261.

Dalai, A.K. & Davis, B.H. (2008). Fischer–Tropsch synthesis: A review of water effects on the performances of unsupported and supported Co catalysts. *Applied Catalysis A: General,* 348, 1-15.

Davis, B.H. (2007). Fischer-Tropsch synthesis: comparison of performances of iron and cobalt catalysts. *Journal of Industrial and Engineering Chemistry Research,* 46, 8938-8945.

Davis, B.H. (2009). Fischer–Tropsch Synthesis: Reaction mechanisms for iron catalysts. *Catalysis Today,* 141, 25-33.

de Klerk, A. & Furimsky, E. (2011). Catalysis in the Refining of Fischer–Tropsch Syncrude. *Platinum Metals Review,* 55, 263-267.

den Breejen, J.P., Radstake, P.B., Bezemer, G.L., Bitter, J.H., Frøseth, V., Holmen, A. & de Jong, K.P. (2009). On the origin of the cobalt particle size effects in Fischer-Tropsch catalysis. *Journal of the American Chemical Society,* 131, 7197-7203.

Digges, T.G., Rosenberg, S.J. & Geil, G.W. (1966). *Heat treatment and properties of iron and steel*. (Library of Congress Catalog, Card No. 66-61523; Monograph 88). U.S. National Bureau of Standards. Department of Commerce, U.S. Government Printing Office, Washington, DC, U.S.A., p.46.

Ding, M., Yang, Y., Wu, B., Xu, J., Zhang, C., Xiang, H. & Li, Y. (2009). Study of phase transformation and catalytic performance on precipitated iron-based catalyst for Fischer–Tropsch synthesis. *Journal of Molecular Catalysis A: Chemical,* 303, 65-71.

Dlamini, M.W., Kumi, D.O., Phaahlamohlaka, T.N., Lyadov, A.S., Billing, D.G., Jewell, L.L. & Coville, N.J. (2015). Carbon spheres prepared by hydrothermal synthesis - A support for bimetallic iron cobalt Fischer-Tropsch catalysts. *ChemCatChem,* 7**,** 3000-3011.

Dry, M.E. (1982). Catalytic aspects of industrial Fischer-Tropsch synthesis. *Journal of Molecular Catalysis,* 17, 133-144.

Dry, M.E. (1990). Fischer-Tropsch synthesis over iron catalysts. *Catalysis Letters,* 7, 241-252.

Dry, M.E. (2002). The Fischer–Tropsch process: 1950–2000. *Catalysis Today,* 71, 227-241.

Ebert, M.P.M. (2013). *Process synthesis and design of low temperature Fischer-Tropsch crude production from biomass derived syngas.* Masters Thesis (MSc.), Chalmers University of Technology, Göteborg, Sweden, p.72.

Enger, B.C. & Holmen, A. (2012). Nickel and Fischer-Tropsch Synthesis. *Catalysis Reviews - Science and Engineering,* 54, 437-488.

Ernst, B., Libs, S., Chaumette, P. & Kiennemann, A. (1999). Preparation and characterization of Fischer–Tropsch active Co/SiO_2 catalysts. *Applied Catalysis A: General,* 186, 145-168.

Escalona, N., Medina, C., García, R. & Reyes, P. (2009). Fischer Tropsch reaction from a mixture similar to biosyngas. Influence of promoters on surface and catalytic properties of Co/SiO_2 catalysts. *Catalysis Today,* 143, 76-79.

Eschemann, T.O., Bitter, J.H. & Jong, K.P.D. (2014). Effects of loading and synthesis method of titania-supported cobalt catalysts for Fischer–Tropsch synthesis. *Catalysis Today,* 228, 89-95.

Farias, F.E.M., Sales, F.G. & Fernandes, F.A.N. (2008). Effect of operating conditions and potassium content on Fischer-Tropsch liquid products produced by potassium-promoted iron catalysts. *Journal of Natural Gas Chemistry,* 17, 175-178.

Fechete, I., Wang, Y. & Védrine, J.C. (2012). The past, present and future of heterogeneous catalysis. *Catalysis Today,* 189, 2-27.

Ferrari, A.C. & Robertson, J. (2000). Interpretation of Raman spectra of disordered and amorphous carbon. *Physical Review B,* 61, 14095.

Fox, J.M. (1993). The different catalytic routes for methane valorization: an assessment of processes for liquid fuels. *Catalysis Reviews - Science and Engineering,* 35, 169-212.

Fu, T. & Li, Z. (2015). Review of recent development in Co-based catalysts supported on carbon materials for Fischer–Tropsch synthesis. *Chemical Engineering Science,* 135, 3-20.

Gaube, J. & Klein, H.F. (2008). The promoter effect of alkali in Fischer-Tropsch iron and cobalt catalysts. *Applied Catalysis A: General,* 350, 126-132.

Gore, J.P. & Sane, A. (2011). Flame synthesis of carbon nanotubes. In: Yellampalli, S. (ed.), *Carbon nanotubes - synthesis, characterization, applications*. InTech, Rijeka, Croatia, 121-146.

Gratuito, M.K.B., Panyathanmaporn, T., Chumnanklang, R.A., Sirinuntawittaya, N. & Dutta, A. (2008). Production of activated carbon from coconut shell: Optimization using response surface methodology. *Bioresource Technology,* 99, 4887-4895.

Hayakawa, H., Tanaka, H. & Fujimoto, K. (2006). The different catalytic routes for methane valorization: an assessment of processes for liquid fuels. *Applied Catalysis A: General,* 310, 24-30.

Herranz, T., Rojas, S., Pérez-Alonso, F.J., Ojeda, M., Terreros, P. & Fierro, J.L.G. (2006). Genesis of iron carbides and their role in the synthesis of hydrocarbons from synthesis gas. *Journal of Catalysis,* 243, 199-211.

Hilmen, A.M., Schanke, D., Hanssen, K.F. & Holmen, A. (1999). Study of the effect of water on alumina supported cobalt Fischer–Tropsch catalysts. *Applied Catalysis A: General,* 186, 169-188.

Hou, W., Wu, B., Yang, Y., Hao, Q., Tian, L., Xiang, H. & Li, Y. (2008). Effect of SiO_2 content on iron-based catalysts for slurry Fischer–Tropsch synthesis. *Fuel Processing Technology,* 89, 284-291.

Hu, J., Yu, F. & Lu, Y. (2012). Application of Fischer–Tropsch synthesis in biomass to liquid conversion. *Catalysts,* 2, 303-326.

Huyser, J., van Vuuren, M.J. & Kupi, G. (2010). The value of a two alpha model in the elucidation of a full product spetrum for Fe-LTFT. In*:* Davis, B.H. & Occelli, M.L. (eds.), *Advances in Fischer-Tropsch Synthesis, Catalysts, and Catalysis*. CRC Press, Boca Raton (FL), USA, p.424.

Jacobs, G., Das, T.K., Zhang, Y., Li, J., Racoillet, G. & Davis, B.H. (2002). Fischer–Tropsch synthesis: support, loading, and promoter effects on the reducibility of cobalt catalysts. *Applied Catalysis A: General,* 233, 263-281.

Jacobs, G., Ma, W., Gao, P., Todic, B., Bhatelia, T., Bukur, D.B. & Davis, B.H. (2013). The application of synchrotron methods in characterizing iron and cobalt Fischer-Tropsch synthesis catalysts. *Catalysis Today,* 214, 100-139.

Jahangiri, H., Bennett, J., Mahjoubi, P., Wilson, K. & Gu, S. (2014). A review of advanced catalyst development for Fischer–Tropsch synthesis of hydrocarbons from biomass derived syn-gas. *Catalysis Science & Technology ,* 4, 2210–2229.

James, O.O., Chowdhury, B., Mesubic, M.A. & Maity, S. (2012). Reflections on the chemistry of the Fischer–Tropsch synthesis. *RSC Advances,* 2, 7347-7366.

Jankhah, S., Abatzoglou, N., Gitzhofer, F., Blanchard, J. & Oudghiri-Hassani, H. (2008). Catalytic properties of carbon nano-filaments produced by iron-catalysed reforming of ethanol. *Chemical Engineering Journal,* 139, 532-539.

Jong, S.-J. & Cheng, S. (1995). Reduction behavior and catalytic properties of cobalt containing ZSM-5 zeolites. *Applied Catalysis A: General,* 126, 51-66.

Jongsomjit, B., Wongsalee, T. & Praserthdam, P. (2006). Catalytic behaviors of mixed TiO_2-SiO_2-supported cobalt Fischer–Tropsch catalysts for carbon monoxide hydrogenation. *Materials Chemistry and Physics,* 97, 343-350.

Kang, S.-H., Bae, J. W., Woo, K.-J., Prasad, P.S.S. & Jun, K.-W. (2010). ZSM-5 supported iron catalysts for Fischer–Tropsch production of light olefin. *Fuel Processing Technology,* 91, 399-403.

Khadzhiev, S.N. & Krylova, A.Y. (2011). Fischer-Tropsch synthesis in a three-phase system over nanocatalysts (Review). *Petroleum Chemistry,* 51, 74-85.

Khassin, A.A., Yurieva, T.M. & Parmon, V.N. (1998). Fischer-Tropsch synthesis over cobalt-containing unsupported catalysts in slurry reactor. Effect of the metallic Co particle size on the catalyst selectivity. *Reaction Kinetics and Catalysis Letters,* 64, 55-62.

Khodakov, A.Y. (2009). enhancing cobalt dispersion in supported Fischer-Tropsch catalysts via controlled decomposition of cobalt precursors. *Brazilian Journal of Physics,* 39, 171-175.

Khodakov, A.Y., Chu, W. & Fongarland, P. (2007). Advances in the development of novel cobalt Fischer-Tropsch catalysts for synthesis of long-chain hydrocarbons and clean fuels. *Chemical Reviews,* 107, 1692-1744.

Kniess, C.T., Lima, J.C.D. & Prates, P.B. (2012). The quantification of crystalline phases in materials: Applications of Rietveld method. In: Shatokha, V. (ed.). *Sintering - Methods and Products*. InTech, Rijeka, Croatia, 293-316.

Kreutz, T.G., Larson, E.D., Liu, G. & Williams, R.H. (2008). *Fischer-Tropsch fuels from coal and biomass*. 25th Annual International Pittsburgh Coal Conference. Conference Proceedings. Pittsburgh, Pennsylvania, USA.

Kwak, G., Kim, D.-E., Kim, Y.T., Park, H.-G., Kang, S. C., Ha, K.-S., Juna, K.-W. & Lee, Y.-J. (2016). Enhanced catalytic activity of cobalt catalysts for Fischer–Tropsch synthesis via carburization and hydrogenation and its application to regeneration. *Catalysis Science & Technology,* 6, 4594-4600.

Li, J., Zhan, X., Zhang, Y., Jacobs, G., Das, T. & Davis, B.H. (2002). Fischer–Tropsch synthesis: effect of water on the deactivation of Pt promoted Co/Al_2O_3 catalysts. *Applied Catalysis A: General,* 228, 203-212.

Li, S., O'Brien, R. J., Meitzner, G.D., Hamdeh, H., Davis, B.H. & Iglesia, E. (2001). Structural analysis of unpromoted Fe-based Fischer-Tropsch catalysts using X-ray absorption spectroscopy. *Applied Catalysis A: General,* 219, 215-222.

Liu, C.-J., Vissokov, G.P. & Jang, B.W.L. (2002). Catalyst preparation using plasma technologies. *Catalysis Today,* 72, 173-184.

Liu, J.-X., Su, H.-Y., Sun, D.-P., Zhang, B.-Y. & Li, W.-X. (2013). Crystallographic dependence of CO activation on cobalt catalysts: HCP versus FCC. *Journal of the American Chemical Society,* 135, 16284-16287.

Lögdberg, S. (2007). *Development of Fischer-Tropsch Catalysts for Gasified Biomass.* PhD Thesis, KTH Royal Institute of Technology, Stockholm, Sweden, p.90.

Lohitharn, N. & Goodwin Jr., J.G. (2008). Impact of Cr, Mn and Zr addition on Fe Fischer–Tropsch synthesis catalysis: Investigation at the active site level using SSITKA. *Journal of Catalysis,* 257, 142-151.

Lu, W., Huang, P., He, C. & Yan, B. (2013). XRD, SEM and XAS studies of FeCo films electrodeposited at different current density. *International Journal of Electrochemical Science,* 8, 914-923.

Luo, M. & Davis, B.H. (2003). Fischer–Tropsch synthesis: Group II alkali-earth metal promoted catalysts. *Applied Catalysis A: General,* 246, 171-181.

Ma, W., Jacobs, G., Sparks, D.E., Gnanamani, M.K., Pendyala, V.R.R., Yen, C.H., Klettlinger, J.L.S., Tomsik, T.M. & Davis, B.H. (2011). Fischer–Tropsch synthesis: Support and cobalt cluster size effects on kinetics over Co/Al_2O_3 and Co/SiO_2 catalysts. *Fuel,* 90, 756-765.

Ma, W., Kugler, E.L. & Dadyburjor, D.B. (2007). Potassium effects on activated-carbon-supported iron catalysts for Fischer−Tropsch synthesis. *Energy & Fuels,* 21**,** 1832-1842.

Madon, R.J. & Iglesia, E. (1993). The importance of olefin readsorption and H_2/CO reactant ratio for hydrocarbon chain growth on ruthenium catalysts. *Journal of Catalysis,* 139, 576-590.

Moodley, D.J., van de Loosdrecht, J., Saib, A.M. & Niemantsverdriet, H.J.W. (2010). The formation and influence of carbon on cobalt-based Fischer-Tropsch synthesis catalysts: An integrated review. In: Davis, B.H. & Occelli, M.L. (eds.). *Advances in Fisher Tropsch synthesis, catalysts and catalysis*. CRC Press, Boca Raton, FL., USA, 49-81.

Morales, F., Smit, E.D., de Groot, F.M.F., Visser, T. & Weckhuysen, B.M. (2007). Effects of manganese oxide promoter on the CO and H_2 adsorption properties of titania-supported cobalt Fischer–Tropsch catalysts. *Journal of Catalysis,* 246, 91-99.

Moussa, S.O., Panchakarla, L.S., Ho, M.Q. & El-Shall, M.S. (2014). Graphene-supported, iron-based nanoparticles for catalytic production of liquid hydrocarbons from synthesis gas: The role of the graphene support in comparison with carbon nanotubes. *ACS Catalysis,* 4, 535-545.

Okamoto, H. (1992). The C-Fe (carbon-iron) system. *Journal of Phase Equilibria,* 13, 543-565.

Okamoto, H. (2008). Co-Fe (Cobalt-Iron). *Journal of Phase Equilibria and Diffusion,* 29, 383-384.

Osswald, S., Chmiola, J. & Gogotsi, Y. (2012). Structural evolution of carbide-derived carbons upon vacuum annealing. *Carbon,* 50, 4880-4886.

Pinna, D., Tronconi, E., Lietti, L., Zennaro, R. & Forzatti, P. (2003). Wax composition transients during Fischer–Tropsch synthesis. *Journal of Catalysis,* 214, 251-260.

Pour, A.N., Housaindokht, M.R., Tayyari, S.F., Zarkesh, J. & Alaei, M.R. (2010a). Kinetic studies of the Fischer-Tropsch synthesis over La, Mg and Ca promoted nano–structured iron catalyst. *Journal of Natural Gas Science and Engineering,* 2, 61-68.

Pour, A.N., Shahri, S.M.K., Zamani, Y., Irani, M. & Tehrani, S. (2008). Deactivation studies of bifunctional Fe-HZSM5 catalyst in Fischer-Tropsch process. *Journal of Natural Gas Chemistry,* 17, 242-248.

Pour, A. N., Shahri, S.M.K., Zamani, Y. & Zamanian, A. (2010b). Promoter effect on the CO_2-H_2O formation during Fischer-Tropsch synthesis on iron-based catalysts. *Journal of Natural Gas Chemistry,* 19, 193-197.

Qin, S., Zhang, C., Xu, J., Wu, B., Xiang, H. & Li, Y. (2009). Effect of Mo addition on precipitated Fe catalysts for Fischer–Tropsch synthesis. *Journal of Molecular Catalysis A: Chemical,* 304, 128-134.

Raupp, G.B. & Delgass, W.N. (1979). Mössbauer investigation of supported Fe and FeNi catalysts: II. Carbides formed Fischer-Tropsch synthesis. *Journal of Catalysis,* 58, 348-360.

Ravel, B. & Newville, M. (2005). ATHENA, ARTEMIS, HEPHAESTUS: Data analysis for X-ray absorption spectroscopy using IFEFFIT. *Journal of Synchrotron Radiation,* 12, 537-541.

Riedel, T. & Schaub, G. (2003). Low-temperature Fischer–Tropsch synthesis on cobalt catalysts - effects of CO_2. *Topics in Catalysis,* 26, 145-156.

Rietveld, H.M. (1969). A profile refinement method for nuclear and magnetic structures. *Journal of Applied Crystallography,* 2, 65-71.

Rohde, M.P., Schaub, G., Khajavi, S., Jansen, J.C. & Kapteijn, F. (2008). Fischer–Tropsch synthesis with in situ H_2O removal – Directions of membrane development. *Microporous and Mesoporous Materials,* 115, 123-136.

Rutkovskii, A.E., Vishnyakov, L.R., Chekhovskii, A.A. & Kirkun, N.I. (2000). Use of plasma technology in creating catalysts on carriers. *Powder Metallurgy and Metal Ceramics,* 39(3), 207-209.

Rytter, E., Skagseth, T.H., Eri, S. & Sjåstad, A.O. (2010). Cobalt Fischer-Tropsch catalysts using nickel promoter as a rhenium substitute to suppress deactivation. *Journal of Industrial and Engineering Chemistry Research,* 49, 4140-4148.

Schulz, H. (1999). Short history and present trends of Fischer–Tropsch synthesis. *Applied Catalysis A: General,* 186, 3-12.

Serp, P. & Machado, B. (2015). *Nanostructured carbon materials for catalysis*. Royal Society of Chemistry (RSC), Cambridge, UK, p.570.

Spath, P.L. & Dayton, D.C. (2003). *Preliminary screening - technical and economic assessment of synthesis gas to fuels and chemicals with emphasis on the potential for biomass-derived syngas*. (A technical report, NREL/TP-510-34929). National Renewable Energy Laboratory (NREL), Department of Energy, Golden, Colorado, U.S.A., p.142.

Tang, Q., Wang, Y., Zhang, Q. & Wan, H. (2003). Preparation of metallic cobalt inside NaY zeolite with high catalytic activity in Fischer–Tropsch synthesis. *Catalysis Communications,* 4, 253-258.

Tao, Z., Yang, Y., Zhang, C., Li, T., Wang, J., Wan, H., Xiang, H. & Li, Y. (2006). Effect of calcium promoter on a precipitated iron–manganese catalyst for Fischer–Tropsch synthesis. *Catalysis Communications,* 7, 1061-1066.

Tavasoli, A., Abbaslou, R.M.M. & Dalai, A.K. (2008). Deactivation behavior of ruthenium promoted Co/γ-Al_2O_3 catalysts in Fischer–Tropsch synthesis. *Applied Catalysis A: General,* 346, 58-64.

Tehrani, M., Boroujeni, A.Y., Luhrs, C., Phillips, J. & Al-Haik, M.S. (2014). Hybrid composites based on carbon fiber/carbon nanofilament reinforcement. *Materials,* 7, 4182-4195.

Terakado, O., Uno, Y. & Hirasawa, M. (2014). Synthesis of fine iron-cobalt alloy particles by the co-reduction of precursors with solvated electrons in sodium ammonia solution. *Materials Transactions,* 55, 517-521.

Thomas, J.M. & Thomas, W.J. (1997). *Principles and Practice of Heterogeneous Catalysis*. Wiley-VCH: Weinheim, Germany, p.669.

Tijmensen, M.J.A., Faaij, A.P.C., Hamelinck, C.N. & van Hardeveld, M.R.M. (2002). Exploration of the possibilities for production of Fischer-Tropsch liquids and power via biomass gasification. *Journal of Biomass and Bioenergy,* 23, 129-152.

Trépanier, M., Tavasoli, A., Dalai, A.K. & Abatzoglou, N. (2009a). Co, Ru and K loadings effects on the activity and selectivity of carbon nanotubes supported cobalt catalyst in Fischer–Tropsch synthesis. *Applied Catalysis A: General,* 353, 193-202.

Trépanier, M., Tavasoli, A., Dalai, A.K. & Abatzoglou, N. (2009b). Fischer–Tropsch synthesis over carbon nanotubes supported cobalt catalysts in a fixed bed reactor: Influence of acid treatment. *Fuel Processing Technology,* 90, 367-374.

Tsakoumis, N.E., Rønning, M., Borg, Ø., Rytter, E. & Holmen, A. (2010). Deactivation of cobalt based Fischer-Tropsch catalysts: A review. *Catalysis Today,* 154, 162-182.

Tuxen, A., Carenco, S., Chintapalli, M., Chuang, C.-H., Escudero, C., Pach, E., Jiang, P., Borondics, F., Beberwyck, B., Alivisatos, A.P., Thornton, G., Pong, W.-F., Guo, J., Perez, R., Besenbacher, F. & Salmeron, M. (2013). Size-dependent dissociation of carbon monoxide on cobalt nanoparticles. *Journal of the American Chemical Society,* 135, 2273-2278.

van Berge, P.J., van de Loosdrecht, J., Barradas, S. & van der Kraan, A.M. (2000). Oxidation of cobalt based Fischer–Tropsch catalysts as a deactivation mechanism. *Catalysis Today,* 58, 321-334.

van de Loosdrecht, J., Balzhinimaev, B., Dalmon, J.A., Niemantsverdriet, J.W., Tsybulya, S.V., Saib, A.M., van Berge, P.J. & Visagie, J.L. (2007). Cobalt Fischer-Tropsch synthesis: Deactivation by oxidation? *Catalysis Today,* 123, 293-302.

van der Laan, G.P. & Beenackers, A.A.C.M. (1999). Hydrocarbon selectivity model for the gas−solid Fischer−Tropsch synthesis on precipitated iron catalysts. *Journal of Industrial and Engineering Chemistry Research,* 38, 1277-1290.

van Steen, E. & Prinsloo, F.F. (2002). Comparison of preparation methods for carbon nanotubes supported iron Fischer–Tropsch catalysts. *Catalysis Today,* 71**,** 327-334.

van Steen, E. & Schulz, H. (1999). Polymerisation kinetics of the Fischer–Tropsch CO hydrogenation using iron and cobalt based catalysts. *Applied Catalysis A: General,* 186, 309-320.

Venugopal, A., Aluha, J., Mogano, D. & Scurrell, M.S. (2003a). The gold–ruthenium–iron oxide catalytic system for the low temperature water–gas-shift reaction: The examination of gold–ruthenium interactions. *Applied Catalysis A: General,* 245, 149-158.

Venugopal, A., Aluha, J. & Scurrell, M.S. (2003b). The water-gas shift reaction over Au-based, bimetallic catalysts. The Au-M (M=Ag, Bi, Co, Cu, Mn, Ni, Pb, Ru, Sn, Tl) on Iron (III) oxide system. *Catalysis Letters,* 90, 1-6.

Visconti, C.G., Lietti, L., Tronconi, E., Forzatti, P., Zennaro, R. & Finocchio, E. (2009). Fischer–Tropsch synthesis on a Co/Al_2O_3 catalyst with CO_2 containing syngas. *Applied Catalysis A: General,* 355, 61-68.

Vo, D.-V. N. & Adesina, A. A. (2011). Fischer–Tropsch synthesis over alumina-supported molybdenum carbide catalyst. *Applied Catalysis A: General,* 399, 221-232.

Vosloo, A.C. (2001). Fischer–Tropsch: a futuristic view. *Fuel Processing Technology* 71, 149-155.

Voss, M., Borgmann, D. & Wedler, G. (2002). Characterization of alumina, silica, and titania supported cobalt catalysts. *Journal of Catalysis,* 212, 10-21.

Wang, C., Xu, L. & Wang, Q. (2003). Review of directly producing light olefins via CO hydrogenation. *Journal of Natural Gas Chemistry,* 12, 10-16.

Xiong, H., Jewell, L.L. & Coville, N.J. (2015). Shaped carbons as supports for the catalytic conversion of syngas to clean fuels. *ACS Catalysis,* 5**,** 2640-2658.

Xiong, H., Motchelaho, M.A.M., Moyo, M., Jewell, L.L. & Coville, N.J. (2011). Correlating the preparation and performance of cobalt catalysts supported on carbon nanotubes and carbon spheres in the Fischer–Tropsch synthesis. *Journal of Catalysis,* 278, 26-40.

Xu, K., Sun, B., Lin, J., Wen, W., Pei, Y., Yan, S., Qiao, M., Zhang, X. & Zong, B. (2014). ε-Iron carbide as a low-temperature Fischer-Tropsch synthesis catalyst. *Nature Communications,* 5:5783, 1-7.

Yang, J., Ma, W., Chen, D., Holmen, A. & Davis, B.H. (2014). Fischer–Tropsch synthesis: A review of the effect of CO conversion on methane selectivity. *Applied Catalysis A: General,* 470, 250-260.

Y Yang, J., Qi, Y., Zhu, J., Zhu, Y.-A., Chen, D. & Holmen, A. (2013). Reaction mechanism of CO activation and methane formation on Co Fischer–Tropsch catalyst: A combined DFT, transient, and steady-state kinetic modeling. *Journal of Catalysis,* 308, 37-49.

Yang, J., Suna, Y., Tanga, Y., Liu, Y., Wang, H., Tian, L., Wang, H., Zhang, Z., Xiang, H. & Li, Y. (2006). Effect of magnesium promoter on iron-based catalyst for Fischer–Tropsch synthesis. *Journal of Molecular Catalysis A: Chemical,* 245, 26-36.

Yang, Y., Xiang, H.-W., Xu, Y.-Y., Bai, L. & Li, Y.-W. (2004). Effect of potassium promoter on precipitated iron-manganese catalyst for Fischer–Tropsch synthesis. *Applied Catalysis A: General,* 266, 181-194.

Yoo, Y.-G., Yang, D.-S., Jiang, B., Yu, S.-C. & Greneche, J.M. (2006). Local ordering study of nanostructured FeCo-C alloys for various Fe contents. *Journal of the Korean Physical Society,* 48, 1463-1467.

Zamani, Y. (2015). Fischer-Tropsch synthesis over nano-sized iron-based catalysts: investigation of promoter and temperature effects on products distribution. *Journal of Petroleum and Coal,* 57, 71-75.

Zennaro, R., Tagliabue, M. & Bartholomew, C.H. (2000). Kinetics of Fischer–Tropsch synthesis on titania-supported cobalt. *Catalysis Today,* 58, 309-319.

Zhang, Y., Bao, J., Nagamori, S. & Tsubaki, N. (2009). A new and direct preparation method of iron-based bimodal catalyst and its application in Fischer–Tropsch synthesis. *Applied Catalysis A: General,* 352, 277-281.

Zhao, G., Zhang, C., Qin, S., Xiang, H. & Li, Y. (2008). Effect of interaction between potassium and structural promoters on Fischer–Tropsch performance in iron-based catalysts. *Journal of Molecular Catalysis A: Chemical,* 286, 137-142.

9. APPENDICES: PUBLICATIONS

This research work has been presented in a series of both local and international conferences and the ensuing results published in a number of journal articles as follows:

Journal Articles:

1. **James Aluha**, Philip Boahene, Ajay Dalai, Yongfeng Hu, Kossi Béré, Nadi Braidy, and Nicolas Abatzoglou, Synthesis and characterization of Co/C and Fe/C nano-catalysts for Fischer-Tropsch synthesis: A comparative study using a fixed-bed reactor, *Journal of Industrial & Engineering Chemistry Research*, Vol. 54(43), (**2015**), 10661–10674.

2. **James Aluha**, Nadi Braidy, Ajay Dalai, and Nicolas Abatzoglou, Low-temperature Fischer-Tropsch synthesis using plasma-synthesized nanometric Co/C and Fe/C catalysts, *Canadian Journal of Chemical Engineering*, Vol. 94, (**2016**), 1504–1515.

3. **James Aluha**, and Nicolas Abatzoglou, Synthetic fuels from 3-φ Fischer-Tropsch synthesis using bio-derived gas feed and novel nanometric catalysts synthesised by plasma, *Journal of Biomass and Bioenergy*, Vol. 95, (**2016**), 330–339.

4. **James Aluha**, Kossi Béré, Nicolas Abatzoglou, and François Gitzhofer, Application of plasma in production of nano-catalysts for Fischer-Tropsch synthesis. *Journal of Plasma Chemistry and Plasma Processing*, Vol. 36, (**2016**), 1325–1348.

5. **James Aluha**, Yongfeng Hu, and Nicolas Abatzoglou, Effect of CO concentration on the α-value of plasma-synthesized Co/C catalyst in Fischer-Tropsch synthesis, *Catalysts*, 7(2), 69, (**2017**), 1–19.

6. **James Aluha,** and Nicolas Abatzoglou, Promotional effect of Mo and Ni in plasma-synthesized Co-Fe/C bimetallic nano-catalysts for Fischer-Tropsch synthesis, *Journal of Industrial and Engineering Chemistry*, (**2017**), (Accepted).

7. **James Aluha**, and Nicolas Abatzoglou, Gold-promoted plasma-synthesized Ni-Co-Fe/C catalyst for Fischer-Tropsch synthesis, *Gold Bulletin*, (**2017**), (Submitted).

Conference Paper(s):

1. **James Aluha**, Nadi Braidy, Ajay Dalai, and Nicolas Abatzoglou, *Low-temperature Fischer-Tropsch synthesis with carbon-supported nanometric iron-cobalt catalysts*, Conference Proceedings; The 23rd European Biomass Conference and Exhibition (EUBCE), Vienna, Austria; (1st – 4th Jun. 2015), ISBN 978-88-89407-516, DOI: 10.5071/23rdEUBCE2015-3CO.15.1, 988–994.

Conference Presentations:

1. **James Aluha**, and Nicolas Abatzoglou. *Effect of Au, Ni, and Mo on plasma-derived Co-Fe/C bimetallic nano-catalysts in Fischer-Tropsch synthesis*, Oral presentation, (16th – 19th Oct. 2016), The 66th Canadian Chemical Engineering (CChE) Conference, Quebec City, (QC), Canada.

2. **James Aluha**, Nadi Braidy, and Nicolas Abatzoglou. *Nano-catalysts produced by suspension plasma spray (SPS) technology for Fischer-Tropsch synthesis*, Poster presentation, (6th – 8th Jul. 2016), The Canadian BiofuelNet (BFN) Advanced Biofuels Symposium, Vancouver, (BC), Canada.

3. **James Aluha**, Nadi Braidy, and Nicolas Abatzoglou. *Nanometric plasma-derived cobalt and iron catalysts supported on carbon for Fischer-Tropsch synthesis in a slurry-CSTR*, Oral presentation, (4th – 7th Oct. 2015), The 65th Canadian Chemical Engineering (CChE) Conference, Calgary, (AB), Canada.

4. **James Aluha**, Nadi Braidy, Yongfeng Hu, and Nicolas Abatzoglou. *Synthetic fuels from 3-φ Fischer-Tropsch synthesis using bio-derived gas feed and novel nanometric catalysts*, Oral presentation, (27th Sept. – 2nd Oct. 2015), Biorefinery I: Chemicals and Materials from Thermo-Chemical Biomass Conversion and Related Processes (ECI Conference), Crete, Greece.

5. **James Aluha**, Nadi Braidy, and Nicolas Abatzoglou. *Plasma-derived nanometric iron and cobalt catalysts on carbon support for low temperature Fischer-Tropsch synthesis*, Oral presentation, (22nd – 24th Jul. 2015), The Canadian BiofuelNet (BFN) Advanced Biofuels Symposium, Montreal, (QC), Canada.

6. **James Aluha**, Nadi Braidy, Ajay Dalai, and Nicolas Abatzoglou. *Low-temperature Fischer-Tropsch reaction using carbon-supported nanometric catalysts of iron and cobalt*, Oral presentation, (1st – 4th Jun. 2015), The 23rd European Biomass Conference and Exhibition (EUBCE), Vienna, Austria.

7. **James Aluha**, Nadi Braidy, Yongfeng Hu, Ajay Dalai, and Nicolas Abatzoglou. *Plasma-derived nanometric Co/C and Fe/C catalysts for Fischer-Tropsch synthesis*, Oral presentation, (22nd – 26th Mar. 2015), The 249th American Chemical Society (ACS) National Meeting & Exposition, Denver, (CO), USA.

8. **James Aluha**, Philip Boahene, Ajay Dalai, Yongfeng Hu, Kossi Bere, François Gitzhofer, Nadi Braidy, and Nicolas Abatzoglou. *A comparative study of carbon-supported iron and cobalt catalysts for Fischer-Tropsch synthesis in a fixed-bed reactor*, Oral presentation, (19th – 22nd Oct. 2014), The 64th Canadian Chemical Engineering (CChE) Conference, Niagara Falls, (ON), Canada.

9. **James Aluha**, Nadi Braidy, and Nicolas Abatzoglou. *Carbon-supported iron and cobalt catalysts for Fischer-Tropsch synthesis*, Poster presentation, (27 – 29th May 2014), The Canadian BiofuelNet (BFN) Advanced Biofuels Symposium, Ottawa, (ON), Canada.

9.1. Appendix A: Article 1 - Catalyst synthesis by SPS technology

Plasma Chem Plasma Process (2016) 36:1325–1348
DOI 10.1007/s11090-016-9734-1

ORIGINAL PAPER

Synthesis of Nano-catalysts by Induction Suspension Plasma Technology (SPS) for Fischer–Tropsch Reaction

James Aluha[1] · Kossi Bere[1] · Nicolas Abatzoglou[1] · François Gitzhofer[1]

Received: 26 February 2016 / Accepted: 10 July 2016 / Published online: 22 July 2016

Abstract Nanometric catalysts were synthesized through induction suspension plasma technology (SPS) for application in the Fischer–Tropsch synthesis (FTS). Carbon-supported single metal catalysts (Co/C, Fe/C), bimetallic formulations (Co–Fe/C), and ternary (Co–Fe–Mo and Co–Fe–Ni) systems have been considered in this work. SPS has been selected because it simultaneously allows for: (1) atomizing and generating metallic nanoparticles; (2) creating particularly Fe carbides, which are important in Fe-based FTS reaction mechanism; (3) in situ production of the nanometric graphitic-carbon matrix; and (4) saving time in catalyst synthesis, limiting sample preparation steps and eliminating post synthesis treatment before use. Porosity measurements by the Brunauer–Emmett–Teller method indicate that the samples are essentially non-porous. The synthesized catalysts characterized by X-ray Diffraction analysis show the presence of both metallic and carbidic species. The graphitic-carbon matrix has substantial structural defects that make it partly amorphous. Scanning Electron Microscopy analysis coupled with Energy Dispersive X-ray Spectroscopy mapping shows uniform dispersion of the metal moieties in the carbon support. Analysis by Transmission Electron Microscopy imaging displays metal nanoparticles with mean particle size within the 9–15 nm range enveloped in the carbon matrix.

Keywords Induction plasma · Suspension plasma · Cobalt–iron–carbon catalyst · Fischer–Tropsch

Introduction

Fischer–Tropsch catalysis is exploited commercially in the production of synthetic automobile fuels such as gasoline and diesel, alongside other associated petrochemical products. For process efficiency therefore, the catalysts employed must meet certain

✉ François Gitzhofer
francois.gitzhofer@usherbrooke.ca

[1] Department of Chemical and Biotechnological Engineering, Université de Sherbrooke, Sherbrooke, QC J1K 2R1, Canada

requirements that produce high activity and selectivity towards the desired fractions. Using syngas as the raw material, the Fischer–Tropsch synthesis (FTS) process polymerizes two simple molecules, namely, carbon monoxide and hydrogen ($CO + H_2$) to produce molecules with varying hydrocarbon chains and molecular weights. In this publication, we report on the application of induction plasma using the suspension plasma-spray (SPS) technology for the production of high quality FTS catalysts by means of a high throughput, single-step continuous method.

We suppose that plasma-synthesized catalysts will find a marketable application in the FTS process, particularly when supported on carbon since one of the greatest advantages derived from such catalysts lies in the concomitant production of both the metallic and carbidic species in the samples. It is presumed that the active species in FTS are metallic cobalt nanoparticles on one hand, and the Fe carbides on the other. In some instances it has been observed that carburization, which produces carbides enhances FTS activity with the Fe-based catalyst [1], but acting as a catalyst poison for the Co-based catalyst [2]. Although catalyst deactivation by carbon deposition is a major challenge when using non-carbon supported FTS catalysts, not all types of carbon (listed as coke, metal carbides, graphitic or hydrogen-containing carbon) lead to deactivation [3].

Several phases have been observed in Fe-based catalysts during FTS, which include metallic iron (Fe°), iron oxides (FeO, Fe_2O_3 and Fe_3O_4), and various forms of iron carbides, Fe_xC_y [4]. Some studies have shown that partially reduced carbon-supported Fe_3O_4 influences both catalyst activity and selectivity by forming the less stable non-stoichiometric iron-oxide-carbide species, which is perceived to be more active and more selective towards the formation of olefins than the known χ-Fe_5C_2 [5]. The formation and composition of these Fe-phases depend on the FTS process conditions, rate of catalyst deactivation and catalyst composition [6]. In order to improve on catalyst durability, some authors have produced carbon supported Fe–Co bimetallic alloys (Fe–Co/C) by mechanical alloying [7], but in this work, such materials were synthesized much faster, through an easy method with potential for scale-up and great reproducibility using the SPS technology.

Catalyst preparation by SPS technology improves synthesis efficiency and brings a lot of flexibility in the materials selection for Fischer–Tropsch synthesis (FTS) [8]. Multi-stage catalyst preparation techniques are tedious, time consuming and escalate both labor and material costs, besides being prone to cumulative errors that lead to variations in catalyst quality. Therefore, the SPS method provides better catalyst reproducibility in shortened preparation time, because it is a single-step approach, producing robust catalysts whose metal components do not sinter [9], have superior catalyst performance [10], with evenly distributed active species characterized by longer catalyst lifetime [11].

Since metal particles injected into the plasma follow various trajectories, the characteristics of any SPS product are determined by gas total *flow rate, velocity and residence time* [12]. An optimum flow rate of the material must therefore be established because sometimes a substantial fraction of the injected material goes unaffected either by failing to atomize or to ionize after melting [13]. Due to the probability of atomization being dependent on both the gas velocity and the particle's specific mass [14], small, spherically-shaped powder particles are most preferable in producing uniformity in the suspension, leading to a smoother flow.

The objective of this work was to produce in a single reaction step both the carbon matrix, which acts as the catalyst support and the metallic particles in the nanometric range alongside the FTS catalytically active Fe carbides. Nanometric catalysts were preferred because they would easily overcome diffusion limitations during FTS since highly porous catalysts get clogged due to unfavorable mass transfer of the large polymeric molecules,

and this leads to catalyst deactivation. At temperatures above 1000 K (727 °C), plasma generates Fe carbides [15], on which the Fe-catalyzed FTS reaction mechanism depends [16]. While the metal particles melt and vaporize in the plasma, the oil in which the metal particles are suspended is thermally cracked. Carbonaceous gases in the plasma react with hydrogen supplied to generate mainly methane and also interact with the metal cluster species (e.g. Fe) to produce carbides (e.g. Fe_2C, Fe_3C or Fe_5C_2). The remaining carbon then accumulates on the metal nanoparticles or the metal-carbide nanoparticles as well as on the cooler walls of the SPS reactor. The Fe_3C phase that was evident in our samples forms at temperatures above 1 373 K (1100 °C), below which it decomposes into graphitic carbon and austenite (FCC structure), and further into the α-Fe (BCC structure) below 973 K (700 °C) [17].

In this study, we synthesized carbon-supported catalysts under identical plasma conditions, sequentially developed from single metal formulations (Co/C, Fe/C), to Co–Fe/C bimetallics in various metal proportions, and then Co–Fe–Mo and Co–Fe–Ni ternary formulations. Our objective was to rationally design catalysts that would operate in a wide range of low-temperature FTS, particularly between 493 and 533 K (220 and 260 °C), without excessive formation of CO_2 and CH_4 at the upper end of the given temperature range. Preliminary catalyst activity tests were conducted in both fixed-bed [9] and slurry reactors [18] and the materials were found to be highly active for FTS, with the single-metal catalysts being more active at the lower temperature of 493 K, while the bimetallic formulations were more selective towards the diesel range at the higher temperature of 533 K [19] and with fine tuning of the catalyst pre-treatment procedure, excessive water production during FTS was cut by half [20]. This paper therefore discusses the catalyst synthesis procedure, and the materials' physicochemical properties as determined through the following characterization techniques: Brunauer–Emmett–Teller (BET) surface area analysis, Scanning Electron Microscopy (SEM) coupled with Energy Dispersive X-ray Spectroscopy (EDX) mapping, Transmission Electron Microscopy (TEM), and X-ray Diffraction (XRD) analysis in conjunction with Rietveld Quantitative Analysis (RQA).

Experimental Methods

Catalyst Synthesis by Plasma

The SPS plasma system using the PL-50 plasma torch supplied by Tekna Inc., operates at 3.2 MHz alongside other system parameters summarized in Table 1. A schematic for catalyst production is provided in Fig. 1, using the method already described [8]. While maintaining the triode plate power at 29 kW, a homogeneous mixture of 60 g of the metal (particle size range 1–10 μm) in 300 ml of mineral oil was introduced directly into the plasma using an atomization probe at a flow rate of 8.2 ml min^{-1} [9]. For the sample preparation in oxidizing medium, the H_2 in the sheath gas was replaced with O_2 gas flowing at 10 SLPM, while all the other conditions were held constant.

During the initials tests with Fe-only samples, a number of parameters were varied in order to assess their influence on the nature of the plasma products as follows:

(a) Plasma catalyst composition: introduction of pure metal (Fe), pure oxide such as nano-hematite, or mixed metal and oxide in mass ratio of Fe to nano-hematite = 2.
(b) Changing the residence time of the suspension in the plasma by altering the initial reactor pressure from 27 to 33 and then 67 kPa (equivalent of 200, 250 and 500 Torr

Table 1 Operating SPS process parameters

Process parameter	Values	
Plasma system	Power system	60 kW
	Plasma torch	Tekna PL-50 (3.2 MHz)
SPS characteristics	Nozzle (fitting the torch)	Subsonic type
	Injection probe	Liquid injection type
Suspension	Metal particle size	1–10 μm
	Concentration	0.2 g of metal/ml of oil
	Feed rate	8.2 ml min^{-1}
Plasma gas flow rates in standard liters per minute (SLPM)	Central gas	Ar: 23
	Atomization gas	Ar: 9.5
	Sheath gas	Ar: 72 H_2: 9.4
Plate power	Wattage	29 kW
	Efficiency	≈40 %
Reactor pressure	Initial pressure	27–67 Torr
	Final pressure	250–300 Torr

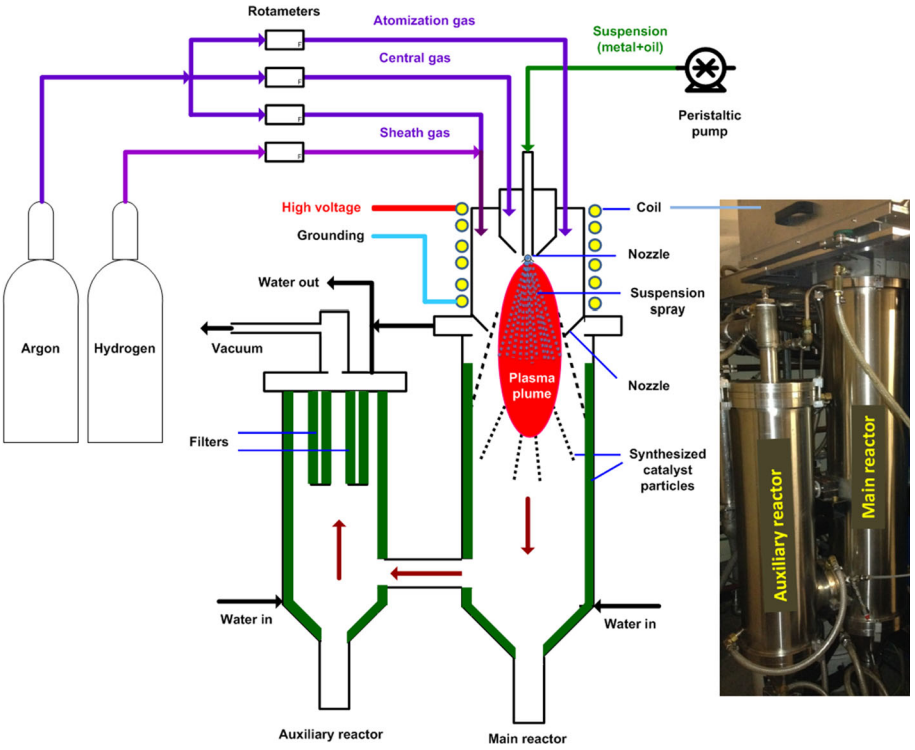

Fig. 1 Schematic of the plasma-reactor system used in catalyst synthesis with a pictorial inset of the setup

respectively). High vacuum (or lower pressure) exerts greater drag on the sample and leads to faster movement (or lower residence times in the plasma), while higher pressures confine the plasma and increases particle residence times in the plasma.

(c) The effect of applying either a reducing (H_2) or an oxidizing (O_2) atmosphere on the plasma product, for which only TEM analysis was used to characterize the samples and is discussed in Sect. 3.2.3.

Analogous Co-only samples were synthesized likewise–in reducing (H_2-rich) atmosphere, followed by Co–Fe bimetallic formulations and ternary systems (Co–Fe–Mo and Co–Fe–Ni), with various metal proportions being used as summarized in Table 2. The resulting powder materials were harvested manually from the walls of the reactors as well as from the filters mounted in the auxiliary reactor, and the catalysts stored away for future usage.

Catalyst Characterization

The synthesized catalysts were analyzed by various characterization techniques involving porosity analysis by the BET method, XRD modeled with the Rietveld Quantitative Analysis (RQA) technique, and Microscopic imaging by both SEM and TEM.

Porosity and the BET Surface Area Analysis

Porosity measurements of the synthesized catalysts were conducted on a Micromeritics Accelerated Surface Area Porosimetry (ASAP 2020) analyzer by determining their BET specific surface areas. Sample mass of about 0.5 g was initially degassed at 363 K (90 °C) for 30 min and then at 523 K (250 °C) for 50 h under evacuation until a pressure of less than 1 Pa (10 μm.Hg) was achieved. After cooling, the sample was re-weighed and then analyzed using N_2 gas physisorption under liquid nitrogen at 77 K (−196 °C) from an initial pressure of about 0.2 Pa (2 μm Hg) to ambient pressure. Adsorption–desorption isotherm plots were extracted to determine the materials' porosity.

Scanning Electron Microscopy (SEM)

A Hitachi S-4700 Scanning Electron Microscope, equipped with an EDX X-Max Oxford spectrometer was utilized for SEM analysis to capture both secondary and backscattered

Table 2 Metal mass injected into plasma to produce the single-metal (Co/C, Fe/C) catalysts, Co–Fe bimetallics or the Ni–Co–Fe and Mo–Co–Fe ternary formulations

Catalyst sample (total mass 60 g)	Mass (g)			
	Co	Fe	Ni	Mo
100 %Fe/C	–	60	–	–
30 %Co–70 %Fe/C	18	42	–	–
50 %Co–50 %Fe/C	30	30	–	–
70 %Co–20 %Fe–10 %Mo/C	42	12	–	6
70 %Co–20 %Fe–10 %Ni/C	42	12	6	–
70 %Co–25 %Fe–5 %Ni/C	42	15	3	–
80 %Co–20 %Fe/C	48	12	–	–
100 %Co/C	60	–		

images. EDX mapping of the samples was performed to determine the metal distribution in the carbon matrix.

Transmission Electron Microscopy (TEM)

TEM analysis using an accelerating electron beam of 120 kV from a tungsten filament was conducted on a Hitachi H-7500 instrument and images captured in the bright field mode by means of a bottom-mounted AMT 4 k × 4 k CCD Camera System Model X41. Particle-size distribution analysis was done by means of the Nano-measurer version 1.2 "Scion Imager" software.

XRD Analysis

A Philips X'pert PRO Diffractometer from PANalytical was used for XRD analysis, set in the Bragg–Brentano configuration with PIXcel-1D detector and operated on the factory installed Analytical Data Collector software. The diffractometer was fitted with Ni-filters for the Cu Kα radiation (1.5406 Å) produced at 40 kV and 50 mA. The XRD patterns were recorded in the range of 20° to 110° [2θ] angle at a scanning speed of about 3° [2θ] min^{-1}, with a step size of 0.040° [2θ] angle. The anti-scatter and divergent slits were fixed at 1°. Data analysis was done using the MDI JADE 2010 (version 2.6.6) software and compared with the Powder Diffraction Files in the Database (version 4.13.0.2) using the PDF-4 + software 2013 (version 4.13.0.6). Since these samples comprise a maximum number of four elements, the number of phases present after synthesis is numerous and the relative mass fraction of each phase was determined using the RQA method [21], in conjunction with the High Score Plus modeling software [22].

Results and Discussion

The Rationale for Catalyst Synthesis

In this work, the use of nanometric carbon matrix as a catalyst support has not been found to adversely affect catalyst activity during FTS through effects such as carburization or coking. This concurs with other authors who have observed that the amorphous carbonaceous species deposited on the catalyst were mere spectators, and did not impair the catalyst activity in the measuring time period of about 500 h [1]. In our case, the plasma-synthesized samples were observed to be highly graphitic, although characterized by some disorder arising from widespread structural defects [9].

Generally, the single metal catalysts (Co/C, Fe/C) were quite active at the low FTS temperature of 493 K. However, at 533 K where formation of the shorter molecular chains was expected, catalyst selectivity shifted disproportionately towards the production of CO_2 and CH_4 gas. For this reason, the Co–Fe bimetallics were formulated in order to improve catalytic selectivity by moderating the formation of CO_2 and CH_4 gas, but their capacity to lower H_2O production was still poor. Therefore, application of metal ternary (Co–Fe–Mo and Co–Fe–Ni) systems was instructive with Ni being introduced into the Co–Fe/C catalytic structure as a first step to suppress water production in FTS by augmenting the water–gas shift reaction rate [23].

On the other hand, Mo was expected to increase the surface acidity of the catalyst in order to improve its selectivity toward the diesel fraction [24]. Additionally, in choosing the three bimetallic compositions, we were testing a hypothesis that, according to the Co–Fe binary phase diagram by Okamoto [25], the plasma-generated 50 %Co–50 %Fe and 30 %Co–70 %Fe formulations would contain identical intermetallic phases while the 80 %Co–20 %Fe formulation would exhibit unique properties since its Co–Fe intermetallic phases would be different. Instead, it was observed that the 50 %Co–50 %Fe formulation was more distinctive with the highest mean particle size (14.4 nm) compared to the other two formulations with a lower mean particle size (9 nm).

Catalyst Characterization

BET Surface Area Analysis

In general, porosity analysis indicated similarities in the adsorption–desorption isotherms, with Fig. 2 representing a typical plot, independent of catalyst composition. For every tested catalyst, the lack of a notable hysteresis loop signifies that the samples were non-porous. The overlaid pore distribution plots shown in Fig. 3 imply that there exists some micro-porosity with pore size of less than 10 nm. However, since microporous materials usually display greater hysteresis, this means that the packing of the nanometric catalyst particles creates some artificial nano-porosity due to gas adsorption between packed nanoparticles [18]. Nevertheless, some disparities were observed particularly from identical samples collected from different reactors. For example, when samples from the main plasma reactor were compared to those that originated from the auxiliary reactor, Co/C catalysts had comparable BET specific surface areas, while the 80 %Co–20 %Fe/C and 70 %Co–20 %Fe–10 %Ni showed a higher surface area in the samples from the main reactor. The rest of the samples (70 %Co–25 %Fe–5 %Ni, 50 %Co–50 %Fe/C, 30 %Co–70 %Fe/C and Fe/C) from the auxiliary reactor indicated higher surface areas, see Table 3. Overall, the properties of the materials collected from the filters as well as the walls of the

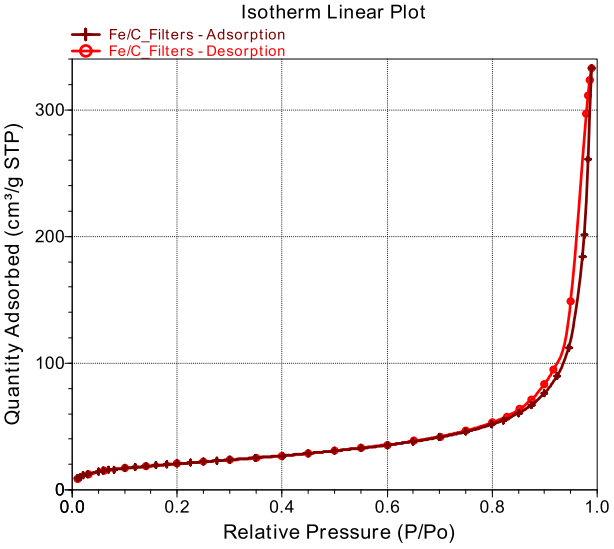

Fig. 2 Representative adsorption–desorption isotherms of the Fe/C catalyst from filters showing limited hysteresis as a sign of non-porosity in the samples

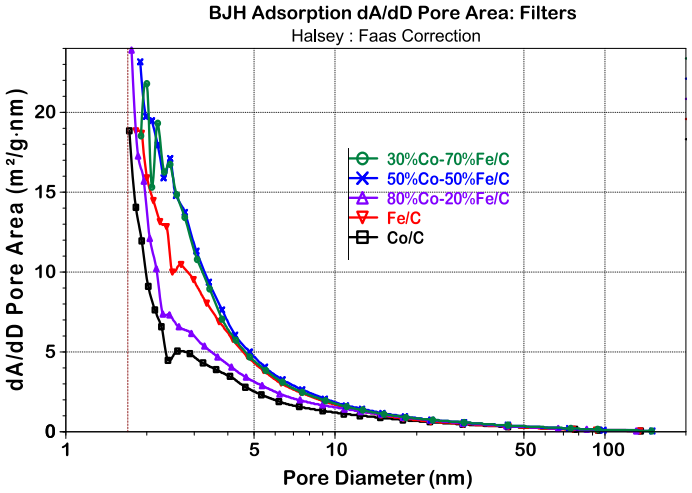

Fig. 3 Pore distribution plots by pore area for the catalysts drawn from the auxiliary reactor

Table 3 Comparative porosity analysis of the catalyst materials by the BET method

Catalyst (expected composition)	BET Surface area (m^2 g^{-1})		Average pore diameter (nm)[a]		Total pore volume (cm^3 g^{-1})[b]	
	Auxiliary reactor	Main reactor	Auxiliary reactor	Main reactor	Auxiliary reactor	Main reactor
100 %Co/C	55.5	54.4	27.4	28.3	0.38	0.39
80 %Co–20 %Fe/C	67.2	72.8	24.4	22.0	0.41	0.42
70 %Co–20 %Fe–10 %Ni/C	69.2	76.3	25.8	19.3	0.45	0.37
70 %Co–25 %Fe–5 %Ni/C	92.6	88.7	20.6	19.1	0.48	0.42
50 %Co–50 %Fe/C	92.2	73.3	22.3	20.8	0.51	0.38
30 %Co–70 %Fe/C	91.1	73.1	22.6	18.9	0.51	0.34
100 %Fe/C	72.2	35.4	21.6	32.6	0.40	0.28

[a] Single point adsorption total pore volume of pores less than 120 nm in diameter at $P/Po = 0.98$

[b] Average pore diameter (4 V/A by BET)

auxiliary and main reactor were similar, with BET specific surface areas that did not exceed 100 m^2 g^{-1}.

Scanning Electron Microscopy (SEM)

Synthesized catalysts were characterized by SEM in conjunction with EDX, where both spot and area analysis indicated uniform distribution of the metal nanoparticles in the carbon matrix of all the samples. Secondary and backscattered SEM images of the 30 %Co–70 %Fe/C catalyst are shown in Fig. 4 as a representative. In addition, EDX

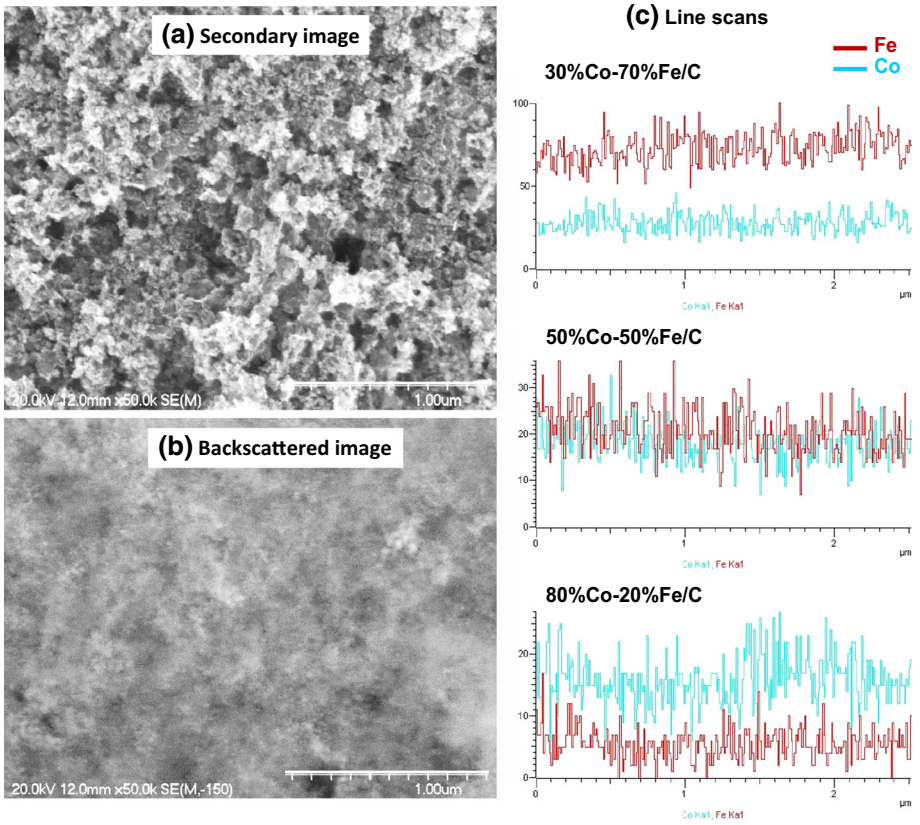

Fig. 4 SEM analysis of the as-synthesized catalyst from the main reactor showing **a** secondary and **b** backscattered images of the 30 %Co–70 %Fe/C sample; **c** EDX *line* scans of the three bimetallic samples

mapping conducted on the bimetallic catalysts confirmed that the mass loading and dispersion of the metal nanoparticles in the carbon matrix was indeed uniform and without particle agglomeration as expected. This is clear from the line scans shown in the same figure. Notice the gradual increase of the red shade in the sample images with higher Co loading as portrayed in Fig. 5 and the blue one for Ni in Fig. 6.

TEM Analysis

The as-synthesized catalysts were analyzed by TEM imaging from which metal particle dispersion and particle-size distribution were determined.

The Effect of Fe Precursor: Pure Metal Versus Oxide feedstock Either pure metal or pure hematite mixed in mineral oil was introduced into the plasma. Since the commercial nano-hematite is fluffy, the intended 60 g could not be accommodated into the 300 g of mineral oil. Therefore, only 20 g have been used instead. It was observed that by using H_2 as the plasma sheath gas, the hematite was reduced to metallic iron during the plasma synthesis step. In both cases (use of pure metal or pure hematite), the spherical metal particles were

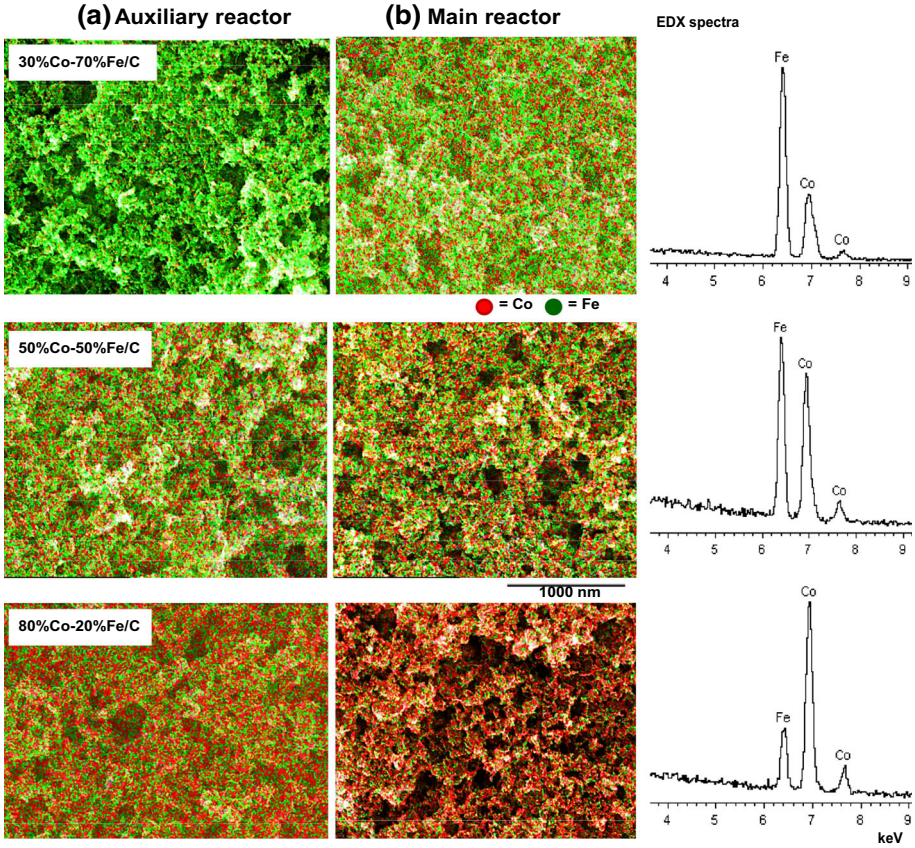

Fig. 5 EDX imaging of the as-synthesized bimetallic catalysts indicating characteristic uniform metal dispersion, with their respective EDX spectra

similar in morphology and completely surrounded by the carbon matrix generated in situ, while some metal nanoparticles were clearly enclosed in a carbon capsule, see Fig. 7. The only difference between samples originating from the different feedstocks was that, where the nano-hematite was used, there was less metal in the carbon matrix since only a third of the original mass was used.

Particle Residence Time in Plasma as an Effect of Pressure on Fe Catalysts Changing the initial pressure in the reactor chamber was intended to determine the residence time of the particles in the plasma. Higher pressure leads to longer residence times while high vacuum shortens the particle residence time in the plasma. It was observed that the residence time of the particles in the plasma did not considerably affect the nature of the catalysts, and morphologically they were similar as depicted in Fig. 8. In this unique test, 20 g of nano-hematite were used instead of 60 g, and as mentioned above, many areas of the carbon matrix in the catalyst were observed to be devoid of metal.

The Effect of Gas on Fe Catalysts: H_2 Versus O_2 When the commercial nano-hematite (with mean particle size of 4 nm) as seen in Fig. 9a was introduced into the plasma, it was

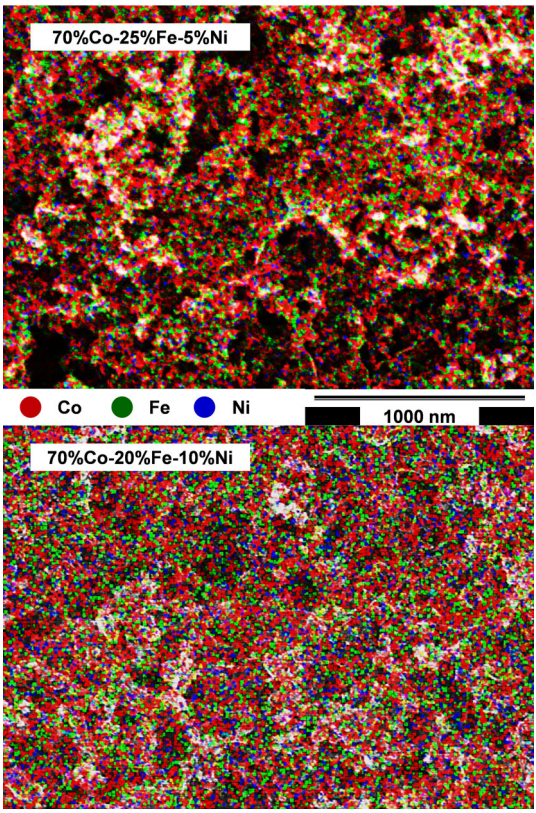

Fig. 6 EDX imaging of the as-synthesized Co–Fe–Ni ternary catalysts from the main reactor indicating uniform metal dispersion

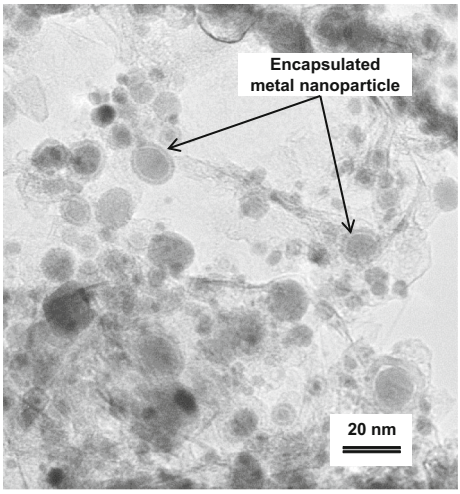

Fig. 7 A sample TEM image of the Fe/C catalyst from the main reactor synthesized from pure metal and oil in H_2 plasma sheath gas

observed that a reducing atmosphere produced metal moieties embedded in a carbon matrix as shown in Fig. 9b, while an oxidizing atmosphere led to substantial particle growth, see Fig. 9c. In a reducing environment, the mineral oil provided the carbon that

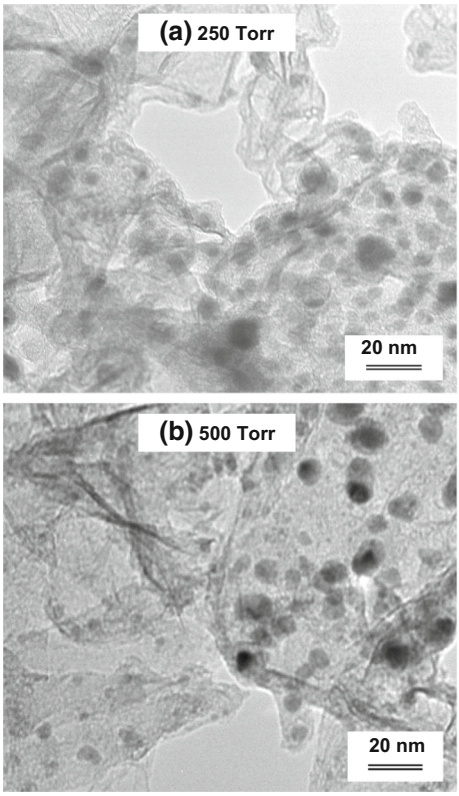

Fig. 8 TEM images of main reactor Fe/C as-synthesized catalysts originated from nano-hematite prepared using different residence times

encaged the metal particles, thereby preventing agglomeration by ring fencing each particle from possible contact with its neighbors. On the other hand, the oxidizing atmosphere consumed the oil meant to produce the carbon matrix in the catalyst resulting in extra enthalpy in the plasma plume. Therefore, a lack of ring fencing and particle lability, coupled with excessive heat led to the fusion and crystal growth of the feedstock nano-hematite particles. Larger particles were thought to have had protracted residence times in the plasma due to local eddies at the reactor top as determined experimentally by Jia [26, p. 75], with typical particle velocity of up to 40 m s^{-1}, as demonstrated by Goortani [27, p. 114]. The observations on particle growth related to the oxidizing-reducing plasma conditions confirmed that a reducing atmosphere was imperative for the plasma-synthesis of active FTS catalysts using this approach.

Comparison of Co/C and Fe/C Catalysts One remarkable feature in the Co-based catalysts was the stacking faults as marked in Fig. 10. Nonetheless, the materials were identical to the Fe-based catalysts, having the metal moieties evenly spread and implanted in the carbon matrix. Overlaid particle size distribution plots for over 750 particles measured per sample indicated no substantial differences in their mean nanoparticles size (Co/C = 11.0 nm; Fe/C = 11.3 nm), as shown in Fig. 11.

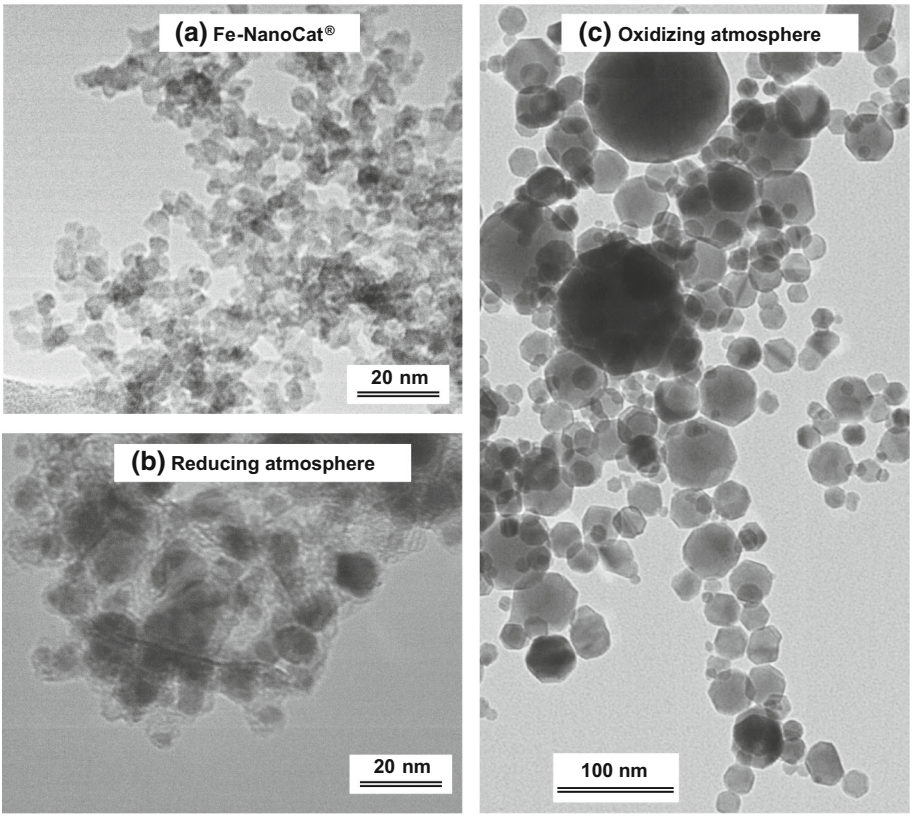

Fig. 9 TEM images of **a** the nano-hematite feedstock; and **b** Fe/C catalyst as derived from oil in H_2 and **c** the plasma product as derived in O_2 (polygons are oxides), collected from the main reactor

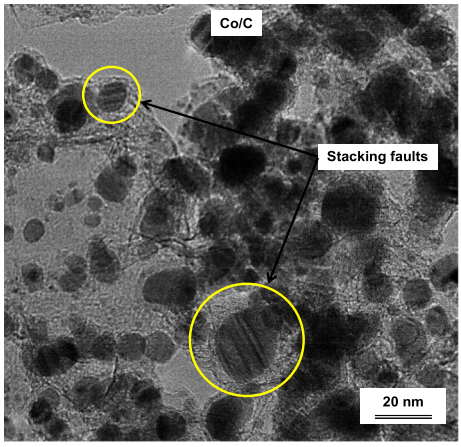

Fig. 10 A characteristic TEM image of the Co/C catalyst sample from the auxiliary reactor

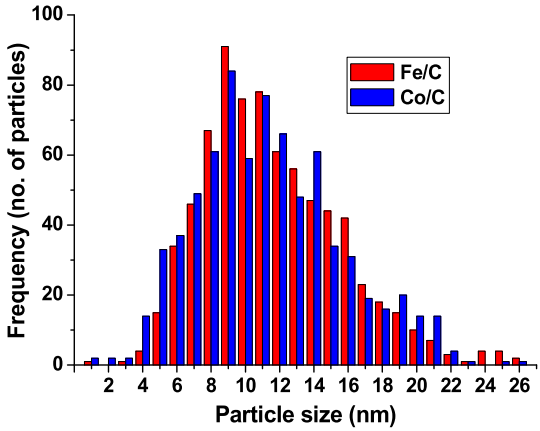

Fig. 11 Overlaid plots showing particle size distribution of Co/C and Fe/C catalysts from the auxiliary reactor

Comparison of the 3 Bimetallic Co–Fe Catalysts Figure 12 illustrates that the SPS method produces bimetallic catalysts with comparable metal nanoparticle dispersion and physical properties. There was no significant variation in the morphology of the materials, whether single metal (Co/C, Fe/C) or Co–Fe/C bimetallics in their various metallic proportions after SPS. This makes the SPS approach unique in producing catalysts with uniform qualities, and provides strong evidence for its capacity to easily reproduce catalyst synthesis.

Notice the carbon nanotube in the micrograph. It has been advanced [28] that plasma temperature, velocity, gas-phase composition fields and precursor injection conditions are the major driving factors that determine the optimum region for carbon nanoparticle growth. A key characteristic of the graphite growth mechanism in the plasma involves carbon nucleation on the surface of the catalyst material (Fe or Co) by the decomposition of gaseous hydrocarbon molecules followed by diffusion of the hydrogen away from the surface. Once the nanoparticle is supersaturated with the carbon atoms, they form hexagonal sheets that conform to the curvature of the particle and this mechanism is energetically favored [28]. Graphite forms when the carbon feedstock is injected into the plasma zone ($T \approx 10{,}000$ K for argon plasma). However, in low-temperature regions of the reactor, typically below the melting point of the Fe catalyst in the plasma (1800 K), particle growth leads to deposition of amorphous carbon products. At temperatures in excess of 1800 K, only graphitic carbon can grow, thereby producing thin sheets. Carbon nanotubes (CNTs) can be considered as tiny rolled up sheets that form single walled, double-walled or multi-walled nanotubes (SWCNTs, DWCNTs, or MWCNTs respectively) and CNTs have also been found to be favorable supports in FTS [29, 30].

In the plasma synthesis of our catalysts, the metal clusters act as the catalytic growth centers for the nanometric carbon matrix, where nano-graphitic sheets and CNTs are formed in the presence of mineral oil as a carbon source [31]. In chemical vapor deposition (CVD), for example, it has been observed that in the presence of a catalyst (Ni, Fe or Co), the hydrocarbon molecules are broken into reactive species at the temperature range of 823–1273 K (550–1000 °C) to produce CNTs [32]. Although some authors claim that metal oxides are necessary for the growth of CNTs and carbon nanofilaments (CNFs) [28], the lack of oxygen in the plasma reactor system precludes the formation of iron oxides, which are precursors of CNFs. Thus, the presence of CNFs are rather scarce, but we

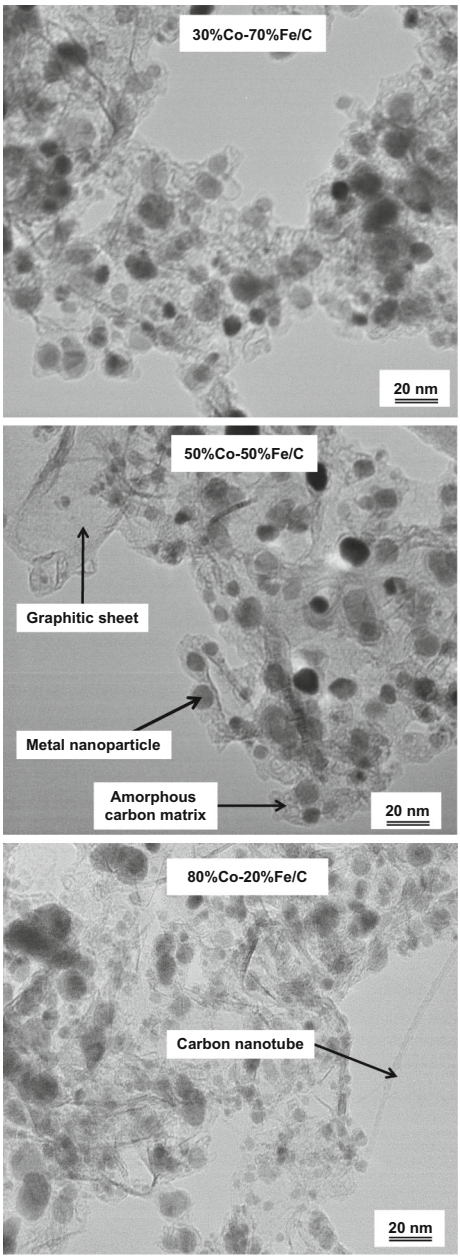

Fig. 12 TEM images of the Co–Fe/C bimetallic catalysts drawn from the auxiliary reactor

extensively observe graphitic sheets where H_2 is used [33]. In this work, the addition of O_2 in the plasma gas stream was intended to ensure that the metal oxides were not completely reduced to the metal during synthesis. Nevertheless, TEM images indicated no morphological variations in the catalysts, whether synthesized in the presence of O_2 or H_2 in the plasma gas, because CNF growth is partly time-depended. The residence time of the precursor catalyst material in the plasma was inevitably too short to allow for CNF growth.

In producing α-Fe and Fe carbide nanoparticles by the use of nano-hematite, it was shown that the process is both temperature and time-dependent, exceeding 503 K and about 15 min [34]. However, due to high temperatures experienced during the production of α-Fe and Fe carbide nanoparticles by plasma synthesis, those reactions are instantaneous [35]. It has been noted that higher carbon feedstock concentration in addition to higher temperature usually offers more carbon species available for nano-sheet growth [36]. In our case the hydrocarbon feedstock to the plasma catalyst (or metal powder) was in the ratio of 5:1 mass by mass, in the plasma gases (Ar and H_2).

Between the three bimetallic compositions, the only difference observed was the average diameter of the particles. A sample of over 250 nanoparticles was measured for each catalyst, and it was observed that the particle-size distribution for both the 80 %Co–20 %Fe/C and 30 %Co–70 %Fe/C bimetallic catalysts was identical (ca. 9 nm), and a similar trend was also recognized for the single metal Co/C and Fe/C catalysts (ca. 11 nm). However, only the 50 %Co–50 %Fe/C bimetallic catalyst displayed a wider particle size distribution with a mean particle size of 14.4 nm, see Fig. 13. Since none of the characterization techniques could provide conclusive information on the nature and quantity of the Co and Fe nanoparticles in the materials, intuitively we suspect that the 50 %Co–50 %Fe sample had comparatively bigger particles due to elaborate CoFe intermetallic formation, thereby enhancing metal–metal cluster agglomeration. Therefore, by inductive argument we think that the 50 %Co–50 %Fe/C sample had more CoFe nano-alloys than the other two bimetallic samples because all the Co could have alloyed with all the Fe and vice versa. However, in the 80 %Co–20 %Fe/C sample, only a maximum of 20 % Co

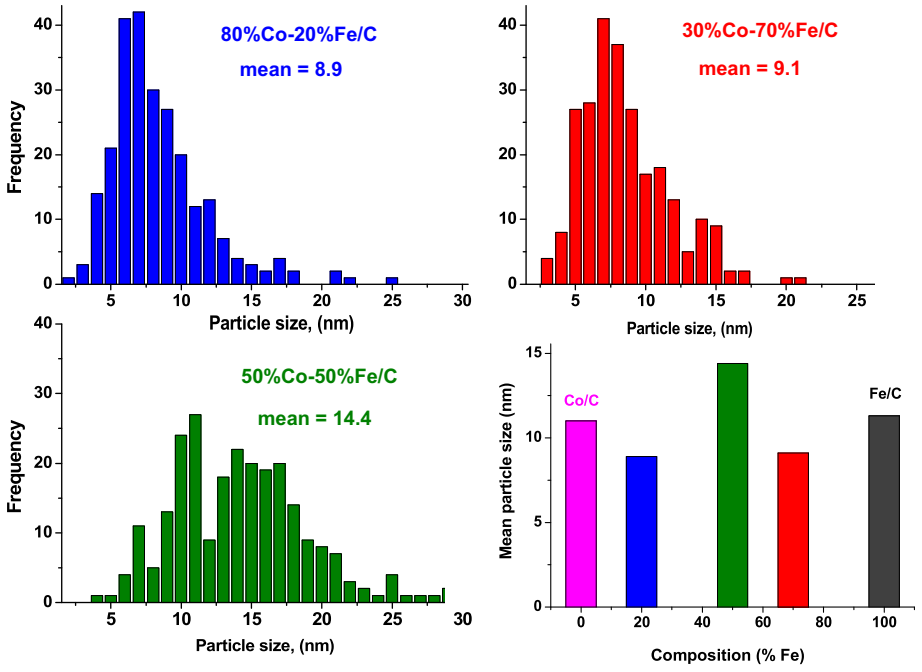

Fig. 13 Plots of the average particle size of catalysts drawn from the auxiliary reactor as analysed by TEM imaging

metal could form the CoFe intermetallic nano-alloy, while in the 30 %Co–70 %Fe/C sample only a maximum of 30 % Fe metal could form the CoFe intermetallic nano-alloy.

Since SPS technology produces metal nanoparticles within a narrow size range, this property becomes increasingly critical in processes such as FTS that are particle-size sensitive. For example, it has been shown that for Co-based FTS catalysis, no intrinsic particle size effect exists for metal particle size between 3.5 and 10.5 nm, but for the smaller particles below 2.5 nm, the metallic Co is easily oxidized by the water vapor, leading to lower turnover frequency (TOF) and higher CH_4 selectivity [37]. This means that a process that generates a higher percentage of catalyst nanoparticles below 2.5 nm will experience faster catalyst deactivation due to the formation of CoO. Other authors using cobalt particles in the size range of 2.6–27 nm found the optimum at 6–8 nm where, larger particles displayed lower catalytic activity while smaller particles recorded both lower activity and lower selectivity towards FTS products [38].

Similar observations on particle-size effect have been made in Fe-based catalysts from a study with particles in the size range of 2–12 nm. The best CO conversion was obtained at 6.1 nm. An increase in the particle size was seen to enhance the reduction capacity of the catalyst, which tends to increase its selectivity towards FTS products, and lowers CH_4 formation. In addition, increasing the particle size from 2.4 to 6.2 nm improved TOF, which remained almost constant up to a particle size of 11.5 nm [39]. Therefore, in view of its perceived potential for easy scale up, we find the plasma method most appropriate for the production of FTS catalysts having the right metal nanoparticle size-range.

Comparison of the Co–Fe–Mo and Co–Fe–Ni Ternary Catalytic Systems Figure 14 shows that the Co–Fe–Mo and Co–Fe–Ni ternary systems have similar metal particle dispersion. The consistency in the quality of the catalysts demonstrates that the SPS process is robust and reliable in reproducing the materials irrespective of the kind of metal used in the range of our operating conditions.

XRD Analysis

XRD analysis as displayed in Fig. 15 shows that all the Fe-containing catalysts comprise considerable amounts of carbides (Fe_3C), which display the major peak at 45° (2θ) angle, although this peak overlaps with those of cobalt's FCC and HCP peaks. With increasing Co-loading in the samples, the peak intensities of Fe gradually diminishes as expected. The 50 %Co–50 %Fe sample shows both metallic Co and Fe phases. In these results, it is clear that none of Co/C catalysts contains significant amount of HCP metallic Co.

XRD phase quantification in the as-synthesized bimetallic catalysts was modeled using the RQA curve fitting, and the 30 %Co–70 %Fe/C catalyst is shown in Fig. 16 as a representative. Although the RQA of the single metal catalysts (Co/C and Fe/C) has already been discussed [18], it is worthwhile comparing their phases with those of the 3 bimetallics here. The analysis showed crystalline phases of both metallic and metal-carbide species in the materials, besides the presence of graphitic carbon. Only the Co/C sample contained Co carbides (Co_3C), which were absent in the bimetallics, while all the Fe-containing samples had Fe carbides particularly in the form of Fe_3C.

The RQA results obtained are summarized in Table 4. The estimated standard deviation (e.s.d) values, which reflects the precision of the refined parameters are indicated in brackets and should tend to zero. Ideally, the curves' goodness of fit (GOF) with the High Score Plus software, should be close to 1 [40], but a value of 2, which is the case with most

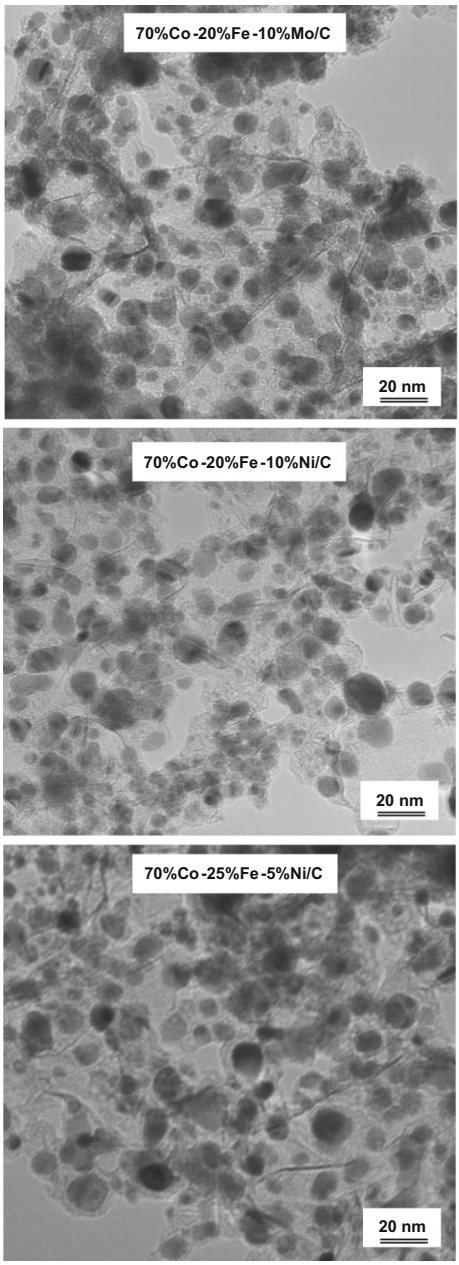

Fig. 14 TEM images of the Co–Fe–Mo and Co–Fe–Ni ternary catalysts from the main reactor

of our analyses should still be acceptable owing to the compounding difficulties encountered that included peak overlaps, peak broadening, peak extinction, and amorphicity arising from disordered carbon characterized by the high noise to signal ratio. In the Mo- or Ni-containing samples, neither Mo nor Ni could be quantified due to a comparatively higher concentration of Co in the samples, as exemplified in Fig. 17 for the Ni-based ternary-system catalyst.

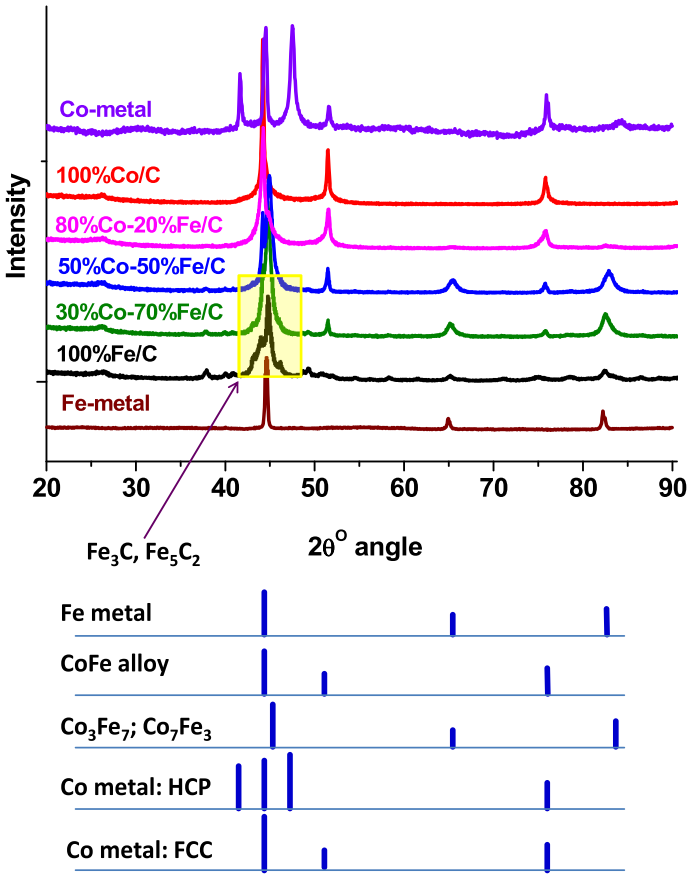

Fig. 15 XRD patterns of the Co–Fe/C bimetallics compared to the single metal Co/C and Fe/C catalysts drawn from the auxiliary reactor

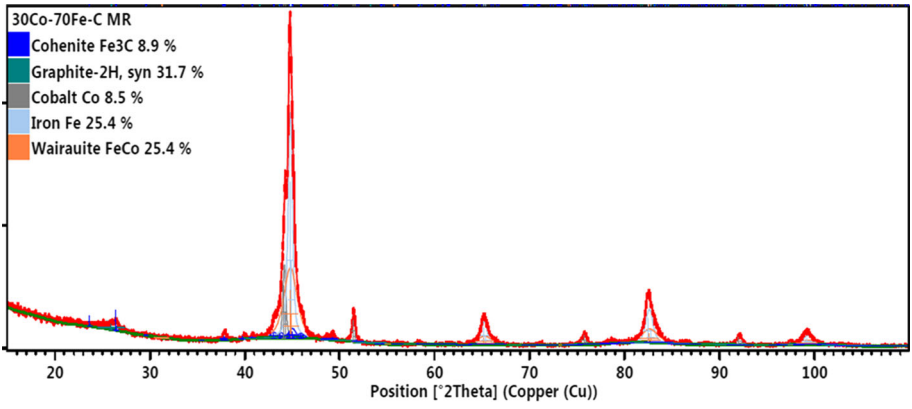

Fig. 16 Curve fitting by Rietveld analysis using XRD spectra of the as-synthesized 30 %Co–70 %Fe/C catalyst from the main reactor

Table 4 Rietveld quantitative analysis of the as-synthesized catalysts (auxiliary reactor)

Phase	Catalyst composition				
	100 %Co	80 %Co–20 %Fe	50 %Co–50 %Fe	30 %Co–70 %Fe	100 %Fe
Co_3C	6.7 (1)	UQ	–	–	–
Fe_3C	–	–	4.6 (2)	8.9 (1)	26.0 (1)
Graphite-2H	54.1 (1)	27.0 (1)	35.0 (1)	28.0 (1)	40.0 (3)
Co (metal)	39.2 (2)	46.3 (3)	10.6 (1)	8.8 (2)	–
Fe (metal)	–	3.5 (2)	25.0 (1)	28.0 (1)	34.0 (3)*
FeCo intermetallic	–	23.0 (1)	24.0 (1)	26.0 (1)	–
Fe_2C	–	UQ			UQ
Other Co–Fe alloys	–	LC			–
Fe_5C_2		PO			UQ
Quality of refinement					
GOF	1.60	2.66	1.57	1.56	1.59

UQ, unquantifiable, but presence likelihood high; PO, present in all samples, but impossible to quantify due to peak overlaps with Co; *Fe*°, *mixed phases: metallic iron 20.9 % (3), Taenite = 13.1 % (3); e.s.d, estimated standard deviation (bracketed values); LC, impossible to quantify for lack of reference patterns with position of atoms; GOF, goodness of fit $(\chi^2) = (R_{wp}/R_{exp})^2$ and should approach unity; R_{exp}, expected R or the "best possible R_{wp}" factor; R_{wp}, weighted profile (R-factor)—weighted to emphasize peak intensity over background

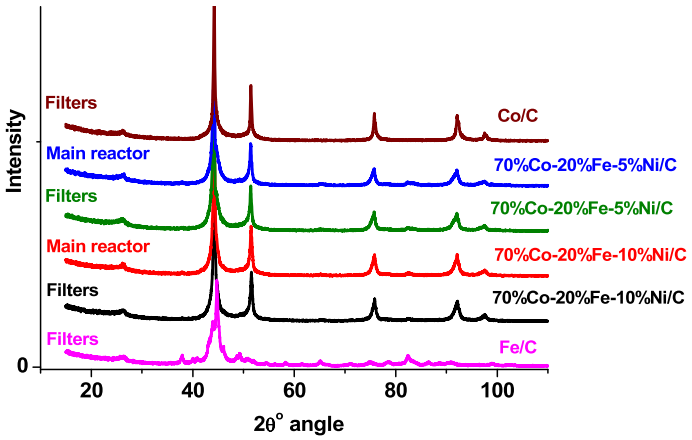

Fig. 17 XRD patterns of Ni–Co–Fe/C ternary system compared to single metal Co/C and Fe/C catalysts

Phase quantification by the Rietveld application of XRD analysis showed that the Fe/C catalyst contained ~40 % graphitic carbon, 34 % Fe° and 26 % Fe_3C. The Co/C sample comprised ~54 % graphitic carbon, 39 % Co°, and 7 % Co_3C. Unique to the Co-containing samples were stacking faults recognized in TEM images. The original Co metal feedstock used in the plasma contained mixed phases of both hexagonal closed packing (HCP) structure (ca. 38 %), and the face-centered cubic (FCC) structure (ca. 62 %). Both structures were evident from the XRD analysis of the original metal. Only nanoparticles with the FCC structure exited the plasma reactor, because Co takes the HCP structure, but

above 693 K (420 °C) the FCC structure prevails, although nano-sized particles in the range of 10–20 nm adopt the FCC phase at room temperature [41].

A good proportion of the metallic phase (Fe° or Co°) was identified in all samples, while the bimetallics consisted of some measure of the CoFe intermetallic phase. Although other alloys were present in the samples, it was impossible to precisely and conclusively identify them, either for lack of reference patterns with the right atom positions such as Fe_2Co, or their determined values were within the error margin, thereby making any such conclusion unreliable. Nonetheless, reflections from the characteristic (111), (200) and (220) crystal planes of CoFe (FCC) solid solution phase were observed at approximately $2\theta = 44°$, 51° and 75°, respectively. In addition, the (110), (200), (211) peaks of α-Co_7Fe_3 (BCC) phase were observed at about 45°, 66° and 84°, respectively [42]. The Co_3Fe_7 seemed to share the same XRD peak positions with Co_7Fe_3 [43].

Besides, some of the phases were below the instrument's detection limits, particularly for the Co–Fe/C bimetallics and ternary systems (Co–Fe–Mo and Co–Fe–Ni/C) due to some of their phases existing in minute quantities. Furthermore, peak overlaps in the samples made it problematic to quantify the other intermetallic phases or metal carbides such as Fe_5C_2 and Fe_2C, which were possibly present. Likewise, additional hitches arose in the analysis since substantial amount of disordered carbon existed in the samples. Complete phase quantification was therefore constrained by various factors such as high noise to signal ratio arising from considerable amorphicity, peak overlaps, highly nanometric samples leading to peak broadening and consequently peak extinction, compounded by software limitations where some reference patterns were lacking.

Benefits of SPS Technology in Catalyst Synthesis

In this work, we opine that catalysts synthesized by the single-step plasma technology are highly reproducible because it is a less complex method. Since it has been established that carbide species enhance FTS activity in Fe-based catalysts, the simultaneous formation of metallic and carbidic species entrenched in a nanometric carbon support provides substantial benefits for such catalysts. This would be in addition to other favorable advantages derived from time, labor and material cost-reduction measures in the process.

Characterization of the plasma-synthesized materials confirmed the catalysts' nanometric properties. From their BET adsorption–desorption isotherms, the samples were found to be identical in nature, having plots that were characteristic of type II isotherms. Such materials are distinctively non-porous. Their pore structure and pore distribution plots were equally comparable. However, it was observed that the single metal catalysts had higher pore diameter measurements than the bimetallics. Conversely, the single metal catalysts had lower BET specific surface areas than their bimetallic counterparts. The small pore volumes (ca. 0.4 $cm^3\ g^{-1}$) alluded to the non-porous nature of the materials. In FTS, non-porous catalysts would be advantageous since mass-transfer limitations are eliminated. Catalyst deactivation as a result of poor mass transfer of the high molecular weight FTS products clog catalyst pores, and for that reason we have argued that porous materials must be avoided [18].

All the samples took the form of spherical metal nanostructures, entrenched in a carbon matrix that is partially hydrogasified by reduction in a H_2 stream at $\sim$673 K (400 °C) in order to expose the metal moieties for FTS catalysis. Both SEM and TEM analysis showed uniform dispersion of the metal nanoparticles in the samples, generally with particle size range between 1 and 30 nm, and a mean size of $\sim$9 nm for the 80 %Co–20 %Fe/C and 30 %Co–70 %Fe/C bimetallics, $\sim$11 nm for the single metal (Co/C, Fe/C) catalysts and

over 14 nm for the 50 %Co–50 %Fe/C bimetallic catalyst. The carbon support in which the metal nanoparticles were lodged was highly graphitic, but with considerable structural defects, which contributed to its partial amorphicity. Carbon supports have been found to be desirable for FTS [44], with graphitic support being more appealing for FTS because it has various advantages that include: its chemical inertness that prevents reaction with the active metal phase, while at the same time inhibiting undesirable reactions with the syngas; its thermal stability at high temperatures; it does not sinter or shrink during reaction, thus exhibiting limited thermally-induced loss of surface area; it has favorable thermal and electrical conductivity properties; and it has good mechanical strength [45].

Conclusion

Novel and high quality nanometric catalysts with potential for application in Fischer–Tropsch synthesis were produced through induction plasma material synthesis using SPS. The catalysts encompassed single metal (Co/C and Fe/C) formulations, Co–Fe/C bimetallics, as well as the Co–Fe–Mo/C and Co–Fe–Ni/C ternary systems, and they were found to be primarily non-porous as determined by BET surface area analysis. Microscopy (SEM) through EDX mapping revealed uniform dispersion of the metal moieties in the carbon matrix, while TEM analysis indicated metal nanoparticle size with mean in the range of 9–15 nm. Although quantitative analysis through XRD coupled with RQA was attempted in order to determine the exact distribution of the phases in the materials, difficulties existed particularly due to the presence of a significant amount of the support being amorphous. Furthermore, peak broadening, peak overlaps, peak extinction and a lack of database reference patterns added to the analysis difficulties. Nevertheless, qualitatively we got cues of the possible phases that were present in the samples, which included pure metal phases (Co° and Fe°), Co–Fe intermetallic alloys (CoFe, Co_3Fe_7 and Co_7Fe_3) and the carbides (Co_3C, Fe_2C, Fe_3C, and Fe_5C_2). The Fe carbides are understood to be the active phase in the Fe-based FTS catalysts, which makes the plasma synthesis a valuable approach in catalyst preparation.

Acknowledgments The authors gratefully acknowledge the Canadian National Centres of Excellence (NCE) BioFuelNet for financial support; Prof. Nadi Braidy in conjunction with the CCM (Centre de Caractérisation des Matériaux, Université de Sherbrooke) staff for facilitating the characterization: Mrs. Irène Kelsey Lévesque and Mr. Carl St.-Louis for BET surface area analysis, Mr. Charles Bertrand for Microscopy (SEM & TEM), and Mr. Stéphane Gutierrez for XRD analysis.

References

1. Ding M, Yang Y, Wu B, Xu J, Zhang C, Xiang H, Li Y (2009) Study of phase transformation and catalytic performance on precipitated iron-based catalyst for Fischer–Tropsch synthesis. J Mol Catal A: Chem 303:65–71
2. Tsakoumis NE, Rønning M, Borg Ø, Rytter E, Holmen A (2010) Deactivation of cobalt based Fischer–Tropsch catalysts: a review. Catal Today 154(3–4):162–182
3. Moodley DJ, van de Loosdrecht J, Saib AM, Niemantsverdriet HJW (2010) The formation and influence of carbon on cobalt-based Fischer–Tropsch synthesis catalysts: an integrated review. In: Davis BH, Occelli ML (eds) Advances in fisher tropsch synthesis, catalysts and catalysis. CRC Press, Boca Raton, pp 49–81
4. Bahgat M (2006) Technology of iron carbide synthesis. J Mater Sci Technol 22(03):423–432

5. Bengoa JF, Alvarez AM, Cagnoli MV, Gallegos NG, Marchetti SG (2007) Influence of intermediate iron reduced species in Fischer–Tropsch synthesis using Fe/C catalysts. Appl Catal A 325:68–75
6. Davis BH (2009) Fischer–Tropsch synthesis: reaction mechanisms for iron catalysts. Catal Today 141:25–33
7. Yoo Y-G, Yang D-S, Jiang B, Yu S-C, Greneche JM (2006) Local ordering study of nanostructured FeCo–C alloys for various Fe contents. J Korean Phys Soc 48(6):1463–1467
8. Blanchard J, Abatzoglou N, Eslahpazir-Esfandabadi R, Gitzhofer F (2010) Fischer–Tropsch synthesis in a slurry reactor using a nano-iron carbide catalyst produced by a plasma spray technique. Ind Eng Chem Res 49(15):6948–6955
9. Aluha J, Boahene P, Dalai A, Hu Y, Bere K, Braidy N, Abatzoglou N (2015) Synthesis and characterisation of nanometric Co/C and Fe/C catalysts for Fischer–Tropsch synthesis: a comparative study using a fixed-bed reactor. Ind Eng Chem Res 54(43):10661–10674
10. Rutkovskii AE, Vishnyakov LR, Chekhovskii AA, Kirkun NI (2000) Use of plasma technology in creating catalysts on carriers. Powder Metall Met Ceram 39(3–4):207–209
11. Liu C-J, Vissokov GP, Jang BWL (2002) Catalyst preparation using plasma technologies. Catal Today 72(3–4):173–184
12. Girshick SL, Chiu CP, Muno R, Wu CY, Yang L, Singh SK, McMurry PH (1993) Thermal plasma synthesis of ultrafine iron particles. J Aerosol Sci 24(3):367–382
13. Dignard NM (1998) Experimental optimization of the spheroidization of metallic and ceramic powders with induction plasma. MSc Thesis. Université de Sherbrooke, Sherbrooke
14. Sanpo N (2014) Solution precursor plasma spray system. Springer, Berlin
15. Okamoto H (1992) The C–Fe (carbon–iron) system. J Ph Equilib 13(5):543–565
16. Bengoa JF, Alvarez AM, Cagnoli MV, Gallegos NG, Marchetti SG (2007) Influence of intermediate iron reduced species in Fischer–Tropsch synthesis using Fe/C catalysts. Appl Catal A 325(1):68–75
17. Digges TG, Rosenberg SJ, Geil GW (1966) Heat treatment and properties of iron and steel. Vol Monograph 88. US Department of Commerce, National Bureau of Standards, Washington
18. Aluha J, Braidy N, Dalai A, Abatzoglou N (2016) Low-temperature Fischer–Tropsch synthesis using plasma-synthesised nanometric Co/C and Fe/C catalysts. Can J Chem Eng. doi:10.1002/cjce.22537
19. Aluha J, Braidy N, Dalai A, Abatzoglou N(2015) Low-temperature Fischer–Tropsch synthesis with carbon-supported nanometric iron-cobalt catalysts. In: 23rd European biomass conference and exhibition, Vienna, 1–4 June, 2015. pp 988–994
20. Aluha J, Abatzoglou N (2016) Synthetic fuels from 3-φ Fischer–Tropsch synthesis using syngas feed and novel nanometric catalysts synthesised by plasma. Biomass Bioenerg. doi:10.1016/j.biombioe.2016.05.010
21. Rietveld HM (1969) A profile refinement method for nuclear and magnetic structures. J Appl Cryst 2:65–71
22. Kniess CT, Lima JCd, Prates PB (eds) (2012) The quantification of crystalline phases in materials: applications of Rietveld method. Sintering—methods and products. InTech, Rijeka
23. Venugopal A, Aluha J, Scurrell MS (2003) The water-gas shift reaction over Au-based, bimetallic catalysts. The Au–M (M = Ag, Bi Co, Cu, Mn, Ni, Pb, Ru, Sn, Tl) on Iron (III) oxide system. Catal Lett 90(1–2):1–6
24. Jong S-J, Cheng S (1995) Reduction behavior and catalytic properties of cobalt containing ZSM-5 zeolites. Appl Catal A 126:51–66
25. Okamoto H (2008) Co–Fe (Cobalt–Iron). J Ph Equilib Diffus 29(4):383–384
26. Jia L (2005) Inductively coupled thermal plasma synthesis of CeO_2-based nano-powders. MSc Thesis. Université de Sherbrooke, Sherbrooke
27. Goortani BM (2006) Synthesis and evaluation of the size and the morphology of SiO_2 nanoparticles in ICP RF plasma reactors. PhD Thesis. Université de Sherbrooke, Sherbrooke
28. Gore JP, Sane A (2011) Flame synthesis of carbon nanotubes. In: Yellampalli S (ed) Carbon nanotubes—synthesis, characterization, applications. InTech, Rijeka, pp 121–146
29. Bahome MC, Jewell LL, Hildebrandt D, Glasser D, Coville NJ (2005) Fischer–Tropsch synthesis over iron catalysts supported on carbon nanotubes. Appl Catal A 287:60–67
30. van Steen E, Prinsloo FF (2002) Comparison of preparation methods for carbon nanotubes supported iron Fischer–Tropsch catalysts. Catal Today 71:327–334
31. Küttel OM, Groening O, Emmenegger C, Schlapbach L (1998) Electron field emission from phase pure nanotube films grown in a methane/hydrogen plasma. Appl Phys Lett 73(15):2113–2115
32. Wang Y, Yeow JTW (2009) A review of carbon nanotubes-based gas sensors. J Sens 493904:1–24
33. Blanchard J, Oudghiri-Hassani H, Abatzoglou N, Jankhah S, Gitzhofer F (2008) Synthesis of nanocarbons via ethanol dry reforming over a carbon steel catalyst. Chem Eng J 143(1–3):186–194

34. Schneeweiss O, Zbořil R, David B, Heřmánek M, Mashlan M (2009) Solid-state synthesis of α-Fe and iron carbide nanoparticles by thermal treatment of amorphous Fe_2O_3. Hyperfine Interact 189(1):167–173
35. Bell MS, Teo KBK, Lacerda RG, Milne WI, Hash DB, Meyyappan M (2006) Carbon nanotubes by plasma-enhanced chemical vapor deposition. Pure Appl Chem 78(6):1117–1125
36. Wang J, Zhu M, Outlaw RA, Zhao X, Manos DM, Holloway BC (2004) Synthesis of carbon nanosheets by inductively coupled radio-frequency plasma enhanced chemical vapor deposition. Carbon 42:2867–2872
37. Z-j Wang, Skiles S, Yang F, Yan Z, Goodman DW (2012) Particle size effects in Fischer–Tropsch synthesis by cobalt. Catal Today 181:75–81
38. Bezemer GL, Bitter JH, Kuipers HPCE, Oosterbeek H, Holewijn JE, Xu X, Kapteijn F, van Dillen AJ, de Jong KP (2006) Cobalt particle size effects in the Fischer–Tropsch reaction studied with carbon nanofiber supported catalysts. J Am Chem Soc 128(12):3956–3964
39. Park J-Y, Lee Y-J, Khanna PK, Jun K-W, Bae JW, Kim YH (2010) Alumina-supported iron oxide nanoparticles as Fischer–Tropsch catalysts: effect of particle size of iron oxide. J Mol Catal A Chem 323(1–2):84–90
40. McCusker LB, Dreele RBV, Cox DE, Louër D, Scardi P (1999) Rietveld refinement guidelines. J Appl Cryst 32:36–50
41. Ram S (2001) Allotropic phase transformations in HCP, FCC and BCC metastable structures in Co-nanoparticles. Mater Sci Eng A 304–306:923–927
42. Lu W, Huang P, He C, Yan B (2013) XRD, SEM and XAS studies of FeCo films electrodeposited at different current density. Int J Electrochem Sci 8:914–923
43. Terakado O, Uno Y, Hirasawa M (2014) Synthesis of fine iron-cobalt alloy particles by the co-reduction of precursors with solvated electrons in sodium ammonia solution. Mater Trans 55(3):517–521
44. Dlamini MW, Kumi DO, Phaahlamohlaka TN, Lyadov AS, Billing DG, Jewell LL, Coville NJ (2015) Carbon spheres prepared by hydrothermal synthesis—a support for bimetallic iron cobalt Fischer–Tropsch catalysts. ChemCatChem 7:3000–3011
45. Fu T, Jiang Y, Lv J, Li Z (2013) Effect of carbon support on Fischer–Tropsch synthesis activity and product distribution over Co-based catalysts. Fuel Process Technol 110:141–149

9.2. Appendix B: Article 2 - Catalyst testing in Fixed-bed reactor

I&EC research
Industrial & Engineering Chemistry Research

Article

pubs.acs.org/IECR

Synthesis and Characterization of Co/C and Fe/C Nanocatalysts for Fischer–Tropsch Synthesis: A Comparative Study Using a Fixed-Bed Reactor

James Aluha,[†] Philip Boahene,[‡] Ajay Dalai,[‡] Yongfeng Hu,[§] Kossi Bere,[†] Nadi Braidy,[†] and Nicolas Abatzoglou*[,†]

[†]Department of Chemical & Biotechnological Engineering, Université de Sherbrooke, Sherbrooke, Quebec, Canada J1K 2R1
[‡]Department of Chemical & Biotechnological Engineering, University of Saskatchewan, Saskatoon, Saskatchewan, Canada S7N 5A9
[§]Canadian Light Source Inc., Saskatoon, Saskatchewan, Canada S7N 2 V3

S *Supporting Information*

ABSTRACT: Production of Fischer–Tropsch catalysts is challenging because it involves controlling and optimizing multiple parameters in numerous technical steps. Here, we present C-supported nanometric Fe and Co catalysts synthesized by plasma spraying, a method that contracts catalyst production into a single step, in contrast to traditional multistep catalyst production by precipitation or impregnation. The catalysts were reduced *in situ* and then tested for Fischer–Tropsch synthesis in a gas–solid fixed-bed reactor at 230 °C and 30-bar pressure for 24 h. The performance of plasma-synthesized catalysts was superior at a gas hourly space velocity of 6,000 $mL \cdot g_{cat}^{-1} \cdot h^{-1}$, with Fe/C catalysts showing about 30% CO conversion per pass while Co/C catalysts yielded about 20% CO conversion. Identical C-supported Co and Fe catalysts prepared by impregnation or precipitation gave CO conversions of about 7% under similar reaction conditions.

1. INTRODUCTION

Prospective renewable sources of energy such as biofuels are receiving growing attention, since they are also perceived to have a fundamental capacity to lower greenhouse gas emissions. Today, utilization of biomass to produce biofuels commercially through the Fischer–Tropsch synthesis (FTS) process is seriously considered. Discovered by Franz Fischer and Hans Tropsch in the 1920s, FTS is a catalytic reaction that polymerizes syngas (a mixture of CO and H_2) to generate synthetic fuels,[1] which can be produced by various methods, such as gas-to-liquid, coal-to-liquid, or biomass-to-liquid.[2] When refined, the hydrocarbons thus produced are comparable to conventional liquid fuels derived from crude oil, which comprise mainly gasoline (C_4–C_{12}) and diesel (C_8–C_{21}) fractions, among other hydrocarbons and oxygenated products formed according to the equations in Table 1.

Higher temperatures tend to lower the average carbon-chain length of product molecules and favor both selective methane formation and C deposition. C deposition is detrimental because it decreases desirable product yield and mainly leads to catalyst deactivation, especially as observed with the Fe catalyst.[3] Nevertheless, we consider that if C support can be utilized in FTS, then C deposition and catalyst carburization during the process will ultimately be inconsequential.

Fischer–Tropsch catalyst preparation techniques are varied and include impregnation methods,[4] precipitation,[5] coprecipitation,[6] ion-exchange,[7] combination of coprecipitation and spray-drying technology,[8] C-vapor deposition,[9] and plasma-spray technology,[10] among others. Plasma-spray technology is one of the most recent approaches in catalyst preparation. The active phase of the catalyst, usually in metallic form, may come unsupported,[11] or supported on pristine metal oxides, including Al_2O_3,[12] SiO_2,[13] and TiO_2.[14] In zeolites,[15] high activity and selectivity toward aromatic products in FTS have been attributed to strong acidity and the unique shape and/or porosity of HZSM-5 zeolite.[16] The use of mixed metal-oxide supports, such as SiO_2–TiO_2,[17] ZrO_2–Al_2O_3, or ZrO_2–SiO_2,[18] has also been reported. Today, C is receiving substantial attention as catalyst support, because of its high external and low internal specific surface area due to its nanometric size and particular forms, such as nanotubes,[19] graphitic nanofibers,[20] or nanofilaments.[21]

The main objective of the present study was to determine the most effective approach to C-supported catalyst preparation. We explored three preparation techniques, namely, impregnation, precipitation, and the plasma-method, aimed at guiding us to rapidly make a rational choice of the most promising catalysts. In addition, we preferred to look at the propensity of early particle agglomeration during FTS,[22] in relation to the sample preparation method. Since most FTS tests are conducted either in continuous flow fixed-bed reactors,[23] or continuously stirred slurry tank reactors (CSSTR),[24] all our catalysts were tested in a fixed-bed reactor.

A plasma-synthesized catalyst based on iron (Fe/C) was described earlier by our group,[25] and now, for the first time, an effective plasma-synthesized Co catalyst supported on C (Co/C) is reported. The preliminary results that cover the performance of these nanometric C-supported Co and Fe catalysts, which are currently being developed for biofuel

Received: August 15, 2015
Revised: October 14, 2015
Accepted: October 15, 2015
Published: October 15, 2015

DOI: 10.1021/acs.iecr.5b03003
Ind. Eng. Chem. Res. 2015, 54, 10661–10674

Table 1

Target	Reaction	Designation
Alkanes	$(2n + 1)H_2 + nCO \rightarrow C_nH_{2n+2} + nH_2O$	eq (1)
Alkenes	$2nH_2 + nCO \rightarrow C_nH_{2n} + nH_2O$	eq (2)
Water-gas shift	$H_2O + CO \rightarrow CO_2 + H_2$	eq (3)
Methane	$3H_2 + CO \rightarrow CH_4 + H_2O$	eq (4)
	$4H_2 + CO_2 \rightarrow CH_4 + 2H_2O$	eq (5)
Alcohols	$2nH_2 + nCO \rightarrow C_nH_{(2n+1)}OH + (n - 1)H_2O$	eq (6)
	$(n + 1)H_2 + (2n - 1)CO \rightarrow C_nH_{(2n+1)}OH + (n - 1)CO_2$	eq (7)

production through the FTS process, are presented here. This is an account outlining procedures followed in catalyst synthesis, testing, and characterization. In this work, an attempt has been made to establish catalyst morphology and that of various species in freshly prepared materials through a number of characterization techniques, which include Brunauer−Emmett−Teller (BET) surface area analysis, Raman spectroscopy, scanning electron microscopy (SEM) coupled with energy dispersive X-ray spectroscopy (EDX), transmission electron microscopy (TEM), as well as X-ray methods, such as X-ray absorption near-edge structure (XANES), X-ray photoelectron spectroscopy (XPS), and X-ray diffraction (XRD) analysis.

2. EXPERIMENTAL METHODS

2.1. Catalyst Synthesis. Three methods were employed to prepare Co- and Fe-based catalysts, namely, plasma spraying, impregnation and precipitation, targeting 40% metal-loading onto C supports. The resulting materials were tested for Fischer−Tropsch activity. Since nanometric metallic particles are pyrophoric, particularly when deposited on nanometric C, and can easily degenerate into fire when exposed to air, all precautions were taken during preparation, general management and treatment of the catalysts to avoid such exposure.

2.1.1. Chemicals and Materials. The raw materials for preparing the catalytic formulations were: Co metal (particle size: 1−10 μm), Co (II) oxide and Co (II).(III) oxide from Aldrich; Fe metal (1−10 μm), Fe (II) oxide, Fe (II).(III) oxide, Fe (III) nitrate nona-hydrate and Co (II) nitrate hexa-hydrate from Alfa Aesar; high purity gases from PRAXAIR: H_2 (N5.0), CO (N2.5), Ar (N5.0); 68% nitric acid and 29% ammonia solution from ACE Chemicals Co; and mineral oil from Fisher Scientific with catalog name "O122-4, Mineral Oil, Heavy; USP/FCC (Paraffin Oil, Heavy)"; 68% nitric acid and 29% ammonia solution from ACE Chemicals Co.

2.1.2. Preparation of C Supports. Carbon nanofilaments (CNFs) were prepared via a patented process,[26] by dry-reforming of ethanol (C_2H_5OH) in a CO_2 stream at 565 °C (see Figure 1 for the reactor setup). The reactor temperature was raised to 550 °C under pure Ar flowing at the rate of 200 SCCM (standard cubic cm per min, or 3.33×10^{-6} $Nm^3.s^{-1}$; where 1 SCCM = 1.67×10^{-8} $Nm^3.s^{-1}$). The stream of C_2H_5OH and CO_2 mixture was then opened at a constant flow rate of 1 O atom for every C atom: ($C_2H_5OH + CO_2 = 3C + 3O$). On a 17-g steel strip with dimensions of 413 mm × 25 mm × 0.5 mm, some 0.3 g/min of liquid C_2H_5OH was reacted with CO_2 at a flow rate of 160 SCCM (or 2.67×10^{-6} $Nm^3.s^{-1}$) at room temperature and barometric pressure (25 °C, 1 atm), and the reaction was left to proceed for about 4−6 h.[27] The

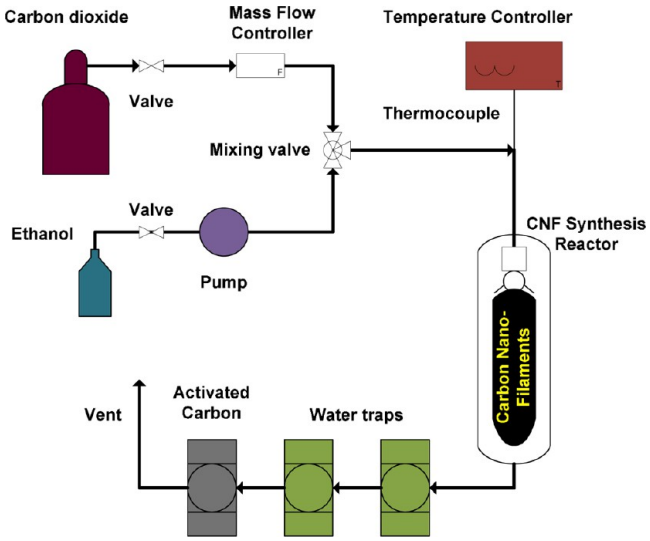

Figure 1. Reactor setup for CNF synthesis.

resulting CNFs, deposited as C according to eq 8, were harvested and then functionalized by acid-activation using dilute 4 M HNO_3 where 250 mL of 68% (15.8 M) concentrated acid was dissolved in a liter of solution using distilled H_2O. About 50 g of the CNFs were refluxed with 4 M HNO_3 at 95 °C for 3 h.[28]

$$C_2H_5OH(l) + CO_2(g) \rightarrow CO + 2H_2(g) + 2H_2O(l) + 2C(s) \quad \text{(eq 8)}$$

2.1.3. Catalyst Preparation by Impregnation. While aiming for 40% metal-loading in the final catalyst sample, 33.7 g of $Co(NO_3)_2.6H_2O$ and 10.2 g of acid-activated CNF support were mixed with H_2O to produce a thick homogeneous paste and left to evaporate slowly to dryness in an oven set at 100 °C for 15 h. A similar homogeneous paste was made from 45.4 g of $Fe(NO_3)_3{\cdot}9H_2O$ and 9.4 g of acid-activated CNF support for Fe-based catalysts. The resulting catalyst precursors were then calcined at 290 °C in Ar current flowing at 400 SCCM (6.67×10^{-6} $Nm^3.s^{-1}$) for 10 h, after which they were cooled to room temperature in the same gas stream.

2.1.4. Catalyst Preparation by Ammonia Precipitation. Similarly, while aiming at 40% metal-loading in the final catalysts, 0.11 M solutions of Co or Fe metal salts were prepared with a mass of 31.6 g of $Co(NO_3)_2.6H_2O$ and 45.1 g of $Fe(NO_3)_3.9H_2O$, respectively. To prepare about 0.15 M NH_4OH solution, 25 mL of 29% (or 15 M) NH_4OH solution was dissolved in 250 mL of solution with distilled H_2O. About 100 mL of this solution was drawn out and used to precipitate

DOI: 10.1021/acs.iecr.5b03003
Ind. Eng. Chem. Res. 2015, 54, 10661−10674

the metals out of their respective solutions, then added instantaneously to 10.0 g of acid-activated CNF support. The ensuing thick homogeneous paste was warmed gently for 30 min on a water bath set at 70 °C to evaporate excess ammonia. The sample was vacuum-filtered and washed with a liter of distilled H_2O, and the residue was left to oven-dry at 100 °C for 10 h. The resulting catalyst precursor was calcined at 290 °C in Ar current flowing at 400 SCCM (6.67×10^{-6} $Nm^3.s^{-1}$) for 10 h, then cooled to room temperature in Ar.

2.1.5. Catalyst Preparation by Plasma. Catalyst synthesis was carried out in a radio frequency (RF) plasma system, which powered the inductively heated torch (PL-50, 3.2 MHz, supplied by Tekna Inc.) equipped with a subsonic nozzle. A 60.0-g mass of Co or Fe was mixed with 300 mL of mineral oil for 2 h to form a homogeneous suspension, which was then introduced directly into the plasma spray at a flow rate of 8.2 $mL.min^{-1}$ by peristaltic pump. As illustrated in Figure 2, the

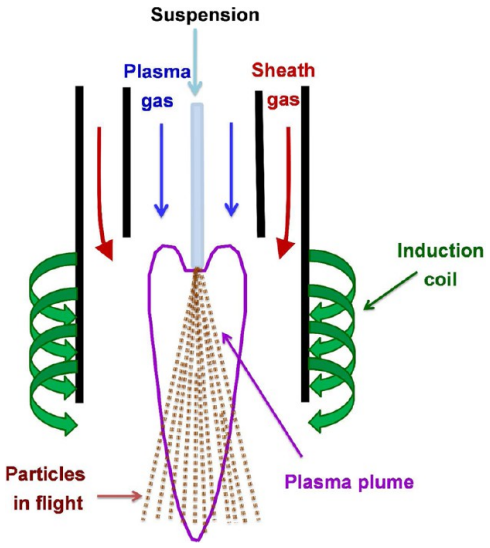

Figure 2. Introduction of metal−oil suspension into plasma to produce Co/C or Fe/C catalysts.

reaction gases were: sheath gas composing Ar at 50 psi, and flowing at 75 SLPM or 1.25×10^{-3} $Nm^3.s^{-1}$ (SLPM = standard liters per minute), H_2 (50 psi, 10 SLPM or 1.67×10^{-4} $Nm^3.s^{-1}$), swirling plasmagenic Ar (23 SLPM or 3.83×10^{-4} $Nm^3.s^{-1}$), and the suspension was atomized with Ar (10.5 SLPM or 1.75×10^{-4} $Nm^3.s^{-1}$). RF plasma power was kept constant at 29 kW, while initial fixed pressure was set at 250 Torr (1 Torr =133.3 Pa). After catalyst synthesis, the reactor was quenched, opened and the materials harvested manually, where the catalyst powder deposited at its walls as well as on the filters (in the auxiliary reactor) were skimmed off, collected and then tested for Fischer−Tropsch activity.

2.2. Catalyst Testing. *2.2.1. Reactor Setup and Reaction Conditions.* Figure 3 depicts a simplified version of the reactor design for catalyst testing. A 1.0-g catalyst mass diluted with 6 mL of silicon carbide (SiC) was loaded systematically with various mesh-size SiC beads into a 50 cm stainless steel fixed-bed reactor. Variations in mesh size served to eliminate both heat and mass transfer problems, an approach typical of the one already prescribed.[29] The catalyst was reduced *in situ* at 350 °C for 10 h in pure H_2 flowing at 55 SCCM (9.17×10^{-7} $Nm^3.s^{-1}$) and then tested for FTS activity at 30-bar pressure and 230 °C, with a gas flow rate of 100 SCCM (1.67×10^{-6} $Nm^3.s^{-1}$) for 24 h. The composition of the syngas mixture was in the ratio of H_2:CO=1.88 as follows: 58.4% H_2, 31.1% CO and 10.5% Ar.

Gas-phase data were collected from a Shimadzu GC-2014 Gas Chromatograph (GC) operated by factory-installed GC Real Time Analysis software. The instrument was fitted with a Porapak N 80/100 GC column of 1.0-m length (L), 3.17 mm inner diameter (ID), and 1.00-μm film thickness (df), operating to a maximum temperature of 250 °C and leading to a thermal conductivity detector. On the other hand, a flame ionization detector (FID) analyzed hydrocarbons present in gas exit samples running through a GC Restek Rtx-1 PONA column with dimensions L = 100.0 m, ID = 0.25 mm, and df =0.50 μm, operating to a maximum temperature of 250 °C. Liquid-phase analysis was conducted on a Varian CP-3800 Gas Chromatograph, also fitted with a FID for hydrocarbon analysis, using a Zebron ZB-1XT SimDist GC column: L = 5 m, ID = 0.53 mm, and df =0.15 μm, suited for operating within a temperature range of −60° to 450 °C.

2.2.2. Mass Balance: Conversion and Selectivity Calculations. About 10% Ar was included in the gas stream for mass balance determination,[30] where catalyst activity was calculated by the amount of CO converted. Thus:

$$\mathrm{CO}\ (\%) = \left[\frac{\mathrm{CO}_{in} - \mathrm{CO}_{out}}{\mathrm{CO}_{in}}\right] \times \left[\frac{\mathrm{Ar}_{in}}{\mathrm{Ar}_{out}}\right] \times 100 \qquad \text{(eq 9)}$$

Since we had 2 separate GCs, one dedicated for gas-phase analysis (online) and the other for liquid-phase analysis (offline), selectivity toward the various products was determined by assuming that the CO feedstock would form either of the 2 classes of compounds: gas or liquid. To ascertain catalyst selectivity, first of all, raw figures of gas concentration (%) for products in the gas phase were applied as collected (P_0, P_1, P_2, ...). This procedure is depicted in Figure 4. Let total CO conversion to gas-phase products be P. If $P = p_0 + p_1 + p_2 + p_3 + p_4$, then total CO conversion to liquid-phase products = (100 − P). In the liquid phase, the selectivity of each product (S_i') was calculated from the area under its corresponding peak (A_i), and then divided by the total sum area of all peaks from C_5 and above. Thus:

$$S_i' = \left(\frac{A_i}{A_5 + A_6 + A_7 + \cdots A_n}\right) \qquad \text{(eq 10)}$$

Overall, the selectivity (S) of any product (C_i) in the liquid phase was then given by the equation:

$$S_{C_i} = \frac{S_i'}{100}(100 - P) \qquad \text{(eq 11)}$$

where C_i = the hydrocarbon product with i C atoms, i = the number of C atoms, i = 5, 6, 7, ⋯, n, and S_i' = selectivity calculated from the area under each peak (A_i).

2.3. Catalyst Characterization. *2.3.1. BET Surface aArea.* Fresh catalysts were characterized on a Micromeritics ASAP 2020 instrument by the BET method. The samples were degassed at 250 °C for 50 h and evacuated until a pressure of less than 10 μmHg was obtained in the sample holder. Analysis by BET physisorption was then carried out with N_2 at −196 °C, starting with initial pressure below 10 μmHg.

2.3.2. SEM and TEM. Catalyst morphology was examined by SEM, and the elements present in each catalyst were confirmed by EDX spectroscopy. A Hitachi S-4700 SEM, equipped with an X-Max Oxford EDX spectrometer, captured both secondary

DOI: 10.1021/acs.iecr.5b03003
Ind. Eng. Chem. Res. 2015, 54, 10661−10674

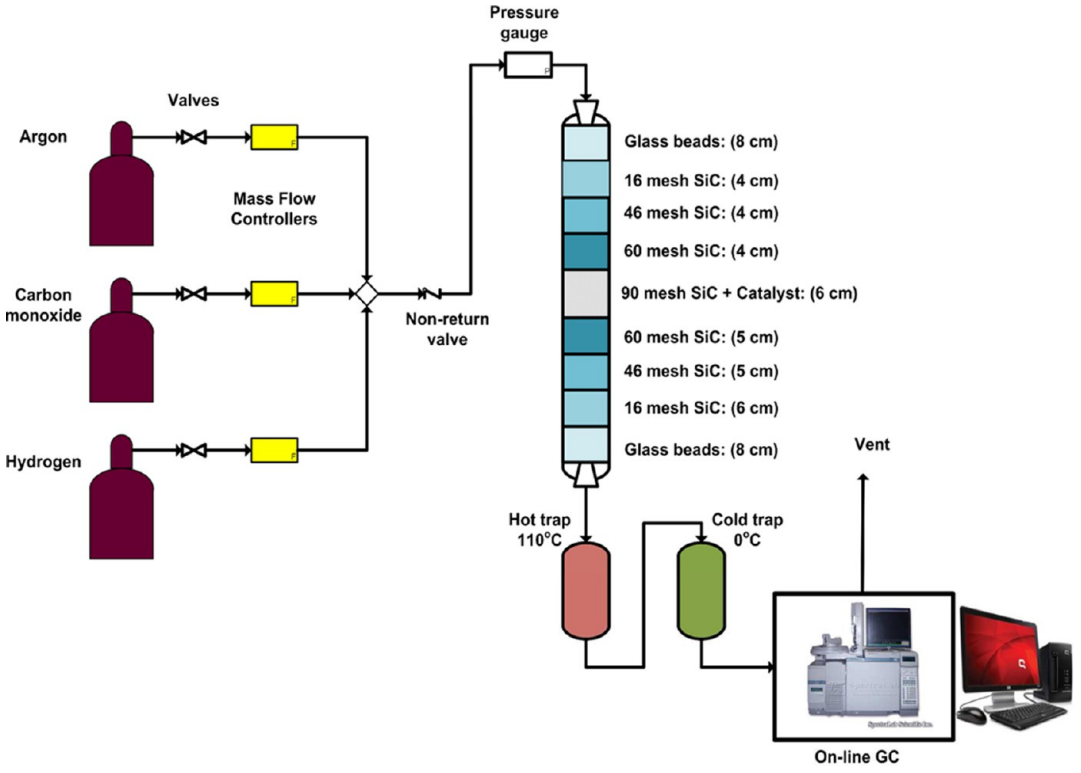

Figure 3. Simplified setup of fixed-bed reactor system.

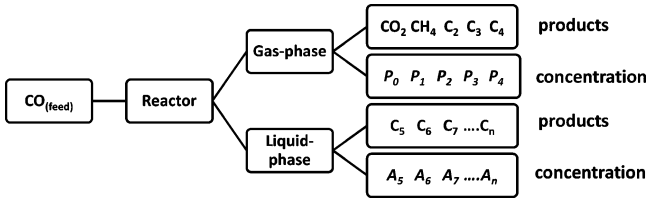

Figure 4. Diagrammatic scheme of selectivity determination.

and backscattered images. On the other hand, a Hitachi H-7500 TEM, fitted with W filament and operated at an accelerating electron beam of 120 kV, analyzed metal particle size distribution. A bottom-mounted AMT 4k x 4k CCD Camera System Model X41 captured images in bright field mode.

2.3.3. Raman Spectroscopy. The nature of the C supports was analyzed by Raman spectroscopy with a LabRam-800 spectrometer equipped with microscope, a He−Ne 632.8 nm laser and a N_2-cooled charge-coupled device detector. To avoid sample overheating during measurements, laser beam power was kept below 2 mW through 50x objective lens, focusing the excitation light on a spot size of 3 μm in diameter. Weak Raman signals were accumulated for a period of 30 min to 1 h to obtain a good signal/noise ratio. Since FT-Raman spectra reproducibility of these materials was poor, the MicroRaman module was favored for material characterization.

2.3.4. XRD Analysis. To identify elemental composition as well as crystalline phases in the catalysts, XRD analysis was conducted with a Philips X'pert PRO Diffractometer from PANalytical, fitted with Ni-filters for Cu Kα radiation of wavelength alpha1 = 1.5406 Å, produced at 40 kV and 50 mA. The instrument was set to Bragg−Brentano configuration with a PIXcel-1D detector, and operated by factory-installed Analytical Data Collector software. XRD patterns were recorded in the range of 20° to 90° [2θ] angle at a scanning speed of about 3° [2θ] min^{-1}, step size of 0.040° [2θ] angle and time of 0.0395 s per step, corresponding to a scan time of 24 min. Antiscatter and divergent slits were fixed at 1°. The collected data were compared with Powder Diffraction Files in the Database (version 4.13.0.2), using 2013 PDF-4+ software (version 4.13.0.6), published by the International Center for Diffraction Data. Data were analyzed by Materials Data Inc. software: MDI JADE 2010 (version 2.6.6).

2.3.5. XPS Analysis. Elemental composition and the oxidation state of elements in the catalysts were ascertained by XPS Kratos Axis Ultra DLD spectrometer. Samples were excited by the Al$K\alpha$ monochromatized line (1486.6 eV) with 225 W of applied power. The analyzer was operated in constant pass energy mode (Epass =160 eV for survey scans and Epass =20 eV for high resolution scans). Work function of the instrument was calibrated to give binding energy (BE) of 83.96 eV for the Au $4f_{7/2}$ line of metallic gold. Spectrometer dispersion was adjusted to give BE of 93.62 eV for the Cu $2p_{3/2}$ line of metallic Cu. A charge neutralizer was used on all samples to compensate for the charging effect and, when needed (particularly for nonconductive samples), no charge corrections were made, and binding energies were referenced to the adventitious carbon C 1s core level (284.8 eV). The powdered catalyst was pressed into a thin pellet in a powder sample holder. The analyzed area was oval with 300 × 700 μm dimensions.[31] Data were analyzed by Casa XPS software (version 2.3.16).

2.3.6. XANES Analysis. Synchrotron light in XANES analysis measured oxidation states of the elements and deciphered the local chemical environment. X-ray absorption spectra of the elements of interest in the catalysts were measured at their respective K-edge energies: at 7,709 (between 7,700 and 7,750 eV) for Co and at 7,112 (between 7,100 and 7,150 eV) for Fe. Measurements were recorded both in transmission mode and

DOI: 10.1021/acs.iecr.5b03003
Ind. Eng. Chem. Res. 2015, 54, 10661−10674

by fluorescence, with 2 ionization chambers for X-ray detection. A Si(111) double-crystal monochromator was calibrated by setting the first inflection point of the K-edge spectrum of the element in question. Data collection in the determined range lasted about 20−30 min. X-ray absorption data were analyzed by the conventional procedure: after background correction, XANES spectra were normalized by edge height. Various reference compounds served to standardize the analysis. For example, crystalline $Co(NO_3)_2$, Co_3O_4, CoO, and Co foil were used for Co-based catalysts,[31] while crystalline $Fe(NO_3)_3$, Fe_3O_4, FeO, and Fe foil were used for Fe-based catalysts. During analysis, samples (~10 mg each) were reduced *in situ* in a H_2 gas-stream at 350 °C for 3 h to simulate the reduction process that the FTS catalyst undergoes before reaction. Hephaestus software analyzed theoretical K-edge energies for Co and Fe standards (metal foils), while data manipulation and interpretation was by Athena software.[32]

3. RESULTS

3.1. Catalyst Activity Tests. *3.1.1. CO Conversion.* Seeing that the reactor was 50 cm long, first of all, its heating profile was ascertained by temperature calibration. From the measurements, the hottest position in the catalyst bed was determined to be at 23 cm from the reactor top, which is where the tip of the thermocouple was directed, and the catalyst was packed in such a way that this was also the center of the catalyst bed. A calibration plot is provided in the Supporting Information (Figure A1). Since it was presumed that the catalyst would be operating at steady state after 18 h on stream, it was observed that the impregnated Co/CNF sample as well as the plasma-synthesized Co/C and Fe/C catalysts yielded more products after 24 h than the rest of the catalysts. Further, it was noted (Figure 5) that at gas hourly space velocity of 6,000 $mL \cdot g_{cat}^{-1} \cdot h^{-1}$,

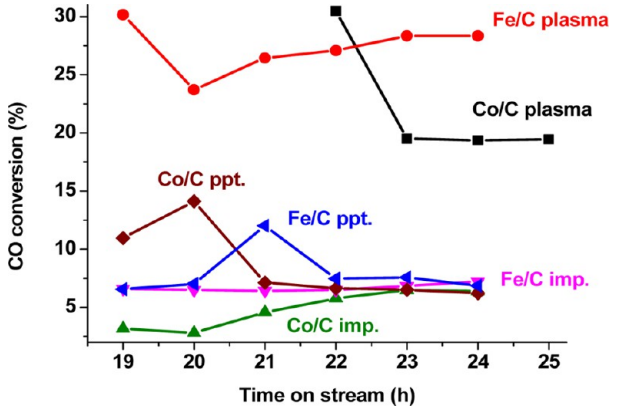

Figure 5. Fischer−Tropsch activity of catalysts prepared by various methods.

plasma-synthesized samples displayed relatively higher CO conversions per pass (28% for Fe/C and 20% for Co/C) than those prepared on CNFs, either by impregnation (imp) or precipitation (ppt). The raw data is given in the Supporting Information (Table S1).

Although the plasma-synthesized Co/C sample yielded more products by weight, it was less active in terms of CO conversion because it generated a significant amount of H_2O, which is undesirable in the process. The sample GC trace in Figure 6 indicates that the anticipated catalyst's product spectrum was attained, mainly in the diesel range (C_{10}−C_{20}). Further

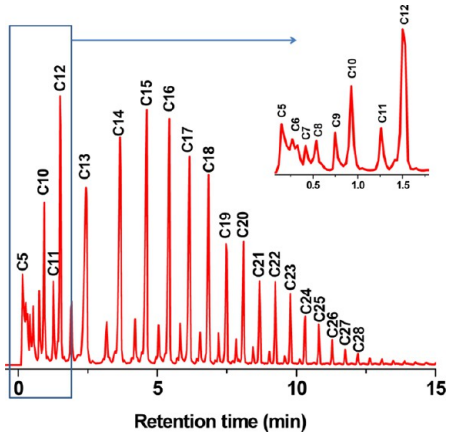

Figure 6. Sample GC trace showing FTS product spectra of plasma-synthesized Fe/C catalyst.

enrichment of petro-diesel fractions could be achieved by thermally hydrocracking FTS products of higher molecular weight (e.g., waxes) to form molecules with shorter C chains.

3.1.2. Catalyst Selectivity. Catalyst selectivity toward each product was calculated using eq 10 and eq 11. The data indicate that catalyst selectivity tended more toward the diesel range, particularly for the plasma-synthesized Fe/C catalyst, which led with 71%, followed by the impregnated Co/CNF catalyst with 56%, and then by the precipitated Fe/CNF catalyst with 51%. Only the plasma-synthesized Co/C catalyst formed products that were richer in the gasoline range, with selectivity of 60%. This information is presented graphically in Figure 7, while the

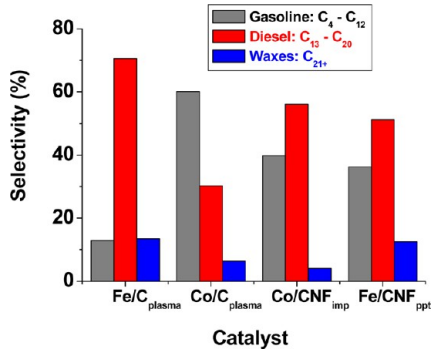

Figure 7. Comparison of catalyst selectivity by product fraction.

raw data is given in the Supporting Information (Table S2). Since hydrocarbon constituents normally overlap in gasoline (C_4−C_{12}) and diesel (C_8−C_{21}) fractions, in this work we prefer to define gasoline as C_4−C_{12} fractions and diesel as C_{13}−C_{20} for simplicity and mass balance purposes.

Producing minute quantities of undesirable products, such as methane, CO_2, and other gaseous short-chain hydrocarbons (totaling less than 5%), was a positive attribute of all six catalysts. This was compelling, particularly for the best-performing catalysts synthesized by the plasma-spray method (Figure 8).

3.2. Catalyst Characterization. *3.2.1. BET Surface Area.* The BET-specific surface area of fresh CNFs was 179 $m^2 \cdot g^{-1}$, but after activation with HNO_3, it increased considerably by ~33% to 237 $m^2 \cdot g^{-1}$. Nevertheless, upon Co or Fe metal deposition and subsequent calcination at 290 °C for 10 h, surface area decreased significantly and lay between 106 and

DOI: 10.1021/acs.iecr.5b03003
Ind. Eng. Chem. Res. 2015, 54, 10661−10674

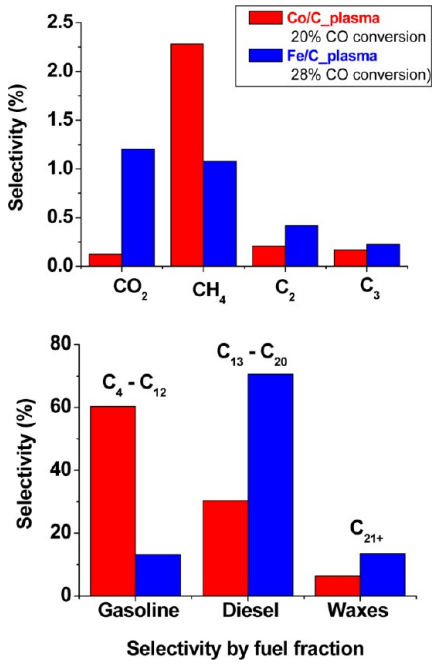

Figure 8. Selectivity plots of plasma-synthesized catalysts.

176 $m^2 \cdot g^{-1}$. This was attributed to partial blockage of the internal surface of CNFs by metal particle deposition. Plasma-synthesized catalysts, on the other hand, had relatively lower surface areas (Co/C = 93 $m^2 \cdot g^{-1}$; Fe/C = 55 $m^2 \cdot g^{-1}$) than those synthesized by precipitation or impregnation. The BET-specific surface area of the samples is summarized in Table 2.

Table 2. BET-Specific Surface Areas of Fresh Catalysts

Sample	BET surface area ($m^2 \cdot g^{-1}$)	
Synthesis method	Co-based	Fe-based
Precipitation	144.5	176.3
Impregnation	105.9	140.2
Plasma spray	92.6	54.5

Their gas adsorption plots were characteristic of type II isotherms, which indicated that the nature of their porosity was similar, tending toward nonporosity with limited hysteresis. Figure 9 is representative of overlaid adsorption−desorption isotherms of impregnated Co/CNF samples, while the rest of the plots are provided for in the Supporting Information (Figure A2).

Nevertheless, since active sites in the catalysts are associated with metal species and not the support, this BET-specific surface area represents the latter. Thus, for turnover frequency considerations, it would be more reasonable to assume an average specific surface area based on a nanometric metal particle size distribution and make the plausible assumption that these particles have no internal surface (existing as compact spheres). The validity of this assumption was reported in a previous publication.[33] The restricted hysteresis observed from isotherms revealed that the samples either had low porosity or generally tended toward nonporosity. Pore distribution plots of the catalysts displayed in Figure 10 showed that the average pore diameter was below 5 nm.

Although some microporosity was observed, it was entirely artificial. Being in the nanometric range, the catalyst particles packed in such a way that they formed artificial voids and channels. Consequently, the sample behaved like microporous material. Constricted deviation between adsorption and desorption isotherms indicated narrow or uniform distribution of pores. Generally, excessive microporosity is not desirable in FTS, since products of large molecular size are expected to diffuse rapidly out of the pores.

3.2.2. SEM. Both area and spot analysis of fresh catalysts characterized by SEM imaging in conjunction with EDX (semiquantitatively) indicated that catalysts, prepared by either the plasma spray or impregnation method, contained metal-loading between 20 and 30 wt %, while the precipitation technique led to metal-loading of about 16−18 wt %. This translates to a metal-loading efficiency of approximately 70% for the impregnation method and less than 50% for the precipitation method. The missing metal was attributed to deposition on the walls of preparation vessels. Representative SEM images in Figure 11 show that (i) plasma-synthesized

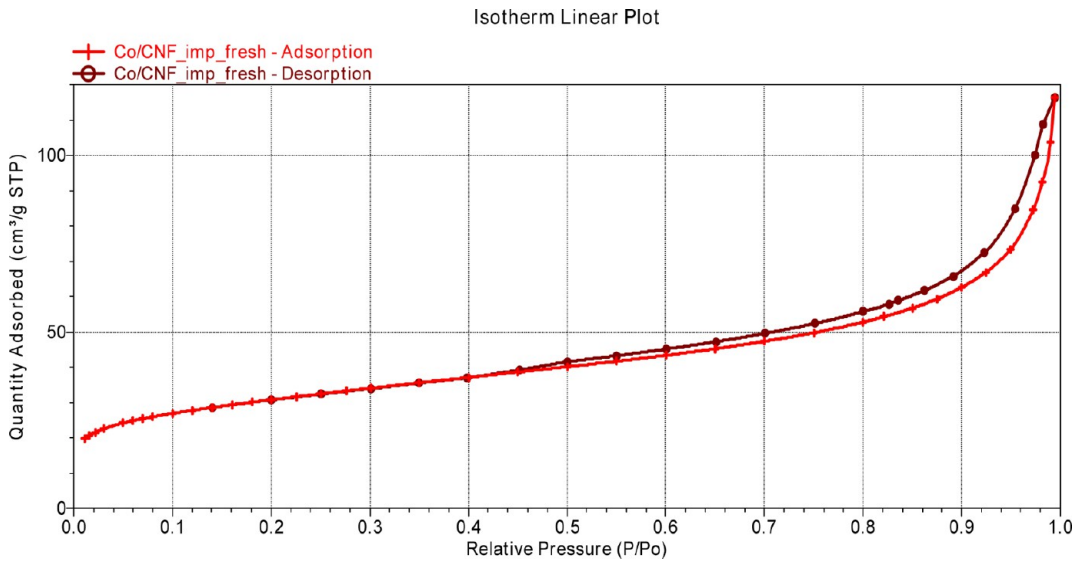

Figure 9. Adsorption−desorption isotherm of fresh Co/CNF catalyst.

DOI: 10.1021/acs.iecr.5b03003
Ind. Eng. Chem. Res. 2015, 54, 10661−10674

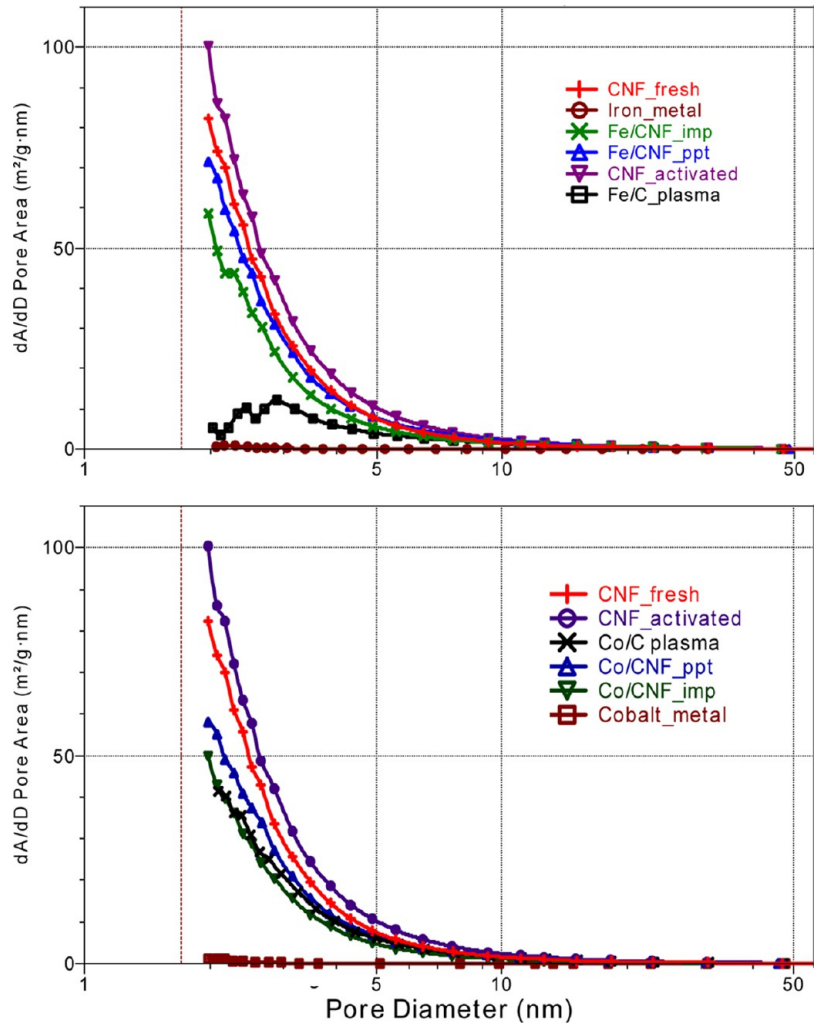

Figure 10. Overlaid pore distribution plots by pore area of fresh catalysts.

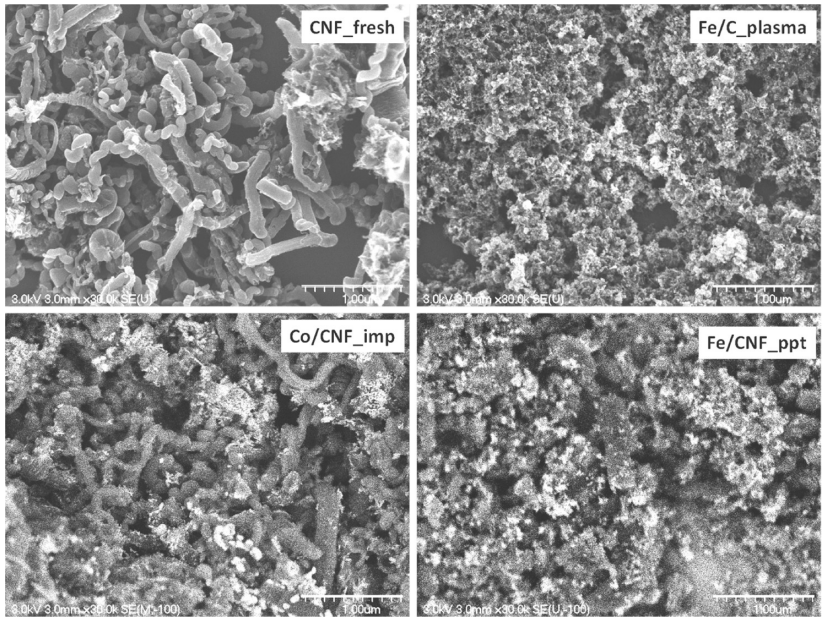

Figure 11. (a) Top: Secondary SEM images of fresh CNFs and plasma-synthesized Fe/C; (b) Bottom: Backscattered SEM images of fresh Co/CNF and Fe/CNF catalysts (same scale).

DOI: 10.1021/acs.iecr.5b03003
Ind. Eng. Chem. Res. 2015, 54, 10661−10674

samples comprising fine nanometric C support had a different morphology from CNFs that had larger strand-like features; (ii) precipitated and impregnated samples displayed greater particle sintering and poor distribution of metal nanoparticles; and (iii) in precipitated and impregnated samples, further heat treatment during oven-drying (100 °C, 15 h), functionalization by acid-treatment (95 °C, 3 h), and calcination (at 290 °C, 10 h) led to the deformation of CNFs.

3.2.3. TEM. Samples prepared by impregnation or precipitation and calcined at 290 °C for 10 h showed signs of particle growth, while plasma-synthesized samples did not. Figure 12

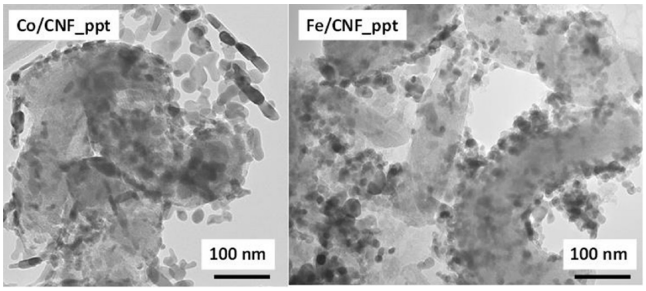

Figure 12. Representative TEM images of freshly precipitated catalysts.

displays characteristic TEM images of the precipitated catalysts, while Figure 13 shows images of impregnated samples. Notice the slack contact with the C support, which led to particle mobility and sintering as a result. This was exemplified by Fe/CNF catalysts prepared by impregnation, which agglomerated away from the support. It contrasts with plasma-synthesized samples, which on the other hand indicated more complex

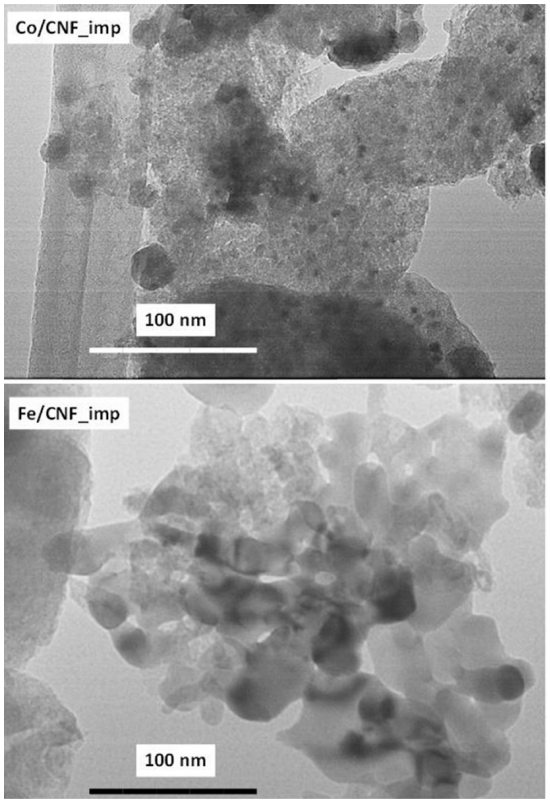

Figure 13. TEM images of freshly impregnated catalysts.

association and metal particles being fully embedded in the C matrix (Figure 14).

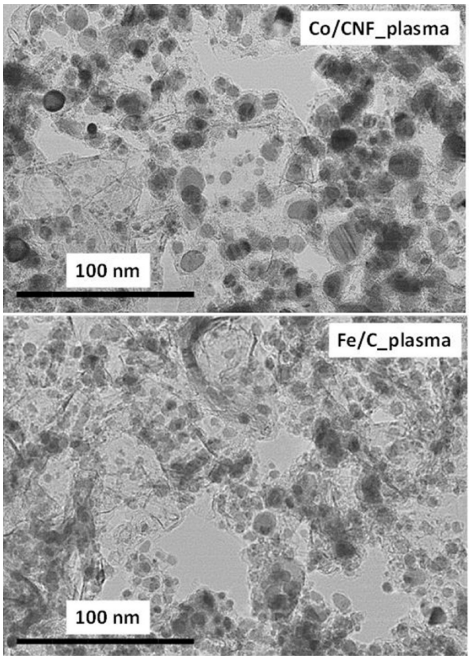

Figure 14. TEM images of fresh plasma-synthesized samples.

Particle size analysis and distribution were evaluated based on at least 150 particles per sample (see plots in Figure 15). Plasma-synthesized samples displayed average particle size of about 12−13 nm, revealing narrow particle size distribution. They were followed closely by precipitated samples, which had a mean size of 18 nm for Fe/CNF and 22 nm for Co/CNF. The impregnation method exhibited particle agglomeration, with some particles being as large as 80 nm in diameter. The mean particle size of the Fe/CNF catalysts was 31 nm, while that of Co/CNF was 37 nm, which had a wide particle size distribution range, comprising both small (*ca.* 10 nm) and large nanoparticles (up to *ca.* 80 nm) (Figure 13).

3.2.4. Raman Spectroscopy. Analysis of fresh supports by Raman spectroscopy showed that CNFs contained the ordered graphitic C (G-line), some of which contained defective graphitic sites giving rise to the disordered form (D-line), as indicated by Figure 16. The Raman spectra of disordered graphite show two distinct sharp modes, the G-peak around 1580−1600 cm^{-1} and the D-peak around 1350 cm^{-1}, whereby the G and D peaks appear to portray varying intensities, position, and width in different nanocrystalline and amorphous carbons, even in samples without widespread graphitic ordering.[34] The diminished G-band in the CNFs after acid treatment showed loss of graphitization during CNF functionalization, leading to the formation of defects, while the augmented G-band in the plasma-synthesized sample was a sign of ensuing graphitization in the carbon support and therefore had a more graphitic structure.[35] It was therefore concluded that the samples, particularly the CNFs, were highly graphitic in nature, but with considerable defects.

3.2.5. XRD Analysis. From XRD analysis (summarized in Figure 17), we observed that amorphous C and a significant amount of carbides, such as cementite (θ-Fe_3C) and Hägg (χ-Fe_5C_2) type, were predominant in fresh CNFs. Fe-based catalysts produced by precipitation or impregnation showed the

DOI: 10.1021/acs.iecr.5b03003
Ind. Eng. Chem. Res. 2015, 54, 10661−10674

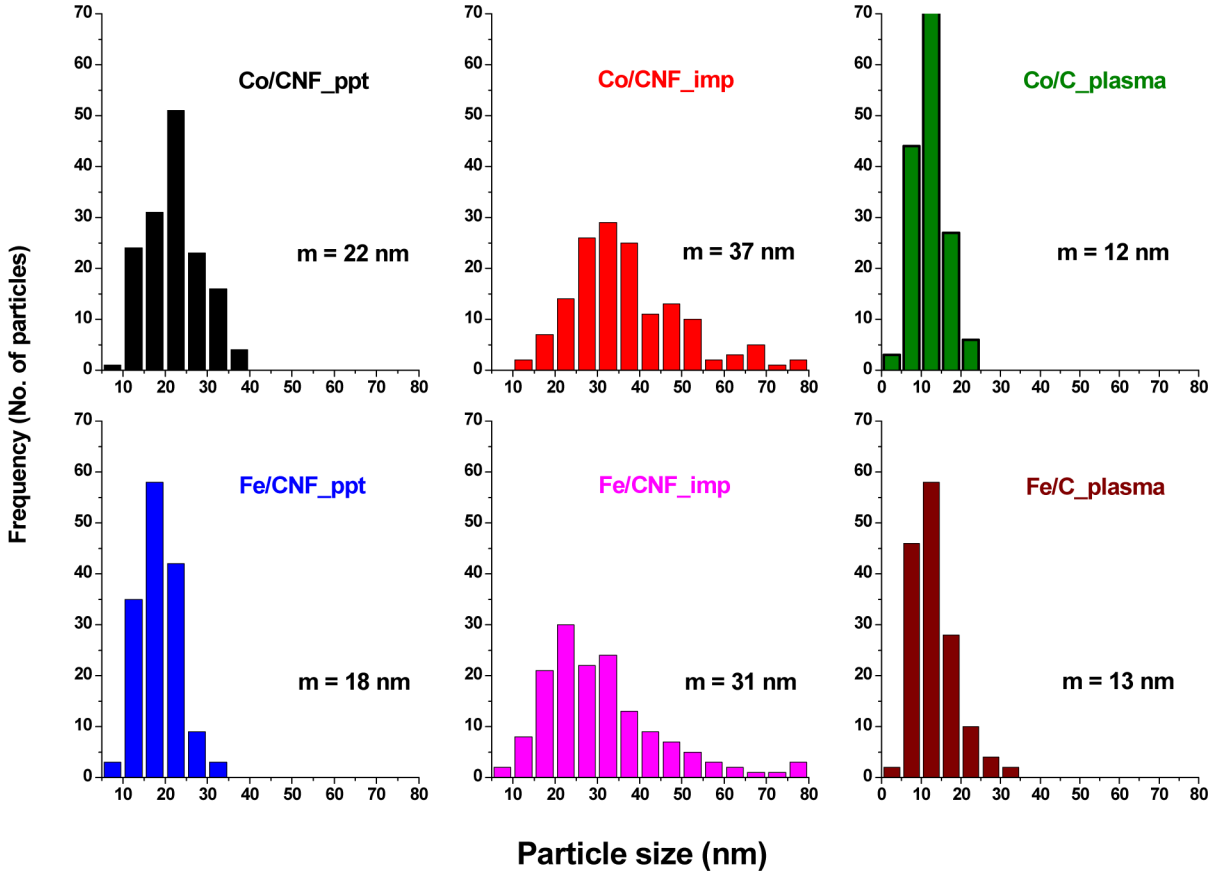

Figure 15. TEM analysis of particle size distribution of fresh catalysts indicating average particle size per catalyst (m = mean; n = 150 particles).

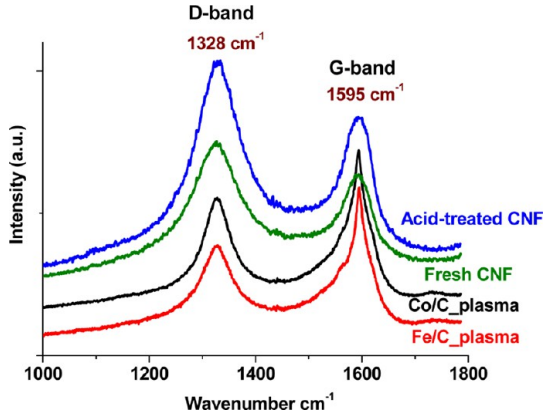

Figure 16. Raman spectra of fresh and acid-treated CNFs compared to plasma-synthesized Co/C and Fe/C catalysts.

hematite phase, as seen in Figure 17(a), while plasma-synthesized Fe/C displayed 1 broadened peak, indicating the possibility of carbides (χ-Fe_5C_2 and/or θ-Fe_3C). The XRD pattern of metallic Fe was absent, despite significant quantities of Fe in plasma-synthesized catalysts, probably because of the peak broadening that accompanies decreasing crystallite or metal particle size. Since the Fe/C catalyst was in the nanometric range, peak extinction would be expected.

In Figure 17(b), the plasma-synthesized Co/C catalyst revealed only the metallic phase (Co°), while impregnated Co/CNF contained both metallic (Co°) and monoxide (CoO) phases, but the precipitated Co/CNF catalyst showed predominant presence of the Co_3O_4 phase. It is believed that

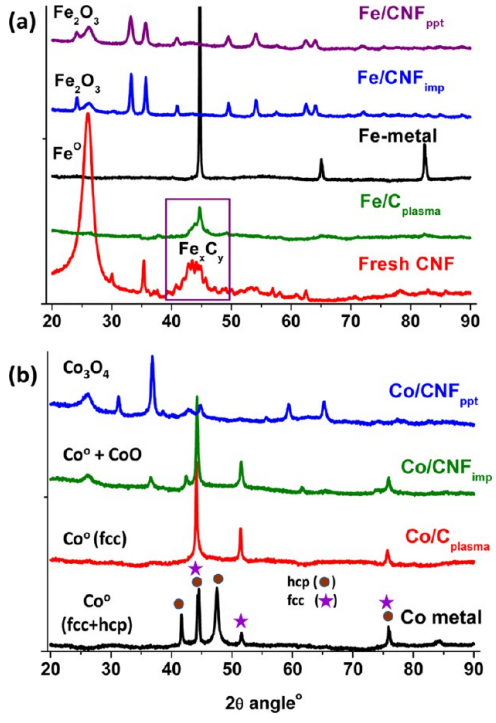

Figure 17. XRD spectra of fresh catalysts: (a) Fe-based; (b) Co-based.

Co carbides were also present in the plasma-derived samples, but existed below the detection limits of our XRD analysis, probably due to peak broadening arising from small crystallites.[36] It was further observed that the original Co

DOI: 10.1021/acs.iecr.5b03003
Ind. Eng. Chem. Res. 2015, 54, 10661−10674

powder used to prepare the plasma-synthesized catalysts consisted of 2 metallic phases, exhibited as face-centerd cubic (fcc) and hexagonal close packing (hcc) structures, giving distinct XRD patterns. In the catalyst, the hexagonal phase (*ca.* 38.1%) was transformed fully into the cubic phase.

3.2.6. XPS Analysis. Analysis of plasma-synthesized samples by XPS indicated metallic species on the surface of the catalysts. Table S3 in the Supporting Information summarizes the semiquantitative results. Mass composition amounting to approximately 20% mass-loading of the metal onto the C support was in close agreement with the EDX results accompanying SEM analysis. Since high-resolution analysis at each peak provides the chemical environment of each element, significant amounts of both metallic and oxidic species (CoO and Co_3O_4) were observed, for example, in the precipitated Co/CNF sample, in addition to trace amounts of hydroxide, $Co(OH)_2$ species, with a peak appearing just above 7,800 eV (Figure 18(a)).

The plasma-synthesized samples were not expected to contain any O. However, surface contamination was suspected to have contributed to this result, as shown by XPS analysis of the metal samples, which contained a significant amount of O and C, probably due to the oxidation and subsequent absorption of atmospheric CO_2 by the oxide layer, forming surface carbonates during storage. Similarly, at about 290 eV, $\pi \rightarrow \pi^*$ electron transitions occurred above the C peak (284 eV), as depicted in Figure 18(b). The π-bonds were indicative of graphitic C in the samples. Nonetheless, despite the substantial and concomitant presence of the metals and C in the materials, there was no significant sign of chemical bonding between them. From the shape of the XPS satellite peaks (see inset), metal carbide peaks expected to appear just below the C peak were not observed.

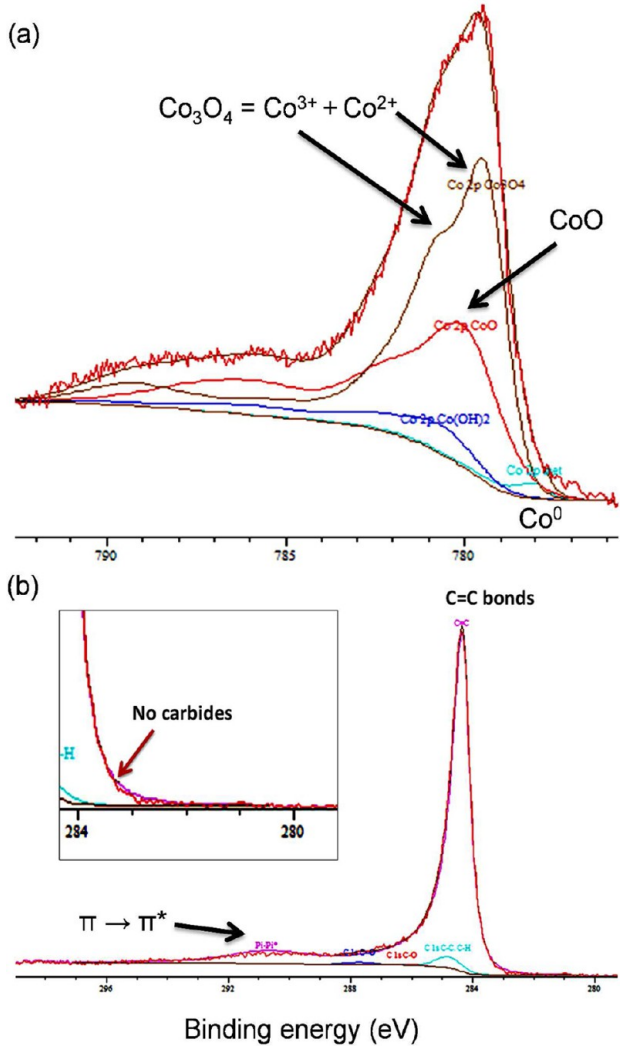

Figure 18. Sample XPS satellite peaks of (a) Co and (b) C in precipitated Co/CNF catalyst showing the $\pi \rightarrow \pi^*$ electron transition but no trace of carbides on the catalyst surface.

3.2.7. XANES Analysis. XANES analysis confirmed that the fresh plasma-synthesized catalysts were predominated by metallic species, as shown in Figure 19 for Co-based materials, and in Figure 20 for Fe-based materials. Figure 19(a) indicates that catalysts synthesized by either impregnation or plasma contained metallic species (Co^o), which was comparable in nature to Co foil. On the other hand, freshly precipitated catalysts were perceived to contain ionic species (possibly Co^{3+}) since their K-edge was found at higher energies than those of the CoO (or Co^{2+}) standard. This observation seemed to confirm the XRD results, which indicated that the precipitated Co/CNF catalyst was indeed composed of Co_3O_4. Figure 19(b) presents the spectra of reduced catalysts (during *in situ* XANES analysis at 350 °C for 3 h): it shows that all the catalysts contained Co^o, since their K-edges were close to that of Co foil (at ∼7,709 eV). This implies that Co-based catalysts were easily reduced.

The first derivatives, with the maxima corresponding to inflection points, established oxidation states at the point of maximum energy absorption. These values are shown in Figure 19(c) for fresh catalysts, while those of reduced catalysts are reported in Figure 19(d). Since most of the catalysts, particularly the plasma-synthesized sample, indicated the presence of metallic Co, their first derivatives disclosed a high peak at 7,709 eV and a relatively smaller peak around 7,723 eV, which corresponded to the presence of Co^0 and Co^{2+}, respectively. The precipitated Co/CNF catalyst showed a higher peak around 7,723 eV, which implied that the sample contained a high concentration of oxidized species.

As shown in Figure 20(a) only the plasma-synthesized Fe/C catalyst contained metallic species, whose nature was identical to the Fe foil, with typical K-edge energy at 7112 eV. Nonetheless, there was a gradual shift in the K-edge to higher energies, as observed in standard samples of higher oxidation states (e.g., FeO, Fe_2O_3, or Fe_3O_4). Precipitated or impregnated Fe/CNF samples contained significant reducible oxide species. XRD analysis also indicated that both samples contained hematite. Upon reduction in H_2, their spectra were found to shift to lower energies, toward the Fe^0 K-edge, as depicted in Figure 20(b). The Fe/CNF sample synthesized by impregnation demonstrated a clear case of partial oxidation during online reduction (at 350 °C, 3 h). However, the used samples after FTS testing indicated complete reduction. Since the samples are pyrophoric, we found that XANES was a convenient method of analyzing used samples while still in the reaction mixture, without having to expose the metallic particles to air.

Similarly, the first derivatives of Fe^0, Fe^{2+}, and Fe^{3+} oxidation states appeared at 7,112, 7,118, and 7,128 eV respectively, as shown in Figure 20(c) for fresh catalysts and in Figure 20(d) for reduced catalysts. Due to protracted reduction during FTS, only the used Fe/CNF sample and the freshly prepared plasma-synthesized sample appeared to trace the Fe foil (Fe^0)

DOI: 10.1021/acs.iecr.5b03003
Ind. Eng. Chem. Res. 2015, 54, 10661−10674

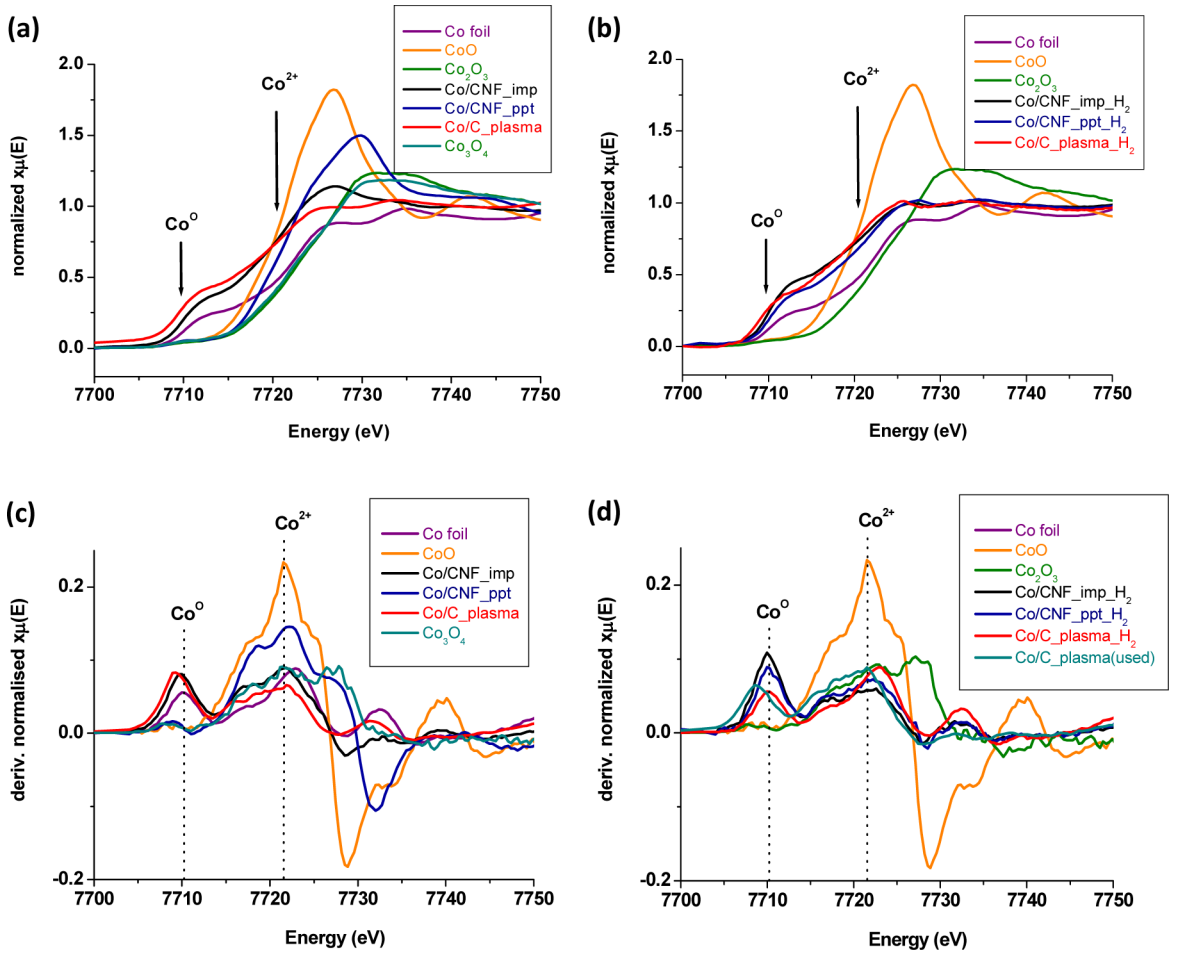

Figure 19. XANES analysis of (a) fresh Co-catalysts; (b) reduced in situ by H_2 for 3 h, with their respective first derivative of (c) raw data and (d) reduced samples.

spectrum. There is no doubt that the samples in Figure 20(d) had only undergone partial reduction, owing to the presence of oxidized species still present in them. Therefore, it seems probable that Fe-based catalysts require optimization through a meticulously designed reduction procedure in comparison to Co-based catalysts.

4. DISCUSSION

4.1. Catalyst Preparation. Since traditional methods of catalyst synthesis are multivariable and involve several stages, with each stage having to control numerous parameters, such approaches are tedious and labor-intensive. In this work, we favored catalyst synthesis by the plasma-spray method. Comparison of catalyst preparation by plasma technology vis-à-vis other techniques, such as impregnation or precipitation, is summarized schematically in Figure A3 of the Supporting Information. For example, the plasma method only takes a single step with 8 parameters to control, while the other procedures require 6 stages, with overall control of about 40 different parameters. Other observed advantages of plasma technology include shortened preparation time, uniformity in quality of materials, achieving highly distributed and, consequently, smaller nanometric size metal particles and active species, superior catalytic performance,[37] and enhanced catalyst lifetime, with overall lower energy requirements.[38]

One remarkable advantage of our catalyst preparation approach by plasma is that it produces core−shell type formulations. Graphitic C acts as an egg-shell that protects the nanometric metallic core (Co or Fe) from coming into contact with air. Since metal nanoparticles in combination with nanometric C are known to be pyrophoric in nature, in this way, our catalysts are safeguarded from oxidation during storage. Moreover, before FTS reaction, the C shell is partially removed (by catalyst activation pretreatment) to expose the encapsulated metal core embedded in the C matrix. Pretreatment is performed *in situ*, in a reducing environment with pure H_2 or CO. Since reduction is done at high temperatures (400 °C), it creates volatile gases presumably rich in methane and other hydrocarbons, which flow out of the reactor, rendering their separation less problematic.

4.2. Catalyst Characterization. Possible species found in the catalysts are summarized in the Supporting Information shown in Table S4. Porosity measurements by the BET method showed that the samples tended toward nonporosity, which is a positive attribute of the catalysts, as it would facilitate easy diffusion of the polymeric FTS products. Evidence from the various characterization techniques (Raman, XPS, and XRD) indicated that catalyst support contained both amorphous and graphitic forms of C. The predominantly ordered graphitic structures found in the CNFs were impaired by acid treatment during functionalization. Functionalization of the support is an important step in catalyst synthesis by precipitation or impregnation because it creates sites for anchoring the metal onto the CNFs. However, the procedure seems to introduce

DOI: 10.1021/acs.iecr.5b03003
Ind. Eng. Chem. Res. 2015, 54, 10661−10674

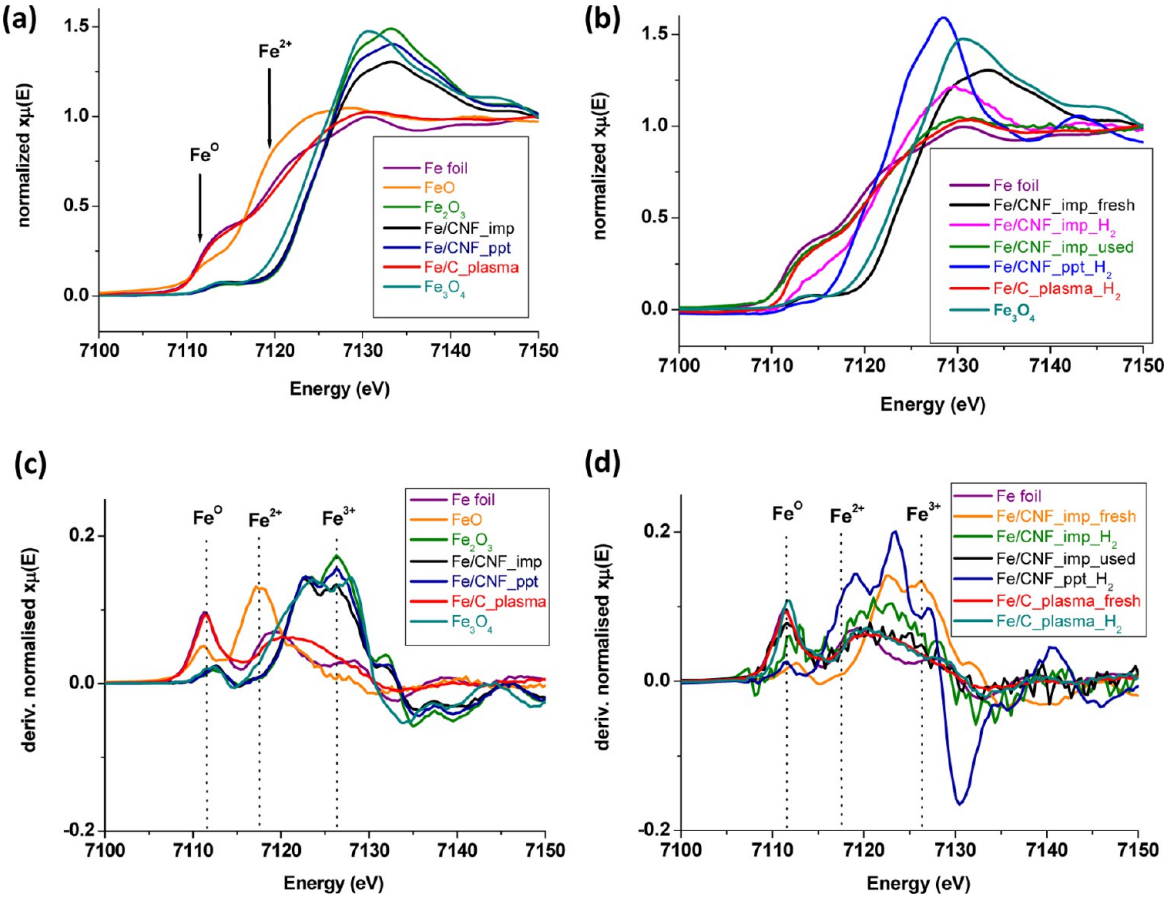

Figure 20. XANES analysis of (a) fresh Fe-catalysts; (b) reduced in situ by H_2 for 3 h with their respective first derivative of (c) raw data and (d) reduced samples.

massive defects in the CNFs, as was evident from the SEM images of the calcined samples. Nevertheless, graphitic C is deemed to be a better catalyst support than amorphous C because of its enhanced mechanical, electrical, and thermal conductivity properties. Graphitic C provides rigid mechanical support for metal particle anchorage, and the parallel sheets prevent mobility of the particles from dislocation. It exhibits high reactivity, specifically because of unsaturated valences at the edges of the graphitic layers, and has been tested as catalyst support for various reactions, including the hydrogenation of CO.[39]

In addition, it was observed from XRD analysis that fresh Fe/CNF catalysts, prepared by impregnation or precipitation, contained substantial amounts of Fe oxides, while XANES analysis revealed that the plasma-synthesized Fe/C catalyst was comprised mainly metallic Fe, a conclusion that could not be drawn from its XRD pattern. Nevertheless, evidence for the presence of Fe carbides (possibly Fe_3C and Fe_5C_2) in fresh CNFs and plasma-synthesized Fe/C catalyst was obtained by XRD analysis, which is a bulk technique. Fe carbides were not evident in XPS analysis, but we suppose that since it is a surface technique, encapsulation of the metal and carbides in the extensive C matrix did not lend the carbides a strong signal for detection. Since various studies show that the active species in Fe-catalyzed FTS are in the form of Fe carbides,[40] we are of the opinion that our acid-treatment to functionalize CNFs vanquished the carbides. As a consequence, catalysts produced by impregnation or precipitation were less active.

On the other hand, it is believed that, for Co-catalyzed FTS, activity is dependent on the reducibility of Co oxides,[20] and partial reduction of Co depresses catalyst activity. It was observed that although all prepared Co/C catalysts contained predominantly Co°, the one prepared by precipitation had a significant amount of Co_3O_4, which led to the lowest CO conversion (6.2%), while Co/CNF by impregnation contained some CoO (6.4% CO conversion). Even after *in situ* reduction, catalysts that originally contained oxidic species were perceived to be less active than plasma-synthesized samples that had none (19.4% CO conversion). Generally, we suspect that 10-h online reduction of the catalysts was not enough to totally reduce Co catalysts to the metallic form. This phenomenon was exemplified by our 3-h *in situ* reduction of Fe-based catalysts during XANES analysis, where a clear but gradual shift of the K-edge was evident due to the catalyst's partial reduction as a function of time, as depicted in Figure 20(b). It was also observed that, in the first-derivative plots, the used Co/C sample synthesized by plasma indicated a peak shift to the lower energies due to the presence of Co carbides. This conclusion was prompted by evidence from EXAFS and XANES in a study where the simultaneous presence of Co_2C and a form of Co exhibiting greater metallic character seemed to appear under FTS conditions.[36] Although not observed through the XRD analysis, it is believed that the Co carbides were present but could not be detected due to their existence as very small crystallites. This may explain the apparent shift of the XANES first-derivative peak in the used catalyst from that of the standard Co°.

DOI: 10.1021/acs.iecr.5b03003
Ind. Eng. Chem. Res. 2015, 54, 10661−10674

XRD analysis showed that the initial Co powder used in sample preparation contained 2 phases: hexagonal (hcp) and cubic (fcc), but given the high quench rates typical of plasma synthesis, the fcc was stabilized. Apparently, as the active phase in the Co catalyst, evidence has shown that the hcp exhibits greater intrinsic activity than fcc Co.[41] It is postulated that, besides metallic species, a good Co-based FTS catalyst is a function of crystallite size as well. Average Co-cluster size greater than 10 nm is supposed to stabilize the catalyst from deactivation. Our Co/CNF catalysts by impregnation and precipitation had average particle size of 37 and 22 nm, and gave CO conversions of 6.4 and 6.2%, respectively, while plasma-synthesized Co/C, which was more active (with 19.4% CO conversions) had average particle size of 12 nm. This means that loss of activity and, consequently, deactivation may be a combined outcome of the reoxidation of active Co particles,[41] as well as a particle-size effect.[20]

4.3. Catalyst Performance. After this investigation, we are inclined to believe that, if well optimized, the most effective method of preparing C-supported nanometric FTS catalysts would be through plasma-spray technology. Plasma-synthesized samples showed better activity with Fe/C giving 28% CO conversion, while Co/C delivered 20% CO conversion, but all catalysts prepared by impregnation or precipitation on CNFs showed CO conversion of less than 10%. Catalyst selectivity was observed to lean more toward the diesel range, with plasma-synthesized Fe/C leading with 71%, followed by the impregnated Co/CNF catalyst with 56%, and then the precipitated Fe/CNF with 51%. Only plasma-synthesized Co/C was more selective toward the gasoline fraction with 60%.

5. CONCLUSION

Six C-supported catalysts with their formulations based on Co or Fe were tested for Fischer−Tropsch activity. They were prepared by impregnation, precipitation, or the plasma-spray method. Overall, CO conversions were ∼28% (Fe/C by plasma), ∼ 20% (Co/C by plasma), and ∼7% (for Co/CNF and Fe/CNF by impregnation or precipitation). The selectivity of the catalysts tended more toward the diesel range, with 71% (Fe/C by plasma), 56% (Co/CNF by impregnation), and 51% (Fe/CNF by precipitation), except for the plasma-synthesized Co/C catalyst, which was richer in the gasoline range with 60% selectivity. These results show that plasma-synthesized catalysts were superior in performance compared to catalysts prepared on CNFs by other methods. From this study, a unique rationale to choose an effective FTS catalyst was developed, and used to rapidly narrow down to plasma technology as the most promising approach for future synthesis of FTS catalysts.

The plasma method produces active nanometallic catalysts in one step, thereby shrinking the preparation protocol. The metal phase is uniformly distributed in the carbon matrix, as indicated by SEM analysis, with an average particle size of about 12−13 nm, as given by TEM analysis. The graphitic nature of the C support was determined from XPS and Raman spectroscopy. Since FTS produces large polymeric products, one advantage of these materials lies in their nonporous nature, as shown by BET surface area analysis, making it possible to operate the reaction away from the diffusion-limited regimes. The presence of plasma-derived carbides, which are useful in the Fe-catalyzed FTS reaction, was evidenced from the X-ray techniques (XRD and XANES).

■ ASSOCIATED CONTENT

Supporting Information

The Supporting Information is available free of charge on the ACS Publications website at DOI: 10.1021/acs.iecr.5b03003.

Temperature profile determining thermocouple depth in the reactor; BET adsorption−desorption isotherms of the fresh CNFs, acid-treated CNFs, and the CNF-supported catalysts as well as the plasma-derived catalysts; Optimization process in catalyst synthesis: plasma-spray method compared to traditional techniques; Summary of catalyst activity comparing the mass of FTS products formed and the % CO conversion (plotted in Figure 5); Raw data for catalyst selectivity (%) toward various FTS products (plotted as Figures 7 and 8); Atomic composition on the surface of plasma-synthesized catalysts by XPS; Summary of possible Co and Fe species in catalyst samples as identified by various analytical techniques (PDF)

■ AUTHOR INFORMATION

Corresponding Author

*E-mail: Nicolas.Abatzoglou@USherbrooke.ca.

Notes

The authors declare no competing financial interest.

■ ACKNOWLEDGMENTS

We thank the BiofuelNet National Centre of Excellence (NCE) of Canada for financial support; Henri Gauvin and Jacques Gagné for their technical expertise in the laboratory; Aimee MacLennan of Canadian Light Source Inc. (CLS Synchrotron, Saskatoon, SK, Canada) for XANES analysis; Centre de Caractérisation des Matériaux (Université de Sherbrooke) personnel for facilitating characterization: Irène Kelsey Lévesque for BET surface area analysis; Kim Doan Nguyen Thi for Raman spectroscopy; Sonia Blais for XPS analysis; Charles Bertrand for SEM and TEM; and Stéphane Gutierrez for XRD analysis.

■ REFERENCES

(1) Khodakov, A. Y.; Chu, W.; Fongarland, P. Advances in the Development of Novel Cobalt Fischer−Tropsch Catalysts for Synthesis of Long-Chain Hydrocarbons and Clean Fuels. *Chem. Rev.* **2007**, *107*, 1692.

(2) de Klerk, A.; Furimsky, E. Catalysis in the Refining of Fischer−Tropsch Syncrude. *Platin. Met. Rev.* **2011**, *55*, 263.

(3) Pour, A. N.; Housaindokht, M. R.; Tayyari, S. F.; Zarkesh, J. Fischer−Tropsch Synthesis by Nano-structured Iron Catalyst. *J. Nat. Gas Chem.* **2010**, *19*, 284.

(4) Morales, F.; de Smit, E.; de Groot, F. M. F.; Visser, T.; Weckhuysen, B. M. Effects of Manganese oxide Promoter on the CO and H_2 Adsorption Properties of Titania-supported Cobalt Fischer−Tropsch Catalysts. *J. Catal.* **2007**, *246*, 91.

(5) Riedel, T.; Schaub, G. Low-Temperature Fischer−Tropsch Synthesis on Cobalt Catalysts - Effects of CO_2. *Top. Catal.* **2003**, *26*, 145.

(6) Yang, Y.; Xiang, H.-W.; Xu, Y.-Y.; Bai, L.; Li, Y.-W. Effect of Potassium Promoter on Precipitated Iron-Manganese Catalyst for Fischer−Tropsch Synthesis. *Appl. Catal., A* **2004**, *266*, 181.

(7) Tang, Q.; Wang, Y.; Zhang, Q.; Wan, H. Preparation of Metallic Cobalt Inside NaY Zeolite with High Catalytic Activity in Fischer−Tropsch Synthesis. *Catal. Commun.* **2003**, *4*, 253.

(8) Hou, W.; Wu, B.; Yang, Y.; Hao, Q.; Tian, L.; Xiang, H.; Li, Y. Effect of SiO_2 Content on Iron-based Catalysts for Slurry Fischer−Tropsch Synthesis. *Fuel Process. Technol.* **2008**, *89*, 284.

DOI: 10.1021/acs.iecr.5b03003
Ind. Eng. Chem. Res. 2015, 54, 10661−10674

(9) Xiong, H.; Motchelaho, M. A. M.; Moyo, M.; Jewell, L. L.; Coville, N. J. Correlating the Preparation and Performance of Cobalt Catalysts Supported on Carbon Nanotubes and Carbon Spheres in the Fischer−Tropsch Synthesis. *J. Catal.* **2011**, *278*, 26.
(10) Blanchard, J.; Abatzoglou, N.; Eslahpazir-Esfandabadi, R.; Gitzhofer, F. Fischer−Tropsch Synthesis in a Slurry Reactor using a Nano-Iron Carbide Catalyst Produced by a Plasma Spray Technique. *Ind. Eng. Chem. Res.* **2010**, *49*, 6948.
(11) Gaube, J.; Klein, H. F. The Promoter Effect of Alkali in Fischer−Tropsch Iron and Cobalt Catalysts. *Appl. Catal., A* **2008**, *350*, 126.
(12) Visconti, C. G.; Lietti, L.; Tronconi, E.; Forzatti, P.; Zennaro, R.; Finocchio, E. Fischer−Tropsch Synthesis on a Co/Al_2O_3 Catalyst with CO_2 Containing Syngas. *Appl. Catal., A* **2009**, *355*, 61.
(13) Ernst, B.; Libs, S.; Chaumette, P.; Kiennemann, A. Preparation and Characterization of Fischer−Tropsch Active Co/SiO_2 Catalysts. *Appl. Catal., A* **1999**, *186*, 145.
(14) Eschemann, T. O.; Bitter, J. H.; de Jong, K. P. Effects of Loading and Synthesis Method of Titania-Supported Cobalt Catalysts for Fischer−Tropsch Synthesis. *Catal. Today* **2014**, *228*, 89.
(15) Kang, S.-H.; Bae, J. W.; Woo, K.-J.; Prasad, P. S. S.; Jun, K.-W. ZSM-5 Supported Iron Catalysts for Fischer−Tropsch Production of Light Olefin. *Fuel Process. Technol.* **2010**, *91*, 399.
(16) Jong, S.-J.; Cheng, S. Reduction Behavior and Catalytic Properties of Cobalt Containing ZSM-5 Zeolites. *Appl. Catal., A* **1995**, *126*, 51.
(17) Jongsomjit, B.; Wongsalee, T.; Praserthdam, P. Catalytic Behaviors of Mixed TiO_2-SiO_2-Supported Cobalt Fischer−Tropsch Catalysts for Carbon Monoxide Hydrogenation. *Mater. Chem. Phys.* **2006**, *97*, 343.
(18) Jacobs, G.; Das, T. K.; Zhang, Y.; Li, J.; Racoillet, G.; Davis, B. H. Fischer−Tropsch Synthesis: Support, Loading, and Promoter Effects on the Reducibility of Cobalt Catalysts. *Appl. Catal., A* **2002**, *233*, 263.
(19) Abbaslou, R. M. M.; Tavassoli, A.; Soltan, J.; Dalai, A. K. Iron Catalysts Supported on Carbon Nanotubes for Fischer−Tropsch Synthesis: Effect of Catalytic Site Position. *Appl. Catal., A* **2009**, *367*, 47.
(20) Bezemer, G. L.; Bitter, J. H.; Kuipers, H. P. C. E.; Oosterbeek, H.; Holewijn, J. E.; Xu, X.; Kapteijn, F.; van Dillen, A. J.; de Jong, K. P. Cobalt Particle Size Effects in the Fischer−Tropsch Reaction Studied with Carbon Nanofiber Supported Catalysts. *J. Am. Chem. Soc.* **2006**, *128*, 3956.
(21) Jankhah, S.; Abatzoglou, N.; Gitzhofer, F. Thermal and Catalytic Dry Reforming and Cracking of Ethanol for Hydrogen and Carbon Nanofilaments' Production. *Int. J. Hydrogen Energy* **2008**, *33*, 4769.
(22) Moodley, D. J.; van de Loosdrecht, J.; Saib, A. M.; Niemantsverdriet, H. J. W. The Formation and Influence of Carbon on Cobalt-based Fischer−Tropsch Catalysts: An Integrated Review. In *Advances in Fischer−Tropsch Synthesis, Catalysts and Catalysis*; Davis, B. H., Occelli, M. L., Eds.; CRC Press: Boca Raton, FL (USA), 2010; p 51.
(23) Zennaro, R.; Tagliabue, M.; Bartholomew, C. H. Kinetics of Fischer−Tropsch Synthesis on Titania-supported Cobalt. *Catal. Today* **2000**, *58*, 309.
(24) Bao, A.; Liew, K.; Li, J. Fischer−Tropsch Synthesis on CaO-promoted Co/Al_2O_3 Catalysts. *J. Mol. Catal. A: Chem.* **2009**, *304*, 47.
(25) Blanchard, J.; Abatzoglou, N.; Eslahpazir-Esfandabadi, R.; Gitzhofer, F. Fischer−Tropsch Synthesis in a Slurry Reactor using a Nano-iron Carbide Catalyst Produced by a Plasma Spray Technique. *Ind. Eng. Chem. Res.* **2010**, *49*, 6948.
(26) Abatzoglou, N.; Gitzhofer, F.; Blanchard, J.; Vigier, K. D. O.; Gravelle, D. Carbon sequestration and dry reforming process and catalysts to produce same. US Patent 7,794,690, 2010.
(27) Blanchard, J.; Oudghiri-Hassani, H.; Abatzoglou, N.; Jankhah, S.; Gitzhofer, F. Synthesis of Nanocarbons via Ethanol Dry Reforming over a Carbon Steel Catalyst. *Chem. Eng. J.* **2008**, *143*, 186.
(28) Abatzoglou, N.; Plascencia, C. R., Ni-doped Carbon Nanofilaments (Ni-CNF): Preparation and Use as Reforming Catalyst. Presented at the *5th International Conference on Nanotechnology: Fundamentals and Applications*, Prague, Czech Republic, 2014; Keynote Lecture V, pp 1−8.
(29) Bej, S. K.; Dalai, A. K.; Maity, S. K. Effect of Diluent Size on the Performance of a Micro-scale Fixed bed Multiphase Reactor in Up Flow and Down Flow Modes of Operation. *Catal. Today* **2001**, *64*, 333.
(30) Bahome, M. C.; Jewell, L. L.; Hildebrandt, D.; Glasser, D.; Coville, N. J. Fischer−Tropsch Synthesis over Iron Catalysts Supported on Carbon Nanotubes. *Appl. Catal., A* **2005**, *287*, 60.
(31) Chu, W.; Chernavskii, P. A.; Gengembre, L.; Pankina, G. A.; Fongarland, P.; Khodakov, A. Y. Cobalt Species in Promoted Cobalt Alumina-supported Fischer−Tropsch Catalysts. *J. Catal.* **2007**, *252*, 215.
(32) Ravel, B.; Newville, M. ATHENA, ARTEMIS, HEPHAESTUS: Data Analysis for X-ray Absorption Spectroscopy using IFEFFIT. *J. Synchrotron Radiat.* **2005**, *12*, 537.
(33) Braidy, N.; Andrei, C.; Blanchard, J.; Abatzoglou, N. From Nanoparticles to Process: An Aberration-corrected TEM Study of Fischer−Tropsch Catalysts at Various Steps of the Process. *Adv. Mater. Res.* **2011**, *324*, 197.
(34) Ferrari, A. C.; Robertson, J. Interpretation of Raman Spectra of Disordered and Amorphous Carbon. *Phys. Rev. B: Condens. Matter Mater. Phys.* **2000**, *61*, 14095.
(35) Osswald, S.; Chmiola, J.; Gogotsi, Y. Structural Evolution of Carbide-derived Carbons upon Vacuum Annealing. *Carbon* **2012**, *50*, 4880.
(36) Mohandas, J. C.; Gnanamani, M. K.; Jacobs, G.; Ma, W.; Ji, Y.; Khalid, S.; Davis, B. H. Fischer−Tropsch Synthesis: Characterization and Reaction Testing of Cobalt Carbide. *ACS Catal.* **2011**, *1*, 1581.
(37) Rutkovskii, A. E.; Vishnyakov, L. R.; Chekhovskii, A. A.; Kirkun, N. I. Use of Plasma Technology in Creating Catalysts on Carriers. *Powder Metall. Met. Ceram.* **2000**, *39*, 207.
(38) Liu, C.-J.; Vissokov, G. P.; Jang, B. W. L. Catalyst Preparation using Plasma Technologies. *Catal. Today* **2002**, *72*, 173.
(39) Serp, P.; Machado, B., Carbon (Nano)materials for Catalysis. In *Nanostructured Carbon Materials for Catalysis*; Royal Society of Chemistry: London, UK, 2015; pp 1−45.
(40) Bengoa, J. F.; Alvarez, A. M.; Cagnoli, M. V.; Gallegos, N. G.; Marchetti, S. G. Influence of Intermediate Iron Reduced Species in Fischer−Tropsch Synthesis using Fe/C Catalysts. *Appl. Catal., A* **2007**, *325*, 68.
(41) Jacobs, G.; Ma, W.; Gao, P.; Todic, B.; Bhatelia, T.; Bukur, D. B.; Davis, B. H. The Application of Synchrotron Methods in Characterizing Iron and Cobalt Fischer−Tropsch Synthesis Catalysts. *Catal. Today* **2013**, *214*, 100.

DOI: 10.1021/acs.iecr.5b03003
Ind. Eng. Chem. Res. 2015, 54, 10661−10674

9.3. Appendix C: Article 3 – Single metal catalyst testing in CSTR

THE CANADIAN JOURNAL OF CHEMICAL ENGINEERING

LOW-TEMPERATURE FISCHER-TROPSCH SYNTHESIS USING PLASMA-SYNTHESIZED NANOMETRIC CO/C AND FE/C CATALYSTS

James Aluha,[1] Nadi Braidy,[1] Ajay Dalai[2] and Nicolas Abatzoglou[1]*

1. Department of Chemical and Biotechnological Engineering, Université de Sherbrooke, Sherbrooke QC, J1K 2R1, Canada

2. Department of Chemical and Biotechnological Engineering, University of Saskatchewan, SK, S7N 5A9, Canada

In this study, two analogous nanometric catalysts consisting of carbon-supported cobalt or iron (Co/C and Fe/C) were synthesized by plasma and tested for Fischer-Tropsch synthesis (FTS) in a continuously-stirred tank slurry reactor (CSTSR). Being pyrophoric in nature, these new materials were reduced in situ at 673 K (400 °C) for 24 h using pure H_2 gas. The FTS reaction was conducted at 493 K (220 °C), 2000 kPa pressure, and gas hourly space velocity (GHSV) of 3600 mL · g_{cat}^{-1} · h^{-1} for 24 h, using a feed stream of 0.6 L/L (60 vol %) H_2 and 0.3 L/L (30 vol %) CO, with 0.1 L/L (10 vol %) Ar for mass balance determination. Devoid of promoters and under similar reaction conditions, the Co/C catalyst showed higher CO conversion (42 %) than the Fe/C (25 %), benchmarked against the commercial Fe-NanoCat® (32 %). Co/C was more selective toward gasoline production, while Fe/C was more selective toward the diesel fraction. From transmission electron microscopy (TEM) analysis, no significant change in the mean particle size (~12 nm) was observed in the plasma-synthesized catalysts before and after FTS reaction, implying that the catalysts did not sinter. Additionally, there were no internal mass transport limitations in these catalysts, making them favourable for FTS. Besides metallic species, X-ray diffraction (XRD) analysis indicated the presence of carbides in fresh catalysts (Fe_3C in Fe/C and Co_3C in Co/C). Magnetite (Fe_3O_4) was the most prevalent phase in the used Fe-NanoCat® sample, a phase that was below the detection limits of XRD in the used plasma-synthesized Fe/C sample.

Keywords: plasma, carbon, iron, cobalt, catalyst, Fischer-Tropsch

INTRODUCTION

Plasma technology is a relatively new Fischer-Tropsch synthesis (FTS) catalysts preparation technique.[1] Commercial applications of FTS produce mainly synthetic liquid fuels that comprise gasoline (C_4–C_{12}), diesel (C_8–C_{21}), and heavier products such as waxes (C_{21+}), among other hydrocarbon products (Equations (1, 2)). The water-gas shift reaction shown in Equation (3) is one of the most important side reactions in the process.

$$n\,CO + 2n\,H_2 \rightarrow [-CH_2-]_n + n\,H_2O \quad (1)$$

$$n\,CO + (2n+1)\,H_2 \rightarrow C_nH_{2n+2} + n\,H_2O \quad (2)$$

$$CO + H_2O \rightarrow CO_2 + H_2 \quad (3)$$

There are several advantages of using plasma over conventional catalyst synthesis techniques. For example, although numerous process variables are necessary to provide the versatility needed to fabricate complex catalysts, plasma is a single-step method that decreases the number of stages in catalyst preparation, an approach that significantly lowers excessive process variables and parameters.[2] Other proposed advantages include superior catalyst performance,[3] achieved from the highly distributed active species, enhanced catalyst lifetime, shortened preparation time, and overall lower energy requirements, especially in cold plasma applications.[4]

The nature and operation of the active species in the FTS catalysts are of substantial interest, having been studied using many characterization methods such as X-ray techniques (EXAFS, XRD, XPS), microscopy (SEM, TEM),[5] temperature-programmed reduction or oxidation (TPR/TPO), and adsorption techniques, namely physisorption and chemisorption,[6] among others. Often, the catalyst remains in a metallic state under FTS conditions, but its composition may change during reaction,[7] ranging from metallic iron (Fe^0), its oxides (FeO, Fe_2O_3 or Fe_3O_4), and carbides (Fe_2C, Fe_3C or Fe_5C_2 among others), represented generally as Fe_xC_y.[8] In the Fe-catalyzed FTS, catalyst synthesis by plasma appears to generate these indispensable Fe carbides, which affords the technique a comparative advantage over other preparation methods.

When compared, reactors with Fe-based catalysts for low-temperature Fischer-Tropsch synthesis (LT-FTS) have received less attention than their Co-based counterparts since Fe catalysts usually exhibit lower activity for the production of diesel and wax yields.[9] In this study, a typical 3-phase bubbled-gas continuously-stirred tank slurry reactor (3φ-BG-CSTSR) was employed, operated isothermally for LT-FTS with an objective of mainly obtaining the diesel fraction. Formation of molecules with higher molecular mass such as waxes was still viewed as favourable since the molecules could be thermally cracked to enrich the diesel fraction. In the chosen 3φ-BG-CSTSR, the simulated syngas feed was bubbled through inert (or rather low reactivity) oil, namely *n*-hexadecane (C_{16}), in which catalyst particles were suspended. Vigorous mixing maximizes phase contact and consequently mass transfer rates in addition to creating uniform temperature distribution. In a relatively small reactor volume, this enhances efficiency when operating within a regime of kinetically-controlled surface reactions.[10] Nowadays, using eggshell catalyst pellets in

* *Author to whom correspondence may be addressed.*
E-mail address: nicolas.abatzoglou@usherbrooke.ca
Can. J. Chem. Eng. 94:1504–1515, 2016

DOI 10.1002/cjce.22537
Supplementary material is available in the online journal.
Published online 19 June 2016 in Wiley Online Library (wileyonlinelibrary.com).

packed-bed reactors introduces design flexibility by separating issues that involve the characteristic diffusion distance in catalyst pellets from pressure drop and other reactor constraints.[11]

This paper is a supplementary article from the recently published work where we compared several catalysts prepared by various methods, and the plasma-synthesized samples were found to be the most promising materials for LT-FTS when tested in the fixed-bed reactor.[2] In this work, we present results from a study comparing two analogous catalysts synthesized through plasma. The materials were based on Co and Fe, supported on carbon (Co/C and Fe/C), prepared under identical plasma conditions, and tested similarly for FTS activity. Since the materials are being projected for industrial application, they were benchmarked against a commercially available FTS catalyst (the Fe-NanoCat®). We describe the catalyst synthesis procedure by plasma and discuss details of the catalyst activity testing with respect to selectivity, specifically toward the diesel range hydrocarbon fraction. Attention is also given to the characterization of these novel materials.

EXPERIMENTAL

Catalyst Synthesis by Plasma

Using a radio frequency (RF) plasma system (PL-50, 3.2 MHz, Tekna Inc.), two analogous catalysts (Co/C and Fe/C) were synthesized by introducing 60 g of metal (mixed in 300 mL of mineral oil) directly into the plasma at a flow rate of 8.2 mL · min^{-1}.[2] The resulting powder material was harvested and tested for FTS.

Catalyst Testing Reaction Conditions

The reactor of choice was a 1.5 L stainless-steel Parr reactor vessel, acting as a 3φ-BG-CSTSR operated isothermally at 493 K (220 °C), under 2000 or 3000 kPa pressure. Figure 1 is a scheme of our catalyst testing reactor system. With a syngas feed volume composition of 0.3 L/L (30 %) CO and 0.6 L/L (60 %) H_2 flowing at 300 mL · min^{-1} (H_2:CO volume ratio of 2) for the FTS provided a gas hourly space velocity (GHSV) of 3600 mL · g_{cat}^{-1} · h^{-1}, using 5.0 g of catalyst; 0.1 L/L (10 %) Ar was included in the gas stream for the overall mass balance determination and CO conversion calculations.[12]

Before the FTS reaction ensued, the catalyst was pre-treated in situ for 24 h in high-purity hydrogen gas (N4.5) flowing at 250 mL · min^{-1} at 673 K (400 °C), at which most of the carbon matrix was presumably gasified to CH_4 and other hydrocarbons, leaving behind nanometric Fe or Co catalysts that were predominantly in a metallic form. The activity of these new materials was benchmarked against the commercial Fischer-Tropsch catalyst (Fe-NanoCat®), which was activated by pure CO (N2.5) instead of hydrogen.

Two offline Varian CP-3800 GC units were used to analyze the FTS product spectra: one for gas-phase products and the other one for the liquid-phase. The gas-phase analysis GC unit was equipped with one flame-ionization detector (FID) and two thermal conductivity detectors (TCDs). One TCD was dedicated to analyzing H_2 only while the other was for analyzing the other gases. The column sequence for the general TCD was Hayesep T (CP81072), followed by Hayesep Q (CP81073) and then Molsieve 13X (CP81071), with He as the carrier gas, while the setup for the H_2 TCD was a Hayesep Q (CP81069) with a Molsieve 5A (CP81025), and N_2 as the carrier gas. The FID detector was in series with the general TCD detector. On the other hand, the liquid-phase GC unit with a FID and He as the carrier gas was fitted with a low-polarity GC column 100–2000 DB-1HT (Agilent Technologies Inc.), having L = 30 m, ID = 0.32 mm, and DF = 100 nm (0.10 μm); suited for operating within a temperature range of 213–673 K (–60 to 400 °C).

Catalyst Characterization

Since the samples are pyrophoric, only the fresh catalysts, and whenever possible the used samples, were analyzed by various characterization techniques, which involved porosity analysis by the Brunauer-Emmett-Teller (BET) method, powder X-ray diffraction (p-XRD) including the Rietveld quantitative analysis (RQA), and both scanning electron microscopy (SEM) and transmission electron microscopy (TEM).

Thermogravimetric analysis (TGA)

The metal mass loading of the catalysts was determined by thermogravimetric analysis using a Setaram Setsys 2400 calorimetric

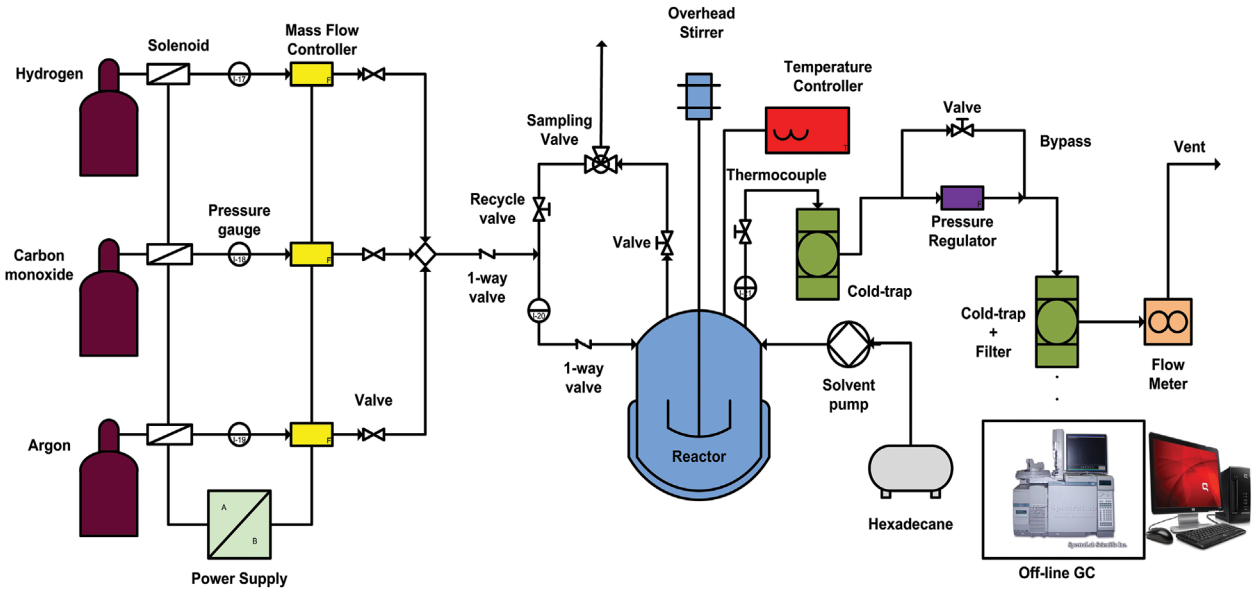

Figure 1. Schematic illustrating the design of our CSTSR catalyst testing system.

system, equipped with a 1873 K TG-DTA sensor. < 25 mg of the sample in an alumina crucible was heated from ambient temperature (~293 K) to 1273 K at a heating rate of 10 K · min^{-1}, first in an inert atmosphere using Ar and then in 0.2 L/L (20 vol %) O_2 balanced in Ar. Mass loss recorded relates to the amount of carbon burned (to CO_2), leaving behind the bare metal, from which the atomic mass loading of the metal in the catalyst is calculated.

Porosity and the BET surface area analysis

The specific surface area of the fresh catalysts was measured by the BET method, using a Micromeritics ASAP 2020 unit. ~0.5 g was degassed at 363 K (90 °C) for 30 min and then at 523 K (250 °C) for 50 h under evacuation until a pressure of < 1 Pa (10 μm_{Hg}) was obtained in the sample holder. After degassing, the sample was re-weighed and then analyzed under liquid nitrogen at 77 K from an initial pressure of ~0.2 Pa (2 μm_{Hg}) to ambient pressure.

Scanning electron microscopy (SEM)

SEM analysis and imaging, which captured both secondary and backscattered images, were conducted on a Hitachi S-4700 Scanning Electron Microscope, equipped with an energy dispersive X-ray (EDX) X-Max Oxford spectrometer.

Transmission electron microscopy (TEM)

TEM analysis was conducted on a Hitachi H-7500 instrument, operated at an accelerating electron beam of 120 kV from a tungsten filament. Images were captured in the bright field mode using a bottom-mounted AMT 4k × 4k CCD Camera System Model X41. Analysis for particle size distribution was done by means of the Nano-measurer version 1.2 "Scion Imager" software.

Powder X-ray diffraction analysis

Powder X-ray diffraction analysis was carried out using a Philips X'pert PRO Diffractometer from PANalytical. The instrument was set in the Bragg-Brentano configuration with PIXcel-1D detector and operated with factory-installed Analytical Data Collector software. It was fitted with Ni filters for the Cu Kα radiation (0.154 nm) produced at 40 kV and 50 mA. XRD patterns were recorded in the range of 20° and 110° [2θ] angles at a scanning speed of ~3° [2θ] min^{-1}, with a step size of 0.040° [2θ] angle and time of 0.0395 s per step corresponding to a scan time of 24 min. The anti-scatter and divergent slits were fixed at 1°. Materials Data Inc. software, MDI JADE 2010 (version 2.6.6), was used in data analysis and the collected data compared with the Powder Diffraction Files in the database (version 4.13.0.2) using the PDF-4+ software 2013 (version 4.13.0.6).

Analysis of the dry powder was conducted for the fresh Co/C and Fe/C samples. After reaction, and due to the pyrophoric nature of the materials, a sample of the slurry containing the solvent and the FTS products was drawn directly from the reactor and analyzed without any further treatment. Modelling with Rietveld refinement[13] to determine the phase fractions in the fresh and used catalysts was done using High Score Plus software for the Rietveld quantitative analysis (RQA), which takes into consideration the relative mass fraction of each phase in a mixture of several phases.[14]

RESULTS

Catalyst Testing

Catalyst activity

The plasma-synthesized Co/C and Fe/C catalysts were pre-treated in a stream of pure H_2 gas at 673 K for 24 h and then tested for Fischer-Tropsch activity at 493 K and 2000 kPa. It was observed that the Co/C was more active than the Fe/C (Figure 2). On average the Co/C catalyst showed a ≥ 40 % CO conversion, and 12 % for the Fe/C catalyst, while the commercial Fe-NanoCat® catalyst (pre-treated in CO) gave a ≥ 30 % CO conversion. The activity of all catalysts was observed to be unstable over time-on-stream (TOS). However, when the catalysts were pre-treated at lower temperatures and shorter periods (623 K, 16 h) and then tested for FTS at 493 K and 3000 kPa, there was an improvement in the Fe/C catalyst, which gave ~25 % CO conversion; the plasma-synthesized Co/C catalyst was still more active with > 40 % CO conversion and more stable over TOS than the Fe/C catalyst, but deteriorating with TOS toward 20 % after 24 h on stream (Figure 3).

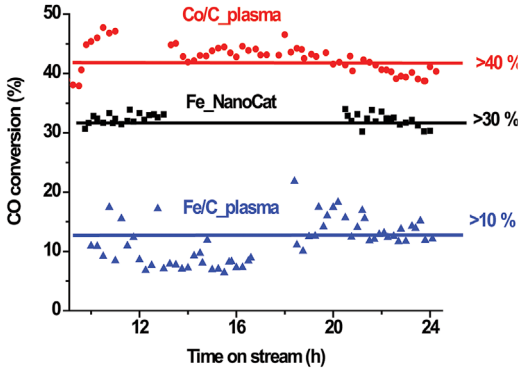

Figure 2. Activity plots for plasma-synthesized Co/C and Fe/C catalysts compared to Fe-NanoCat® pretreated at 673 K (400 °C) for 24 h; tested at 2000 kPa pressure, 493 K (220 °C) for 24 h.

The Co/C catalyst shows a higher propensity to create a full spectrum of products than the Fe/C catalyst, running from low to high molecular mass products including waxes (Figure 3). A typical effluent gas analysis is summarized in Table 1, which clearly shows that under 2000 kPa pressure, at T = 493 K the average CO conversion lies between 10–45 % with low formation of CO_2 and CH_4 from all the catalysts. However, at T = 543 K, the CO conversion approached 100 %, but with increased CO_2 and CH_4 formation. In addition, the Fe-based catalysts had a lower tendency to produce CH_4 in comparison to the Co/C catalyst. All the catalysts has a limited capacity to form C_2–C_5 products.

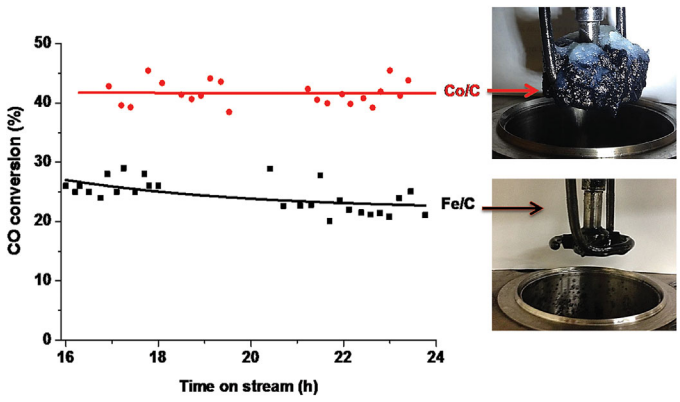

Figure 3. Activity plots for the plasma-synthesized Co/C and Fe/C catalysts reduced at 623 K (350 °C) for 16 h and tested at 493 K (220 °C) under 3000 kPa pressure with insets of images of the reactor at the end of reaction.

Table 1. GC analysis showing typical gas composition from the reactor exit at 2000 kPa for 493 K and 543 K (220 °C, 270 °C)

Catalyst	% CO conversion	Concentration (%) CO_2	CH_4	C_2H_6	C_2H_4	C_3–C_5
(a) 493 K						
Fe/C_{plasma}	25	2.8	2.0	0.4	0.1	–
Fe-NanoCat®	32	2.8	1.3	0.4	0.3	–
Co/C_{plasma}	45	2.0	8.8	0.3	0.0	–
(b) 543 K						
Fe/C_{plasma}	80	12.5	5.6	1.4	0.6	–
Fe-NanoCat®	89	15.1	5.4	1.1	0.5	–
Co/C_{plasma}	100	18.0	42.0	1.1	0.0	–

Liquid-phase analysis indicated a product spectrum of C_6–C_{40} (Figure S1a of Supporting Information; see overlaid sample GC traces of Co/C and Fe/C catalysts). Since the hexadecane (C_{16}) solvent camouflages the FTS products at C_{16}, the peak was deleted from the GC trace and replaced with that of C_{18} to determine its appropriate value. This conclusion was arrived at because from the previous work using the fixed-bed reactor where the same catalysts were tested,[2] it was observed that analysis of only the liquid-phase components produced a maximum at the C_{17} peak (Figure S1b). Integration of the area under each peak provided for the means of determining the selectivity of each catalyst.

Effect of pre-treatment

The Co/C catalyst was found to be relatively less sensitive to the pre-treatment procedure than the Fe/C catalyst, whether reduced for 10 h or for longer (24 h), as seen in Figure 4. The same was observed with temperature: for both 523 and 673 K, the catalyst performance was comparable, with CO conversions remaining at ~40 % in all cases. In contrast, Fe/C was more sensitive to pre-treatment. For example, catalyst reduction at 593 K for 10 h led to 10 % CO conversion, but gave 25 % CO conversion at 24 h. This implies that prolonged reduction at lower temperatures may be more desirable since a longer reduction period (24 h) only managed 10 % CO conversion when performed at elevated temperatures (673 K). In fact, reduction of the catalyst for a shorter time (10 h) at a high temperature (673 K) was equally effective, leading to 25 % CO conversion. These observations agreed with earlier work performed on identical Fe-based catalysts, where under mild low-T pretreatment conditions for a short time, not enough carbon was removed from the metal catalyst, leading to low CO conversion. In contrast, under severe high-T pretreatment conditions for prolonged periods, the catalyst suffered from sintering and/or decarburization, which by the same token lowered catalytic activity.[1]

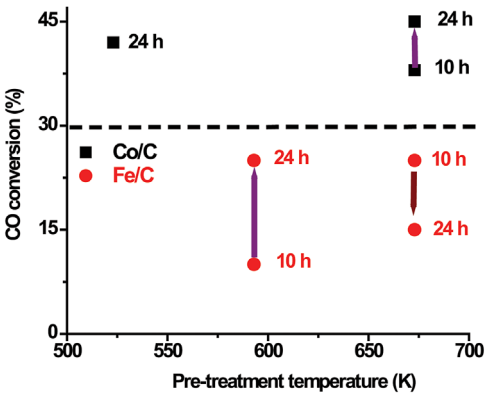

Figure 4. Activity plots for plasma-derived Co/C and Fe/C catalysts reduced under various conditions of time and temperature.

Catalyst selectivity

Values derived from the GC analysis of the liquid phase were adapted by integrating the area under each peak and dividing by the total area of all the peaks (Equation (4)). The selectivity (S) towards any FTS product with i number of carbon atoms was therefore calculated to be directly proportional to the area under its peak (A_i), thus the following is true:

$$S_i = \frac{(A_i)\, x\, 100}{\sum_{i=5}^{n} A_i} \tag{4}$$

where the hydrocarbon molecules have at least five carbon atoms.

After determining the selectivity of each product, peak areas of isomers and hydrocarbons with a similar number of carbon atoms were lumped together (Figure 5), after which they were further summed up to determine the different fuel fractions. In reality, the gasoline fraction is a mixture that ranges between C_4–C_{12}, while the diesel range is C_8–C_{21}, but in this work, we shall take the gasoline fraction to mean C_4–C_{12} and diesel as C_{13}–C_{20} for mass balance and in order to lessen the confusion that may arise from peak overlaps. Figure 4 depicts the commercial Fe-NanoCat® sample as having a relatively narrower product distribution than the plasma-synthesized catalysts (Co/C and Fe/C), both of which displayed a much broader product spectrum, progressively distributed across most of the carbon molecular chains. Note that most of the fraction in the wax range produced by the Co/C sample may not be reflected in this plot, since it had solidified and may not be fully represented in the liquid analysis. Nevertheless, the current objective was to assess, among several catalysts,[2] the ones that are more selective towards the diesel range.

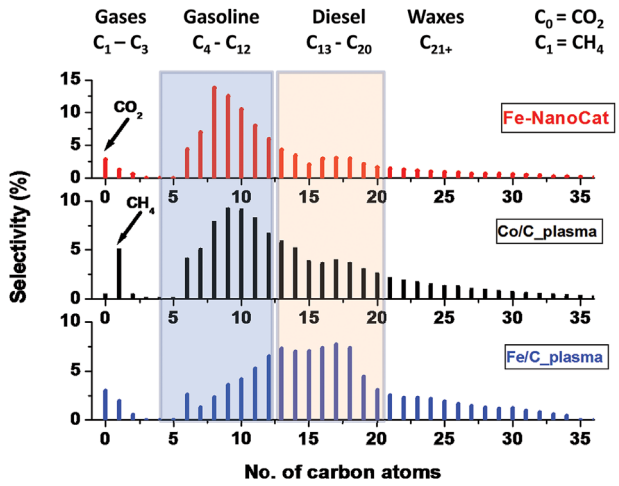

Figure 5. Full spectrum selectivity plots (combining gas and liquid fractions) for catalysts reduced at 673 K (400 °C) for 24 h, and tested at 493 K (220 °C), under a pressure of 2000 kPa, for 24 h at various CO conversions (x): Fe/C (x = 12 %); Fe-NanoCat® (x = 32 %); and Co/C (x = 45 %).

Integrating data from both gas-phase and liquid-phase analyses, the combined selectivity results for the three catalysts are presented in Table A1 of the supporting information. In graphical format in Figure 6, it separates the gases, and lumps together the gasoline and diesel fractions independently, for catalysts reduced at 673 K (400 °C) for 24 h, and then tested at 493 K (220 °C), 2000 kPa, for 24 h at various CO conversions (x): Fe/C (x = 12 %); Fe-NanoCat® (x = 32 %); and Co/C (x = 45 %).

It was observed that overall, the plasma-synthesized Fe/C sample was more selective toward the formation of the diesel fraction (51 %), followed by Co/C (31 %), and then Fe-NanoCat® catalyst (23 %) (Figure 6a). In contrast, Figure 6b shows that the commercial Fe-NanoCat® catalyst produced the richest gasoline fraction (62 %), followed by Co/C (50 %), and then Fe/C (26 %). In fact, all three catalysts showed that they had equal capacity to form the normal diesel fraction (C_8-C_{21}), with a constant selectivity approaching 75 %. Nevertheless, as per our definition, diesel fraction was taken as C_{13}-C_{20} for easy mass balance, where overlaps of hydrocarbon fractions were avoided. It is important to note that the full mass balance of the waxes is not shown in these plots; only the soluble waxes were analyzed by the liquid GC, while the insoluble waxes (Figure 3) still remain unaccounted for.

Production of the diesel fraction decreases in the order of Fe/C ≫ Co/C>Fe-NanoCat® (Figure 6b). The Co/C catalyst had a higher selectivity toward methane formation than the Fe-based catalysts.

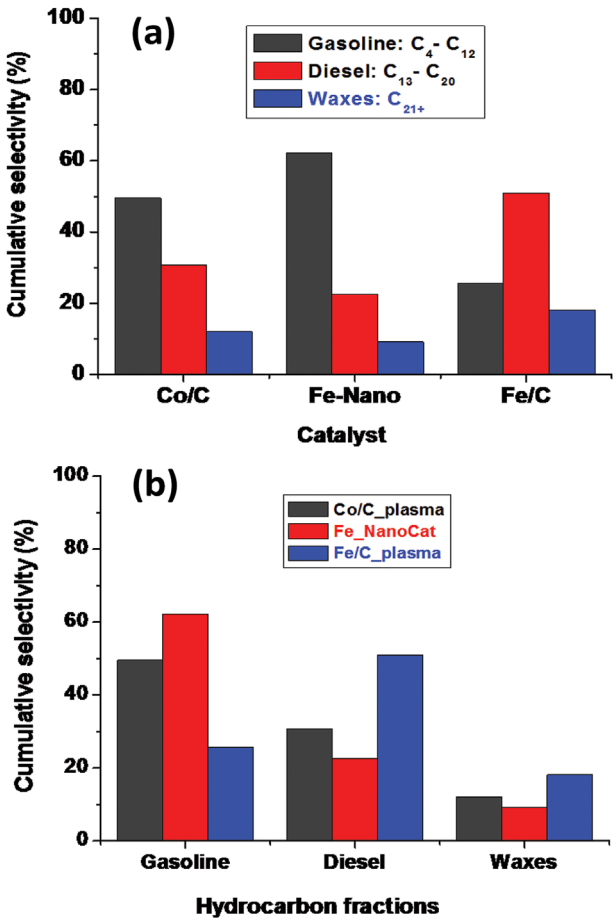

Figure 6. Accumulated selectivity (a) per catalyst and (b) by hydrocarbon fractions, at various CO conversions (x): Fe/C (x = 12 %); Fe-NanoCat® (x = 32 %); and Co/C (x = 45 %); for catalysts reduced at 673 K (400 °C) for 24 h and tested at 493 K (220 °C).

However, the Fe-based catalysts produced more CO_2 than the Co/C catalyst, probably because of their capability to catalyze the water-gas shift reaction given by Equation (3), which may be beneficial in restoring H_2 back into the FTS system.

Catalyst Characterization

Thermogravimetric analysis (TGA)

Samples were heated to 1273 K in Ar to drive off volatile organic compounds, cooled to ambient temperature, and then reheated in air using the same program. The atomic mass loading of the metals onto the C support in the fresh plasma-synthesized catalysts was found to be ~0.25 g/g (25 wt%) in Fe/C or Co/C. The TGA plots and tabulated calculations are displayed in Figure S2 and Table A2, respectively (provided in the supporting information).

BET surface area analysis

The plasma-synthesized Co/C and Fe/C catalysts tested in this work originated from the auxiliary reactor and their BET specific surface areas were 56 and 75 $m^2 \cdot g^{-1}$ respectively. Normally, high surface areas are desirable in catalysts in order to enhance metal nanoparticle dispersion. According to the behaviour of the isotherms given in Figure 7a, these materials are typical of type II isotherms and may be classified as largely tending towards non-porosity. This is because their adsorption and desorption isotherms were almost superimposable and presented no significant hysteresis loop.

Although the pore distribution plots portrayed in Figure 7b indicated pore sizes of < 10 nm, which revealed some degree of microporosity, it would be expected that microporous materials should display both greater hysteresis and a sharp rise in the plot at the lower pressures, thereby exhibiting type I isotherms. Nevertheless, earlier studies of our catalysts have pointed to the fact that the perceived micro-porosity is an artificial phenomenon arising from

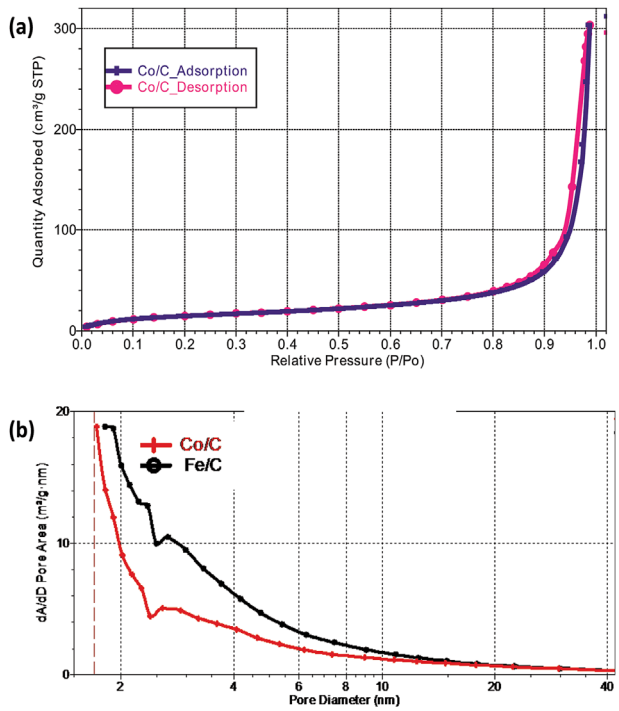

Figure 7. Sample plots for: (a) BET isotherm showing limited hysteresis as a sign of non-porosity, and (b) pore size distribution by pore area.

the physical packing of the nanoparticles.[2] Figure S3 in the supporting information clarifies this impression.

Given that FTS is a multi-dimensional reaction involving multifaceted kinetics, with the movement of reactants and products of the reaction prevailing in various phases (solid, liquid, and gas) through a complex network of pores in the catalyst, highly micro-porous catalysts are undesirable in FTS, considering that the hydrocarbons so formed must diffuse out of the catalyst before a buildup of molecules with higher molecular masses such as waxes clog the pores. It is noted that in light of mass transport requirements, catalyst porosity influences diffusion, and is characterized by what is regarded as the effective diffusivity, D_e (in $m^2 \cdot s^{-1}$), given by Equation (5):[15]

$$D_e = \frac{D.\phi_p.\sigma_c}{\tau} \tag{5}$$

where $\boldsymbol{D}$ = diffusion coefficient in gas or liquid filling the pores ($m^2 \cdot s^{-1}$),

$$\boldsymbol{\phi_p} = pellet\ porosity = \frac{void\ space\ volume}{total\ volume(solid + voids)}$$

$$\boldsymbol{\sigma_c} = constriction\ factor\ for\ variation\ in\ cross\text{-}sectional\ area$$

$$\boldsymbol{\tau} = tortuosity = \frac{Distance\ a\ molecule\ travels\ between\ two\ points}{Shortest\ distance\ between\ the\ two\ points}$$

The existence of constrictions in porous materials, the 'hindrance factor,' determines how fast the molecules navigate through the pores, and porosity will in turn influence the tortuosity, or the rate at which the reactants as well as the products enter or leave the catalyst pellet. Tortuosity then is a function of pellet particle size, whereby large or highly porous pellets result in the molecules taking extended periods of time to diffuse out. In addition, since our reaction products are polymeric in nature, high residence times in a porous catalyst material would lead to the formation of larger molecules such as waxes, and this in turn results in the entrapment and subsequent blockage of the pores, thereby causing catalyst deactivation. On the contrary, since our catalysts have no internal porosity, they are ideal materials for such a polymerization reaction as LT-FTS.

Scanning electron microscopy (SEM)

In this work, fresh plasma-synthesized catalysts characterized by SEM in conjunction with EDX indicated no obvious signs of bulk metal segregation. Both spot and area analysis showed uniform dispersion of the nanoparticles in the carbon matrix, as shown in Figure 8 for Co/C and Figure 9 for Fe/C catalysts, with semi-quantitative EDX analysis indicating that both the catalysts had metal mass loadings ranging from 0.2–0.3 g/g (20–30 %) on the C support.

Transmission electron microscopy (TEM)

Fresh and used catalysts were analyzed by TEM imaging for particle size distribution and Figure 10 depicts images of the commercial Fe-NanoCat® materials, with an obvious transformation in catalyst morphology, indicated by particle growth after reaction, from an average of 4 nm in the fresh hematite, seen in Figure 10a, to a wide particle size distribution ranging from 4–60 nm in the used catalyst. The solid boulder-like features in the used Fe-NanoCat® catalysts presented in Figure 10b have the

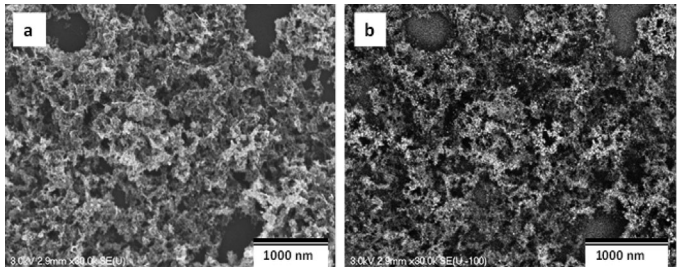

Figure 8. SEM images of the fresh plasma-synthesized Co/C catalyst from the auxiliary reactor by: (a) secondary imaging, and (b) backscattered imaging.

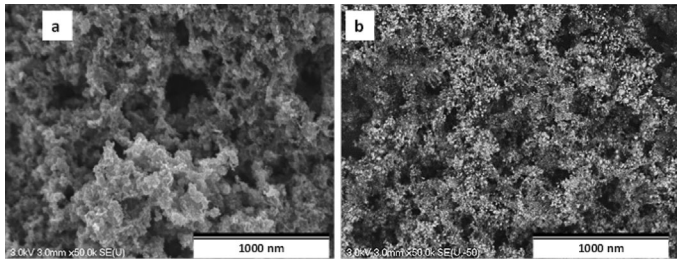

Figure 9. SEM images of the fresh plasma-synthesized Fe/C catalyst from the auxiliary reactor by: (a) secondary imaging, and (b) backscattered imaging.

typical morphology of magnetite,[16] most of which were not encapsulated by the carbon. At least 420 particles were measured in the used catalyst, and their size distribution is plotted in Figure 10c. In the used Fe-NanoCat® sample, the nanoparticle labelled (1b) may be an encapsulated metal or encapsulated oxide or even metal core-oxide shell encapsulated with carbon since we can actually observe a double shell on that nanoparticle.

For the plasma-synthesized samples (Fe/C and Co/C, Figures 11 and 12 respectively), at least 750 particles were measured for each fresh and used catalyst. There was a noticeable display of the catalysts' morphological stability in the samples before and after reaction since very limited variations in their particle size were observed (see particle size distribution plots).

X-ray diffraction analysis

In the XRD studies, Rietveld quantitative analysis (RQA) was used in an attempt to quantify the species in the fresh catalyst materials. Figures 13 and 14, respectively, represent the XRD patterns of the fresh plasma-synthesized Co/C and Fe/C catalysts with the RQA curve fitting. A database search showed that the two catalysts contained both amorphous and graphitic carbon as well as both metallic and metal-carbide species. The results are summarized in Table 2. Comparatively, the Fe catalyst had significant amounts of carbides (Fe_3C) indicated by the major peak at the 45° (2θ) angle. The curves' goodness of fit (GOF) with the High Score Plus software was ~1.6, rendering our analysis objectively acceptable. Ideally GOF should be 1, but a value of 2 is still tolerable.[17] We take this view because there was a considerable amount of unquantifiable amorphous material, which we believe made quantification difficult. In addition, since nanometric metallic particles lead to peak broadening and subsequent peak extinction, it complicates the analytical problem.

The estimated standard deviation (ESD), which reflects the precision of the refined parameters, is bracketed in Table 2 and

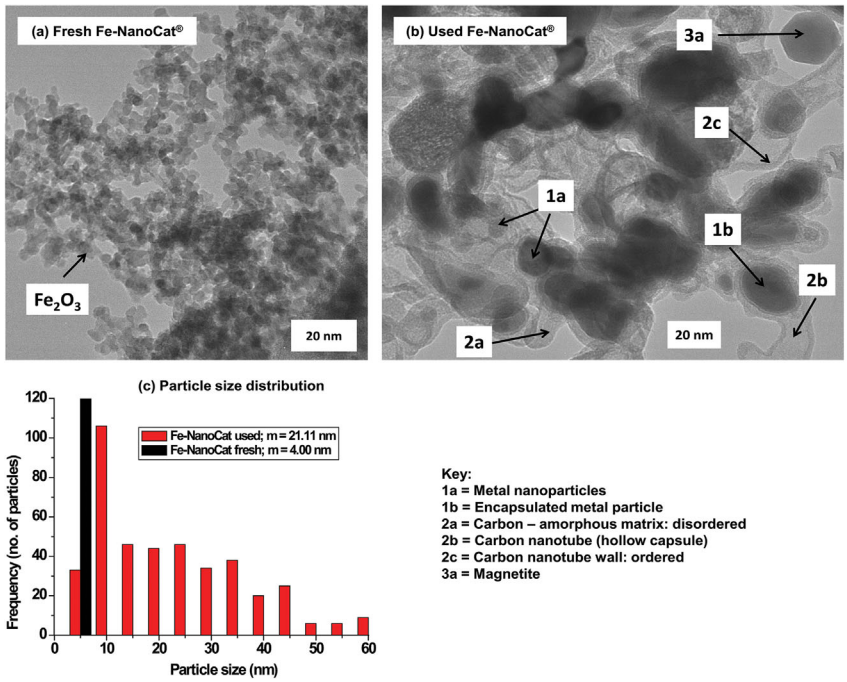

Figure 10. TEM images of the commercial Fe-NanoCat® catalyst before and after FTS.

should tend to 0. In our case it was mostly 1, but the highest ESD was 3. RQA was used despite the low signal-to-noise ratio associated with the small crystallites in our samples. Even if statistical parameters such as χ^2, GOF, or R_{wp} are deemed acceptable, ESD may overestimate the precision of the results. In fact, it has been shown that while smaller error index values designate a more suitable model fit to the data, improper models with poor quality data may exhibit smaller error index values than some superb models with very high quality data.[18] Nevertheless, the presence of carbides and metals is certainly consistent with the synthesis pathway of these materials.

The XRD patterns of the fresh and used catalysts are shown in Figure 15, Co/C in (a) and Fe/C in (b). The diffractogram of the used commercial Fe-NanoCat® also appears in Figure 15b for comparison. Evidence from RQA showed that the fresh Co/C catalyst comprised metallic cobalt (~39 % Co^o) in a face-centred cubic (FCC) structure, while the sample collected following FTS reaction exhibited a large fraction of amorphous carbon observed

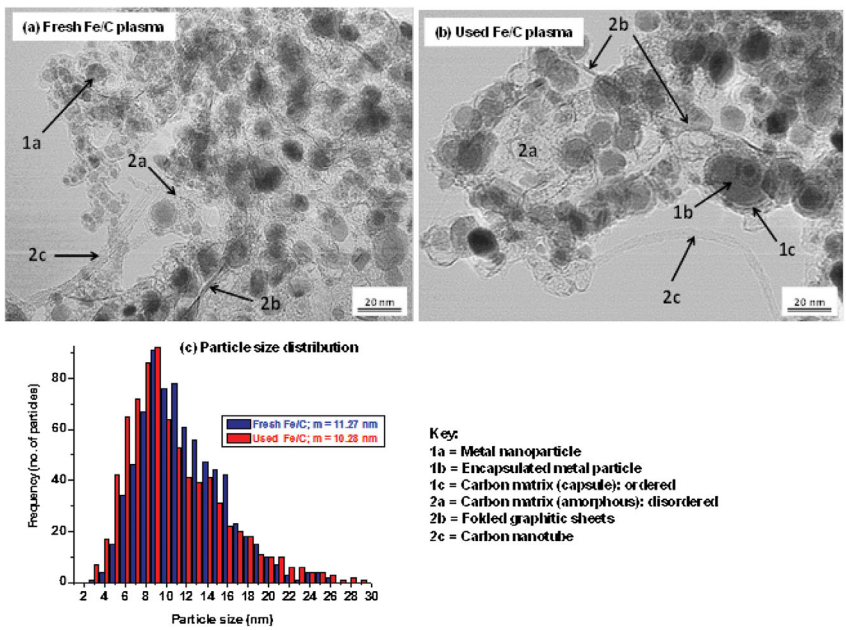

Figure 11. TEM images of the plasma-synthesized Fe/C catalyst before and after FTS.

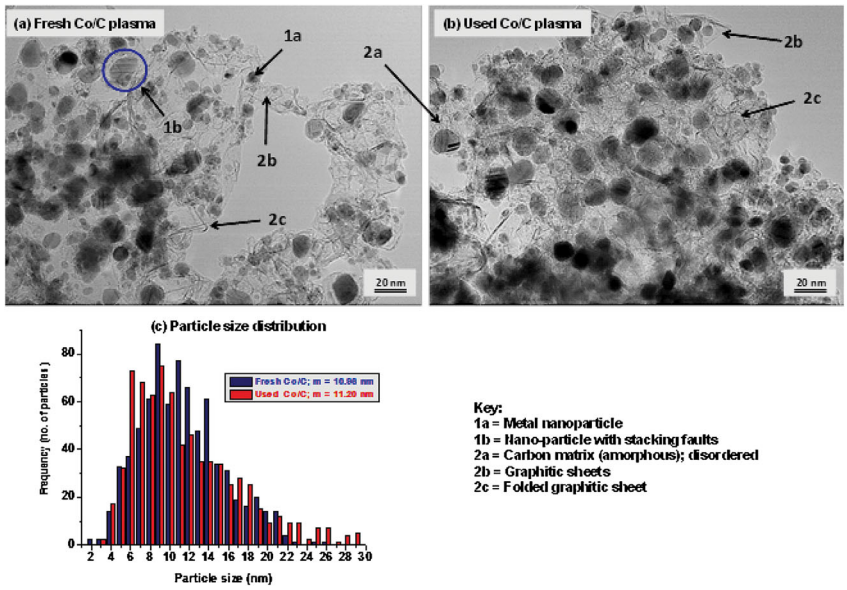

Figure 12. TEM images of the plasma-synthesized Co/C catalyst before and after FTS.

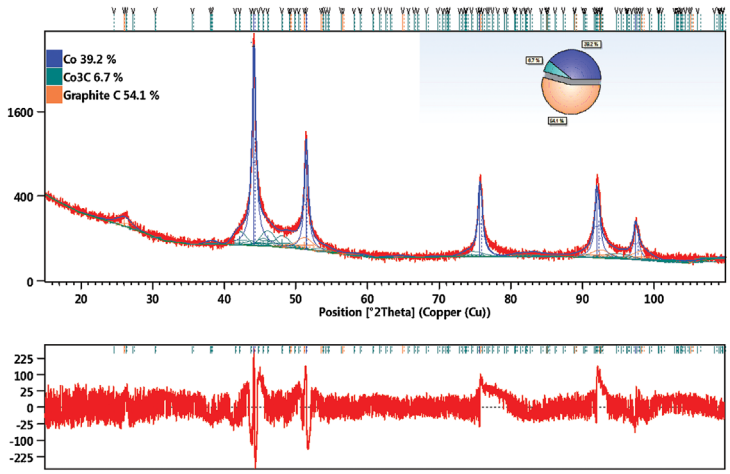

Figure 13. XRD spectra of fresh Co/C catalyst by Rietveld quantitative analysis.

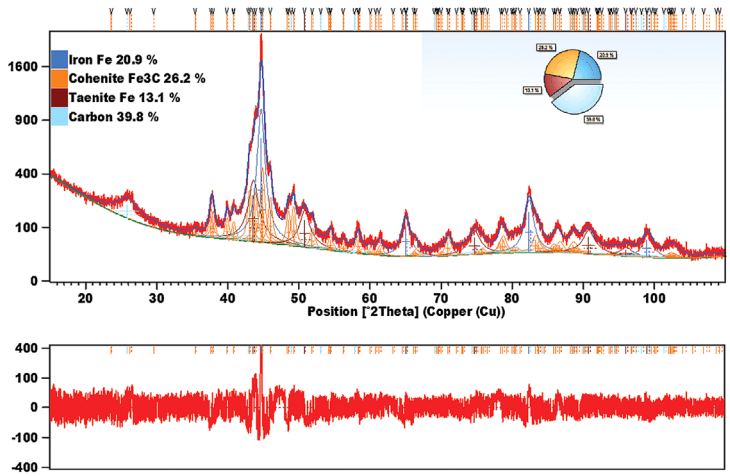

Figure 14. XRD spectra of fresh Fe/C catalyst by Rietveld quantitative analysis.

Table 2. Quantitative analysis of the fresh catalysts

Quantities by RQA, % (ESD)	Metal (Co^o, Fe^o)	Carbides (Co_3C, Fe_3C)	Carbon: Graphite	Carbon: Amorphous
Co/C	39.2 (2)[#]	6.7 (1)	54.1 (1)	unquantifiable
Fe/C	34.0 (3)[*]	26.0 (1)	40.0 (3)	unquantifiable
Quality of refinement	R_{exp}	$R_{profile}$	R_{wp}	GOF
Co/C	8.31	7.97	10.50	1.60
Fe/C	8.31	7.97	10.50	1.59

Co^o = [#]Metallic cobalt: face-centered cubic (FCC) structure
Fe^o = [*]Mixture: taenite = 13.1 % (3); metallic iron 20.9 % (3): cubic (FCC)
ESD = estimated standard deviation (bracketed values)
$R_{profile}$ = quantity being minimized during fitting procedures (by least-squares)
R_{exp} = expected R or the "best possible R_{wp}" factor
R_{wp} = weighted profile (R-factor) – weighted to emphasize peak intensity over background
GOF = Goodness of fit $(\chi^2) = (R_{wp}/R_{exp})^2$ should approach unity

from the broad peaks at 2θ angles below 30°, rendering quantification difficult. Due to their pyrophoric nature, the used samples were analyzed in their slurry form directly from the FTS reactor, hence the source of this amorphicity arising from the presence of the hexadecane solvent.

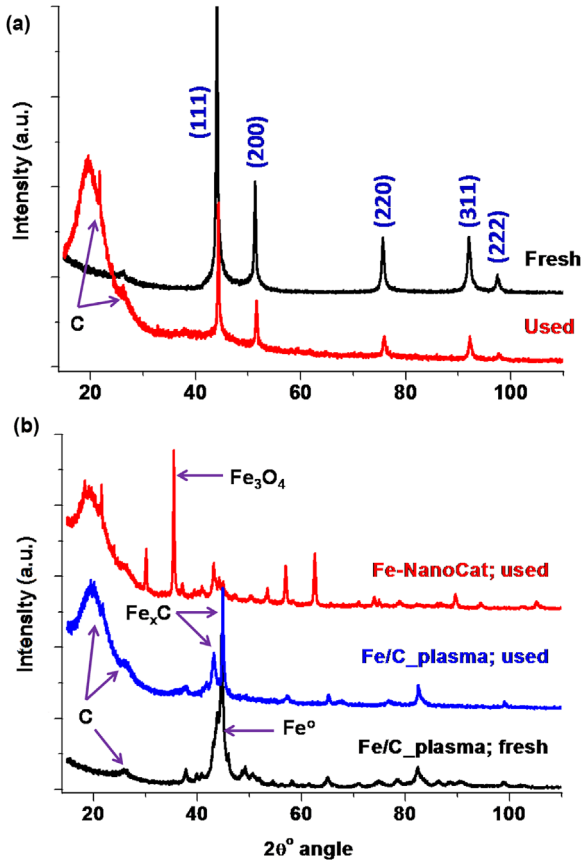

Figure 15. XRD spectra of the fresh and used: (a) cobalt and (b) iron catalysts.

Nonetheless, the original Co^o, Co_3C, and $C_{graphite}$ species could still be identified in the used sample. Before reaction, the fresh commercial Fe-NanoCat® was composed of pure hematite (Fe_2O_3) only, but after use, Fe_3O_4 (hexagonal structure) was the predominant phase. Other species observed in the used Fe-NanoCat® sample were: amorphous and graphitic carbon, Fe^o, FeO, Fe_5C_2, and minute quantities of Fe_7C_3. No Fe_2O_3 was detected. The fresh plasma-synthesized Fe/C catalyst consisted initially of metallic Fe^o (cubic, FCC structure) and Fe_3C (cohenite), supported in a mixed carbon matrix (graphitic and amorphous), while in the used sample, possible phases recognized were Fe^o (FCC), Fe_2C, and ε-Fe_3C. Figure S4 in the supporting information compares these spectra and the XRD patterns of standard materials as found in the database. Although expected, there was almost no evidence for the presence of Fe_3O_4 or Fe_2O_3, probably due to their low concentrations in the used samples, or that they were camouflaged in the diffractogram by the higher signal-to-noise ratio associated with the liquid matrix of the hexadecane solvent in the slurry.

DISCUSSION

Mass Transfer with Plasma-Synthesized Catalysts

In FTS, low temperatures of ~473 K favour the formation of longer carbon chains, while mid-range temperatures such as 573 K produce shorter carbon chains, but above 673 K, selectivity toward mainly CO_2 and CH_4 is promoted. Firstly, increasing temperature lowers (exothermic) gas adsorption rates, in addition to higher temperatures increasing the thermal cracking rate of the longer carbon chains into shorter ones. Therefore, operating optimally at lower temperatures (~473 K) provides just enough activation energy to support the reaction. In our 3ϕ-BG-CSTSR, mixing takes into consideration factors such as the fluid density, viscosity, and critical stirrer rotational speed, beyond which one cannot economically justify the corresponding energy consumption.[19] In our system, proper mixing in the turbulent regime was observed with high gas flow rates (300 $mL \cdot min^{-1}$), the introduction of the feed gas being set at the bottom of the reactor, high stirring rates set at ~2000 rpm to enhance both heat and mass transfer, high catalyst particle dispersion, and uniform catalyst distribution in the reactor, ensuring that the reaction rate was not diffusion-limited. Furthermore, viscosity and fluid density were kept low by using more solvent (150 mL) and less solid catalyst (5.0 g), because too much solid catalyst causes particle attrition and high energy demand during mixing. In commercial versions of the technology, stirring would ideally be replaced by an optimized bubble-column operation.

Clogging of the pores due to product entrapment fundamentally deactivates the catalyst as the micro-pores limit the movement of large molecules from the interior of the catalyst. Therefore, an effective FTS catalyst should comprise small metal particles, preferably in the nanometric range, and be non-porous in nature in order to enhance both heat and mass transfer, a description that fits our plasma-synthesized catalysts. An added advantage of using our nanometric and non-porous catalysts is that it circumvents susceptibility to temperature and gas concentration gradients, which normally occur in large-sized pellet catalysts. Although small catalyst particles could produce characteristically smaller carbon-content fractions, this provides us with the flexibility to alter the residence time in the reactor and enhance the production of the heavier carbon fractions.

Quick adsorption of reactants onto the metal nanoparticles, followed by fast desorption of the products from the catalyst

surface, is desired if FTS targets the relatively low MW area defined by C_5-C_{20} carbon chains. In some studies involving large metal particles or catalysts that are highly micro-porous, it was observed that only the smaller molecules are detected in the product stream due to the entrapment of the high carbon fractions (C_{30+}) in the pores.[20] The authors did not witness significant amounts of *n*-paraffins with more than 35 carbon atoms, probably due to space limitations inside the catalyst pores. Moreover, in the slurry FTS reactor, the chief cause of retardation in the reaction rates is the restricted mobility of the reactant molecules (CO and H_2) into the liquid-filled catalyst pores, arising from the liquid phase or the heavier hydrocarbons produced during FTS.[21] Syngas conversion decreases considerably when the average particle size is increased,[22] pointing to the importance of mass transport effects within the pellet. Since FTS produces polymeric products, highly porous catalytic materials impede the reaction due to diffusion limitations. Our catalysts, being both nanometric and non-porous, operate away from the diffusion-limited regimes, while the low-T operation also diminishes the possibility of metal-phase sintering.

Catalyst Composition Analysis

During catalyst synthesis, Fe carbides, particularly cementite (Fe_3C), are formed at temperatures > 1373 K, being stable at room temperature, but may decompose into graphitic carbon and austenite (FCC structure) below 1373 K, or into body-centred cubic (BCC) α-Fe below 973 K.[23] Our freshly prepared Co/C and Fe/C catalysts by plasma were spherical core-shell metal nanostructures with a mean particle size of $\sim$11 nm, apparently encapsulated by several layers of graphitic and amorphous carbon. The RQA application of XRD analysis showed that the plasma-synthesized Co/C sample comprised 0.54 g/g (54 mass%) graphitic carbon, 0.39 g/g (39 mass%) metallic Co, 0.07 g/g (7 mass%) Co carbides (Co_3C), and some unquantifiable amorphous carbon, but no Co oxides were identified. In the TEM images, stacking faults were recognized in Co-containing samples, probably existing as residuals from the initial Co metal that had a mixture of both hexagonal closed packing (HCP) structure ($\sim$38 %), and FCC structure ($\sim$62 %), both of which were evident from the XRD analysis of the original metal.[2] After catalyst synthesis by plasma, all the HCP crystallite forms were transformed into the FCC structure.

Particle size distribution by TEM analysis showed restrained particle growth in the plasma-synthesized Co/C and Fe/C samples even after 48 h on stream; that is, with 24 h reduction at 673 K, and 24 h FTS reaction at 493 K; this implies that plasma-synthesized catalysts inhibit sintering, since the metal nanoparticles do not seem to interact. Although it is well-known that the melting point of a substance decreases with decreasing particle size, under our high-pressure and LT-FTS conditions, the temperatures are not high enough to promote melting, vaporization, or local diffusion of the nanoparticles. Therefore, using graphite and amorphous carbon capsules as a support creates a rigid frame where the nanoparticles are immobilized. This steric barrier prevents close metal particle interaction, thereby forestalling both surface diffusion and lattice diffusion. In addition, the fast movement ($\sim$2000 rpm) of the catalyst nanoparticles in the reactor minimizes particle interaction, which is critical in sintering.

Catalyst Performance in FTS Reaction

In this study, we investigated catalysts that can find application effectively at $\sim$493 K (220 °C) in the LT-FTS operation, targeting the production of gasoline or diesel fuel. In the pretreatment, the carbon shell around the core metal nanoparticles in the plasma-synthesized Co/C or Fe/C catalysts was removed through reduction in a H_2 gas stream to activate the catalysts for FTS reaction. Reduction releases gaseous products such as CO_2, CH_4, and other hydrocarbons, which facilitate easy separation from the FTS system. There are two benefits of using the plasma technique in our catalyst preparation:

(i) Since the metal nanoparticles deposited on nanometric carbon have the potential to be pyrophoric, the graphitic encapsulation of the metals in the carbon matrix protects the catalysts from catching fire and therefore makes them safe for storage.
(ii) Plasma leads to direct production of the carbide phases, which are deemed to be active in Fe-catalyzed FTS, and losing them during the reduction phase means losing that advantage.

While benchmarking with the fresh commercial Fe-NanoCat® (Fe_2O_3), the catalyst was activated by carburization according to Equation (6), using CO to generate the much-needed Fe carbides in the FTS process.[24]

$$Fe_2O_3 \rightarrow Fe_3O_4 \rightarrow Fe_xC_y \tag{6}$$

Some studies on C-supported Fe catalysts have shown that partially-reduced Fe oxide influences both catalyst activity and selectivity. Reduction of fresh Fe_3O_4 leads to the formation of non-stoichiometric Fe-oxide-carbide species in the catalyst, which is less stable, but more active and more selective toward the formation of olefins than the known χ-Fe_5C_2 carbide.[25] This implies that total reduction of the catalyst to metallic state, or formation of pure Fe carbides, may not be beneficial to the reaction. It has been observed that the development and composition of these Fe phases depends on the process conditions, catalyst deactivation, and catalyst composition.[26] A correlation between FTS reaction rates and Fe carbide concentration has been observed. The unexpected re-oxidation of the catalysts as CO conversion decreased has suggested that deactivation of Fe catalysts in FTS reactions is due, at least partially, to the conversion of Fe carbides to Fe_3O_4. It appears that the CO activation steps, which are responsible for replenishing carbidic surface species and for removing chemisorbed oxygen, are selectively inhibited by deactivation of surface sites, leading to the oxidation of Fe carbide even in the presence of a remarkably reducing reactant mixture. Where some Fe carbide species were responsible for Fischer-Tropsch activity, oxidation of the Fe carbide to Fe oxide led to catalyst deactivation.[27]

Authors have agreed almost unanimously that the active species in the Co catalysts are in metallic form, with the HCP crystal structure demonstrating greater intrinsic activity than the FCC structure.[28] In addition, particle size effects arising from crystallite size influence FTS activity,[29] and our plasma-synthesized Co/C, which was substantially more active than the Fe/C, had an average particle size of 12 nm. Since loss of activity is always attributed to the re-oxidation of Co to its oxides,[28] or sintering,[29] the deactivation observed in our Co/C system was due to excessive water formation. This was confirmed by the short-lived improvement observed in catalyst performance at the removal of water at various intervals before activity dropped again.

In the Fe-catalyzed FTS, controversy still exists over the real active species due to the high number of phases formed in the system and isolation of the active species being practically difficult. Nevertheless, total reduction of the catalyst to metallic state as in Co catalysts, or to pure iron carbides, is certainly not

Table 3. Summary of the catalyst characteristics used in FTS

Properties	Catalyst		
	Co/C	Fe/C	Fe-NanoCat®
Elemental analysis: Metal loading	25 %	25 %	–
BET surface area ($m^2 \cdot g^{-1}$)	55.8	74.8	–
Pore size/distribution (nm)	< 10	< 10	–
Particle size:			
fresh catalyst (nm)	11.0	11.3	4.0
used catalyst (nm)	11.2	10.3	21.1
Activity: CO conversion (%)*	45 %	25 %	32 %
Selectivity:			
(i) gasoline (C_4–C_{12})	49.5	25.6	62.2
(ii) diesel ($C_{13} - C_{20}$)	30.8	50.9	22.5
(iii) waxes, etc. (C_{21+})	12.0	18.1	9.1
Phases present in used catalysts:			
(i) metallic species	Co^o (fcc)	Fe^o (fcc)	–
(ii) oxides	–	–	FeO Fe_3O_4
(iii) carbides	Co_3C	Fe_2C ε-Fe_3C	Fe_3C Fe_5C_2 Fe_7C_3
(iv) carbon - ordered - disordered	$C_{graphite}$ $C_{amorphous}$	$C_{graphite}$ $C_{amorphous}$	$C_{graphite}$ $C_{amorphous}$

*Maximum CO conversion observed under our reaction conditions

beneficial.[25] This work confirms this phenomenon of under-treatment (at low temperature, for a limited time) and over-reduction (high temperature, for a long time), particularly with the Fe-based catalysts during activation. The Co/C catalyst, on the other hand, is less sensitive to the pretreatment procedure.

In our used plasma-synthesized Fe/C sample, we observed only two phases: the metallic structure, and Fe carbides. Similarly, in the commercial Fe-NanoCat® sample, we observed only two phases: Fe oxides and Fe carbides. It was therefore concluded that the metallic Fe^o in the plasma-synthesized Fe/C sample were spectator species, and may need activation through carburization (to form Fe carbides) during the optimization process. It is also known that Fe oxides on their own cannot catalyze FTS, an observation that strongly indicates that the perceived carbides in the samples were necessary for the reaction. XRD analysis showed the presence of oxidic species in the used catalysts, while TEM showed that even after reduction the used catalysts were still encapsulated in a much thinner carbon matrix, and with little change in their metal particle sizes. The thermodynamics of the two FTS systems show that, at equilibrium, the most stable forms of the catalysts will lead to deactivation of the catalysts as they form spinel oxides (Fe_3O_4 or Co_3O_4). The advantage of the plasma-synthesized samples is that they constrain deactivation arising from the re-oxidation of the metals to form Fe_3O_4 or Co_3O_4 since such species were not detectable in the used samples. Whereas Co_3C may not be useful to FTS, the disappearance of the Fe carbides would be detrimental to the reaction because Fe carbides are essential to the propagation of the FTS carbon-chain. Nevertheless, the gas feedstock can be established such that the ratio of H_2, CO, and CO_2 ensures that the metal oxides are converted back to the metal (Co^o) or Fe carbides in a way that regenerates the catalysts, because theoretically, if the syngas has a ratio of $[H_2:(2CO + 3CO_2)] \approx 1.05$, all of the H_2, CO, and CO_2 can be converted to FTS products.[30]

Both the Fe-only and Co-only catalysts show promise for this application, comparing favourably to the existing commercial Fe-NanoCat® material when tested under similar reaction conditions. A summary of the catalysts' properties is provided in Table 3. The plasma-synthesized catalysts have demonstrated an acceptable combined selectivity towards the formation of gasoline and diesel fractions (80 % for Co/C and 76 % for Fe/C), which compares well with the Fe-NanoCat® (85 %). The plasma-synthesized Co/C with a CO conversion of 45 % presented a much better performance than the commercial Fe-NanoCat® (with 32 %). These two were in fact more stable and less sensitive online than the plasma-synthesized Fe/C, which showed CO conversion of between 10–25 %, depending on the pre-treatment conditions such as temperature and duration.

CONCLUSIONS

Two nanometric catalysts supported on carbon (Co/C and Fe/C) were synthesized through plasma and tested for LT-FTS in a CSTSR. At steady state (presumably after 18 h on stream, at T = 493 K (220 °C), p = 2000 kPa, GHSV = 3600 $mL \cdot g_{cat}^{-1} \cdot h^{-1}$), the Co/C catalyst was observed to be comparatively more active and more stable online than the Fe/C catalyst. The Co/C catalyst also showed higher propensity to produce a full spectrum of products, including those with heavier molecular mass such as wax. Without any promoters, the catalysts were benchmarked against the commercially available Fe-NanoCat® catalyst, and the activity decreased in the order of Co/C ≫ Fe-NanoCat® > Fe/C with their respective CO conversions being 45 %, 32 %, and 25 %. This study confirmed that both the plasma-synthesized catalysts have potential for industrial applications since they were remarkably selective (∼80 %) towards the formation of both gasoline and diesel combined, competing favourably with the current commercial catalyst (with selectivity ∼85 %). Selectivity towards the production of the diesel fraction alone (C_{13}–C_{20}) decreased in the order of Fe/C ≫ Co/C > Fe-NanoCat® (with 51 %, 31 %, and 22 % respectively).

ACKNOWLEDGEMENTS

We thank the Canadian BiofuelNet National Centre of Excellence (NCE) for financial support; Jasmin Blanchard, Henri Gauvin, and Jacques Gagné for their technical expertise in the labs; and the CCM (Centre de Caractérisation des Matériaux, Université de Sherbrooke) staff for facilitating the characterization: Irène Kelsey Lévesque for BET surface area analysis, Carl St-Louis for thermogravimetric analysis, Charles Bertrand for microscopy (SEM & TEM), and Stéphane Gutierrez for XRD analysis.

NOMENCLATURE

A_i	relative area under peak for hydrocarbon with i carbon atoms (%)
ASAP	accelerated surface area porosimeter (Micromeritics unit)
bcc	body-centred cubic structure
BET	Brunauer-Emmett-Teller
C_4–C_{12}	gasoline fraction
C_{13}–C_{20}	diesel fraction
C_{16}	*n*-hexadecane
C_{21+}	high molecular hydrocarbons, such as waxes
$[—CH_2—]_n$	alkene polymers
C_nH_{2n+2}	alkanes
Co/C	cobalt catalyst supported on carbon
CSTR	continuously-stirred tank reactor

D	diffusion coefficient in pores ($m^2 \cdot s^{-1}$)
D_e	effective diffusivity ($m^2 \cdot s^{-1}$)
df	film thickness of GC column (μm)
EDX	energy dispersive X-ray spectroscopy
ESD	estimated standard deviation
EXAFS	extended X-ray absorption fine structure
FCC	face-centred cubic structure
Fe/C	iron catalyst supported on carbon
Fe-NanoCat®	commercial Fischer-Tropsch nano-hematite catalyst
FID	flame-ionization detector
FTS	Fischer-Tropsch synthesis
GC	gas chromatography
GHSV	gas hourly space velocity ($mL \cdot g_{cat}^{-1} \cdot h^{-1}$)
GOF	goodness of fit: $(\chi^2) = (R_{wp}/R_{exp})^2$
HCP	hexagonal closed packing
id	inner diameter of GC column (mm)
l	length (m)
LT-FTS	low-temperature Fischer-Tropsch synthesis
N2.5	gas purity for CO; two nines = 99.5 %
N4.5	gas purity for H_2 and Ar; four nines = 99.995 %
p	pressure (Pa)
R_{exp}	expected R or the "best possible R_{wp}" factor
RF	radio frequency (Hz)
$R_{profile}$	quantity being minimized during fitting procedures (by least-squares)
RQA	Rietveld quantitative analysis
R_{wp}	weighted profile (R-factor) ratio of peak intensity to background
p-XRD	powder X-ray diffraction
S	selectivity (%)
SEM	scanning electron microscopy
T	temperature (K)
TCD	thermal conductivity detector
TG-DTA	thermogravimetric-differential thermal analysis
TEM	transmission electron microscopy
TOS	time-on-stream
TPR/TPO	temperature-programmed reduction/oxidation
XPS	X-ray photoelectron spectroscopy
3φ-BG-CSTSR	three-phase bubbled-gas continuously-stirred tank slurry reactor
Vol.	volume (L)

Greek Letters

φ	phase (3-φ = 3 phase: gas, liquid, solid)
σ_c	constriction factor for variation in cross-sectional area
τ	tortuosity
χ^2	measure of a curve's goodness of fit
ϕ_p	pellet porosity

REFERENCES

[1] J. Blanchard, N. Abatzoglou, R. Eslahpazir-Esfandabadi, F. Gitzhofer, *Ind. Eng. Chem. Res*. **2010**, *49*, 6948.

[2] J. Aluha, P. Boahene, A. Dalai, Y. Hu, K. Bere, N. Braidy, N. Abatzoglou, *Ind. Eng. Chem. Res*. **2015**, *54*, 10661.

[3] A. E. Rutkovskii, L. R. Vishnyakov, A. A. Chekhovskii, N. I. Kirkun, *Powder Metall. Met. C+* **2000**, *39*, 207.

[4] C.-J. Liu, G. P. Vissokov, B. W. L. Jang, *Catal. Today* **2002**, *72*, 173.

[5] B. Ernst, S. Libs, P. Chaumette, A. Kiennemann, *Appl. Catal. A-Gen*. **1999**, *186*, 145.

[6] M. Voss, D. Borgmann, G. Wedler, *J. Catal*. **2002**, *212*, 10.

[7] T. Herranz, S. Rojas, F. J. Pérez-Alonso, M. Ojeda, P. Terreros, J. L. G. Fierro, *J. Catal*. **2006**, *243*, 199.

[8] M. Bahgat, *J. Mater. Sci. Technol*. **2006**, *22*, 423.

[9] M. P. M. Ebert, *Process synthesis and design of low temperature Fischer-Tropsch crude production from biomass derived syngas*, MSc thesis, Chalmers University of Technology, Göteborg **2013**, p. 23.

[10] T. G. Kreutz, E. D. Larson, G. Liu, R. H. Williams, "Fischer-Tropsch Fuels from Coal and Biomass," *25th Annual International Pittsburgh Coal Conference*, Princeton University, Pittsburgh, 29 September−2 October **2008**.

[11] E. Iglesia, *Appl. Catal. A-Gen*. **1997**, *161*, 59.

[12] M. C. Bahome, L. L. Jewell, D. Hildebrandt, D. Glasser, N. J. Coville, *Appl. Catal. A-Gen*. **2005**, *287*, 60.

[13] C. T. Kniess, J. C. de Lima, P. B. Prates, "The quantification of crystalline phases in materials: Applications of Rietveld method," in *Sintering − Methods and Products*, D. V. Shatokha, Ed., InTech, Rijeka **2012**, p. 293–316.

[14] H. M. Rietveld, *J. Appl. Crystallogr*. **1969**, *2*, 65.

[15] H. S. Fogler, *Elements of chemical reaction engineering*, 4th edition, Pearson Education, Upper Saddle River **2006**.

[16] N. Braidy, C. Andrei, J. Blanchard, N. Abatzoglou, *Adv. Mater. Res*. **2011**, *324*, 197.

[17] L. B. McCusker, R. B. V. Dreele, D. E. Cox, D. Louër, P. Scardi, *J. Appl. Crystallogr*. **1999**, *32*, 36.

[18] B. H. Toby, *Powder Diffr*. **2006**, *21*, 67.

[19] J. Domínguez, A. M. Abreu, R. McCalla, J. Borroto, M. Ortueta, E. Pérez, *J. Radioanal. Nucl. Ch*. **1999**, *241*, 337.

[20] F. E. M. Farias, F. G. Sales, F. A. N. Fernandes, *J. Nat. Gas Chem*. **2008**, *17*, 175.

[21] O. O. James, B. Chowdhury, M. A. Mesubic, S. Maity, *RSC Advances* **2012**, *2*, 7347.

[22] M. F. M. Post, A. C. van't Hoog, J. K. Minderhoud, S. T. Sie, *AIChE J*. **1989**, *35*, 1107.

[23] T. G. Digges, S. J. Rosenberg, G. W. Geil, *Vol. Monograph 88*, US Department of Commerce, National Bureau of Standards, Washington DC **1966**.

[24] M. Ding, Y. Yang, B. Wu, Y. Li, T. Wang, L. Ma, *Energy Procedia* **2014**, *61*, 2267.

[25] J. F. Bengoa, A. M. Alvarez, M. V. Cagnoli, N. G. Gallegos, S. G. Marchetti, *Appl. Catal. A-Gen*. **2007**, *325*, 68.

[26] B. H. Davis, *Catal. Today* **2009**, *141*, 25.

[27] S. Li, R. J. O'Brien, G. D. Meitzner, H. Hamdehd, B. H. Davis, E. Iglesia, *Appl. Catal. A-Gen*. **2001**, *219*, 215.

[28] G. Jacobs, W. Ma, P. Gao, B. Todic, T. Bhatelia, D. B. Bukur, B. H. Davis, *Catal. Today* **2013**, *214*, 100.

[29] G. L. Bezemer, J. H. Bitter, H. P. C. E. Kuipers, H. Oosterbeek, J. E. Holewijn, X. Xu, F. Kapteijn, A. J. van Dillen, K. P. de Jong, *J. Am. Chem. Soc*. **2006**, *128*, 3956.

[30] M. E. Dry, *Catal. Today* **2002**, *71*, 227.

Manuscript received October 29, 2015; revised manuscript received November 24, 2015; accepted for publication November 25, 2015.

9.4. Appendix D: Article 4 – α-value determination of the Co/C catalyst

catalysts

MDPI

Communication

Effect of CO Concentration on the α-Value of Plasma-Synthesized Co/C Catalyst in Fischer-Tropsch Synthesis

James Aluha [1], Yongfeng Hu [2] and Nicolas Abatzoglou [1,*]

[1] Department of Chemical & Biotechnological Engineering, Université de Sherbrooke, Sherbrooke, QC J1K 2R1, Canada; james.aluha@usherbrooke.ca

[2] Canadian Light Source Inc., Saskatoon, SK S7N 2 V3, Canada; yongfeng.hu@lightsource.ca

* Correspondence: nicolas.abatzoglou@usherbrooke.ca; Tel.: +1-819-821-7904

Academic Editor: Leonarda F. Liotta

Received: 28 December 2016; Accepted: 13 February 2017; Published: 21 February 2017

Abstract: A plasma-synthesized cobalt catalyst supported on carbon (Co/C) was tested for Fischer-Tropsch synthesis (FTS) in a 3-phase continuously-stirred tank slurry reactor (3-ϕ-CSTSR) operated isothermally at 220 °C (493 K), and 2 MPa pressure. Initial syngas feed stream of H_2:CO ratio = 2 with molar composition of 0.6 L/L (60 vol %) H_2 and 0.3 L/L (30 vol %) CO, balanced in 0.1 L/L (10 vol %) Ar was used, flowing at hourly space velocity (GHSV) of 3600 $cm^3 \cdot h^{-1} \cdot g^{-1}$ of catalyst. Similarly, other syngas feed compositions of H_2:CO ratio = 1.5 and 1.0 were used. Results showed ~40% CO conversion with early catalyst selectivity inclined towards formation of gasoline (C_4–C_{12}) and diesel (C_{13}–C_{20}) fractions. With prolonged time-on-stream (TOS), catalyst selectivity escalated towards the heavier molecular-weight fractions such as waxes (C_{21+}). The catalyst's α-value, which signifies the probability of the hydrocarbon chain growth was empirically determined to be in the range of 0.85–0.87 (at H_2:CO ratio = 2), demonstrating prevalence of the hydrocarbon-chain propagation, with particular predisposition for wax production. The inhibiting CO effect towards FTS was noted at molar H_2:CO ratio of 1.0 and 1.5, giving only ~10% and ~20% CO conversion respectively, although with a high α-value of 0.93 in both cases, which showed predominant production of the heavier molecular weight fractions.

Keywords: alpha-value; cobalt-catalyst; plasma-synthesis; carbon; Fischer-Tropsch

1. Introduction

At present, South African Synthetic Oil Ltd., (SASOL) operates the world largest coal liquefaction plants and it produces synthetic fuels commercially through Fischer-Tropsch catalysis. Syngas, a mixture of carbon monoxide and hydrogen (CO + H_2) is polymerized to a myriad of hydrocarbon products with –CH_2– being considered as the basic monomer, as illustrated in sample Equation (1) by Thomas and Thomas [1] (p. 526). In addition to fuels and oils, Sasol produces locomotive and industrial lubricants, greases and solid waxes, cleansers and degreasing agents, besides a full spectrum of chemicals that include solvents, ammonia, mining reagents, explosives and polymers such as polyethylene, polypropylene and polyvinyl chloride.

$$n\,\mathbf{CO} + 2n\,\mathbf{H_2} \;\rightarrow\; -[\mathbf{CH_2}]_n - + n\,\mathbf{H_2O} \tag{1}$$

In the production of high molecular-weight hydrocarbons such as diesel and waxes, a Co-based catalyst is normally preferred. Although the catalyst exhibits high activity and long life in the low-temperature Fischer-Tropsch synthesis (LT-FTS) regime, exposure to high temperatures results

in carbon deposition on metal-oxide supports such as Al_2O_3, SiO_2 or TiO_2, which is detrimental to the catalyst's structural integrity [2]. However, there is a view that a carbon-supported catalyst may not be impacted in a similar way because of its resistance to both carbon fouling and carburization effects [3]. For this reason, we are advocating for the application of plasma-generated graphitic carbon as an effective FTS catalyst support in this study. Indeed some authors have observed the value carburization process can offer in catalyst regeneration. For example, Equation (2) shows a proposed mechanism of regenerating a Co-based FTS catalyst through carburization by initially forming the less active Co_2C phase, followed by reduction in H_2 [4].

$$\mathbf{CoO} \overset{\mathbf{CO}}{\rightarrow} \mathbf{Co_2C} \overset{\mathbf{H_2}}{\rightarrow} \mathbf{Co} \tag{2}$$

Moreover, the graphitic carbon-support structure has been noted to enhance catalyst selectivity towards high molecular weight fractions with more than five carbon atoms in the hydrocarbon chain (C_{5+}) by facilitating electron transfer between the Co metal and CO molecules during FTS [5]. It has been observed that certain desirable properties of the C support can easily be activated, enhanced or varied by functionalization using either basic or acidic media [6]. In fact, the very presence of carbon as a support does not seem to negatively influence the performance of the nanometric carbon-supported catalysts that were synthesized through plasma [7]. In the recent past, great interest has been stimulated in catalyst preparation by various plasma technologies because plasma produces materials that have improved LT-FTS activity, enhanced stability, and have better anti-carbon deposition performance [8]. In LT-FTS, a comparative study of identical single-metal Co/C catalysts produced by various methods showed that induction suspension plasma-spray (SPS) technology produces superior FTS catalysts [9].

Another approach that has been applied in FTS to improve selectivity towards the C_{5+} products is through CO-enriched syngas feeds, which lowers CH_4 formation [10]. Nevertheless, where gas composition has been used to determine the product spectrum, low CO conversions have prevailed, with an increased reaction rate being observed at higher H_2:CO ratios above 1.6, and this has an added advantage of using less catalyst quantities for the same feed conversion [2]. Since natural resources such as coal are finite, pursuit for alternative carbon sources and the use of CO-rich syngas of biomass origin is contemplated [11], and may present benefits that comprise sustainability through production of biomass-derived fuels. Interest in a Biomass to Liquid process via Fischer–Tropsch (BTL-FT) synthesis is growing steadily from both academia and industry because of its ability to produce carbon neutral and environmentally friendly clean fuels [12]. Commercial production of such fuels while simultaneously satisfying the increasing energy demand and meeting stringent environmental regulations is inevitable in the foreseeable future, particularly with the push towards sulphur-free diesel [13]. The world today is therefore bracing itself for compliance in automobile fuel production; to shift away from fossil fuels towards renewable sources of energy such as biomass.

A number of theories have been developed to elucidate the polymerization mechanisms that influence FTS product selectivity. In order to determine α, the probability of a catalyst being selective towards the formation of C_{5+} products, the Anderson-Schulz-Flory (ASF) distribution model shown in Equation (3) is normally applied [14]. The α-value is calculated from the gradient of the linearized expression in the plot of $\log(M_n/n)$ versus n, given as Equation (4) [15] (p. 403).

$$\frac{\boldsymbol{M_n}}{\boldsymbol{n}} = (\mathbf{1}-\boldsymbol{\alpha})^{\mathbf{2}} \cdot \boldsymbol{\alpha}^{(\boldsymbol{n}-\mathbf{1})} \tag{3}$$

$$\boldsymbol{ln\alpha} = \boldsymbol{nln\alpha} + \boldsymbol{ln}\left[\frac{(\mathbf{1}-\boldsymbol{\alpha})^{\mathbf{2}}}{\boldsymbol{\alpha}}\right] \tag{4}$$

where:

M_n = mole fraction of a hydrocarbon with chain length n
n = number of total carbon atoms

α = probability of chain growth ($\alpha < 1$)
$(1 - \alpha)$ = probability of chain termination

Although being more expensive than the Fe-based catalyst, the Co catalyst is preferred for the production of long-chain paraffins because of its high activity and low water-gas shift activity [16]. On one hand, strong interaction between the metallic phase and the support has been observed to improve catalytic activity [17], but on the other hand, it may be detrimental due to the formation of irreducible metal-support compounds such as cobalt aluminate or cobalt silicate by way of incorporating CoO into the Al_2O_3 or SiO_2 support respectively [18], thereby leading to catalyst deactivation. In addition, carburization of the Co catalyst may lead to deactivation since the cobalt carbide (Co_2C) formed is not a catalytically active material for FTS [4], though it has been observed to enhance the activity of the Fe-based catalyst [19]. Other causes of catalyst deactivation include coking, surface restructuring of the Co metal phase in syngas, and sintering of the Co nanoparticles [20]. Some authors have equally suggested that Co-metal re-oxidation may also lead to catalyst deactivation [21], although there are some disagreements based on particle size effects as shown by empirical data [22].

Nevertheless, one method that has been adopted in solving catalyst deactivation issues is by addition of promoters. For example, precious metals like Au [23], and Pt [24], or in some cases, Ru have been employed to create multi-component catalysts such as (Ru + Co + Mn/Zr/SiO_2) to enhance Co reducibility [25]. This alters catalyst activity and selectivity or the catalyst's preference for a specific reaction mechanism [26], although some elements acting as promoters have been observed to aggravate metal particle sintering of the metal nanoparticles [27]. Other complex catalyst formulations such as carbon-supported cobalt manganese oxide ($CoMnO_x$) catalysts [28], are currently being developed.

In this article, we limit our discussion to an approach that does not involve promoters because the single-metal Co/C catalyst is under scrutiny. Since one of the major causes of deactivation in Co-based catalysts is carbon deposition [29], in this project, a carbon support was envisaged for a permanent solution. Table 1 indicates a selected number of Co-based catalysts used in FTS reaction that were supported on various materials ranging from metal oxides to elemental carbon that has received considerable attention in the recent past. The Co metal may be added to the support using different approaches such as impregnation or precipitation, but currently the plasma technology is advancing, both in catalyst synthesis and activation. Although most researchers test the catalysts in the fixed-bed reactor with the H_2:CO ratio of ~2 at 220 °C and 2 MPa pressure, in this study the slurry reactor operating under similar reaction conditions has been chosen.

In our earlier work, catalyst activity was determined by real-time analysis of the unreacted CO in the reactor effluent-gas stream, from which CO conversion was calculated. However, one of the constraints of our earlier reactor set-up was that similar real-time liquid-phase analysis was not possible, since it required total cooling of the reactor preferably overnight in order to sample the slurry. In doing so, a lot of valuable information from the liquid-phase was inaccessible until after over 36 h from the commencement of the reaction. This necessitated for a modification of our reactor system, where we have devised a method of analyzing the liquid-phase in order to determine the composition of the heavier hydrocarbons (C_{5+}) in real time as the reaction progresses. Having a family of eight plasma-synthesized catalysts based on Co and Fe [30], the most active material at the lower temperatures of 160–220 °C was the single Co/C catalyst, which we have selected to use in this study.

Since the previous publication on the single-metal Co/C was centred on catalyst synthesis, characterization and benchmarking with the commercially available Fe-NanoCat® catalyst [7], one of the limitation in determining the true α-value of the catalyst was due to the reactor set-up. The plasma-synthesized Co/C was tested in a closed 3-ϕ-CSTSR for FTS. In the current reactor set up, the true α-value of the catalyst may be calculated because there is minimum time required to generate a reasonable amount of polymerization, which if not observed can lead to a wrong determination.

Table 1. Some Co catalysts that have been tested in typical FTS reaction conditions.

Catalyst	Catalyst			FTS Reaction						Reference
	Synthesis Method *	Support #	Metal Particle Size (nm) θ	Reactor	GHSV ($cm^3 \cdot g^{-1} \cdot h^{-1}$)	H_2:CO	Pressure (MPa)	Temp (°C)	% CO Conversion $	
Co/Al_2O_3	IWI	Al_2O_3	11–28	Fixed-bed	6100–9500	2.1	2	210	50	[31]
Co/C	IWI	CNTs	9–24	Fixed-bed	2000	2	2	270	90	[32]
Co/C	IWI	CNTs	4–20	Fixed-bed	3600	2	2	220	50	[33]
Co/C	DBD-plasma	CNTs	5–26	Fixed-bed	1800	2	2	230	95	[34]
Co/C	IWI, DP, IA	CNFBs	2.6–27	Plug-flow	-	2	3.5	210–250	60–80	[35]
Co/C	Induction SPS	Carbon	9–11	CSTR	3600	2	2	220	42	[7]
Co/SiC	IM	SiC	15–35	Fixed-bed	6000	2	2	220 250	25 92	[36]
Co/SiO_2	-	SiO_2	-	Fixed-bed	6000	1.9	1.5–2.5	230	42	[37,38]
Co/SiO_2	IWI, GD-plasma	SiO_2	5.8–10.2	Fixed-bed	1800	2	0.1	220	22	[39]
Co/TiO_2	DP, IWI	TiO_2	2–13	Fixed-bed	3450–5850	2	2	220	35	[40]

FTS = Fischer-Tropsch synthesis; GHSV = gas hourly space velocity; CSTR = continuously-stirred tank reactor. * CP = Co-precipitation; DP = Deposition-precipitation; IA = Ion adsorption; IM = Impregnation method; IWI = Incipient wetness impregnation; DBD = dielectric-barrier discharge plasma (*treatment*); GD = Glow discharge (*treatment*); SPS = suspension-plasma spray (*synthesis*); θ Mean metal particle size varies in the data depending on analytical technique applied (e.g., Transmission Electron Microscopic (TEM) imaging, X-ray Diffraction (XRD), Chemisorption); $ The highest CO conversion achieved is reported here; # CNT = Carbon nanotubes; CNFBs = Carbon nanofibres.

Therefore, the objectives of this work was: (i) to develop a safe sampling method of the slurry from the reactor, which was both hot and at high-pressure, without significantly interrupting the FTS reaction process or being exposed to the highly toxic CO; (ii) to illustrate hydrocarbon–chain propagation with TOS by providing empirical evidence for the gradual development of the longer-chain hydrocarbons using this novel sampling method; (iii) to determine the true α-value of the Co/C catalyst, while observing for the least time required for maximum possible polymerization to occur; and (iv) to investigate the effect of using CO-rich syngas feed stream on the LT-FTS product distribution, with a view that the current H_2-rich syngas derived from natural gas will eventually be replaced by the CO-rich biomass-derived syngas. In characterizing the materials' properties, we have motivated for the catalysts' potential suitability in FTS application since the materials have been found to be both nanometric and non-porous [30]. Therefore, in this paper, we report for the first time the effect of feed gas composition on the catalyst's α-value with TOS as projected from the FTS product distribution using the plasma-synthesized catalyst supported on carbon (Co/C).

2. Results

2.1. Catalyst Characterization

The catalyst under review has already been fully characterized by Brunauer-Emmett-Teller (BET) specific surface area analysis and porosity, Raman spectroscopy, Thermogravimetric analysis (TGA), X-ray diffraction (XRD) coupled with Rietveld quantitative analysis (RQA), and X-ray absorption near-edge structure (XANES) studies. In addition, the microscopic properties of the catalyst were revealed by Transmission electron microscopy (TEM) as well as with Scanning electron microscopy (SEM) coupled with the Energy dispersive X-ray spectroscopy (EDX). Since the details of this catalyst's properties are available in earlier work [7], the results are summarized here for the benefit of the reader.

2.1.1. BET Surface Area Analysis

The fresh Co-only (Co/C) catalyst was determined to be both nanometric and non-porous in nature, but with a high BET specific surface area of about 56 $m^2 \cdot g^{-1}$, pore diameter of about 28 nm and total pore volume of 0.39 $cm^3 \cdot g^{-1}$ as given in Table 2.

Table 2. Catalyst porosity analysis results by the BET method.

Property	Auxiliary Plasma Reactor *	Main Plasma Reactor *
BET surface area ($m^2 \cdot g^{-1}$)	55.5	54.4
Average pore diameter (nm) $^{\$}$	27.4	28.3
Total pore volume ($cm^3 \cdot g^{-1}$) $^{\#}$	0.38	0.39

BET = Brunauer-Emmett-Teller specific surface area analysis. * The plasma reactor design in catalyst synthesis comprises the auxiliary and main reactors, see Section 4.3.1. $^{\$}$ Single point adsorption total pore volume of pores less than 120 nm in diameter at $P/Po = 0.98$. $^{\#}$ Average pore diameter (4V/A by BET).

Figure 1a depicts the non-porous nature of the material from its adsorption-desorption isotherms and Figure 1b provides the basis of interpretation. A steep isotherm in the low pressure region below $P/Po = 0.30$ means that the sample is micro-porous (type I isotherm), but since our plot was almost flat in that portion (type II isotherm), it implied that the catalyst was not microporous. In addition, the lack of hysteresis in the desorption arm of the isotherm indicated that the sample was non-porous. Figure 1c shows the BET transform plot with a perfect linear fit on the adsorption isotherm, indicating the high reliability of the method. Normally, solid powder samples with particle diameter in the micrometer range have BET specific surface area of ~1 $m^2 \cdot g^{-1}$. However, when the powder particles are transformed into the nanometer range through plasma, their surface area significantly increases. For example, compact Co spheres of average diameter of 11 nm have a geometrically calculated

external specific surface of about 70 $m^2 \cdot g^{-1}$. Therefore, the measured BET surface area of 56 $m^2 \cdot g^{-1}$ is representative of the tested catalyst.

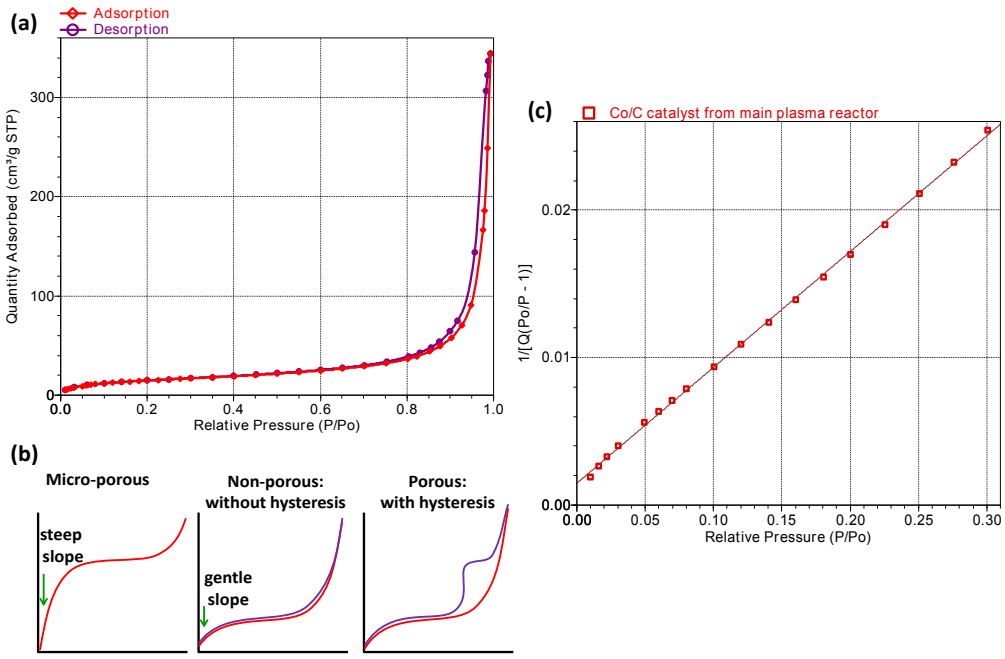

Figure 1. Porosity analysis of the fresh Co/C catalyst showing (**a**) overlaid adsorption-desorption isotherms; (**b**) cartoons with various impressions of isotherm interpretations; and (**c**) the BET transform plot.

2.1.2. Elemental Analysis

Due to the difficulties experienced in digesting the graphitic C-support for analysis by inductively-coupled plasma mass spectrometry (ICP-MS), TGA by carbon ignition was utilized, which revealed that the Co atomic-mass loading in the C matrix was approximately 0.25 g/g (25-wt. %) in the freshly synthesized catalysts through plasma.

2.1.3. Microscopy: Elemental and Particle Size Analysis

Semi-quantitative SEM analysis coupled with EDX facility showed a Co metal-loading between 20%–30% in the carbon support, as confirmed by TGA (25-wt. %). Metal nanoparticle-size analysis by TEM imaging manifested a mean size of about 11.0 nm (counting 750 particles) before and after the reaction [7], as portrayed in Figure 2. This observation alluded to the absence of nanoparticle agglomeration in the spent catalyst sample after a 24-h reduction at 400 °C followed by another 24 h of FTS reaction. Figure 3 provides the metal nanoparticle size distribution of 695 particles of the fresh catalyst by TEM analysis, which exhibits a near Gaussian-type distribution, with a standard deviation of 4.4.

2.1.4. XRD and RQA Analysis

XRD analysis revealed the presence of metallic and carbidic species in the catalyst. In order to maximize the catalytic activity measured by CO conversion during FTS, prior catalyst reduction is paramount because the active species in Co-containing samples are construed to be metallic (Co°) in nature. Some authors have asserted that the highest CO conversions in FTS are attributed to higher Co reducibility [33], while the oxidation of the Co metal leads to catalyst deactivation [21]. Figure 4 presents the XRD patterns of the fresh Co metal injected into the plasma, which comprised two phases as analysed by RQA: 62% having face centred cubic (FCC) structure, and 38% hexagonal closed packing

(HCP) structure [7]. After plasma synthesis, the Co moieties were perceived to be encapsulated in the carbon matrix and the metal contained only the FCC crystal structure, a phase that prevailed even after the FTS reaction. Since the Co/C catalyst is entirely nanometric, we are convinced that the material probably contains other phases that could be beyond the detection limits of the XRD instrument. However, in the absence of such evidence, we think that the FCC phase is the active form of this catalyst.

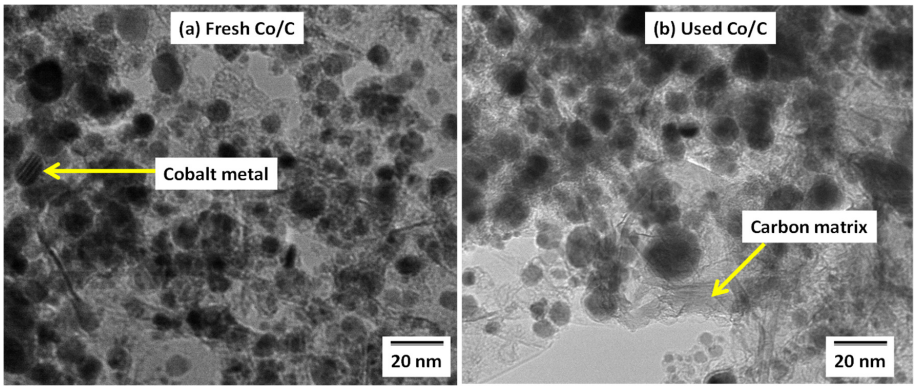

Figure 2. Transmission Electron Microscopic (TEM) images for the fresh and used plasma-synthesized Co/C samples.

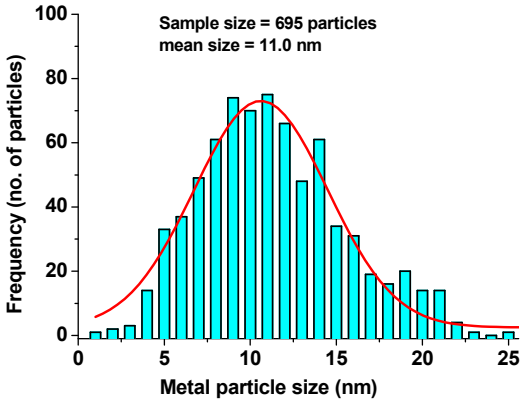

Figure 3. Normal metal particle-size distribution of the fresh Co/C catalyst by TEM analysis.

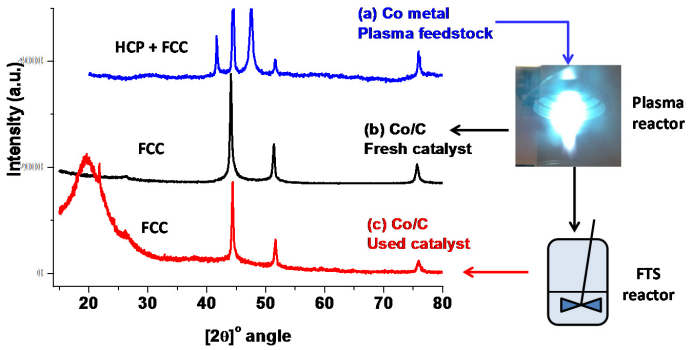

Figure 4. X-ray diffraction (XRD) patterns for the (**a**) Co metal; (**b**) freshly plasma-synthesized Co/C catalyst and (**c**) used sample.

2.1.5. XANES Analysis

Spectral analysis of the fresh and used catalysts by X-ray absorption near-edge structure (XANES) did not indicate any form of oxidation in the samples. However, when compared to the metal-Co standard, a shift of the edge peak in both the fresh and used Co/C catalysts was observed, particularly when the derivative plots were examined, as seen in Figure 5. The Co species in the catalysts seemed to have become 'more metallic' in the sense of its electron-donating capability and hence the edge shift to the lower energies of the spectrum [41]. This was perhaps due to the simultaneous presence of metallic and carbidic species in the Co/C catalyst samples, as discussed in an earlier article [9]. The carbidic species in the samples were only evidenced by the XRD data analysis through RQA modeling using the High Score Plus software [7]. XANES peak-edge shift to the right implies occurrence of Co oxidation and more often than not leads to catalyst deactivation, whereas peak-edge shift to the left as was observed here, in both the fresh and used samples has a connotation of preventing deactivation, which may prove to be advantageous to the longevity of the catalyst material.

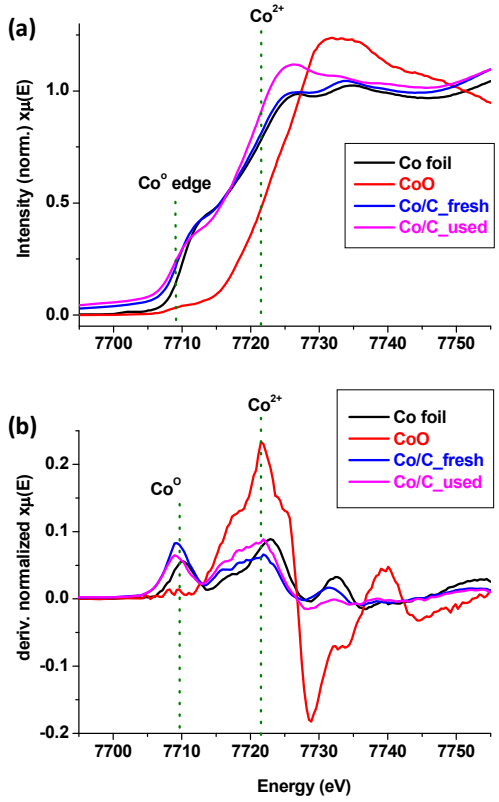

Figure 5. XANES spectra (**a**) normalized and (**b**) first derivative of the fresh and used Co/C samples compared with the Co^0 and CoO standards.

2.2. Catalyst Activity Testing

Figure 6 represents the catalytic activity at gas hourly space velocity (GHSV) of 3600 $cm^3 \cdot g^{-1} \cdot h^{-1}$ of catalyst, which presented between 38% and 43% CO conversion for the molar feed-gas ratio of H_2:CO = 2. This finding was consistent with our earlier work [7]. For the CO-rich feed gas of molar ratio of H_2:CO = 1.5 and 1.0, catalytic activity dropped to 20% and 10% CO conversion respectively.

2.3. Catalyst Selectivity

Since the modification on the FTS reactor system offered capacity to simultaneously perform both gas-phase and liquid-phase analysis, combining the results provided a full portrait of the FTS product-spectrum in real time. Figure 7 demonstrates the progressive polymerization occurring in the

liquid-phase with TOS. The slurry was sampled 5 times (after 2 h, 5 h, 8 h, 17 h and 19 h of FTS reaction). This procedure was repeated for another experiment, which produced similar results displaying the incremental change perceived in the liquid-phase of the FTS product distribution.

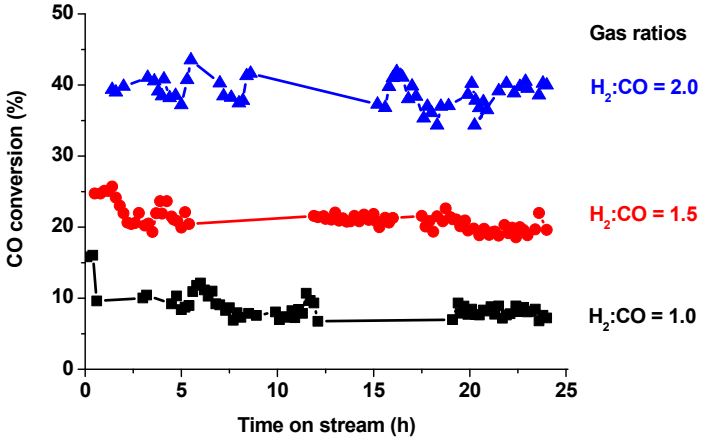

Figure 6. Plots showing the positive influence of H_2 on FTS reaction with TOS using the Co/C catalyst tested at 220 °C, 2 MPa and GHSV of 3600 $cm^3 \cdot g^{-1} \cdot h^{-1}$.

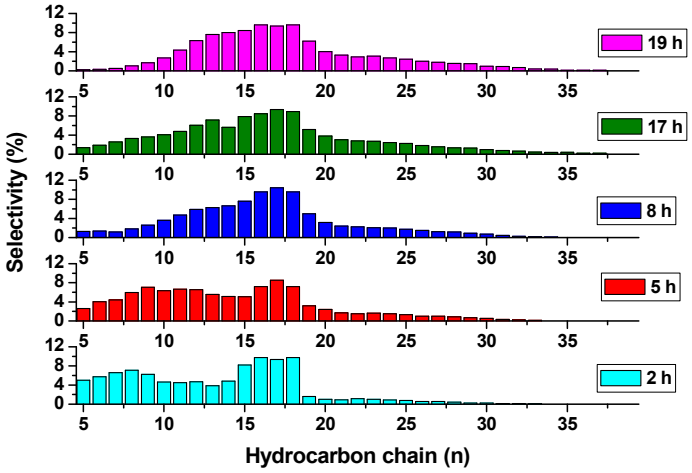

Figure 7. Catalyst selectivity from liquid-sample analysis at various TOS for reaction performed at 220 °C, 2 MPa and GHSV of 3600 $cm^3 \cdot g^{-1} \cdot h^{-1}$ with H_2:CO ratio = 2.

The emerging trend indicated that with passage of time from 2 h to 19 h, there was a substantial transformation from the shorter hydrocarbon chains to the higher molecular-weight fractions. For example, about 5% of C_5 existed at 2 h, diminishing to almost zero at 19 h. At the same time, the waxes that were present in very minute quantities at 2 h had increased considerably at 19 h. From the gas-phase analysis, a high production of CH_4 was recorded initially, making up to 11%, but dropped to approximately 8% after 6 h, and below 4% at 24 h. The combined C2's (C_2H_6 and C_2H_4) gave a total of about 0.6%, while the composition of CO_2 was only 0.5% in the effluent stream. No C_3 or C_4 compounds were detectable. Figure 8 provides the full spectrum of the FTS product distribution at various H_2:CO ratios of 2.0, 1.5 and 1.0 that indicated a shift to the lower molecular weights as the H_2:CO ratio increased from 1 to 2.

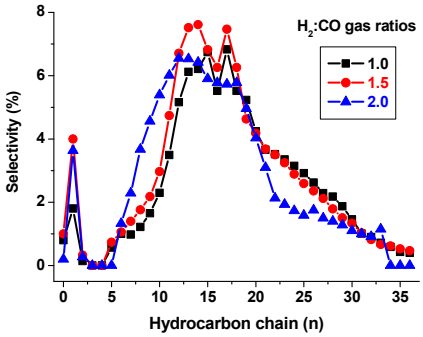

Figure 8. Effect of gas composition on the product spectrum of Fischer-Tropsch synthesis (FTS) after 24 h on stream at 220 °C, 2 MPa and gas hourly space velocity (GHSV) of 3600 $cm^3 \cdot g^{-1} \cdot h^{-1}$.

2.4. Determination of α-Values

Since our GC column was incapable of distinguishing the hydrocarbon compounds entirely by their various functional groups, in combining together all molecules with equal number of carbon atoms (alkanes, alkenes oxygenates, etc.), it was assumed that the formation of FTS products conformed to the conventional (ASF) polymerization kinetics, quantitatively described as requiring the presence of only one type of chain-growth site. Given that the catalyst was both nanometric and non-porous, heat and mass transport effects were essentially eliminated, so we suppose since earlier optimization tests indicated the same [42]. As presented in Figure 9, results of $\log(M_n/n)$ versus n demonstrated the typical deviation from the normal ASF distribution [43], due to the formation of significant amounts of CH_4 followed immediately by almost a non-existent (C_2–C_5) portion. This created a dip in the plot as seen in Figure 9a: with very little of C_2H_6 and C_2H_4 observed (amounting to less than 1%, when combined).

From C_4 there was a sharp rise towards C_6 that gently increased to C_{10}. Beyond C_{10} one may observe two definite gradients: a gentle one between C_{10}–C_{16} and a steeper one above C_{16} that is detectable from Figure 9b. Solving for $\log(\alpha)$ in Equation (4) revealed that the α-value for the Co/C catalyst was approximately 0.87, which was attained very quickly at low GHSV of 1800 $cm^3 \cdot h^{-1} \cdot g^{-1}$ of catalyst using H_2:CO = 2. Analyses for samples tested at GHSV of 3600 $cm^3 \cdot h^{-1} \cdot g^{-1}$ using various H_2:CO ratios of 2.0, 1.5 and 1.0 are provided in Figure 10 showing that the CO-rich gas streams (of H_2:CO ratios of 1.5 and 1.0) displayed the higher α-value of 0.93, and attained the maximum value within ~6 h, while the H_2-rich gas stream (H_2:CO = 2) showed a lower α-value of 0.85, which was only attained after over 15 h on stream.

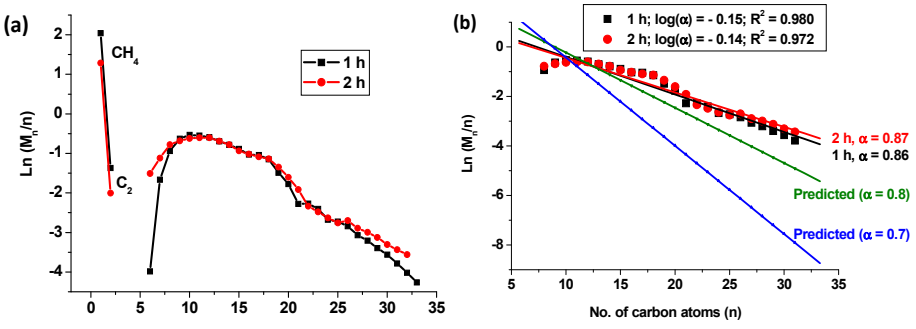

Figure 9. Plots of $\log(M_n/n)$ versus n comparing predicted (literature data value) and the measured α-values of Co/C catalyst after 1–2 h on stream, tested at 220 °C, 2 MPa and GHSV = 1800 $cm^3 \cdot h^{-1} \cdot g^{-1}$.

Table 3 summarizes the aggregate product fractions as obtained at the end of the reaction (TOS = 24 h) using the various gas feeds, which when the liquid-phase products were transmuted into the graphical format as shown in Figure 11 indicated that application of low H_2:CO ratios suppresses

H_2O production, but enhances wax formation. High H_2:CO ratio of 2 only influences additional formation of gasoline, because diesel production remains more or less constant at all H_2:CO ratios. Prolonged reaction times were observed to shift the product spectrum from the gasoline fraction to the wax fraction, with little net impact on the quantity of diesel formed. Nonetheless, overall the catalyst was perceived to be more selective towards the production of the diesel-fraction (~45%), which was in fact, our target product. A convergence of gradients towards the highest possible α-value (~0.85) was observed to form a common product spectrum at higher residence times (above 15 h).

Table 3. Product fractions with various feed gas compositions at 24 h of FTS reaction tested at 220 °C, 2 MPa and GHSV of 3600 $cm^3 \cdot g^{-1} \cdot h^{-1}$.

Feed Gas (H_2:CO Ratio)	Product Fraction (%)							α-Value
	CO_2	CH_4	C_2	C_5–C_{12}	C_{13}–C_{20}	C_{21+}	H_2O (cm^3)	
1.0	0.8	1.8	0.1	16.4	46.4	31.1	21	0.93
1.5	1.0	4.0	0.3	21.6	45.6	28.5	33	0.93
2.0	0.2	3.6	0.3	29.8	45.1	20.6	52	0.85

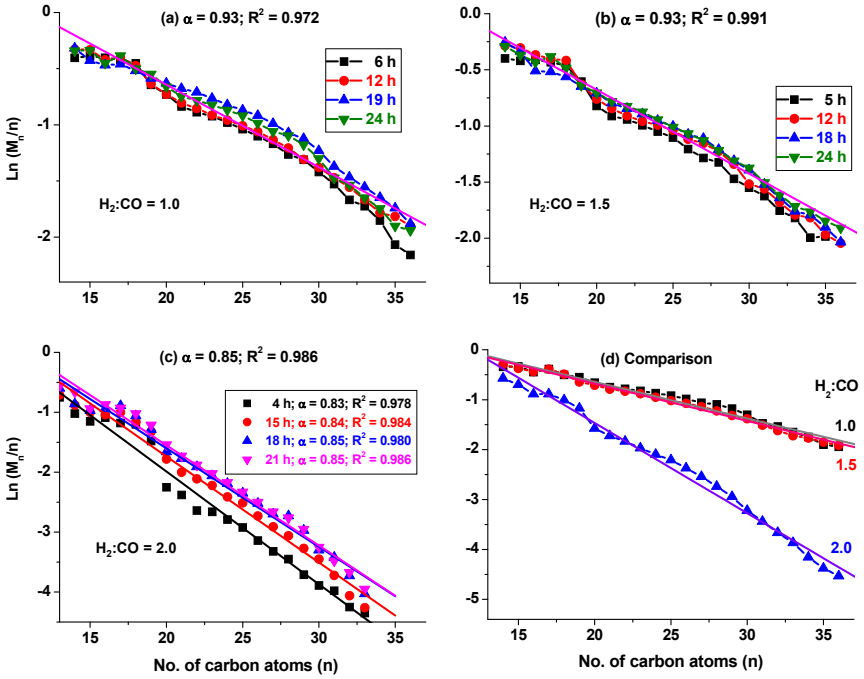

Figure 10. Plots displaying fast convergence and higher α-values for CO-rich feed gases with H_2:CO ratio of (**a**) = 1.0, (**b**) 1.5, (**c**) 2.0, and (**d**) their comparison after 24 h on stream at 220 °C, 2 MPa and GHSV of 3600 $cm^3 \cdot g^{-1} \cdot h^{-1}$.

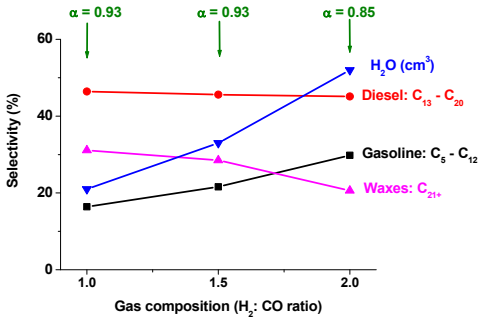

Figure 11. Impact of gas composition on FTS product fractions after 24 h on stream with catalyst samples tested at 220 °C, 2 MPa and GHSV of 3600 $cm^3 \cdot g^{-1} \cdot h^{-1}$.

3. Discussion

3.1. Evaluation of Research Objectives

The application of nanometric catalysts in this work was targeted for two main reasons: that the FTS product selectivity is strongly influenced by the size of Co nanoparticles [30], and that it is desirable to operate the reactor away from diffusion-limiting regimes. Due to the nature of the reaction, the large polymeric molecules especially the waxes generated in due course may easily clog catalyst pores and lead to catalyst deactivation. Therefore, the application of both nanometric and non-porous catalysts with high BET specific surface area of ~56 $m^2 \cdot g^{-1}$ of catalyst have been posited to be ideal for LT-FTS [7]. From our initial research objectives, it is hereby concluded that the plans were successfully executed and our product targets achieved since we were able to:

(i) Use a specially designed liquid sampling column to provide empirical evidence for the gradual development of the longer-chain hydrocarbons from real-time liquid-phase analysis, illustrating hydrocarbon-chain propagation with TOS;
(ii) Determine the true α-value of the plasma-synthesized Co/C catalyst as being above 0.85, which could only be ascertained after over 15 h on stream, since any α-values determined below this time period may be misleading;
(iii) Establish that the application of CO-rich syngas, which may in future be derived from biomass, is a viable alternative that can replace the current use of H_2-rich syngas in generating high molecular FTS products.

Microscopy through SEM coupled with EDX indicated uniform distribution of metal moieties in the carbon matrix, while TEM analysis showed highly dispersed Co nanoparticles of mean particle size of ~11 nm. Both XANES and XRD hinted to the fact that the used catalyst samples did not undergo metal oxidation, a characteristic that may prove to be beneficial to the longevity of the catalyst. In addition, XRD analysis revealed that the FCC crystal structure of the Co catalyst was the predominant and possibly the active phase in the FTS reaction [7], although some scholars have provided evidence for potentially greater intrinsic activity displayed by the HCP phase of the Co catalyst [44]. The catalytic activity for CO conversion was shown to greatly increase for catalysts with a majority of HCP stacking compared to those containing mostly the FCC phase particles [45]. In our plasma-synthesized Co/C sample, the existing HCP phase in the initial Co metal was completely transformed into the FCC phase and the catalyst was still very active. This contrasts with literature data where catalysts that contain mainly the HCP crystal structure show more active catalysis for CO hydrogenation than the FCC crystal structure of the Co metal obtained from Co_3O_4 reduction [4]. Besides, the HCP structure favours a different reaction mechanism, which involves direct CO dissociation, while the FCC structure kinetically favours the H-assisted CO dissociation mechanism on the Co metal [44]. We are of the opinion that there is full dependence on the presence of H_2 to dissociate CO on the FCC phase, because the metal nanoparticle-size range in our samples can only produce the stable FCC structure, while the HCP would automatically undergo a phase transformation. A summary of the catalyst's properties are provided in Table 4.

3.2. Application of Biomass and Bio-Syngas as Game Changer in Fuel Industry

This study intended to investigate the possible outcomes of exposing our recently formulated plasma-synthesized Co/C catalyst [9], to a CO-rich FTS feedstock because the composition of syngas feedstock was observed to impact on the FTS product distribution [46]. In this work, application of CO-rich gas feed simulating bio-syngas has established the practicality of producing higher molecular-weight hydrocarbons in FTS, although with lower CO conversions when compared to the H_2-rich feeds. The high α-value of 0.93 obtained (at 220 °C and 2 MPa) for CO-rich inlet stream would be a beneficial characteristic to the plasma-synthesized Co/C catalyst, particularly when considering the use of biomass-derived syngas feeds.

Table 4. Summary details of the properties of the plasma synthesized Co/C catalyst.

Measurement	Method	Catalyst Property	Values
Metal loading in carbon support	Carbon ignition, SEM	Co atomic-mass (g/g)	0.25
Catalyst composition	XRD, XANES	Phases present Dominant structure	Co^0, Co_3C FCC
Porosity	N_2 physisorption by BET	BET surface area ($m^2 \cdot g^{-1}$) Mean pore diameter (nm) Total pore volume ($cm^3 \cdot g^{-1}$)	56 28 0.39
Metal nanoparticles	Microscopy, TEM	Mean particle size (nm)	11
Alpha-values	ASF product distribution	H_2:CO ratio 1.0 H_2:CO ratio 1.5 H_2:CO ratio 2.0	0.93 0.93 0.85
Catalyst activity	GC analysis	CO conversion (220 °C, 2 MPa) H_2:CO ratio 1.0 H_2:CO ratio 1.5 H_2:CO ratio 2.0	10% 20% 40%
Selectivity	Liquid-GC analysis FTS at 220 °C, 2 MPa, H_2:CO = 2.0	Sample product distribution: CO_2 CH_4 C_2–C_4 C_5–C_{12} (Gasoline) C_{13}–C_{20} (Diesel) C_{21+} (Wax)	0.2 3.6 0.3 29.8 45.1 20.6

Since low CO conversions could be expected in the FTS using CO-rich feed stocks, a slight increase in temperature above 220 °C may enhance catalytic activity and enrich the diesel fraction. Alternatively, the waxes so produced can be converted to diesel fuel by way of thermal or hydrocracking of the waxes so produced. In industry, Co catalysts are designed for maximum selectivity in wax production that in turn acts as a feedstock for hydrocracking, and it is projected that an 80% selectivity towards diesel fuel can be achieved by blending both the FTS and hydrocracking processes [47]. One of the advantages observed from these results is the rapid chain growth experienced by use of the plasma-derived catalyst, particularly with the application of low H_2:CO ratios. In addition, since the hydrocarbon-chain growth begins at C_5, very limited quantities of CO_2, C2's (ethane and ethene), C3's and C4's were detected, and in fact the CH_4 production diminishes with TOS.

3.3. Catalyst Selectivity and α-Values

In this investigation, there was the typical deviation from the ASF distribution observed at the lower carbon values of ($n \leq 10$) due to reaction thermodynamics favouring CH_4 formation in appreciable quantities (up to 12%). However, the conspicuous absence of the C_2–C_4 portion cannot be explained from their thermodynamics point of view. For example, in the Fe-catalyzed LT-FTS, a two-α-model has been advanced to describe product selectivity, which is correlated to the catalyst's surface properties. The non-polar Fe-carbide surface seems to be responsible for the production of paraffins and olefins, while the polar Fe-oxide surface could be responsible for the production of light hydrocarbons, olefins and oxygenates [48]. The deviation from the ASF distribution has been noted particularly for its poor suitability for nanometric catalytic systems, and this could be an indicator of critical variations in the dominant growth mechanisms of FTS catalyzed by nanoparticles [49]. Since the predicted α-values for the Co catalyst by the ASF model is in the range of 0.70–0.80, our Co/C catalyst depending on reaction conditions was found to be greater, in the range of 0.78–0.87 (for H_2:CO = 2), and 0.93 (for H_2:CO $\leq$ 1.5). The higher α-values were validated by the substantial conspicuous solid wax, visible to the naked eye [7]. This creates the impression that liquid GC analysis may only be partially effective since the wax may not dissolve fully in the solvent during analysis.

When heavier components of the product stream are unable to dissolve or accumulate in the solvent, it lowers its amount in the sample drawn for analysis ($\alpha = M_{n+1}/M_n$). A noted classic example is the slow accumulation of the heavier products in the solvent that can lead to negative deviation from the α-values predicted by ASF [50]. However, in our case, the values were higher than those predicted. A possible explanation is that with the use of nanometric and non-porous materials, no diffusion limitations existed and hence the apparent instantaneously availability of the FTS products in the

solvent for analysis. Besides, it is also thought that since the heavier hydrocarbons take longer to move away from the catalyst surface, by virtue of their size, they have greater re-adsorption probability after formation [51]. Other authors indeed agree with the supposition that the olefin-chain length influences re-adsorption rate because the strength of molecular physisorption on catalyst surface increases its solubility in FTS wax with growing chain length and this olefin re-adsorption model was used to accurately predict product selectivity over the entire range of their experimental conditions [14]. It is for this reason that we think our nanometric catalysts are efficient in the process of hydrocarbon chain-growth propagation because no diffusion limitations seem to exist.

4. Experimental Section

4.1. Catalyst Synthesis: Reagents

The raw materials used for catalyst synthesis and testing were: cobalt metal powder with particle size range of 1–10 μm and cobalt (II) oxide (Aldrich, Milwaukee, WI, USA); high purity FTS feed stock gases (PRAXAIR, Sherbrooke, QC, Canada) composing H_2 (N5.0), CO (N2.5), and Ar (N5.0); mineral oil (Fisher Scientific, Ottawa, ON, Canada), with catalog name "O122-4, Mineral Oil, Heavy; USP/FCC (Paraffin Oil, Heavy)", and 99% pure n-hexadecane solvent (Fisher Scientific, Whitby, ON, Canada).

4.2. Catalyst Characterization

The Co/C catalyst under review has already been fully characterized: initially by XANES (Canadian Light Source (CLS) Synchrotron, Saskatoon, SK, Canada), and for porosity and BET specific surface area using the Accelerated Surface Area Porosimeter (ASAP) 2020 instrument (Micromeritics, Norcross, GA, USA) [9], and later the quantitative elemental analysis for the Co metal in the C support was performed by the carbon ignition method using a TG-DTA Setsys 2400 instrument (Setarum, Hillsborough, NJ, USA), while phase analysis was conducted on a Philips X'pert PRO X-ray Diffractometer (PANalytical, EA Almelo, The Netherlands), which is fitted with Ni-filters for the Cu Kα radiation of wavelength alpha1 = 1.5406 Å, produced at 40 kV and 50 mA (PANalytical, EA Almelo, The Netherlands). Curve-fitting modeling to determine the various amounts of each species in the catalyst was done using the PANalytical's High Score Plus software by Rietveld Quantitative Analysis (RQA).

In addition, the microscopic properties of the material were revealed by a Hitachi S-4700 Scanning Electron Microscope (SEM), equipped with an X-Max Oxford EDX spectrometer for elemental analysis (Hitachi, Tokyo, Japan). On the other hand, analysis by Transmission Electron Microscopy (TEM) was conducted on a Hitachi H-7500 Microscope, fitted with tungsten filament operated at an accelerating electron beam of 120 kV. A bottom-mounted AMT 4k x 4k CCD Camera System Model X41 captured images in bright field mode. (Hitachi, Tokyo, Japan) [7]. Comprehensive test procedures and analysis conditions are therefore provided in the cited articles.

4.3. Reactor Designs

4.3.1. Plasma Synthesis Reactor

The reactor set-up and detailed production of the catalyst synthesis method through plasma has been provided in an earlier article [30], where two reactor vessels were used to trap the synthesized materials. The first vessel, which confines the plasma plume is regarded as the main plasma reactor, while the auxiliary reactor lies adjacent to the main plasma reactor and both of them are connected through a junction where the fine-powder catalyst particles are captured on filters during the high vacuum evacuation.

4.3.2. Fischer-Tropsch Synthesis Reactor (3-ϕ-CSTSR)

The catalyst was tested in a 3-phase continuously-stirred tank slurry reactor vessel with a holding capacity of 0.5 L (Autoclave Engineers, Erie, PA, USA). In the current work, the original reactor design [7] was modified, in that, a liquid-phase sampling line was introduced into the reactor as shown in Figure 11. The sampling pipe for the slurry originated from the bottom of the vessel, while the gas-phase sampling pipe originated from the top of the reactor. The scheme incorporated a method intended to draw the slurry safely at high temperature and pressure without interrupting the reaction by use of a 15-cm long liquid-sampling column having a 1.5-cm internal diameter.

4.4. Liquid Sampling

Before sampling the slurry, all valves were shut, then valve-1 in Figure 12 was opened to allow the reactor pressure (2 MPa) to push the piston and hence the liquid, up the sampling column. After shutting valve-1, valve-2 was opened slowly to release the pressure in the column. While valve-2 was still open and valve-3 shut, valve-4 was opened carefully to draw out about 1–2 cm^3 sample of the slurry into a vial. Having all valves shut, the pressure in the air cylinder was raised slightly above the reactor pressure (e.g., 2.2 MPa). Valve-3 was then opened progressively in order to push the piston back to the bottom of the sampling column thereby pushing the untapped slurry back into the reactor for further reaction. The valve was shut again and by keeping all valves closed, valve-2 was opened to release the pressure that originated from the air bottle and then the valve was shut again. At the appointed time, the cycle was repeated at various time intervals without interrupting the reaction considerably. The drawn slurry sample was then filtered before injecting about 0.1 µm of the liquid sample into the liquid-based GC for analysis.

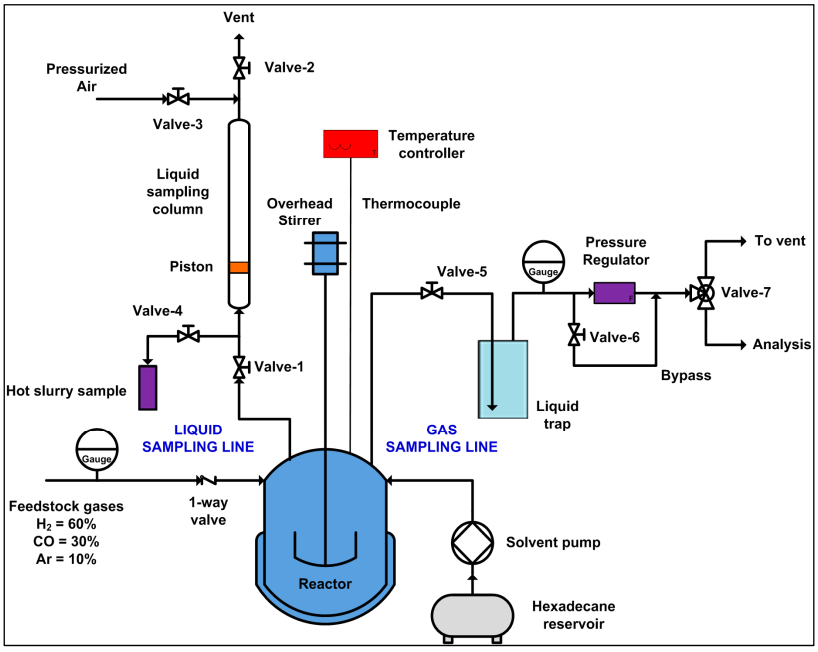

Figure 12. Design of our 3-ϕ-CSTSR incorporating both liquid and gas sampling lines.

4.5. Catalyst Testing

All catalyst samples were pre-treated at 400 °C for 24 h in a pure H_2 (N5.0) gas stream flowing at RTP, at the rate of 250 SCCM, (standard cubic cm per min or 4.17×10^{-6} $Nm^3 \cdot s^{-1}$; where 1 SCCM = 1.67×10^{-8} $Nm^3 \cdot s^{-1}$), while the FTS reaction was carried out in 3-ϕ-CSTSR operated isothermally at 220 °C and 2 MPa pressure with a stirring rate of over 2000 rpm. The purpose of pre-treatment by reduction is to gasify some of the excess carbon matrix in order to increase exposure

of the metal nanoparticles to the FTS gas reactants. The initial gas composition was set in the H_2:CO ratio of 2:1 flowing at 300 SCCM (or 5.01×10^{-6} $Nm^3 \cdot s^{-1}$), containing 0.6 L/L (60 vol %) H_2 and 0.3 L/L (30 vol %) CO, balanced in 0.1 L/L (10 vol %) Ar, for mass-balance calculation. At higher temperature (e.g., 260 °C), the catalyst became less useful for evaluating the α-value due to excessive CH_4 production (up to ~46%) [52]. Hexadecane (C_{16}) solvent was used to make up a reactor volume of 210 cm^3, and a mass of 5.0 g of catalyst utilized to create a gas flow rate with GHSV of 3600 $cm^3 \cdot g^{-1} \cdot h^{-1}$ of catalyst. The catalyst was doubled to 10.0 g to deliver a GHSV of 1800 $cm^3 \cdot g^{-1} \cdot h^{-1}$ of catalyst, while holding all the other reaction parameters constant. In other experiments, the feed gas composition was altered from H_2:CO ratio of 2.0 to 1.5 or to 1.0.

During the reaction, the gas-phase was sampled and tested for CO conversion using an at-line GC, while small quantities (1–2 cm^3) of the slurry were drawn about five times at various intervals within the 24-h reaction for real-time liquid-phase analysis. The solid-liquid sample was filtered before injecting into the liquid-based GC. From the GC charts, peak areas were computed to determine the selectivity of the product spectrum for both the gas-phase and liquid-phase analyses by a method already described in an earlier article [7]. The α-values were obtained by the least-squares linear regression of Equation (3), but in the logarithmic form expressed as Equation (4), where $\log(M_n/n)$ is plotted against n (the hydrocarbon-chain length) [15]. The following typical characteristic ranges of α-values for various catalysts: for Ru = 0.85–0.95; Co = 0.70–0.80; and Fe = 0.50–0.70, which are designated in this article as the "predicted" α-values [53].

5. Conclusions

From the objectives of this work, we developed a safe sampling method of drawing small portions of the hot slurry from a pressured 3-ϕ-CSTSR vessel without significantly interrupting the FTS reaction process. This approach enabled us to provide tangible evidence for the gradual formation and shift of the FTS fractions towards the heavier hydrocarbons with TOS. When tested at 220 °C (493 K), 2 MPa pressure, and GHSV = 3600 $cm^3 \cdot g^{-1} \cdot h^{-1}$ of catalyst, results showed that there was lower catalyst activity of ~10% and ~20% CO conversion at H_2:CO ratio of 1.0 and 1.5 respectively, with a predominant production of the heavier molecular weight fractions (diesel = C_{13}–C_{20} and waxes = C_{21+}), giving an α-value of 0.93. A higher catalyst activity (~40% CO conversion) was witnessed for H_2:CO ratio of 2.0 with prevalent tendency to produce more light-weight hydrocarbons (gasoline = C_4–C_{12}) and this led to relatively lower α-value of 0.85. Although our target fraction in this reaction was to produce diesel fuel as the principal fraction, the α-values higher than the predicted figure of 0.8 imply that the catalyst has great propensity to produce C_{20+} fractions too, particularly under CO-rich gas-feed streams.

Acknowledgments: We thank the Canadian BiofuelNet National Centre of Excellence (NCE) for financial support, Henri Gauvin for technical expertise in the labs; the CCM (Centre de Caractérisation des Matériaux, Université de Sherbrooke) staff for facilitating the characterization: Irène Kelsey Lévesque and Carl St.-Louis for BET surface area analysis, Charles Bertrand for Microscopy (SEM & TEM), and Stéphane Gutierrez for XRD analysis.

Author Contributions: Catalyst synthesis, testing, characterization, data analysis and manuscript drafting was done by James Aluha, while Nicolas Abatzoglou supervised the entire work and proofread the document. Yongfeng Hu provided access to the Canadian Light Source (CLS) Synchrotron and supervised the XANES analysis.

Conflicts of Interest: The authors declare no conflict of interest.

Abbreviations

The following abbreviations have been used in this manuscript:

ASF	Anderson-Schulz-Flory distribution
ASAP	Accelerated surface area porosimeter (Micromeritics ASAP-2020) instrument
BET	Brunauer-Emmett-Teller method for specific surface area analysis
EDX	Energy dispersive X-ray spectroscopy
FCC	Face centred cubic structure
FTS	Fischer-Tropsch synthesis

GC	Gas chromatography
GHSV	Gas hourly space velocity
HCP	Hexagonal closed packing structure
ICP-MS	Inductively-coupled plasma mass spectrometry
LT-FTS	Low-temperature Fischer-Tropsch synthesis
RQA	Rietveld quantitative analysis
RTP	Room temperature and pressure
SASOL	South African Synthetic Oil Ltd.
SCCM	Standard cubic centimetre per minute
SEM	Scanning electron microscopy
SPS	Suspension plasma-spray technology
TEM	Transmission electron microscopy
TGA	Thermogravimetric analysis
TOS	Time-on-stream
XANES	X-ray absorption near-edge structure analysis by Synchrotron light
XRD	X-ray diffraction analysis
3-ϕ-CSTSR	Three-phase continuously-stirred-tank slurry reactor

References

1. Thomas, J.M.; Thomas, W.J. *Principles and Practice of Heterogeneous Catalysis*; Wiley: Hoboken, NJ, USA, 1997; p. 526.
2. Vosloo, A.C. Fischer–Tropsch: A futuristic view. *Fuel Process. Technol.* **2001**, *71*, 149–155. [CrossRef]
3. Ding, M.; Yang, Y.; Wu, B.; Xu, J.; Zhang, C.; Xiang, H.; Li, Y. Study of phase transformation and catalytic performance on precipitated iron-based catalyst for Fischer-Tropsch synthesis. *J. Mol. Catal. A Chem.* **2009**, *303*, 65–71. [CrossRef]
4. Kwak, G.; Kim, D.-E.; Kim, Y.T.; Park, H.-G.; Kang, S.C.; Ha, K.-S.; Juna, K.-W.; Lee, Y.-J. Enhanced catalytic activity of cobalt catalysts for Fischer-Tropsch synthesis via carburization and hydrogenation and its application to regeneration. *Catal. Sci. Technol.* **2016**, *6*, 4594–4600. [CrossRef]
5. Fu, T.; Jiang, Y.; Lv, J.; Li, Z. Effect of carbon support on Fischer–Tropsch synthesis activity and product distribution over Co-based catalysts. *Fuel Process. Technol.* **2013**, *110*, 141–149. [CrossRef]
6. D'Souza, L.; Barnes, S.; Regalbuto, J.R. The simple, effective synthesis of highly dispersed Pd/C and CoPd/C heterogeneous catalysts via charge-enhanced dry impregnation. *Catalysts* **2016**, *6*, 1–11. [CrossRef]
7. Aluha, J.; Braidy, N.; Dalai, A.; Abatzoglou, N. Low-temperature Fischer-Tropsch synthesis using plasma-synthesised nanometric Co/C and Fe/C catalysts. *Can. J. Chem. Eng.* **2016**, *94*, 1504–1515. [CrossRef]
8. Liu, C.-J.; Zou, J.; Yu, K.; Cheng, D.; Han, Y.; Zhan, J.; Ratanatawanate, C.; Jang, B.W.-L. Plasma application for more environmentally friendly catalyst preparation. *Pure Appl. Chem.* **2006**, *78*, 1227–1238. [CrossRef]
9. Aluha, J.; Boahene, P.; Dalai, A.; Hu, Y.; Bere, K.; Braidy, N.; Abatzoglou, N. Synthesis and characterisation of nanometric Co/C and Fe/C catalysts for Fischer-Tropsch synthesis: A comparative study using a fixed-bed reactor. *Ind. Eng. Chem. Res.* **2015**, *54*, 10661–10674. [CrossRef]
10. Tristantini, D.; Lögdberg, S.; Gevert, B.; Borg, Ø.; Holmen, A. The effect of synthesis gas composition on the Fischer–Tropsch synthesis over Co/γ-Al_2O_3 and Co–Re/γ-Al_2O_3 catalysts. *Fuel Process. Technol.* **2007**, *88*, 643–649. [CrossRef]
11. Chaudhari, S.T.; Bej, S.K.; Bakhshi, N.N.; Dalai, A.K. Steam gasification of biomass-derived char for the production of carbon monoxide-rich synthesis gas. *Energy Fuels* **2001**, *15*, 736–742. [CrossRef]
12. Hu, J.; Yu, F.; Lu, Y. Application of Fischer-Tropsch synthesis in biomass to liquid conversion. *Catalysts* **2012**, *2*, 303–326. [CrossRef]
13. Aluha, J.; Braidy, N.; Dalai, A.; Abatzoglou, N. Low-temperature fischer-tropsch synthesis with carbon-supported nanometric iron-cobalt catalysts. In Proceedings of the 23rd European Biomass Conference and Exhibition, Vienna, Austria, 1–4 June 2015.
14. van der Laan, G.P.; Beenackers, A.A.C.M. Hydrocarbon selectivity model for the gas-solid Fischer-Tropsch synthesis on precipitated iron catalysts. *Ind. Eng. Chem. Res.* **1999**, *38*, 1277–1290. [CrossRef]
15. Bartholomew, C.H.; Farrauto, R.J. *Fundamentals of Industrial Catalytic Processes*; John Wiley & Sons, Inc.: Hoboken, NJ, USA, 2006; p. 403.

16. Fu, T.; Li, Z. Review of recent development in Co-based catalysts supported on carbon materials for Fischer-Tropsch synthesis. *Chem. Eng. Sci.* **2015**, *135*, 3–20. [CrossRef]
17. Jacobs, G.; Das, T.K.; Zhang, Y.; Li, J.; Racoillet, G.; Davis, B.H. Fischer-Tropsch synthesis: Support, loading, and promoter effects on the reducibility of cobalt catalysts. *Appl. Catal. A* **2002**, *233*, 263–281. [CrossRef]
18. Jacobs, G.; Ma, W.; Gao, P.; Todic, B.; Bhatelia, T.; Bukur, D.B.; Davis, B.H. The application of synchrotron methods in characterizing iron and cobalt Fischer-Tropsch synthesis catalysts. *Catal. Today* **2013**, *214*, 100–139. [CrossRef]
19. Ding, M.; Yang, Y.; Wu, B.; Li, Y.; Wang, T.; Ma, L. Study on reduction and carburization behaviors of iron-based Fischer-Tropsch synthesis catalyst. *Energy Procedia* **2014**, *61*, 2267–2270. [CrossRef]
20. Khodakov, A.Y.; Chu, W.; Fongarland, P. Advances in the development of novel cobalt Fischer-Tropsch catalysts for synthesis of long-chain hydrocarbons and clean fuels. *Chem. Rev.* **2007**, *107*, 1692–1744. [CrossRef] [PubMed]
21. van Berge, P.J.; van de Loosdrecht, J.; Barradas, S.; van der Kraan, A.M. Oxidation of cobalt based Fischer-Tropsch catalysts as a deactivation mechanism. *Catal. Today* **2000**, *58*, 321–334. [CrossRef]
22. Van de Loosdrecht, J.; Balzhinimaev, B.; Dalmon, J.A.; Niemantsverdriet, J.W.; Tsybulya, S.V.; Saib, A.M.; van-Berge, P.J.; Visagie, J.L. Cobalt Fischer-Tropsch synthesis: Deactivation by oxidation? *Catal. Today* **2007**, *123*, 293–302. [CrossRef]
23. Nabaho, D.; Niemantsverdriet, J.W.H.; Claeys, M.; van Steen, E. Hydrogen spillover in the Fischer-Tropsch synthesis: An analysis of gold as a promoter for cobalt-alumina catalysts. *Catal. Today* **2016**, *275*, 27–34. [CrossRef]
24. Den Otter, J.H.; Nijveld, S.R.; de Jong, K.P. Synergistic promotion of Co/SiO_2 Fischer-Tropsch catalysts by niobia and platinum. *ACS Catal.* **2016**, *6*, 1616–1623. [CrossRef]
25. Miyazawa, T.; Hanaoka, T.; Shimura, K.; Hirata, S. Ruthenium modification on Mn and Zr-modified Co/SiO_2 catalysts for slurry-phase Fischer-Tropsch synthesis. *Catalysts* **2015**, *5*, 26–37. [CrossRef]
26. Fajín, J.L.C.; Cordeiro, M.N.D.S.; Gomes, J.R.B. Fischer-Tropsch synthesis on multicomponent catalysts: What can we learn from computer simulations? *Catalysts* **2015**, *5*, 3–17. [CrossRef]
27. Jacobs, G.; Ma, W.; Davis, B.H. Influence of reduction promoters on stability of cobalt/γ-alumina Fischer-Tropsch synthesis catalysts. *Catalysts* **2014**, *4*, 49–76. [CrossRef]
28. Iqbal, S.; Davies, T.E.; Morgan, D.J.; Karim, K.; Hayward, J.S.; Bartley, J.K.; Taylor, S.H.; Hutchings, G.J. Fischer Tropsch synthesis using cobalt based carbon catalysts. *Catal. Today* **2016**, *275*, 35–39. [CrossRef]
29. Rytter, E.; Holmen, A. Deactivation and regeneration of commercial type Fischer-Tropsch Co-catalysts—A mini-review. *Catalysts* **2015**, *5*, 478–499. [CrossRef]
30. Aluha, J.; Bere, K.; Abatzoglou, N.; Gitzhofer, F. Synthesis of nano-catalysts by induction suspension plasma technology (SPS) for Fischer-Tropsch reaction. *Plasma Chem. Plasma P* **2016**, *36*, 1325–1348. [CrossRef]
31. Borg, Ø.; Eri, S.; Blekkan, E.A.; Storsæter, S.; Wigum, H.; Rytter, E.; Holmen, A. Fischer-Tropsch synthesis over γ-alumina-supported cobalt catalysts: Effect of support variables. *J. Catal.* **2007**, *248*, 89–100. [CrossRef]
32. Abbaslou, R.M.M.; Tavassoli, A.; Soltan, J.; Dalai, A.K. Iron catalysts supported on carbon nanotubes for Fischer-Tropsch synthesis: Effect of catalytic site position. *Appl. Catal. A* **2009**, *367*, 47–52. [CrossRef]
33. Trépanier, M.; Tavasoli, A.; Dalai, A.K.; Abatzoglou, N. Fischer-Tropsch synthesis over carbon nanotubes supported cobalt catalysts in a fixed bed reactor: Influence of acid treatment. *Fuel Process. Technol.* **2009**, *90*, 367–374. [CrossRef]
34. Fu, T.; Huang, C.; Lv, J.; Li, Z. Fuel production through Fischer-Tropsch synthesis on carbon nanotubes supported co catalyst prepared by plasma. *Fuel* **2014**, *121*, 225–231. [CrossRef]
35. Bezemer, G.L.; Bitter, J.H.; Kuipers, H.P.C.E.; Oosterbeek, H.; Holewijn, J.E.; Xu, X.; Kapteijn, F.; van Dillen, A.J.; de Jong, K.P. Cobalt particle size effects in the Fischer-Tropsch reaction studied with carbon nanofiber supported catalysts. *J. Am. Chem. Soc.* **2006**, *128*, 3956–3964. [CrossRef] [PubMed]
36. De la Osa, A.R.; Romero, A.; Dorado, F.; Valverde, J.L.; Sánchez, P. Influence of cobalt precursor on efficient production of commercial fuels over FTS Co/SiC catalyst. *Catalysts* **2016**, *6*, 98. [CrossRef]
37. Moazami, N.; Mahmoudi, H.; Rahbar, K.; Panahifar, P.; Tsolakis, A.; Wyszynski, M.L. Catalytic performance of cobalt-silica catalyst for Fischer-Tropsch synthesis: Effects of reaction rates on efficiency of liquid synthesis. *Chem. Eng. Sci.* **2015**, *134*, 374–384. [CrossRef]

38. Moazami, N.; Wyszynski, M.L.; Mahmoudi, H.; Tsolakis, A.; Zou, Z.; Panahifar, P.; Rahbar, K. Modelling of a fixed bed reactor for Fischer–Tropsch synthesis of simulated N_2-rich syngas over Co/SiO_2: Hydrocarbon production. *Fuel* **2015**, *154*, 140–151. [CrossRef]
39. Hong, J.; Chu, W.; Chernavskii, P.A.; Khodakov, A.Y. Cobalt species and cobalt-support interaction in glow discharge plasma-assisted Fischer-Tropsch catalysts. *J. Catal.* **2010**, *273*, 9–17. [CrossRef]
40. Eschemann, T.O.; Bitter, J.H.; de Jong, K.P. Effects of loading and synthesis method of titania-supported cobalt catalysts for Fischer-Tropsch synthesis. *Catal. Today* **2014**, *228*, 89–95. [CrossRef]
41. Mohandas, J.C.; Gnanamani, M.K.; Jacobs, G.; Ma, W.; Ji, Y.; Khalid, S.; Davis, B.H. Fischer-Tropsch synthesis: Characterization and reaction testing of cobalt carbide. *ACS Catal.* **2011**, *1*, 1581–1588. [CrossRef]
42. Blanchard, J.; Abatzoglou, N. Nano-iron carbide synthesized by plasma as catalyst for Fischer-Tropsch synthesis in slurry reactors: The role of iron loading and K, Cu promoters. *Catal. Today* **2014**, *237*, 150–156. [CrossRef]
43. Davis, B.H. *The Two-Alpha Value for Iron Fischer-Tropsch Catalysts: Fact or Fiction?* ACS Fuel: San Francisco, CA, USA, 2006; Argonne National Laboratory: San Francisco, CA, USA; pp. 173–183.
44. Liu, J.-X.; Su, H.-Y.; Sun, D.-P.; Zhang, B.-Y.; Li, W.-X. Crystallographic dependence of Co activation on cobalt catalysts: HCP versus FCC. *J. Am. Chem. Soc.* **2013**, *135*, 16284–16287. [CrossRef] [PubMed]
45. Ducreux, O.; Rebours, B.; Lynch, J.; Roy-Auberger, M.; Bazin, D. Microstructure of supported cobalt Fischer-Tropsch catalysts. *Oil Gas Sci. Technol. Rev. IFP* **2009**, *64*, 49–62. [CrossRef]
46. Farias, F.E.M.; Sales, F.G.; Fernandes, F.A.N. Effect of operating conditions and potassium content on Fischer-Tropsch liquid products produced by potassium-promoted iron catalysts. *J. Nat. Gas Chem.* **2008**, *17*, 175–178. [CrossRef]
47. Schulz, H. Short history and present trends of Fischer-Tropsch synthesis. *Appl. Catal. A* **1999**, *186*, 3–12. [CrossRef]
48. Huyser, J.; van Vuuren, M.J.; Kupi, G. Advances in Fischer-Tropsch synthesis, catalysts, and catalysis. In *The Value of a Two Alpha Model in the Elucidation of a Full Product Spetrum for Fe-LTFT*; Davis, B.H., Occelli, M.L., Eds.; CRC Press: Boca Raton, FL, USA, 2010; pp. 185–197.
49. Tavakoli, A.; Sohrabi, M.; Kargari, A. Application of Anderson-Schulz-Flory (ASF) equation in the product distribution of slurry phase FT synthesis with nanosized iron catalysts. *Chem. Eng. J.* **2008**, *136*, 358–363. [CrossRef]
50. Dictor, R.A.; Bell, A.T. An explanation for deviations of Fischer-Tropsch products from a Schulz-Flory distribution. *Ind. Eng. Chem. Proc. Des. Dev.* **1983**, *22*, 678–681. [CrossRef]
51. Iglesia, E.; Reyes, S.C.; Madon, R.J.; Soled, S.L. Selectivity control and catalyst design in the Fischer-Tropsch synthesis: Sites, pellets, and reactors. *Adv. Catal.* **1993**, *39*, 221–302.
52. Aluha, J.; Abatzoglou, N. Synthetic fuels from 3-ϕ Fischer-Tropsch synthesis using syngas feed and novel nanometric catalysts synthesised by plasma. *Biomass Bioenergy* **2016**, *95*, 330–339. [CrossRef]
53. Dry, M.E. Catalytic aspects of industrial Fischer-Tropsch synthesis. *J. Mol. Catal.* **1982**, *17*, 133–144. [CrossRef]

9.5. Appendix E: Article 5 – Bimetallic catalysts tested in CSTR

Biomass and Bioenergy 95 (2016) 330–339

Contents lists available at ScienceDirect

Biomass and Bioenergy

journal homepage: http://www.elsevier.com/locate/biombioe

Research paper

Synthetic fuels from 3-ϕ Fischer-Tropsch synthesis using syngas feed and novel nanometric catalysts synthesised by plasma

James Aluha, Nicolas Abatzoglou*

Department of Chemical & Biotechnological Engineering, Université de Sherbrooke, Sherbrooke, QC, J1K 2R1, Canada

ARTICLE INFO

Article history:
Received 13 February 2016
Received in revised form
6 May 2016
Accepted 8 May 2016
Available online 17 June 2016

Keywords:
Fischer-Tropsch
Plasma
Carbon
Iron
Cobalt
Catalyst

ABSTRACT

Nanometric carbon-supported catalysts based on cobalt and iron (Co/C, Fe/C and Co–Fe/C) were synthesised by plasma method for application in Fischer-Tropsch synthesis (FTS). FTS tests were conducted at reaction conditions (*ca* 533 K, 2 MPa) over the catalyst, in a feed stream of 60% mol fraction H_2 and 30% mol fraction CO at 1.0 $cm^3 s^{-1} g^{-1}$ of catalyst for 24 h. Prior to this, the catalysts were pre-treated at 673 K either in pure H_2 or CO flowing at 250 cm^3 min^{-1} for 24 h. Results showed that higher temperature promoted better CO conversion; up to 100% for the Co/C catalyst at 533 K. However, lower temperatures were more conducive for the selectivity of Co/C catalyst towards gasoline (C_4–C_{12}) and diesel (C_{13}–C_{20}) fractions, since production of undesired products such as CO_2 and CH_4 was prevalent at higher temperatures. At 493 K, the Co–Fe/C bimetallics were almost inert, but at 533 K, they showed improved CO conversion. When compared to the Co/C catalyst, Fe-containing catalysts suppressed both CO_2 and CH_4 production. Moderated H_2O production was witnessed in the CO-reduced catalysts, contrasting with catalysts pre-treated in H_2 gas. Catalyst characterisation by BET surface area, XRD analysis and microscopy (SEM & TEM) showed that plasma synthesis produces catalysts with consistency, having highly dispersed nanoparticle metal moieties, interspersed with various forms of metallic, carbidic and intermetallic Co–Fe species in the carbon matrix support.

1. Introduction

The industrial FTS process polymerises syngas (a mixture of H_2 and *CO*) at H_2:CO mol ratio of ~2 over a Co or Fe catalyst, forming hydrocarbon chains with a widespread product distribution [1]. Alkane formation is favoured by hydrogen-rich feed streams as represented by Eq. (1), while alkene production is favoured by hydrogen-poor feed streams given by Eq. (2). The co-produced H_2O is undesirable though inevitable and participates in parallel reactions with H_2 and CO, particularly in the presence of Fe-based catalysts, such as the reverse water-gas shift (WGS) reaction as given in Eq. (3).

$$(2n+1)H_2 + nCO \rightarrow C_nH_{(2n+2)} + nH_2O \quad (1)$$

$$2nH_2 + nCO \rightarrow C_nH_{2n} + nH_2O \quad (2)$$

$$CO + H_2O \leftrightarrow CO_2 + H_2 \quad (3)$$

Different mechanisms have been proposed for FTS reaction, with evidence pointing towards the active phase involving metallic Co or Fe-carbides species [2]. For example, the Fe/C catalyst efficiency is drastically decreased once the carbides are converted to metallic Fe-only-containing formulations. A choice FTS catalyst should therefore have the active metallic phase supported on inert material such as graphitic carbon [3], and preferably being nanometric in nature, with high surface area to augment the rate of reaction, but low porosity ideally for overcoming diffusion limitations since the reaction forms polymeric molecules. Additionally, an inert support prevents side reactions that may interfere with the active metallic phase, reactants or products. In earlier works, we have shown that our catalyst materials comprise encapsulated metal nanoparticles in a carbon matrix, where the matrix can be removed by a careful *in situ* reduction process in order to expose the metal nanoparticles for catalysis. For example, in a 100-h-long test with the plasma-synthesised Fe/C catalyst after a 6 h reduction at 723 K and FTS performed at 493 K, under 3.1 MPa pressure, and gas hourly space velocity (GHSV) of 2725 cm^3 h^{-1} g^{-1} of catalyst, the

* Corresponding author.
E-mail address: nicolas.abatzoglou@usherbrooke.ca (N. Abatzoglou).

http://dx.doi.org/10.1016/j.biombioe.2016.05.010
0961-9534/

average CO conversion was relatively high (*ca.* 40%) in the first 8 h, dropping quickly to an average of approximately 25%, with CH_4 selectivity of below 5% [4].

The objective of this work was to develop by rational design, a potential FTS catalyst for industrial application. Using a step-wise approach, catalysts were synthesised and tested with increasing process complexity: improving from single-metal to bimetallics, from low-temperature to high temperature tests, and from observing the hydrocarbon product spectrum to water management issues. The plasma-synthesis method was chosen because it forms nano-metallic moieties simultaneously with the nanometric carbon support *in situ*. It has been shown that the Co-based FTS catalysis thrives on the metallic species (Co°), while the Fe-catalysed reaction is dependent on its Fe carbides [5], which may appear in various forms as Fe_xC_y [6]. Both the metallic and carbide species are generated by plasma [7], an approach that we found to be relatively more efficient in sample preparation since it is a single-step method [8], and would potentially save time and lower both labour and material costs when commercialised. Although it has been advanced that non-stoichiometric iron-oxide-carbide species are the active phase in FTS [5], our used samples did not seem to contain any metal-oxide species, which have been established to be the origin of catalyst deactivation [2]. This is a positive attribute of our samples that do not show deactivation either on stream or by morphological changes.

In this study, we compare the performance of carbon-supported catalysts based on Co and Fe, synthesised through plasma under identical conditions. The materials were either single metal formulations (Co/C, Fe/C) or Co–Fe/C bimetallic formulations prepared in various metal proportions. Preliminary tests for FTS activity was conducted for H_2-reduced Co/C and Fe/C formulations in a fixed-bed reactor [8], and then in a three-phase slurry continuously-stirred tank reactor (3-ϕ-SCSTR) [9], while the Co–Fe/C bimetallic formulations were tested in the 3-ϕ-SCSTR only [10]. In this article, the influence of the pre-treatment gas on the FTS product spectrum in the 3-ϕ-SCSTR is discussed, comparing the use of H_2 versus CO as reduction media.

2. Experimental methods

2.1. Catalyst synthesis by plasma

The Radio-Frequency (RF) plasma system (PL-50, 3.2 MHz) was used for catalyst production by the method already described for the single-metal (Co/C, Fe/C) catalysts [8], and the bimetallic (Co–Fe/C) formulations [10]. The resulting powder materials were then tested for FTS activity.

2.2. Catalyst characterisation

The catalysts were analysed by various characterisation techniques, whose details can be found in an earlier article [9]. Nevertheless, a summarised view includes BET specific surface area analysis, Scanning Electron Microscopy (SEM), Transmission Electron Microscopy (TEM) and X-ray Diffraction. Porosity and surface area measurements were conducted on a Micromeritics ASAP 2020 analyser using N_2 gas physisorption where the adsorption-desorption isotherm plots were extracted to determine the materials' porosity. SEM analysis captured both secondary and back-scattered images using the Hitachi S-4700 Scanning Electron Microscope, coupled with an X-Max Oxford EDX (Energy Dispersive X-ray) spectrometer and X-ray mapping to display the metal distribution in the carbon matrix. Imaging by TEM analysis in bright-field mode was captured by a bottom-mounted AMT 4 k × 4 k CCD Camera System Model X41 using an accelerating electron beam of 120 kV from a tungsten filament on a Hitachi H-7500 instrument. Particle-size distribution was analysed using the Nano-measurer version 1.2 "Scion Imager" software. A Philips X'pert PRO Diffractometer from PANalytical was used in powder-XRD analysis, fitted with Ni-filters for the Cu Kα radiation (1.5406 Å) produced at 40 kV and 50 mA. The XRD patterns were recorded in the range of 5° and 110° [2θ] angle, and data analysis done using the MDI JADE 2010 (version 2.6.6) software, compared with Powder Diffraction Files in the Database (version 4.13.0.2) using the PDF-4+ software 2013 (version 4.13.0.6).

2.3. Catalyst testing: reaction conditions

Before FTS tests, catalysts were preferably activated by *in situ* reduction because the materials are pyrophoric. The pre-treatment was conducted at 673 K (400 °C) for 24 h using either high purity H_2 gas (99.998%) or CO (99.5%) flowing at 250 $cm^3\ min^{-1}$. Reduction exposes the nanometric Fe or Co moieties for reaction by partly gasifying the surrounding carbon matrix into CH_4 and other hydrocarbon gases. A typical FTS feed gas stream comprising 60 mol.% fraction H_2 and 30 mol.% fraction CO (H_2:CO ratio = 2:1) balanced in Ar, flowing at 300 $cm^3\ min^{-1}$ was then introduced into the 1.5-L Parr reactor vessel, acting as a 3-ϕ-SCSTR. The reactor was operated isothermally at temperatures within the range of 493–533 K (220–260 °C), at 2 MPa pressure, GHSV of 1.0 $cm^3 s^{-1} g^{-1}$ of catalyst using 5.0 g of catalyst with the gas volume measured at reaction conditions. Ar was included for CO conversion calculations where composition of effluent gases and FTS products in the liquid phase were analysed by gas chromatography as described before [9].

3. Results

3.1. Catalyst characterisation

3.1.1. BET surface area analysis

There was an increase in BET specific surface areas of the bimetallic Co–Fe/C catalysts followed by a drop at both edges of the single metal catalysts (Co/C and Fe/C), as graphically represented in Fig. 1 part (a). A similar trend is depicted in Fig. 1 part (b) for their respective pore volumes, determined by "single point adsorption for total pore volume less than 120 nm in diameter (at P/Po = 0.98)". However, the converse was observed for their average pore diameters using the relationship (4 V/A by BET), where the single metal catalysts had higher pore diameters than the bimetallic catalysts, see Fig. 1 part (c).

3.1.2. Scanning Electron Microscopy (SEM)

The freshly synthesised catalysts comprised finely divided metal moieties evenly distributed across the carbon matrix. Fig. 2 is a representative secondary image of the fresh 30%Co–70%Fe/C catalyst showing the nanometric nature of the carbon support, while the EDX spectrum provides evidence for the expected higher mass Fe:Co ratio in this catalyst. Increasing Co loading becomes even more evident in the X-ray mapping as provided in Fig. 3 for the other two fresh bimetallic catalysts (50%Co–50%Fe/C and 80% Co–20%Fe/C).

3.1.3. Transmission Electron Microscopy (TEM)

Analysis by TEM imaging for catalyst morphology and particle size distribution showed that in the single metal catalysts, the fresh and used samples did not exhibit any morphological changes during FTS. An illustration is provided in Fig. 4 comparing the image of a fresh Co/C catalyst, which did not change after use, benchmarked with the commercial nano-hematite (Fe-NanoCat®) FTS catalyst, where nanoparticle sintering was rampant, leading to the

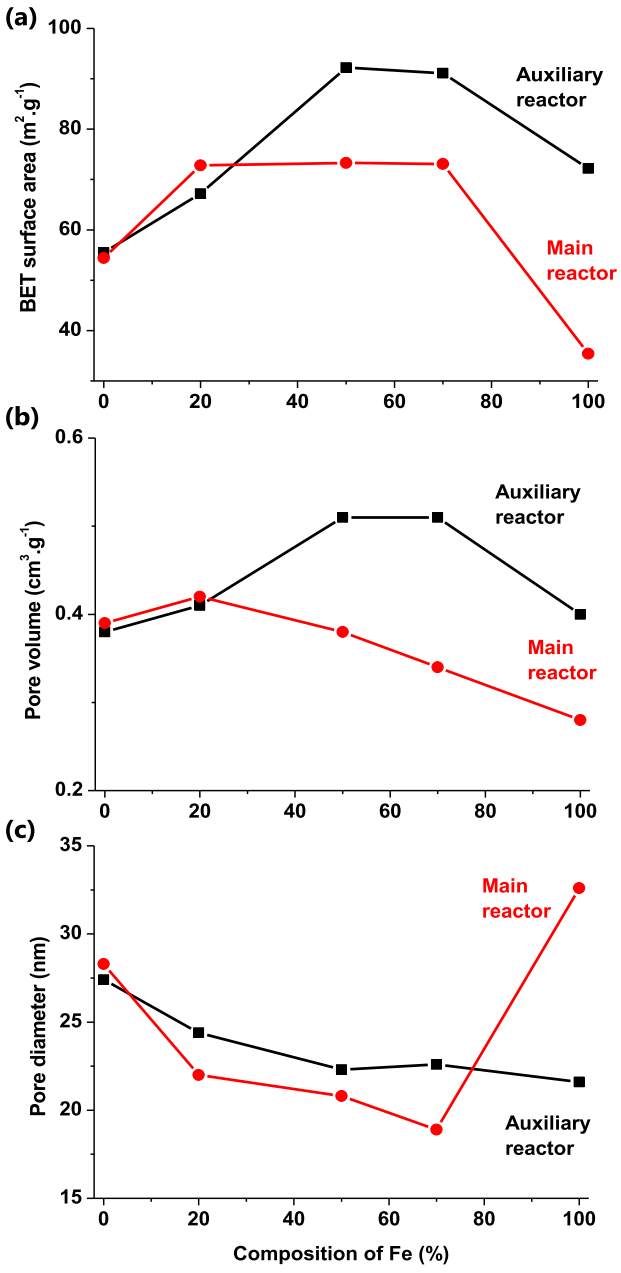

Fig. 1. Plots of (a) BET specific surface area; (b) pore volume; and (c) pore diameter against increasing Fe-loading in the catalysts.

conclusion that plasma-synthesised catalysts were apparently not prone to particle agglomeration and hints to their long-term durability [9]. Summary plots in Fig. 5 graphically display the particle-size distribution of each catalyst for a sample size of 250 nanoparticles. The 80%Co–20%Fe/C and 30%Co–70%Fe/C bimetallics had the lowest mean of ~9 nm followed by the single metal Co/C and Fe/C catalysts with a mean of ~11 nm, while the bimetallic 50%Co–50%Fe/C catalyst demonstrated a wider particle size distribution with a mean of over 14 nm.

Thermal treatment (~50 h) did not seem to adversely affect the morphology of the plasma-derived catalysts since no significant changes were evident before and after reaction (reduced at 673 K for 24 h; then FTS at 493–533 K for a further 24 h). However, when the same catalyst samples were reduced in CO under identical conditions, carbon nanofilaments (CNFs) were created in all

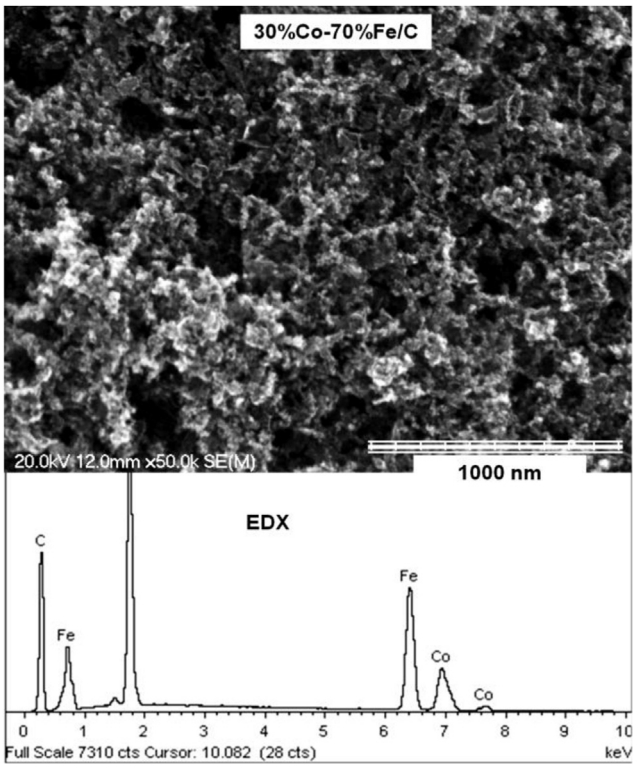

Fig. 2. Secondary SEM image of the fresh 30%–70%Fe/C catalyst.

catalysts, perceived to be growing away from the metal centres (in the direction of the arrows) as portrayed in Fig. 6. It has been advanced that metal oxides are necessary for CNT growth [11], and similar images to ours have been identified from the catalytic chemical vapour deposition of Ni-activated growth of CNFs, whose structures were described more effectively as multi-wall carbon nanotubes (MWCNTs) [12]. The images in the first row of Fig. 6 (a_1, b_1 and c_1) represent the fresh bimetallic catalysts, while those in the second row (a_2, b_2 and c_2) display images of their corresponding catalysts after use in FTS reaction. Fig. 7 is a supplementary TEM image of the CNFs at higher magnification.

3.1.4. XRD analysis

Fig. 8 shows the XRD patterns of the fresh single metal (Co/C and Fe/C) and Co–Fe/C bimetallic catalysts, overlaid with the used Co–Fe/C bimetallics after pre-treatment in H_2, while Fig. 9 compares the used bimetallic Co–Fe/C catalysts pre-treated in either H_2 or CO. Greater amorphicity was observed in catalysts pre-treated in CO than those pre-treated in H_2 due to the CNF production with CO reduction, which amplified the presence of graphitic carbon shown by the large broadened peak below the 30° [2θ]-angle. Possible phases identified in the used bimetallic samples are summarised in Table 1. Since analysis of used samples provides evidence of the phases that were present in the material during reaction, it was observed that all used bimetallic samples comprised a mutual presence of metallic Co and Fe as expected. Nonetheless, the 80% Co–20%Fe/C catalyst had the highest amount of Co, but its metallic phase was apparently missing in both the H_2- and CO-reduced samples probably due to peak extinction arising from their nanometric nature or the FCC phase overlapping with the CoFe peaks. In addition, all the catalysts showed the presence of CoFe intermetallic except the H_2-reduced 30%Co–70%Fe/C sample. Instead it displayed the presence of Co_3Fe_7 that was missing in all the other catalysts. It was also observed that both the 30%Co–70%Fe/C and 80%Co–20%

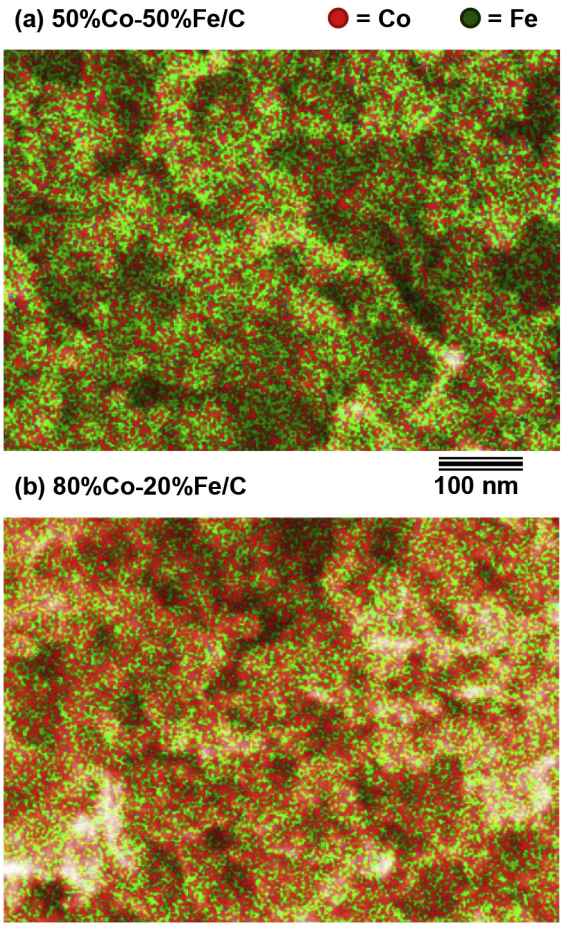

Fig. 3. X-ray mapping of (a) 50%–50%Fe/C and (b) 80%–20%Fe/C catalyst by SEM imaging.

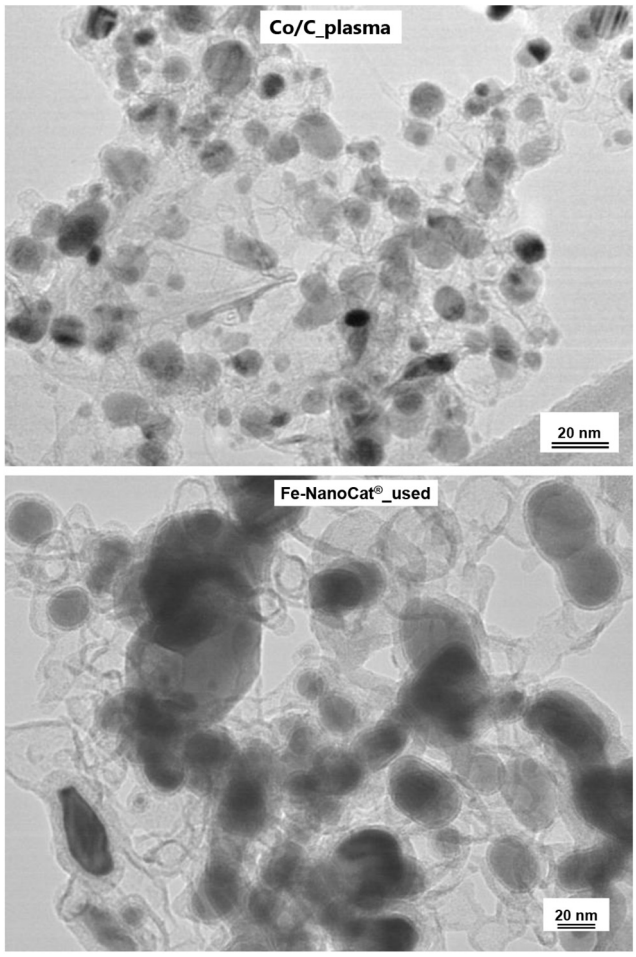

Fig. 4. TEM images contrasting metal nanoparticles in the fresh Co/C catalyst with the agglomerated nanoparticles in the used commercial Fe-NanoCat® catalyst.

Fe/C contained Fe_3Co and Co_7Fe_3 phases mutually except in the CO-reduced 80%Co–20%Fe/C sample that did not have the Co_7Fe_3 phase. The 50%Co–50%Fe/C sample lacked all these phases (Fe_3Co, Co_3Fe_7 and Co_7Fe_3).

Evidence for metal carbides prevailed in the CO-reduced 30% Co–70%Fe/C and 80%Co–20%Fe/C samples, which indicated having cohenite (Fe_2C) and cementite (Fe_3C), while the 50%Co–50%Fe/C sample displayed none of these carbides, whether reduced in H_2 or CO. Nevertheless, only the H_2-reduced 30%Co–70%Fe/C sample showed some evidence for both cementite (Fe_3C) and Hägg carbides (Fe_5C_2). Further, all catalysts (both H_2 and CO-reduced samples) had the unique martensite ($FeC_{0.016}$) phase, except in the CO-reduced 30%Co–70%Fe/C and 50%Co–50%Fe/C samples.

A striking observation was that Co carbides were apparently missing in all the used samples, even after 24 h of carburisation with CO and a further 24 h in the presence of the CO-rich FTS feedstock (*ca.* 30% CO). In addition, there is no evidence of the presence of any metal oxide in the samples. It is therefore assumed that both Co carbides and metal oxides existed (if at all), in minute quantities below the equipment's detection limit. This finding is remarkably important for our samples because it points towards their robustness and resistance to deactivation, since oxidation of metal nanoparticles to form Co_3O_4 or Fe_3O_4 is thermodynamically favoured and would lead to irreversible catalyst deactivation. Therefore, by leveraging on this aspect of synthesising catalysts by plasma, the FTS process efficiency can be improved by prolonged catalysts' lifespan.

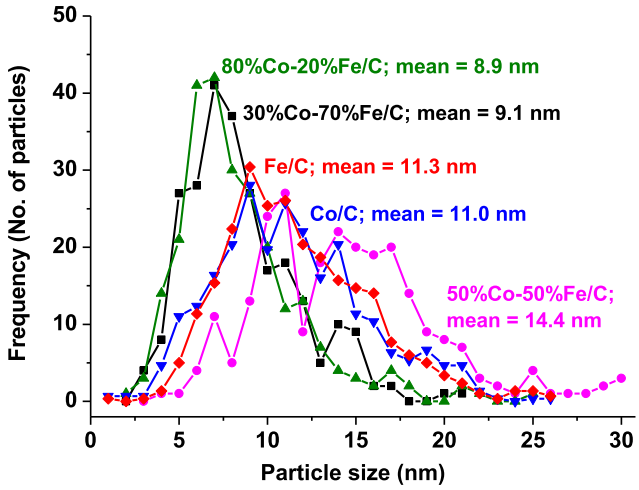

Fig. 5. Particle size distribution of fresh plasma-synthesised catalysts by TEM imaging.

3.2. Catalyst testing

3.2.1. Catalyst pre-treatment in H_2

Activity plots in Fig. 10 show a decreasing CO conversion in the order of Co/C ≫ Fe/C > Co–Fe/C bimetallics for the FTS reaction at

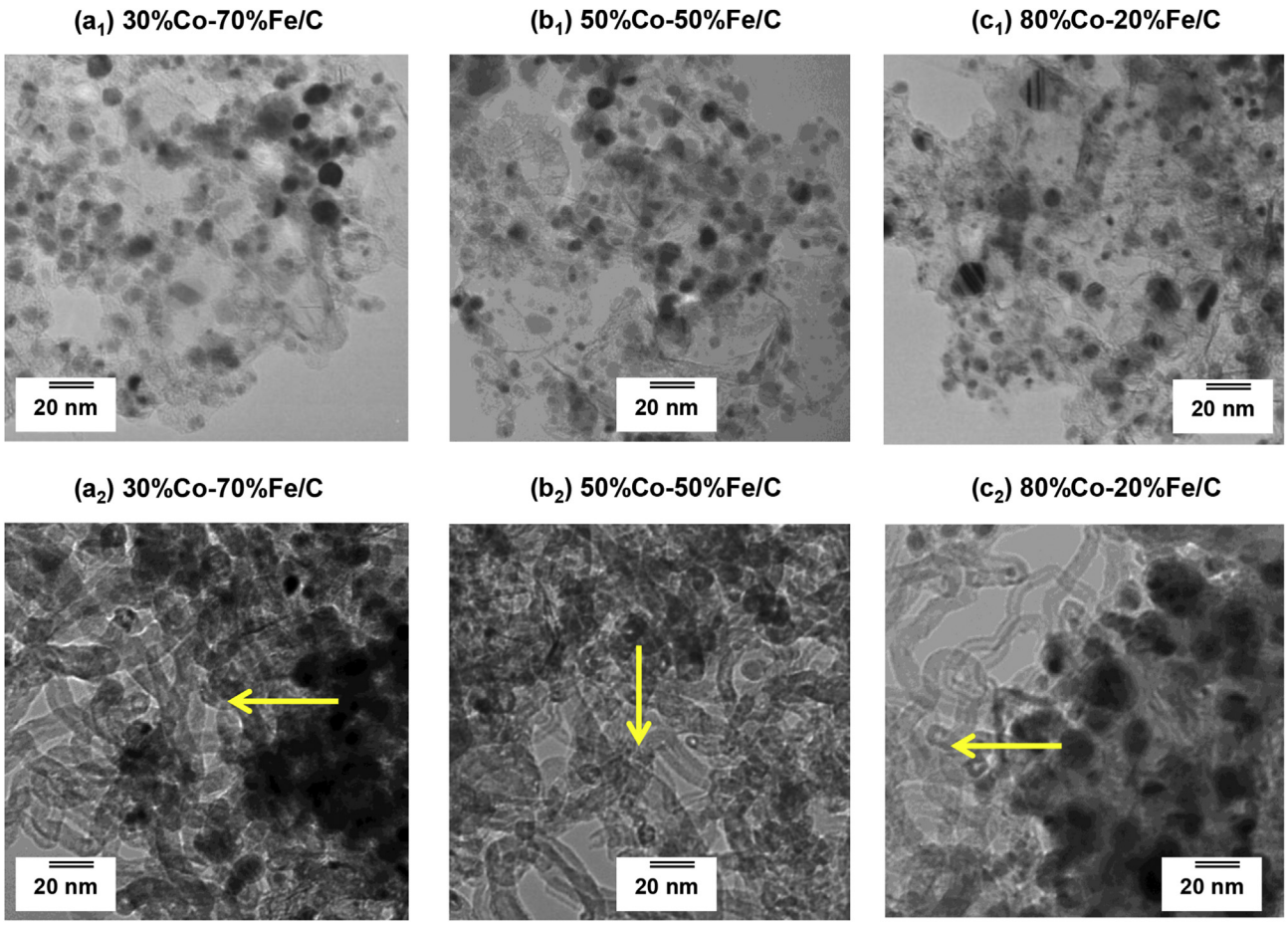

Fig. 6. TEM imaging showing similarities in the fresh bimetallic Co-Fe/C catalysts (row 1) and used catalysts after a CO pre-treatment (row 2) with the nanofilaments seen growing away from the metal centres.

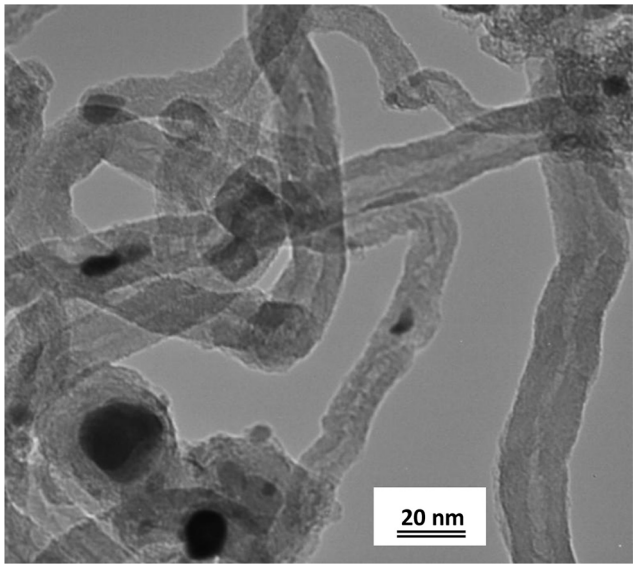

Fig. 7. TEM image of the multi-wall carbon nanofilaments in the CO-reduced 30% Co–70%Fe/C catalyst.

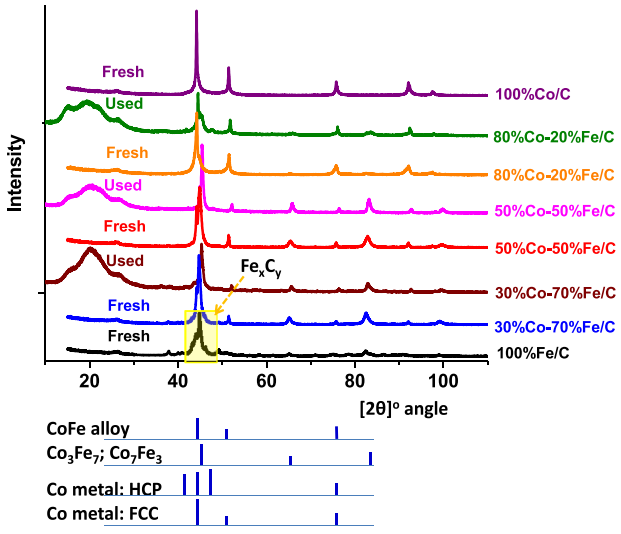

Fig. 8. XRD patterns of fresh and used Co-Fe/C bimetallics after H_2 pre-treatment, benchmarked against the fresh plasma-synthesised Fe/C and Co/C catalysts.

533 K (260°C), while Fig. 11 indicates the final CO conversions at 24 h for the tests done at 493 K or 533 K. Among the bimetallics, only the 80%Co–20%Fe/C catalyst showed some activity at 533 K with a 10% CO conversion, while the single metal Co/C catalyst displayed complete CO conversion. Analysis of the catalysts' selectivity is summarised in Table 2, which gives the catalysts' product spectrum in both gas phase and liquid phase. The product

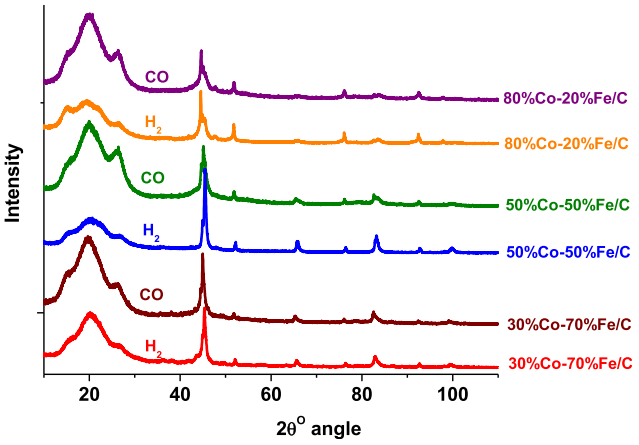

Fig. 9. XRD patterns of the used Co-Fe/C bimetallics, with CO pre-treated catalysts showing higher amorphicity than those pre-treated in H_2.

mass including wax at the lower temperatures (~493 K), as seen in Fig. 12(a). In principle, this is desirable because one can enrich the diesel fraction by raising the FTS reaction temperature, which alters selectivity towards the shorter-chain hydrocarbons by thermal cracking or by increased chain termination mechanisms such as faster molecule desorption. At 533 K, complete CO conversion by the Co/C catalyst was witnessed, with disproportionate production of CH_4 (~46%) and CO_2 (~20%), resulting in a dismal aggregate selectivity of only 19% towards the diesel fraction, see Fig. 12(b). For this reason bimetallic catalysts were formulated to operate in a wider range of conditions without excessive production of CH_4 or CO_2 at the upper end of the temperature range.

Representative selectivity using the 80%Co−20%Fe/C catalyst is shown in Fig. 12(c) and (d) for 493 K and 533 K respectively. Generally, for the bimetallic catalysts operating at comparable CO conversions of approximately 45% (Figs 10 and 11), selectivity towards the formation of gasoline and diesel was more than 80% collectively, since the production of both CH_4 and CO_2 combined

Table 1
Possible phases present in the Co−Fe/C bimetallic catalysts as identified through XRD analysis.

Pre-treatment	Metals		Intermetallic alloys				Carbides			
CO-reduced	Co°	Fe°	Fe_3Co	Co_3Fe_7	CoFe	Co_7Fe_3	Cohenite (Fe_2C)	Hägg (Fe_5C_2)	Cementite (Fe_3C)	Martensite $FeC_{0.016}$
30%Co−70%Fe/C	x	x	x	–	x	x	x	–	x	–
50%Co−50%Fe/C	x	x	–	–	xx	–	–	–	–	–
80%Co−20%Fe/C	–	xx	x	–	x	–	x	–	xx	x
H_2-reduced										
30%Co−70%Fe/C	x	xx	x	x	–	x	–	x	x	xx
50%Co−50%Fe/C	x	x	–	–	x	–	–	–	–	x
80%Co−20%Fe/C	–	xx	x	–	x	x	–	–	–	x

(−) = no phase identified.
(X) = presence of one phase identified.
(XX) = different phases identified, but with similar composition; for example, Fe with space group = cFm3m (225).
Kamacite = with space group cIm-3m (229) were the most prevalent metallic iron phases.

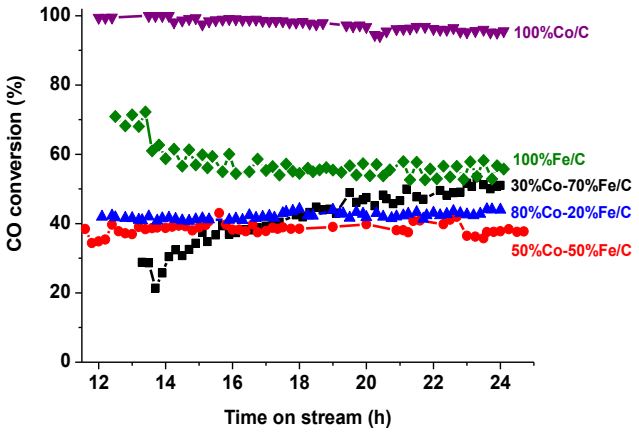

Fig. 10. Activity plots for plasma-synthesised Co/C and Fe/C single metal catalysts compared to the Co-Fe/C bimetallic catalysts tested at 533 K (260 °C) for 24 h.

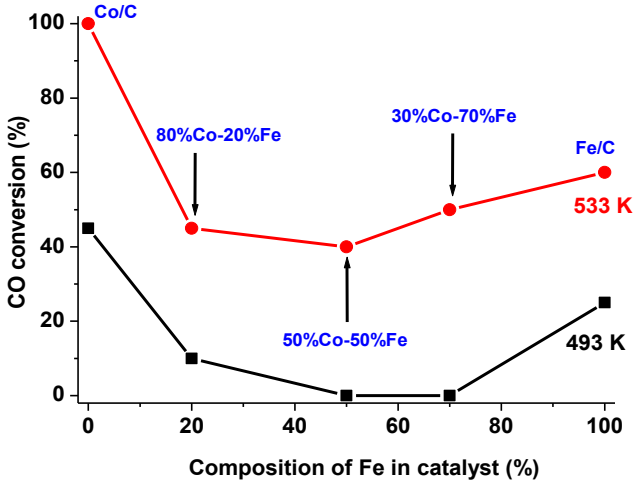

Fig. 11. Activity plots for the plasma-synthesised catalysts with various metal compositions tested at 493 K (220 °C) and 533 K (260 °C).

distribution was plotted according to the number of carbon atoms present in each hydrocarbon chain. Catalyst selectivity was further aggregated in terms of gasoline fraction (C_4-C_{12}), diesel fraction (C_{13}-C_{20}) and waxes (C_{21+}), but analytical limitations existed since the waxes, which are partly solid could not be fully accounted for by our GC systems.

Apparently, the catalysts were quite selective towards diesel production, which was our target fraction. In addition, the Co/C catalyst seemed to generate hydrocarbons of higher molecular was less than 15%, making bimetallic catalysts more attractive for higher-temperature applications. In summary, the following observations were made:

(i) The cobalt-based (Co/C) catalyst was more active and more selective towards the diesel fraction in comparison to the Fe-

Table 2
Summary of catalyst activity and selectivity as determined by GC analysis.

Catalyst	Temperature (K)	Activity	Selectivity						
		% CO conversion[a]	CO_2	CH_4	C_2-C_3	Gasoline C_4-C_{12}	Diesel C_{13}-C_{20}	Wax C_{21+}	H_2O (cm^3)
	493								
100%Fe/C		12	3.0	2.0	0.5	25.6	50.9	18.1	–
30%Co–70%Fe/C		0	–	–	–	–	–	–	–
50%Co–50%Fe/C		0	–	–	–	–	–	–	–
80%Co–20%Fe/C		10	0.4	4.8	0.4	26.9	56.4	11.2	–
100%Co/C		42	0.3	4.9	0.4	49.5	30.8	12.0	55
	533								
100%Fe/C		60	10.2	5.1	1.3	19.4	55.2	8.7	30
30%Co–70%Fe/C		50	7.8	6.8	1.4	29.0	44.5	10.5	25
50%Co–50%Fe/C		40	8.4	9.6	1.4	48.9	24.6	7.5	30
80%Co–20%Fe/C		45	3.2	9.8	0.8	19.1	54.7	12.5	50
100%Co/C		100	19.8	45.6	2.3	8.6	18.7	5.1	40

[a] Conversion at time t = 24 h.

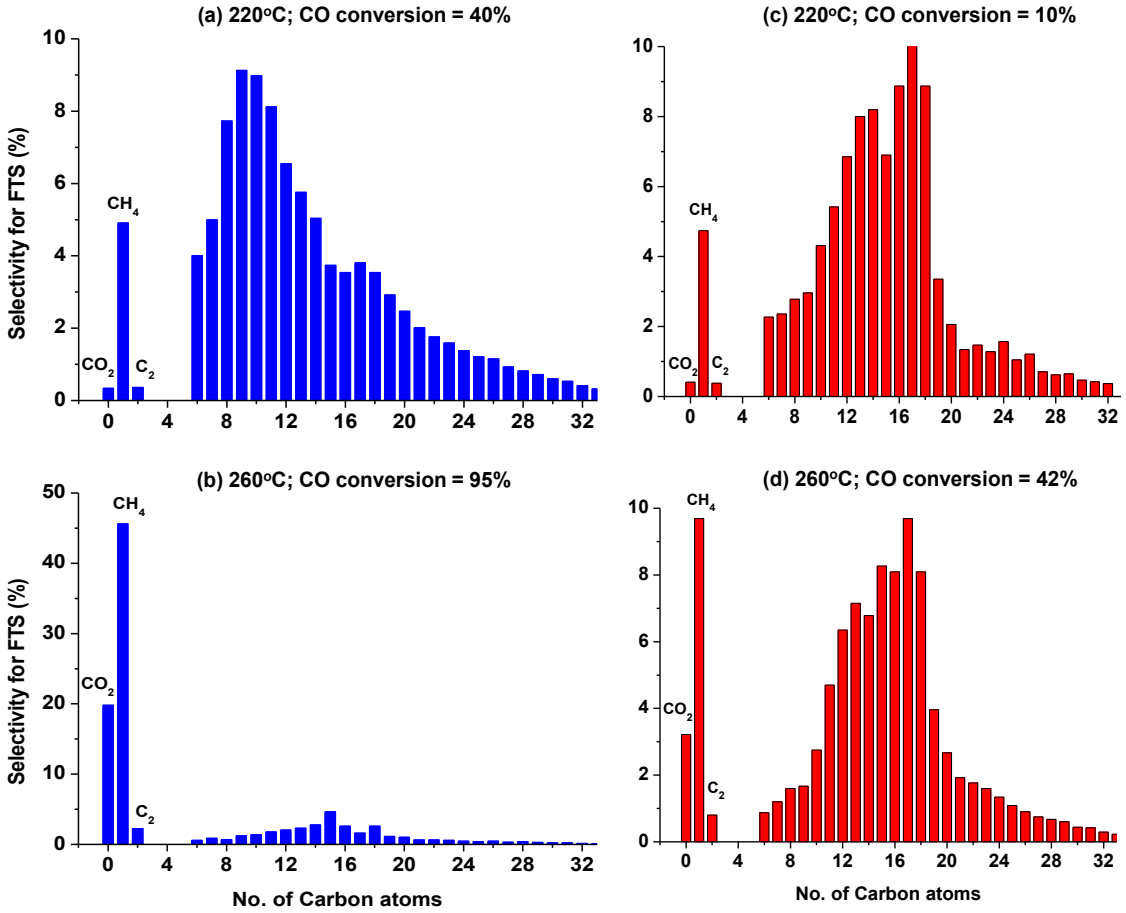

Fig. 12. (a) FTS product spectrum of Co/C catalyst at 493 K (220 °C) and (b) 533 K (260 °C); (c) similar selectivity plots for 80%Co–20%Fe/C at 493 K and (d) 533 K.

based one, which was dependent on other factors such as temperature and reduction conditions.

(ii) Only the Fe/C and 80%Co–20%Fe/C catalysts gave a 50+ % selectivity towards the diesel fraction at both 493 K and 533 K.

(iii) At the higher temperature of 533 K, the Co/C catalyst produced more methane (~46%), but incorporation of Fe in the catalyst significantly lowered the CH_4 selectivity to less than 10% in all the cases.

(iv) At 533 K, all the bimetallics were less selective towards CO_2 formation in comparison to their single-metal counterparts.

(v) All the catalysts displayed limited capacity to form C_2–C_3 products.

(vi) Catalysts with more than 50%Fe in composition produced less water.

3.2.2. *Catalyst pre-treatment in CO*

It was observed that all the catalysts had comparable activity,

with CO conversions of 40+ %, as presented graphically in Fig. 13. Selectivity plots in Fig. 14 demonstrated that all the catalysts had a greater capacity to produce the diesel fraction (C_{13}-C_{20}) than gasoline (C_4-C_{12}).

The Co-only catalyst generated the most water when compared to the other Fe-containing catalysts. The Co/C catalyst produced 55 cm^3 of H_2O at 493 K (40% CO conversion) and 40 cm^3 at 533 K (95% CO conversion), while the Fe/C catalyst produced only 20 cm^3 of H_2O at 493 K (25% CO conversion) and 30 cm^3 at 533 K (55% CO conversion). This was a clear indication of the inability of the Co-based catalyst to lower water formation, while the presence of Fe in the bimetallics can be used to improve the catalysts' capacity to manage water production, as shown in Fig. 15.

In consideration of bimetallic catalysts only, a comparison of their aggregated selectivity obtained at 533 K within a range of 40–50% CO conversion is summarised in Fig. 16. The FTS product fractions for 30%Co–70%Fe/C, 50%Co–50%Fe/C and 80%Co–20%Fe/C catalysts are shown in columns 1, 2 and 3 respectively, where the upper row displays images of H_2-reduced catalysts while the lower row is for CO-reduced samples. From the plots, the following inferences were established:

(i) All the catalysts gave a 50+ % selectivity towards the diesel fraction except the H_2-reduced 30%Co–70%Fe/C and 50% Co–50%Fe/C catalysts, with respective selectivity of 45% and 25%.
(ii) Only the H_2-reduced 50%Co–50%Fe/C catalyst was more selective towards gasoline production (49%), while the other catalysts followed a similar pattern of producing hydrocarbon fractions in decreasing order of diesel ≫ gasoline > wax.
(iii) CO-reduced catalysts produced more diesel than the H_2-reduced catalysts, increasing directly with the Co content in the catalysts.

4. Discussion

4.1. The evolution of an effective FTS catalyst

For catalysts pre-treated in H_2 and tested at 493 K, Co/C was the most active, and it also produced substantial amount of the heavier FTS products such as waxes. Since higher temperatures favour the production of lower molecular fractions, the temperature was raised to 533 K in order to enrich the diesel fraction from the waxes, but the Co/C catalyst generated more of the undesired products such as methane (46%) and CO_2 (20%). Upgrading to the use of bimetallic formulations significantly lowered CH_4 production (<10%) and led to lower selectivity towards CO_2 in comparison to their single-metal counterparts at 533 K.

Besides, catalysts with more than 50%Fe in composition produced less water, probably due to the capacity of the Fe component to perform the reversible WGS reaction. Ordinarily in the WGS reaction given in Eq. (3), the presence of H_2O induces production of H_2 by CO consumption, while the presence of CO_2 produces CO by the consumption of H_2; and both scenarios enrich the syngas composition, thereby improving the FTS reaction. With catalysts pre-treated in CO, the quantity of H_2O produced contracted significantly in all bimetallic formulations, seemingly converging to almost an equivalent amount (*ca.* 20 cm^3) in 24 h.

Generally, it was observed that at equal CO conversions (40–50%), the bimetallic catalysts were more selective towards the production of the diesel fraction after CO-reduction than after

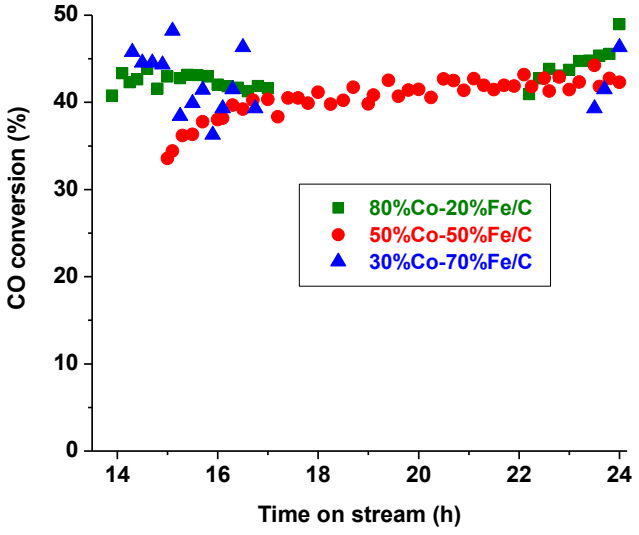

Fig. 13. Activity plots for Co-Fe/C bimetallic catalysts reduced in CO at 673 K for 24 h and tested at 533 K for 24 h.

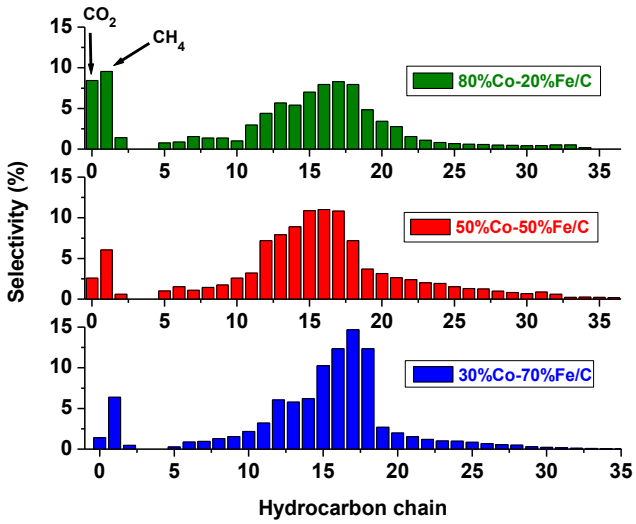

Fig. 14. Selectivity plots of CO-reduced bimetallics, tested at 533 K for 24 h.

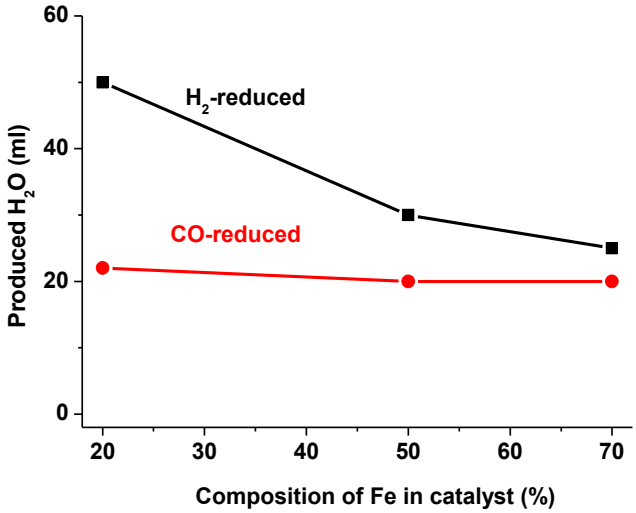

Fig. 15. Plots indicating the amount of water produced after 24 h of FTS by the bimetallic catalysts pre-treated either in H_2 or CO and tested at 533 K.

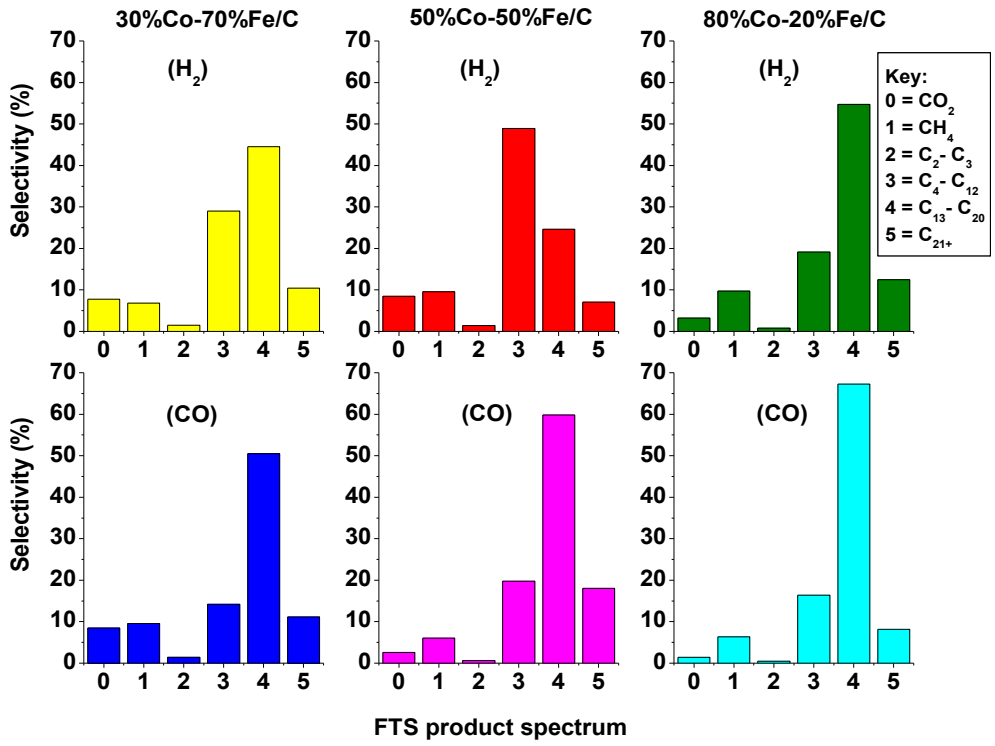

Fig. 16. Aggregate selectivity of the bimetallics at 40 – 50 % CO conversion: 30%Co–70%Fe/C (column 1); 50%Co–50%Fe/C (column 2); and 80%Co–20%Fe/C (column 3); tested at 533 K after reduction in H_2 (row 1) or CO (row 2).

reduction in H_2, particularly the 50%Co–50%Fe/C formulation that showed incomparable gasoline production. The plasma-generated Fe–Co/C bimetallic nano-alloys were designed in order to improve on catalyst durability, and in choosing their Co–Fe binary compositions in reference to Okamoto's phase diagram [13], it was expected that 50%Co–50%Fe and 30%Co–70%Fe formulations would contain identical intermetallic Co–Fe phases, characteristically different from the 80%Co–20%Fe formulation. However, it was observed that the 50%Co–50%Fe formulation had a higher average particle size of 14.4 nm, while the other two formulations had a mean particle size of 9 nm.

Evidence from porosity and surface area analysis, microscopy (SEM and TEM) as well as XRD analysis attested to the suitability of the materials as FTS catalysts. Attributes of a choice FTS catalyst include a non-porous nature and preferably nanometric, with highly dispersed metal nanoparticles entrenched in a graphitic matrix. The inertness of the support inhibits undesirable side reactions. The concomitant existence of metallic Co species with Fe carbides contribute to the catalyst's activity, whereas the manifest absence of metal oxides in the used samples is a noteworthy indicator that these catalysts may not be susceptible to deactivation.

4.2. Potential industrial application

In this study, two reducing media were employed: H_2 or CO gas stream at 673 K for 24 h. Since metallic Co is the active phase in Co-based FTS, carburising Co to carbides is perceived to be detrimental to the process and the use of CO pre-treatment should be avoided. Therefore, the use of hydrogen for the Co-based catalyst would be more desirable, leading to a two-step reduction process: $Co_3O_4 \rightarrow CoO \rightarrow Co^{\circ}$ [14]. However, deactivation of FTS catalysts results from the converse reactions, oxidising the metallic species back to its oxides [15].

On the other hand, the reduction of the Fe-based catalyst is more complex. For example, in the commercial Fe-NanoCat® catalyst that was used in benchmarking the new catalysts: the nano-hematite (Fe_2O_3) is initially reduced to magnetite. Two possible scenarios arise, where H_2 is used to reduce the magnetite to iron (II) oxide and then further to metallic Fe following the trend α-$Fe_2O_3 \rightarrow Fe_3O_4 \rightarrow FeO \rightarrow \alpha$-Fe; or the magnetite is carburised by CO to form Fe carbides as follows: α-$Fe_2O_3 \rightarrow Fe_3O_4 \rightarrow Fe_xC$ [16].

In our case, the Fe-NanoCat® was activated by carburisation using a CO-reduction step. This information is illustrated in the reaction scheme shown in Fig. 17, with the dotted arrows showing that carburisation of FeO and metallic Fe is so rapid that the two phases are basically not observed in the presence of CO. In addition, it has been established that the carburisation ability of reduced Fe species is in the order of α-Fe > FeO > Fe_3O_4 and the conversion of FeO and α-Fe to Fe carbides provides active sites for FTS. This may provide an answer as to why no Fe oxide was observed in our samples by XRD analysis. In principle, it means that alternating the

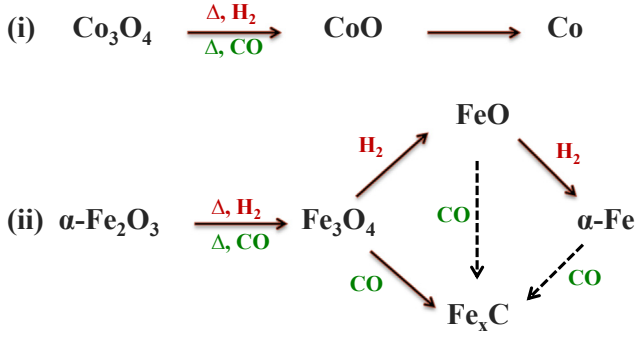

Fig. 17. Possible low pressure reduction routes of nanometric oxides of cobalt and iron using H_2 or CO.

pressure in cycles between high pressure (during FTS) and ambient pressure (during catalyst pre-treatment) can lead to catalyst regeneration without catalyst removal from the reactor.

Since these FTS system is highly reducing comprising a feedstock of 60% H_2 and 30% CO, thermodynamically, the final products of the catalysts are expected to be Co_3O_4 in the Co-catalysed FTS reaction and $Fe_2O_3.H_2O$ or Fe_3O_4 in the Fe-catalysed reaction. Thermodynamic data was obtained using the FactSage™ software (version 6.4) and the summary plots are provided in the supporting information as Figs. S1 and S2.

Under the given FTS reaction conditions, catalyst transformations are most likely to be irreversible in the long term. Nevertheless, in this work we have shown that plasma-synthesised catalysts only have Fe carbides that are active for FTS. This is due to (a) the lack of oxygen during catalyst synthesis and (b) the fact that the plasma process operates far from equilibrium. Should the oxides be formed during FTS, the systems may be regenerated back to the metallic Co or the active Fe_xC species at ambient pressure without sintering, making the FTS attractive for future production of synthetic fuels. A major expectation is the use of biomass-derived syngas in its application, and we recommend the use of plasma-synthesised catalysts for improving the process efficiency.

5. Conclusion

A comparative study was conducted using carbon-supported Co and Fe catalysts synthesised through plasma. The materials were tested for FTS in a 3-ϕ-SCSTR operated isothermally at 493 or 533 K, 2 MPa pressure, and GHSV of 1.0 $cm^3s^{-1}g^{-1}$ of catalyst. The Co/C catalyst was relatively the most active, showing greater propensity to produce a full spectrum of products, including waxes. At 533 K where it had total CO conversion, high selectivity towards production of CO_2 (~20%) and CH_4 (~46%) also advanced. However, both partial and total substitution of Co with Fe in the catalyst significantly lowered the CH_4 selectivity to less than 10% in all the cases. Catalysts with more than 50% Fe in composition produced less H_2O.

It was observed that all the catalysts displayed limited capacity to form C_2–C_3 products, but the Fe/C and 80%Co–20%Fe/C catalysts gave 50+ % selectivity towards the diesel fraction at both 493 K and 533 K. However, only the 50%Co–50%Fe/C catalyst was more selective (49%) towards gasoline fraction at 533 K. All bimetallics were less selective towards CO_2 formation in comparison to their single-metal counterparts at 533 K. Pre-treatment of the bimetallics in CO was observed to create carbon nanofilaments, which led to decreased water production by more than half when compared to the Co-rich catalysts reduced H_2.

Acknowledgements

This research is funded by BioFuelNet NCE Grants, Canada (NSERC grant# 419517-2011 and SSHRC grant #: 900-2011-0001), a network focusing on the development of advanced biofuels. BioFuelNet is a member of the Networks of Centres of Excellence of Canada program. Dr. Kossi Béré, Dr. Jasmin Blanchard and Mr. Henri Gauvin for their technical expertise in the labs; Prof. Nadi Braidy and staff at CCM (Centre de Caractérisation des Matériaux, Université de Sherbrooke) for facilitating the characterisation: Mrs. Irène Kelsey Lévesque and Mr. Carl St.-Louis for BET surface area analysis, Mr. Charles Bertrand for Microscopy (SEM & TEM), and Dr. Stéphane Gutierrez for XRD analysis.

Appendix A. Supplementary data

Supplementary data related to this article can be found at http://dx.doi.org/10.1016/j.biombioe.2016.05.010.

References

[1] A.Y. Khodakov, Enhancing cobalt dispersion in supported Fischer-Tropsch catalysts via controlled decomposition of cobalt precursors, Braz. J. Phys. 39 (2009) 171–175.
[2] S. Li, R.J. O'Brien, G.D. Meitzner, H. Hamdeh, B.H. Davis, E. Iglesia, Structural analysis of unpromoted Fe-based Fischer-Tropsch catalysts using X-ray absorption spectroscopy, Appl. Catal. A 219 (2001) 215–222.
[3] G.L. Bezemer, J.H. Bitter, H.P.C.E. Kuipers, H. Oosterbeek, J.E. Holewijn, X. Xu, et al., Cobalt particle size effects in the Fischer-Tropsch reaction studied with carbon nanofiber supported catalysts, J. Am. Chem. Soc. 128 (2006) 3956–3964.
[4] J. Blanchard, N. Abatzoglou, R. Eslahpazir-Esfandabadi, F. Gitzhofer, Fischer-Tropsch synthesis in a slurry reactor using a nano-iron carbide catalyst produced by a plasma spray technique, Ind. Eng. Chem. Res. 49 (2010) 6948–6955.
[5] J.F. Bengoa, A.M. Alvarez, M.V. Cagnoli, N.G. Gallegos, S.G. Marchetti, Influence of intermediate iron reduced species in Fischer-Tropsch synthesis using Fe/C catalysts, Appl. Catal. A 325 (2007) 68–75.
[6] M. Bahgat, Technology of iron carbide synthesis, J. Mater. Sci. Technol. 22 (2006) 423–432.
[7] H. Okamoto, The C-Fe (carbon-iron) system, J. Phase Equilib. 13 (1992) 543–565.
[8] J. Aluha, P. Boahene, A. Dalai, Y. Hu, K. Bere, N. Braidy, et al., Synthesis and characterisation of nanometric Co/C and Fe/C catalysts for Fischer-Tropsch synthesis: a comparative study using a fixed-bed reactor, Ind. Eng. Chem. Res. 54 (2015) 10661–10674.
[9] J. Aluha, N. Braidy, A. Dalai, N. Abatzoglou, Low-temperature Fischer-Tropsch synthesis using plasma-synthesised nanometric Co/C and Fe/C catalysts, Can. J. Chem. Eng. (May 13, 2016), http://dx.doi.org/10.1002/cjce.22537 (online).
[10] J. Aluha, N. Braidy, A. Dalai, N. Abatzoglou, Low-temperature Fischer-Tropsch synthesis with carbon-supported nanometric iron-cobalt catalysts, in: 23rd European Biomass Conference and Exhibition. Vienna, Austria; 1-4 June, 2015, pp. 988–994.
[11] J.P. Gore, A. Sane, Flame synthesis of carbon nanotubes, in: S. Yellampalli (Ed.), Carbon Nanotubes – Synthesis, Characterization, Applications, InTech, Rijeka, Croatia, 2011, pp. 121–146.
[12] M. Tehrani, A.Y. Boroujeni, C. Luhrs, J. Phillips, M.S. Al-Haik, Hybrid composites based on carbon fiber/carbon nanofilament reinforcement, Materials 7 (2014) 4182–4195.
[13] H. Okamoto, Co-Fe (Cobalt-Iron), J. Phase Equilib. Diff. 29 (2008) 383–384.
[14] A. Tuxen, S. Carenco, M. Chintapalli, C.-H. Chuang, C. Escudero, E. Pach, et al., Size-dependent dissociation of carbon monoxide on cobalt nanoparticles, J. Am. Chem. Soc. 135 (2013) 2273–2278.
[15] G. Jacobs, W. Ma, P. Gao, B. Todic, T. Bhatelia, D.B. Bukur, et al., The application of synchrotron methods in characterizing iron and cobalt Fischer-Tropsch synthesis catalysts, Catal. Today 214 (2013) 100–139.
[16] M. Ding, Y. Yang, B. Wu, Y. Li, T. Wang, L. Ma, Study on reduction and carburization behaviors of iron-based Fischer-Tropsch synthesis catalyst, Energy Procedia 61 (2014) 2267–2270.

9.6. Appendix F: Conference paper – Bimetallic catalysts tested in CSTR

23rd European Biomass Conference and Exhibition, 1-4 June 2015, Vienna, Austria

LOW-TEMPERATURE FISCHER-TROPSCH SYNTHESIS WITH CARBON-SUPPORTED NANOMETRIC IRON-COBALT CATALYSTS

James Aluha[1], Nadi Braidy[1], Ajay Dalai[2], and Nicolas Abatzoglou*[,1]
[1]Department of Chemical & Biotechnological Engineering, Université de Sherbrooke, Sherbrooke, QC, Canada J1K 2R1
[2]Department of Chemical & Biotechnological Engineering, University of Saskatchewan, Saskatoon, SK, Canada S7N 5A9
*Corresponding author: Nicolas.Abatzoglou@USherbrooke.ca

ABSTRACT: Marketable fuel production from biomass through Fischer-Tropsch synthesis (FTS) process is the main objective of this work. Today, there is need for higher performance FTS catalysts that will lead to sustainable production of biofuels because of the global escalating energy prices, developing environmental concerns and more stringent legislation, particularly the push towards sulphur-free diesel. By developing efficient non-porous catalysts in the nanometric range, operating in the diffusion-controlled 3-phase FTS regime is avoided; this is a must in this direction and constitutes an experimentally proven choice. Potential carbon-supported bimetallic formulations based on iron and cobalt, synthesised by plasma-spray method were produced and tested as FTS nanocatalysts in a continuously-stirred slurry tank reactor (CSSTR) at 260°C, 20-bar pressure and gas hourly specific velocity (GHSV) of 3,600 $ml.g^{-1}.h^{-1}$ for 24 h. Three catalytic formulations tested were: 30%Co-70%Fe, 50%Co-50%Fe, and 80%Co-20%Fe. Their analysis by Transmission Electron Microscopy (TEM) indicated an average particle size of 9.1, 14.4 and 8.9 nm, and BET specific surface areas of 89, 89 and 65 $m^2.g^{-1}$ respectively. Overall, the materials showed comparable selectivity of ~76% towards the production of C_5-C_{22} (petrol + diesel fractions), but catalyst activity decreased in the order of 30%Co-70%Fe >> 80%Co-20%Fe > 50%Co-50%Fe, with carbon monoxide (CO) conversions of 50, 42 and 35% respectively after 24 h on stream.
Keywords: plasma, carbon-supported, iron-cobalt, catalysts, Fischer-Tropsch

1 INTRODUCTION

Low temperature Fischer-Tropsch Synthesis (LTFTS) is one of the targeted technologies for the production of biofuels from renewable resources. With higher and more volatile prices for crude oil, coupled with increasing demand, the pursuit for alternative sources of energy is escalating. Prospective renewable sources such as biofuels are progressively receiving attention because they can also lower greenhouse gas emissions. Since FTS is a commercially viable process, conversion of biomass into syngas – a mixture of H_2 and CO – can be integrated into the scheme. As it is today, syngas is reacted over a cobalt (Co) or iron (Fe) metal catalyst to form polymeric hydrocarbon chains that constitute petrol (C_5-C_{11}) and diesel (C_{12}-C_{22}), among other products.

In principle, syngas may be produced from any hydrocarbon feedstock such as fossil fuel, natural gas, coal or biomass. For commercial production of gasoline or diesel, the lowest cost path would be the most favourable. Biomass is apparently one of the most abundant and cheapest renewable resources of hydrocarbons in nature. Since Co catalysts are more sensitive to sulphur-poisoning than Fe catalysts, and given the relatively higher cost of Co to Fe, more efficient removal of sulphur is required for the Co-catalysed reaction than for the Fe catalysts that are more sulphur-tolerant [1]. Feed stock from biomass may involve minor costs in syngas clean-up, particularly from sulphur present in minute quantities [2].

Various techniques have been employed in the preparation of these catalysts, including impregnation, precipitation or ion-exchange among others, but the current plasma spray method is gaining traction although it is a relatively new technique [3]. Plasma technology has highly-coveted benefits such as shortened preparation time, decreased number of preparation steps, lower overall energy requirements, production of uniform metal particle size, high distribution of nanometric and active species as well as enhanced lifespan [4], [5]. Since we reported the use of plasma [3], it goes hand in hand with carbon as our support of choice, making the catalysts not susceptible to poisoning or deactivation from the effect of coking [6], [7], or carburization particularly for Co-based catalysts [8]. It is believed that non-stoichiometric Fe-oxide-carbide species are the active phase in the Fe-based catalysts [9], while Co must be in the metallic state for the Co-based catalysts [10]. By converting syngas mixtures originating from natural gas, which is rich in hydrogen (with ratio H_2:CO ≈ 2:1), the Co catalysts deliver higher conversions in comparison to Fe catalyst, besides giving higher selectivity towards paraffins [11]. Moreover, since cobalt operates better at lower temperatures, it forms more of the longer chain fractions, which makes it more selective towards the desired diesel fraction than the petrol. Moreover, the waxes so produced can be hydrothermally cracked to generate the shorter chain fractions that could enrich the biofuels.

Over Co catalysts, approximately 2 H_2 molecules react with 1 CO molecule to produce 1 hydrocarbon unit [-CH_2-] and 1 H_2O molecule. This molar H_2:CO ratio is normally taken as 2.1 since a ratio of 2.15 is required for Co catalysts, but may be as low as 1.7 for Fe-based catalysts in LTFTS. At higher temperatures, water-gas shift (WGS) rapidly goes into equilibrium, allowing any CO_2 formed to be converted to FTS products via reverse WGS reactions. Theoretically, if the syngas ratio of [H_2:(2CO+3CO_2)] approaches 1.05, all of the H_2, CO and CO_2 can be converted to Fischer-Tropsch products [12]. Since the Fe-catalyst inherently performs the WGS reaction, it supplements the feed stock by generating additional H_2 gas back into the FTS reaction [13].

In addition, since metallic species have been found to be the active phase in Co-based FTS, catalyst deactivation results from Co^o re-oxidation to the oxidic phase. Therefore, operating in a highly-reducing environment, such as that of syngas mixtures is seen as an advantage since the catalyst's long-term activity and stability will be highly dependent on its reducibility. Nevertheless, it has been shown that Co is poor in enhancing WGS reaction, and high vapour pressure of water in the system leads to its re-oxidation and

subsequent deactivation [14], [15]. Co-based catalysts have also been found to deactivate due to the formation of irreducible metal-support compounds, such as $CoAl_2O_4$, by way of incorporating CoO in the Al_2O_3 support [16]. In an effort to improve catalyst performance, the promotional effect of other elements has been investigated for both Co- and Fe-based systems. For example, increasing the basicity of a catalyst surface by adding Ca, Mg or La influences the rate constant of FTS reaction [17], while K promotes selectivity towards the production of olefins, but restrains the formation of methane (CH_4) and light hydrocarbons in Fe-Mn catalysts [18]. It has been observed that Au improves the reducibility of Co on Al_2O_3 support. Since an effective Co catalyst must be in the metallic state, the strong metal-support interaction in Co/Al_2O_3 hinders the Co reduction [19]. Where deliberate studies of bimetallic formulations were conducted, including Co-Fe [20], [21], [22], Fe-Cu [23], [24], Co-Mn [25], [26], and Fe-Mn [18], [27], [28], the catalysts were not plasma-synthesised and supported on carbon at the same time.

Since our previous investigations were based on a plasma-synthesised Fe-only formulation [3], in this work, we report for the first time nanometric plasma-derived catalysts based on Co-Fe bimetallics and supported on carbon, which are currently being developed for application in LTFTS. The catalysts were tested in a 3-phase continuously-stirred slurry tank reactor (CSSTR) at 20-60 bar pressure, within the typical low-temperature regimes of 200-240°C and extrapolated to 260°C. High pressure is warranted to enhance CO conversion and lower both the process and reactor volume. The low-temperature operation leads to linear alkane structures as well as the production of longer chain hydrocarbons in the C_{10}-C_{20} range that is characteristic of excellent diesel fuel and minimises the formation of C_5-C_9 fractions. The catalysts were characterised by various techniques, such as Brunauer-Emmett-Teller (BET) surface area, Transmission Electron Microscopy (TEM), and X-ray diffraction (XRD) analysis, among others. This paper discusses catalyst synthesis procedures with the testing and characterisation of the new materials.

2 EXPERIMENTAL METHODS

2.1 Catalyst synthesis

To prepare catalysts of bimetallic compositions, various masses of Co and Fe amounting to 60 g of the metals were mixed under stirring conditions with 300 ml of mineral oil for at least 2 h, forming a homogeneous suspension, which was then introduced directly into the plasma spray at a flow rate of 8.2 $ml.min^{-1}$. The HF-60 kW plasma system operates with PL-50 coil and subsonic nozzle. Gas flow rates in the sheath of the flame were: 75 SLPM (standard litres per minute) for Argon (Ar) and 10 SLPM for H_2. The other Ar gas flow rates were 23 SLPM (central) and 10.4 SLPM (powder). Voltage was set at 6.6 kV, with current at 4.4 A and 0.5 A (grounding), which provided power of about 29 kW during the process. Fixed pressure was set at 250 Torr, but initial and final pressure values were kept approximately at 30 and 304 Torr, respectively. Pressure of 1 Torr = 1/760 of a standard atmosphere (~133 Pa). After catalyst synthesis, the materials were harvested and tested for FTS. Table I lists the mass of each metal employed in catalyst preparation.

Table I: Co and Fe powder masses used for catalyst preparation

Sample (expected composition)	Powder mass (g)		
	Co	Fe	Total
30%Co-70%Fe/C	18	42	60
50%Co-50%Fe/C	30	30	60
80%Co-20%Fe/C	48	12	60

2.2 Catalyst testing

A 3-phase CSSTR system was deployed. The syngas mixture ratio of H_2:CO = 2:1 was 60% H_2 and 30% CO balanced with 10% Ar for mass balance determination. Catalyst activity was calculated with CO amount converted in the Fischer-Tropsch reaction according to the equation [29]:

$$CO\ conversion\ (\%) = \left[\frac{CO_{in} - CO_{out}}{CO_{in}}\right] x \left[\frac{Ar_{in}}{Ar_{out}}\right] x\ 100$$

A typical run involved about 5 g of catalyst, which was reduced at 400°C in pure H_2 gas flowing at the rate of 250 SCCM (standard cubic centimetres per minute) for 24 h and then tested for FTS for at least 24 h in 150 ml of hexadecane solvent (C_{16}). This amounts to gas hourly specific velocity GHSV of 3,600 $ml.g^{-1}.h^{-1}$. Reaction conditions were initially set at 220°C and 20-bar pressure, with a high stirring rate of about 2,000 rpm prescribed to circumvent operation in the diffusion-limited regime. Further tests were conducted at 260°C.

2.3 Catalyst characterization

2.3.1 BET surface area

Fresh catalysts were analysed for their BET specific surface areas using the Micromeritics Accelerated Surface Area Porosimeter (ASAP 2020), according to the BET method. Samples were degassed at 250°C for 50 h and evacuated until a pressure of less than 10 µmHg was obtained in the sample holder. BET physisorption was then performed using nitrogen at –196°C starting with a pressure below 10 µmHg.

2.3.2 Transmission Electron Microscopy (TEM)

TEM imaging and analysis was conducted on a Hitachi H-7500 Microscope, which is fitted with a tungsten filament operated at an accelerating electron beam of 120 kV. Images in the bright field mode were captured by the AMT 4k x 4k CCD Camera System Model X41.

2.3.3 X-ray Diffraction (XRD)

Elemental composition and crystalline phases in the catalysts were identified by XRD analysis using a Philips X'pert PRO Diffractometer from PANalytical. The system is fitted with a PIXcel-1D detector and Ni-filters for the Cu Kα radiation produced at 40 kV and 50 mA with the wavelength of alpha1 being 1.5406 Å. The instrument was set in the Bragg-Brentano configuration. The XRD patterns were recorded in the range of 20° to 110° [2θ] angle at a step size of 0.040° [2θ] angle. Data analysis was conducted using the Materials Data Inc. software: MDI JADE 2010 (version 2.6.6) and HighScore Plus (version 3.0e) for Rietveld Quantitative Analysis.

3 RESULTS

3.1 Catalyst activity

Gas-phase data, collected at the reactor exit, indicated that all catalysts produced less than 10% CO_2 and CH_4 each, with very low generation of C_2-C_4 molecules, primarily C_2, (Table II).

Table II: Product spectra in gas effluents

Catalyst	Temp°C	X *	Concentration (%)				H_2O
		(%)	CO_2	CH_4	C_2H_6	C_2H_4	(ml)
30%Co	220	0	0.0	0.0	0.0	0.0	-
50%Co	220	0	0.0	0.0	0.0	0.0	-
80%Co	220	10	0.4	4.8	0.4	0.0	-
30%Co	260	50	6.3	6.6	1.3	0.1	25
50%Co	260	35	7.5	8.5	1.3	0.1	30
80%Co	260	42	3.2	9.8	0.7	0.1	50

*X = Final CO conversion at the end of 24 h.

It was observed that only the 80%Co-20%Fe/C catalyst indicated some activity at 220°C, with a CO conversion of 10%. Nevertheless, on average the activity was almost identical for all the catalysts at 260°C, giving CO conversion of over 40%, (Fig. 1). However, the 30%Co-70%Fe/C catalyst was the best performing catalyst at the 24th h, sitting at 50% CO conversion and still showing some improvement in activity, while the 50%Co-50%Fe/C catalyst was the least performing catalyst formulation with 35% CO conversion, exhibiting some deactivation. The activity of 80%Co-20%Fe/C catalyst remained stable at 42% CO conversion. Within 24 h, 80%Co-20%Fe/C generated the highest amount of water, totalling 50 ml, followed by 50%Co-50%Fe/C with 30 ml, and lastly, by 30%Co-70%Fe/C, with 25 ml.

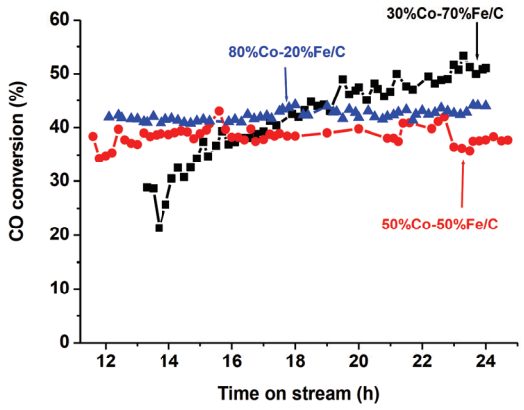

Figure 1: Catalyst activity at 260°C, 20-bar

3.2 Catalyst selectivity

At 220°C, 30%Co-70%Fe/C and 50%Co-50%Fe/C catalysts did not show any significant activity; only the 80%Co-20%Fe/C formulation was active. At both 220 and 260°C, it was observed to be consistent in its product distribution (C_6-C_{32+}) having CO conversions of 10 and 42% respectively. The distribution of molecules by the number of carbon atoms in the hydrocarbon chains produced represents the catalyst's selectivity, (Fig. 2).

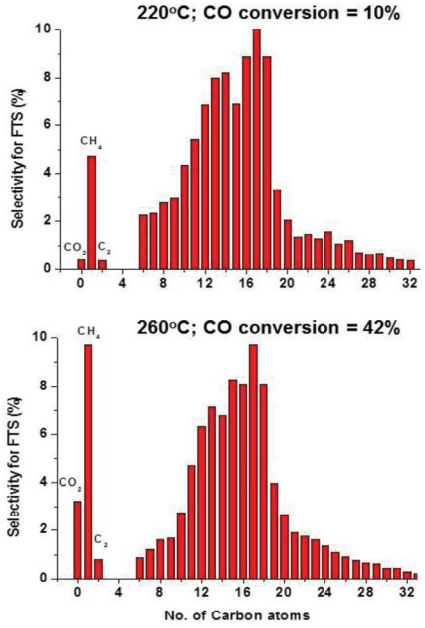

Figure 2: Selectivity of 80%Co-20%Fe/C tested at 220°C and 260°C with 20-bar pressure for 24 h

Cumulatively, 50%Co-50%Fe/C seemed to produce more undesired by-products (methane and CO_2 combined) than the other 2 catalysts. In terms of fuel fractions formed, the 80%Co-20%Fe/C and 30%Co-70%Fe/C were found to be richer in diesel fractions at average CO conversions of 42 and 45%, respectively (Fig. 3), while 50%Co-50%Fe/C was more selective towards the production of petrol fractions, with CO conversion of less than 40%.

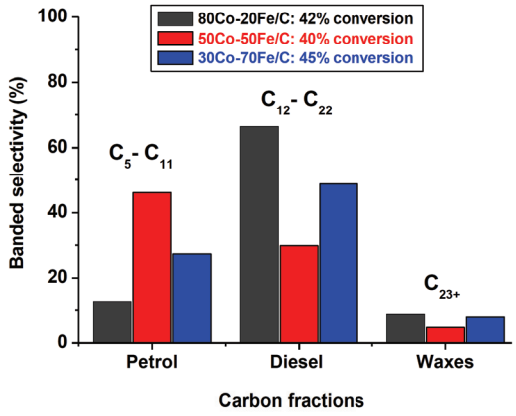

Figure 3: Comparison of catalyst selectivity towards the liquid-phase fractions.

Therefore, overall, 50%Co-50%Fe/C was the least performing catalyst in the pack, with total selectivity of 83% towards C_{6+} and activity of ~40%, while the other 2 formulations had total selectivity of 86% towards C_{6+} and activity greater than 40% CO conversion. Although steadily active, the major disadvantage with the 80%Co-20%Fe/C catalyst was that it generated twice as much water as the 30%Co-70%Fe/C formulation.

3.3 Catalyst characterisation

3.3.1 BET surface area

BET-specific surface area was 89 $m^2.g^{-1}$ for both the 30%Co-70%Fe/C and 50%Co-50%Fe/C catalysts, and somewhat lower for the 80%Co-20%Fe/C formulation, at 65 $m^2.g^{-1}$. All samples seemed to display some degree of micro-porosity, with pore size distribution of less than 10 nm. Since the samples were nanometric, this could be explained by nano-porosity of the carbon matrix of the catalytic formulations tested.

3.3.2 Transmission Electron Microscopy

A representative TEM image of fresh bimetallic catalysts (Fig. 4) and overlaid plots of their particle size distribution (Fig. 5) are provided. In each case, 250 nanoparticles were measured. Mean particle size of 30%Co-70%Fe/C and 80%Co-20%Fe/C was identical, and equivalent to 9.1 and 8.9 nm, respectively, while that of 50%Co-50%Fe/C was the largest, at 14.4 nm.

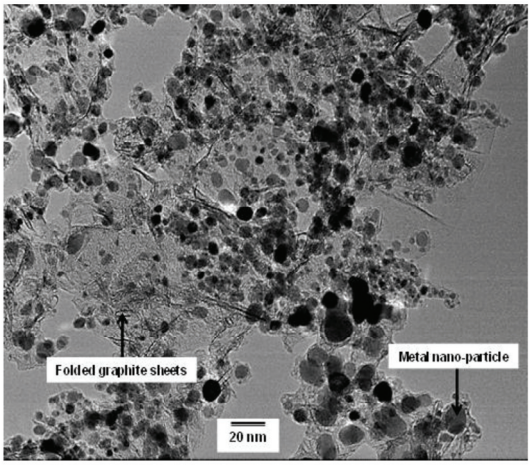

Figure 4: TEM image of 50%Co-50%Fe/C

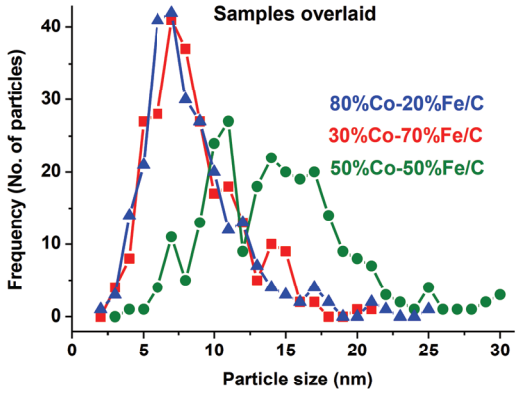

Figure 5: Particle size distribution plots from TEM imaging

3.3.3 XRD Analysis

Evidence from advanced XRD analysis indicated that augmenting the amount of Co in the bimetallic samples increased Co peak size and decreased Fe-related peaks (Fig. 6). As references XRD patterns of the Co-only and Fe-only catalysts were compared to those of the bimetallics. It was observed that the typical intense Fe peaks were extinct in the Fe/C catalyst probably due to diminished crystallite size, which leads to peak broadening, or as a result of being supported on an amorphous carbon support.

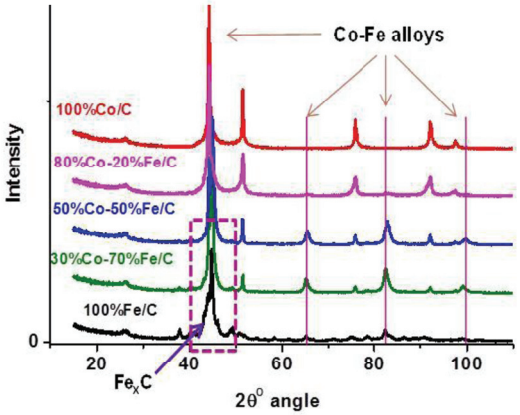

Figure 6: XRD patterns of Co-Fe/C bimetallics compared to single metal catalysts

It was found that the 30%Co-70%Fe/C formulation contained both Co and Fe metallic species, and carbides, namely cementite (θ-Fe_3C), and the Co_3Fe_7 alloy. Similarly, the 80%Co-20%Fe/C formulation comprised of segregated metallic species (Co^o and Fe^o), in addition to two types of carbides: cementite, and the Hägg carbides, (χ-Fe_5C_2). On the other hand, the 50%Co-50%Fe/C did not show any carbides, but consisted of 3 alloy species (Co-Fe, Fe_3Co_7 and Co_3Fe_7) far and above the concurrent presence of Co^o and Fe^o. It is plausibly speculated that in the 50%Co-50%Fe/C formulation, the presence of many alloy phases as well as the lack of Fe-carbides species could have contributed largely to its relatively inferior performance in FTS.

4 DISCUSSION

4.1 Fischer-Tropsch catalysis from biomass

Challenges are numerous in the petrochemical industry, and one of them mainly involves the production of effective catalysts: with good activity, high selectivity and long lifespan. It is desirable for catalysts to be produced under milder conditions and with relatively fewer steps at an acceptable price. To lower costs, using biomass in the production of for example, diesel that is free of sulphur, nitrogen and aromatic compounds seems attractive besides base metal (Fe and Co) catalysts being tailored at the nanoscale level for the application. Such a measure would reduce process costs and limit prevalence of catalyst poisoning, which in turn would prolong the catalyst's chemical reactivity and lifespan. Factors that are presently believed to play a significant role in FTS include the overall capacity of the nano-catalysts to create high CO conversions, small metal clusters (particle size within the 25-300 nm range), the catalyst structure (pellet size and shape), low porosity, chemical composition, metal oxidation state, and synergistic inter-particle interactions [30].

By using syngas originating from biomass feedstock, limited catalyst poisoning is anticipated from sulphur,

because biomass is very low in sulphur content. In addition, eliminating the sulphur purification step in fuel production would lead to significant energy and cost savings, besides the sulphur-free diesel fuel creating a platform for cheaper metals like palladium to be used in the auto-catalyst instead of platinum or rhodium, since sulphur poisons the Pd-based catalyst in diesel-driven cars. Furthermore, sulphur-free diesel emits lower particulate pollutants from car exhausts (such as SO_2, H_2SO_4). These emissions are the foundation of acid rain that has disastrous environmental effects such as causing corrosion on buildings, respiratory health problems, and death of aquatic life, among other negative impacts.

Nonetheless, over the past 20 years, regulations to curb exhaust emissions in the car industry have led to dramatic improvements in air quality owing to the incremental implementation of Euro I to Euro VI standards. This is a fine example of the development of new technologies being motivated by environmental concerns and stringent legislation, which has caused a considerable drop in the levels of nitrogen oxides (NOx) and particulate matter such as unburnt hydrocarbons from diesel engines.

Some of the issues addressed by our approach in Fischer-Tropsch catalysis are summarised in Table III.

Table III: Industrial concerns addressed by our catalysts

Approach	Rationalisation	Industrial concern	Ref.
1. Plasma Technology	**(a) Simplicity:** Plasma spray method is a single-step application; it is simpler, yet effective	Application of complex methods of catalyst synthesis	[31]
	(b) Metal dispersion: Highly dispersed metal nano-particles embedded in a carbon matrix	Catalyst deactivation - sintering	[12]
2. Biomass Feedstock	**Low-sulphur content:** Biomass feedstock contains less sulphur than fossil fuel feedstock	Catalyst deactivation - sulphur poisoning	[1] [7] [32]
3. Carbon support	**(a) Cost reduction:** Carbon is cheap and abundant in nature; cost of catalyst = cost of (metal + support)	High capital costs	[32]
	(b) Carburization: no impact Carbon does not adversely affect catalyst performance	Catalyst carburization	[8]
	(c) Deactivation: no impact Carbon support does not impact the catalyst negatively	Catalyst deactivation - coking	[7] [6]

4.2 Summary: catalyst performance

Whereas it is easier to optimize macro-level parameters, such as catalyst pellet dimension and shape, fluid flow and hydrodynamics, reactor pressure drop as well as mass and heat transfer effects in the reactor, it is more difficult to optimise micro-level parameters that involve nano-particle structures and local reaction conditions around the nano-particles which, in turn, significantly impact catalyst activity, selectivity and stability. Success in FTS will mean precise control of size, shape, spatial particle distribution of active species, surface composition, electronic structure, and both the thermal and chemical stability of individual nano-components.

The strategic advantage of nano-materials lies in utilizing the large surface area of nano-crystals, in addition to their surface electronic properties. Metallic nano-particles have a large surface-to-volume ratio when compared to bulk materials, a property that could be appropriate in speeding up chemical reactions. In our case, we found plasma synthesis in catalyst production to be the most ideal method of producing high quality FTS catalysts with uniform and reproducible attributes. In addition, the potential for large scale production is practically viable to a large extent.

Furthermore, we noticed from the various analyses that a good proportion of our materials contained segregated phases of pure metal (Co^o and Fe^o). Since it has been postulated that FTS activity of Co-based catalysts is a function of both metallic state and crystallite size [33], it is well fitting to observe that a predominant presence of Co^o phase in all our catalysts could have contributed considerably to their performance.

It is suspected that the larger particle size (~14 nm) in the 50%Co-50%Fe sample resulted from particle fusion, giving rise to the numerous alloy phases (Co-Fe, Co_3Fe_7 and Fe_3Co_7), and we therefore think that these alloys are not active for FTS reaction. Evidence indicates that the active species in the Fe-based FTS catalysts are the Fe-carbides [9]. We are inclined to concur with this observation because amongst the three catalysts that we tested, only the Co-rich 80%Co-20%Fe formulation consisted of the unique Hägg Fe-carbides (χ-Fe_5C_2). Not only was this the most active catalyst at both 220 and 260°C, but it also indicated consistent CO conversion of 42% right from the offset of the reaction (Fig. 2). Likewise, we observed that the 30%Co-70%Fe formulation also had carbides, but of the cementite type (θ-Fe_3C), which did not seem to promote the activity of the catalyst from its onset. We are therefore of the opinion that the Hägg Fe-carbides provide the most active phase in the Fe-based Fischer-Tropsch catalysis.

Other properties of the catalyst as well as the possible species found in the fresh catalysts are summarised in Table IV.

Table IV: Summary of catalyst properties of Co-Fe bimetallic samples

Property		Sample		
Composition		30%Co	50%Co	80%Co
BET surface area (m^2/g)#		89	89	65
Particle size (nm)†		9.1	14.4	8.9
Conversion of CO (%)	220°C	0	0	10
	260°C‡	45	40	42
Selectivity (%)*	Petrol	27.3	46.1	12.8
	Diesel	48.7	29.9	64.7
	Total	76.0	76.0	77.5
	H_2O (ml)	25	30	50
XRD analysis	Metals	Fe^o Co^o	Fe^o Co^o	Fe^o Co^o
	Alloys	Co_3Fe_7	Co-Fe Co_3Fe_7 Co_7Fe_3	-
	Carbides	Fe_3C	-	Fe_3C Fe_5C_2

#Fresh catalyst;
†Particle size analysis by TEM;
‡Average CO conversion over 24 h;
*Activity at 260°C, 20-bar; petrol fraction (C_5-C_{11}) and diesel fraction (C_{12}-C_{22}).

5 CONCLUSION

Bimetallic Co and Fe formulations synthesised by plasma spray technology have not been studied before. In this work, we have established potential carbon-supported catalysts for FTS, aiming at nanometric Co-Fe bimetallics. The catalysts were tested for Fischer-Tropsch activity in a CSSTR for 24 h at 220 and 260°C, 20-bar pressure and GHSV of 3,600 $ml.g^{-1}.h^{-1}$. Prior to the test,

the catalyst was reduced *in situ* at 400°C in hydrogen gas flowing at 250 SCCM (1-2 bar pressure) for 24 h.

Three catalyst formulations – 30%Co-70%Fe, 50%Co-50%Fe, and 80%Co-20%Fe – were evaluated. They showed that, on average, they were comparable in performance, giving activity of ~40% CO conversion and ~76% selectivity towards the production of petrol and diesel fractions combined (C_5-C_{22}). However, after 24 h on stream, 30%Co-70%Fe/C presented signs of activity improvement towards 50% CO conversion, 80%Co-20%Fe/C remained stable at 42% CO conversion, while 50%Co-50%Fe/C showed deactivation with activity dropping to 35% CO conversion.

6 REFERENCES

[1] T.L. Chew, S. Bhatia, Catalytic processes towards the production of biofuels in a palm oil and oil palm biomass-based biorefinery, Bioresour. Technol. 99 (2008) 7911-7922.

[2] J. Hu, F. Yu, Y. Lu, Application of Fischer-Tropsch synthesis in biomass to liquid conversion, Catalysts 2 (2012) 303-326.

[3] J. Blanchard, N. Abatzoglou, R. Eslahpazir-Esfandabadi, F. Gitzhofer, Fischer-Tropsch synthesis in a slurry reactor using a nano-iron carbide catalyst produced by a plasma spray technique, Ind. Eng. Chem. Res. 49 (2010) 6948-6955.

[4] C.J. Liu, G.P. Vissokov, B.W. Jang, Catalyst preparation using plasma technologies, Catal. Today 72 (2002) 173-184.

[5] A.E. Rutkovskii, L.R. Vishnyakov, A.A. Chekhovskii, N.I. Kirkun, Use of plasma technology in creating catalysts on carriers, Powder Metall. Met. C+, 39 (2000) 207-209.

[6] A.N. Pour, S.M. Shahri, Y. Zamani, M. Irani, S. Tehrani, Deactivation studies of bifunctional Fe-HZSM5 catalyst in Fischer-Tropsch process, J. Nat. Gas Chem. 17 (2008) 242-248.

[7] M.E. Dry, Fischer-Tropsch synthesis over iron catalysts, Catal. Lett. 7 (1990) 241-252.

[8] M. Ding, Y. Yang, B. Wu, J. Xu, C. Zhang, H. Xiang, Y. Li, Study of phase transformation and catalytic performance on precipitated iron-based catalyst for Fischer-Tropsch synthesis, J. Mol. Catal. A: Chem. 303 (2009) 65-71.

[9] J.F. Bengoa, A.M. Alvarez, M.V. Cagnoli, N.G. Gallegos, S.G. Marchetti, Influence of intermediate iron reduced species in Fischer-Tropsch synthesis using Fe/C catalysts, Appl. Catal. A: Gen. 325 (2007) 68-75.

[10] W. Chu, P.A. Chernavskii, L. Gengembre, G.A. Pankina, P. Fongarland, A.Y. Khodakov, Cobalt species in promoted cobalt alumina-supported Fischer-Tropsch catalysts, J. Catal. 252 (2007) 215-230.

[11] V.R. Calderone, N.R. Shiju, D. Curulla-Ferré, S. Chambrey, A. Khodakov, A. Rose, J. Thiessen, A. Jess, G. Rothenberg, De novo design of nanostructured iron-cobalt Fischer-Tropsch catalysts, Angew. Chem. Int. Ed. Engl. 52 (2013) 4397 -4401.

[12] M.E. Dry, The Fischer-Tropsch process: 1950-2000, Catal. Today 71 (2002) 227-241.

[13] P.L. Spath, D.C. Dayton, Preliminary screening – technical and economic assessment of synthesis gas to fuels and chemicals with emphasis on the potential for biomass-derived syngas, in: Technical Report by NREL, National Renewable Energy Laboratory (December 2003), Department of Energy, U.S.A.

[14] P.J. van Berge, J. van de Loosdrecht, S. Barradas, A.M. van der Kraan, Oxidation of cobalt based Fischer-Tropsch catalysts as a deactivation mechanism, Catal. Today 58 (2000) 321-334.

[15] A.M. Hilmen, D. Schanke, K.F. Hanssen, A. Holmen, Study of the effect of water on alumina supported cobalt Fischer-Tropsch catalysts, Appl. Catal. A: Gen. 186 (1999) 169-188.

[16] G. Jacobs, W. Ma, P. Gao, B. Todic, T. Bhatelia, D.B. Bukur, B.H. Davis, The application of synchrotron methods in characterizing iron and cobalt Fischer-Tropsch synthesis catalysts, Catal. Today 214 (2013) 100-139.

[17] A.N. Pour, M.R. Housaindokht, S.F. Tayyari, J. Zarkesh, M.R. Alaei, Kinetic studies of the Fischer-Tropsch synthesis over La, Mg and Ca promoted nano-structured iron catalyst, J. Nat. Gas Sci. Eng. 2 (2010) 61-68.

[18] Y. Yang, H.W. Xiang, Y.Y. Xu, L. Bai, Y.W. Li, Effect of potassium promoter on precipitated iron-manganese catalyst for Fischer-Tropsch synthesis, Appl. Catal. A: Gen. 266 (2004) 181-194.

[19] N. Ahmad, S.T. Hussain, B. Muhammad, J.A. Anderson, N. Ali, S.M. Abbas, Influence of gold promoter on Fischer Tropsch synthesis over Co/Al_2O_3 catalysts, in: 10th International Bhurban Conference on Applied Sciences & Technology (IBCAST), Islamabad, Pakistan (January 15-19, 2013), 11-15.

[20] S. Ali, N.A. Zabidi, D. Subbarao, Correlation between Fischer-Tropsch catalytic activity and composition of catalysts, Chem. Central J. 5:68 (2011) doi: 10.1186/1752-153X-5-68.

[21] S. Lögdberg, Development of Fischer-Tropsch catalysts for gasified biomass, in: Licentiate Thesis in Chemical Engineering, Norwegian University of Science and Technology (Trondheim), Stockholm, Sweden, 2007, p. 90.

[22] C. Wang, L. Xu, Q. Wang, Review of directly producing light olefinns via CO hydrogenation, J. Nat. Gas Chem. 12 (2003) 10-16.

[23] A.N. Pour, S.M. Shahri, Y. Zamani, A. Zamanian, Promoter effect on CO_2-H_2O formation during Fischer-Tropsch synthesis on iron-based catalysts, J. Nat. Gas Chem. 19 (2010) 193-197.

[24] A.N. Pour, M.R. Housaindokht, S.F. Tayyari, J. Zarkesh, Fischer-Tropsch synthesis by nano-structured iron catalyst, J. Natur. Gas Chem. 19 (2010) 284-292.

[25] M. Voss, D. Borgmann, G. Wedler, Characterization of alumina, silica, and titania supported cobalt catalysts, J. Catal. 212 (2002) 10-21.

[26] F. Morales, E. de Smit, F.M.F. de Groot, T. Visser, B.M. Weckhuysen, Effects of manganese oxide promoter on the CO and H_2 adsorption properties of titania-supported cobalt Fischer-Tropsch catalysts, J. Catal. 246 (2007) 91-99.

[27] Z. Tao, Y. Yang, C. Zhang, T. Li, J. Wang, H. Wan, H. Xiang, Y. Li, Effect of calcium promoter on a precipitated iron-manganese catalyst for

Fischer-Tropsch synthesis, Catal. Comm. 7 (2006) 1061-1066.
[28] B.T. Teng, J. Chang, C.H. Zhang, D.B. Cao, J. Yang, Y. Liu, X.H. Guo, H.W. Xiang, Y.W. Li, A comprehensive kinetics model of Fischer-Tropsch synthesis over an industrial Fe-Mn catalyst, Appl. Catal. A: Gen. 301 (2006) 39-50.
[29] M.C. Bahome, L.L. Jewell, D. Hildebrandt, D. Glasser, N.J. Coville, Fischer-Tropsch synthesis over iron catalysts supported on carbon nanotubes, Appl. Catal. A: Gen. 287 (2005) 60-67.
[30] G. Hawkins, Nanocatalysts in Refining & Petrochemical Processes, GBII Enterprises Ltd., www.slideshare.net (2013) PowerPoint presentation, http://www.slideshare.net/GerardBHawkins/nanocatalysts-in-refining-petrochemical-processes.
[31] Y. Zhang, J. Bao, S. Nagamori, N. Tsubaki, A new and direct preparation method of iron-based bimodal catalyst and its application in Fischer-Tropsch synthesis, Appl. Catal. A: Gen. 352 (2009) 277-281.
[32] A.C. Vosloo, Fischer-Tropsch: a futuristic view, Fuel Processing Technol. 71 (2001) 149-155.
[33] G.L. Bezemer, J.H. Bitter, H.P. Kuipers, H. Oosterbeek, J.E. Holewijn, X. Xu, F. Kapteijn, A.J. van Dillen, K.P. de Jong, Cobalt particle size effects in the Fischer-Tropsch reaction studied with carbon nanofiber supported catalysts, J. Am. Chem. Soc. 128 (2006) 3956-3964.

7 ACKNOWLEDGEMENTS

We thank Dr. Kossi Bere and Mr. Henri Gauvin (Université de Sherbrooke) for their valuable technical contribution towards the project and the BioFuelNet National Center of Excellence of Canada for financial support.

8 LOGO SPACE

9.7. Appendix G: Residuals from the XRD analysis by RQA

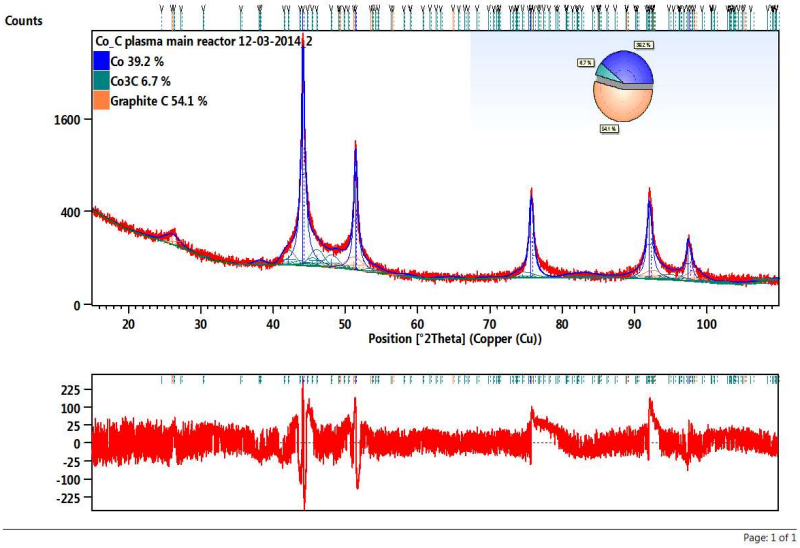

Page: 1 of 1

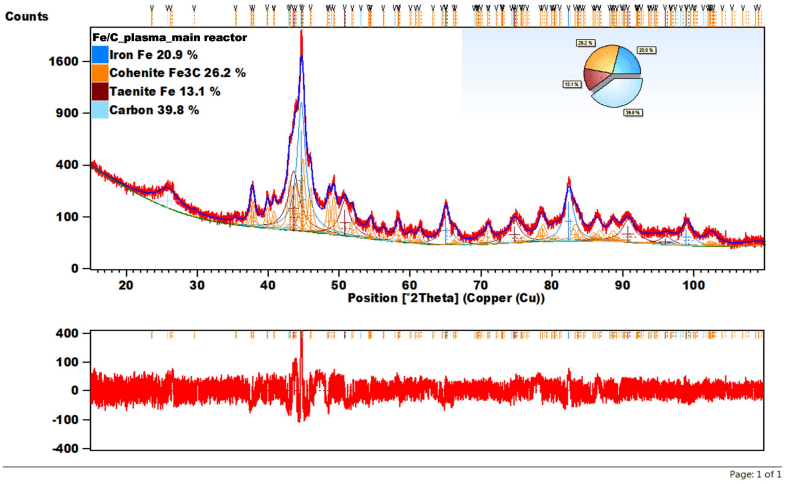

Page: 1 of 1

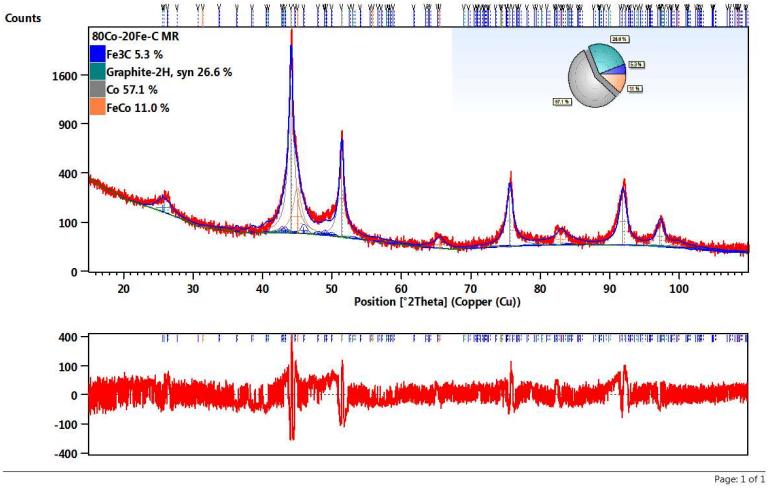

Page: 1 of 1

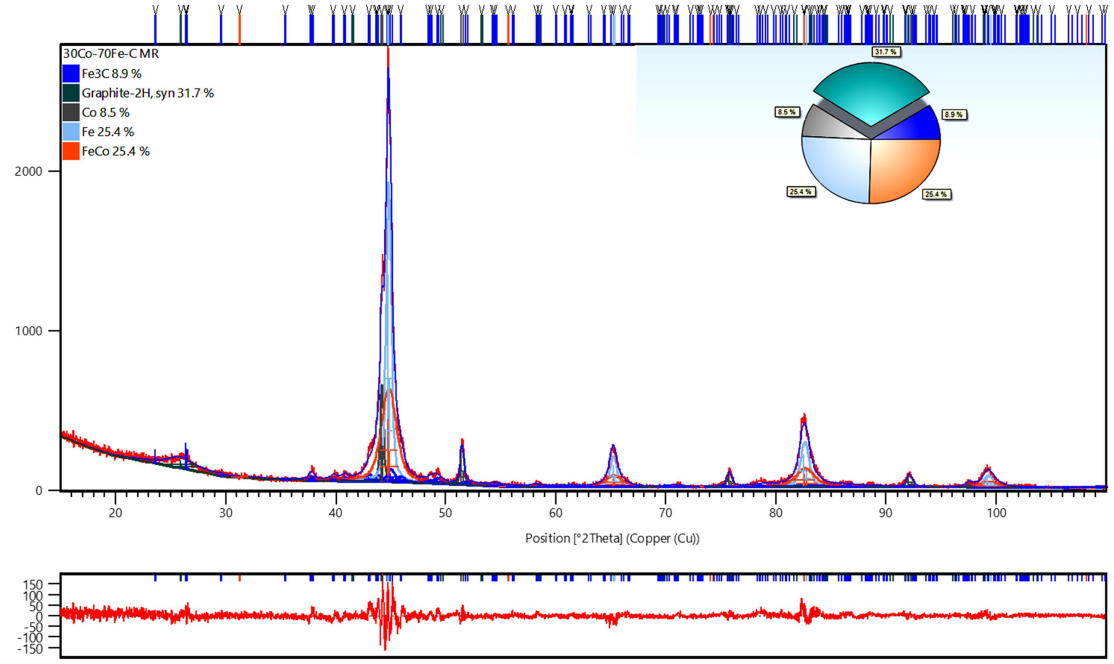
30Co-70Fe-C MR
Fe3C 8.9 %
Graphite-2H, syn 31.7 %
Co 8.5 %
Fe 25.4 %
FeCo 25.4 %
31.7 %
8.9 %
25.4 %
25.4 %
8.5 %
2000
1000
0
20
30
40
50
60
70
80
90
100
Position [°2Theta] (Copper (Cu))
150
100
50
0
-50
-100
-150

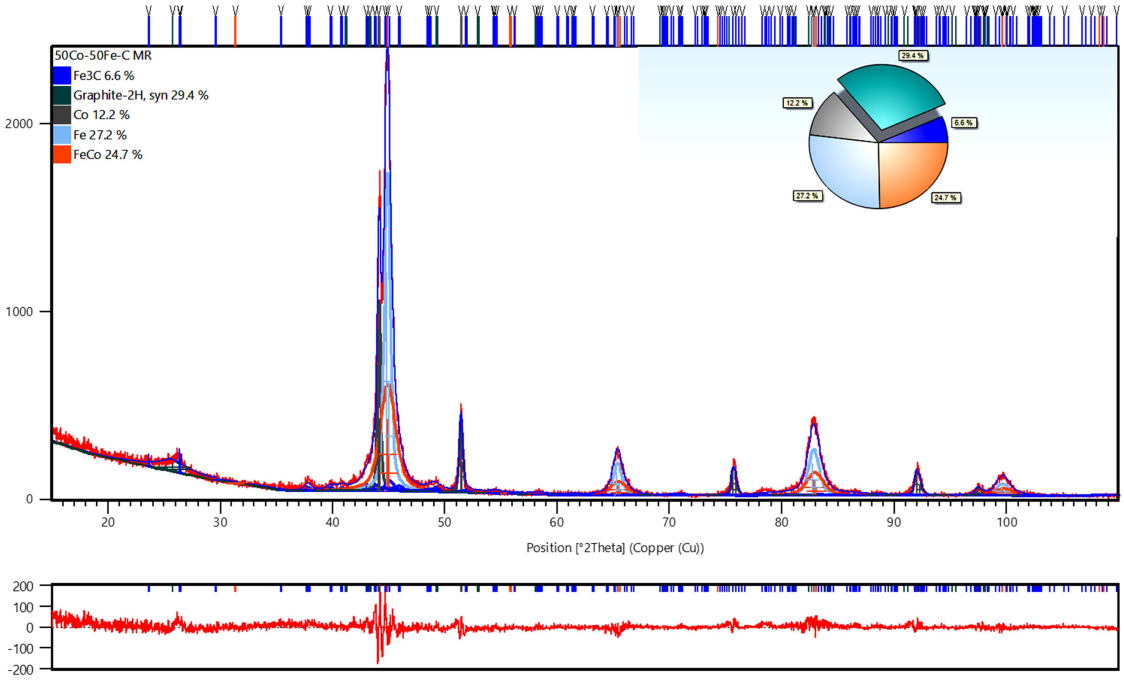
50Co-50Fe-C MR
Fe3C 6.6 %
Graphite-2H, syn 29.4 %
Co 12.2 %
Fe 27.2 %
FeCo 24.7 %
29.4 %
12.2 %
6.6 %
27.2 %
24.7 %
2000
1000
0
20
30
40
50
60
70
80
90
100
Position [°2Theta] (Copper (Cu))
200
100
0
-100
-200

9.8. Appendix H: Article 6 – Promotional effect of Mo and Ni

Promotional effect of Mo and Ni in plasma-synthesized Co-Fe/C bimetallic nano-catalysts for Fischer-Tropsch synthesis

James Aluha and Nicolas Abatzoglou*

Department of Chemical & Biotechnological Engineering, Université de Sherbrooke, QC, Canada J1K 2R1

*Corresponding author: nicolas.abatzoglou@usherbrooke.ca

Abstract

Two carbon-supported Fischer-Tropsch Synthesis (FTS) catalysts with ternary metallic formulations (10%Mo-70%Co-20%Fe and 10%Ni-70%Co-20%Fe) were synthesized through suspension plasma-spray (SPS) technology. Their average particle size determined by Transmission Electron Microscopy was 8.4 and 13.3 nm respectively and their BET specific surface areas were between 69 – 85 $m^2.g^{-1}$. As their analogous monometallic and bimetallic formulations presented in previous publications, these catalysts were both non-porous and nanometric with Scanning Electron Microscopy showing uniform metal-nanoparticle distribution in the carbon-support matrix. FTS test conditions in a 3-phase continuously stirred-tank slurry reactor operated for 24 h were: 260°C, 2 MPa pressure, H_2:CO = 2, gas hourly specific velocity = 3 600 $cm^3.h^{-1}.g^{-1}$ of catalyst. Basing catalyst performance on the bimetallic 80%Co-20%Fe/C catalyst, Ni-addition enhanced catalyst activity from ~42 to 50% CO conversion, and boosted selectivity towards gasoline fraction (C_5 – C_{12}) from ~19 to 50%. Enriching the catalyst-surface acidity by Mo-promotion improved selectivity for both gasoline-fraction (19→33%) and the C_5 – C_{20} fraction (74→87%) and lowered H_2O production by 30%, although at lower CO conversion (~38%). The catalysts' α-values were ~0.8 in the C_{10+} region, and from mass balance their estimated H_2 efficiency decreased in the order of Mo-Co-Fe/C >> Co-Fe/C > Ni-Co-Fe/C.

Key words:

Fischer-Tropsch, plasma-synthesis, molybdenum, nickel promotion, cobalt-iron catalysts

Graphical abstract:

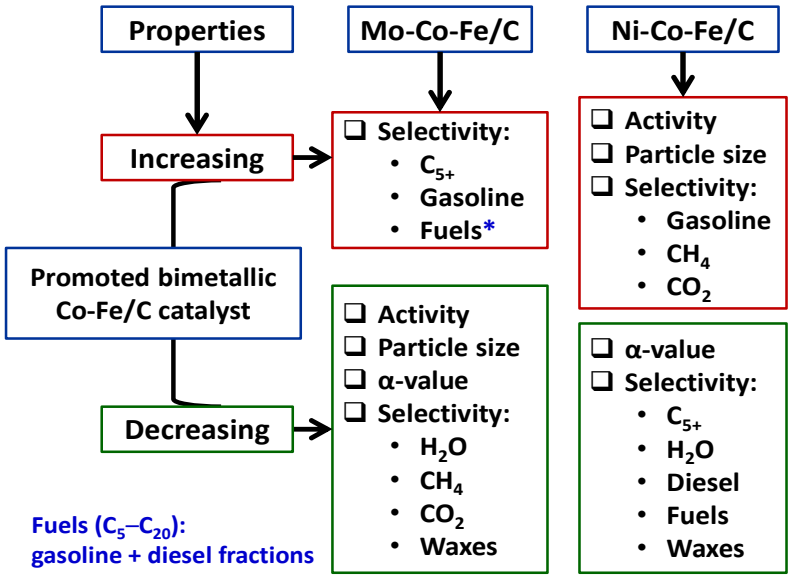

1. INTRODUCTION

Carbon is an attractive support for the production of Fischer-Tropsch catalysts. A number of authors have observed higher activity in carbon-supported catalysts than in those supported on metal oxides [1], and some of the authors attribute this behaviour to the lower interaction between carbon and the active metal phase [2]. When compared to its analogous unsupported Co-based catalyst [3], the carbon-supported catalyst demonstrated increased activity and selectivity towards C_{5+} hydrocarbons with concurrent decrease in the selectivity towards CH_4 and CO_2 production, and it attained steady state performance far more rapidly than the unsupported catalyst. In addition, carbon exists in a variety of forms and morphologies that have been applied in Fischer-Tropsch synthesis (FTS), displaying enormous capacity for modification to produce diverse porous microstructures [4], which include among others, charcoal [5], activated carbon [6], carbon nanotubes [7], graphitic nano-fibres [8], carbon nanofilaments [9], carbon spheres with mean size 600 nm [10], graphene nano-sheets [11], reduced graphene oxide [12], carbon nanotube carpets [13], carbon black, glassy carbon, ordered mesoporous carbon, and diamond [1].

The most critical factors normally used to evaluate the viability of potential catalysts for application in industry are catalyst activity, selectivity and durability [14]. Product selectivity towards gasoline and diesel fractions is the hallmark of an effective FTS catalyst, which can be exploited commercially by converting syngas, a mixture of H_2 and CO to synthetic fuels. Equally, and of great interest is the selectivity for wax production [15], since the heavier molecular-weight hydrocarbons can be isomerized [16], used in personal care lotions and creams [17], or thermally cracked to enrich the gasoline and diesel fuel fractions [18]. Ordinarily, the Co catalyst has higher activity for CO-hydrogenation than the Fe catalyst, but the Fe catalyst is relatively more versatile, and may be manipulated depending on the reaction conditions and promoter effects to produce more branched hydrocarbons, alkenes and oxygenates [14].

One of the approaches employed in improving FTS catalyst selectivity is by the promotional effect of adding other elements in Co- or Fe-based catalysts. For Fe-based catalysts, there exists a wide window in which one could vary its selectivity properties, while selectivity-

linked promoters in the Co catalyst have been limited to date, because of the unfavourable effect the promoters have on catalytic activity [19]. Furthermore, since H_2O greatly impacts on the selectivity of CO to CH_4 in Co catalysts, promoter choice and process conditions are critical in lowering CH_4 production [20]. Beyond the classic single-metal (Co and Fe) catalysts, the Co-Fe bimetallics [21], in addition to many others including Co-Mn [22], Co-Ni [23], Fe-Cu [24], Fe-Mn [25], and Fe-Ni [26] have been examined in order to improve the performance of the Co-only or Fe-only catalysts.

Moreover, the influence of many elements on catalyst selectivity have been studied, and among them are Ba, Be, Ca, and Mg [27], Cu, Re, Ru and Zn [28], Mn [29], and Pt [30]. For example, it has been observed that K-promoted catalysts enhance olefin selectivity while restraining CH_4 and light-hydrocarbons formation [31], and high activity and selectivity towards the aromatic products in FTS has been attributed to the strong acidity and the unique shape or porosity found in the HZSM-5 zeolite [32]. Nevertheless, not all elements produce a positive promotional effect as was the case in using La, Mg or Ca to raise the basicity of the Fe-catalyst surface, which increased the activation energy to 70, 78 and 92 $kJ.mol^{-1}$ respectively, thus worsening the FTS reaction rate [33].

However, many multi-metallic systems create synergistic effects that produce highly active, selective and stable catalysts due to changes in both their electronic and geometric structures, with the catalytic performance being determined by the atomic composition of the crystallite surface and not merely by the overall bulk composition [34]. Some of the ternary systems that have been considered include the addition of Ni [35], or Mn [36] to the Fe-Co bimetallic system. On one hand, the addition of Mo to Fe catalyst remarkably improves selectivity towards the diesel range hydrocarbons (C_{12+}) and suppresses production of the $C_2 – C_8$ hydrocarbons [37]. On the other hand,, the acid-enhancing effect of Mo has a negative influence on its FTS activity, an impact that is also experienced by increasing the basicity of a catalyst surface by adding Ca, Mg or La, which lowers the reaction rate [33]. This implies that extreme surface acidity or basicity on FTS catalysts may not be beneficial to the reaction and the optimal conditions must be determined on a case-by-case study as they are a function of the catalyst’s specificity.

In some Co-based catalysts, Ni promotion has been noted to produce stability with time-on-stream (TOS) [38]. Presence of Ni in Fe catalysts has been shown to improve Fe-oxide particle dispersion, shrinking the crystallite size, while increasing the rate of Fe-oxide reduction in H_2 and boosting the rate of Fe-oxide carburization by CO, but it subdues Fe-carbide formation by syngas reduction [39]. Besides, high Ni-content catalysts suppress selectivity towards heavier hydrocarbons (C_{5+}) and result in greater CH_4 selectivity.

Since various studies show that the active species in Fe-catalyzed FTS are in the form of Fe-carbides [40], the earliest work by this research group using the induction suspension plasma-spray (SPS) technology showed production of such species at temperatures above 1 000 K, and the catalysts were found to be highly active for FTS [41]. Comparing single-metal Co/C and Fe/C catalysts in subsequent studies, it was advanced that since catalyst synthesis by the plasma method involves only a single step with 8 parameters to control, it simplifies the catalyst synthesis significantly when compared to the other traditional synthesis techniques such as impregnation or precipitation that require 6 stages, with overall control of about 40 different parameters [42]. Samples prepared by impregnation or precipitation contained residual metal oxides and indicated early metal nanoparticle agglomeration after 24 h of FTS reaction. Both phenomena (presence of oxidic species and sintering) contribute to catalyst deactivation considerably.

In contrast, the plasma-synthesized samples were devoid of metal oxides and did not exhibit signs of sintering under comparable reaction conditions [43]. Preliminary studies of the Co-Fe/C bimetallics indicated that catalysts produced through plasma displayed identical physical characteristics [44], and the samples did not need elaborate activation procedures; unlike other FTS catalysts that demand optimization and further development of activation methods [23]. Other authors have observed various benefits in using plasma technology because of the shortened preparation time, uniformity in the quality of materials produced, creation of smaller metal particles in the nanometric range as the active species with superior in catalytic performance [45], and enhanced catalyst lifetime, with the plasma method presenting potential for lowering overall process energy requirements [46].

In this investigation, the influence of Mo and Ni addition on the performance of carbon-supported Co-Fe bimetallic catalyst synthesized using induction SPS technology was

evaluated. Since Ni has been shown to increase Co-based catalyst stability and yet there are no studies on combining bimetallic (Co-Fe)-based catalyst with Ni, we decided to conduct this study using our SPS technology to produce the formulations. The main obstacle towards commercial application of Ni-based FTS catalysts lies in its excessive production of CH_4 as well as its tendency to form volatile carbonyls that lead to catalyst deactivation and loss of the active phase [47]. Regarding the use of Mo though its acidity might be detrimental to the FTS activity, its proven ability to result in higher selectivity for longer-chain hydrocarbons [48], with Mo-carbides being the active phase [49], is the main reason of studying its addition to our bimetallic (Co-Fe/C) catalytic formulation.

Although some researchers have tested ternary metallic systems such as the Ni-Co-Fe for FTS, their samples were not supported on carbon and neither were they produced through SPS technology [35]. The encompassing objective of this work was to design and evaluate the properties of potential carbon-supported FTS catalysts among a family of plasma-synthesized materials, which demonstrate selective production of synthetic fuels richer in diesel fraction (C_{13} – C_{20}). Therefore, 10% of either Mo or Ni was introduced into the Co-Fe/C sample, and two hypotheses were examined using the proposed catalysts, thus:

(i) *Presence of Ni*: Since it has been reported that Ni could replace Re as a reduction and activity promoter in the Co-based FTS catalyst [38], we postulated that Ni addition to the Co-Fe/C bimetallic catalysts could – (a) give higher stability to the catalyst, and (b) boost the production of shorter hydrocarbon-chain molecules because Ni promotes early molecular desorption by lowering its activation energy [47];

(ii) *Presence of Mo*: It was advanced that catalyst synthesis of Mo-Co-Fe/C through SPS technology would create Mo-carbides, which are selective for olefin production [49], and that increased surface acidity by Mo-addition to the Co-Fe/C bimetallic would augment the electron-withdrawing character in the catalyst sample and intensify FTS-product selectivity, especially towards the diesel fraction production [50].

This study focuses for the first time on the catalytic performance of the ternary metallic catalysts of 10%Mo-70%Co-20%Fe/C and 10%Ni-70%Co-20%Fe/C, synthesized through SPS technology. In the text, their formulations are abbreviated as Mo-Co-Fe/C and Ni-Co-Fe/C respectively. These catalysts were benchmarked against other plasma-synthesized

Co/C, Fe/C and Co-Fe/C catalysts, with the results showing potential for future application in FTS industry. Results on catalyst comparisons in earlier considerations are available on single-metal Co/C and Fe/C catalysts [42], the bimetallic Co-Fe/C materials [51], and a comprehensive treatment of the rationale administered towards catalyst choice, the theory behind catalyst formulation, the catalyst synthesis procedure and production, as well as the materials' characterization aspects being sufficiently expounded [52]. In this paper, we limit the discussion to our primary findings on catalyst activity and selectivity when Mo or Ni was incorporated in the carbon-supported Co-Fe bimetallic catalyst through the plasma-spray method. Nevertheless, we have provided a succinct, but sufficient coverage of catalyst characterization to support the results presented in this article.

2. EXPERIMENTAL METHODS

2.1 Catalyst Synthesis

The single metal Co/C and Fe/C catalysts [42], in addition to the bimetallic Co-Fe/C catalysts [51], were prepared by the induction suspension plasma-spray (SPS) process, which uses high temperatures to atomize and ionize the solid/liquid sample flowing in a stream of hot gas at particle velocities below 100 $m.s^{-1}$ [53]. A mass of 60 g of the metals in various proportions were mixed in 300 cm^3 mineral oil and the suspension injected into the plasma at a flow rate of 8.2 $cm^3.min^{-1}$. This produced carbon-supported catalysts with metal nanoparticle moieties appearing to be encapsulated in the carbon matrix. Details of this technique have already been prescribed in earlier works and the overall catalyst composition (expressed at ~25-wt% metal loading) is based on "mass" of the metal relative to that of the carbon support in the catalyst formulations. The carbon-supported Ni-Co-Fe and Mo-Co-Fe catalysts were synthesized similarly through the plasma process [52].

2.2 Catalyst Testing

A fresh catalyst (5.0 g each) was first reduced *in situ* at 400^{o}C for 24 h in the FTS reactor using pure H_2 gas (N5.0) flowing at 250 $cm^3.min^{-1}$. The intention of the reduction procedure was to gasify a part of the carbon matrix surrounding the metal so as to amplify contact between the metal and the reactants during FTS. The reactor was then cooled, followed by introduction of 150 cm^3 of hexadecane solvent (C_{16}) to create a three-phase continuously stirred-tank slurry reactor (3-φ-CSTSR).

The pre-treated catalyst was then tested for FTS activity at 260°C and 2 MPa pressure for 24 h on stream. An artificial syngas mixture was used, with composition set at 0.6 L/L (60-vol%) H_2 and 0.3 L/L (30-vol%) CO, balanced in Ar. The gas flow rate streaming in from the bottom of the reactor was 300 $cm^3.min^{-1}$, which translated into a gas hourly specific velocity (GHSV) of 3 600 $cm^3.g^{-1}.h^{-1}$ of catalyst, with the gas volume being considered at the reaction conditions. The FTS product spectrum was analyzed by gas chromatography (GC) at standard conditions according to the protocol reported in earlier works for the single metal Co/C and Fe/C catalysts [43] and the Co-Fe/C bimetallic catalysts [51].

Since the typical FTS product spectrum of a catalyst is predicted by the Anderson-Schulz-Flory (ASF) distribution [54], the probability for the hydrocarbon-chain growth was determined by α-values derived from the expressions given below [34], thus:

$$\frac{M_n}{n} = (1-\alpha)^2.\alpha^{(n-1)} \qquad \text{Eqn. (1)}$$

$$ln\,\alpha = n\,ln\,\alpha + ln\left[\frac{(1-\alpha)^2}{\alpha}\right] \qquad \text{Eqn. (2)}$$

$$\alpha = \frac{M_{n+1}}{M_n} = \frac{r_p}{(r_p+r_t)} \qquad \text{Eqn. (3)}$$

where: M_n = mole fraction of a hydrocarbon with chain length *n*

n = number of total carbon atoms

α = probability of chain growth (α < 1)

(1 - α) = probability of chain termination

r_p = the rate of chain propagation

r_t = the rate of chain termination

The α-values are obtained by the least-squares linear regression of Equation (1) in the logarithmic form expressed as Equation (2), where $\log(M_n/n)$ is plotted against *n*, the hydrocarbon-chain length as indicated by Bartholomew and Farrauto (p.403) [55].

2.3 Catalyst Characterization

The catalysts were characterized by various analytical techniques comprising (a) Brunauer-Emmett-Teller (BET) method for porosity and specific surface area determination; (b) morphological and particle size analysis using both Scanning and Transmission Electron Microscopy (SEM and TEM) coupled with Energy Dispersive X-ray Spectroscopy (EDX); (c) crystalline phases nature and composition analysis by X-ray diffraction (XRD) and Rietveld Quantitative Analysis (RQA); as well as (d) X-ray photoelectron spectroscopy (XPS). The characterization test conditions and analyses results are available in an earlier article for BET, SEM, TEM and XRD [52], and for XPS [42]. In this paper, only the results that support the current discussion are presented.

3. RESULTS AND DISCUSSION

3.1 Catalyst Synthesis

Catalyst synthesis using SPS technology has been found to create nanometric materials with remarkably uniform characteristics. In this study, it was observed that even after introduction of 10% Mo or Ni in the Co-Fe bimetallics, the physical properties of the catalysts by and large remained identical [52]. The high reproducibility of catalyst properties imply that plasma application in catalyst synthesis presents stately potential for the large-scale catalyst production.

3.2 Catalyst Testing

3.2.1 Catalyst activity

In this work, we tested two ternary formulations of Mo-Co-Fe/C and Ni-Co-Fe/C catalysts at 260^{o}C and 2 MPa pressure, and referenced their catalytic performance with a sample bimetallic catalyst (80%Co-20%Fe/C, in here referred to as Co-Fe/C). Figure 1 presents

catalyst activity plots by % CO conversion. In comparison to the Co-Fe/C bimetallic catalyst with ~42% CO conversion at time = 24 h, the Mo-containing catalyst was slightly less active (38%) probably due to a prolonged induction period, while the Ni-containing catalyst was more active showing increasing CO conversion toward 50%.

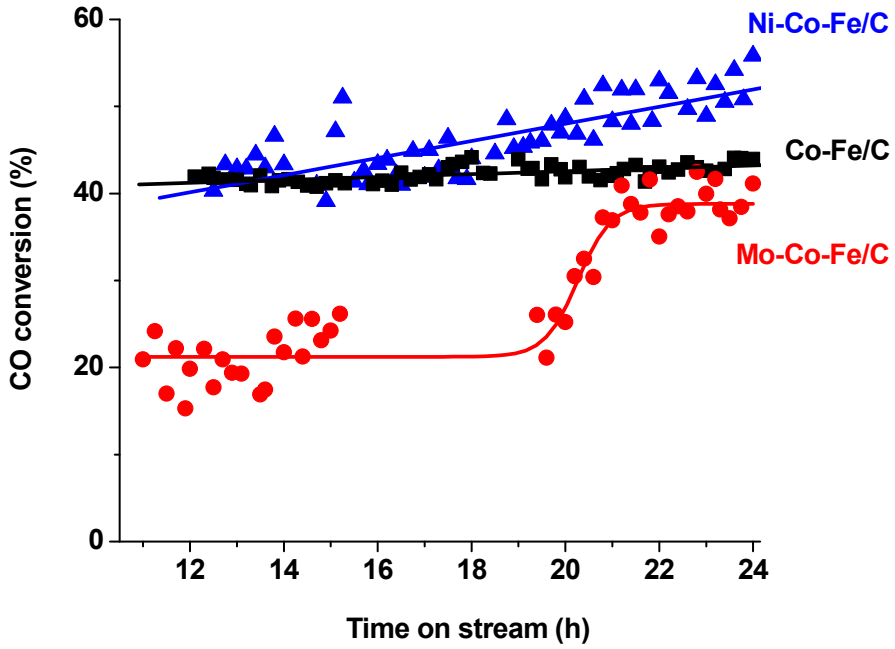

Figure 1: Activity plots for the Co-Fe/C, Mo-Co-Fe/C, and Ni-Co-Fe/C catalysts

3.2.2 Catalyst selectivity

Figure 2 provides summary plots of the corresponding catalyst selectivity for the materials presented in Figure 1. On the x-axis, zero represents CO_2 and one represents CH_4, while all other integer numbers represent the number of C atoms in the hydrocarbon molecules. Since no C3's and C4's were detected by our GC columns in addition to very little of C_2H_6 and C_2H_4 being observed (amounting to less than 0.5% when combined), it was therefore prudent to round off the numbers to the nearest whole numbers for ease of reading the manuscript. For example, in the Mo-based catalyst the reactor-exit concentration of ethane was about 0.4% while that of ethene was 0.08%. Figure 3 indicates the combined fractions in terms of gasoline ($C_5 – C_{12}$), diesel ($C_{13} – C_{20}$), and waxes (C_{21+}). It should be noted that the normal diesel fraction contains a mixture of hydrocarbons in the range of $C_8 – C_{21}$ tailing off at both ends, but in this study, the definition of the diesel fraction was taken strictly as

between C_{13} – C_{20} to simplify catalyst performance evaluation and for easy mass balance, where overlaps of hydrocarbon fractions for gasoline and diesel were avoided.

The product spectrum shows that the bimetallic Co-Fe/C was comparatively more selective towards production of the longer-chain hydrocarbon components such as diesel (55%) and waxes (13%) than the promoted catalysts where there was a perceived enhancement of catalyst selectivity towards gasoline fraction after Mo, or Ni addition (19%→33%→50% respectively). However, the Ni-Co-Fe/C catalyst produced substantial quantities of CO_2 and CH_4 totalling to 22%, which lowered selectivity for the diesel fraction from ~55% to 22%. On the contrary, Mo addition to the Co-Fe/C catalyst depressed the production of CO_2 and CH_4 to a combined value of less than 10% in total. A more detailed analysis follows below.

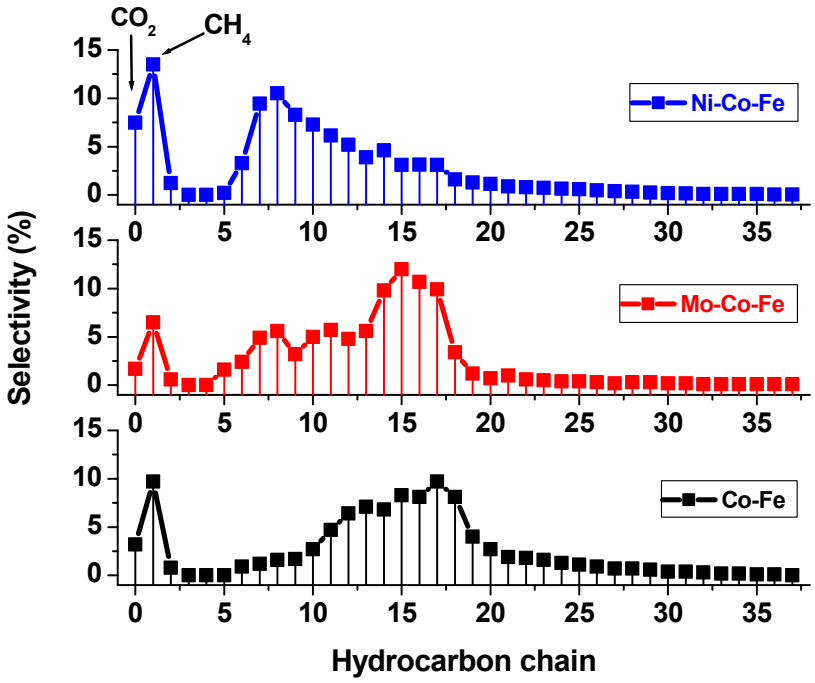

Figure 2: Catalyst selectivity as portrayed by hydrocarbon distribution plots for the Co-Fe/C, Mo-Co-Fe/C, and Ni-Co-Fe/C catalysts

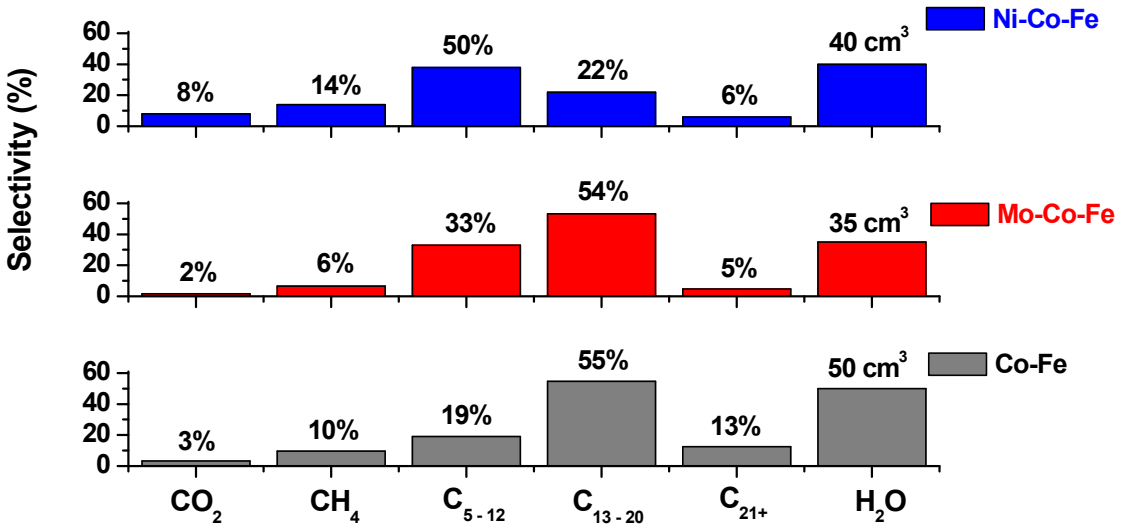

Figure 3: Plots of aggregated FTS fraction distribution after 24 h of reaction for the Co-Fe/C, Mo-Co-Fe/C, and Ni-Co-Fe/C catalysts

3.2.3 Hydrogen efficiency

The amount of H_2O produced in the experiments was utilised in hydrogen mass balance to determine a rough estimate of the H_2 efficiency for each catalyst. Equations (4) and (5) show that for every H_2O molecule released, there is production of either one $-CH_2-$ group that is formed in the hydrocarbon chain, or one CH_4 molecule with each reaction taking up 2 or 3 molecules of H_2 respectively. In addition to these reactions, there are other various chemical reactions that impact differently on H_2 in FTS. For example, there is a variation in the amounts of H_2 used up towards the selectivity of alkanes, alkenes, alcohols, and aldehydes in addition to water gas shift (WGS) reaction, which consumes H_2O and generates H_2 in FTS shown in Equation (6).

$$CO + 2H_2 \rightarrow -[CH_2]- + H_2O \qquad \text{Eqn. (4)}$$

$$CO + 3H_2 \rightarrow CH_4 + H_2O \qquad \text{Eqn. (5)}$$

$$CO + H_2O \rightarrow CO_2 + H_2 \qquad \text{Eqn. (6)}$$

Since FTS chemistry is highly convoluted and our analytical equipment has a limitation of being unable to discriminate between the various hydrocarbon groups, we assumed that the principal product of this analysis was the alkene, (C_nH_{2n}) and H_2O, which is measurable. The purpose of this estimation was to apply a simple method to articulate the catalytic behaviour of each catalyst with respect to H_2 consumption, without going into complex details. On the basis of this assumption, while ignoring the consequences of WGS reaction, the amount of H_2O formed was split in the same proportions as they appear in the selectivity data between CH_4 on one hand and overall FTS products (C_{5+}) on the other.

Therefore, Figure 4 exemplifies how the calculation was performed using the Co-Fe/C catalyst data, while Table 1 provides a summary of the results for all the three catalysts. The total amount of H_2 gas that was delivered in the 24-h experiment was equivalent to 10.8 moles = (300 $cm^3.min^{-1}$) x (60% H_2) x (60 min.) x (24 h)/(24,000 cm^3 at RTP).

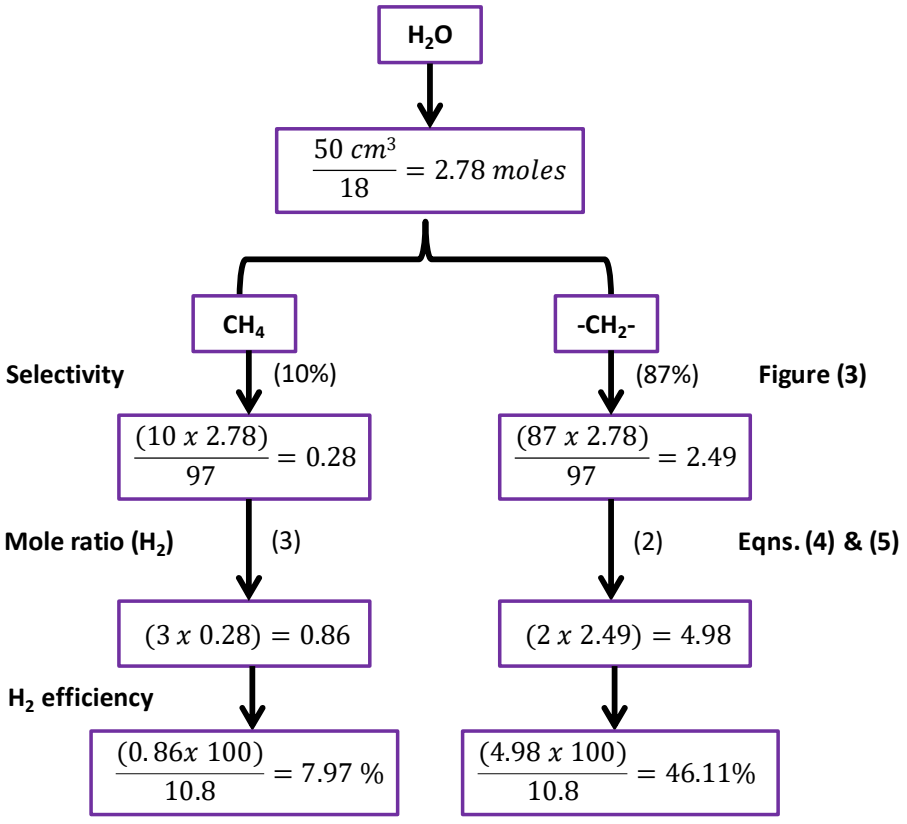

Figure 4: Sample calculation for H_2 efficiency determination after 24 h of reaction

Table 1: Determination of the H_2 efficiency per catalyst

Catalyst	H_2O produced		Selectivity (%)		H_2 efficiency (%)		
	(cm^3)	moles	C_{5+}	CH_4	C_{5+}	CH_4	$[C_{5+}]$:CH_4
Co-Fe/C	50	2.78	87	10	46.1	8.0	5.7
Mo-Co-Fe/C	35	1.94	91	6	33.3	3.3	10.0
Ni-Co-Fe/C	40	2.22	78	14	34.9	9.4	3.7

From these results, it was observed that the ratio of H_2 consumed between C_{5+} and CH_4 production decreased in the order of Mo-Co-Fe/C >> Co-Fe/C > Ni-Co-Fe/C. This implies that for every CH_4 molecule produced, there were ten -$[CH_2]$- monomers added to the hydrocarbon-growth chain in the Mo-Co-Fe/C formulation, making it the most hydrogen-efficient catalyst, while the least efficient catalyst was in the Ni-Co-Fe/C formulation.

3.2.4 Benchmarking: Rationale for catalyst selection

These catalysts were benchmarked under similar FTS reaction conditions (260^{o}C; 2 MPa pressure; and GHSV = 3 600 $cm^3.h^{-1}.g^{-1}$ of catalyst) against the original plasma-synthesized Co/C and Fe/C single-metal catalysts [43], and further evaluated against the previously considered Co-Fe/C bimetallics [51]. In this discussion, the 80%Co-20%Fe/C catalyst acts as the bimetallic representative, since it had comparable average nanoparticle size of the metal (within the 9–11 nm range), besides having almost equal metal proportions with the other materials under examination: Co (~70%) and Fe (~20%).

Selectivity towards the diesel fraction was our target, with the preliminary tests performed at 220^{o}C using the single metal Co/C and Fe/C catalysts, and their respective CO conversions were 45 and 25% [43]. Kinetically, increasing temperature should enhance the reaction, in addition to promoting the formation of lower-molecular weight hydrocarbons. Therefore, at 260^{o}C, the Co/C catalyst was expected to produce more gasoline fraction at a faster rate. Indeed, it displayed improved activity to complete CO conversion, but with very poor selectivity (27%) towards the fuels (S_{fuels} = C_5 – C_{20}). In this section of the discussion, S_{fuels} is designated as the combined selectivity of gasoline and diesel fractions only.

Figure 5 provides a summary spatial chart offering information on the evolution of the FTS catalyst in this study: from the single-metal formulations (step 1) to the bimetallic systems (step 2), through to the ternary-metal formulations (steps 3 and 4) and the rationale of scrutinizing the materials for their performance at 260°C is provided. Since selectivity towards diesel fraction ($C_{13} - C_{20}$) was our targeted product overall, raising the temperature to 260°C for Co/C produced dismal performance, with a paltry 19%. The Fe/C catalyst on the other hand showed lower catalyst activity of 60% CO conversion, but with better overall selectivity towards the FTS fuels (S_{fuels} = 74%) at 260°C (step 1). It was more selective towards the diesel fraction (55%) than the Co/C (19%), forming less CO_2 (10%) than the Co/C catalyst (20%), and it generated significantly lower amounts of CH_4 (5%) compared to 46% in Co/C [43].

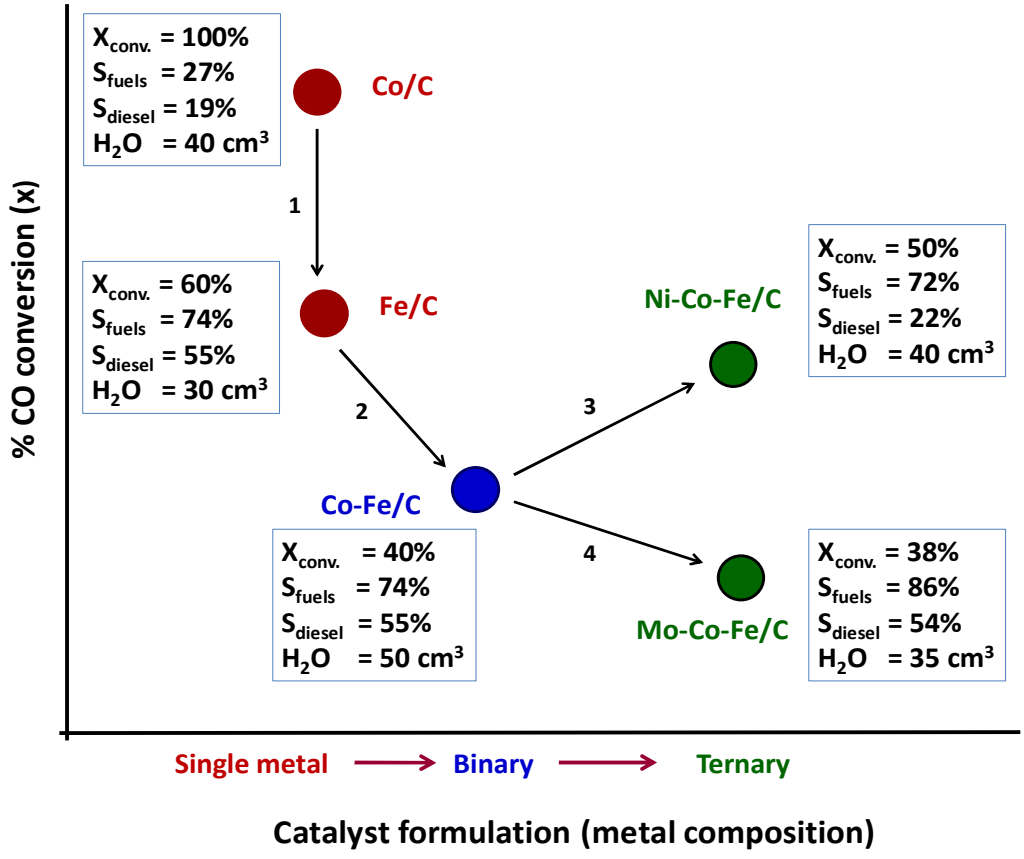

Figure 5: A chart summarizing the process of assessing catalyst performance at 260°C for Co/C, Fe/C, Co-Fe/C, Mo-Co-Fe/C, and Ni-Co-Fe/C, indicating catalyst activity as $X_{conv.}$ = CO conversion (%); selectivity, S_{fuel} (%) = gasoline (C_5–C_{12}) + diesel (C_{13}–C_{20}); selectivity for diesel = S_{diesel} (%); and water (H_2O)

These findings then necessitated the development of the Co-Fe/C bimetallics in order to further improve on the catalyst selectivity towards production of the diesel fraction (step 2). A family of three bimetallics (30%Co-70%Fe/C, 50%Co-50%Fe/C and 80%Co-20%Fe/C) were synthesized and when tested were found to be rather inactive at 220^{o}C except for the 80%Co-20%Fe/C catalyst, which gave a 10% CO conversion only. FTS operation at higher temperature (260^{o}C) manifested almost equivalent catalytic activity in all the three bimetallics, with overall CO conversion occurring in the range of 40 – 50% [51]. Being represented in the chart of Figure 5 by the 80%Co-20%Fe/C catalyst, the application of bimetallics did not seem to make a big difference when compared to the Fe/C catalyst operated at 260^{o}C, since the selectivity towards the diesel and gasoline fractions (S_{fuels}) seemed to remain unchanged (55%), prompting us to explore the ternary systems. Nevertheless, it has been shown that larger metal nanoparticles are more selective towards the formation of light-weight hydrocarbons [56], and since the mean particle size of the 50%Co-50%Fe/C sample was larger (14.4 nm), it led to a higher selectivity towards the gasoline fraction [51].

It was observed that under similar FTS reaction conditions, the addition of 10%Ni to the Co-Fe/C bimetallic led to a 10% increase in CO conversion from 40 to 50% (step 3). Whereas the Co-Fe/C bimetallic catalyst gave S_{fuels} = 74% (with 3% CO_2, 10% CH_4 and 50 cm^3 H_2O), the S_{fuels} = 72% for Ni-Co-Fe/C catalyst with only 22% apportioned towards the diesel fraction. The presence of Ni prompted excessive production of CO_2 (8%) and CH_4 (14%), but with less H_2O generation (40 cm^3).

The Mo-Co-Fe/C catalyst on the other hand presented a slightly lower catalytic activity (~38% CO conversions) in comparison to Co-Fe/C (~42%) at 260^{o}C, and, as seen in Figure 1, it had a sluggish start (step 4). It is hypothesized that the catalyst experienced a protracted induction period, possibly with considerable surface reconstruction. In parallel, it was observed that, relative to the Co-Fe/C catalyst, the presence of Mo improved the overall selectivity towards the fuels (S_{fuels} = 86% up from 73%). However, diesel fraction selectivity remained constant (55%), implying that probably the enhanced surface acidity enriched the gasoline fraction more, in addition to suppressing production of CO_2 (2%) and CH_4 (6%). In comparison to the Fe/C catalyst, the Mo-Co-Fe/C catalyst had better

selectivity towards fuel production, (S_{fuels} = 86% : 74%), although it was less active (38% : 60%).

3.2.4 Determination of the catalysts' α-values

The α-values of both the Mo-Co-Fe/C and Ni-Co-Fe/C catalysts were found to be 0.78 at high C-numbers (C_{10+}), although the Co-Fe/C bimetallic had a higher value of 0.81, see Figure 6. This means that the addition of Mo or Ni to the Co-Fe/C catalyst apparently had the similar impact of lowering the α-value to 0.78 and leading to the production of the shorter-chain hydrocarbons.

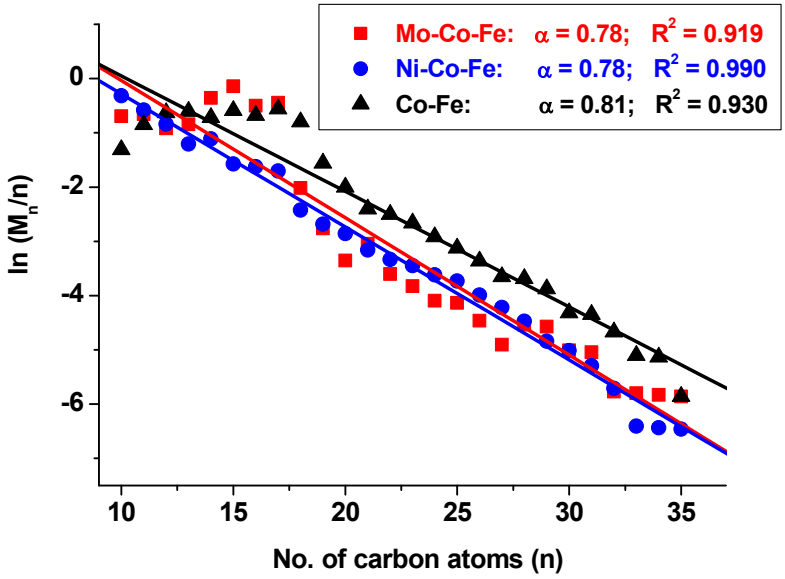

Figure 6: Plots for determining catalysts' α-values using log(M_n/n) versus n

3.3 Catalyst Characterization

3.3.1 BET surface area analysis

Porosity analysis by the BET method showed that the catalysts had characteristics that were consistent with non-porous materials, and were construed to be devoid of internal porosity as exemplified by the absence of hysteresis in their overlaid adsorption-desorption isotherms provided in Figure 7. Largely, the plasma-generated Co-Fe/C bimetallics and the ternary Ni-Co-Fe/C and Mo-Co-Fe/C systems had BET specific surface areas that were in

the range between 67 – 93 $m^2.g^{-1}$. Moreover, they exhibited higher surface areas than the single metal Co/C and Fe/C catalysts, typically producing a crescent-looking plot as shown in Figure 8. These results were comparable to other conventional nanometric metal-oxide supported FTS catalysts, with an example of the Co/MnO_2 catalyst that was found to have BET specific surface areas of 74 $m^2.g^{-1}$ [57].

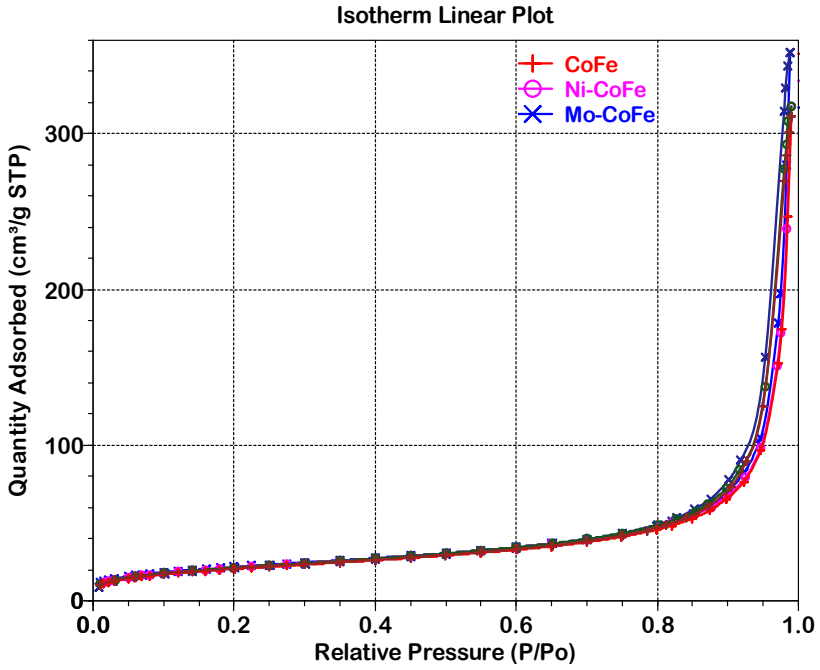

Figure 7: Overlaid adsorption-desorption isotherms derived from N_2 physisorption indicating similarities in the 80%Co-20%Fe/C, 10%Mo-70%Co-20%Fe/C and 10%Ni-70%Co-20%Fe/C samples collected from the main plasma reactor

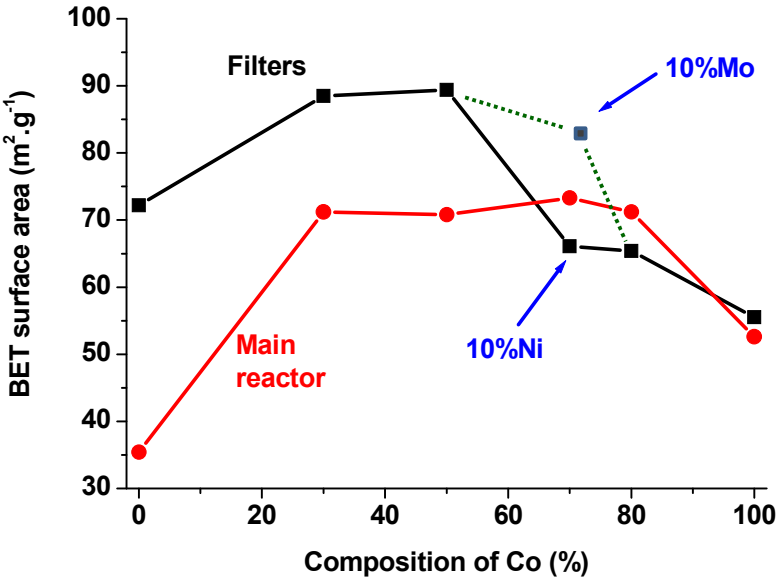

Figure 8: Plots of BET specific surface area against increasing Co-metal concentration in the samples for the single metal Co/C and Fe/C samples; bimetallic 30%Co-70%Fe/C, 50%Co-50%Fe/C, 80%Co-20%Fe/C catalysts; and the ternary 10%Mo-70%Co-20%Fe/C, and 10%Ni-70%Co-20%Fe/C systems.

From the plasma reactor set-up discussed in an earlier article [52], the catalyst samples were collected from both the main reactor (where the metal-oil suspension is injected into the plasma plume), and the adjacent auxiliary reactor (into which some of the nanoparticles migrate and get trapped onto the filters mounted therein). Generally, it was observed that samples collected from the filters in the auxiliary reactor had a slightly higher surface area than those collected from the main plasma reactor. For example, the respective BET specific surface areas of the Mo-Co-Fe/C sample from the auxiliary reactor and the main reactor were 85 and 77 $m^2.g^{-1}$ of catalyst, while those of the Ni-Co-Fe/C sample were 69 and 76 $m^2.g^{-1}$ of catalyst respectively. Presumably, samples from the auxiliary reactor had less metal moieties in the carbon support, a disposition that resultantly made them lighter and smaller in particle size probably aiding their migration away from the main reactor into the auxiliary reactor, with some getting trapped onto the filters.

3.3.2 SEM analysis

Since SEM analysis data for the Ni-Co-Fe/C was provided in the synthesis and characterization article [52], in this work we present data on the Mo-Co-Fe/C catalyst. The striking dispersion and uniform distribution of the metal nanoparticles in the samples was evident from the backscattered SEM imaging and EDX mapping shown in Figure 9. The light areas in Figure 9(a) represent the presence of the heavier elements (the metals), while the dark areas represent the lighter element, which is the carbon support. Elemental distribution captured by X-ray mapping in Figure 9(b) confirmed the uniform metal dispersion in the carbon matrix. Elemental line scan analysis on the secondary image provided in Figure 10 demonstrated that the metal concentration of the 10%Mo-70%Co-20%Fe/C catalyst in the support matrix existed in the expected proportions of Mo:Fe:Co ≈ 1:2:7 (resulting from the arbitrary scale of ≈ 7:15:50 units), with the EDX spectrum confirming presence of all the three elements.

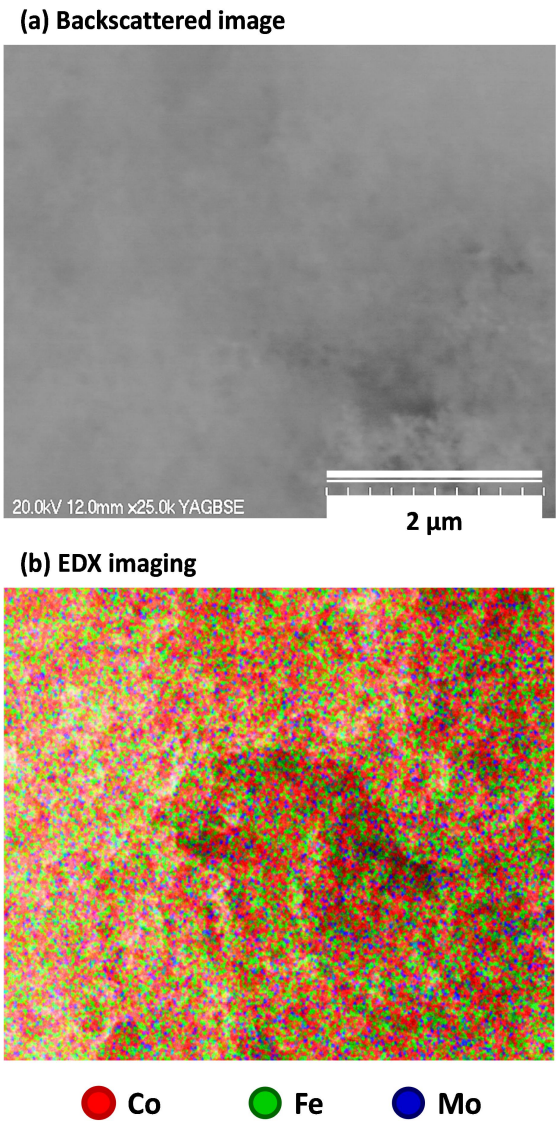

Figure 9: (a) A backscattered SEM image of the fresh 10%Mo-70%Co-20%Fe/C catalyst, and (b) image of elemental X-ray mapping.

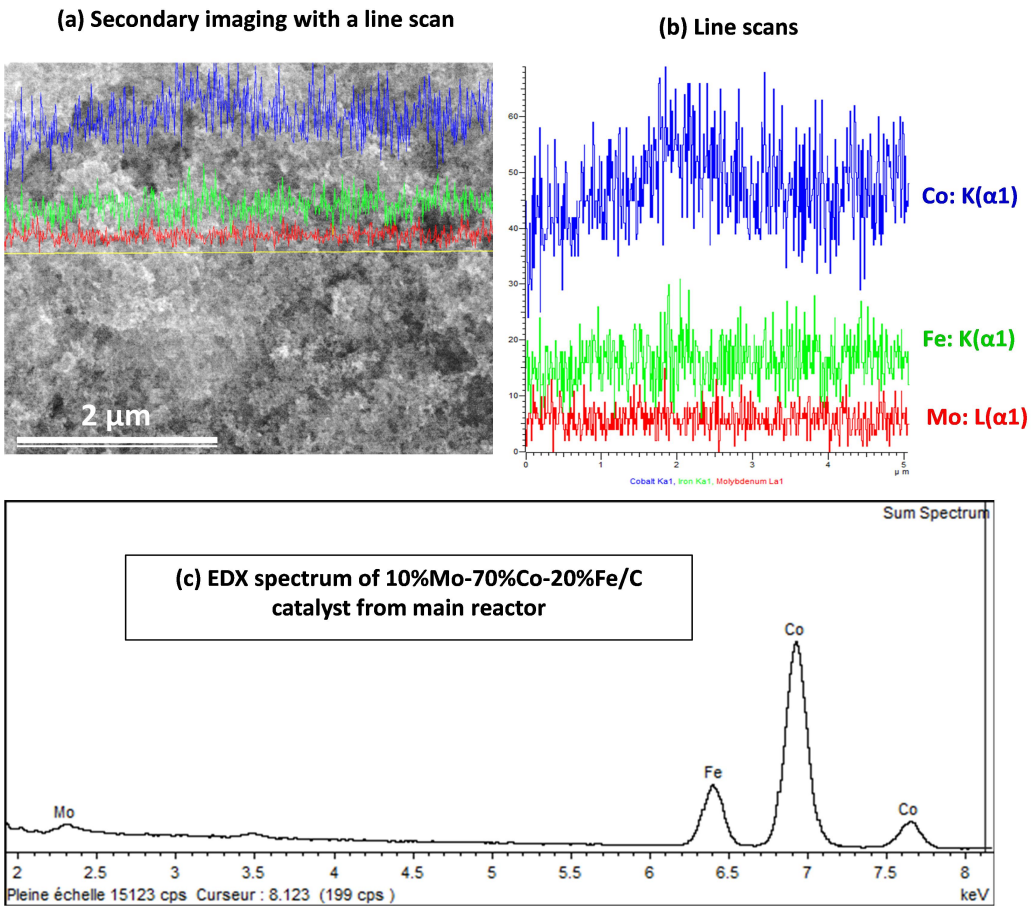

Figure 10: SEM analysis for the fresh 10%Mo-70%Co-20%Fe/C catalyst showing (a) a sample secondary image with (b) line scan analysis, and (c) the EDX spectrum.

3.3.3 TEM analysis

TEM analysis revealed a catalyst support consisting of a blend between amorphous carbon and graphitic-carbon sheets that were saturated with metal nanoparticle moieties, uniformly distributed and displaying widespread dispersion in the carbon matrix. Earlier studies indicated the average metal nanoparticle size in the freshly-synthesized samples were in close range with Co/C having a mean particle size of 11.0 nm, that of Fe/C was 11.3 nm [43], while both the 80%Co-20%Fe/C and 30%Co-70%Fe/C bimetallics had a mean size of 8.9 and 9.1 nm respectively, except for the 50%Co-50%Fe/C bimetallic, which had a mean of 14.4 nm [51]. In this work, 450 nanoparticles were measured and the mean particle size for the fresh Mo-Co-Fe/C and Ni-Co-Fe/C catalysts was found to be 8.4 nm and 13.3 nm respectively as depicted in Figure 11. The representative bimetallic catalyst is the 80%Co-20%Fe/C with mean 8.9 nm.

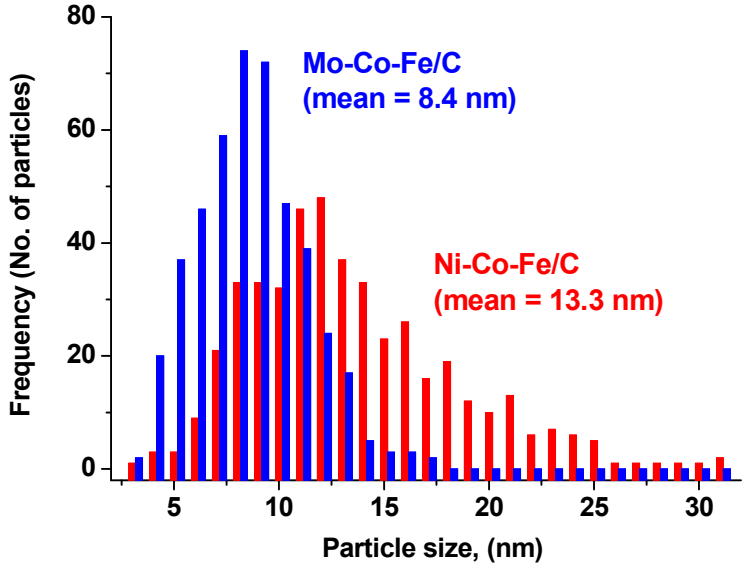

Figure 11: TEM analysis indicating metal nanoparticle-size distribution for the fresh catalysts: Mo-Co-Fe/C (8.4 nm); and Ni-Co-Fe/C (13.3 nm)

There was no apparent particle agglomeration observed, even after high-temperature exposure during pre-treatment at 400^{o}C for 24 h, followed by FTS reaction at 260^{o}C for another 24 h. Sample TEM images shown in Figure 12 indicated that in the used plasma-synthesized samples, there was no conceivable sintering or metal segregation away from the support particularly when compared to the magnitude of metal agglomeration experienced with the commercial Fe-NanoCat® tested under similar reaction conditions as already discussed in an earlier article [43].

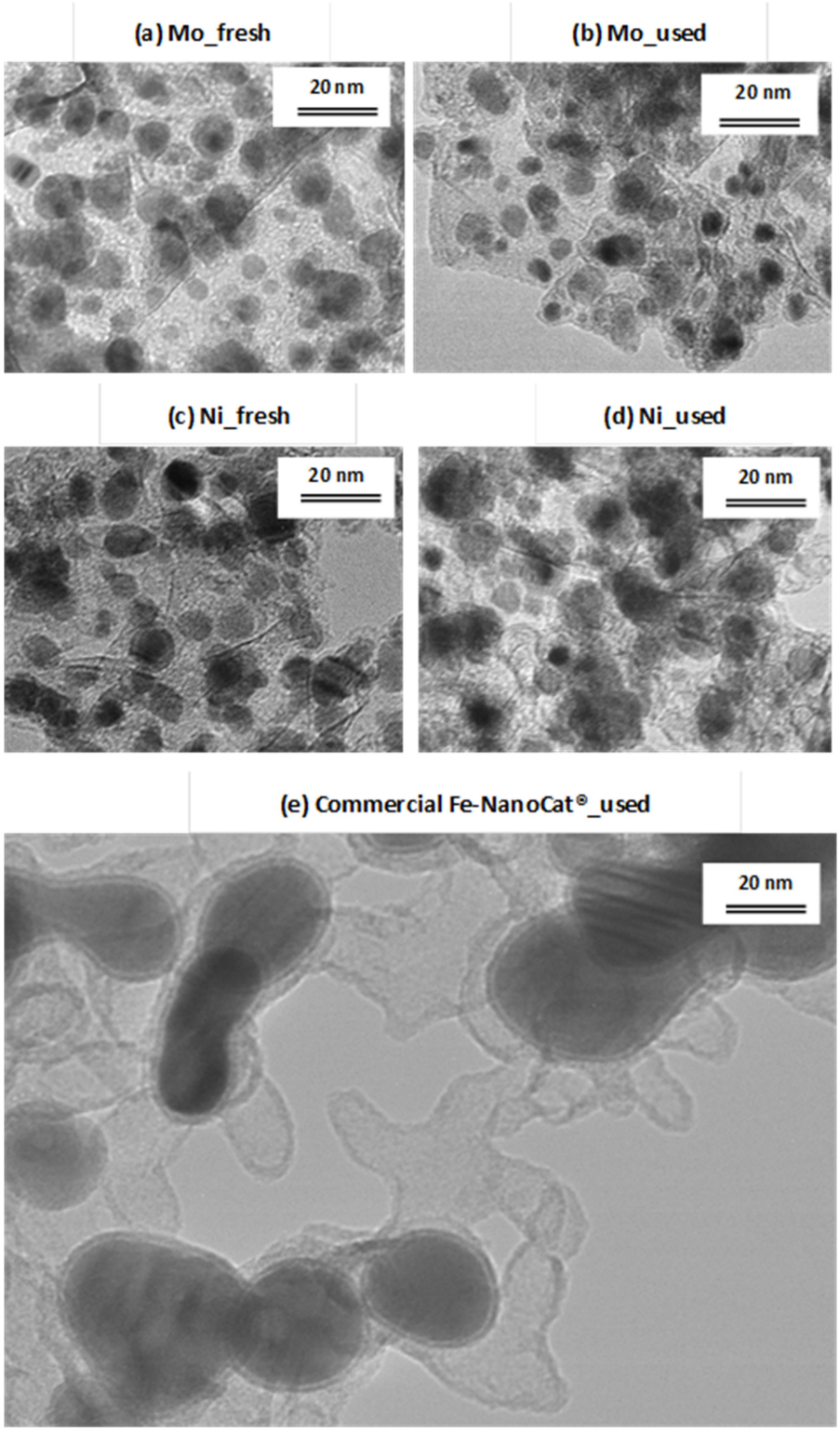

Figure 12: Sample TEM images showing a lack of sintering for plasma-synthesized (a) fresh Mo-Co-Fe/C, (b) used Mo-Co-Fe/C, (c) fresh Ni-Co-Fe/C, and (d) used Ni-Co-Fe/C catalysts compared to (e) the commercial Fe-based catalyst after FTS reaction

3.3.4 XRD analysis

Powder XRD analysis of the Ni-Co-Fe/C was not successful due to major peak overlaps with the cobalt's overarching face-centred cubic (FCC) crystal structure as well as the metallic (Fe^0) XRD pattern. Besides, the presence of Ni did not seem to make any difference to the XRD pattern of its sample as seen in Figure 13, probably because either Ni was below the instrument's detection limits or, the nanometric nature of the crystallites was the overriding factor, since it leads to peak broadening and ultimately peak extinction. Decreasing the scanning step size of the XRD instrument from 0.040° [2θ] angle to 0.020° did not show any improvement for Ni detection in the XRD spectrum.

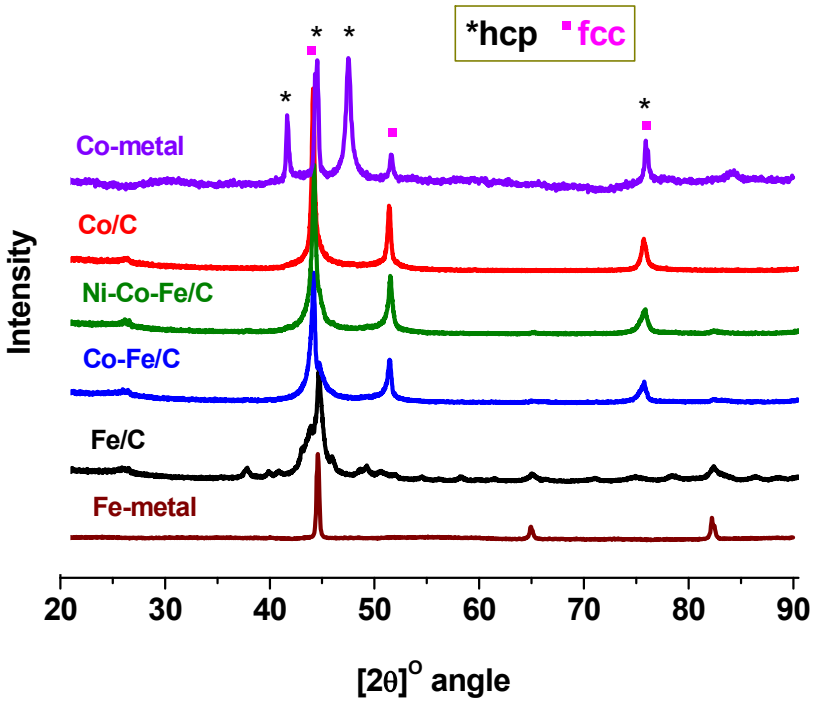

Figure 13: XRD patterns for the fresh Ni-Co-Fe/C catalyst compared to Fe and Co metals as well as the Co-Fe/C bimetallic obtained from the main reactor

Attempted phase quantification of the Mo-Co-Fe/C catalyst by RQA was equally not effective due to high sample amorphicity as confirmed by the broad peak at around 20° [2θ] angle in Figure 14. Both peak broadening as well as peak extinction made analysis difficult due to the nanometric nature of the catalysts. However, some characteristic peaks still revealed valuable information such as the possibility of having numerous phases existing in

the samples such as those rich in Fe-carbides (Fe_2C, Fe_3C, Fe_5C_2) being evident at approximately 45° [2θ] angle. In addition to the CoFe intermetallic with noticeable peaks at 44°, 52° and 75° [2θ] angle, the Co_3Fe_7 and Co_7Fe_3 nano-alloys were possibly present. The FCC phase of metallic Co° was more apparent than the HCP (hexagonal close packing) phase in both the fresh and used samples.

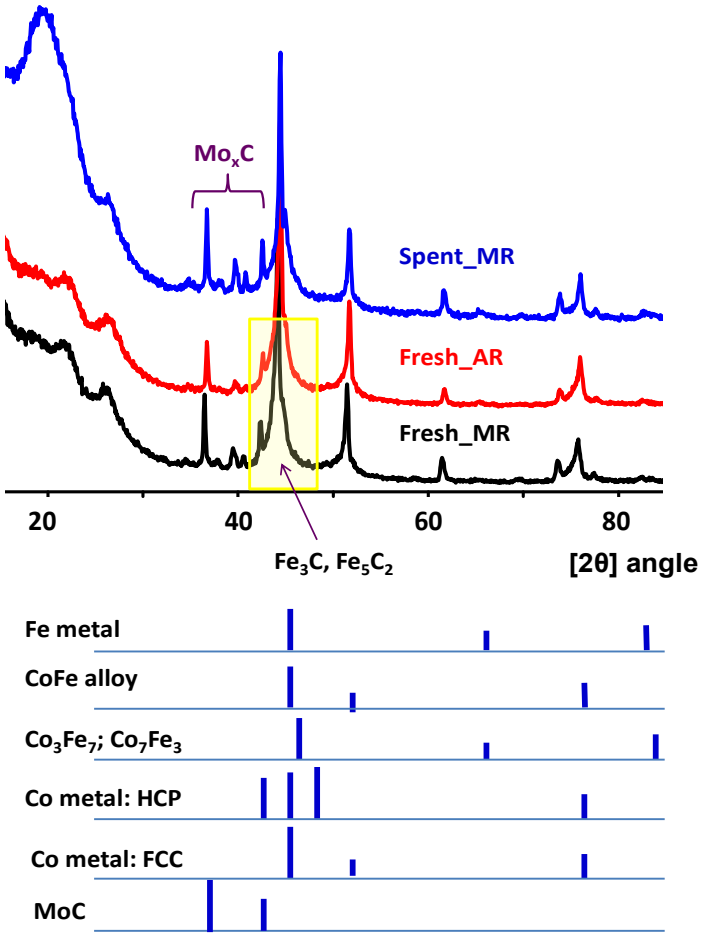

Figure 14: XRD patterns for the fresh Mo-Co-Fe/C catalysts showing similarity in those obtained from the main reactor (MR) and the auxiliary reactor (AR) with some differences in the spent catalyst (MR) arising from the reduction effect

Ostensibly, the Mo-based samples contained both forms of MoC and Mo_2C before and after use in FTS reaction. Greater prevalence of metallic forms was manifested in the used samples than in the fresh samples, with the Mo° and Fe° displaying characteristic peaks at 41° and 45° [2θ] angles respectively, as seen in Figure 15. There was no substantial evidence for the presence of metal-oxides (i.e. for Co, Fe or Mo), even after exposure to the

CO and H_2O during FTS reaction. However, their presence is still conceivable, albeit in minute quantities beyond the instrument's detection limits, since they are thermodynamically more stable than the metallic species.

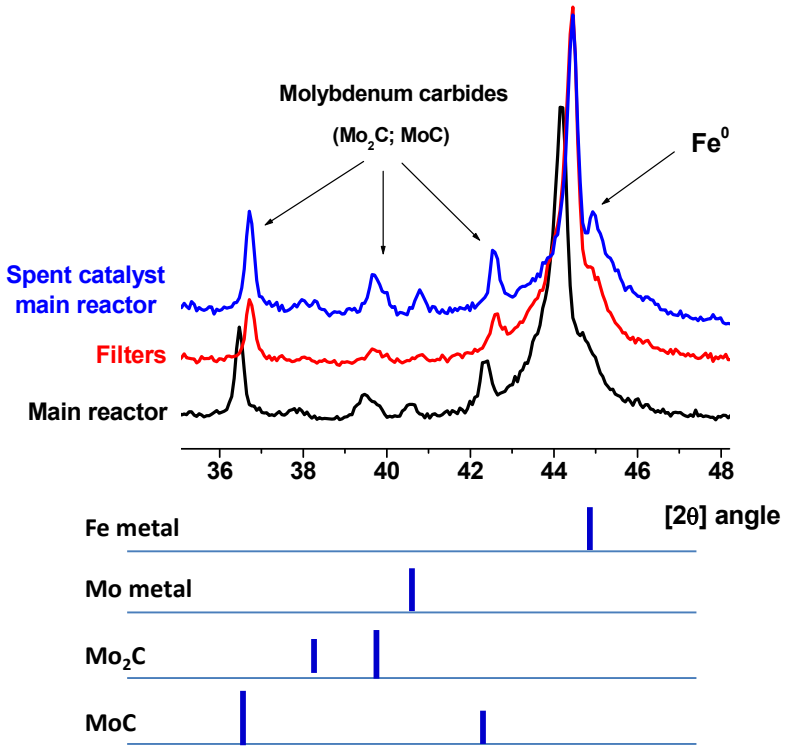

Figure 15: Comparison of XRD patterns of the fresh and used Mo-Co-Fe/C catalysts revealing more metallic Fe and Mo in the used materials as a result of catalyst reduction

3.3.5 XPS analysis

Figure 16 presents the XPS spectra of the fresh Ni-Co-Fe/C catalyst drawn from both the main plasma reactor as well as the auxiliary plasma reactor to prove that although XRD analysis was unable to ascertain the presence of Ni in the samples, analysis by XPS was very effective in doing so. This finding confirmed the results obtained from EDX mapping using the SEM imaging technique [52]. Table 2 indicates a summary of the calculated atomic concentrations of each element in the samples. Since the materials are highly pyrophoric, they are easily oxidized by atmospheric oxygen, and hence the considerable presence of oxygen on the catalyst surface.

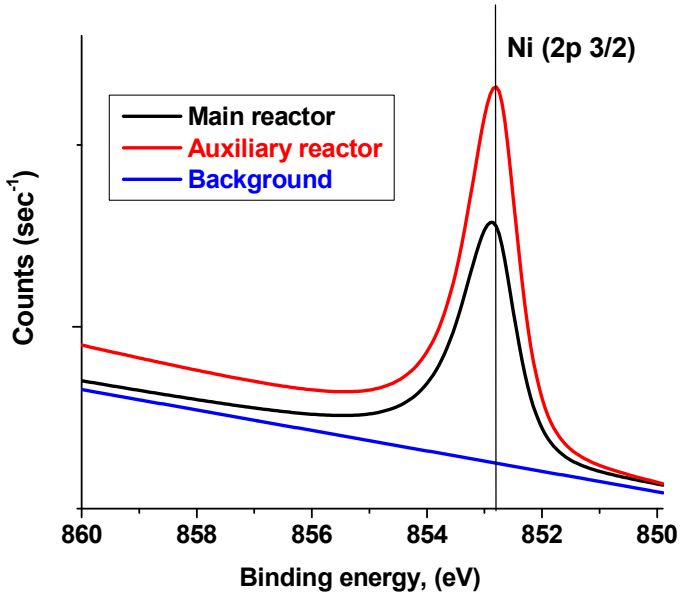

Figure 16: Evidence of Ni in the fresh plasma-synthesized Ni-Co-Fe/C catalyst by XPS

Table 2: XPS analysis data for plasma-synthesized Ni-Co-Fe/C catalyst

Element	Main reactor			Auxiliary reactor		
	Peak position (eV)	FWHM*	% atomic concentration	Peak position (eV)	FWHM	% atomic concentration
C (1s)	284.5	2.76	93.14	284.5	2.72	93.21
O (1s)	532.5	3.77	2.58	532.5	4.21	1.87
Co (2p)	778.5	3.66	2.02	778.5	3.74	2.31
Fe (2p)	713.5	9.87	1.76	712.5	9.81	2.12
Ni (2p)	852.5	2.68	0.50	853.5	3.90	0.50

* FWHM = Full width at half maximum of peaks

For the Mo-Co-Fe/C formulation, the overlaid XPS spectra of samples drawn from the main plasma reactor and auxiliary plasma reactor (fresh catalysts) as well as the spent catalyst obtained from the main plasma reactor are displayed in Figure 17. A summary of their peak positions and elemental atomic concentrations are provided in Table 3. It was observed that the chemical composition of the sample collected from the main plasma reactor was significantly different from that obtained from the auxiliary plasma reactor, which contained mainly metallic (Mo^0) and oxidized (Mo^{4+}) species with peak positions at approximately 228.1 and 231.3 eV respectively, which concurred with data interpretation in literature [58]. However, both the fresh and used catalysts from the main plasma reactor had some

similarities since they contained mixed Mo^0, Mo^{4+} and Mo^{6+} species, which had their respective peak positions at about 228.1, 231.3 and 232.6 eV in the fresh sample and 228.2, 231.3 eV and 232.2 eV in the used catalyst. The peak at ~236 eV is a doublet due to the Mo-3d spin-orbital splitting in Mo (VI) atoms, which concurrently appears with the peak at ~232 eV and is usually indicative of the presence of MoO_3 species [59].

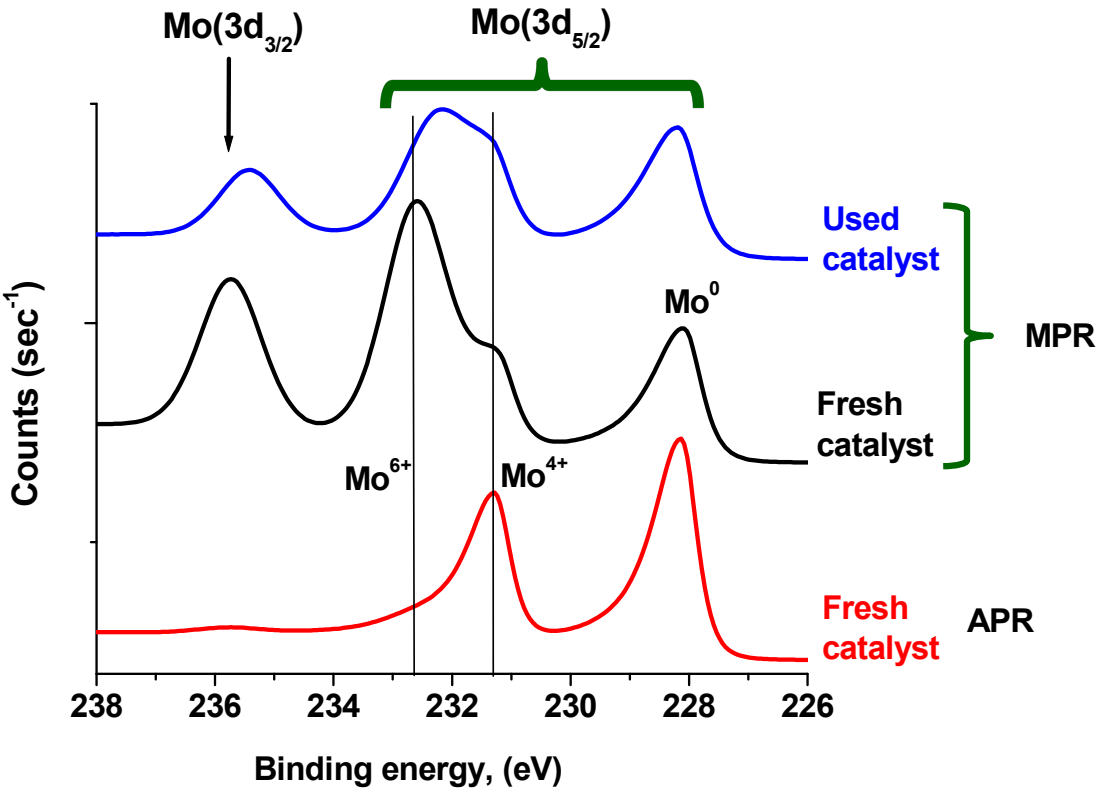

Figure 17: XPS envelopes of the fresh Mo-Co-Fe/C catalyst from the auxiliary plasma reactor (APR), alongside the fresh and used catalysts from the main plasma reactor (MPR)

Table 3: XPS analysis data for plasma-synthesized Mo-Co-Fe/C catalyst

Element	Auxiliary reactor: fresh catalyst			Main reactor: fresh catalyst			Main reactor: used catalyst		
	Peak (eV)	FWHM	% At. Conc.	Peak (eV)	FWHM	% At. Conc.	Peak (eV)	FWHM	% At. Conc.
O 1s	529.9	3.71	3.13	529.9	3.69	5.13	529.8	3.41	7.93
C 1s	284.8	2.84	91.54	284.8	2.89	90.00	284.5	2.78	86.71
Co 2p	778.2	3.45	3.14	777.9	4.63	2.83	778.2	5.83	3.53
Fe 2p	711.9	9.97	2.08	711.9	9.67	1.80	712.9	8.90	1.78
Mo 3d	228.1	3.27	0.11	228.1	5.90	0.23	228.2	2.48	0.05

4. DISCUSSION

4.1 Catalyst Synthesis and Characterization

In this paper we report findings that are unique to the production of synthetic fuels, where new catalyst formulations have been produced, composing ternary Mo-Co-Fe and Ni-Co-Fe metallic systems, supported on nanometric carbon that has been generated by an induction plasma-spray technique. The nature of this plasma-synthesized carbon support meets the properties of carbon black as was shown by Raman spectroscopy in earlier work [42]. The carbon is characteristically a mixture of graphitic carbon with a considerable portion of it having varying degrees of structural defects that it tends towards amorphous carbon. This carbon support is unique and, during FTS reaction, (a) remains unaffected when reduced in pure H_2 at 400^{o}C for 24 h whilst (b) its graphitic sheets fold into carbon nanofilaments when the reduction is done in CO; and the carbon-nanofilament growth is seen to progress away from the metal centres [51].

Since the use of carbon support in FTS is receiving considerable attention today, plasma application provides numerous benefits in catalyst preparation, particularly where reproducibility of highly active catalytic materials is critical to the success of process execution. In this study, we show that both the promoted catalysts (Mo-Co-Fe/C and Ni-Co-Fe/C), were essentially nanometric and non-porous, having comparable properties to all the other plasma-synthesized materials reported earlier. The promoted as well as the bimetallic catalysts generally had BET specific surface area in the range of 67 – 93 $m^2.g^{-1}$. In this work we underscore the importance of applying non-porous catalysts with high surface area because this is fundamental to the FTS reaction as it targets production of large molecular-weight hydrocarbons, and one must avoid operating in diffusion-limited regimes.

Our plasma-synthesized samples have presented uniform metal distribution as observed from SEM imaging and EDX elemental mapping, while metal nanoparticle size measurement by TEM analysis has indicated an average in the range of 8.9 – 14.4 nm for the single metal Co/C, Fe/C and the bimetallic Co-Fe/C catalysts. It is therefore notable that the promoted Mo-Co-Fe/C and Ni-Co-Fe/C catalysts also exhibit similar characteristics with mean metal nanoparticle size of 8.4 and 13.3 nm respectively. These distinctive properties

underpin the reliability and capacity SPS technology presents in catalyst production, reproducibility and its great potential for future scale up.

Some authors have observed that during FTS reaction, stronger CO adsorption exists in the smaller Co particles of less than 7 nm, leading to low turnover frequency [60]. Therefore, our samples aimed at consistently producing metal nanoparticles above 8 nm makes our plasma approach highly successful at lab-scale and extremely promising for a scale-up endeavour and eventual industrial applications. In addition, since the smaller Co particles exhibit higher selectivity for CH_4 formation, mainly due to their heightened capacity for hydrogen coverages, this is a phenomenon that our samples have overcome.

Moreover, having the particle-size distribution of the samples remaining unaffected after FTS reaction was an early indication of their intrinsic resistance to sintering, catalyst deactivation and ultimate long-term durability. Although some authors claim that their carbon-supported catalyst attained steady state operation more quickly (after 45 h with TOS) when compared to other catalysts (90 h) [3], our plasma-synthesized catalysts continued to show an upward trend of improving activity after 24 h as depicted in Figure 1. This is clearly an early sign that catalyst deactivation was distant.

XRD analysis of the catalysts showed a myriad of phases present in the catalysts, ranging from metallic forms (Co^o, Fe^o, Mo^o and Ni^o), to nano-alloys (CoFe, Co_3Fe_7, Co_7Fe_3, etc.), and their corresponding metal carbides (Fe_2C, Fe_3C, Fe_5C_2; MoC, Mo_2C, etc.). Incidentally, the main purpose of catalyst synthesis by plasma technology was to generate the nanometric carbon support concomitantly with this mixture of metallic and carbidic moieties, which are known to be the active phases in the FTS reaction, depending on the metal involved. Whereas Fe-carbides are perceived to be the fundamental species in the Fe-based FTS catalysis, metallic Co is instrumental to the Co-based catalyst, while the Mo-based catalyst seems to require the carbidic phase also.

The negative consequence of having nanometric catalysts with extremely small crystallite sizes of the catalyst was that it led to rampant peak broadening as well as peak extinctions in the XRD patterns, and this rendered phase identification in our analyses only partly

conceivable, but phase quantification by RQA absolutely difficult. Nevertheless, analysis exploiting XPS was able to confirm the presence of Ni in the Ni-Co-Fe/C sample since XRD failed to detect it. In addition, analysis of the Mo-Co-Fe/C sample by XPS indicated the presence of both metallic and oxidized species (Mo^0, Mo^{4+} and Mo^{6+}). Some of the Mo-species in the oxidized state may be construed to be carbidic in nature as observed from the XRD analysis, although the carbide peak in XPS was not conspicuous (expected to appear below the carbon peak at 284 eV).

Since the Mo-catalyst that was used in the FTS reaction was collected from the main plasma reactor, it indicated a considerable presence of MoO_3, which could be difficult to reduce at our pre-treatment temperature of 673 K (400^oC). Some authors have indicated that a reduction temperature of over 873 K (600^oC) is required to reduce the nanometric MoO_3 to metallic Mo because below 883 K, the original morphology of MoO_2 was conserved [61]. Probably, this could be the reason why we still find the Mo^{6+} species persisting in the used sample as shown in Figure 17. Unlike the Ni-promoted catalyst, the Mo-Co-Fe/C sample went through an extended induction period, which was exhibited by the step change in the FTS reaction after 20 h on stream. However, it should be noted that this explanation is still speculative and validation may require advanced equipment such as *in situ* XRD tests, where the catalyst's phase transformations could be monitored with TOS.

From this investigation, it has been established that the principal advantage of SPS technology in catalyst synthesis is to concurrently create a nanometric carbon-support matrix alongside metal nanoparticles in various phases ranging from metallic to carbidic moieties, which are highly active for the FTS reaction. Since a reduction process plays a vital role in activating the FTS catalyst, it has been shown that increasing the catalyst particle size decreases the rate of catalyst reduction [62]. This implies that the size of the metal nanoparticles significantly impacts on the FTS reaction. Therefore, plasma technology offers an effective method of producing ready-to-use nanometric catalysts, which are potentially easy to reduce *in situ* due to the particle size effect.

4.2 Evaluation of Hypotheses Tested

Two hypotheses were tested on a limited scale using the 80%Co-20%Fe/C bimetallic catalyst. The study, which investigated the promotional effects of Mo and Ni on the FTS product spectrum showed that addition of 10% Ni to the Co-Fe/C bimetallic catalyst resulted in higher production of CH_4 and shorter hydrocarbon-chain molecules, while increased surface acidity by addition of 10% Mo to the Co-Fe/C bimetallic boosted gasoline production by ~74% (from 19% to 33% of the total selectivity).

4.2.1 Promotion of Co-Fe/C catalyst with Ni

These research findings have confirmed our initial assertion that a Ni-based catalyst would be more selective towards gasoline fraction, with a lower wax fraction. Performing the FTS reaction at 260^{o}C showed higher catalyst activity in Ni-Co-Fe/C (50% CO conversion) than with the initial Co-Fe/C bimetallic (42% CO conversion), although the Ni-Co-Fe/C had greater propensity for producing CH_4 (23%) and CO_2 (14%), both of which were undesirable products. However, since it was advanced that promotion of the Co-Fe/C bimetallic catalyst with Ni would improve the production of shorter hydrocarbon chains, it means that our first hypothesis was accurate: that is, Ni enhances mechanisms that involve lower activation energy, early chain-growth termination, fast hydrocarbon desorption and poor molecular readsorption. Some of the catalysts tested earlier have shown a remarkable stability and the hypothesis that Ni enhances this stability is not yet proven because it requires hundreds or even thousands of hours TOS.

4.2.2 Presence of molybdenum

In our second hypothesis it was proposed that enhanced surface acidity by Mo-promotion in Co-Fe/C catalyst would stimulate the production of longer-chain hydrocarbons, targeting to enrich the diesel-fraction. In addition, a Mo-based catalyst would be desirable because of its resistance to the deactivation that originates from carburization. In fact, the creation of Mo-carbide species is central to their operation in FTS catalysis [49]. Therefore, these research findings have disapproved our claim that Mo-promotion would amplify product selectivity towards diesel fraction. Instead, presence of Mo enhances gasoline fraction, while the quantity of diesel generated by both the promoted and un-promoted catalysts (Mo-Co-Fe/C and Co-Fe/C) remained constant (at ~55%).

4.2.3 Reaction mechanism

It has been posited that the Mo-catalyzed FTS reaction progresses by the Eley–Rideal mechanism, which arises from the strong CO adsorption to the electron-withdrawing Mo-carbide catalyst surface [49]. The associatively chemisorbed CO is therefore thought to react with the H_2 in gas phase to form HCOH as the chain-initiator species, which propagates to higher olefin and paraffin species. In fact, in the Ni-based catalyst, density functional calculations suggest that direct CO dissociation is relatively less viable than the dissociation of intermediate FTS species such as the hydroxymethylidyne (COH) or formyl (HCO). Consequently, the reactions toward CH_3OH and CH_4 formation preferentially evolve through the HCO intermediate on all the surfaces [63]. This means that since our reaction is operated at high H_2 concentration (H_2:CO = 2), both the proposed "*Carbide*" and "*CO-insertion*" mechanisms could take the same pathway as depicted in Equation (7) leading to excessive CH_4 production. This assertion was found to be true for our Ni-promoted catalyst because it generated 14% CH_4, while the Mo-catalyst gave only 6%.

$$\boldsymbol{CO \xrightarrow{+H} C \xrightarrow{+H} CH \xrightarrow{+H} CH_2 \xrightarrow{+H} CH_3 \xrightarrow{+H} CH_4} \quad \text{Eqn. (7)}$$

For other hydrocarbon-chain growths, it has been observed that the molecular structures of the transition states may be quite similar, but there is a substantial variation in the energy barriers involved between the various C–C coupling reactions among the transition elements, resulting into different preferential paths for the chain growth in each metal. For example, Co favours the [CH_2 + CH_2] coupling, while Fe favours [C + CH_3] coupling [63].

It was our intention to identify, quantify and correlate the amount of each phase in the catalysts to its activity and selectivity, but this investigation was less productive because of the nanometric nature of materials, which rendered accurate determination of phase composition by XRD analysis to be nearly impossible. Therefore, there is no sufficient exploitable information from which we can draw authoritative conclusions on the nature of the reaction mechanisms using the available characterization data. However, it is evident that both Mo- and Ni-addition produced more gasoline (33% and 50% respectively) than the Co-Fe/C bimetallic (19%), and less waxes (5% and 6% respectively) relative to Co-Fe/C

(13%). This means that Mo promoted the low molecular-weight FTS products, although with the advantage of limiting the generation of CO_2 (2%) and CH_4 (6%), whereas the Ni-Co-Fe/C catalyst produced more CO_2 (8%) and sizable quantities of CH_4 (14%).

In addition, when the ratio between the overall FTS products (C_{5+}) and CH_4 is considered in the light of H_2-efficiency, the Mo-promoted catalyst seems to outperform the other two catalysts, with increasing H_2-efficiency in the order of Ni-Co-Fe/C followed by Co-Fe/C and then Mo-Co-Fe/C with (C_{5+} : CH_4) = 3.7, 5.7 and 10 respectively. Therefore, in terms of selectivity and H_2 efficiency, the best catalyst is the Mo-Co-Fe/C.

4.3 Evaluation of α-values

It was observed that both Ni- and Mo-promotion, whose presence was confirmed by XRD, XPS, SEM and EDX analyses, only enriched the production of the gasoline fraction, and that both the ternary catalytic systems (Mo-Co-Fe/C and Ni-Co-Fe/C) had the lower α-value of 0.78 as compared to 0.81 of the Co-Fe/C bimetallic catalyst. Since Co has a typical range of α-values between 0.70 – 0.80 and Fe between 0.50 – 0.70 [64], these results show that the high amounts of Co (having 70 – 80% of metal loading) in the samples took precedence in the reactivity of the materials. However, it also shows that the presence of Fe or Ni had a positive impact on the product distribution towards the lighter hydrocarbons. This finding is in agreement with literature data where low α-values exhibited by Mo- and Ni-promoted catalysts at high temperature (260^{o}C) is perceived to maximize on gasoline production, with low yields of high molecular-weight products [65]. On the other hand, low-temperature operation and catalysts with higher α-values such as the Co-Fe/C bimetallic produce more compounds with longer carbon-chains (e.g. waxes), but less of gasoline and low molecular-weight olefins.

5. CONCLUSION

Two analogous ternary catalysts (Mo-Co-Fe and Ni-Co-Fe), supported on carbon were synthesized through plasma to produce catalysts that were both nanometric and non-porous with BET specific surface area in the range of 69 – 85 $m^2.g^{-1}$. Various phases were evident from XRD analysis ranging from metal carbides to metallic and nano-alloy forms,

but they were not fully quantifiable by RQA due to peak broadening and peak extinctions arising from the nanometric nature of the materials. XPS confirmed presence of Ni in the Ni-Co-Fe/C sample, which went undetected by XRD analysis, besides indicating the presence of Mo^0, Mo^{4+} and Mo^{6+} in the Mo-Co-Fe/C sample. Due to the pyrophoric nature of the samples, it is speculated that exposure to air leads to the formation of MoO_3 in the catalyst, which may require protracted activation times before FTS. Microscopic imaging (by SEM, EDX & TEM) indicated uniform metal distribution in the carbon matrix and had average particle size of 8.4 nm for Mo-Co-Fe/C and 13.3 nm for Ni-Co-Fe/C catalyst. There were no significant signs of early carbon-support degradation or metal nanoparticle agglomeration in the catalysts as seen from TEM analysis particularly after the prolonged thermal treatment of 24 h by H_2-reduction at 400^{o}C, followed by another 24 h of FTS reaction at 260^{o}C.

These catalysts were tested under realistic FTS reaction conditions (260^{o}C; 2 MPa pressure; H_2:CO ratio = 2; GHSV = 3 600 $cm^3.h^{-1}.g^{-1}$ of catalyst). It was observed that the presence of Mo favoured higher production of gasoline fraction and not diesel as initially thought. Selectivity of Mo-Co-Fe/C towards the diesel fraction ($C_{13} – C_{20}$) remained constant (at ~55%), while the gasoline ($C_5 – C_{12}$) selectivity stood at 33% compared to 19% in the Co-Fe/C bimetallic. Similarly, Ni-promotion improved the reaction rate from 42 to 50% CO conversion and enhanced the production of shorter-chain hydrocarbons generating 50% gasoline, but with excessive formation of CO_2 (14%), CH_4 (23%), and H_2O (55 cm^3). The α-values determined from the higher molecular-weight hydrocarbons (C_{10+}) were 0.81 for the Co-Fe/C catalyst and 0.78 for both the Mo-Co-Fe/C and Ni-Co-Fe/C catalysts. Mass balance calculations indicated that the catalysts' H_2-efficiency, that is, the ratio between C_{5+} and CH_4 production decreased in the order of Mo-Co-Fe/C >> Co-Fe/C > Co-Fe/C with values given as 10, 5.7 and 3.7 respectively.

6. ACKNOWLEDGEMENTS

The financial support granted by the Canadian BiofuelNet National Centre of Excellence (NCE) is gratefully acknowledged. Special thanks are addressed to: Dr. Kossi Béré for technical expertise in the Plasma Synthesis lab; the staff at CCM (Centre de

Caractérisation des Matériaux, Université de Sherbrooke) for facilitating the characterization of the materials: more specifically, Mrs. Irène Kelsey Lévesque and Mr. Carl St.-Louis for BET surface area analysis; Mr. Charles Bertrand for Microscopy (SEM & TEM) and Mr. Stéphane Gutierrez for XRD analysis.

7. REFERENCES

[1] H. Xiong, L.L. Jewell, N.J. Coville, ACS Catalysis 5 (2015) 2640-2658.

[2] Z.-r. Li, Y.-l. Fu, M. Jiang, T.-d. Hu, T. Liu, Y.-n. Xie, J. Catal. 199 (2001) 155-161.

[3] S. Iqbal, T.E. Davies, D.J. Morgan, K. Karim, J.S. Hayward, J.K. Bartley, S.H. Taylor, G.J. Hutchings, Catal. Today 275 (2016) 35-39.

[4] T. Fu, Z. Li, Chem. Eng. Sci. 135 (2015) 3-20.

[5] J.W. Dun, E. Gulari, K.Y.S. Ng, Applied Catal. 15 (1985) 247-263.

[6] W. Ma, E.L. Kugler, D.B. Dadyburjor, Energy & Fuels 21 (2007) 1832-1842.

[7] J. Chen, C. Xue, R. Ramasubramaniam, H. Liu, Carbon 44 (2006) 2142-2146.

[8] G.L. Bezemer, J.H. Bitter, H.P.C.E. Kuipers, H. Oosterbeek, J.E. Holewijn, X. Xu, F. Kapteijn, A.J. van Dillen, K.P. de Jong, J. Am. Chem. Soc. 128 (2006) 3956-3964.

[9] S. Jankhah, N. Abatzoglou, F. Gitzhofer, J. Blanchard, H. Oudghiri-Hassani, Chem. Eng. J. 139 (2008) 532-539.

[10] M.W. Dlamini, D.O. Kumi, T.N. Phaahlamohlaka, A.S. Lyadov, D.G. Billing, L.L. Jewell, N.J. Coville, ChemCatChem 7 (2015) 3000-3011.

[11] S.O. Moussa, L.S. Panchakarla, M.Q. Ho, M.S. El-Shall, ACS Catalysis 4 (2014) 535-545.

[12] Y. Cheng, J. Lin, K. Xu, H. Wang, X. Yao, Y. Pei, S. Yan, M. Qiao, B. Zong, ACS Catalysis 6 (2016) 389-399.

[13] H. Almkhelfe, J. Carpena-Núñez, T.C. Back, P.B. Amama, Nanoscale 8 (2016) 13476-13487.

[14] M.E. Dry, Catal. Today 71 (2002) 227-241.

[15] D. Pinna, E. Tronconi, L. Lietti, R. Zennaro, P. Forzatti, J. Catal. 214 (2003) 251-260.

[16] S.M. Davis, D.F. Ryan, Distillate fuel production from Fischer-Tropsch wax, in: US-Patent No. 5378348A, Exxon Research and Engineering Company, USA, 1995.

[17] M. Bekker, N.R. Louw, V.J.J. van Rensburg, J. Potgieter, Int. J. Cosmet. Sci. 35 (2013) 99-104.

[18] X. Dupain, R.A. Krul, C.J. Schaverien, M. Makkee, J.A. Moulijn, Appl. Catal., B. 63 (2006) 277-295.

[19] B.H. Davis, Ind. Eng. Chem. Res. 46 (2007) 8938-8945.

[20] J. Yang, W. Ma, D. Chen, A. Holmen, B.H. Davis, Appl. Catal. A. 470 (2014) 250-260.

[21] M. Shiva, H. Atashi, F.F. Tabrizi, A.A. Mirzaei, M. Arsalanfar, J. Ind. Eng. Chem. 19 (2013) 172-181.

[22] F. Morales, E.d. Smit, F.M.F. de Groot, T. Visser, B.M. Weckhuysen, J. Catal. 246 (2007) 91-99.

[23] A. Zare, A. Zare, M. Shiva, A.A. Mirzaei, J. Ind. Eng. Chem. 19 (2013) 1858-1868.

[24] A.N. Pour, S.M.K. Shahri, Y. Zamani, A. Zamanian, J. Nat. Gas Chem. 19 (2010) 193-197.

[25] Z. Tao, Y. Yang, C. Zhang, T. Li, J. Wang, H. Wan, H. Xiang, Y. Li, Catal. Comm. 7 (2006) 1061-1066.

[26] A.A. Mirzaei, R.M. Kiai, H. Atashi, M. Arsalanfar, S. Shahriari, J. Ind. Eng. Chem. 18 (2012) 1242-1251.

[27] M. Luo, B.H. Davis, Appl. Catal. A. 246 (2003) 171-181.

[28] N. Escalona, C. Medina, R. García, P. Reyes, Catal. Today 143 (2009) 76-79.

[29] Z. Tao, Y. Yang, C. Zhang, T. Li, M. Ding, H. Xiang, Y. Li, J. Nat. Gas Chem. 16 (2007) 278-285.

[30] W. Chu, P.A. Chernavskii, L. Gengembre, G.A. Pankina, P. Fongarland, A.Y. Khodakov, J. Catal. 252 (2007) 215-230.

[31] Y. Yang, H.-W. Xiang, Y.-Y. Xu, L. Bai, Y.-W. Li, Appl. Catal. A. 266 (2004) 181-194.

[32] S.-J. Jong, S. Cheng, Appl. Catal. A. 126 (1995) 51-66.

[33] A.N. Pour, M.R. Housaindokht, S.F. Tayyari, J. Zarkesh, M.R. Alaei, J. Nat. Gas Sci. Eng. 2 (2010) 61-68.

[34] C. Wang, L. Xu, Q. Wang, J. Nat. Gas Chem. 12 (2003) 10-16.

[35] S. Vahid, A.A. Mirzaei, J. Ind. Eng. Chem. 20 (2014) 2166-2173.

[36] M. Arsalanfar, A.A. Mirzaei, H.R. Bozorgzadeh, A. Samimi, R. Ghobadi, J. Ind. Eng. Chem. 20 (2014) 1313-1323.

[37] S. Qin, C. Zhang, J. Xu, B. Wu, H. Xiang, Y. Li, J. Mol. Catal. A: Chem. 304 (2009) 128-134.

[38] E. Rytter, T.H. Skagseth, S. Eri, A.O. Sjåstad, Ind. Eng. Chem. Res. 49 (2010) 4140-4148.

[39] T. Li, H. Wang, Y. Yanga, H. Xiang, Y. Li, Fuel Process. Technol. 118 (2014) 117-124.

[40] J.F. Bengoa, A.M. Alvarez, M.V. Cagnoli, N.G. Gallegos, S.G. Marchetti, Appl. Catal. A. 325 (2007) 68-75.

[41] J. Blanchard, N. Abatzoglou, R. Eslahpazir-Esfandabadi, F. Gitzhofer, Ind. Eng. Chem. Res. 49 (2010) 6948-6955.

[42] J. Aluha, P. Boahene, A. Dalai, Y. Hu, K. Bere, N. Braidy, N. Abatzoglou, Ind. Eng. Chem. Res. 54 (2015) 10661-10674.

[43] J. Aluha, N. Braidy, A. Dalai, N. Abatzoglou, Can. J. Chem. Eng. 94 (2016) 1504-1515.

[44] J. Aluha, N. Braidy, A. Dalai, N. Abatzoglou, Low-temperature Fischer-Tropsch synthesis with carbon-supported nanometric iron-cobalt catalysts, 23rd European Biomass Conference and Exhibition, Vienna, Austria, 1-4 June, 2015, pp. 988-994.

[45] A.E. Rutkovskii, L.R. Vishnyakov, A.A. Chekhovskii, N.I. Kirkun, Powder Metall. Met. C+ 39 (2000) 207-209.

[46] C.-J. Liu, G.P. Vissokov, B.W.L. Jang, Catal. Today 72 (2002) 173-184.

[47] B.C. Enger, A. Holmen, Cat. Rev. - Sci. Eng. 54 (2012) 437-488.

[48] S. Zamana, K.J. Smitha, Catal. Rev. - Sci. Eng. 54 (2012) 41-132.

[49] D.-V.N. Vo, A.A. Adesina, Appl. Catal. A. 399 (2011) 221-232.

[50] C.G. Cooper, T.-H. Nguyen, Y.-J. Lee, K.M. Hardiman, T. Safinski, F.P. Lucien, A.A. Adesina, Catal. Today 131 (2008) 255-261.

[51] J. Aluha, N. Abatzoglou, Biomass Bioenerg. 95 (2016) 330-339.

[52] J. Aluha, K. Bere, N. Abatzoglou, F. Gitzhofer, Plasma Chem. Plasma P. 36 (2016) 1325-1348.

[53] N. Sanpo, Springer Brief (2014) 31-32.

[54] G.P. van der Laan, A.A.C.M. Beenackers, Ind. Eng. Chem. Res. 38 (1999) 1277-1290.

[55] C.H. Bartholomew, R.J. Farrauto, Fundamentals of Industrial Catalytic Processes, John Wiley & Sons, Inc., Hoboken, New Jersey (USA), 2006.

[56] A.A. Khassin, T.M. Yurieva, V.N. Parmon, React. Kinet. Catal. Lett. 64 (1998) 55-62.

[57] M. Mansouri, H. Atashi, F.F. Tabrizi, A.A. Mirzaei, G. Mansouri, J. Ind. Eng. Chem. 19 (2013) 1177-1183.

[58] K. Oshikawa, M. Nagai, S. Omi, J. Phys. Chem. B. 105 (2001) 9124-9131.

[59] J. Baltrusaitisa, B. Mendoza-Sanchez, V. Fernandez, R. Veenstra, N. Dukstiene, A. Roberts, N. Fairley, Appl. Surf. Sci. 326 (2015) 151-161.

[60] J.P. den Breejen, P.B. Radstake, G.L. Bezemer, J.H. Bitter, V. Frøseth, A. Holmen, K.P. de Jong, J. Am. Chem. Soc. 131 (2009) 7197-7203.

[61] L. Wang, G.-H. Zhang, J.-S. Wang, K.-C. Chou, J. Phys. Chem. C. 120 (2016) 4097-4103.

[62] A.N. Pour, M.R. Housaindokht, E.G. Babakhani, M. Irani, S.M.K. Shahri, J. Ind. Eng. Chem. 17 (2011) 596-602.

[63] J.L.C. Fajín, M.N.D.S. Cordeiro, J.R.B. Gomes, Catalysts 5 (2015) 3-17.

[64] M.E. Dry, J. Mol. Catal. 17 (1982) 133-144.

[65] A. Tavakoli, M. Sohrabi, A. Kargari, Chem. Eng. J. 136 (2008) 358-363.

9.9. Appendix I: Article 7 – Promotion of Ni-Co-Fe catalyst using Au

Gold-promoted plasma-synthesized Ni-Co-Fe/C catalyst for Fischer-Tropsch synthesis

James Aluha and Nicolas Abatzoglou*

Department of Chemical & Biotechnological Engineering, Université de Sherbrooke, QC, Canada, J1K 2R1

*Corresponding author: nicolas.abatzoglou@usherbrooke.ca

Abstract

From this study, we present results of a nanometric, gold-promoted Fischer-Tropsch synthesis (FTS) catalyst, with carbon support. A ternary 5%Ni-70%Co-25%Fe/C formulation was synthesized using induction suspension plasma-spray (SPS) technology; the so-produced formulation was doped with 5%Au through the impregnation method. The catalysts (Au-Ni-Co-Fe/C and Ni-Co-Fe/C) were tested for 24 h in a continuously-stirred tank reactor (CSTR) operated at 260°C, 2 MPa pressure and H_2:CO molar ratio of 2 using feed gas composition set at 0.6 L/L (60-vol%) H_2 and 0.3 L/L (30-vol%) CO balanced in Ar flowing at gas hourly specific velocity (GHSV) of 3 600 $cm^3.h^{-1}.g^{-1}$ of catalyst. Catalyst performance was benchmarked against comparable plasma-synthesized bimetallic 80%Co-20%Fe/C and ternary 10%Ni-70%Co-20%Fe/C formulations. The bimetallic Co-Fe/C showed: (a) catalytic activity of ~40% CO conversion, and (b) selectivity of ~19% for gasoline fraction (C_5 – C_{12}) and 55% towards diesel (C_{13} – C_{20}). Addition of 10%Ni to the Co-Fe/C improved CO conversion from 40 to 50% with enhanced selectivity for gasoline from 19 to 50%, but the diesel fraction dropped from 55 to 22%. Incorporation of 5%Au in the 5%Ni-Co-Fe/C catalyst led to 60% CO conversion, yet when compared to the un-promoted 5%Ni-Co-Fe/C catalyst that showed 90% CO conversion with relatively high selectivity of 34% towards CO_2 and CH_4 combined, it cut H_2O production by almost half and improved selectivity for gasoline fraction from 38 to 41% and for diesel from 20 to 32%. All tested catalysts' α-values lay between 0.78 – 0.88 in the C_{10+} region.

Key words:

Fischer-Tropsch, plasma-synthesis, molybdenum, gold-nickel promotion, cobalt-iron catalysts

1. INTRODUCTION

Great interest in alternative energy sources has been stimulated as a result of the increasing obligation to lower the global impact of greenhouse gases. Some technical feasibility studies and analyses of biomass economics are showing promise for production of bio-derived fuels in the transport sector [1]. Renewable energy sources such as biomass can be incorporated in mature technologies such as Fischer-Tropsch synthesis (FTS) in order to make them 'greener' [2]. FTS for example, involves the commercial hydrogenation of CO to synthetic fuels composing gasoline and diesel with comparable quality as those derived from petroleum feedstocks. Since a biomass feedstock is most likely to be low in sulphur content [3], we foresee its application in FTS as a possible sustainable process towards biofuel production. Depending on the nature of the catalyst and FTS reaction conditions, CO can be polymerized to produce hydrocarbons of various chain lengths using supported Co- or Fe-based catalyst materials. Unfortunately, fast accumulation of the large polymeric molecules so formed has a tendency of clogging the catalyst pores, thereby leading to catalyst deactivation [4].

In view of the current challenges in Fischer-Tropsch catalysis research, we have argued that a catalyst, which is both nanometric and non-porous, would overcome limitations related to all mass transfer steps because the reaction occurs outside the catalyst particle [5]. In addition, the use of a carbon support could make the catalyst resistant to deactivation that originates from sintering. Besides, since there are no pores inside the catalytically active metallic phases, deactivation due to carbon deposition becomes highly depressed. Moreover, we have asserted that catalysts characterized by such attractive properties are best synthesized through induction suspension plasma-spray (SPS) technology because of its ability to simultaneously atomize, vaporize and produce numerous catalytic phases that are active for FTS [6]. In these catalysts, the nanometric carbon support is produced in plasma concomitantly with the metallic Co^0 species that is necessary for FTS in cobalt-based catalysts, or the carbide species (such as Fe_3C, Fe_5C_2, etc.) in iron-based FTS catalysts. This information is summarized in Table 1, having been adopted from our previously published findings [7]. Furthermore, we think that catalyst promotion with Au has potential to boost water-gas shift (WGS) reaction [8], and by enhancing the reducibility of the metallic Co^0 species, it could improve on FTS capabilities.

Table 1 Industrial concerns our catalysts have attempted to address [7]

	Approach	Influence on overall FTS process	Industrial concern	Ref.
1.	**Biomass Feedstock**	**Low-sulphur content:** Biomass feedstock contains less sulphur than fossil fuel feedstock.	Catalyst deactivation: - by sulphur poisoning	[3]
2.	**Nanometric catalysts**	**Turnover frequency (TOF)**: Application of high surface area per unit mass of the metal exposes more reactant per unit time	Reaction kinetics; Diffusion and mass transfer limitations	[9]
3.	**Non porous catalysts**	**Mass transfer effect**: Elimination of porosity increases contact between reactants and the active metal phase, and fast product desorption	Diffusion and mass transfer limitations	[10]
4.	**Carbon support**	**(a) Carburization: no impact** Carbon does not adversely affect catalyst performance	Catalyst deactivation: - by carburization	[11]
		(b) Deactivation: no impact: Carbon support does not impact the catalyst negatively	Catalyst deactivation: - by coking	[12] [13]
5.	**Plasma Technology**	**(a) Process efficiency:** Single-step application uses a simpler, yet highly effective method in catalyst synthesis	Application of complex methods during catalyst synthesis	[14]
		(b) Metal dispersion: Highly dispersed, uniformly distributed metal nano-particles embedded in a carbon matrix	Catalyst deactivation: - sintering	[15]
6.	**Au-promotion**	**(a) Water management**: Water removal through enhanced of water-gas shift reaction	High water vapour pressure lowers FTS activity	[16]
		(b) Maintaining the metallic phase: Enhancement of Co reduction.	Catalyst deactivation: - metal oxidation - reaction of metal phase with support.	[17] [18] [19]

Since CO adsorption on Fe is stronger than on Co, it creates high activation barriers for product desorption as noted by Bartholomew and Farrauto (p.408) [20]. This explains the higher tendency for the Fe to form carbides and oxides when compared to Co, which does not produce any bulk carbides. In the recent past, special attention has been given to Co-Fe alloys on a variety of supports [21], and while there is a wide window of choice in Fe-based catalysts for selectivity-linked promoters, that of Co-based catalysts is limited due to the unfavourable effect it imposes on catalytic activity [22]. For example, an attempt to raise the Fe's catalyst-surface basicity using La, Mg or Ca was perceived to worsen the FTS reaction rate due to increased activation energy from 70, to 78 and to 92 kJ.mol^{-1} respectively [23].

During FTS, CO_2 production must be suppressed as it acts as an inert component in the system [24]. On the other hand, CH_4 formation is equally undesirable because it consumes the valuable H_2 feedstock in the process [25], and therefore promoter choice and process conditions are key to lowering CH_4 production [26]. Since generation of H_2O as a by-product in FTS is inevitable, it may lead to catalyst deactivation [27]. Nonetheless, the Fe-based catalyst inherently participates in the WGS reaction, shown in Equation (1), through the *in situ* generated Fe-oxides, and the WGS reaction is perceived to boost FTS by enriching the H_2 gas stream [28].

$$H_2O + CO \xrightarrow{WGS} CO_2 + H_2 \quad Eqn.(1)$$

Although the Au-Co bimetallic is relatively poorer at the WGS reaction [29], it has been observed that when Au is associated with Ru or Ni, both of which are FTS-active metals, the Fe_2O_3-supported Au-Ru and Au-Ni bimetallic combinations become effective low-temperature water-gas shift (LT-WGS) catalysts [30]. Therefore, having an active Au-promoted bifunctional FTS-WGS catalyst containing Ni that encourages fast desorption of FTS products provides the benefit of producing a wide-range of both long and shorter chain hydrocarbons [31]. In this study, we investigated the effect of adding Au and Ni to the bimetallic Co-Fe/C catalyst because currently, there is very limited research directed towards Au-promoted, carbon-supported FTS catalysts that have been synthesized through plasma, as indicated in Table 2.

Table 2 Comparison of some unique properties of catalysts that have been tested in FTS

Targeted configuration	Catalyst		Synthesis method *	Ref.
	Active phase	Support		
Gold promotion	Au-Co	Al_2O_3	IM, IE	[32]
	Au-Co	Al_2O_3	CP, IM	[18]
	Au-Co	Al_2O_3	IM	[33]
	Au-Co	TiO_2	DP	[34]
	Au-Ru	MgO, SiO_2	IM	[35]
	Pt/Au-Co	TiO_2	IM	[36]
Carbon support	Co	CNTs[#]	IWI	[37]
	Co	CNTs	IWI	[38]
	Co	Carbon nanofibres	IWI, DP, IA	[39]
	Co, Ru, K	CNTs	IM	[40]
	Fe	Activated carbon	IM	[41]
	Fe	CNTs	IWI, DP	[42]
Plasma synthesis	Co	CNTs	DBD-plasma	[43]
	Pt-Co	Al_2O_3	GD-plasma	[44]
	Co, Ru-Co	SiO_2	GD-plasma	[45]
	Fe, K, Cu	Carbon	Induction SPS	[46]
	Co-Fe	Carbon	Induction SPS	[47]
	Fe-Ru oxide	Unsupported	LPP	[48]

[#] CNT = Carbon nanotubes;

* CP = Co-precipitation; DP = Deposition-precipitation; IE = Ion exchange; IA = Ion adsorption; IM = Impregnation method; IWI = Incipient wetness impregnation;

DBD = dielectric-barrier discharge plasma (*treatment*); GD = Glow discharge (*treatment*);

LLP = Liquid-phase plasma (*synthesis*); SPS = suspension-plasma spray (*synthesis*);

The overall objective of this work was to evaluate the properties of potential FTS catalysts among a family of plasma-synthesized materials, which demonstrate selective production of synthetic fuels that are primarily richer in the diesel range fraction (C_{13} – C_{20}). We therefore present the catalytic performance of the quaternary metallic formulation of the Au-promoted Ni-Co-Fe/C catalyst synthesized though plasma. The catalyst was benchmarked against the bimetallic Co-Fe/C catalyst [47], which we reported earlier. In this study, Ni or Au with Ni was introduced into the Co-Fe/C sample, and the two hypotheses tested were that:

(i) The presence of Ni in the catalyst could lead to selective enrichment of the gasoline fraction in FTS, because Ni promotes early molecular desorption [31];

(ii) Creating the Au-Ni-Fe nexus by incorporating Au in the catalyst sample produces synergistic effects that enhance LT-WGS reaction, which enriches the feed-gas composition with H_2 and improves FTS [29].

We therefore present for the first time the FTS test results on the effect of incorporating Au in carbon-supported Ni-Co-Fe catalyst synthesized by plasma, limiting the discussion to the key outcomes on catalyst activity and selectivity investigations, with the findings showing potential for future FTS application. Even so, we only provide a succinct, but sufficient treatment of catalyst synthesis and characterization to support results presented in this article, because they can be found in an earlier publication [6].

2. EXPERIMENTAL METHODS

2.1 Catalyst Synthesis

The single metal Co/C and Fe/C catalysts [5], in addition to the bimetallic Co-Fe/C catalysts [47], were prepared by the induction suspension plasma-spray (SPS) process. A mass of 60 g of the metals in various proportions were mixed in 300 cm^3 mineral oil and the suspension injected into the plasma at a flow rate of 8.2 $cm^3.min^{-1}$. Details of this technique have already been prescribed in earlier works and the overall catalyst composition (expressed at ~25-wt% metal loading) is based on “mass” of the metal relative to that of the carbon support in the catalyst formulations. The carbon-supported Ni-Co-Fe catalysts were synthesized similarly through the plasma process [6].

The Ni-Co-Fe catalyst was further doped with about 5%Au using impregnation method, in order to minimize the loss of the precious metal through the plasma system due to vaporization. A mass of 9.8 g from the 5%Ni-70%Co-25%Fe/C catalyst was mixed with 50 cm^3 of Au-solution prepared by adding 250 cm^3 of distilled H_2O to 1.0 g of chloro-auric acid trihydrate, $AuCl_4.3H_2O$. Since the catalyst is highly hydrophobic as a result of the residual mineral oil from the plasma reactor, 5 cm^3 of absolute ethanol was added to the mixture in order to dissolve the carbon-supported catalyst in the Au solution. The resulting slurry was left to oven-dry at 105^oC for 22 h, after which the dried crust was crushed and then tested for FTS activity after *in situ* reduction in H_2 gas.

2.2 Catalyst Testing

A fresh catalyst (5.0 g each) in the FTS reactor was first reduced *in situ* at 400^{o}C for 24 h using pure H_2 gas (N5.0) flowing at 250 $cm^3.min^{-1}$. After cooling the reactor and flushing it with inert gas, 150 cm^3 of hexadecane solvent (C_{16}) was introduced in to create a 3-phase continuously stirred-tank slurry reactor (3-φ-CSTSR). The pre-treated catalyst was then tested for FTS activity for 24 h on stream at 260°C and 2 MPa pressure using an artificial syngas mixture of composition H_2:CO ratio = 2, with flow rate fixed at 300 $cm^3.min^{-1}$ (at RTP), having 0.6 L/L (60-vol%) H_2 and 0.3 L/L (30-vol%) CO balanced in Ar, which translates into a gas hourly specific velocity (GHSV) of 3 600 $ml.g^{-1}.h^{-1}$ of catalyst. The FTS product spectrum was analysed by gas chromatography (GC) at standard conditions according to the protocol reported in earlier works for the single metal Co/C and Fe/C catalysts [49] and the Co-Fe/C bimetallic catalysts [47].

2.3 Catalyst Characterization

The catalysts were characterized by a number of analytical techniques that included porosity measurements through the Brunauer-Emmett-Teller (BET) method for specific surface area determination, morphological and particle size analysis using both Scanning and Transmission Electron Microscopy (SEM and TEM) coupled with Energy Dispersive X-ray Spectroscopy (EDX), in addition to phase identification and composition analysis by XRD analysis, and X-ray photoelectron spectroscopy (XPS). The characterization test conditions and analysis results are available in earlier articles for BET surface area, SEM, TEM and XRD [6], and XPS [5]. In this paper, only the results that support the current discussion are presented.

3. RESULTS AND DISCUSSION

3.1 Catalyst Synthesis

Although Au-addition to the catalyst was achieved by impregnation, the ternary Ni-Co-Fe/C catalyst was synthesized through plasma, which has been found to create nanometric materials with remarkably uniform characteristics. In principle, SPS technology should be used in the synthesis of all catalysts, but since Au is a precious metal we intended to

minimize losses during synthesis due to vaporization. Nevertheless, this was treated as an initial catalyst selection process and it was observed that even after introduction of Ni in the Co-Fe bimetallics, the catalysts' physical properties remained remarkably identical [6]. The high reproducibility of the catalysts indicates that synthesis through plasma presents notable prospects for industrial-scale catalyst production.

3.2 Catalyst Testing

3.2.1 Catalyst activity

The ternary Ni-Co-Fe/C formulation was tested alongside the Au-promoted Ni-Co-Fe/C catalysts at 260^{o}C and 2 MPa pressure, benchmarking their catalytic performance with a sample Co-Fe/C bimetallic catalyst. Figure 1 presents catalyst activity plots after 12 h on stream. In comparison to the Co-Fe/C bimetallic with over 40% CO conversion, the Ni-containing catalysts were more active; hence the one with 10%Ni exhibited a higher CO conversion of ~50%, while halving the amount of Ni and replacing it with Au-promotion (i.e. the 5%Au-5%Ni-Co-Fe/C) increased the activity further to ~60% CO conversion. Nevertheless, the un-promoted 5%Ni-Co-Fe/C formulation was relatively the most active with ~90% CO conversion, although with very poor selectivity towards FTS products.

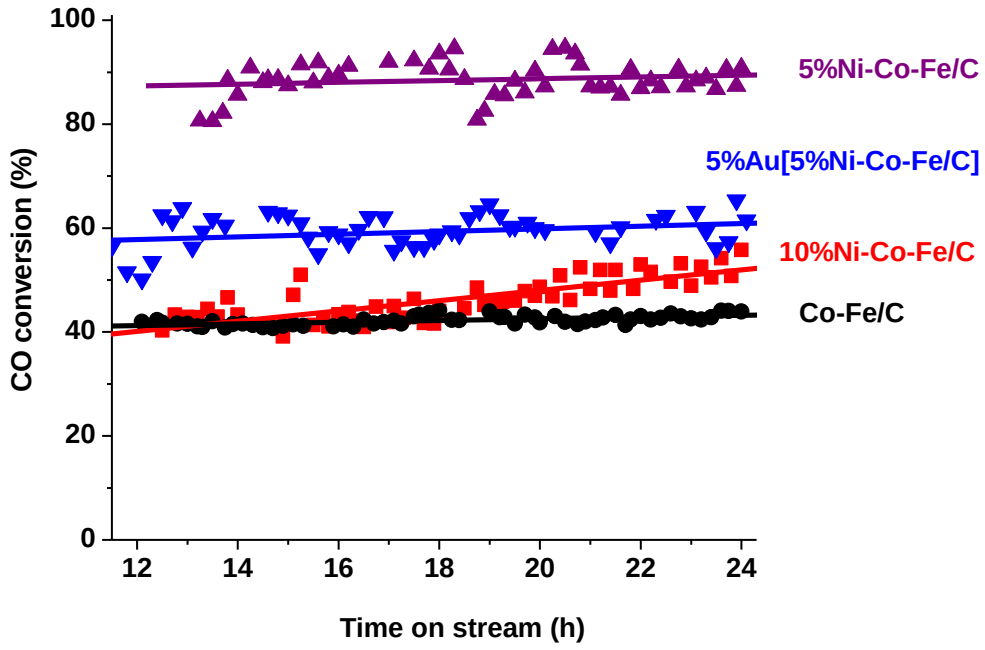

Fig. 1 Catalyst activity plots for the (a) Co-Fe/C; (b) 10%Ni-Co-Fe/C; (c) 5%Ni-Co-Fe/C; and (d) Au-5%Ni-Co-Fe/C formulations

3.2.2 Catalyst selectivity

Figure 2 provides summary plots of the corresponding catalyst selectivity for the materials presented in Figure 1. On the x-axis, zero represents CO_2 and one represents CH_4, while the ascending integer numbers indicate the number of C atoms in the hydrocarbon molecules. For ease of mass balance evaluation, data analysis and presentation, Figure 3 indicates the aggregate fractions in terms of gasoline (C_5 – C_{12}), diesel (C_{13} – C_{20}), and waxes (C_{21+}). The product spectrum shows that the bimetallic Co-Fe/C was comparatively more selective towards production of the longer-chain hydrocarbon components such as diesel (55%) and waxes (13%). Basing on the Co-Fe/C bimetallic catalyst, addition of Ni or Au-Ni was noted to enhance selectivity towards the gasoline fraction from 19%, to 38 and 41% respectively. Promotion of the Ni-Co-Fe/C catalyst with Au substantially lowered CO_2 and CH_4 production and improved selectivity for the diesel fraction from 20% to 32%. Moreover, there was a sizable decline in H_2O production for the Au-promoted sample.

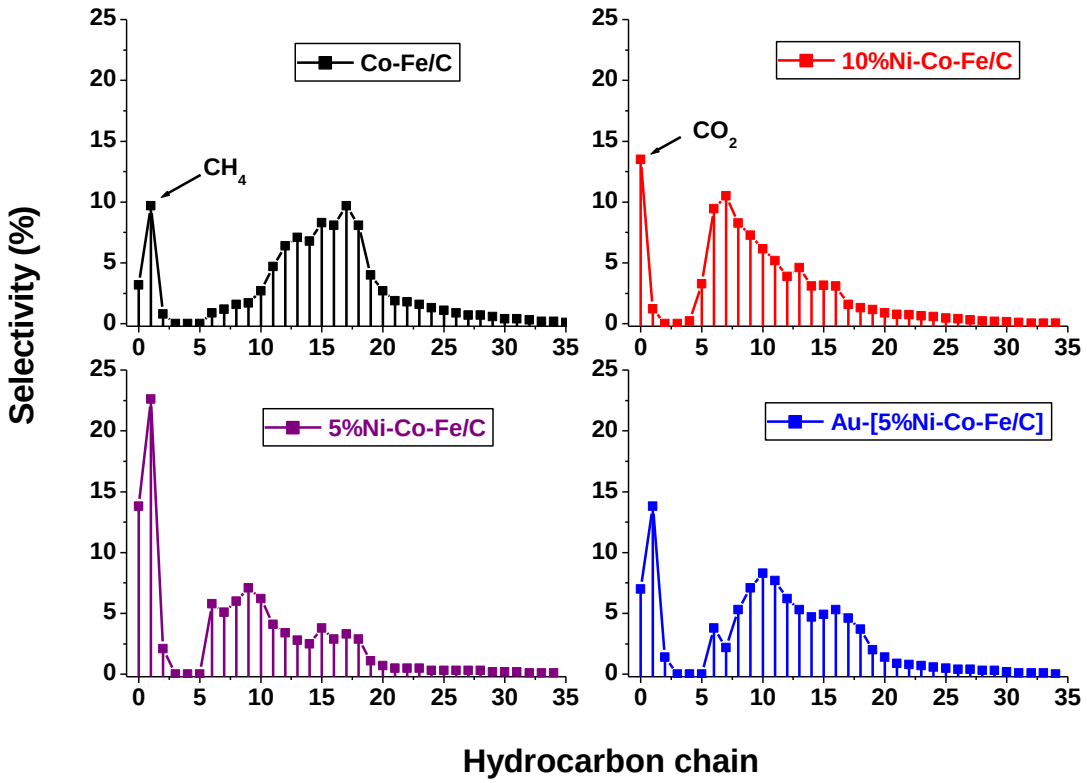

Fig. 2 Catalyst selectivity as portrayed by the FTS product distribution plots for (a) Co-Fe/C; (b) 10%Ni-Co-Fe/C; (c) 5%Ni-Co-Fe/C; and (d) 5%Au[5%Ni-Co-Fe/C]

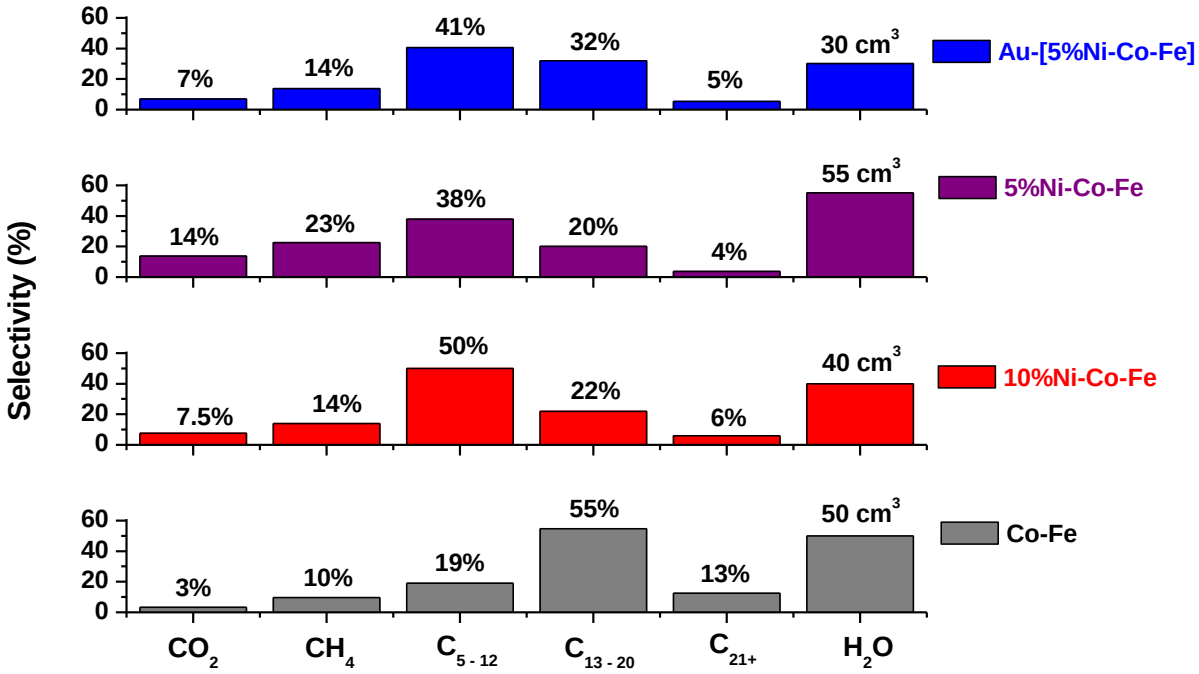

Fig. 3 Plots comparing aggregated FTS fraction distribution of (a) Co-Fe/C; (b) 10%Ni-Co-Fe/C; (c) 5%Ni-Co-Fe/C; and (d) 5%Au[5%Ni-Co-Fe/C] catalysts after 24 h of reaction

3.2.3 Determination of the catalysts' α-values

Since Co has a typical range of α-values between 0.70 – 0.80, and Fe between 0.50 – 0.70 [50], for our catalysts α ≥ 0.78 at high C-numbers (C_{10+}) because of the high Co content (>70%). Figure 4 provides plots that were used to define the catalysts' α-values. It was observed that comparatively, the Co-Fe/C bimetallic formulation had the highest α-value of 0.88, although with poor linear regression analysis of R^2 = 0.633. Addition of 10%Ni to the Co-Fe/C catalyst produced the lowest α-value of 0.78, and addition of 5%Ni or 5%Au gave ~0.84, but with better curve fitting of R^2 > 0.94. This means that higher production of the light-weight hydrocarbons would be expected from the Ni- and Au-containing catalysts relative to the bimetallic Co-Fe/C catalyst. This may be deciphered from Table 3, which shows that under similar reaction conditions (260^{o}C, 2 MPa, GHSV = 3 600 $cm^3.h^{-1}.g^{-1}$ of catalyst), the least attractive catalyst was the 5%Ni-Co-Fe/C formulation because of its combined selectivity towards the fuels (gasoline and diesel = 58%) being very low. Although the 5%Ni-Co-Fe/C exhibited the highest CO conversion (90%), its overall selectivity was poor due to high production of CH_4 (23%) and CO_2 (14%), besides generating the greatest amount of H_2O (55 cm^3).

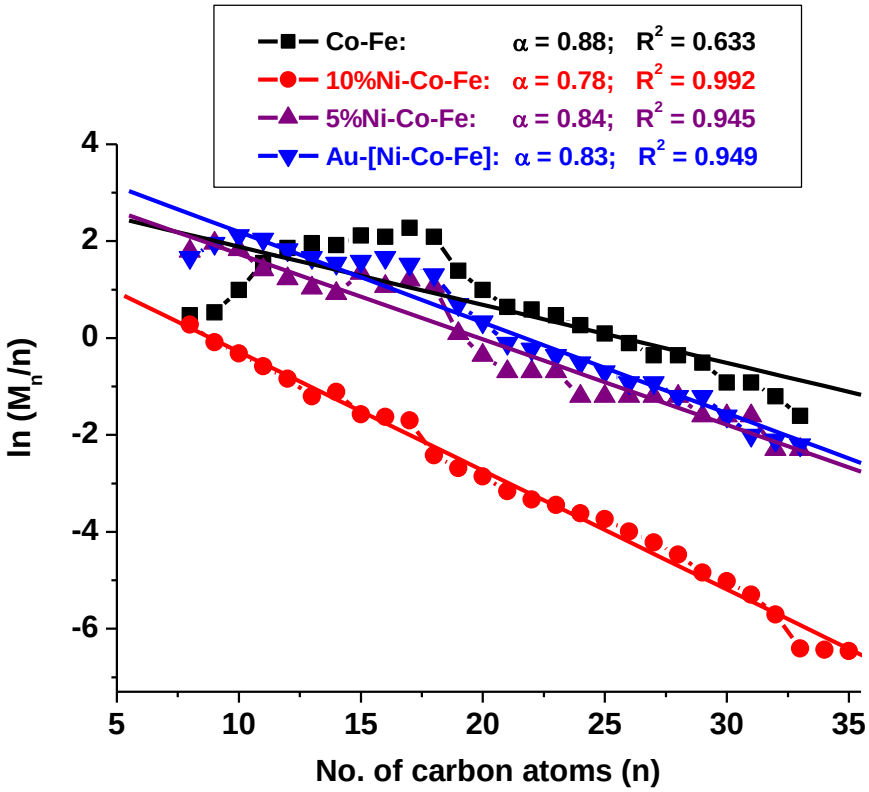

Fig. 4 Graph summarizing determination of catalysts' α-values using log(M_n/n) versus n plots

Table 3 Summary catalyst properties for (a) Co-Fe/C; (b) Ni-Co-Fe/C; (c) Ni-Co-Fe/C; and (d) Au-Ni-Co-Fe/C after 24 h of FTS reaction at 260°C

Catalyst	Activity (%)	Selectivity (%)			H_2 efficiency, E (%)		
	CO conversion	(D+G)*	(D/G) ratio	α-value	H_2O (cm^3)	CH_4	C_{5+}
Co-Fe	42	74	2.89	0.88	50	8	46
10%Ni-Co-Fe	50	72	0.44	0.78	40	9	35
5%Au[5%Ni-Co-Fe]	60	73	0.78	0.83	30	7	26
5%Ni-Co-Fe	90	58	0.53	0.84	55	23	41

* *(D = Diesel; G = Gasoline)*

Conversely, the most attractive catalyst would have been the Co-Fe/C, because (i) its product spectrum was richer in diesel, having the highest diesel to gasoline ratio (~2.9); (ii) it had the highest α-value of 0.88; and (iii) it exhibited lowest selectivity towards CH_4 (10%) and CO_2 (3%). However, it displayed the minimum CO conversion (at 42%) and produced much H_2O (50 cm^3). Therefore, between the Au-Ni-Co-Fe/C and 10%Ni-Co-Fe/C formulation, we found the Au-promoted catalyst as more appealing because it had a higher

catalytic activity of 60% CO conversion compared to 50% in the 10%Ni-Co-Fe/C, it produced the least amount of H_2O (30 cm^3 compared to 40 cm^3), it had a higher α-value (0.83 compared to 0.78), and it produced relatively more diesel with a high diesel to gasoline ratio (~0.78 compared to 0.44). However, both the catalysts exhibited comparable selectivity towards CH_4 (~14%), CO_2 (~7%) and wax (~5%).

3.2.4 Catalysts' H_2 efficiency

By using the total quantity of H_2O generated in the reaction over the 24-h period, a rough estimate of the catalysts' H_2 efficiency could be determined since H_2O is measurable. However, WGS activity presents a technical difficulty in the calculation because it consumes some of the H_2O generated thereby enriching the H_2 stream [51]. Assuming that the principal product of the FTS reaction was the alkene, (C_nH_{2n}) there is a 1:2 mole ratio between the H_2O generated and the H_2 consumed for every $–CH_2–$ formed in the hydrocarbon according to Equation (2). If we neglect the WGS effect, then the maximum amount of H_2O to be generated within the 24 h of FTS reaction would be about 5.04 moles (or 90.72 cm^3) because the total amount of H_2 gas delivered during the 24-h experiment was equivalent to 10.8 moles = (300 $cm^3.min^{-1}$) x (60% H_2) x (60 min.) x (24 h)/(24,000 cm^3 at RTP).

$$CO + 2H_2 \xrightarrow{FTS} -[CH_2]- + H_2O \quad Eqn.(2)$$

$$CO + 3H_2 \rightarrow CH_4 + H_2O \quad Eqn.(3)$$

Secondly, the total amount of H_2O formed was divided in equal ratio in terms of its origin, either from $–CH_2–$ or CH_4 formation according to Equation (3). A summary of the calculated values are presented in the last column of Table 3. From this determination, it was observed that the Co-Fe/C catalyst was the most efficient in CO hydrogenation by converting ~46% of the H_2 supplied to C_{5+} products, while the Au-Ni-Co-Fe/C formulation was the least efficient with only 26% conversion towards C_{5+} products. It was equally evident that Ni-containing samples were the most inefficient by converting considerable quantities of H_2 to CH_4; the 5%Ni-Co-Fe/C displayed a 23% efficiency and the 10%Ni-Co-

Fe/C had a 9% efficiency. The Au-promoted Ni catalyst was the least efficient in converting H_2 to CH_4 (showing a 7% efficiency).

Since the Au-promoted catalyst converted the least amount of H_2 from the feed stream to both $–CH_2–$ and CH_4, this can be perceived as a positive attribute because the rest of the H_2 is in excess and can lead to significant reduction in the H_2 flow rates, and subsequently the recycle streams of the whole process. On the other hand, the Co-Fe/C catalyst can be viewed as one requiring large quantities of H_2. Therefore, the perceived lower H_2 efficiency in the Au-promoted catalyst could present the beneficial scenario of using CO-rich feedstocks possibly of a bio-syngas origin. This is because WGS reaction seems to be enriching the H_2 feed stream in the Au-promoted catalyst, which is evident from the lower H_2O production accompanied by substantial CO_2 formation, unlike with the Co-Fe/C catalyst.

In conclusion, we found that overall, the Au-Ni-Co-Fe/C formulation was comparatively a more balanced catalyst in the light of great activity, good selectivity for both gasoline and diesel fuels, high α-value, limited H_2O and CH_4 production. It was also characterized by elevated WGS activity that enriches the H_2 stream in FTS as evidenced from the CO_2 formed. This may pave way for the use of CO-rich feedstocks such as bio-syngas towards the application of renewable energy resources in producing biofuels.

3.3 Catalyst Characterization

3.3.1 Porosity measurement by N_2 physisorption

From the SPS reactor set-up discussed in an earlier article [6], indicating that generally, the BET specific surface areas of the plasma-synthesized bimetallic and ternary metallic samples were in close range between 65–90 $m^2.g^{-1}$. In this article, we are discussing the bimetallic Co-Fe/C, and the ternary 10%Ni-Co-Fe/C and 5%Ni-Co-Fe/C catalysts. For example, the BET specific surface areas of the samples that were collected from the main plasma reactor were 73, 76 and 89 $m^2.g^{-1}$ respectively. Due to the pyrophoric nature of the samples, the Au-promoted 5%Ni-Co-Fe/C catalyst was not analysed for surface area because it was assumed that it had similar physical characteristics as the 5%Ni-Co-Fe/C catalyst. Pre-treatment was performed *in situ* to activate the material before FTS catalysis.

3.3.2 SEM analysis

Since SEM analysis data for the Ni-Co-Fe/C was discussed exhaustively in the previous article [6], Figure 5 provides a glimpse of the even dispersion and uniform distribution of the various metal nanoparticles in the samples. This was evident from the backscattered SEM imaging and EDX mapping, which indicated the capability of the SPS technology in reproducing high quality FTS catalysts.

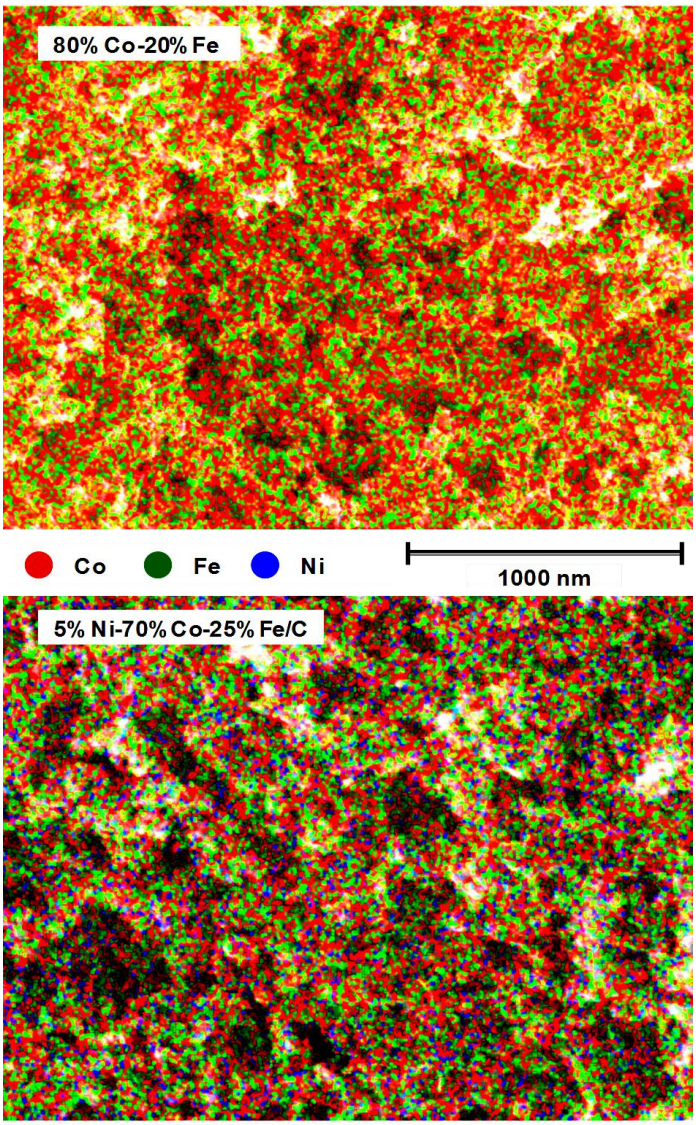

Figure 5: EDX mapping by SEM imaging indicating the presence of Co, Fe and Ni in the plasma-synthesized catalysts

3.3.3 TEM analysis

Imaging by TEM analysis revealed metal nanoparticle moieties supported in a carbon matrix. Earlier studies indicated that the mean metal-nanoparticle size was around 9–11 nm in the freshly plasma-synthesized catalysts [49], except for the 50%Co-50%Fe/C bimetallic, which had a mean of 14.4 nm [47]. A similar observation is reflected in this study, where Figure 6 provides the micrographs of the fresh and used 5%Ni-Co-Fe/C catalysts as well as the Au-promoted 5%Ni-Co-Fe/C sample. Figure 7 portrays the particle size distribution plots of the same catalysts where a sample size of 500 metal nanoparticles was analyzed.

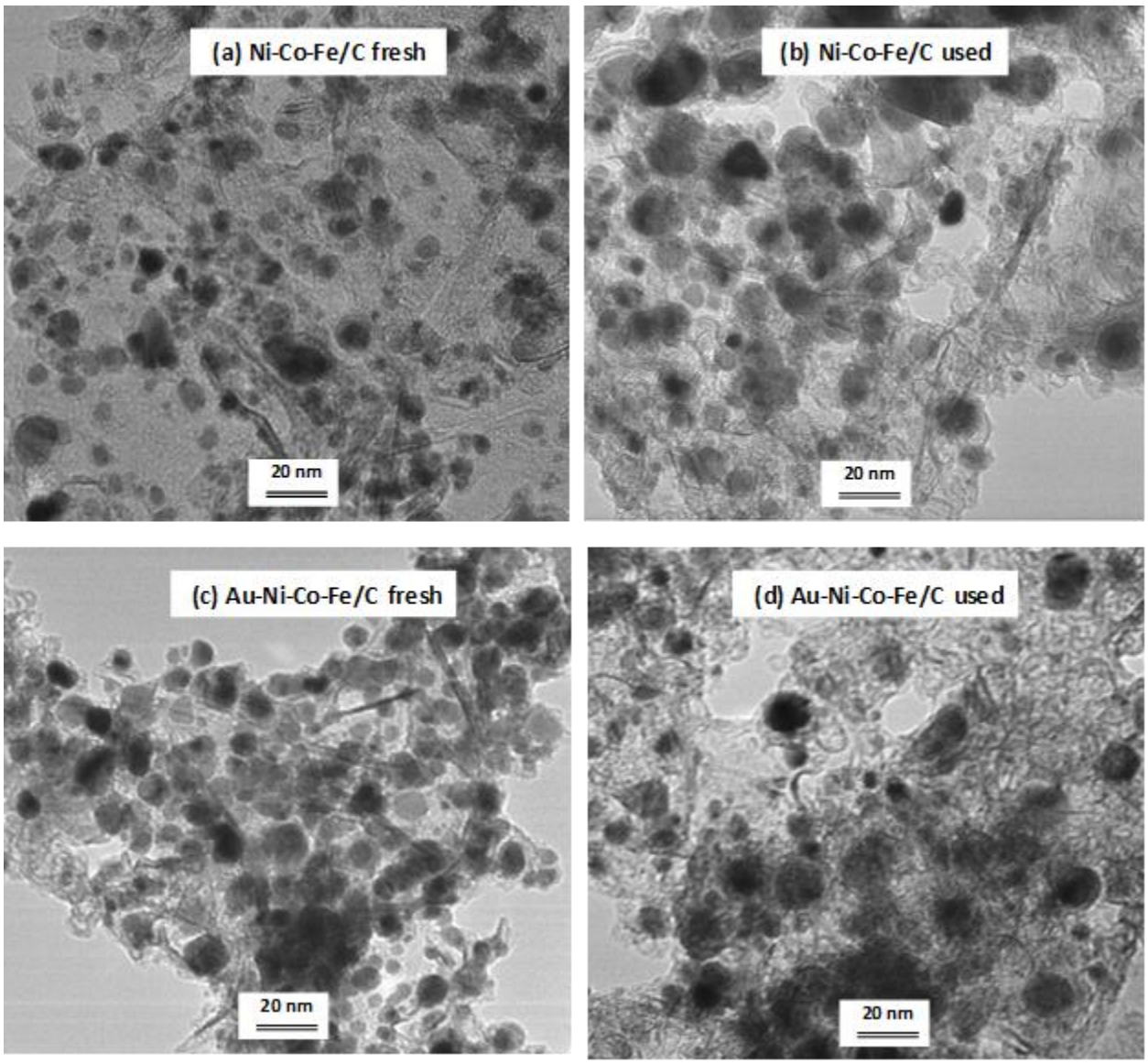

Fig. 6 Sample TEM images of the (a) fresh 5%Ni-Co-Fe/C; (b) used 5%Ni-Co-Fe/C; (c) fresh Au-Ni-Co-Fe/C; and (d) used Au-Ni-Co-Fe/C showing early sintering after FTS reaction

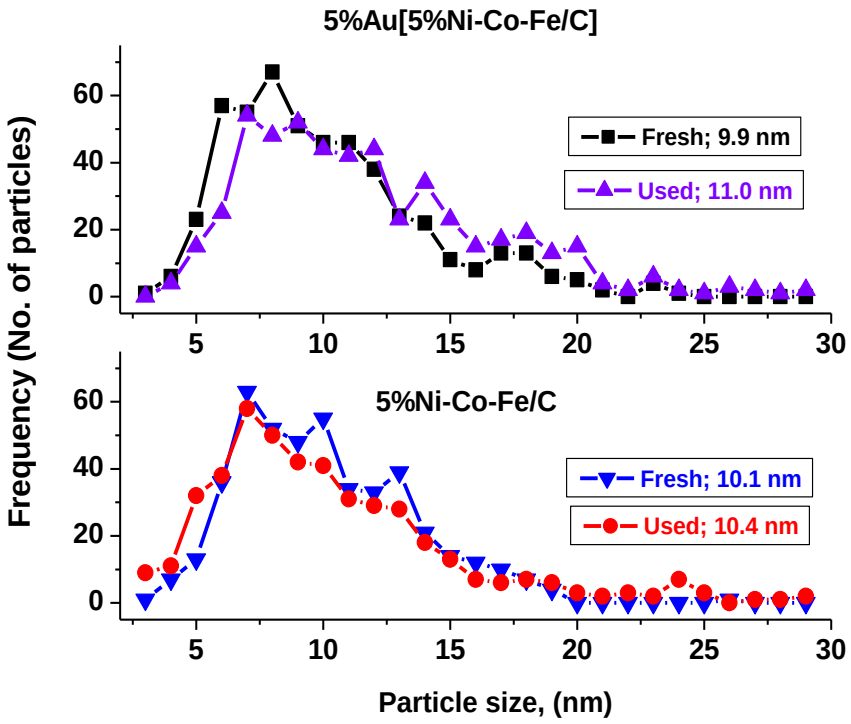

Fig. 7 Metal nanoparticle-size distribution (n = 500) for the fresh and used catalysts by TEM analysis, indicating (a) 5%Ni-Co-Fe/C catalyst, (b) after promotion with Au

The fresh and used 5%Ni-Co-Fe/C catalysts showed mean particle size of 10.1 and 10.4 nm respectively, while the Au-promoted 5%Ni-Co-Fe/C catalyst had an average metal particle size of 9.9 and 11.0 nm respectively. Except for the used Au-Ni-Co-Fe/C catalyst that has some large nanoparticles above 13 nm, there was no other conceivable particle agglomeration observed in the used samples, even after high-temperature exposure during pre-treatment at 400^{o}C for 24 h, followed by the FTS reaction at 260^{o}C for another 24 h.

3.3.4 XRD analysis

The nanometric nature of the metallic component in the catalysts was confirmed through XRD studies coupled with Rietveld quantitative analysis (RQA) as exemplified by peak broadening and peak extinction in the materials' XRD patterns provided in Figure 8. Although this finding has been discussed exhaustively elsewhere [6], it is important to highlight it here; that all the Co-rich catalyst samples took the XRD pattern of the face-centred cubic structure of Co^{0} because it was the dominant metal in the samples [5]. For example, in Figure 8, all the catalysts (100%Co/C, 80%Co-20%Fe/C, 10%Ni-70%Co-20%Fe/C, and the 5%Ni-70%Co-25%Fe/C formulations) had identical XRD patterns. Proof

of the presence of other metals had to be sought through various means alongside XRD, including XANES for Fe, and analysis particularly for Ni by XPS, and SEM imaging through EDX mapping.

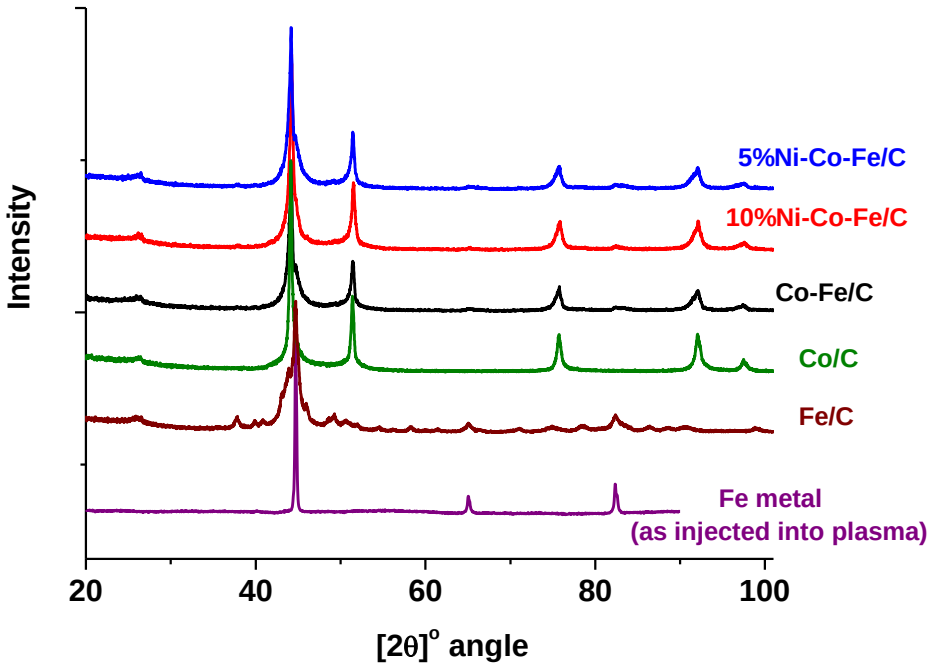

Fig. 8 Powder XRD patterns of the freshly plasma-synthesized catalyst for (a) Co/C, (b) Fe/C, (c) Co-Fe/C, (d) 5%Ni-Co-Fe/C and, (e) 10%Ni-Co-Fe/C compared with the Fe metal

3.3.5 XPS analysis

Due to the difficulty experienced in detecting Ni in the samples through XRD analysis, XPS succeeded in establishing the presence of metallic Ni in the catalysts as demonstrated by the peak with binding energy of around 852.8 eV as given in Figure 9.

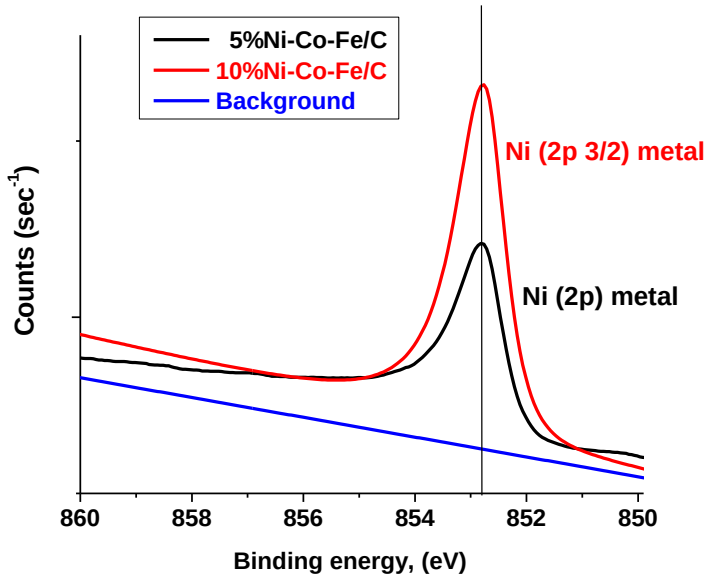

Fig. 9 XPS analysis establishing the presence of Ni in freshly synthesized (a) 5%Ni-Co-Fe/C and (b) 10%Ni-Co-Fe/C catalysts collected from the auxiliary plasma reactor

4. DISCUSSION

4.1 Catalyst Synthesis and Characterization

All the plasma-synthesized catalyst samples exhibited uniform metal distribution as observed from SEM analysis, while particle size measurement by TEM imaging indicated an average of 9–11 nm, which is a distinctive property that underpins the capacity SPS technology presents for reproducibility, with great potential for future scale up. Although stronger CO adsorption has been observed in the smaller Co particles (< 7 nm), which leads to low TOF in FTS reaction [52], our samples aimed at producing metal nanoparticles above 8 nm, which was successful. In addition, the smaller Co particles exhibit higher selectivity for CH_4 formation mainly due to their heightened capacity for hydrogen adsorption and coverage, a property that our samples have overcome. Since the particle-size distribution of our samples by and large remained unaffected after FTS reaction, it was an early indication of their intrinsic resistance to sintering, catalyst deactivation and ultimate long-term durability.

4.2 Promotion of Co-Fe/C catalyst with Ni

It was advanced that the presence of Ni in the Co-Fe/C bimetallic catalysts could boost production of the shorter hydrocarbon chains. This means that our first hypothesis was correct: that Ni enhances mechanisms that lead to early chain-growth termination, fast hydrocarbon desorption and low molecular-readsorption rates. For this reason, the quantity of Ni in the catalyst was lowered from 10 to 5% and the Ni-Co-Fe/C catalyst became even more active showing up to 90% CO conversion, although with higher selectivity towards production of the low-molecular weight hydrocarbons such as gasoline (38%) than the diesel fraction (20%), while the initial Co-Fe/C bimetallic catalyst was more selective towards diesel (55%) than gasoline (19%).

It was observed that at 260^{o}C, addition of 10%Ni in the Co-Fe/C catalyst exhibited higher catalyst activity (from 42 to 50% CO conversion), although with greater propensity to produce CH_4 (23%) and CO_2 (14%), both of which are undesirable products. The high activity witnessed in the 5%Ni catalyst (with up to 90% CO conversion) was probably due to the production of hydrogen radicals, which are extremely reactive because Ni has been found to catalyze a wide variety of reactions due to its marked ability to activate the H_2 molecule by dissociative chemisorption [53]. We can therefore speculate that perhaps the presence of Ni in our materials could benefit the FTS reaction at much lower temperature operations. Higher temperature operations in this study were used because the bimetallic catalysts were almost inert at the lower temperatures of ~220^{o}C [47], and carrying out a comparative study within that temperature regime would not have been fruitful.

4.3 Presence of Au and Ni for Water-Gas Shift

4.3.1 Testing hypotheses with Au-catalyzed WGS reaction

In the second hypothesis, it was advanced that the simultaneous presence of Au and Ni in the Co-Fe/C bimetallic would improve FTS activity through the synergistic effect of Au-Ni-Fe performing WGS reaction. In our samples, the presence of Au was perceived to elevate both the catalyst activity and selectivity. By replacing half of the Ni with Au in the 10%Ni-Co-Fe/C sample, the activity rose from 50 to 60% CO conversion, while the selectivity towards FTS products improved with C_{5+} rising from 62 to 78% in the 5%Au-5%Ni-Co-Fe/C catalyst sample. Analysis of the total amount of H_2O produced within the 24 h of each

experiment showed the highest H_2 efficiency depicted by the 5%Ni-Co-Fe/C sample at 41% leading to FTS products (C_{5+}) and 23% to CH_4, which made the catalyst unattractive. The sample also displayed the greatest CO and H_2 conversions of 89 and 78% respectively, with the mass balance indicating an excess of H_2 that was in agreement with gas analysis of the effluent reactor stream as shown in Table 4.

Table 4 Mass balance in evaluating the catalysts' H_2 efficiency, at t = 24 h

Property		**Catalyst**		
		80%Co-20%Fe/C	5%Ni-Co-Fe/C	5%Au-Ni-Co-Fe/C
Conversion, X (%)	X_{CO}	42	89	59
	X_{H2}	38	78	51
Excess H_2, F_{exit} (%)*		52	20	49
Mass balance: (X_{H2} + F_{exit}) (%)		90	98	100
H_2 efficiency, E (%)#	$E_{(CH4)}$	8	23	7
	$E_{(C5+)}$	46	41	26
Ratio (X_{CO} : X_{H2})		1.11	1.14	1.16
Difference, (X_{CO} – X_{H2}) (%)		4	12	13
Evolution of CO_2 (%)**		3	14	7

* Concentration of H_2 in the exit flow (F_{exit} rate ≤ 250 $cm^3.min^{-1}$) as determined by GC analysis

\# H_2 efficiency as calculated from the measured H_2O quantities as apparent H_2 conversion

** CO_2 concentration measurement as determined by GC analysis

High selectivity towards CH_4 in the Ni-based sample proved the Au-promoted catalyst to be the best alternative having respective CO and H_2 conversions of 59 and 51%, relative to the Co-Fe/C bimetallic that showed 42 and 38% CO and H_2 conversions respectively. Nevertheless, the Au catalyst had the least H_2 efficiency towards the FTS products (26%) and CH_4 (7%), yet when the ratio of the used CO to that of H_2 was determined for the three catalysts (80%Co-20%Fe/C, 5%Ni-Co-Fe/C, and 5%Au-Ni-Co-Fe/C), it gave a constant number of ~ 1.1. This means that no matter how much H_2 was added to the feed stream the reaction will proceed in a constant CO:H_2 gas ratio of ~1.1, indicating that these catalysts could operate optimally in a CO-rich feed gas. Therefore, the excess H_2 gas in the feed must be lowered to typify a bio-syngas feedstock and in so doing, the Au-promoted sample would be the best catalyst that can produce biofuels while generating the least amounts of CH_4 and H_2O.

Some authors have showed that 1.5-wt%Au loading increases CO conversion to produce higher selectivity towards C_{5+} hydrocarbons alongside decreased CH_4 formation [18]. Indeed, in our samples CH_4 production was lowered from 23 to 14% by Au-addition in the 5%Ni-Co-Fe/C catalyst, while at the same time CO_2 production was halved from 14 to 7%. Since it was observed that the presence of Au in the 5%Ni-Co-Fe/C catalyst improved its selectivity by suppressing H_2O formation from 55 to 30 cm^3 (in 24 h), we are convinced that the WGS process internally generates H_2 that improves FTS product development and lowers H_2O production. Other authors have observed that the Au in Au-Co/Al_2O_3 acts as an effective WGS catalyst during the early stages of the reaction only, but loses this characteristic as the FTS reaction progresses due to metallic-phase redistribution [33]. Although the Au-Co bimetallic has been shown to be poor at WGS reaction, the performance of Au-Ni or Au-Fe bimetallics seem to be relatively better [29].

Considering the bimetallic Co-Fe/C catalyst that generated only 3% CO_2, there was an increase in the CO_2 production with the addition of 10%Ni (7.5%) or after partial replacement of the 10%Ni with 5%Au, in Au-Ni-Co-Fe/C catalyst, which generated 7% CO_2. Since WGS reaction enhances CO_2 production, it was observed that H_2O consumption according to Equation (1) was accompanied by an increase in the quantity of CO_2 formed. However, an exact match in the amounts of CO_2 generated was only reflected in the bimetallic Co-Fe/C catalyst (~4%) and the Ni-Co-Fe/C catalyst (~12%) represented by the difference between the two conversions ($X_{CO} – X_{H2}$), see Table 4. Instead, Au-addition to the 5%Ni-Co-Fe/C catalyst remarkably lowered both CO_2 and H_2O production by almost half (from 14 to 7% for CO_2 and 55 to 30 cm^3 in H_2O), while at the same time improving the FTS product stream.

4.3.2 Mechanism of Au promoted Ni-Co-Fe catalyst in WGS reaction

Although Ni is a proven hydrogenation catalyst, its potential for H_2 production in WGS reaction is already reported; however, high efficiency (94% CO conversion) was demonstrated only at elevated temperatures, typically above 450^oC [51]. On the other hand, Au has been shown to be an active LT-WGS catalyst, since Au-promoted Co catalysts exhibit higher TOF, which is attributed to H_2-spillover effect. This is a phenomenon

that usually involves the diffusion of atomic hydrogen from a noble metal to another surface such as the catalyst's support. The noble metal, for example, facilitates the Co reduction, which in turn enables the production of dissociated hydrogen atoms to diffuse over to the moieties of the Co-oxide support [54].

One major benefit observed in the spillover effect is that it facilitates the removal of non-reactive species that block the metal's active sites because the catalyst promoter encourages the desorption of such species, thus increasing the H_2:CO ratio on the catalyst surface. The consequence of a high H_2:CO ratio on the catalyst surface is to enhance FTS reaction rates [32]. During the dissociative adsorption of H_2O on Au/Fe_2O_3 the H_2O adsorbs strategically at the interface between Au nanoparticles and the oxide support, followed by a spillover of active OH^- groups onto adjacent sites of the ferric oxide. Although this results in the cyclic re-oxidation of Fe^{2+} to Fe^{3+}, this mechanism has been found to be unfavourable thermodynamically [55].

Therefore, two other complimentary mechanisms have been advanced; the first relates to a regenerative-redox mechanism where the CO reacts with a reducible oxide support, partially reducing the support to form CO_2, which is then followed by the associate mechanism where H_2O oxidizes the partially reduced support to release H_2 [56]. Since a substantial amount of Fe_3O_4 had already been identified in the active Fe/C catalyst during FTS in our early works [57], its presence as the reducible support alongside Ni and Au was expected to enhance WGS reaction in the FTS system. Already, the Au-Ni-Fe_2O_4 has been shown to be an effective hydrogenation catalyst in the removal of H_2 from CO_2 gas streams at 350 – 470 K [53].

4.3.3 Benefits of Au-promoted FTS catalysts

Tests, where Au/$Ni(OH)_2$ was the active WGS catalyst, yielded excessive CH_4 after total reduction to elemental Ni [55]. Although many authors concur that Au-promoted catalysts have high CH_4 selectivity, low olefin and poor C_{5+} selectivity that result in low α-values when compared to the un-promoted samples [54], our results were much superior to these outcomes. The tested un-promoted Co/C catalyst had shown poor FTS selectivity at 20% CO_2, 46% CH_4, 7% gasoline, and 19% diesel, but the Au-promoted catalyst, operating at

similar reaction conditions (260^{o}C, 2 MPa), exhibited higher chain-growth probability with α-value > 0.80. The Au-Ni-Fe-Co/C displayed comparatively lower CH_4 and high C_{5+} selectivity as follows: 7% CO_2, 14% CH_4, 41% gasoline, 32% diesel and 5% waxes.

Incidentally, the amount of H_2O produced by the Co/C single-metal and Co-Fe/C bimetallic catalysts was ~40 and 50 cm^3 respectively, while the Au-promoted sample produced only 30 cm^3, which was equivalent to that produced by the single-metal Fe/C [47]. Since we know that the Fe catalyst is good at LT-WGS reaction, it is reasonable to impute the Au-Ni-Fe as an active component in the WGS reaction. However, as CO_2 is a by-product of WGS, the lower amount of CO_2 produced in the process by the Au-promoted sample (7%) when compared to Fe/C (10%) strengthens this thesis. Nevertheless, since an equal amount of CO_2 was expected in case of Au-enhanced WGS, there was a 3% drop, probably because the presence of Au introduced a different reaction mechanism which, at least partially, bypassed the WGS reaction.

Moreover, Au-addition was perceived to be advantageous since the Au-Ni-Co-Fe/C catalyst produced more gasoline (41%) than all the other catalysts tested, including the un-promoted 5%Ni-Co-Fe/C (38%). The Au-Ni-Co-Fe/C catalyst gave 33% selectivity towards diesel fraction, while the 5%Ni-Co-Fe/C made only 20%. The performance of the Au-Ni-Co-Fe/C catalyst is, thus, considered, superior because it generated less CO_2 (7%) and CH_4 (14%) relative to that of 5%Ni-Co-Fe/C, which had produced 14% of CO_2 and 23% of CH_4 under similar reaction conditions.

5. CONCLUSION

A nanometric plasma-synthesized 5%Ni-Co-Fe/C catalyst, supported on carbon with BET specific surface area of ~90 $m^2.g^{-1}$ was promoted by Au-addition to produce a highly active FTS catalyst. Microscopic imaging analysis (by TEM and SEM coupled with EDX and X-ray mapping) revealed uniform metal distribution in the carbon matrix with average nanoparticle size in the range of 10 – 11 nm. The nanoparticles remained generally unaffected after a 24-h thermal treatment by H_2-reduction at 400^{o}C, followed by another 24-h FTS reaction at 260^{o}C. Various phases were evident from XRD analysis ranging from metal carbides to

metallic and nano-alloy forms, but they were not fully quantifiable by RQA due to peak broadening and peak extinctions arising from the nanometric nature of the materials.

Both the un-promoted Ni-Co-Fe/C and the Au-promoted Ni-Co-Fe/C catalysts were tested under identical FTS reaction conditions (260^{o}C; 2 MPa pressure; H_2:CO ratio = 2; GHSV = 3 600 $cm^3.h^{-1}.g^{-1}$ of catalyst) and benchmarked against the Co-Fe/C bimetallic. It was observed that addition of Ni alone to the Co-Fe/C bimetallic was not beneficial as it enhanced the production of shorter-chain hydrocarbons with excessive formation of CO_2 (14%), CH_4 (23%), and H_2O (55 cm^3). These values were almost halved (CO_2 = 7%; CH_4 = 14%; and H_2O = 30 cm^3) by the introduction of Au in the catalyst. The Au-Ni-Co-Fe/C catalyst produced more gasoline than all the other catalysts, with selectivity of ~41%, perhaps aided by the presence Ni. The α-values of the catalysts were calculated to be between 0.78 – 0.88 as determined from the higher molecular-weight hydrocarbons (C_{10+}).

6. ACKNOWLEDGEMENTS

We appreciate the financial support we obtained from the Canadian BiofuelNet National Centre of Excellence (NCE); Dr. Kossi Béré for technical expertise in the Plasma Synthesis lab; the staff at CCM (Centre de Caractérisation des Matériaux, Université de Sherbrooke) for facilitating the characterization of the materials: Mrs. Irène Kelsey Lévesque and Mr. Carl St.-Louis for BET surface area analysis, Mr. Charles Bertrand for Microscopy (SEM & TEM), Mrs. Sonia Blais for XPS, and Mr. Stéphane Gutierrez for XRD analysis.

7. REFERENCES

1. Tijmensen MJA, Faaij APC, Hamelinck CN, van Hardeveld MRM (2002) Exploration of the possibilities for production of Fischer-Tropsch liquids and power via biomass gasification. Biomass Bioenerg 23:129-152

2. Maitlis P, de Klerk A (2013) Fischer–Tropsch Catalyst Life Cycle. In: Pretorius J, de Klerk PA (eds) Greener Fischer-Tropsch Processes for Fuels and Feedstocks pp 267-279

3. Chew TL, Bhatia S (2008) Catalytic processes towards the production of biofuels in a palm oil and oil palm biomass-based biorefinery. Bioresour Technol 99:7911-7922

4. Khodakov AY, Chu W, Fongarland P (2007) Advances in the Development of Novel Cobalt Fischer-Tropsch Catalysts for Synthesis of Long-Chain Hydrocarbons and Clean Fuels. Chem Rev 107:1692-1744

5. Aluha J, Boahene P, Dalai A, Hu Y, Bere K, Braidy N, Abatzoglou N (2015) Synthesis and characterisation of nanometric Co/C and Fe/C catalysts for Fischer-Tropsch synthesis: A comparative study using a fixed-bed reactor. Ind Eng Chem Res 54 (43):10661-10674

6. Aluha J, Bere K, Abatzoglou N, Gitzhofer F (2016) Synthesis of nano-catalysts by induction Suspension Plasma Technology (SPS) for Fischer-Tropsch reaction. Plasma Chem Plasma P 36 (5):1325-1348.

7. Aluha J, Braidy N, Dalai A, Abatzoglou N Low-temperature Fischer-Tropsch synthesis with carbon-supported nanometric iron-cobalt catalysts. In: 23rd European Biomass Conference and Exhibition, Vienna, Austria, 1-4 June, 2015. pp 988-994

8. Andreeva D (2002) Low temperature water gas shift over gold catalysts. Gold Bull 35/3:82-88

9. Zohdi-Fasaei H, Atashi H, Tabrizi FF, Mirzaei AA (2016) Effects of mass transfer on Fischer-Tropsch kinetics over mesoporous silica-supported Co-Mn-Ce nano catalysts in a fixed-bed reactor. J Nat Gas Sci Eng 32:262-272

10. Vahid S, Mirzaei AA (2014) An investigation of the kinetics and mechanism of Fischer–Tropsch synthesis on Fe–Co–Ni supported catalyst. J Ind Eng Chem 20:2166-2173

11. Ding M, Yang Y, Wu B, Xu J, Zhang C, Xiang H, Li Y (2009) Study of phase transformation and catalytic performance on precipitated iron-based catalyst for Fischer–Tropsch synthesis. J Mol Catal A: Chem 303:65-71

12. Dry ME (1990) Fischer-Tropsch synthesis over iron catalysts. Catal Lett 7:241-252

13. Pour AN, Shahri SMK, Zamani Y, Irani M, Tehrani S (2008) Deactivation studies of bifunctional Fe-HZSM5 catalyst in Fischer-Tropsch process. J Nat Gas Chem 17:242-248

14. Zhang Y, Bao J, Nagamori S, Tsubaki N (2009) A new and direct preparation method of iron-based bimodal catalyst and its application in Fischer–Tropsch synthesis. Appl Catal A 352:277-281

15. Dry ME (2002) The Fischer–Tropsch process: 1950–2000. Catal Today 71 227-241

16. Rohde MP, Schaub G, Khajavi S, Jansen JC, Kapteijn F (2008) Fischer–Tropsch synthesis with in situ H_2O removal – Directions of membrane development. Micropor Mesopor Mater 115:123-136

17. Rytter E, Skagseth TH, Eri S, Sjåstad AO (2010) Cobalt Fischer-Tropsch catalysts using nickel promoter as a rhenium substitute to suppress deactivation. Ind Eng Chem Res 49:4140-4148

18. Ahmad N, Hussain ST, Muhammad B, Anderson JA, Ali N, Abbas SM Influence of Gold Promoter on Fischer Tropsch Synthesis Over Co/Al_2O_3 Catalysts. In: 10th International Bhurban Conference on Applied Sciences & Technology (IBCAST), Islamabad, Pakistan, 15^{th}-19^{th} Jan. 2013. pp 11-15

19. Jacobs G, Ma W, Gao P, Todic B, Bhatelia T, Bukur DB, Davis BH (2013) The application of synchrotron methods in characterizing iron and cobalt Fischer-Tropsch synthesis catalysts. Catal Today 214:100-139

20. Bartholomew CH, Farrauto RJ (2006) Fundamentals of Industrial Catalytic Processes. John Wiley & Sons, Inc., Hoboken, New Jersey (USA)

21. Calderone VR, Shiju NR, Ferré DC, Rothenberg G (2011) Bimetallic catalysts for the Fischer–Tropsch reaction. Green Chem 13:1950-1959

22. Davis BH (2007) Fischer-Tropsch synthesis: comparison of performances of iron and cobalt catalysts. Ind Eng Chem Res 46 (26):8938-8945

23. Pour AN, Housaindokht MR, Tayyari SF, Zarkesh J, Alaei MR (2010) Kinetic studies of the Fischer-Tropsch synthesis over La, Mg and Ca promoted nano–structured iron catalyst. J Nat Gas Sci Eng 2: 61-68

24. Riedel T, Schaub G (2003) Low-temperature Fischer–Tropsch synthesis on cobalt catalysts - effects of CO_2. Top Catal 26 (1-4):145-156

25. Schulz H (1999) Short history and present trends of Fischer–Tropsch synthesis. Appl Catal A 186 3-12

26. Yang J, Ma W, Chen D, Holmen A, Davis BH (2014) Fischer–Tropsch synthesis: A review of the effect of CO conversion on methane selectivity. Appl Catal A 470:250–260

27. Li J, Zhan X, Zhang Y, Jacobs G, Das T, Davis BH (2002) Fischer–Tropsch synthesis: effect of water on the deactivation of Pt promoted Co/Al_2O_3 catalysts. Appl Catal A 228:203-212

28. Spath PL, Dayton DC (2003) Preliminary Screening - Technical and Economic Assessment of Synthesis Gas to Fuels and Chemicals with Emphasis on the Potential for Biomass-Derived Syngas: A Technical Report. NREL/TP-510-34929. National Renewable Energy Laboratory, U.S.A.

29. Venugopal A, Aluha J, Scurrell MS (2003) The water-gas shift reaction over Au-based, bimetallic catalysts. The Au-M (M=Ag, Bi, Co, Cu, Mn, Ni, Pb, Ru, Sn, Tl) on Iron (III) oxide system. Catal Lett 90 (1-2):1-6

30. Venugopal A, Aluha J, Mogano D, Scurrell MS (2003) The gold–ruthenium–iron oxide catalytic system for the low temperature water–gas-shift reaction: The examination of gold–ruthenium interactions. Appl Catal A 245:149-158

31. Enger BC, Holmen A (2012) Nickel and Fischer-Tropsch Synthesis. Cat Rev - Sci Eng 54 (4):437-488.

32. Nabaho D, Niemantsverdriet JWH, Claeys M, van Steen E (2016) Hydrogen spillover in the Fischer–Tropsch synthesis: An analysis of gold as a promoter for cobalt–alumina catalysts. Catal Today 275:27-34

33. McCue AJ, Aponaviciute J, Wells RPK, Anderson JA (2013) Gold modified cobalt-based Fischer-Tropsch catalysts for conversion of synthesis gas to liquid fuels. Front Chem Sci Eng 7 (3):262–269.

34. Jalama K, Coville NJ, Hildebrandt D, Glasser D, Jewell LL, Anderson JA, Taylor S, Enache D, Hutchings GJ (2007) Effect of the addition of Au on Co/TiO_2 catalyst for the Fischer-Tropsch reaction. Top Catal 44 (1):129-136

35. Datye AK, Schwank J (1985) Fischer-Tropsch synthesis on bimetallic ruthenium-gold catalysts. J Catal 93:256-269

36. Kunene A, Claeys M, van Steen E (2014) Pt/Au alloys as reduction promoters for Co/TiO_2 Fischer-Tropsch catalysts. Adv Mater Res 1019:365-371

37. Abbaslou RMM, Tavassoli A, Soltan J, Dalai AK (2009) Iron catalysts supported on carbon nanotubes for Fischer–Tropsch synthesis: Effect of catalytic site position. Appl Catal A 367:47-52

38. Trépanier M, Tavasoli A, Dalai AK, Abatzoglou N (2009) Fischer–Tropsch synthesis over carbon nanotubes supported cobalt catalysts in a fixed bed reactor: Influence of acid treatment. Fuel Process Technol 90:367-374

39. Bezemer GL, Bitter JH, Kuipers HPCE, Oosterbeek H, Holewijn JE, Xu X, Kapteijn F, van Dillen AJ, de Jong KP (2006) Cobalt particle size effects in the Fischer-Tropsch reaction studied with carbon nanofiber supported catalysts. J Am Chem Soc 128 (12):3956-3964

40. Trépanier M, Tavasoli A, Dalai AK, Abatzoglou N (2009) Co, Ru and K loadings effects on the activity and selectivity of carbon nanotubes supported cobalt catalyst in Fischer–Tropsch synthesis. Appl Catal A 353:193-202

41. Sun B, Xu K, Nguyen L, Qiao M, Tao FF (2012) Preparation and catalysis of carbon-supported Iron catalysts for Fischer–Tropsch synthesis. ChemCatChem 4:1498-1511

42. van Steen E, Prinsloo FF (2002) Comparison of preparation methods for carbon nanotubes supported iron Fischer–Tropsch catalysts. Catal Today 71:327-334

43. Fu T, Huang C, Lv J, Li Z (2014) Fuel production through Fischer–Tropsch synthesis on carbon nanotubes supported Co catalyst prepared by plasma. Fuel 121:225-231

44. Chu W, Wang L-N, Chernavskii PA, Khodakov AY (2008) Glow-discharge plasma-assisted design of cobalt catalysts for Fischer–Tropsch synthesis. Angew Chem Int Ed 47:5052-5055

45. Hong J, Chu W, Chernavskii PA, Khodakov AY (2010) Cobalt species and cobalt-support interaction in glow discharge plasma-assisted Fischer–Tropsch catalysts. J Catal 273:9-17

46. Blanchard J, Abatzoglou N (2014) Nano-iron carbide synthesized by plasma as catalyst for Fischer–Tropsch synthesis in slurry reactors: The role of iron loading and K, Cu promoters. Catal Today 237:150-156

47. Aluha J, Abatzoglou N (2016) Synthetic fuels from 3-φ Fischer-Tropsch synthesis using syngas feed and novel nanometric catalysts synthesised by plasma. Biomass Bioenerg 95 (1):330-339.

48. Lee S-J, Lee H, Jeon K-J, Park H, Park Y-K, Jung S-C (2016) Characterization of bimetallic Fe-Ru oxide nanoparticles prepared by liquid-phase plasma method. Nanoscale Res Lett 11:344:1-8

49. Aluha J, Braidy N, Dalai A, Abatzoglou N (2016) Low-temperature Fischer-Tropsch synthesis using plasma-synthesised nanometric Co/C and Fe/C catalysts. Can J Chem Eng 94 (8):1504–1515.

50. Dry ME (1982) Catalytic aspects of industrial Fischer-Tropsch synthesis. J Mol Catal 17:133-144

51. Haryanto A, Fernando SD, To SDF, Steele PH, Pordesimo L, Adhikari S (2009) Hydrogen production through the water-gas shift reaction: Thermodynamic equilibrium versus experimental results over supported Ni catalysts. Energy Fuels 23:3097-3102

52. den Breejen JP, Radstake PB, Bezemer GL, Bitter JH, Frøseth V, Holmen A, de Jong KP (2009) On the origin of the cobalt particle size effects in Fischer-Tropsch catalysis. J Am Chem Soc 131:7197-7203

53. Bond GC, Thompson DT (1999) Catalysis by Gold. Cat Rev - Sci Eng 41 (3-4):319-388.

54. de Beer M, Kunene A, Nabaho D, Claeys M, van Steen E (2014) Technical and economic aspects of promotion of cobalt-based Fischer-Tropsch catalysts by noble metals – A review. J South Afr Inst Min Metall 114:157-165

55. Andreeva D (2002) Low temperature water gas shift over gold catalysts. Gold Bull 35 (3):82-88

56. Tao FF, Ma Z (2013) Water–gas shift on gold catalysts: catalyst systems and fundamental studies. Phys Chem Chem Phys 15:15260-15270

57. Braidy N, Andrei C, Blanchard J, Abatzoglou N (2011) From nanoparticles to process: an aberration-corrected TEM study of Fischer-Tropsch catalysts at various steps of the process. Adv Mater Res 324:197-200